BOTTOM-UP NANO-ENGINEERING OF SOME FUNCTIONAL SEMICONDUCTING MATERIALS FOR THERMOELECTRICS AND SPINTRONICS APPLICATIONS

THESIS SUBMITTED TO **AcSIR** FOR THE AWARD OF

THE DEGREE OF

DOCTOR OF PHILOSOPHY

IN ENGINEERING SCIENCES

By

AKSHAY V. R.

Registration No: 20EE14A39012

Under the guidance of

Dr. M. VASUNDHARA

MATERIALS SCIENCE AND TECHNOLOGY DIVISION

NATIONAL INSTITUTE FOR INTERDISCIPLINARY

SCIENCE AND TECHNOLOGY (CSIR-NIIST)

THIRUVANANTHAPURAM- 695 019

KERALA, INDIA

JUNE 2019

Dedicated to……
My family

<u>DECLARATION</u>

I hereby declare that the matter embodied in the Ph.D. thesis entitled "**Bottom-up Nano-Engineering of some functional semiconducting materials for thermoelectrics and spintronics applications**" is the result of the investigations carried out by me at the Functional Materials Section, Materials Science and Technology Division, CSIR-National Institute for Interdisciplinary Science and Technology, Thiruvananthapuram, under the supervision of Dr. M. Vasundhara and the same has not been submitted elsewhere for any other degree, diploma or title.

In keeping with the general practice of reporting scientific observations, due acknowledgement has been made wherever the work described is based on the findings of other investigators.
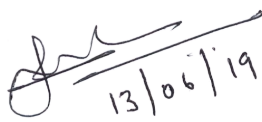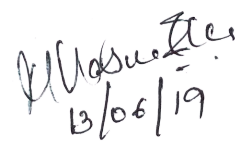
13/06/19

Akshay V. R.

Thiruvananthapuram

CERTIFICATE

This is to certify that the work incorporated in this Ph.D. thesis entitled "**Bottom-up Nano-Engineering of some functional semiconducting materials for thermoelectrics and spintronics applications**" submitted by **Mr. Akshay V. R.** to the Academy of Scientific and Innovative Research (AcSIR) in partial fulfillment of the requirements for the award of the **Degree of Doctor of Philosophy in Engineering Sciences** embodies original research work carried out by him under my supervision. I further certify that this work has not been submitted to any other University or Institution in part or full for the award of any degree or diploma. Research material obtained from other sources such as text, illustration, table etc., used in the thesis have been duly cited and acknowledged.

13/06/19

Akshay V. R.

(Research Scholar)

13/06/19

Dr. M.Vasundhara

(Research supervisor)

<u>CONTENTS</u>

List of Figures

List of Tables

Abbreviations

TE	Thermoelectric
DMS	Dilute magnetic semiconductor
ZT	Figure of merit
FM	Ferromagnetic/ferromagnetism
RTFM	Room temperature ferromagnetism
TM	transition metal
S	Seebeck coefficient
σ	electrical conductivity
κ	thermal conductivity
PGEC	phonon-glass electron-crystal
PF	power factor ($S^2\sigma$)
κ_L	lattice thermal conductivity
κ_e	electronic thermal conductivity
n	carrier concentration
η	efficieny
T_H	Temperature at hot side
T_C	Temperature at cold side
T_m	Mean temperature of both T_H and T_C
T	absolute temperature
k_B	Boltzmann constant
h	Planck's constant
*m**	effective mass of the carrier
ρ	electric resistivity
e	electrical charge of an electron
μ	carrier mobility
L	Lorenz factor
QLs	quintuple layers
SS	solvothermal
SPS	spark plasma sintering
MSS	microwave solvothermal
1D	one dimensional
2D	two dimensional
CP	cold pressing
SG	solution grow
HP	hot pressing
LIE	lithium ionic exfoliation
BMA	ball milling alloy
MA	melting alloy
BS	Bridgman–Stockbarger
BM	ball milling
THM	travelling heater method
MS	melt spinning
Te-MS	Te rich melt spinning
ZM	zone melting
HF	Hot forging
T_C	Curie temperature
M_s	saturation magnetization
PM	Paramagnetism/paramagnetic

AFM	Antiferromagnetism/antiferromagnetic
PLD	pulsed laser deposition
H	magnetic field
χ	susceptibility
M	magnetization
M_r	remanent magnetization
H_C	coercivity
SE	Superexchange
DE	Double exchange
O	oxygen
RKKY	Ruderman-Kittel-Kasuya-Yosida
k_F	radius of the Fermi surface
r	distance
BMP	bound magnetic polaron
BT	Bismuth telluride
$NaBH_4$	Sodium borohydride
EDTA	ethylenediaminetetraacetic acid
h	hour
XRD	X-ray diffraction
HR-TEM	High Resolution-Transmission Electron Microscopy
EDS	energy dispersive X-ray spectroscopy
XPS	X-ray photoelectron spectroscopy
SEM	Scanning Electron Microscopy
AFM	atomic force microscopy
HPHTS	high-pressure and high temperature sintering
ETO	electrical transport option
PPMS	Physical Property Measurement System
ρ_{xy}	Hall resistivity
χ^2	goodness of fit
R_{wp}	R factor
R_{exp}	expected R factor
SAED	selected area diffraction patterns
FFT	Fast Fourier Transform
R_H	Hall coefficient
HP	hot pressed
E_F	Fermi level
ED-XRFS	energy dispersive X-ray Fluorescence Spectrometry
ICP-MS	Inductive Coupled Plasma – Mass Spectroscopy
FT-IR	Fourier Transform-Infrared
VSM	vibrating sample magnetometer
FWHM	full width at half maximum
E_g	optical band gap
α	absorption coefficient
PL	Photoluminescence
STE	self-trapped excitons
OH	hydroxyl
N	BMP concentration
$m_{s} = m_{eff}$	Spontaneous magnetic moment
χ_m	magnetic susceptibility
f_N	atomic form factor

F	Structure factor
E	photon energy
E_u	Urbach energy
SSP	size strain plot
CB	conduction band
VB	valence band
ZFC	Zero Field Cooled
FC	Field Cooled
SPM	superparamagnetic
V_o	oxygen vacancy defects

Abstract

Thermoelectrics and spintronics enable the optimization of transport properties and spin characteristics of functional semiconductors that provides opportunity to address upcoming challenges in terms of environmental problems, energy crisis and energy storage. This key issue forces us to think about materials for devices that can tackle energy issues with high efficiency. One of the possible ways to achieve this goal is to develop technologies based on any of the renewable energy sources. Thermoelectric (TE) devices based on Bi_2Te_3 based materials hence attract the attention of scientific community which consists of both p-type and n-type materials that can enable a direct and reversible conversion of thermal energy to electrical energy. Energy conversion efficiency of a TE material is directly related with the dimensionless figure of merit, $ZT = S^2\sigma T/\kappa$, where S, σ, κ, and T are the Seebeck coefficient, electrical conductivity, thermal conductivity, and the absolute temperature, respectively. Another way to achieve the above mentioned problem is to develop functional devices by utilizing the spin of an electron and in this regard, oxide based dilute magnetic semiconductor (DMS) materials holds good for spintronic and magneto-optic devices. DMSs are the materials in which a small fraction of cations in the host lattice is replaced by magnetic impurities. Room-temperature ferromagnetism (RTFM) is required for spintronic devices for their practical utilization, and also the ferromagnetism should be intrinsic. However, in spite of a good amount of work on oxide based DMSs is done, the origin of RTFM in TiO_2 is still under debate. Even RTFM has been found in undoped and nonmagnetic elements doped TiO_2 and other oxides which help to understand the role of defects in creating ferromagnetic ordering. However, due to the unambiguous nature of defects, controversies regarding the existence of RTFM remain a challenge for the researchers. Nevertheless, there are several issues ultimately restricting the applications of both Bi_2Te_3-based TE materials and TiO_2 based DMS materials.

Issues with Bi_2Te_3-based TE materials:

- ❖ The conventional synthesis methods are mainly based on organic solvents and product yield by different chemical methods are really too low.

- ❖ The κ values of most of the TE materials are very much high which is limited by the alloy limit of κ.

- ❖ For Bi_2Te_3 based TE materials, while focusing on nanostructuring, phonon scattering and charge carrier scattering becomes so crucial resulting in a rapid decrease in carrier mobility.

❖ Further possibilities on structural and morphological control to minimize κ, to enhance the ZT value at room temperature and reaction mechanisms extending to other chalcogenide systems such as Sb_2Te_3, SnTe and Sb-doped Bi_2Te_3 is to be explored more.

Issues with TiO_2-based DMS materials:

❖ The possibility of RTFM in nanostructured TiO_2 in comparison to the bulk counterpart requires further deep analysis based on defect centres.

❖ There are controversial reports regarding the existence of RTFM in TiO_2, i.e., reports suggesting the origin of RTFM due to intrinsic defects like oxygen vacancy or Ti interstitials and reports on the nature of extrinsic factors arising from magnetic clusters due to transition metal doping, requires further clarity.

❖ Very few studies have explored the possibilities of both significant narrowing of band gap and observation of RTFM in undoped as well as doped TiO_2 nanostructures.

❖ It is well known that despite doping agents both optical and magnetic properties depend on fabrication and annealing conditions. Still, the possibilities of annealing atmospheres on undoped TiO_2 nanostructures are to be explored further.

In order to address the above issues, I have carried out my research in PhD program in the following steps.

Bi_2Te_3 nanostructures:

✓ A simple, cost-effective, surfactant assisted, and aqueous-based low-temperature reflux method has been employed for the synthesis of Bi_2Te_3 nanocrystals and TE properties of Bi_2Te_3 nanostructures are reported by varying the morphology and crystal structure using different reaction times and surfactant concentrations.

✓ The nanocrystals inherited from the optimized reaction conditions and high densification of nanoparticle interfaces contribute to the considerable reduction of κ in Bi_2Te_3 nanostructures, especially, uniformly distributed nanocrystals of Bi_2Te_3 formed for 24 h reaction time and 75 mmol surfactant concentration demonstrate a promising ZT of 0.67 at 300 K, which can be attributed to their κ while the high σ is maintained.

✓ Tuning the surfactant concentration from 50 to 100 mmol facilitates the formation of low-dimensional structures and Bi_2Te_3 nanostructures inherited from 24 h reaction time with 100 mmol surfactant concentration exhibit a highest value of ZT of 0.75 at 300 K among the studied samples

✓ An in-depth understanding of the reaction mechanism to form Bi_2Te_3, Sb_2Te_3, SnTe and Sb-doped Bi_2Te_3 nanostructures is explained in detail and TE properties of Sb-doped Bi_2Te_3 nanostructures is presented with n to p-type transition from 1 to 5 atomic weight % of Sb substitution.

TiO$_2$ nanostructures:

✓ A simple, low-temperature sol-gel method is developed for the synthesis of low-dimensional and highly efficient stable anatase undoped and transition metal (TM=Cr, Mn, Fe, Co, Ni, Cu and Zn) element doped TiO_2 nanocrystals.

✓ Narrowing of the band gap is witnessed in TiO_2 nanocrystals with the substitution of TM ions into TiO_2 lattice. X-ray photoelectron spectra and PL spectra together confirm the oxygen vacancy defects leading to the formation of bound magnetic polarons (BMPs).

✓ It is observed that irrespective of the dopant ions (whether magnetic or nonmagnetic), the magnetic behavior of undoped and doped TiO_2 nanocrystals is decided by either intrinsic contributions i.e, the nature of BMPs (isolated or overlapped) or extrinsic contributions (i.e the magnetic contributions of dopant ions) or both.

✓ TiO_2 nanocrystals are prepared by sol-gel technique under different atmospheres, i.e, in air, oxygen, argon, vacuum and hydrogen and studied their optical and magnetic properties. It is witnessed that the RTFM with band gap of 0.34 eV is achieved in undoped TiO_2 nanocrystals developed without using any hazardous gases as well as without use of high temperature annealing conditions, which can have wide applications in environmental remediation, photocatalysis and spintronics.

Overall, aiming at the issues of hindering both the TE and spintronics applications, some new concepts have been presented in this thesis, which were realized during our extensive research and experimental studies on nanostructure Bi_2Te_3 and TiO_2 for functional applications.

Chapter 1

Introduction

This chapter introduces the significance of functional semiconductors in the development of various nanostructures for both thermoelectric and spintronics applications. The recent trends in utilizing nanostructuring approach in both chalcogenide thermoelectrics and oxide based dilute magnetic semiconductor materials are explained here. The major objectives and organization of the thesis are briefly outlined at the end of the chapter.

1. Introduction

1.1. Background

Semiconductors can be considered as materials which possess electrical conductivity in a range between that of insulators and conductors. These materials are categorized by highest occupied valence band and the empty conduction band. As a result of this interesting band structure, the magnitude of electrical conductivity of a semiconductor can be altered significantly by doping with suitable elements or by means of other factors such as intrinsic defects associated with the system.[1-3] It is to be noted that conducting materials possess ultra-low resistivity where the resistance is considered to be difficult to alter specifically due to the overlapping of valence band and conduction band where the governing mechanism for different properties are owing to the flow of electrons and in contrast, an insulator is categorized with its very high resistivity. Extrinsic or intrinsic factors very rarely affect the resistivity of an insulator where the band gap between the valence band and the conduction band is considerably large. Hence, semiconducting materials are the interesting class of materials showing a compromise between two extreme ends, i.e., between conducting materials and insulating materials. When these materials are deployed for the most advanced applications, they can be called as functional semiconductors. Specifically when we talk about functional semiconductors, the beauty of these materials lies with the interesting properties governed either by the flow of negatively charged electrons or by the positively-charged holes in the electronic structure of the material.[2,3]

Narrow band gap semiconductors and wide band gap semiconductors equally dominate the electronic industry in variety of technological applications. In semiconducting industry, narrow band gap materials serve the role of a chip-cooler whereas wide band gap semiconducting oxide films will be used for spintronic devices. A possible relation between thermoelectric (TE) and spintronics can be given on the basis of utilization of charge and spin of an electron.[4] When we utilize the possibilities lying with charge of an electron, it could provide an optimization on the transport properties, pointing towards the TE applications. Whereas, utilization of spin of an

electron directly focuses on the spintronic industry, the utilization of both charge and spin of the electron ultimately provides a new scheme of devices and electronics which could be sensed in the near future.

In the last few decades, semiconducting functional nanocrystals are attracting wider attention among the interdisciplinary area of research and nanostructuring enables these materials to be applicable for a variety of applications in the field of photocatalysis, solar cells, thermoelectrics, biomedical and electronic industries.[5-9] Considering the new era of modern technologies, TE materials and dilute magnetic semiconductor (DMS) oxide materials is bringing a fresh momentum to the field of TE and spintronics by enabling interesting material properties.

In the nano regime, most of these semiconducting materials physical and chemical properties vary drastically leading to unique properties owing to the quantum confinement effect. The thermal conductivity, electrical conductivity, optical properties and magnetic properties of the semiconductor can be altered significantly due to this quantum confinement effect. Even though the functional semiconductor nanomaterials and devices are promising candidates for a variety of applications in different areas, these materials are still in the research stage and many of their property governing mechanisms and other different possible interactions need to be investigated in detail. Further implication of nanotechnology in to the semiconductor industry could successfully impart significant breakthroughs in modern technologies in the near future. Some of the semiconductor nanocompounds such as Si, Si-Ge, Bi_2Te_3, Bi_2Se_3, Sb_2Te_3, Sb_2Se_3, GaAs, InP, GaN, SiC, ZnS, ZnSe, CdSe, CdS, HgCdTe and few of the dilute magnetic oxide based semiconducting systems such as ZnO, TiO_2, SnO_2 etc., exhibit excellent applications in electronic industry such as memory unit of computers, chip cooling in laptops, cell phones, CD players etc.[10-17]

1.1.1. Bottom-up nanoengineering of functional semiconductors

Among the unique properties of nanomaterials, the movement of electrons and holes in semiconductor nanomaterials is primarily governed by the well-known quantum confinement, and the transport properties related to phonons and photons are

largely affected by the size and geometry of the materials. The specific surface area and surface-to-volume ratio increase drastically as the size of the material decreases. Parameters such as size, shape, and surface characteristics can be varied to control their properties for different applications of interest. These novel properties of semiconductor nanomaterials have attracted significant attention in research and applications in emerging technologies such as nanoelectronics, nanophotonics, energy conversion, non-linear optics, miniaturized sensors and imaging devices, detectors, photography biomedicine etc., In this work, we demonstrate the nanoengineering of TE and DMS materials which facilitates the desired transport and magnetic properties and make them exactly suited for the advanced functional applications.

1.1.1.1. Nanoengineering of narrow band gap semiconductors for thermoelectric applications

Recently there has been greatly expanded interest in the nanostructuring of narrow band gap materials. This is specifically due to the fact that there is an alloy limit of thermal conductivity in bulk TE materials arising as a result of less grain boundary scattering which limits the practical applications.[10-11] In comparison to the bulk counterpart, significant grain boundary scattering in TE nanostructures could provide drastic reduction in thermal conductivity makes them suitable for practical devices. Bismuth Telluride (Bi_2Te_3) is one of the prominent narrow band gap semiconductors having a band gap of 0.2 eV. Bi_2Te_3 nanostructures have the highest figure of merit (***ZT***) and are extensively employed in refrigeration and have a maximum operating range near room temperature.[18] To meet the necessity for the design of a practical TE device, both p and n type nanostructured materials are required and the best materials currently being used in TE applications are $Bi_{2-x}Sb_xTe_3$ and $Bi_2Te_{3-y}Se_y$ for 'p' and 'n' type materials respectively. It is quite interesting that the Bi_2Te_3 can be made n-or p-type by increasing or decreasing respectively the tellurium concentration in the stoichiometric ratio and the hexagonal crystal structure of Bi_2Te_3 may lead to anisotropic electronic properties. On these potential benefits, the n and p-type Bi_2Te_3 based nanomaterials have been developed and the transport properties are investigated in detail for device applications.

1.1.1.2. Nanoengineering of wide band gap semiconductors for spintronics applications

Wide band gap semiconductor materials have been of great interest over the years due to its potential use in spintronic devices, but one of the challenging hurdles in these materials is to achieve intrinsic ferromagnetism (FM) at room temperature. Generally, bulk DMS materials provide less electron interaction with defect sites, limiting the spintronic applications. Nanoengineering induces maximum surface defects and oxygen vacancy centers to trap the electrons making them interesting candidates for spin based devices. Oxide based nanostructured DMSs are the most promising candidates owing to their possible high Curie temperature, compared to the III-V compound based DMSs, such as (Ga,Mn)As.[19,20] As a particular example, titanium dioxide (TiO_2) nanostructures, is one of the most promising DMS materials with a band gap of 3.3 eV. Extensive efforts have been devoted to improve the room temperature ferromagnetism (RTFM) of TiO_2 nanocrystals by enhancing the intrinsic FM. However, reproducibility problems of oxide DMSs have been reported in several cases, where FM is only apparent in samples prepared in a poor oxygen environment. Magnetic clusters and secondary phases have been shown to lead to extrinsic FM in these systems. Therefore, understanding the origin of FM in nanostructured oxide DMSs is still an object of intense debate. Therefore, TiO_2 and transition metal (TM) doped TiO_2 nanocrystals have been developed with tailored band gaps and enhanced RTFM.

1.2. Statement of the problem

Bi_2Te_3 as a TE material and TiO_2 as a DMS material has been a hot topic since last few decades. Although *ZT* value of Bi_2Te_3 has been approved remarkably by nanostructuring, there are still some problems, which should be tackled to further optimize TE properties. Similarly the mechanism underlying the magnetic interactions involved in TM doped nanostructured TiO_2 is still under controversy and requires further clarifications.

1.3. Objectives and scope of the present work

The objectives of this thesis are to develop functional semiconductor nanomaterials and to study their TE, optical and magnetic properties. As state-of-the-art bulk TE materials, nanostructured Bi_2Te_3 family naturally has better performance compared with bulk counterparts. Integrating this advantage, the use of nanostructures can tune the *ZT* through new methods such as quantum confinement, dimensional restriction, and modulation doping. This work concentrates on fabricating nanostructured Bi_2Te_3 by reflux method and measuring the TE properties. The main goal is to enhance the TE performance through nanostructuring, structural and morphological tailoring. What's more, this work is aimed to exploit alternative eco-friendly as well as aqueous medium for the reflux technique, which can improve the yields so as to make it possible to produce TE nanostructures efficiently and cost-effectively. Apart from nanostructured synthesis, the challenges on optimizing the *ZT* highlight the need to establish a comprehensive understanding of electron-hole-phonon transport. In order to obtain a better predetermination of TE performance, the concepts used in this work include various factors such as electron and phonon mean free path, electron mobility, effect of quantum confinement etc. Similarly, challenges in explaining the long range RTFM behavior and optical band gap narrowing in TiO_2 nanocrystals have been demonstrated in a decent manner.

1.4. Organization of the thesis

The entire thesis has been divided into six chapters. The first-chapter describes the significance of functional semiconductors in the development of various nanostructures for both TE and DMS applications. The major objectives of the thesis are briefly outlined at the end of the chapter. Second-chapter describes the fundamental aspects, detailed literature review and the recent progress in development of nanostructures for both TE and DMS materials.

The third chapter deals with the synthesis of nanocrystals of narrow band gap semiconductor, Bi_2Te_3 using an aqueous based reflux method. The effect of surfactant concentration and reaction time on the structural, morphological and TE properties of

nanocrystalline Bi_2Te_3 has been analysed by using different analytic techniques. A systematic study of surfactant-assisted aqueous-based low-temperature chemical method for the synthesis of different phases of Bi-Te-based nanostructures with different morphologies ranging from nanocrystals to nanorods/nanosheets is presented in detail. Simultaneous optimization of reaction time and surfactant concentration yields the formation of hexagonal Bi_2Te_3 nanocrystals even with lower reaction time, which is the desirable crystal structure for obtaining enhanced TE properties. Tuning the surfactant concentration from 50 to 100 mmol facilitates the formation of low-dimensional structures of Bi_2Te_3, and exhibit a promising ***ZT*** of 0.75 at 300 K. An in-depth understanding of the reaction mechanism to form Bi_2Te_3-based nanostructured materials and the possibility of Sb and Se based chalcogenide nanostructure formation in aqueous medium is explained towards the end of this chapter. Overall, the chapter describes an efficient and simple method to develop low dimensional nanostructures for enhanced TE performance.

Fourth chapter illustrates the development of wide band gap semiconductors using sol-gel synthesis where pristine and TM doped anatase-TiO_2 nanocrystals have been synthesized with tailored band gaps and enhanced magnetization. Here, in-depth understanding regarding the contribution of non-magnetic (Cu and Zn), magnetic (Fe, Co and Ni) and antiferromagnetic (Cr and Mn) TM elements on the structural, morphological, optical and magnetic properties have been presented in detail. Oxygen vacancy defects lead to the formation of bound magnetic polarons which induces a weak ferromagnetic behavior in TiO_2 nanocrystals at room temperature. The observed band gap narrowing in these TiO_2 nanostructures and the mechanism underlying the magnetic interactions associated with the magnetic impurity concentration are advantageous from an applied perspective, especially in the field of spintronic and magneto-optic devices.

In the fifth chapter, defect modulation of TiO_2 nanocrystals by varying annealing atmosphere to tailor the NIR range optical absorption, band gap narrowing and ferromagnetic response have been presented. Detailed structural, optical and magnetic study of TiO_2 nanocrystals prepared by simple sol-gel technique annealed in

air, oxygen, argon, vacuum and hydrogen atmospheres has been carried out. Large absorption in Visible and IR region along with much reduced band gap is observed in argon, hydrogen and vacuum annealed samples. The long range RTFM observed in argon annealed TiO_2 nanocrystals is explained by taking into consideration of bound magnetic polarons. The summary of entire thesis work has been provided in the last chapter which also includes the future perspectives of the present study.

1.5. References

1. D. A. Neamen, Semiconductor physics and devices, Q Richard D. Irwin, Inc.(1992)
2. R. F. Pierret, Semiconductor Device Fundamentals, (1996)
3. Y. Li, Y. Weng, X. Yin, X. Yu, S. R. Sarath Kumar, N. Wehbe, H. Wu, H. N. Alshareef, S. J. Pennycook, M. B. H. Breese, J. Chen, S. Dong, T. Wu, Orthorhombic Ti_2O_3: A Polymorph-Dependent Narrow-Bandgap Ferromagnetic Oxide, *Adv. Funct. Mater.*, 28 (2018) 1705657.
4. I. Žutic´, J. Fabian, S. Das Sarma, Spintronics: Fundamentals and applications, *Rev. Mod. Phys.,* 76 (2004**)**, 323
5. A. Yoshikawa, in *Wide Bandgap Semiconductors* (Eds: A. Yoshikawa, H. Matsunami, Y. Nanishi), Springer, Berlin, Heidelberg (2007) p. 2.
6. X. Z. Kong, C. X. Liu, W. Dong, X. D. Zhang, C. Tao, L. Shen, J. R. Zhou, Y. F. Fei, S. P. Ruan, Metal-semiconductor-metal TiO_2 ultraviolet detectors with Ni electrodes, *Appl. Phys. Lett.* 94 (2009), 123502.
7. T. Wang, J. Bai, S. Sakai, J. K. Ho, Investigation of the emission mechanism in InGaN/GaN-based light-emitting diodes, *Appl. Phys. Lett.* 78 (2001) 2617.
8. A. Bera, K. W. Wu, A. Sheikh, E. Alarousu, O. F. Mohammed, T. Wu, Perovskite Oxide $SrTiO_3$ as an Efficient Electron Transporter for Hybrid Perovskite Solar Cells, *J. Phys. Chem. C,* 118 (2014) 28494.
9. K. Nakata, A. Fujishima, TiO_2 photocatalysis: Design and applications, *J. Photochem. Photobiol., C,* 13 (2012) 169
10. C. Han, Z. Li, S. Dou, Recent progress in thermoelectric materials, *Chin. Sci. Bull.* 59 (2014) 2073.
11. G. A. Slack, New Materials and Performance Limits for Thermoelectric Cooling, *In: CRC Handbook of Thermoelectrics.* Rowe DM, editor. Boca Raton, FL: *CRC Press* (1995).
12. J.-C. Zheng, Recent advances on thermoelectric materials, *Front. Phys. China*, 3(3) (2008) 269.
13. D. M. Rowe, Recent developments in thermoelectric materials, *Appl. Energy,* 24 (1986) 139.
14. T. Bland, K. Lee and S. Steinmuller, The spintronics challenge, *Phys. World,* 21(2008) 24.
15. D. D. Awschalom and M. E. Flatté, Challenges for semiconductor spintronics, *Nature Phys.,* 3 (2007) 153.

16. R. Janisch, P. Gopal and N. A. Spalding, Transition metal-doped TiO_2 and ZnO-present status of the field, *J. Phys.: Condens. Matter,* 17 (2005) R657.
17. J. K. Furdyna, Diluted magnetic semiconductors, *J. Appl. Phys.,* 64 (1988) R29.
18. L. Yang, Z. –G. Chen, M. Hong, G. Han, J. Zou, Enhanced thermoelectric performance of nanostructured Bi_2Te_3 through significant phonon scattering, *ACS Appl. Mat. Interfaces,* 7 (2015) 23694
19. H. Ohno, A. Shen, F. Matsukura, A. Oiwa, A. Endo, S. Katsumoto and Y. Iye, (Ga,Mn)As: A new diluted magnetic semiconductor based on GaAs, *Appl. Phys. Lett.*, 69 (1996) 363.
20. Y. J. Matsumoto, M. Murakami, T. J. Shono, T. Hasegawa, T. Fukumura, M. Kawasaki, P. Ahmet, T. Chikyow, S. Y. Koshihara and H. Koinuma, Room temperature ferromagnetism in transparent transition metal-doped titanium dioxide, *Science*, 291 (2001) 854.

Chapter 2

Fundamental Aspects and Literature review on chalcogenide thermoelectric and TiO$_2$ based nanostructured dilute magnetic semiconductors

This chapter describes the detailed literature review and the recent progresses in development of nanostructures for both chalcogenide thermoelectrics and oxide based DMS materials. The first part of this chapter describes in detail regarding the synthesis and thermoelectric characterization of the narrow band-gap semiconductor, Bi$_2$Te$_3$ and up to date progress of their thermoelectric figure of merit. The second part deals with a detailed literature on TiO$_2$ based wide band-gap semiconductors and the mechanism underlying the magnetic interactions involved in transition metal ion-doped TiO$_2$ which is still under controversy and requires further clarifications.

2.1. Introduction to thermoelectric materials

Development of highly efficient TE materials is hindered by the conflicting properties deciding the figure of merit of these materials. In order to improve the figure of merit and overall efficiency of a TE material, different key factors are demonstrated in this chapter. Materials from chalcogenide family are focused here owing to their excellent and tunable transport properties; bismuth-tellurium based materials are focused in the present study. Here, we clearly demonstrate fundamental theories determining TE properties and time line progress in TE research as well as emerging ideas and trends on Bi_2Te_3-based TE materials.

2.1.1. Factors affecting TE efficiency

By analyzing the TE principles, the TE performance of materials can efficiently be optimized. A material which has a high TE performance should have a good electrical conductivity (σ), high Seebeck coefficient (S) for electronic transport, appropriate carrier concentration and low thermal conductivity (κ) for maintaining the temperature difference. Tuning the carrier concentration and κ through various methods is an efficient way to adjust the TE properties of materials.

2.1.1.1. Figure-of-merit and thermoelectric efficiency

A dimensionless quantity called as figure of merit (***ZT***) is a measure of TE efficiency of any material which is generally expressed using the following relation[1]

$$ZT = S^2 \sigma \frac{T}{\kappa} = \frac{S^2 T}{\rho} \frac{1}{\kappa_L + \kappa_e} \qquad 2.1$$

Specifically focusing on to a high performance TE devices which is composed of n and p-type legs derived from high ***ZT*** materials. A series connection is maintained electrically and a parallel connection is maintained thermally on these TE devices or module. From equation (2.1), it is clear that a good TE material should possess a "phonon-glass electron-crystal" (PGEC) behavior and the subsequent result is a large S.[2] Interestingly our aim is to win the conflict among the interdependent parameters S, σ

and κ and generally it is extremely a tedious job to satisfy these criteria in any TE material possessing simple crystal structure. As these properties are really conflicting, any attempt to improve any of S, σ or κ may significantly deteriorate the other properties and overall TE performance as well. By considering this key issue, it is interesting to observe that there is a possibility of getting a prominently increased value of Power factor ($S^2\sigma$) when the carrier concentration is nearly 10^{19} which is exhibited by the materials in the region where there is a crossover among metals and semiconductors as shown in the Fig.2.1. The following representation could be useful in isolating and concentrating on highly efficient and high performance TE materials.
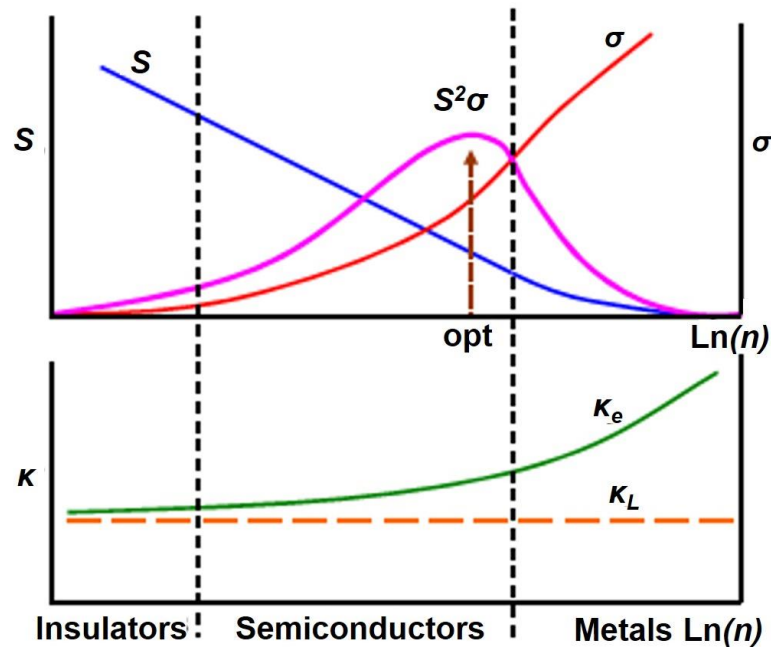
Fig. 2.1. *S*, *σ*, *S²σ*, and electronic (*κₑ*) and lattice (*κ_L*) thermal conductivities as a function of free-charge-carrier concentration ***n***.[3]

Due to this reason, semiconducting materials, more specifically, narrow band gap semiconductors are considered to be the suitable materials for TE applications. A high **ZT** value is observed in these state-of-the-art TE materials especially in chalcogenide based materials, where it is possible to achieve a ZT_{max} by optimizing the value of carrier concentration (**n**). By considering the Carnot efficiency and **ZT** value, the device performance can be assessed using the conversion efficiency equation as represented in equation (2.2).

The maximum value of conversion efficiency, η, is derived using this relation as:[4-6]

$$\eta = \frac{T_H - T_C}{T_H}\left[\frac{\sqrt{1+ZT_m}-1}{\sqrt{1+ZT_m}+\dfrac{T_C}{T_H}}\right] \qquad 2.2$$

In equation (2.2), T_H corresponds to temperature at hot side, T_C the temperature at cold side, and T_m representing the mean temperature of both T_H and T_C. The relation $(T_H-T_C)/T_H$ in the above equation denotes the Carnot efficiency. This is the maximum efficieny (η) that a heat engine or a refrigerator can have by considering the thermodynamic limitations and till date the maximum η of any TE device is around 10% which is much lower than the Carnot efficiency which is near 60%. This fact energizes the current research as there is a huge possibility of improving TE efficiency to a great extent despite the low efficiency exhibited by most of the current TE materials. Nowadays, TE technology is employed in waste heat recovery from automobiles, industries, conversion of solar thermal energy in to waste heat and in the advanced cooling applications. Fig. 2.2. shows the efficiency of TE devices as a function of temperature difference.[7]
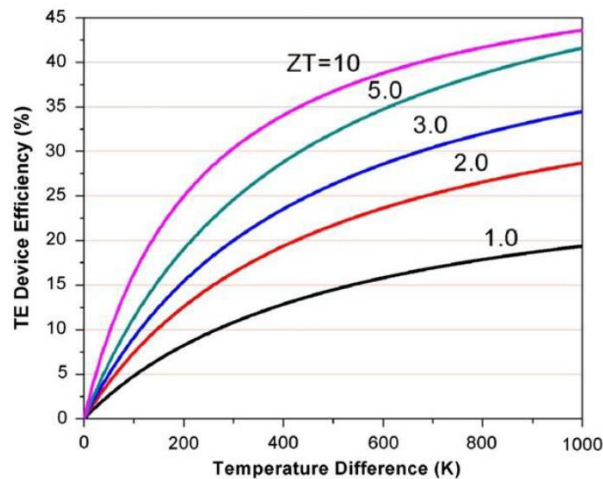
Fig. 2.2. Efficiency of TE devices as a function of temperature.

From the equations mentioned above, we could see that apart from the Carnot efficiency, a TE device performance is directly related to the higher ***ZT*** value of both n and p-type material. A diagrammatic representation based on the previous report is shown in the above figure which clearly validates the importance of equation (2.2) in

determining the TE device efficiency. The diagram gives a clear indication on the variation of *ZT* values to achieve high efficiency and with temperature range of operation and higher *ZT* value contributes a significant improvement in both power generation and refrigeration efficiencies. It is believed that room temperature applications of TE devices are numerous and interestingly, from the above representation, at room temperature if the *ZT* value is around 2, the efficiency will be near or above 15%, ultimately leading to the availability of practical devices for the advanced functional applications. Hence, it is clear that development of materials with attractive *ZT* value makes the TE research more competitive. In order to accomplish and optimize the conflicting properties deciding the *ZT* value, one should follow an approach to maximize the *PF* ($S^2\sigma$) by lowering the κ as much as possible. Two different approaches can be followed to accomplish this major goal; one is to identify the new group of materials with complex crystal structures to improve the room temperature TE performance and another approach lies with the improvement in *ZT* value of the currently available materials, mostly, chalcogenide based materials such as Bi_2Te_3, PbTe, SnTe compounds.

2.1.1.2. Carrier Concentration

The *PF* determines the thermal function of materials. So for a good TE performance, high *S* and high σ should be achieved synchronously. Both the *S* and σ are related to the carrier concentration of materials.[8]

$$S = \frac{8\pi^2 k_B^2}{3eh^2} m^* T \left(\frac{\pi}{3n} \right)^{2/3} \qquad 2.3$$

$$\sigma = \frac{1}{\rho} = ne\mu \qquad 2.4$$

where *n* represents the carrier concentration, k_B is the Boltzmann constant, *h* is the Planck's constant, m^* is the effective mass of the carrier, ρ is the electric resistivity, *e* is the electrical charge of an electron, *T* is the absolute temperature and μ is the carrier mobility. These equations show us that lower carrier concentration leads to lower σ but higher *S*. Hence, it is difficult to achieve a high *S* with a high σ due to the complex

connection between **S**, **σ** and **n**. Hence, optimizing the value of **n** is crucial for maximizing the value of **ZT**. For an ideal TE material, the value of **n** should lie between 10^{19} and 10^{21}.

2.1.1.3. Thermal Conductivity

Thermal conductivity of materials comes from two sources:[8] electrons and holes transporting heat (κ_e) and lattice thermal conductivity (κ_L). The total thermal conductivity is the sum of these two terms represented by

$$\kappa = \kappa_e + \kappa_L \qquad\qquad 2.5$$

$$\kappa_e = L\sigma T = ne\mu LT \qquad\qquad 2.6$$

where L is the Lorenz factor for free electrons, T is the absolute temperature. As κ_e is directly related to the **n**, controlling the carrier concentration is a crucial strategy to obtain high **ZT**.

2.1.2. Different Classes of TE materials

In 1995, Slack described a good TE material as a material with a narrow band gap, high carrier mobility, and low κ.[9] He suggested that the best TE material should possess the electrical properties of a crystalline material and the thermal properties of a glass material, similar to a PGEC.[9] Theoretically, the values of the **ZT** has no restriction, but Slack estimated that the **ZT** of an optimized PGEC material is about 4 in the temperature range from 77 K to 300 K. Different classes of TE materials used today include ceramic materials, semiconducting materials, high temperature performance oxide materials and organic materials. Depending upon the synthesis and processing conditions, these materials could be synthesized in the form of bulk, superlattices, nanocrystals or nanowires.[10-19] A representation of different classes of current TE materials are summarized in Fig.2.3 which gives an overall idea regarding the temperature range of application and **ZT** values of different TE materials. In general, highly efficient TE materials should be chosen depending upon the abundance,

availability and toxicity of elements present in these systems. Fig. 2.4 gives the percentage of different TE materials used globally today.
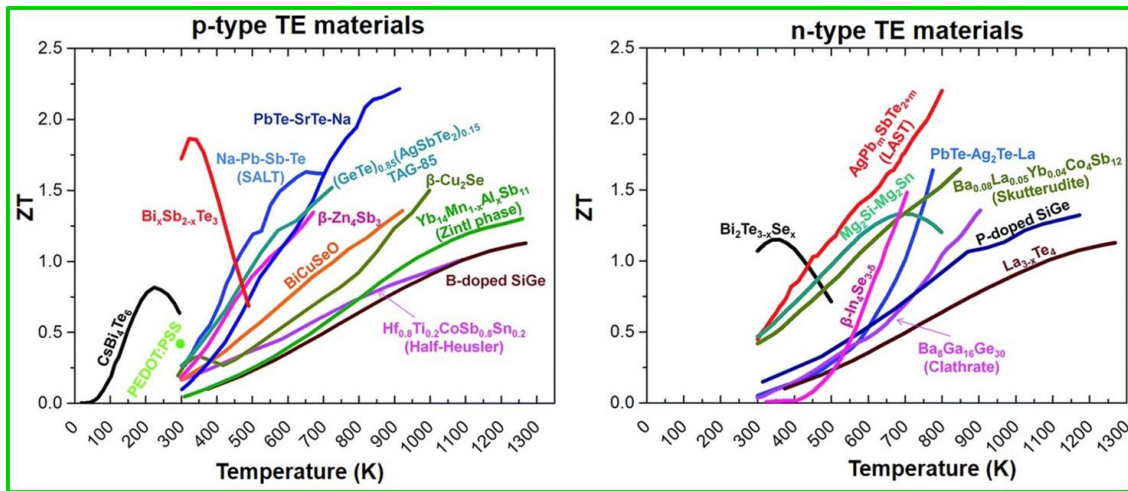
Fig.2.3. Different classes of current n-type and p-type TE materials[20]

Here, a detailed literature review is presented based on different categories of materials available right now and the mechanism underlying the actual performance of these materials.
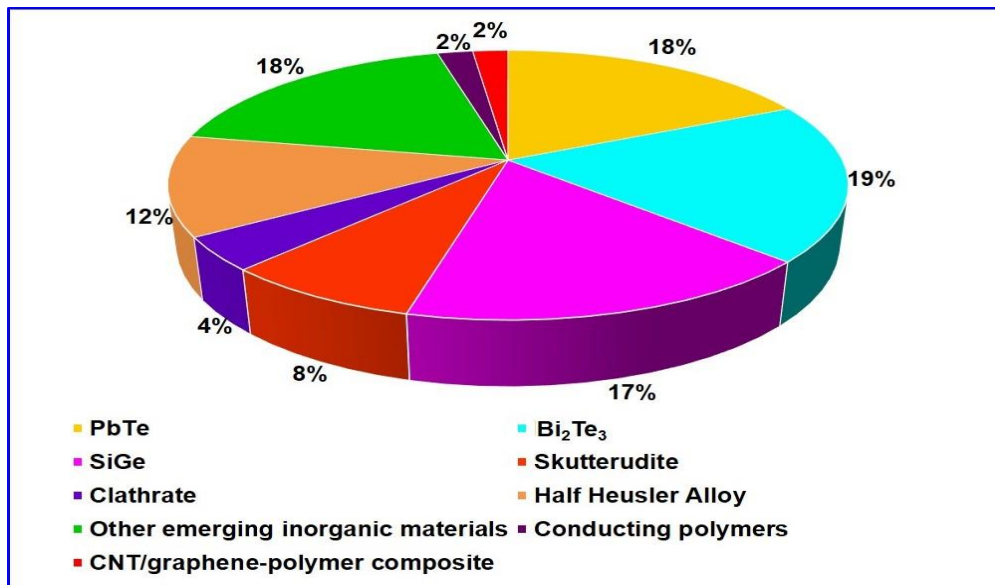
Fig. 2.4. Percentage of different TE materials used in the world today.[21]

2.1.2.1. Metal chalcogenide based materials

Among the inorganic TE material, metal chalcogenides are one of the interesting class of materials having numerous applications in most modern devices and

technologies.[22-27] Specifically, targeting the TE industry, metal chalcogenides can be considered as the best for both power generation and cooling applications as a result of their high performance when compared with other oxides or organic materials. Also, commercialization of these materials in the form of devices is also accomplished with considerable efficiency.[28] Recent reports suggests that a remarkable improvement in *ZT* value could be accomplished in these materials by some different approaches using nanostructuring, elemental doping of these nanocrystals, engineering defect centres and electronic structure of these materials. Superlattices of these materials are supposed to exhibit a record *ZT* value above the conventional values as reported recently.[29,30-32] Chalcogenides materials contain one or more chalcogen elements such as S, Se or Te as a substantial constituent. Lead chalcogenides (PbTe) and Bismuth chalcogenides (Bi_2Te_3) are the most widely used TE materials.

Lead (Pb) is one among the widely used elements in the design of TE materials and has been playing a vital role in TE power generation for more than 50 years owing to its abundance in the Earth's crust and easy processability. Moreover, the heavy atomic weight of Pb could help in the reduction of lattice vibration and κ. In 2005, Harman et al. reported PbTe/PbTeSe quantum-dot superlattices with a *ZT* of 3.0 at 550 K.[33] In 2006, Snyder and his co-workers[34] carefully studied the κ of PbTe using laser flash technique and they could improve the *ZT* of Na-doped PbTe (p-type) from 0.8 to 1.5 and I-doped PbTe (n-type) from 0.7 to 1.4 at 750 K, respectively.[34-36] The major advancement in this field was the use of nano-inclusions to reduce the κ of PbTe by enhancing the phonon scattering.[37-44] Nano-inclusions form a well-dispersed second phase in the host phase and are divided into ''coherent'' and ''incoherent'' ones. Both these nano-inclusions can significantly reduce the κ of PbTe-based TE materials. However, they work by different mechanisms and hence show different effects. The coherent nano-inclusions, which are slightly mismatched with the matrix act as point defects and scatter short wavelength phonons, while the incoherent ones, which show a clear boundary with the host, act as nanoparticles which scatter the mid-wavelength to long-wavelength phonons. An *ZT* value of 1.7-1.8 for both n-type and p-type PbTe has been realized through the use of coherent nano-inclusions of $NaSbTe_2$,[38] $AgSbTe_2$,[39]

and SrTe.[40] Similarly, an *ZT* value of 1.4-1.5 was achieved in n-type PbTe by the incoherent nano-inclusions of Ag_2Te and Sb,[41-42] which is slightly lower than that obtained by coherent nano-inclusions. In 2012, Kanishka *et al.* achieved the maximum decrease in the κ_L and a *ZT* of 2.2 in p-type PbTe-doped with 4 % SrTe at 915 K which was attributed to the improvement in phonon scattering.[45] Biswas *et al.* observed that the doping of Se into p-type PbTe could increase the carrier mobility without decreasing carrier concentration and hence a *ZT* value of 1.8 can be achieved in $Na_{0.02}Pb_{0.98}Te_{0.85}Se_{0.15}$ which was due to the convergence of electronic bands.[40] In 2013, Ibanez *et al.* synthesized core-shell PbTe@PbS nanoparticles in organic solvent using a hot injection method and obtained a *ZT* of 1.07 at 700 K.[46] In 2011, Wang *et al.*, doped PbSe with Na and achieved an *ZT* of 1.2 at 850 K.[47] In 2012, Zhang *et al.* doped PbSe with Al to obtain n-type PbSe with a large *ZT* value of 1.3 at 850 K.[48] In 2017, Ahn *et al.* synthesized 2% ZnTe-doped $Pb_{0.985}Na_{0.015}Te$ and achieved a maximum *ZT* of 1.73 at 700 K.[49]

Bi_2Te_3 and Antimony telluride (Sb_2Te_3) have been widely investigated as a TE material operating at 300 K. The remarkable TE properties of Bi_2Te_3 was attributed to its large mean molecular mass, low melting temperature, and partial degeneracy of the conduction and valence bands.[50] It has a non-cubic tetradymite structure with space group R3m which.is explained in detail in the next section. Sb_2Te_3 also has a similar structure to that of Bi_2Te_3. The low κ, the high σ, and relatively good *ZT* of 0.78, makes Sb_2Te_3 a good choice for use with Bi_2Te_3 to build efficient TE devices.[50]

2.1.3. Measures to improve *ZT*

Ideal TE materials are known as PGEC and require materials with high *PF*, high electronic properties, low κ and low κ_L.[51] Recently, a high *ZT* (>1) was achieved in heavily doped semiconductors,[8,52,53] nanostructures[53-56] and superlattice structures.[53,57-59] High *ZT* achieved by both nano-miniaturization and using nanocomposites have proved to be efficient approaches for the enhancement in TE properties, which increase the *S* value while decreasing the κ_L due to the quantum confinement and the strong scattering by phonons.

2.1.3.1. Tuning the band gap

Bipolar conductivity is one of the main reasons which limit the *ZT* in TE materials used at intermediate or high temperatures.[60,61] This is due to the fact that with increase in temperature, minority carriers[62] are significantly increased due to enhanced thermal excitation, thus, increasing κ_e, therefore, the total κ. These inspired researchers to increase the band gap of materials while reducing the thermal excitation of minority carriers at high temperature. It has been proved theoretically[63,64] and experimentally[61,65] that the band structures can be efficiently tuned by doping semiconductors with other elements. For example, the doping of Cd[66] or Ag[67] in PbTe resulted in an enhancement in the band gap, which further stabilized the carrier concentration of PbTe at high-temperature, leading to a high *ZT*.

2.1.3.2. Effect of nanostructuring: Low Dimensional Thermoelectric Materials

With the advancement in technology, nanostructure engineering has been realized as an effective method to develop high-performance TE materials.[7, 66, 68-70] This includes the development of low dimensional and nanocomposites which benefit from reducing the size and dimensions of materials. The enhancement of *ZT* in low dimensional TE materials is mainly due to the quantum confinement effects[58] while complex phonon scattering[71] and low energy carrier filtering[66] by the nano-scaled substructures enhance the performance of TE nanocomposites.

Hicks and Dresselhaus[57] suggested that low-dimensional or nanocrystalline materials could achieve a remarkable enhancement in *ZT* due to the quantum size effects caused by the increase of phonon scattering[72-75] which result in a higher density of states and a decreased κ_L. When the size of the materials is reduced to the nano regime, the quantum confinement effects increase which results in a decrease in the electron energy band structure resulting in a large *S*. In 2001, Venkatasubramanian[73] reported the highest *ZT* of ~2.4 in Bi_2Te_3/Sb_2Te_3 superlattice films, which boosted the TE property compared to the bulk materials. Lin[76] and Dresselhaus predicted that heterostructure nanowires could have better TE performances than superlattice films or conventional nanowires, which attract much attention to study nanowires.

2.1.3.3. Effect of nanostructuring: Nanocomposite Thermoelectric Materials

Nanocomposites[74] materials are easier to be fabricated when compared to nanomaterials. By adopting appropriate synthesis procedures,[71, 77-79] bulk TE materials with nano-sized substructures can be synthesized successfully. The introduction of nanostructures into bulk materials will create a high density of interfaces or grain boundaries, defects and lattice distortion[70] which can significantly scatter phonons which contribute to the κ_L, therefore, reduce the κ. The phonons with medium and long-wavelength could be strongly scattered by the nano-sized grains, grain boundaries, while the short-wavelength phonons can be scattered by the point defects. Such strong scattering to the phonons can reduce the κ_L at most 50% and lead to a 2-fold increase in **ZT**.[80] Meanwhile, electrons which have a much shorter wavelength than phonon would not be scattered so strongly, which means that the κ_e will not be significantly influenced by the nanocomposites.
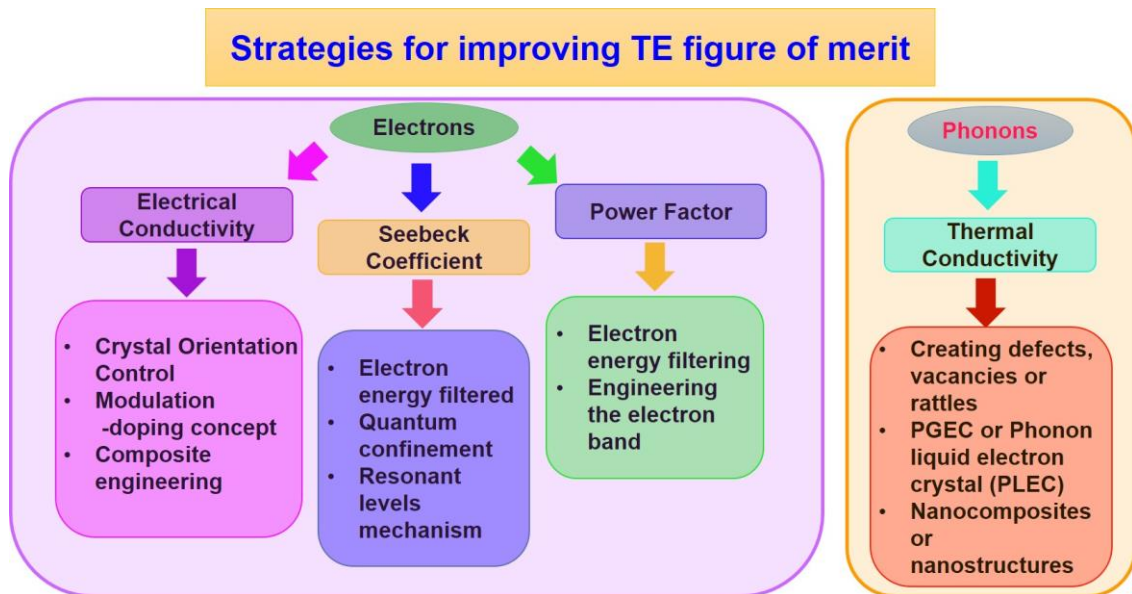
Fig. 2.5. Schematic diagram that briefly summarizes some of the main strategies for the improvement of the figure of merit[81]

In addition, nanocomposites act as a boundary between the nano-participates and the host materials which can filter the lower-energy charge carriers due to the existing potential barrier.[66] As can be seen from equation 2.3, the **S** value strongly related with the **n**. When the carriers transport through the boundary potential barrier between grains, lower-energy charge carriers will be filtered, therefore, the average carrier

energy can be increased, and the *S* can be increased as a consequence while σ will not be significantly reduced. Fig. 2.5. gives a schematic diagram that briefly summarizes some of the main strategies for the improvement of the *ZT*.

2.1.4. Introduction to Bismuth chalcogenides

Bismuth telluride is considered to be one of the best TE materials since it has the capability to convert waste heat energy into beneficial electrical energy operating in a temperature range between 200 and 400 K. Bi physically behaves like a metal. But when it is alloyed with Te, then it behaves like an efficient semiconductor type TE material. In addition, the *S* value of bulk Bi_2Te_3 becomes compensated around room temperature, demanding the materials used in power-generation devices to be an alloy of bismuth, antimony, tellurium, and selenium.

2.1.4.1. Structure of M_2Te_3 (M=Bi, Sb)

Bi_2Te_3 is a narrow-gap layered semiconductor with a rhombohedral unit cell belonging to R-3m space group. It has a layered sandwich structure with five monoatomic sheets stacked along the c axis (z-direction) of the hexagonal lattice as Te(1)-M-Te(2)-M-Te(1) known as quintuple layers (QLs). The coupling is strong between two atomic layers within one QL. The QLs form covalently bonded sheets linked together from each other by weak van der Waals forces. Te atoms exist in two essentially different sites. The Te (1) atom is strongly bound to three Bi atoms on one side and weakly bound to three Te atoms on the other side as its nearest neighbours, while the Te(2) atom forming the middle atomic sheets is octahedrally coordinated to six M atoms. The inner atoms in the same QL are strongly bound together via covalent bonds while the Te(1)-Te(1) bond between different QL is weak and correspond to the largest atomic spacing 0.358 nm. The quintuple layers are separated from each other by weak van der Waals forces.[7] Sb_2Te_3 is isomorphic to Bi_2Te_3. The crystal structure of M_2Te_3 (M=Bi, Sb) is shown in Fig. 2.6 (a). The top view and side view of the QLs is shown in Fig. 2.6 (b) and (c).

Bi$_2$Te$_3$ families crystalize in layered structures and consist of heavy atoms, which can potentially ensure low κ. Moreover, the narrow band gaps can secure a high σ, and the large band degeneracy is also beneficial to produce a high **PF**. Because of these advantages, great efforts have been dedicated to enhance the TE efficiencies of Bi$_2$Te$_3$ families. Single-crystal of Bi$_2$Te$_3$ is formed by the stacks of repeating layers of Te(1)-Bi-Te(2)-Bi-Te(1), whereas the weak van-der Waals force bonds the adjacent quintuples. In consequence of the strong anisotropy, larger **PF** is achieved for the Bi$_2$Te$_3$-based alloys measured parallel to the ab plane (basal plane) than that obtained perpendicular to the basal plane. High κ is also expected as measuring parallel to the ab plane, and thus degrades the **ZT** values. In view of anisotropic transport properties, the **ZT** improvements could only be fulfilled if one can strike the balance between κ reduction and **PF** enhancement through further nanostructuring or doping.
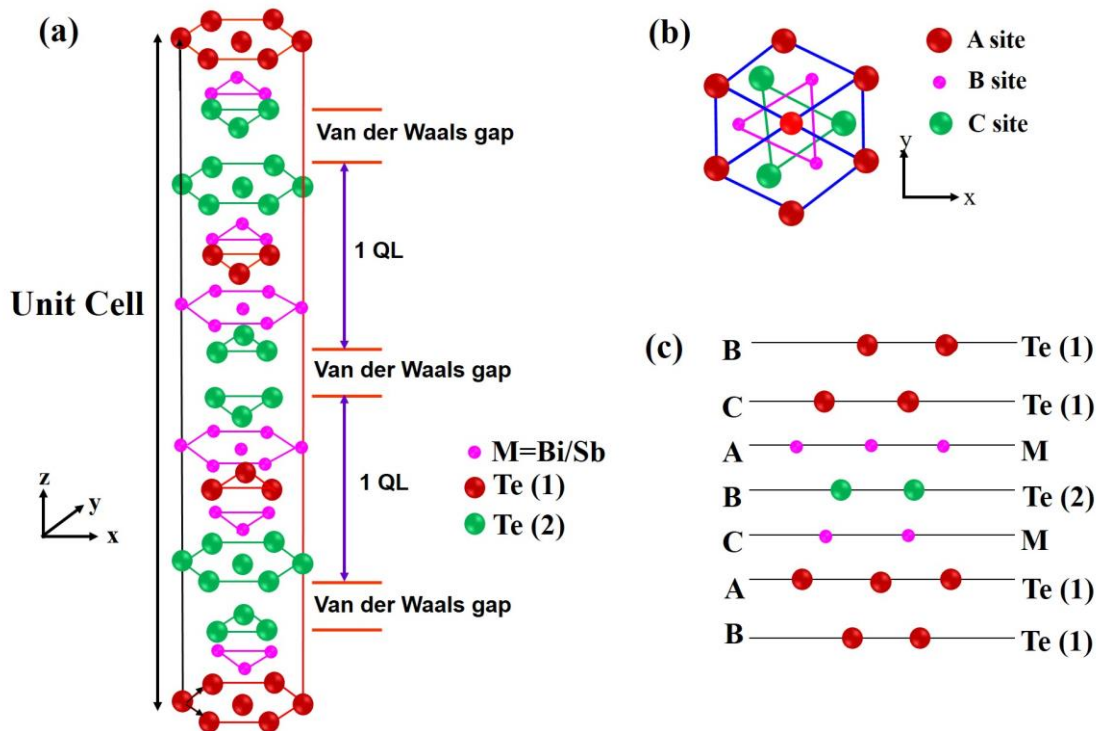
Fig. 2.6. (a) Crystal structure of M$_2$Te$_3$ (M=Bi/Sb), (b) Top view along the z-direction. The triangle lattice in one QL has three different positions, (c) Side view of the QL structure.

2.1.4.2. Literature Review on Bi$_2$Te$_3$ -based materials

Recently, many researchers have attempted to improve the TE efficiency of Bi$_2$Te$_3$-based materials by creating nanostructures in which one or more dimensions are reduced to the nanometric regime. Bi$_2$Te$_3$ can be synthesized in nanostructured form by two methods: top-down and bottom-up approach.[82] The top-down approach includes the synthesis of nanostructured materials from the bulk by physical methods involving evaporation, sputtering and spray pyrolysis methods. In the bottom-up approach, the nanostructured form is constituted by self-assembly, i.e. atom by atom, molecule by molecule, etc. Among these, the bottom-up approach is employed for the synthesis of nanostructures owing to its several advantages such as morphological control with less defects, ability to maintain uniform chemical composition and better short-range and long-range ordering. In bottom-up approach, chemical synthesis is mainly employed which includes sol-gel, electrochemical, chemical vapor, laser chemical vapour, electrolysis deposition, hydrothermal and solvothermal (SS) processes.

Nanostructuring have helped to improve the TE properties of Bi$_2$Te$_3$. In 2001, a ***ZT*** of 2.4 was obtained at 300 K from a p-type superlattice film of Bi$_2$Te$_3$–Sb$_2$Te$_3$ which was attributed to the nanoscale effects.[73] This development led to a surge of research on TE nanomaterials. In 2008, Poudel *et al.* [83] achieved a ***ZT*** of 1.4 at 373 K in p-type nanocrystalline BiSbTe bulk alloys synthesized by ball milling and followed by dc hot pressing. The improvement in ***ZT*** was due to the low κ caused by the increased phonon scattering by grain boundaries and defects. Xie *et al.*[84] synthesized nanostructured p-type (Bi,Sb)$_2$Te$_3$ bulk materials by melt-spinning individual elements of Bi, Sb, and Te followed by a spark plasma sintering (SPS) and achieved an ***ZT*** 0f 1.5 around 370 K. Yan *et al.* successfully increased the ***ZT*** of n-type Bi$_2$Te$_{2.7}$Se$_{0.3}$ to 1.04 by improving its σ through the reorientation of the ab planes of small crystals during multiple-step hot pressing of ball-milled nanopowders.[85] In 2010, Ferdows and Roger theoretically calculated the ***ZT*** of Bi$_2$Te$_3$ thin films to be as high as 7.15 at room temperature which was presumed to be due to the change in the distribution of the valence band density of modes due to the quantum confinement effects in the thin films.[86] Liu *et al.*[87] achieved a ***ZT*** of 0.99 at 373 K in n-type Cu$_{0.01}$Bi$_2$Te$_{2.7}$Se$_{0.3}$ without

texturing. Upon texturing by re-pressing, the *ZT* increased to 1.06 and further increased to 1.1 with aging in air for 5 months. Ko *et al.* also observed an increase in the *S* due to a carrier-selective scattering effect in Pt-doped Sb_2Te_3. The improvement in S was ascribed to the increase in carrier concentration due to the introduction of Pt nanocrystals which partially compensates for the reduced σ due to the decreased μ.[88] In addition to thin films, the *ZT* of Bi_2Te_3 nanowires has also been theoretically calculated, and the results show strong diameter dependence, e.g., the *ZT* value can be greater than 6 if the nanowire diameter is smaller than 5 nm. Inspired by the high *ZT* of nanowires from theoretical predictions, in 2012, Zhang *et al.*[89] synthesized uniform 8-nm Bi_2Te_3 nanowires and achieved a *ZT* of 0.96 at 380 K. The authors also fabricated Bi_2Te_3 nanowire based heterostructures, such as $Te@Bi_2Te_3$, $Bi_2Te_3@PbTe$, although the *ZT* of the $Te@Bi_2Te_3$ heterostructure was only around 0.23 at 400 K.[90] Saleemi *et al.* synthesised nanostructures bulk Bi_2Te_3 through chemical alloying and obtained a *ZT* of 1.1 at 340 K.[91] In 2013, Puneet *et al.* synthesized n-type Bi_2Te_3 by wet chemical exfoliation followed by SPS and achieved a *ZT* of 1.00 at 430 K.[92] In 2015, Yang *et al.* achieved a *ZT* of 0.88 at 400 K in Bi_2Te_3 nanostructures synthesized by SS method followed by SPS.[77] Later, Hong *et al.* achieved large values of *ZT* of 1.23 and 1.2 in n-type $Bi_2Te_{3-x}Se_x$ and p-type $Bi_{0.5}Sb_{1.5}Te_3$ synthesized by microwave assisted surfactant free SS technique and microwave solvothermal method (MSS) respectively.[93,94] Liu *et al.* synthesized n-type $Bi_2Te_{3-x}Se_x$ by hot pressing and obtained a *ZT* of 1.31 at 438 K.[95] In 2019, Te- Bi_2Te_3 heteronanostructures were synthesized by SS method followed by SPS by Mei *et al.* and *ZT* of 0.54 was obtained at 398 K.[96] Bi_2Te_3 alloyed with GeTe and iodine was successfully synthesized by Wu *et al.* and a large *ZT* of 2.2 at 723 K was obtained.[97]

Besides the use of zero-dimensional nanoparticles or 1D nanowires to improve their TE performance, introduction of 2D nanosheets into bismuth chalcogenides can also lead to a high *ZT*. Li *et al.* mixed graphene with Bi_2Te_3 to improve its conductivity, resulting in a 1.5 times higher *ZT* (0.3 at 350 K) for the composites than for single crystal Bi_2Te_3. Although the *ZT* value is low, their work provides an idea to prepare hybrid TE composites with enhanced performance.[98] Various synthesis techniques have

been adopted for synthesis of Bi_2Te_3 both in bulk and nanostructured form which are tabulated in Tables 2.1 and 2.2.. The methods include SS, MSS, cold pressing (CP), solution grow (SG), spark plasma sintering (SPS), hot pressing (HP), lithium ionic exfoliation (LIE), ball milling alloy (BMA), melting alloy (MA), Bridgman–Stockbarger (BS), ball milling (BM), travelling heater method (THM), melt spinning (MS), Te rich melt spinning (Te-MS), zone melting (ZM), Hot forging (HF), etc.

Table 2.1. *ZT* values and temperature of operation for bulk Bi_2Te_3

Sl. No:	Materials	Type-ZT_{max}	Temperature [K]	Synthesis method	Year	Ref.
1	$Bi_2Te_{2.925}Se_{0.075}$	n-0.85	293	THM	1995	99
2	$Bi_{0.5}Sb_{1.5}Te_3$	p-1.4	373	BM+HP	2008	83
3	$Bi_{0.5}Sb_{1.5}Te_3$	p-1.3	373	BMA+HP	2008	100
4	Bi_2Te_3	n-1.2	425	BMA+HP	2008	101
5	$Bi_{0.52}Sb_{1.48}Te_3$	p-1.56	300	MS	2009	102
6	$Bi_2Te_{2.7}Se_{0.3}$	n-1.18	410	BS	2009	103
7	$Bi_2Te_{2.7}Se_{0.3}$	n-1.04	400	BMA+HP	2010	87
8	$Bi_{0.5}Sb_{1.5}Te_3$	p-1.4	300	MA+HP	2010	104
9	$Bi_{0.4}Sb_{1.6}Te_3$	p-1.8	316	MA+MS+HP	2010	105
10	$Cu_{0.01}Bi_2Te_{2.7}Se_{0.3}$	n-1.06	373	BM+HP	2011	85
11	$Bi_{0.5}Sb_{1.5}Te_3$	p-1.10	300	Slip-casting under high magnetic field	2011	106
12	$Bi_2(Te_{1-x}Se_x)_3$-I(0.08%)	n-1.1	340	ZM	2012	107
13	$Bi_2(Te_{0.5}Se_{0.5})_3$-I(0.1%)	n-0.85	570	ZM	2012	107
14	$Bi_{0.5}Sb_{1.5}Te_3$	p-1.21	323	Slip casting under high magnetic feld, SPS	2012	108
15	Bi_2Te_2S/Se	n-0.80	573	Effect of alloying	2013	109
16	$Bi_2Te_{2.3}Se_{0.7}$	n-1.2	445	MA+BM+HP	2014	110

17	$Bi_{0.3}Sb_{1.7}Te_3$	p-1.3	380	MA+BM+HP	2014	110
18	$Bi_{0.05}(PbTe)_{0.95}$	n-1.10	773	Bi doping, Co-ball milling	2014	111
19	$Bi_{0.4}Sb_{1.6}Te_3$	p-1.20	673	BM, hot extrusion	2014	112
20	$Bi_{0.5}Sb_{1.5}Te_3$	p-0.64	300	Effect of severe plastic deformation	2014	113
21	$Bi_2Te_{2.79}Se_{0.21}$	n-1.2	357	HP	2015	114
22	$Bi_{0.5}Sb_{1.6}Te_3$	p-1.86	320	Te-MS+SPS	2015	115
23	$Bi_{0.4}Sb_{1.6}Te_3$	p-1.36	400	ZM, hot deformation	2015	116
24	$Ge_{0.93}Bi_{0.07}Te_{1.005}I_{0.03}$	p-2.2	723	Iodine doping and water quenching	2019	97

Table 2.2. *ZT* values and temperature of operation for nanostructured Bi_2Te_3 based materials

Sl. No:	Materials	Type-ZT_{max}	Temperature [K]	Synthesis method	Year	Ref.
1	$Bi_{0.5}Sb_{1.5}Te_3$	p-1.40	373	BM+SPS, preserved nanostructures	2008	83
2	$Bi_{0.5}Sb_{1.5}Te_3$	p-1.56	300	MS+SPS, nanostructures	2009	117
3	Bi_2Te_3	n-0.94	398	BM+ Hot press, nanograins	2009	118
4	Bi_2Te_3	p-1.18	425	Mechano-chemical process, nanograins	2010	119
5	Bi_2Te_3	p-1.38	473	Nanopores in the bulk	2010	120
6	$Bi_{0.4}Sb_{1.6}Te_3$	p-1.12	350	HP, nanograins	2010	121
7	$Bi_2Se_{0.3}Te_{2.7}$	n-0.93	300	HE, orientation of the nanocrystals	2010	122
8	$Bi_2Se_{0.3}Te_{2.7}$	n-1.04	398	Deformation induced defects	2010	87
9	$Bi_2Se_{0.21}Te_{2.79}$	n-1.14	300	Grown in space, less defects	2010	123

10	$Bi_{0.4}Sb_{1.7}Te_3$	p-0.9	413	SG+SPS	2010	124
11	$Bi_2Se_{0.36}Te_{2.67}$	p-1.20	300	Optimized single crystal	2011	125
12	$Bi_{0.5}Sb_{1.5}Te_3$	p-1.11	300	HF caused nanograins	2011	126
13	$1 vol\% Al_2O_3 + Bi_2Te_3$	n-0.99	400	Dispersed nanoparticles	2011	127
14	$Bi_2Te_ySe_{3-y}$	n-0.70	373	Wet chemical method, nanoparticles	2011	128
15	Bi_2Te_3	n-0.61	423	Wet chemical method, nanoparticles	2011	129
16	$Bi_2Se_{0.3}Te_{2.7}$	n-1.11	423	Nanograins, SiC did not increase **ZT**	2011	130
17	$0.1 vol\%\ SiC + 0.2\ Bi_{0.5}Sb_{1.5}Te_3$	p-0.97	323	Nanograins produced by p-type SiC	2011	130
18	$0.015 vol\%\ MWCNTS + Bi_2(Te_{0.9}Se0.1)_3$	n-0.98	423	Carbon nanotubes as electron donors, composite	2011	131
19	$(Bi_{0.99}Ag_{0.04})_2 (Te_{0.96}Se_{0.04})_3$	n-0.74	373	Effect of Ag doping	2011	132
20	$Bi2Te3-Te$	n-0.6	390	SG+HP	2011	133
21	Nanostructured bulk Bi_2Te_3	n-1.1	340	Chemical alloying	2012	91
22	$Bi0_.5Sb_{1.5}Te_3$	p-1.10	300	Wet chemical method	2012	134
23	Bi_2Te_3	n-0.91	350	MSS+CP	2012	134
24	$Bi_{0.5}Sb_{1.5}Te_3$	p-1.2	363	MSS+CP	2012	134
25	$Bi_2Se_{0.3}Te_{2.7}$	n-1.00	300	BM, hot press, controlled nanostructures	2012	135
26	$Bi_2Se_{0.3}Te_{2.7}$	n-0.54	300	Wet chemical method	2012	136
27	$Bi_2Te_{2.7}Se_{0.3}$	n-0.55	300	SG+SPS	2012	137
28	Bi_2Te_3	n-0.66	470	SG+HP	2012	138
29	Bi_2Te_3	n-0.62	400	SG+SPS	2012	139
30	Bi_2Se_3	n-0.35	400	LIE+HP	2012	140
31	S dopedSb_2Te_3	p-0.95	423	MSS+ CP	2012	141

32	$Bi_{0.5}Sb_{1.5}Te_3$	p-1.79	373	Improved parameters for BM+SPS process, nanograins	2013	142
33	Bi_2Te_3	p-0.97	365	Synthesis under high pressure	2013	143
34	$Cr0.1Bi_2Te_3$	p-0.80	325	Effect of Cr doping	2013	144
35	$Bi_{0.5}Sb_{1.5}Te_3+$ 0.2%Mn	p-1.47	310	Wet chemical method, metal nanoparticle decoration	2013	145
36	0.5at% In+ $Bi_{0.4}Sb_{1.6}Te_3$	p-1.20	320	Effects of Ga and In doping: no effect on σ	2013	146
37	0.4 vol% SiC + $B_{i0.3}Sb_{1.7}Te_3$	p-1.33	373	Effect of SiC	2013	147
38	5 wt% Cu_7Te_4 + $Bi_{0.4}Sb_{1.6}Te_3$	p-1.14	444	Composite, nanograins	2013	148
39	$Bi_{0.5}Sb_{1.5}Te_3$ + Te	p-1.05	425	In-situ formed Te nanoparticles	2013	149
40	Bi_2Te_3	n-1.00	430	Wet chemical exfoliation, SPS	2013	92
41	Bi_2Te_3	n-1.16	420	Wet chemical method, flower-like nanostructure	2013	150
42	$Bi_2Te_{2.994}Cl_{0.006}$+ 0.5wt% In_2Te_3	n-0.94	300	Phase separation	2013	151
43	$(Bi_2Te_3)_{0.85}$ $(Bi_2Se_3)_{0.15}$	n-0.71	480	SG+SPS	2013	152
44	$Bi_{0.5}Sb_{1.5}Te_3$	p-1.60	323	HF, led to orientation of the polycrystals	2014	153
45	$Bi_{0.5}Sb_{1.5}Te_3$	p-1.00	300	BM+Reduction method, nanograins	2014	154
46	$Bi_{0.4}Sb_{1.6}Te_3$	p-1.19	373	Mixture of nanopowder and micropowder	2014	155
47	$Bi_{0.48}Sb_{1.52}Te+$ 4 mol% WSe_2	p-1.27	360	Composite, nanograins	2014	156

48	$Bi_{0.48}Sb_{1.52}Te_3$	p-1.40	340	In-situ exfoliation, SPS	2014	157
49	Bi_2Se_3	p-0.41	533	Nanoplatelets, thermochemical method	2014	158
50	$Bi_2Se_{0.3}Te_{2.7}$	n-1.20	445	Defect engineering	2014	110
51	1.5vol% Ag NW+Bi_2Te_3	n-0.71	475	Effect of Ag nanowires	2014	159
52	Bi_2Te_3 polycrystalline whiskers	n-0.71	673	Template synthesis + HP	2015	160
53	$Bi_{0.42}Sb_{1.5535}Ga_{0.025}Ag_{0.0015}Te_3$	p-1.15	360	Effect of co-doping	2015	161
54	$Bi_{0.5}Sb_{1.5}Te_3$+ 1 vol% Cu_3SbSe_4	p-1.60	476	Carrier fltering effect, nanocomposite	2015	162
55	$Bi_{0.5}Sb_{1.5}Te_3$	p-1.71	323	Melt-solidifcation under high magnetic field	2015	163
56	1at% Fe+ $Bi_{0.48}Sb_{1.52}Te_3$	p-1.09	300	Effect of Fe doping	2015	164
57	$Ce_{0.1}Bi_{1.9}Te_3$	p-1.22	386	Wet chemical method, nanoflowers	2015	165
58	2vol% Ag + Bi_2Te_3	n-0.77	475	Ag nanoparticles	2015	166
59	Bi_2Se_3	n-0.75	423	Single crystal	2015	167
60	$Bi_2Te_{2.4}Se_{0.6}$/ CNT	n-0.80	425	BM, SPS, carbon nanotube (CNT) decrease grain size	2015	168
61	$Bi_2Te_3Se_{0.3}I_{0.0075}$	n-1.13	423	Effect of I doping	2015	169
62	$(Bi_2Se_3)_2(Bi_2Te_3)_8$	n-0.71	450	Wet chemical method, multishell structure	2015	170
63	$Bi_{0.5}Sb_{1.5}Te_3$	p-1.13	360	MSS+ SPS	2015	171
64	Bi_2Se_3	n-0.48	425	MSS+ SPS	2015	172
65	Bi_2Te_3 nanostructures	n-0.88	400	SS and sintered using SPS	2015	77
66	$Bi_2Te_{3-x}Se_x$	n-1.23	480	Microwave, surfactant free SS method	2016	93

67	$Bi_{0.5}Sb_{1.5}Te_3$	p-1.2	320	MSS+SPS	2016	94
68	$Bi_2Te_{3-x}Se_x$	n-1.31	438	Hot pressing	2018	95
69	Te-Bi_2Te_3 hetero-nanostructure	n-0.54	398	SS+SPS	2019	96
70	1.5 vol% Graphene/ Bi_2Te_3	n-0.55	488	composite	2019	173

2.2. Introduction to Dilute Magnetic semiconductors

Dilute magnetic semiconductors (DMSs) are new class of materials which are very useful for spintronics applications. Spintronics devices are based on active spin-based devices that utilize the manipulation of spin-polarized electrons in a host semiconductor.[174,175] However, the polarization of the spin polarized electrons must be preserved to realize a spintronic device. The design of materials possessing both semiconducting and ferromagnetic (FM) properties would be crucial in the development of highly miniaturized devices and presents a serious materials physics challenge. The performance of these devices can be greatly enhanced, if the charge and spin of the electrons are utilized in a single device called spintronic device, which is possible by developing DMSs, which can be easily integrated with the existing semiconducting technology but also is highly spin polarized. Fig. 2.7 shows a schematic representation of a magnetic semiconductor, a non-magnetic semiconductor and a DMS material.
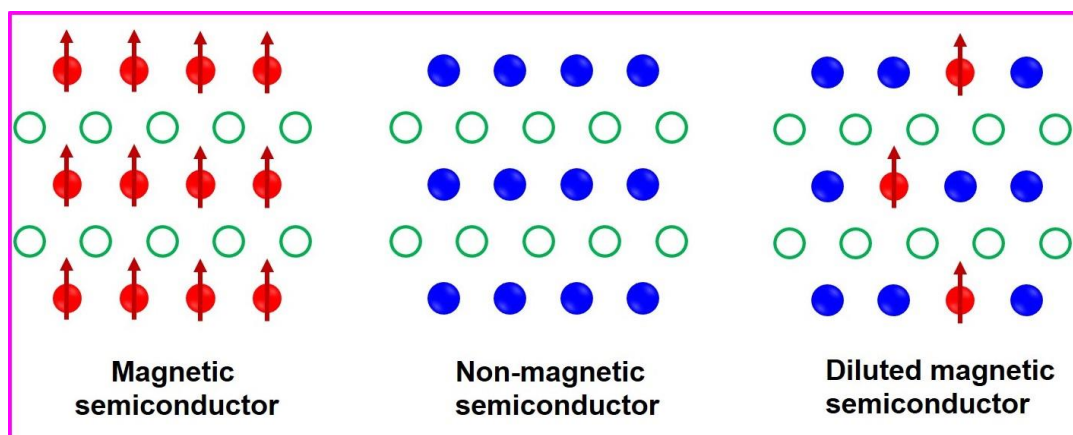
Fig.2.7. Schematic showing (a) a magnetic semiconductor, (b) a non-magnetic semiconductor material and (c) a DMS[176]

The search for material possessing semiconducting and magnetic properties accelerated in recent decades bringing about a new era of DMSs. The first DMS studied were II-VI semiconductor alloys with the general formula $A^{II}_{1-x}Mn_xB^{VI}$ like $Zn_{1-x}Mn_xB$, $Cd_{1-x}Mn_xB$ and $Hg_{1-x}Mn_xB$ where B=S, Se, Te.[177,178] More recently, Mn-doped III–V semiconductors such as $In_{1-x}Mn_xAs$[179,180] and $Ga_{1-x}Mn_xAs$[181,182] showed FM at a higher temperature. Mn-doped GaAs showed a T_C of 173 K, which was quite promising, [183,184] but still too low for RT applications. All these materials exhibited carrier-mediated FM, which provides an opportunity to tune the magnetic behaviour through charge manipulation. This, in turn, has motivated researchers to search for materials which exhibit carrier mediated FM and even higher T_C. In this quest, oxide-based DMS materials came into the picture and became the key materials in the development of spintronic devices. The search for a FM semiconductor at RT was accelerated with the predictions of Dietl *et al.* who performed an exhaustive theoretical study on DMS materials in 2000.[185] The discovery of RTFM in Mn-doped ZnO by Sharma *et al.* [186] and in Co-doped anatase TiO_2 thin films by Matsumoto *et al.* [187] provided an increased sense of enthusiasm for developing magnetically doped semiconductors. A report on RTFM in 2001 in Co-doped TiO_2 by Matsumoto *et al. al.*[187] gave the hope that $Ti_{1-x}Co_xO_2$ thin film can also be used for spintronics. The M_s value was reported to be $0.32\mu_B$/Co-ion and the observed low M_s value was explained in terms of low spin state of Co. The resistivity and carrier concentrations were 0.1-1 Ω-cm and 10^{18} cm^{-3} respectively. This discovery revolutionized considerable research in oxide-based DMS materials such as transition metal (TM) elements-doped ZnO,[188] Cu_2O,[189] SnO_2[190] and $In_{1.8}Sn_{0.2}O_3$.[191] In 2003 Sharma *et al.*[186] reported an ab-initio total energy calculations using projector-augmented wave for $Zn_{0.958}Mn_{0.042}O$ within generalized gradient approximations for exchange-correlation and showed carrier induced FM is stabilized for Mn concentrations less than 5 at.% but AFM above 5 at.%. They have reported RTFM for ZnO: Mn experimentally with a T_C of 425 K when the Mn doping concentration is less than 4 at.%. Sato *et al.*[192] predicted that the FM state in Fe-, Co- or Ni-doped ZnO could be stabilized by s-d hybridization and pointed out that n-type ZnO could be candidates for high T_C materials DMS materials. In 2005, Lawes *et al.* conducted a study on bulk $Zn_{1-x}Mn_xO$ and $Zn_{1-x}Co_xO$ with x=0.02 and 0.15 and

observed FM only at 2 K.[193] Rao *et al.* claimed that the doping of TMs such as Mn and Co in ZnO cannot provide robust FM in these materials and FM can only be achieved by additional co-doping of Mn or Co-doped semiconductors.[194] FM was observed in undoped and nonmagnetic Zn-substituted nanorods of SnO_2 reported by Liu *et al.* The saturation magnetization (M_s) of these nanorods was reported to be sensitive to the Zn concentration where a physical model based on BMP formation was proposed to establish the magnetic ordering of these nanostructures.[195] Ma *et al.* found defect mediated RTFM in Cu-doped ZnO thin films synthesized by reactive magnetron sputtering and pulsed laser deposition (PLD) which could be due to the presence of oxygen vacancies around Zn and Cu ions.[196] The capability of high electron doping in oxide-based semiconductors and the heavy effective electron mass of oxide semiconductors are quite efficient to realize high T_C in these systems.[197] Moreover, most of the oxide-based DMSs are wide band gap semiconductors (>3eV) forming the new generation of spintronic devices.

To exploit the spin and to realize the integration of the DMS material in today's electronics, the development of low dimensional nanostructures is highly crucial. In particular, the long spin coherence length of electrons suggests that the movement of spin, like the flow of charge, could be used to carry information. Such spin-polarized electronic devices could be much smaller, they consume less electricity and could be more useful for advanced computations than today's systems,[198] which are based on electron charge only. Hence, to assimilate electronics, magnetism, and photonics together into a single platform for the next generation multifunctional devices, it is vital to discover a magnetic semiconductor that is not only FM at high temperatures, but also has a tunable carrier density, high magnetic moment, large mobility and is optically transparent to be used in devices for spin injection and detection. The developments in nanotechnology and the demonstration of various quantum size effects in nanoscale systems implies that most of the novel devices of the future will be based on nanostructured DMS which are much more miniaturized and efficient than the existing systems. Among the oxide-based DMS materials investigated, nanostructured TiO_2 system seems to be the most consistently reported *n*-type semiconducting material to

present FM order far above room temperature $(T_C > 650 \text{ K})$[199] Moreover, the possibility of tuning the magnetic states due to the different oxidation states present in TiO_2 through the doping of various TM encouraged us to choose TiO_2 as the DMS material for the present study.

2.2.1. Magnetism in solids

Different types of magnetic materials and magnetic interactions are discussed below. A brief idea regarding the different theoretical models used in DMS materials is also explained here.

2.2.1.1. Types of magnetic materials

All materials can be classified in terms of their magnetic behavior. The two most common type of magnetism are diamagnetism and paramagnetism (PM), which accounts for the magnetic properties of most of the elements in the periodic table at room temperature. These elements are usually referred to as non-magnetic. Based on the spin ordering or exchange interactions, magnetic materials can also be classified into FM, antiferromagnetic (AFM) and ferrimagnetic. Diamagnetism is a very weak form of magnetism exhibited by atoms possessing completely filled electron shells and hence possesses no net magnetic moment. It arises due to the change in the orbital motion of electrons caused by an external magnetic field (H). The induced magnetic moment is very small and acts in a direction opposite to that of H. Hence, diamagnetic materials tend to expel magnetic flux from their interior, and therefore, they exhibit negative χ. Superconductors are perfect diamagnets, most of semiconductors like ZnO, SnO_2 etc. are diamagnetic in nature. In PM materials, the individual atoms or molecules have a net orbital or spin magnetic moment, which are randomly oriented. These moments are only weakly coupled to each other, and the thermal energy causes random alignment of the magnetic moments, and hence there is no net magnetization (M). When H is applied, the moments start to align, but only a small fraction of them are aligned in the direction of field. Hence, they have a small and positive χ between 10^{-3} and 10^{-5} and μ_r slightly greater than one. However, they do not retain magnetism once the field is removed. PM occurs in atoms and molecules with unpaired electrons, such as, free atoms, free

radicals, and in compounds of TMs containing ions with unfilled electron shells. FM materials exhibit spontaneous magnetization and a clear magnetic ordering temperature. In ferromagnets, there is a strong internal interaction between the atomic magnetic moments which aligns them parallel to each other. The T_C of Fe, Co and Ni are 1043 K, 1404 K and 631 K respectively; thus at 300K, only Fe, Co, and Ni are the available FM elements. A ferromagnet in the demagnetized state is composed of a number of small regions called domains. Each domain is spontaneously magnetized to its saturation value of magnetization. But the magnetization vectors in different domains have different orientations, and hence, the total M averages to zero. For an FM material, the field dependence of M is nonlinear, and at large values of H, the M becomes constant at its saturation value called saturation magnetization (M_s). But once saturated, a decrease in H to zero does not reduce M to zero. Hence, it possesses some magnetization called remanent magnetization (M_r). To demagnetize the material, a reverse field is required and the magnitude of this field is called coercivity (H_C). It represents the energy loss during the process of magnetization and demagnetization and this amount of energy (the hysteresis loss) is proportional to the area inside the loop. The variation of M with H for a diamagnet, paramagnet and ferromagnet is shown in Fig. 2.8.
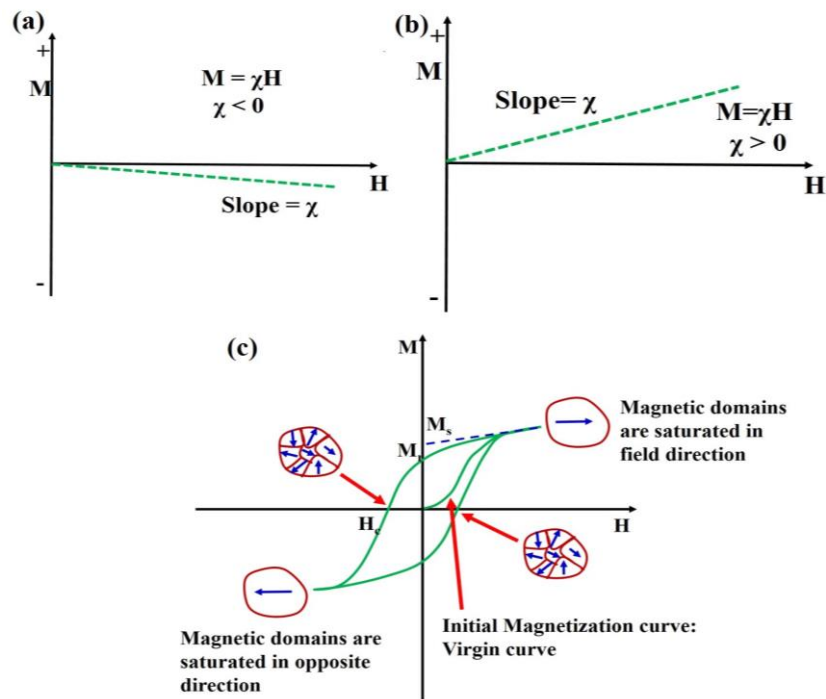
Fig. 2.8. M vs H for a (a) diamagnet, (b) paramagnet and (c) ferromagnet

2.2.1.2. Magnetic exchange interactions

The magnetic order in magnetic systems arises due to the co-operative effects between magnetic moments located at constituent ions. The interaction among the spins is mediated by spin dependent electrostatic interaction known as the exchange interaction. The lowering of the free energy of a magnetic material due to the exchange interaction leads to magnetic order, and it persists below a definite temperature T_C.

Direct exchange interaction occurs between ions whose spins are close enough to have sufficient overlap of their wave functions. Electrons spend most of their time between neighboring atoms when the interatomic distance is small. This gives rise to antiparallel alignment and therefore negative exchange (AFM). If the atoms are far apart the electrons spend their time away from each other to minimize the electron-electron repulsion. This gives rise to parallel alignment or positive exchange (FM).

Indirect exchange interactions are classified into Superexchange (SE) and Double exchange interactions (DE). SE interaction occurs between two nearest-neighbour cations joined through a shared non-magnetic ion such as oxygen (O). TM oxides are excellent models for SE interaction. It is an oxygen-mediated exchange between TM ions based on the virtual hopping of the O_{2p_z} electrons. The O^{2-} ion with the electronic configuration $1s^2\ 2s^2\ 2p^6$ have fully occupied triply degenerate p orbitals ($2p_x$, $2p_y$, $2p_z$) with six electrons. In oxide systems, the five d orbitals of TM are not degenerate, but they split into triply degenerate t_{2g} orbitals ($3d_{xy}$, $3d_{yz}$, $3d_{xz}$), and doubly degenerate e_g orbitals ($3d_z^2$, $3d_{x^2-y^2}$). The e_g orbitals point along the crystal axes, and, therefore, overlap with the O_{2p_z} orbitals. The SE interaction between Mn^{3+} ions is illustrated in Fig. 2.9. Mn^{3+} with electronic configuration [Ar] $3d^4$ has four electrons in the five $3d$ orbitals, three of them occupying the t_{2g} orbitals and the fourth is located in one of the two e_g orbitals, which point along the crystal axes and therefore overlap with the O-2p orbitals. Virtual hopping of O-2p electrons to these overlapping Mn e_g orbitals leads to virtual excited states which can result in a reduction of the total energy of the system depending on the spin directions.[200] The relation between the SE interaction and

the symmetry of electron orbital is described by the Goodenough-Kanamori-Anderson rules which are summarized below: [201-204]

1. The 180° exchange interaction between two half-filled or two empty TM orbitals will be strongly AFM.

2. The 180° exchange interaction between one half-filled and one empty TM orbitals is weakly FM.

3. The 90° exchange interaction between two half-filled TM orbitals is weak and FM.
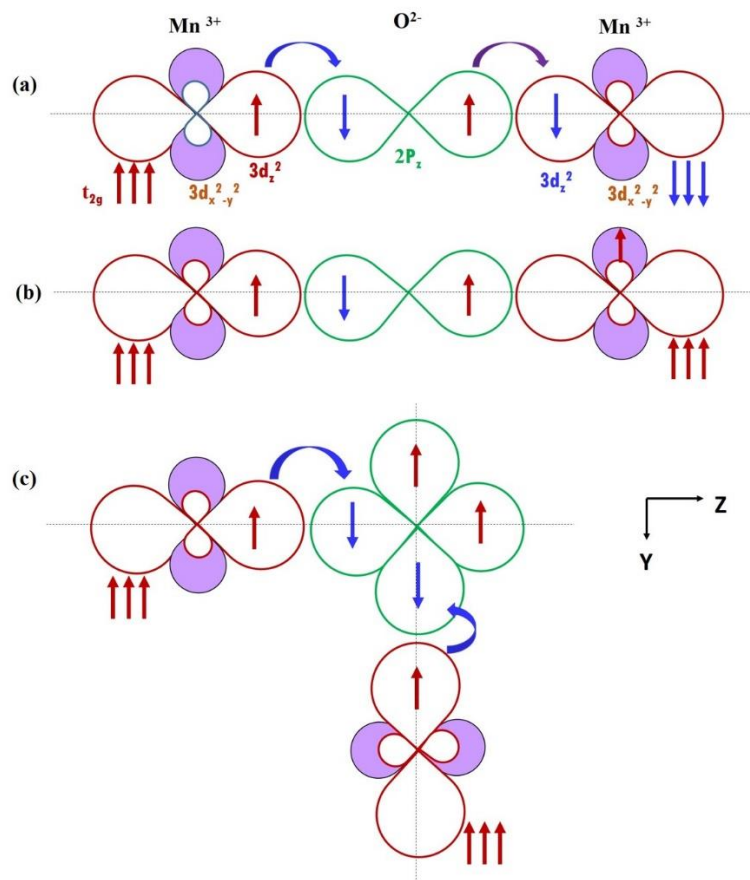
Fig. 2.9. SE interaction between Mn^{3+} ions in manganites.

DE is usually observed in mixed valence manganites containing Mn^{3+} and Mn^{4+} ions or Mn^{3+} and Mn^{2+} ions and is based on the real hopping of electrons between the manganese ions. The innermost electron in the $3d_{z^2}$ orbital of Mn^{3+} ion can hop via the O_{2p_z} orbital to the $3d_{z^2}$ orbital of Mn^{4+} ion and its spin gets coupled with those of both ion cores. The DE mechanism, observed in $La_{0.7}A_{0.3}MnO_3$ (A= tetravalent ions such as Te, Ce, etc), between Mn^{3+} and Mn^{2+} ion separated by an O^{2-} ion, is illustrated in Fig.

2.10 and the FM alignment due to the DE mechanism can be understood from the figure. The e_g electron on the Mn^{2+} ion hop to the e_g orbital of the Mn^{3+} ion favoring DE.
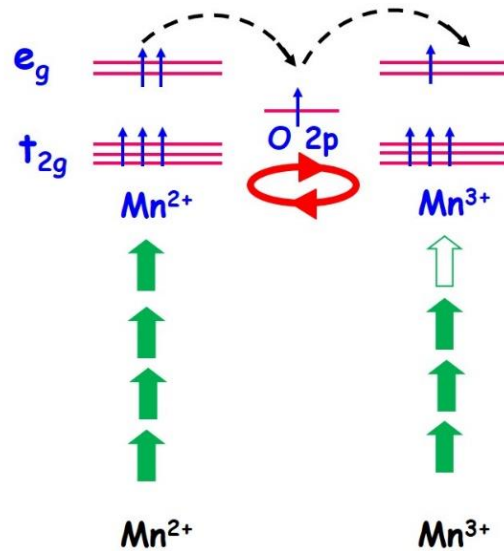
Fig. 2.10. DE interaction in manganites.

2.2.2. Theoretical Models explained in DMS materials

Many theoretical models have been proposed to explain the FM ordering in DMS materials. However, a complete understanding of the origin of FM interactions in these DMS materials is yet to be solved. The theoretical models most commonly used for explaining the FM in DMS materials include the RKKY model, Zener model, mean-field Zener model and the bound magnetic polaron.

2.2.2.1. RKKY model

The RKKY (Ruderman-Kittel-Kasuya-Yosida) interaction describes the magnetic interaction between the localized d or f electron spins (magnetic ion) and the delocalized conduction band electrons (sp-band). The localized moments in the 4f shell interact via electrons in the 5d/6s conduction band. As a result of RKKY interaction, the conduction electrons close to the magnetic ion are magnetized and act as an effective field to influence the polarization of neighbouring magnetic ions. RKKY interaction is long range and has an oscillatory dependence which decays with distance from the

magnetic ion, causing indirect SE interaction between two magnetic ions. This coupling, depending on the separation results in a parallel (FM) or an antiparallel (AFM) alignment of moments. The coupling takes the form of an r-dependent exchange interaction J_{RKKY} (r) given by

$$J_{RKKY}(r) \propto \frac{\cos(2k_F r)}{r^3} \qquad (2.7)$$

where, k_F is the radius of the Fermi surface. Thus the RKKY model is efficient when a high concentration of delocalized carriers is present in the host material. A schematic representation of RKKY interaction is shown in Fig. 2.11.
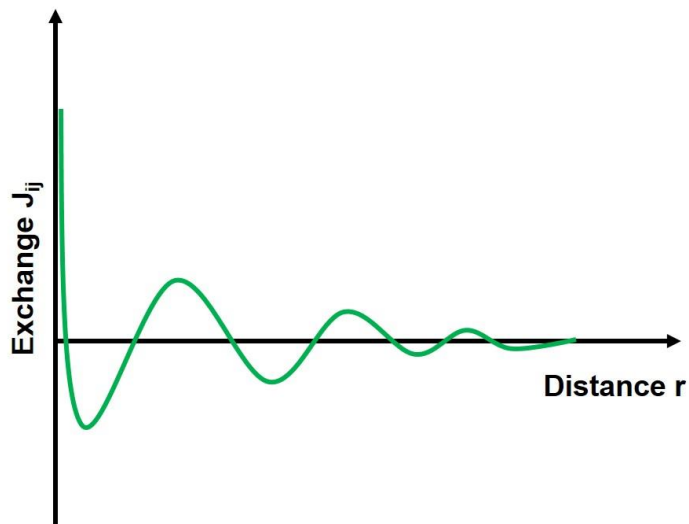
Fig. 2.11. RKKY interaction in metals.

2.2.2.2. Zener Model

Zener proposed the model of FM which is driven by the exchange interaction between carriers and localized spins.[205-207] In the Zener model, the direct exchange interaction between d shells of the adjacent TM atoms (SE) will lead to AFM ordering of the d shell spins because the TM-d shell is half-filled whereas the indirect coupling of spins through the itinerant carriers lead to FM ordering. Dietl *et al.* first explained the observed FM in Zinc Blende and $Ga_{1-x}Mn_xAs$ based on the Zener model.[208] According to him, the divalent Mn^{2+} ions in $Ga_{1-x}Mn_xAs$ provide the localized spins and at the same time act as acceptors which compensate for the deep antisite donors present in

GaAs and produce p-type conduction in them. In the Zener model, the FM ordering was due to the spin-polarized conduction electrons, while in $Ga_{1-x}Mn_xAs$, the FM ordering was mediated by spin-polarized free holes.

2.2.2.3. The mean-field Zener model

The mean-field Zener model was proposed by Dietl *et al.*,[208] which is based on the original model of Zener[206] and the RKKY model. In this model, the delocalized hole carriers mediate an RKKY-like interaction among localized TM ions resulting in FM. The holes need to be spatially delocalized or weakly localized to induce long-range FM. The mean-field Zener model takes into account the anisotropy of the carrier-mediated exchange interaction associated with the spin-orbit coupling in the valence band of the host material in determining the magnitude of the T_C, the carrier correlation and the direction of the easy axis in p-type FM semiconductors. This model predicts that ZnO and Mn-doped p-type GaN are FM with T_C values above room temperature. This model also indicates the dominance of hole exchange of Sato *et al.*[209] and predicts that the high T_C ferromagnetism could also be stabilized in n-type ZnO.

2.2.2.4. Bound Magnetic Polaron model

The polaron percolation theory was developed by Kaminski and Das Sarma [210] in 2002 for explaining the magnetic behaviour in $Mn_xGa_{1-x}As$ and later in 2005, Coey *et al.* applied the theory to magnetically doped oxides.[211] According to the polaron percolation theory, the exchange interaction of localized holes with magnetic impurities leads to the formation of bound magnetic polarons (BMPs). The polaron model can be applied to both n-type and p-type host materials.[212] The BMP model could successfully explain the FM ordering in the transition metal doped ZnO. A BMP consists of a collection of electrons (or holes) bound to impurity atoms through exchange interactions within an orbit. To explain the physics of this polaron model, let us consider two neighbouring polarons. The localized holes of these polarons both act on the impurities surrounding them, producing a high magnetic field. This effective magnetic field is maximum when the spins of the localized polarons are parallel and the magnetic impurity atoms can effectively couple with one another via their respective coupling to

a single polaron. The coupling with polaronic electron is parallel or anti-parallel depending on whether the cation 3d orbital is less than half full or half full or more respectively. These configurations differ in energy and result in a non-zero spin flip energy which is a characteristic of BMPs. Hence, by their coupling to the polaron, the cation impurities become ferromagnetically coupled to each other. The net energy of the system can be lowered by parallel alignment of ions, since they all interact with carriers the same way. At low temperatures, the s-d exchange energy exceeds k_BT, so the mutual alignment of ions and carriers results in an FM "bubble". However, at higher temperatures, the spins of magnetic ions are not constant. Coey *et al.* proposed a model for n-type DMS materials based on exchange interaction between highly correlated narrow impurity bands and the atomic spin moments on dopant ions.[211] The defects such as oxygen vacancies act as the electron source and these electrons interact with all magnetic ions that lie within their orbit. If there is enough number of magnetic spins within the orbital, the electron is completely spin polarized. Furthermore, the atomic magnetic moments have an indirect exchange interaction mediated by carriers, resulting in FM ordering. Fig. 2.12 shows a schematic of BMP interaction in oxides.
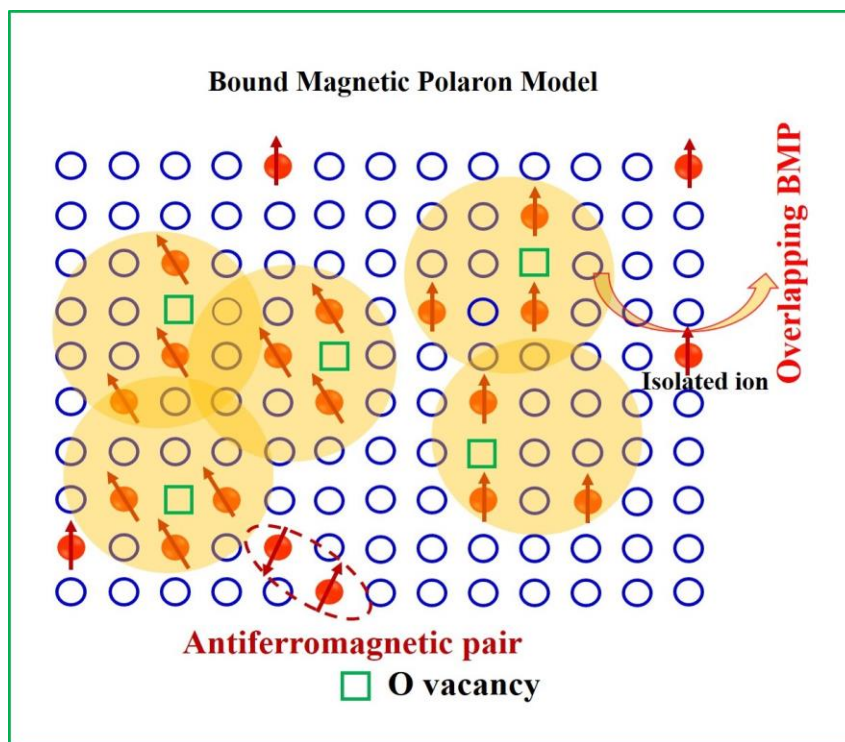
Fig. 2.12. Schematic representation of BMP interaction in oxides

2.2.3. Structure and Literature review on TiO_2 nanomaterials

TiO_2 crystallizes mainly into three phases: anatase, brookite and rutile. The rutile phase is found to be the most stable one. The anatase and brookite structures are converted to rutile form upon heating. The anatase and rutile structures belong to the tetragonal crystal structure while the brookite structure crystallizes into orthorhombic structure. The crystal structures of anatase, rutile and brookite are shown in Fig. 2.13.
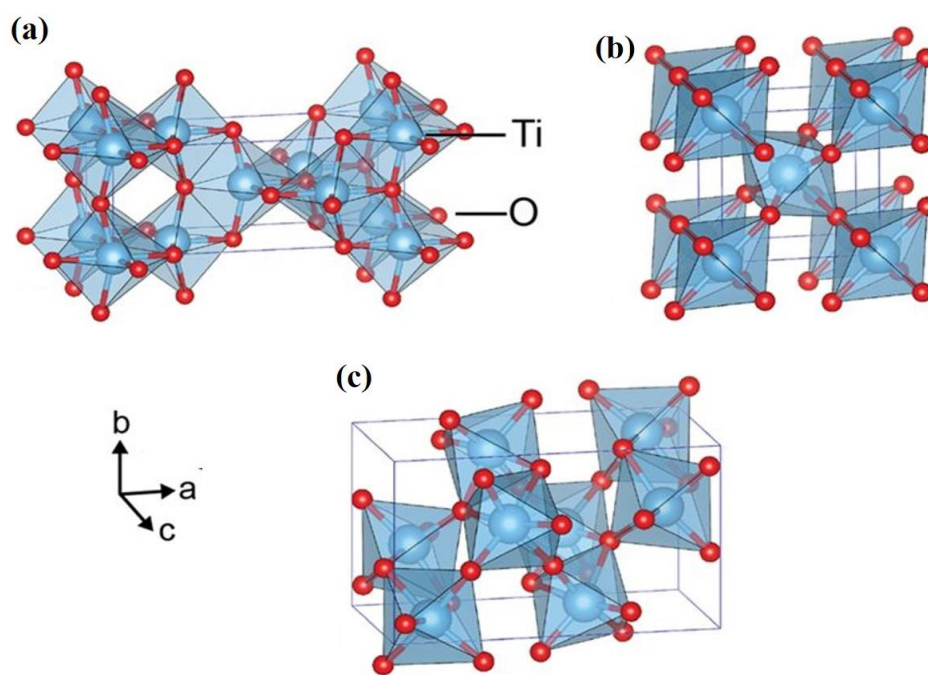
Fig. 2.13. Crystal structures of (a) Anatase, (b) Rutile and (c) Brookite [213]

Among the three polymorphs, rutile is the most stable and the most compact one. The different structures of TiO_2 are constituted by different arrangement of the same building block: a TiO_6 group where the titanium atom (the cation) sits in the center and is surrounded by six oxygen atoms (the anions) situated at the corners of a distorted octahedron. In the rutile phase, each octahedron is in contact with 10 neighbour octahedrons i.e., two sharing edge oxygen pairs and eight sharing corner oxygen atoms while in anatase structure, each octahedron is in contact with eight neighbours i.e. four sharing an edge and four sharing a corner. The octahedral linkage in brookite is such that three edges are shared per octahedron.[214] The lattice parameters of anatase, brookite and rutile phases are shown in Table 2.3.[215]

Table 2.3. Lattice parameters of Anatase, Brookite and Rutile phases

TiO_2	Space Group	Lattice Parameters			Number of Formula Units per unit cell (Z)
		a (Å)	b (Å)	c (Å)	
Anatase	$I4_1/amd$	3.785	3.785	9.514	4
Brookite	Pbca	5.456	9.182	5.143	8
Rutile	$P4_2/mnm$	4.594	4.594	2.959	2

2.2.3.1. Review on non-magnetic elemental substitution in TiO_2

Stoichiometric, bulk crystals of TiO_2 are essentially diamagnetic but undoped TiO_2 nanostructures show FM at room temperature which is attributed to oxygen vacancies,[216,217] Ti vacancies,[218,219] or Ti^{3+} ions[220] present on or near the interface. The oxygen vacancies or Ti interstitials can cause intrinsic defects in TiO_2 and magnetic clusters due to TM doping can induce extrinsic contributions ultimately leading to the controversies regarding the magnetic behavior.[219,221-225] Hence, it could be affirmed that defects associated with the system are mainly responsible for creating FM ordering in these systems.[226] It is interesting to find that some defect-containing undoped (without introducing any magnetic impurities in the materials) and other oxides[225,226] also exhibit RTFM although TiO_2 itself is intrinsically non-magnetic. Yoon *et al.*[223] observed high-temperature FM with a T_C up to 880 K in oxygen-deficient anatase TiO_2 film. Kim *et al.*[224] theoretically found that the FM in undoped TiO_2 was the result of the charge redistribution due to the oxygen-vacancy-induced lattice distortion. Zhou *et al.* observed FM in Ti^{3+} self-doped rutile TiO_2 single crystal prepared by oxygen ion irradiation method.[220] Zou *et al.* observed the co-existence of FM and PM in porous amorphous TiO_2 with a large number of Ti^{3+} prepared by a photochemical method[227] but it was quite interesting to find the diamagnetic nature of TiO_2 when the Ti^{3+} in TiO_2 was completely consumed by air which strongly confirmed that the magnetism of TiO_2 was intrinsic in nature associated with the Ti^{3+} species. Santara *et al.* observed oxygen vacancy induced above room temperature FM in undoped TiO_2 nanoporous nanoribbons.[228] Inspite of various studies based on oxygen vacancy/Ti^{3+} related defects mediated FM, the exact mechanism is still not very clear in the current stage. This invites further experimental and theoretical investigation on this unusual magnetic behavior.

Very few studies have reported about the origin of magnetic behavior of non-magnetic TM-doped TiO_2 such as Cu and Zn and the formation of both TM ion site vacancies and oxygen site vacancies. In 2005, Duhalde *et al.*[229] observed RTFM in Cu-doped TiO_2 where the observed FM was explained based on the formation of oxygen defects near the Cu ion. Hou *et al.* observed RTFM at 350 K in Cu-doped TiO_2 thin films grown by reactive magnetron sputtering and annealed in vacuum. They attributed the FM due to the presence of oxygen vacancies and the distance between nearest-neighbour copper atoms.[230] You *et al.* synthesized Cu-doped TiO_2 nanorods via a controlled hydrolysis method. $Ti_{1-x}Cu_xO_2$ nanorods with x varying from 1.7-3.2 at % displayed FM behaviour at room temperature which was explained on the basis of the concentration of oxygen vacancies present in the system.[231] Choudhary *et al.* found a reduction in band gap with Cu doping and attributed this to the formation of band states due to the oxygen defects present in the system.[221] Zheng *et al.* reported the observation of RTFM in Cu-doped anatase TiO_2 films grown by magnetron sputtering. Here FM was due to the creation of grain boundary defects. Also the presence of oxygen defects resulting in increasing the saturation moment of 0.19% Cu-doped TiO_2 thin film from 0.56 to 26.42 emu/cm^3. Zheng *et al.* also observed that this RTFM could be enhanced or destroyed corresponding to the low or high Cu concentration in TiO_2 via vacuum annealing.[232] Anitha *et al.* synthesized undoped and Cu-doped TiO_2 by peroxide sol-gel method and observed a weak FM superimposed on a diamagnetic background while Cu-doped TiO_2 samples exhibited a weak FM in the low-field region with a PM component in the high-field region. This low field FM behavior was attributed to the defects and oxygen vacancies present in the system.[233]

2.2.3.2. Review on ferromagnetic elemental substitution in TiO_2

Several authors have reported the study of Fe-doped TiO_2 nanocrystals to understand the modifications undergone by the TiO_2 lattice and for using Fe-doped TiO_2 for practical applications.[234,235] George *et al.*[236] reported the synthesis of Fe doped nanoparticles of TiO_2 containing 1–10 wt% Fe which was homogeneously distributed in the TiO_2 matrix by the spray pyrolysis technique. Very recently, Li *et al.*[237] reported the successive layer-by-layer doping method for homogeneous distribution of dopants in

nanoparticles. The Fe doping in TiO$_2$ was found to yield M$_s$ value ranging from 0.14 μ$_B$/Fe-ion to 2.4 μ$_B$/Fe-ion.[238-240] Xiaoyan *et al*. reported that ball milled α-Fe doped TiO$_2$ exhibits FM with T$_C$ = 650 K and M$_s$ = 0.15 μ$_B$/Fe-ion.[241] The observed FM was found to be an intrinsic property. Patel *et al*. observed RTFM in Ti$_{1-x}$Fe$_x$O$_{2-\delta}$ ($0 \leq x \leq 0.03$) nanoparticles synthesized by sol-gel route which was ascribed to the oxygen vacancy defects in the system and was explained in terms of the BMP model.[242] Santara *et al*. observed a 4.8 fold increase in RTFM in Fe-doped TiO$_2$ nanoribbons grown by solvothermal process, compared to the undoped due to the existence of oxygen vacancies. However, the RTFM decreases at higher Fe concentrations due to the AFM ordering between nearby Fe^{3+} ions caused by a super exchange interaction.[217] Navarro *et al*. reported the existence of FM in Fe-doped rutile TiO$_2$ nanopowders which was attributed to the formation of oxygen vacancies in the system.[243] Prajapati *et al*. reported RTFM in undoped and Fe-doped TiO$_2$ and attributed this to the oxygen vacancies present in the system.[244] Ahmed *et al*. observed RTFM in Fe-doped TiO$_2$ nanopowder samples and found that Fe-doped TiO$_2$ samples have a magnetic moment of 4.58 μ$_B$/Fe.[245]

Cobalt (Co) is an effective dopant to improve the optical as well as magnetic properties of TiO$_2$. The observation of RTFM in Co-doped TiO$_2$ thin films by Matsumoto *et al*.[187, 246] excited much interest in this area and several interesting results have been reported. Several reports in the literature show that Co doping can induce FM, PM or superparamagnetism in TiO$_2$ nanocrystals and thin films.[247-250] Shinde *et al*. reported Tc close to 650 K in laser deposited anatase Ti$_{1-x}$Co$_x$O$_{2-\delta}$ films under low doping regime and explained that it is due to intrinsic DMS effect. A T$_C$ up to 400 K was reported by several other authors in Co:TiO$_2$.[187,251-253] The highest Ms value of 1.7μ$_B$/Co-ion was measured by Stampe *et al*. in 7 at % Co-doped sample on LaAlO$_3$ substrate.[254] The M$_s$ values in the range of 0.94μ$_B$/Co-ion to 1.4 μ$_B$/Co-ion were reported by several authors.[187,251,252,255] In 2004, Shinde *et al*. observed superparamagnetic behavior of highly reduced Co-doped rutile film and this was attributed to arise from the presence of superparamagnetic Co clusters in the films at the interface.[256] Bryan *et al*. synthesized colloidal Co^{2+} doped TiO$_2$ nanorods and observed high TC FM and attributed the FM to the creation of grain boundary defects, proposed

to be oxygen vacancies at nanocrystal fusion interfaces.[257] Pereira *et al.* showed that oxygen vacancies play an important role in promoting long-range FM in bulk Co-doped TiO_2 which could be explained based on the concept of BMPs.[258] Santara *et al.*, pointed out the possibility of FM behavior in TiO_2 nanoparticles, which was assumed to be generated as a result of defects related to oxygen site deficiencies due to the Co incorporation into the TiO_2 lattice, where a mechanism for the origin of FM is given and is based on BMP formation.[259] In 2013, Kaushik *et al.* observed RTFM in 10% Co-doped TiO_2 with a Ms of 0.937 emu/g and H_C of 65 Oe, which was attributed to the intrinsic exchange interaction of magnetic moments.[260] PM behavior was observed by Tseng *et al.* in Co-doped TiO_2 nanorods while the undoped samples showed strong FM at room temperature.[261] In 2016, Anitha *et al.* reported PM behaviour in Co-doped TiO_2 nanocrystals which was attributed to an increased concentration of Co^{2+} ions and an increased presence of Co_3O_4 phase near the surface of the TiO_2 as a result of self-purification mechanism.[262]

Ni doping also opens up the possibilities of controlling the morphology[263] and tailoring the band gap. Hou *et al.* observed RTFM in Ni-doped TiO_2 thin films fabricated by reactive magnetron sputtering and explained the FM as originating from the doped matrix and the enhancement/suppression of FM is due to the increase/decrease of oxygen vacancies.[264] Recently, it is reported that Ni-doping can induce reversible FM in single crystals of rutile TiO_2[265] in which the role of Ni clusters are emphasized more as an extrinsic factor contributing to the magnetic moment. Parveen *et al.* also observed RTFM in Ni-doped TiO_2 thin films.[266] Another report suggests that the magnetic moment of mixed crystalline TiO_2 powders decreases with Ni doping which was attributed to oxygen vacancies destroying the spin ordering.[267] Dakhel *et al.* synthesized Ni-doped anatase TiO_2 by thermal co-decomposition of a mixture of metal complexes and revealed the importance of hydrogenation in boosting RTFM in Ni-doped samples.[268] A very few reports have explained the origin of different magnetic behavior and the formation of the oxygen site vacancies in Ni-doped TiO_2.

2.2.3.3. Review on antiferromagnetic elemental substitution in TiO$_2$

Doping transition elements such as Fe, Co and Ni induces weak FM in TiO$_2$ as per the recent reports.[242] However, Cr itself is AFM at 293 K and there are various reports on the origin of FM in Cr-doped TiO$_2$ nanostructures. In comparison to the FM TMs such as Fe, Co and Ni, Cr can be considered as a nonmagnetic transition element intrinsically and as a result, FM may not be observed as a result incorporation. However, Cr^{3+} ions arising as a result of Cr doping is expected to show 3d^3 high-spin electronic configuration, ultimately leading to increased PM moment in the TiO$_2$ system.[269-271] The origin of FM nature was attributed to the formation of BMPs arising due to the coupling between the oxygen vacancies and the unpaired electrons of Cr. [269-271] The solubility limit of Cr was found to be 16 at % and its M$_s$ value was found to vary from 2.9 μ_B/Cr-ion to 0.9 μ_B/Cr-ion with increase in Cr concentration from 0.06 to 0.12%.[272-274] Patel *et al.* reported the observance of RTFM in Cr-doped TiO$_2$ nanorods synthesized via hydrothermal method and attributed them to the oxygen vacancies existing in the system.[269] Similarly, oxygen vacancies played a crucial role in enhancing FM in Cr-doped anodic TiO$_2$ nanotubes.[275] Da Pieve *et al.* reported that in Cr-doped TiO$_2$, F-center mediated mechanism is not responsible for inducing FM and proposed an alternative mechanism of SE interaction between the t$_{2g}$ electrons coupled with structural defects and oxygen vacancies for FM.[271] The creation of grain boundary defects at the interfaces together with oxygen vacancies was also proposed as the mechanism for the origin of FM in Cr-doped TiO$_2$.[257] Santara *et al.* observed a strong correlation between oxygen vacancies and RTFM in undoped and Cr-doped TiO$_2$ grown by hydrothermal method and annealed in vacuum.[276] Haq *et al.* observed FM in 1.5, 3 and 4.5 % Cr doped TiO$_2$ and attributed it to the coupling of neighboring Cr^{3+} ions with the oxygen vacancies.[277] Naseem *et al.* also observed RTFM in undoped and Cr-doped TiO$_2$ synthesized by sol-gel method which was presumed to be due to oxygen vacancy related defects, distribution of dopant concentration and their exchange interactions in TiO$_2$ nanoparticles.[278]

Many reports have explained the observation of RFTM in Mn-doped TiO$_2$ nanoparticles, thin films, etc. The Mn^{2+} ions are considered as a PM center in the magnetic systems and since a long back it is used as a spin injector in most of the

technological applications.[279] RTFM was observed in Mn-doped TiO$_2$ film prepared by PLD which was attributed to the coupling of Mn ions to holes.[280] On the contrary, Hong *et al.* did not observe magnetism in Mn-doped TiO$_2$ film prepared by PLD technique. He reported that at low dopant concentration ($<$ 5%), the Mn atoms substitute for the Ti atoms while maintaining the anatase structure, which enhances the magnetic moment of the TiO$_2$ lattice. But at higher dopant concentrations, ($>$ 10%), Mn doping destroys FM along with the destruction of anatase structure.[281] It is interesting to observe that doping of Mn ions into TiO$_2$ lattice is a tedious process as a result of the self-purification mechanism and hence the possibility of Mn to get expelled onto surface of the TiO$_2$ nanocrystals cannot be ruled out completely leading to controversial reports on magnetic behavior as well.[282] Bhattacharya *et al.* observed FM at low doping concentrations in Mn-doped TiO$_2$ nanocrystals encapsulated in a carbon layer and attributed it to the coupling between Mn spins and the carriers, while at higher doping concentrations, a PM behaviour was observed.[283] Tian *et al.* observed RTFM in polycrystalline samples of Mn-doped TiO$_2$ with a M$_s$ of 0.019μ_B/Mn which was attributed to the presence of oxygen vacancies present in the sample. However, the magnetization decreases with increasing annealing temperature which was attributed to the decrease in the number of oxygen vacancies with increasing annealing temperature.[284] The coexistence of FM and AFM was observed by Mie *et al.* in Mn-doped TiO$_2$ nanoparticles.[285] As a consequence of the difficulty in doping process associated with TiO$_2$ wide band gap materials, various magnetic behavior are expressed by Mn-doped TiO$_2$ nanocrystals which include FM, superparamagnetism, PM and AFM behavior.[286-289]

2.2.3.4. Review on effect of annealing atmosphere in TiO$_2$

Recently, a lot of attention has been given to produce dopant free pure TiO$_2$ phase which can overcome this limitation. It has also been found that without doping, band gap can be reduced by using proper synthesis techniques like reduction or oxidation of TiO$_2$ in proper environment through which defects such as oxygen vacancies and Ti^{3+} can be enhanced/reduced which largely modify the optical and magnetic properties. Recently black TiO$_2$ obtained through hydrogenation of TiO$_2$ has

attracted great attention, which has been used as an effective technique to increase the visible and infrared light absorption under different conditions. Chen *et al.* produced black TiO_2 nanoparticles with 1.0 eV band gap through high-pressure hydrogenation of crystalline TiO_2 [290] which was obtained due to surface disorder. Chen and Mao first reported introduction of in gap defect levels in black TiO_2 due to lattice distortion caused by surface hydrogen. Naldoni *et al.* observed Ti^{3+} inside hydrogenated black TiO_2 particles.[291] After that, Liu *et al.* studied in detail the relation between lattice distortion and VBM shift.[292] A successive work by Chen reported that hydrogenation of surfaces induces a deep level 1.8 eV above VBM giving rise to a greatly narrowed band gap due to distortion of surface lattice.[293] Self-doping with Ti^{3+} has also been used which shows the role of point defects such as oxygen vacancies and Ti interstitial in reducing the band gap of TiO_2.[294] It has also been found that bulk defects also affect the absorption giving rise to enhanced photocatalytic efficiency. Zhou *et al.* reported black color of ordered anatase in a mesoporous structure after hydrogenation in high temperature.[295] Therefore, the black color of anatase TiO_2 along with much reduced band gap have been attributed to multiple origins which invites great attention. The concentration of intrinsic defects mostly depends on the growth conditions. Various techniques have been used to produce surface oxygen vacancies and Ti^{3+} such as UV irradiation, annealing TiO_2 in vacuum or in reducing atmosphere, ion sputtering and high energy particle bombardment etc. Surface disorder and point defects such as O_v and Ti_i not only play the role in reducing the band gap and enhancing the optical absorption, these also largely affect the magnetic behavior of the materials.

Reports suggest that doping can alter the optical and magnetic properties of TiO_2 nanocrystals. Continuous efforts have been made to dope metal and/or non-metal impurities to reduce the band gap and to extend the solar absorption to visible and IR region.[296-301] Along with changes in band gap, doping can change the structural as well as magnetic properties. It can induce disorder in the structures and produce defects. Despite the tremendous efforts on TiO_2 based DMSs to improve its magnetic properties; the origin of RTFM in these compounds is still unclear. Different methods have been suggested for the synthesis of TiO_2 nanocrystals which includes the sol-gel technique,

electrochemical coating, hydrothermal method, chemical vapor deposition, etc.[263,302-306] Sol-gel technique is often considered as an efficient process to precisely control the stoichiometry and is a low-temperature synthesis technique giving high crystallinity and high purity samples.[267,307,308] Hence, we have adopted a simple sol-gel route for the synthesis of TM-doped TiO_2 nanocrystals and investigate the role of TM ions and oxygen mediated defects in promoting magnetism in TiO_2 and hence TM-doped TiO_2 could serve as an efficient material for DMS application.

2.3. References

1. C. Han, Z. Li, S. Dou, Recent progress in thermoelectric materials, *Chin. Sci. Bull.* 59 (2014) 2073.
2. G. A. Slack, New Materials and Performance Limits for Thermoelectric Cooling, *In: CRC Handbook of Thermoelectrics*. Rowe DM, editor. Boca Raton, FL: *CRC Press* (1995).
3. J.-C. Zheng, Recent advances on thermoelectric materials, *Front. Phys. China*, 3(3) (2008) 269.
4. Y. C. Lan, A. J. Minnich, G. Chen, Z. F. Ren, Enhancement of thermoelectric figure-of-merit by a bulk nanostructuring approach, *Adv. Funct. Mater.,* 20 (2010) 357.
5. H. J. Goldsmid, In Handbook of Thermoelectrics, *CRC Press LLC* (1995).
6. Y. G. Deng, J. Liu, Recent advances in direct solar thermal power generation, *J. Renew. Sustain. Energy*, 1(2009) 052701.
7. Z. G. Chen, G. Han, L. Yang, L. Cheng, J. Zou, Nanostructured thermoelectric materials: Current research and future challenge, *Prog. Nat. Sci.* 22 (2012) 535.
8. J. Y. Cho, Y. S. Lim, S. M. Choi, K. H. Kim, W. S. Seo, H. H. Park, Thermoelectric properties of spark plasma-sintered In_4Se_3-In_4Te_3, *J. Electron. Mater.*, 40 (2011) 1024.
9. G. A. Slack, New Materials and Performance Limits for Thermoelectric Cooling, *In: CRC Handbook of Thermoelectrics*. Rowe DM, editor. Boca Raton, FL: *CRC Press* (1995).
10. J. He, Y. F. Liu, Oxide thermoelectrics: the challenges, progress, and outlook, *J. Mater. Res.*, 26 (2011) 1762.
11. O. Bubnova, X. Crispin, Towards polymer-based organic thermoelectric generators, *Energy Environ. Sci.*, 5 (2012) 9345.
12. D. M. Rowe, Recent developments in thermoelectric materials, *Appl. Energy,* 24 (1986) 139.
13. J. R. Sootsman, D. Y. Chung, M. G. Kanatzidis, New and old concepts in thermoelectric materials, *Angew. Chem. Int. Ed.*, 48 (2009) 8616.
14. W. S. Liu, X. Yan, G. Chen, Z. Ren, Recent advances in thermoelectric nanocomposites, *Nano Energy*, 1 (2012) 42.
15. Z. Li, Q. Sun, X. D. Yao, Z. H. Zhu, G. Q. Lu, Semiconductor nanowires for thermoelectrics, *J. Mater. Chem.*, 22 (2012) 22821.

16. Z. Li, O. Kurtulus, F. Nan, Z. Wang, A. Kornowski, U. Pietsch, A. Mews, Controlled synthesis of CdSe nanowires by solution–liquid–solid method, *Adv. Funct. Mater.*, 19 (2009) 3650.
17. Z. Li, L. N. Cheng, Q. Sun, Z. Zhu, M. J. Riley, M. Alijada, Z. Cheng, X. Wang, G. R. Hanson, S. Z. Qiao, S.C. Smith, G.Q. Lu, Diluted magnetic semiconductor nanowires prepared by the solution–liquid–solid method, *Angew. Chem. Int. Ed.*, 49 (2010) 2777.
18. Z. Li, A. J. Du, Q. Sun, M. Alijada, L. N. Cheng, M. J. Riley, Z. H. Zhu, Z. X. Cheng, X. L. Wang, J. Hall, E. Krausz, S. Z. Qiao, S. C Smith, G.Q. Lu, Cobalt-doped cadmium selenide colloidal nanowires, *Chem. Commun.*, 47 (2011) 11894.
19. Z. Li, A. J. Du, Q. Sun, M. Alijada, Z. H. Zhu, G. Q. Lu, Field-effect transistors fabricated from diluted magnetic semiconductor colloidal nanowires, *Nanoscale,* 4 (2012) 1263.
20. M. Rull-Bravo, A. Moure, J. F. Fernández, M. Martín-González, Skutterudites as thermoelectric materials: revisited, *RSC Adv.*, 5 (2015) 41653.
21. C. -J. Yao , H. -L. Zhang, Q. Zhang, Recent Progress in Thermoelectric Materials Based on Conjugated Polymers, *Polymers*, 11 (2019) 107.
22. Y. J. Wang, D. P. Wilkinson, J. Zhang, Noncarbon support materials for polymer electrolyte membrane fuel cell electrocatalysts, *Chem. Rev.*, 111 (2011) 7625.
23. A. A. Gewirth, M. S. Thorum, Electroreduction of dioxygen for fuel-cell applications: materials and challenges, *Inorg. Chem.,* 49 (2010) 3557.
24. G. Q. Zhang, S. Finefrock, D. X. Liang, G. G. Yadav, H. Yang, H. Fang, Y. Wu, Semiconductor nanostructure-based photovoltaic solar cells, *Nanoscale,* 3 (2011) 2430.
25. M. Gratzel, Photoelectrochemical cells, *Nature,* 414 (2001) 338.
26. J. M. Tarascon, M. Armand, Issues and challenges facing rechargeable lithium batteries, *Nature,* 414 (2001) 359.
27. H. Li, Z. X. Wang, L. Q. Chen, X. Huang, Research on advanced materials for Li-ion batteries, *Adv. Mater.,* 21 (2009) 4593.
28. K. Ikoma, M. Munekiyo, K. Furuya, M. Kobayashi, T. Izumi, K. Shinohara, Thermoelectric generator for gasoline engine vehicles using Bi_2Te_3 modules, *J. Jpn. Inst. Met.,* 63 (1999) 1475.
29. R. Venkatasubramanian, E. Siivola, T. Colpitts, B. O'Quinn, Thin-film thermoelectric devices with high room-temperature figures of merit, *Nature,* 413 (2001) 597.
30. H. Y. Lv, H. J. Liu, J. Shi, X. F. Tang, C. Uher, Optimized thermoelectric performance of Bi_2Te_3 nanowires, *J. Mater. Chem. A*, 1 (2013) 6831.
31. X. F. Tang, W. J. Xie, H. Li, W. Zhao, Q. Zhang, Preparation and thermoelectric transport properties of high-performance p-type Bi_2Te_3 with layered nanostructure, *Appl. Phys. Lett.,* 90 (2007) 012102.
32. T. C. Harman, P. J. Taylor, M. P. Walsh, B. E. LaForge, Quantum dot superlattice thermoelectric materials and devices, *Science,* 297 (2002) 2229.

33. T. C. Harman, M. P. Walsh, B. E. LaForge, G. W. Turner, Nanostructured thermoelectric materials, *J. Electron. M*ater., 34 (2005) L19.

34. A. Lalonde, Y. Z. Pei, G. J. Snyder, Reevaluation of $PbTe_{1-x}I_x$ as high performance n-type thermoelectric material, *Energy Environ. Sci.*, 4 (2011) 2090.

35. Y. Z. Pei, A. Lalonde, S. Iwanaga, G. J. Snyder, High thermoelectric figure of merit in heavy hole dominated PbTe, *Energy Environ. Sci*, 4 (2011) 2085.

36. Y. Z. Pei, X. Y. Shi, A. Lalonde, H. Wang, L. Chen, G. J. Snyder, Convergence of electronic bands for high performance bulk thermoelectrics, *Nature,* 473 (2011) 66.

37. J. Q. He, J. R. Sootsman, S. N. Girard, J. C. Zheng, J. Wen, Y. Zhu, M. G. Kanatzidis, V. P. Dravid, On the origin of increased phonon scattering in nanostructured PbTe based thermoelectric materials, *J Am. Chem. Soc.,* 132 (2010) 8669.

38. P. F. P. Poudeu, J. J. D'Angel, A. D. Downey, J. L. Short, T. P. Hogan, M. G. Kanatzidis, High thermoelectric figure of merit and nanostructuring in bulk p-type $Na_{1-x}Pb_mSb_yTe_{m+2}$, *Angew. Chem. Int. Ed.,* 45 (2006) 3835.

39. K. F. Hsu, S. Loo, F. Guo, W. Chen, J. S. Dyck., C. Uher, T. Hogan, E. K. Polychroniadis, M. G. Kanatzidis, Cubic $AgPb_mSbTe_{2+m}$: bulk thermoelectric materials with high figure of merit, *Science,* 303 (2004) 818.

40. K. Biswas, J. Q. He, Q. C. Zhang, G. Wang, C. Uher, V. P. Dravid, M. G. Kanatzidis, Strained endotaxial nanostructures with high thermoelectric figure of merit, *Nat. Chem.,* 3 (2011) 160.

41. J. R. Sootsman, H. J. Kong, C. Uher, J. J. D'Angel, C. I. Wu, T. P. Hogan, T. Caillat, M. G. Kanatzidis, Large enhancements in the thermoelectric power factor of bulk PbTe at high temperature by synergistic nanostructuring, *Angew. Chem. Int. Ed.*, 47 (2008) 8618.

42. Y. Z. Pei, J. Lensch-Falk, E. S. Tobber, D. L. Medlin, G.J. Synder, High thermoelectric performance in PbTe due to large nanoscale Ag_2Te precipitates and La doping, *Adv. Funct. Mater*., 21(2011) 241.

43. K. Ahn, M. K. Han, J. Q. He, J. Androulakis, S. Ballikaya, C. Uher, V. P. Dravid, M. G. Kanatzidis, Exploring resonance levels and nanostructuring in the PbTe–CdTe system and enhancement of the thermoelectric figure of merit, *J. Am. Chem. Soc.,* 132 (2010) 5227.

44. J. Androulakis, C. H. Lin, H. J. Kong, C. Uher, C.-I Wu, T. Hogan, B. A. Cook, T. Caillat, K. M. Paraskevopoulos, M. G. Kanatzidis, Spinodal decomposition and nucleation and growth as a means to bulk nanostructured thermoelectrics: enhanced performance in $Pb_{1-x}Sn_xTe–PbS$, *J. Am. Chem. Soc.,* 129 (2007) 9780.

45. B. Kanishka, J. Q. He, D. B. Ivan, High-performance bulk thermoelectrics with all-scale hierarchical architectures, *Nature,* 489 (2012) 414.

46. M. Ibanez, R. Zamani, S. Gorsse, J. Fan, S. Ortega, D. Cadavid, J. R. Morante, J. Arbiol, A. Cabot, Core-shell nanoparticles as building blocks for the bottom-up production of functional nanocomposites: PbTe–PbS thermoelectric properties, *ACS Nano*, 7 (2013) 2573.

47. H. Wang, Y. Z. Pei, A. D. Lalonde, J. F. Synder, Heavily doped p-type PbSe with high thermoelectric performance: an alternative for PbTe, *Adv. Mater.,* 23 (2011) 1366.

48. Q. Y. Zhang, H. Wang, W. S. Liu, H. Wang, B. Yu, Q. Zhang, Z. Tian, G. Ni, S. Lee, K. Esfarjani, G. Chen, Z. Ren, Enhancement of thermoelectric figure-of-merit by resonant states of aluminium doping in lead selenide, *Energy Environ. Sci.*, 5 (2012) 5246.

49. K. Ahn, H. Shin, J. Im, S. H. Park, I. Chung, ZnTe Alloying Effect on Enhanced Thermoelectric Properties of p-Type PbTe, *ACS Appl. Mater. Interfaces*, 9 (4) (2017) 3766.

50. E. A. Skrabek, D. S. Trimmer in '*CRC Handbook of Thermoelectrics*', ed. Rowe, D. M., 267–275, CRC, Boca Raton (1995).

51. C. L. Wan, Y. F. Wang, N. Wang, W. Norimatsu, M. Kusunoki, K. Koumoto, K., Development of novel thermoelectric materials by reduction of lattice thermal conductivity, *Sci. Technol. Adv. Mater.,* 11 (2010) 1.

52. G. S. Nolas, J. Poon, M. Kanatzidis, Recent developments in bulk thermoelectric materials, *MRS Bull.,* 31 (2006) 199.

53. R. G. Yang, G. Chen, Nanostructured thermoelectric materials: from superlattices to nanocomposites, *Mat.Integration*, 18 (2006) 31.

54. A. I. Hochbaum, R. Chen, R. D. Delgado, W. Liang, E. C. Garnett, M. Najarian, A. Majumdar, P. Yang, Enhanced thermoelectric performance of rough silicon nanowires, *Nature*, 451 (2008) 163.

55. M. S. Dresselhaus, G. Chen, M. Y. Tang, R. G. Yang, H. Lee, D. Z. Wang, Z. F. Ren, J. P. Fleurial, P. Gogna, New directions for low-dimensional thermoelectric materials, *Adv. Mater.,*19 (2007) 1043.

56. A. M. Rao, X. H. Ji, T. M. Tritt, Properties of nanostructured onedimensional and composite thermoelectric materials, *MRS Bull.,* 31 (2006) 218.

57. L. D. Hicks, T. C. Harman, M. S. Dresselhaus, Use of quantum-well superlattices to obtain a high figure of merit from nonconventional thermoelectric materials, *Appl. Phys. Lett.,* 63 (1993) 3230.

58. L. D. Hicks, T. C. Harman, X. Sun, M. S. Dresselhaus, Experimental study of the effect of quantum-well structures on the thermoelectric figure of merit, *Phys. Rev. B*, 53 (1996) 10493.

59. H. Bottner, G. Chen, R. Venkatasubramanian, Aspects of thin-film superlattice thermoelectric materials, devices, and applications, *MRS Bull.,* 31 (2006) 211.

60. J. -H. Bahk, A. Shakouri, Enhancing the thermoelectric figure of merit through the reduction of bipolar thermal conductivity with heterostructure barriers, *Appl. Phys. Lett.,* 105 (2014) 052106.

61. L. D. Zhao, H. J. Wu, S. Q. Hao, C. I. Wu, X. Y. Zhou, K. Biswas, J. Q. He, T. P. Hogan, C. Uher, C. Wolverton, V. P. Dravid, M. G. Kanatzidis, All-scale hierarchical thermoelectrics: MgTe in PbTe facilitates valence band convergence and suppresses bipolar thermal transport for high performance, *Energy Environ. Sci.,* 6 (2013) 3346.

62. Y. Pei, H. Wang, G. J. Snyder, Band engineering of thermoelectric materials, *Adv. Mater.*, 24 (2012) 6125.

63. N. Boukhris, H. Meradji, S. Ghemid, S. Drablia, F. E. Hassan, Ab initio study of the structural, electronic and thermodynamic properties of $PbSe_{1-x}S_x$, $PbSe_{1-x}Te_x$ and $PbS_{1-x}Te_x$ ternary alloys, *Phys. Scr.,* 83 (2011) 065701.

64. K. Hoang, S. D. Mahanti, M. G. Kanatzidis, Impurity clustering and impurity induced bands in PbTe-, SnTe-, and GeTe-based bulk thermoelectrics. *Phys. Rev. B.,* 81 (2010) 115106.

65. Y. Z. Pei, N. A. Heinz, G. J. Snyder, Alloying to increase the band gap for improving thermoelectric properties of Ag_2Te, *J. Mater. Chem.,* 21 (2011) 18256.

66. A. J. Minnich, M. S. Dresselhaus, Z. F. Ren, G. Chen, Bulk nanostructured thermoelectric materials: current research and future prospects, *Energy Environ. Sci.,* 2 (2009) 466.

67. Y. Pei, A. F. May, G. J. Snyder, Self-tuning the carrier concentration of $PbTe/Ag_2Te$ composites with excess Ag for high thermoelectric performance, *Adv. Energy Mater.*, 1 (2011) 291.

68. A. I. Boukai, Y. Bunimovich, J. Tahir-Kheli, J. –K. Yu, W. A. Goddard III, J. R. Heath, Silicon nanowires as efficient thermoelectric materials, *Nature*, 451 (2008) 168.

69. J. P. Heremans, M. S. Dresselhaus, L. E. Bell, D. T. Morelli, When thermoelectrics reached the nanoscale, *Nat. Nano.*, 8 (2013) 471.

70. W. Kim, R. Wang, A. Majumdar, Nanostructuring expands thermal limits, *Nano Today,* 2 (2007) 40.

71. K. Biswas, J. He, I. D. Blum, C.-I Wu, T. P. Hogan, D. N. Seidman, V. P. Dravid, M. G. Kanatzidis, High-performance bulk thermoelectrics with all-scale hierarchical architectures, *Nature*, 489 (2012) 414.

72. Y. N. Xia, P. D. Yang, Y. G. Sun, Y. Y. Wu, B. Mayers, B. Gates, Y. D. Yin, F. Kim, Y. Q. Yan, One-dimensional nanostructures: Synthesis, characterization, and applications, *Adv. Mater.*, 15 (2003) 353.

73. R. Venkatasubramanian, E. Siivola, T. Colpitts, B. O'Quinn, Thin-film thermoelectric devices with high room-temperature figures of merit, *Nature,* 413 (2001) 597.

74. X. A. Fan, J. Y. Yang, Z. Xie, K. Li, W. Zhu, X. K. Duan, C. J. Xiao, Q. Q. Zhang, Bi_2Te_3 hexagonal nanoplates and thermoelectric properties of n-type Bi_2Te_3 nanocomposites, *J. Phys. D Appl. Phys.*, 40 (2007) 5975.

75. W. G. Lu, Y. Ding, Y. X. Chen, Z. L. Wang, J. Y. Fang, Bismuth telluride hexagonal nanoplatelets and their two-step epitaxial growth, *J. Am. Chem. Soc.,* 127 (2005) 10112.

76. Y. M. Lin, M. S. Dresselhaus, Thermoelectric properties of superlattice nanowires, *Phys. Rev. B,* 68 (2003) 075304.

77. L. Yang, Z. –G. Chen, M. Hong, G. Han, J. Zou, Enhanced thermoelectric performance of nanostructured Bi_2Te_3 through significant phonon scattering, *ACS Appl. Mat. Interfaces,* 7 (2015) 23694.

78. Z. –G. Chen, L. Yang, S. Ma, L. Cheng, G. Han, Z.-d Zhang, J. Zou, Paramagnetic Cu-doped Bi_2Te_3 nanoplates, *Appl. Phys. Lett.,* 104 (2014) 053105.

79. L. Cheng, Z. G. Chen, L. Yang, G. Han, H. Y. Xu, G. J. Snyder, G. Q. Lu, J. Zou, T-Shaped Bi_2Te_3–Te heteronanojunctions: epitaxial growth, structural modeling, and thermoelectric properties, *J. Phys. Chem. C,* 117 (2013) 12458.

80. W. Kim, J. Zide, A. Gossard, D. Klenov, S. Stemmer, A. Shakouri, A. Majumdar, Thermal conductivity reduction and thermoelectric figure of merit increase by embedding nanoparticles in crystalline semiconductors, *Phys. Rev. Lett.,* 96 (2006) 045901.

81. W. G. Zeier, J. Schmitt, G. Hautier, U. Aydemir, Z. M. Gibbs, C. Felser, G. J. Snyder, Engineering half-Heusler thermoelectric materials using Zintl chemistry, *Nat. Rev. Mat.* 1 (2016) 16032.

82. P. Gary Wiederrecht, Handbook of Nanoscale Optics and Electronics. Elsevier; (2010) 75.

83. B. Poudel, Q. Hao, Y. Ma, Y. Lan, A. Minnich, B. Yu, X. Yan, D. Wang, A. Muto, D. Vashaee, X. Chen, J. Liu, M. S. Dresselhaus, G. Chen, Z. Ren, High-thermoelectric performance of nanostructured bismuth antimony telluride bulk alloys, *Science,* 320 (2008) 634.

84. W. J. Xie, J. He, H. J. Kang, X. Tang, S. Zhu, M. Laver, S. Wang, J. R. D. Copley, C. M. Brown, Q. Zhang, T. M. Tritt, Identifying the specific nanostructures responsible for the high thermoelectric performance of (Bi, Sb)$_2$Te$_3$ nanocomposites. *Nano Lett.,* 10 (2010) 3283.

85. X. Yan, B. Poudel, Y. Ma, W. S. Liu, G. Joshi, H. Wang, Y. Lan, D. Wang, G. Chen, Z. F. Ren, Experimental studies on anisotropic thermoelectric properties and structures of n-type $Bi_2Te_{27}Se_{0.3}$, *Nano Lett.*, 10 (2010) 3373.

86. Z. Ferdows, L. Roger, Thermoelectric properties of Bi_2Te_3 atomic quintuple thin films, *Appl. Phys. Lett.*, 97 (2010) 212102.

87. W. S. Liu, Q. Y. Zhang, Y. C. Lan, S. Chen, X. Yan, Q. Zhang, H. Wang, D. Wang, G. Chen, Z. Ren, Thermoelectric property studies on Cu-doped n-type $Cu_xBi_2Te_{2.7}Se_{0.3}$ nanocomposites. *Adv. Energy Mater.*, 1 (2011) 577.

88. D. K. Ko, Y. J. Kang, C. B. Murray, Enhanced thermopower via carrier energy filtering in solution-processable Pt–Sb_2Te_3 nanocomposites. *Nano Lett.,* 11(2011) 2841.

89. G. Q. Zhang, B. Kirk, L. A. Jauregui, H. Yang, X. Xu, Y. P. Chen, Y. Wu, Rational synthesis of ultrathin n-type Bi_2Te_3 nanowires with enhanced thermoelectric properties. *Nano Lett.,* 12 (2012) 56.

90. G. Q. Zhang, H. Y. Fang, H. R. Yang, L. A. Jauregui, Y. P. Chen, Y. Wu, Design principle of telluride-based nanowire heterostructures for potential thermoelectric applications. *Nano Lett.,* 12 (2012) 3627.

91. M. Saleemi, M. S. Toprak, S. Li, M. Johnsson, M. Muhammed, Synthesis, processing, and thermoelectric properties of bulk nanostructured bismuth telluride (Bi_2Te_3), *J. Mater. Chem.*, 22 (2012) 725.

92. P. Puneet, R. Podila, M. Karakaya, S. Zhu, J. He, T. M. Tritt, M. S. Dresselhaus, A. M. Rao, Preferential scattering by interfacial charged defects for enhanced thermoelectric performance in few-layered n-type Bi_2Te_3, *Sci. Rept.*, 3 (2013) 3212.

93. M. Hong, T. C. Chasapis, Z.-G. Chen, L. Yang, Mercouri G. Kanatzidis, G. J. Snyder, J. Zou, *n*-Type $Bi_2Te_{3-x}Se_x$ Nanoplates with Enhanced Thermoelectric

Efficiency Driven by Wide-Frequency Phonon Scatterings and Synergistic Carrier Scatterings, *ACS Nano*, *10* (4) (2016) 4719.

94. M. Hong, Z. G. Chen, L. Yang, J. Zou, $Bi_xSb_{2-x}Te_3$ nanoplates with Enhanced Thermoelectric Performance due to Sufficiently Decoupled Electronic Transport Properties and Strong Wide-Frequency Phonon Scatterings, *Nano Energy,* 20 (2016) 144.

95. Y. Liu, Y. Zhang, K. H. Lim, M. Ibáñez, S. Ortega, M. Li, J. David, S. Martí-Sánchez, K. Mi. Ng, J. Arbiol , M. V. Kovalenko, D. Cadavid, A. Cabot, High Thermoelectric Performance in Crystallographically Textured n-Type $Bi_2Te_{3-x}Se_x$ Produced from Asymmetric Colloidal Nanocrystals, *ACS Nano*, *12* (7) (2018) 7174.

96. Z.-Y. Mei, J. Guo, W. Yi, J. Feng, Z.-H. Ge, Shashlik-Like $Te-Bi_2Te_3$ Hetero-nanostructures: One-pot Synthesis, Growth Mechanism and Their Thermoelectric Properties, *Cryst. Eng. Comm.*, (2019) Accepted manuscript.

97. Di Wu, Lin Xie, Xiaolian Chao, Zupei Yang, Jiaqing He, Step-Up Thermoelectric Performance Realized in Bi_2Te_3 Alloyed GeTe via Carrier Concentration and Microstructure Modulations, *ACS Appl. Energy Mater.*, 2 (3) (2019) 1616

98. A. H. Li, M. Shahbazi, S. H. Zhou, G. X. Wang, C. Zhang, P. Jood, G. Peleckis, Y. Du, Z. X. Cheng, X. L. Wang, Y. K. Kuo, Electronic structure and thermoelectric properties of Bi_2Te_3 crystals and graphene doped Bi_2Te_3. *Thin Solid Films,* 518 (2010) e57.

99. M. Carle, P. Pierrat, C. Lahalle-Gravier, S. Scherrer, H. Scherrer, Transport Properties of *n*-Type $Bi_2(Te_{1-x}Se_x)_3$ Single Crystal Solid Solutions (x = 0.05), *J. Phys. Chem. Solids,* 56 (1995) 201.

100. Y. Ma, Q. Hao, B. Poudel, Y. C. Lan, B. Yu, D. Z. Wang, G. Chen, Z. F. Ren, Enhanced Thermoelectric Figure-of-Merit in p-Type Nanostructured Bismuth Antimony Tellurium Alloys Made from Elemental Chunks, *Nano Lett.,* 8 (2008) 2580

101. L. D. Zhao, B. P. Zhang, J. F. Li, H. L. Zhang, W. S. Liu, Enhanced Thermoelectric and Mechanical Properties in Textured *n*-Type Bi_2Te_3 Prepared by Spark Plasma Sintering, *Solid State Sci.,* 10 (2008) 651.

102. W. Xie, X. Tang, Y. Yan, Q. Zhang, T. M. Tritt, Unique Nanostructures and Enhanced Thermoelectric Performance of Melt-Spun BiSbTe Alloys, *Appl. Phys. Lett.,* 94 (2009) 102111.

103. L. V. Prokofieva, D. A. Pshenay-Severin, P. P. Konstantinov, A. A. Shabaldin, Optimum Composition of a $Bi_2Te_{3-x}Se_x$ Alloy for the *n*-Type Leg of a Thermoelectric Generator, *Semiconductors,* 43 (2009) 973.

104. J.-J. Shen, T.-J. Zhu, X.-B. Zhao, S.-N. Zhang, S.-H. Yang, Z.-Z. Yin, Recrystallization Induced in situ Nanostructures in Bulk Bismuth Antimony Tellurides: a Simple Top Down Route and Improved Thermoelectric Properties. *Energy Environ. Sci.* 3 (2010) 1519.

105. S. Fan, J. Zhao, J. Guo, Q. Yan, J. Ma, H. H. Hng, p-Type $Bi_{0.4}Sb_{1.6}Te_3$ Nanocomposites with Enhanced Figure of Merit. *Appl. Phys. Lett.* 96 (2010) 182104.

106. D. H. Kim, C. Kim, K.-C. Je, G. H. Ha, H. Kim, Fabrication and thermoelectric properties of *c*-axis-aligned $Bi_{0.5}Sb_{1.5}Te_3$ with a high magnetic field, *Acta Mater.* 59 (2011) 4957.

107. S. Wang, G. Tan, W. Xie, G. Zheng, H. Li, J. Yang, X. Tang, Enhanced Thermoelectric Properties of $Bi_2(Te_{1-x}Se_x)_3$-Based Compounds as *n*-Type Legs for LowTemperature Power Generation. *J. Mater. Chem.,* 22 (2012) 20943.

108. H. Kim, D. H. Kim, C. Kim, S. Park, Thermoelectric properties of c-axis aligned Bi-Te materials, *AIP Confer. Proceeds.* 1449 (2012) 139.

109. W. Liu, K. C. Lukas, K. McEnaney, S. Lee, Q. Zhang, C. P. Opeil, G. Chen, Z. Ren, Studies on the Bi_2Te_3–Bi_2Se_3–Bi_2S_3 system for mid-temperature thermoelectric energy conversion, *Energy Environ. Sci.*, 6 (2013) 552.

110. L. Hu, T. Zhu, X. Liu, X. Zhao, Point Defect Engineering of High-Performance Bismuth-Telluride-Based Thermoelectric Materials, *Adv. Funct. Mater.* 24, (2014) 5211.

111. O. Falkenbach, D. Hartung, P. Klar, G. Koch, S. Schlecht, Thermoelectric Properties of Nanostructured Bismuth-Doped Lead Telluride $Bi_x(PbTe)_{1-x}$ Prepared by Co-Ball-Milling, *J. Electron. Mater.* 43 (2014) 1674.

112. Y. Nagami, K. Matsuoka, T. Akao, T. Onda, T. Hayashi, Z.-C. Chen, Preparation and Characterization of $Bi_{0.4}Sb_{1.6}Te_3$ Bulk Thermoelectric Materials, *J. Electron. Mater.* 43 (2014) 2262.

113. S.-J. Jung, S. Kim, H.-H. Park, D.-B. Hyun, S.-H. Baek, J.-S. Kim, Thermoelectric Properties of Highly Deformed and Subsequently Annealed *p*-Type $(Bi_{0.25}Sb_{0.75})_2Te_3$ Alloys, *J. Electron. Mater.* 43 (2014) 1726.

114. L. Hu, H. Wu, T. Zhu, C. Fu, J. He, P. Ying, X. Zhao, Tuning Multiscale Microstructures to Enhance Thermoelectric Performance of *n*-Type Bismuth-Telluride Based Solid Solutions, *Adv. Energy Mater.,* 5 (2015) 1500411.

115. S. I. Kim, K. H. Lee, H. A. Mun, H. S. Kim, S. W. Hwang, J. W. Roh, D. J. Yang, W. H. Shin, X. S. Li, Y. H. Lee, G. J. Snyder, S. W. Kim, Dense Dislocation Arrays Embedded in Grain Boundaries for High-Performance Bulk Thermoelectrics. *Science,* 348 (2015) 109.

116. Z. J. Xu, L. P. Hu, P. J. Ying, X. B. Zhao, T. J. Zhu, Enhanced thermoelectric and mechanical properties of zone melted *p*-type $(Bi,Sb)_2Te_3$ thermoelectric materials by hot deformation, *Acta Mater.* 84 (2015) 385.

117. W. Xie, X. Tang, Y. Yan, Q. Zhang, T. M. Tritt, High thermoelectric performance BiSbTe alloy with unique low-dimensional structure, *J. Appl. Phys.* 105 (2009) 113713.

118. F. Yu, J. Zhang, D. Yu, J. He, Z. Liu, B. Xu, Y. Tian, Enhanced thermoelectric figure of merit in nanocrystalline Bi_2Te_3 bulk, *J. Appl. Phys.* 105 (2009) 094303.

119. K. Kim, K. Kim, G. Ha, Thermoelectric properties of P-type bismuth telluride powders synthesized by a mechano-chemical process, *Electron. Mater. Lett.* 6 (2010) 177.

120. Y. H. Zhang, G. Y. Xu, F. Han, Z. Wang, C. C. Ge, Preparation and Thermoelectric Properties of Nanoporous Bi_2Te_3-Based Alloys, *J. Electron. Mater.* 39 (2010) 1741.

121. L. P. Bulat, V. T. Bublik, I. A. Drabkin, V. V. Karataev, V. B. Osvenskii, Y. N. Parkhomenko, G. I. Pivovarov, D. A. Pshenai-Severin, N. Y. Tabachkova, Bulk

Nanostructured Polycrystalline *p*-Bi-Sb-Te Thermoelectrics Obtained by Mechanical Activation Method with Hot Pressing, *J. Electron. Mater.* 39 (2010) 1650.

122. R. Srinivasan, N. Gothard, J. Spowart, Improvement in thermoelectric properties of an n type bismuth telluride ($Bi_2Se_{0.3}Te_{2.7}$) due to texture development and grain refinement during hot deformation, *Mater. Lett.* 64 (2010) 1772.

123. Y. Zhou, X. Li, S. Bai, L. Chen, Comparison of space- and ground-grown $Bi_2Se_{0.21}Te_{2.79}$ thermoelectric crystals, *J. Cryst. Growth* 2010, 312, 775.

124. M. Scheele, N. Oeschler, I. Veremchuk, K.-G. Reinsberg, A.-M. Kreuziger, A. Kornowski, J. Broekaert, C. Klinke, H. Weller, ZT Enhancement in Solution-Grown $Sb_{(2-x)}Bi_xTe_3$ Nanoplatelets, *ACS Nano,* 4 (2010) 4283.

125. N. Keawprak, S. Lao-ubol, C. Eamchotchawalit, Z. M. Sun, Thermoelectric properties of $Bi_2Se_xTe_{3-x}$ prepared by Bridgman method, *J. Alloys Compd.* 509 (2011) 9296.

126. J. J. Shen, Z. Z. Yin, S. H. Yang, C. Yu, T. J. Zhu, X. B. Zhao, Improved Thermoelectric Performance of *p*-Type Bismuth Antimony Telluride Bulk Alloys Prepared by Hot Forging, *J. Electron. Mater.* 40 (2011)1095.

127. F. Li, X. Huang, Z. Sun, J. Ding, J. Jiang, W. Jiang, L. Chen, Enhanced thermoelectric properties of *n*-type Bi_2Te_3-based nanocomposite fabricated by spark plasma sintering, *J. Alloys Compd.*, 509 (2011) 4769.

128. C. Kim, D. H. Kim, J. S. Kim, Y. S. Han, J. S. Chung, H. Kim, A study of the synthesis of bismuth tellurium selenide nanocompounds and procedures for improving their thermoelectric performance, *J. Alloys Compd.*, 509 (2011) 9472.

129. C. Kim, D. H. Kim, Y. S. Han, J. S. Chung, S. Park, H. Kim, Fabrication of bismuth telluride nanoparticles using a chemical synthetic process and their thermoelectric evaluations, *Powder Technol.*, 214 (2011) 463.

130. D.-W. Liu, J.-F. Li, C. Chen, B.-P. Zhang, Effects of SiC Nanodispersion on the Thermoelectric Properties of *p*-Type and *n*-Type Bi_2Te_3-Based Alloys, *J. Electron. Mater.* 40 (2011) 992.

131. D.-H. Park, M.-Y. Kim, T.-S. Oh, Thermoelectric energy-conversion characteristics of n-type $Bi_2(Te,Se)_3$ nanocomposites processed with carbon nanotube dispersion, *Curr. Appl. Phys.* 11 (2011) S41.

132. X. Zhang, X.-y. Ma, Q.-m. Lu, F.-p. Zhang, Y.-q. Liu, J.-x. Zhang, L. Wang, Thermoelectric Properties of Ag-Doped *n*-Type $(Bi_{2-x}Ag_xTe_3)_{0.96}-(Bi_2Se_3)_{0.04}$ Pseudobinary Alloys, *J. Electron. Mater.,* 40 (2011) 773.

133. Y. Zhang, H. Wang, S. Kräemer, Y. Shi, F. Zhang, M. Snedaker, K. Ding, M. Moskovits, G. J. Snyder, G. D. Stucky, Surfactant-Free Synthesis of Bi_2Te_3-Te Micro-Nano Heterostructure with Enhanced Thermoelectric Figure of Merit, *ACS Nano,* 5 (2011) 3158.

134. R. J. Mehta, Y. Zhang, C. Karthik, B. Singh, R. W. Siegel, T. Borca-Tasciuc, G. Ramanath, A new class of doped nanobulk high-figure-of-merit thermoelectrics by scalable bottom-up assembly, *Nat. Mater.,* 11 (2012) 233.

135. C. E. Carlton, C. A. Kuryak, W.-s. Liu, Z. Ren, G. Chen, Y. Shao-Horn, Disordered stoichiometric nanorods and ordered off-stoichiometric nanoparticles in n-type thermoelectric $Bi_2Te_{2.7}Se_{0.3}$, *J. Appl. Phys.* 112 (2012) 093518.

136. A. Soni, Z. Yanyuan, Y. Ligen, M. K. K. Aik, M. S. Dresselhaus, Q. Xiong, Enhanced Thermoelectric Properties of Solution Grown $Bi_2Te_{3-x}Se_x$ Nanoplatelet Composites, *Nano Lett.,* 12 (2012) 1203.

137. A. Soni, Y. Shen, M. Yin, Y. Zhao, L. Yu, X. Hu, Z. Dong, K. A. Khor, M. S. Dresselhaus, Q. Xiong, Interface Driven Energy Filtering of Thermoelectric Power in Spark Plasma Sintered $Bi_2Te_{2.7}Se_{0.3}$ Nanoplatelet Composites, *Nano Lett.,* 12 (2012) 4305.

138. Y. Zhang, T. Day, M. L. Snedaker, H. Wang, S. Krämer, C. S. Birkel, X. Ji, D. Liu, G. J. Snyder, G. D. Stucky, A Mesoporous Anisotropic n-Type Bi_2Te_3 Monolith with Low Thermal Conductivity as an Efficient Thermoelectric Material, *Adv. Mater.,* 24 (2012) 5065.

139. J. S. Son, M. K. Choi, M.-K. Han, K. Park, J.-Y. Kim, S. J. Lim, M. Oh, Y. Kuk, C. Park, S.-J. Kim, T. Hyeon, *n*-Type Nanostructured Thermoelectric Materials Prepared from Chemically Synthesized Ultrathin Bi_2Te_3 Nanoplates, *Nano Lett.,* 12 (2012) 640.

140. Y. Sun, H. Cheng, S. Gao, Q. Liu, Z. Sun, C. Xiao, C. Wu, S. Wei, Y. Xie, Atomically Thick Bismuth Selenide Freestanding Single Layers Achieving Enhanced Thermoelectric Energy Harvesting, *J. Am. Chem. Soc.,* 134 (2012) 20294.

141. R. J. Mehta, Y. Zhang, H. Zhu, D. S. Parker, M. Belley, D. J. Singh, R. Ramprasad, T. Borca-Tasciuc, G. Ramanath, Seebeck and Figure of Merit Enhancement in Nanostructured Antimony Telluride by Antisite Defect Suppression through Sulfur Doping, *Nano Lett.* 12 (2012) 4523.

142. H. Li, H. Jing, Y. Han, G.-Q. Lu, L. Xu, Effects of mechanical alloying process and sintering methods on the microstructure and thermoelectric properties of bulk $Bi_{0.5}Sb_{1.5}Te_3$ alloy, *Intermetallics*, 43 (2013) 16.

143. X. Guo, X. Jia, K. Jie, H. Sun, Y. Zhang, B. Sun, H. Ma, Investigating the thermoelectric properties of synthesized Bi_2Te_3 under different synthesis pressures, *Chem. Phys. Lett.* 568–569 (2013) 190.

144. M.-K. Han, H. Ryu, S.-J. Kim, Effect of Chromium Doping on the Thermoelectric Properties of Bi_2Te_3: $Cr_x Bi_2Te_3$ and $Cr_x Bi_{2-x} Te_3$, *J. Electron. Mater.* 42 (2013) 2758.

145. S. Hwang, S.-I. Kim, K. Ahn, J. Roh, D.-J. Yang, S.-M. Lee, K.-H. Lee, Enhancing the Thermoelectric Properties of *p*-Type Bulk Bi-Sb-Te Nanocomposites via Solution-Based Metal Nanoparticle Decoration, *J. Electron. Mater.,* 42 (2013) 1411.

146. K.-H. Lee, S. Hwang, B. Ryu, K. Ahn, J. Roh, D. Yang, S.-M. Lee, H. Kim, S.-I. Kim, Enhancement of the Thermoelectric Performance of $Bi_{0.4}Sb_{1.6}Te_3$ Alloys by In and Ga Doping, *J. Electron. Mater.*, 42 (2013) 1617.

147. J. Li, Q. Tan, J.-F. Li, D.-W. Liu, F. Li, Z.-Y. Li, M. Zou, K. Wang, BiSbTe-Based Nanocomposites with High ZT: The Effect of SiC Nanodispersion on Thermoelectric Properties, *Adv. Funct. Mater.* 23 (2013) 4317.

148. L. P. Tan, T. Sun, S. Fan, L. Y. Ng, A. Suwardi, Q. Yan, H. H. Hng, Facile synthesis of Cu_7Te_4 nanorods and the enhanced thermoelectric properties of Cu_7Te_4–$Bi_{0.4}Sb_{1.6}Te_3$ nanocomposites, *Nano Energy*, 2 (2013) 4.

149. T. Zhang, J. Jiang, Y. Xiao, Y. Zhai, S. Yang, G. Xu, In situ precipitation of Te nanoparticles in p-type BiSbTe and the effect on thermoelectric performance, *Appl. Mater. Interfaces,* 5 (2013) 3071.

150. F. Wu, H. Song, F. Gao, W. Shi, J. Jia, X. Hu, Effects of Different Morphologies of Bi_2Te_3 Nanopowders on Thermoelectric Properties, *J. Electron. Mater.* 2013, 42, 1140.

151. Y. Zhai, T. Zhang, Y. Xiao, J. Jiang, S. Yang, G. Xu, Enhanced thermoelectric performance in *n*-type $Bi_2Te_{2.994}Cl_{0.006}/In_2Te_3$ composite, *J. Alloys Compd.* 2013, 563, 285.

152. Y. Min, J. W. Roh, H. Yang, M. Park, S. I. Kim, S. Hwang, S. M. Lee, K. H. Lee, U. Jeong, Surfactant-Free Scalable Synthesis of Bi_2Te_3 and Bi_2Se_3 Nanoflakes and Enhanced Thermoelectric Properties of Their Nanocomposites, *Adv. Mater.* 25 (2013) 1425.

153. Q. Jiang, H. Yan, J. Khaliq, H. Ning, S. Grasso, K. Simpson, M. J. Reece, Large *ZT* enhancement in hot forged nanostructured p-type $Bi_{0.5}Sb_{1.5}Te_3$ bulk alloys, *J. Mater. Chem. A,* 2 (2014) 5785

154. G. Lee, G. Ha, Synthesis of $Bi_{0.5}Sb_{1.5}Te_3$ Thermoelectric Powder Using an Oxide-Reduction Process, *J. Electron. Mater.*, 43 (2014) 1697.

155. P.-Y. Lee, J. Hao, T.-Y. Chao, J.-Y. Huang, H.-L. Hsieh, H.-C. Hsu, Thermoelectric Properties of Nano/microstructured *p*-Type $Bi_{0.4}Sb_{1.6}Te_3$Powders Fabricated by Mechanical Alloying and Vacuum Hot Pressing, *J. Electron. Mater.* 43 (2014) 1718.

156. Y. Xiao, G. Chen, H. Qin, M. Wu, Z. Xiao, J. Jiang, J. Xu, H. Jiang, G. Xu, Enhanced thermoelectric figure of merit in p-type $Bi_{0.48}Sb_{1.52}Te_3$ alloy with WSe_2 addition, *J. Mater. Chem. A*, 2, (2014) 8512.

157. W.-T. Zhu, W.-Y. Zhao, H.-Y. Zhou, J. Yu, D.-G. Tang, Z.-Y. Liu, Q.-J. Zhang, Cost-Efficient Preparation and Enhanced Thermoelectric Performance of $Bi_{0.48}Sb_{1.52}Te_3$ Bulk Materials with Micro- and Nanostructures, *J. Electron. Mater.* 43 (2014) 1768.

158. Z. Ali, S. Butt, C. Cao, F. K. Butt, M. Tahir, M. Tanveer, I. Aslam, M. Rizwan, F. Idrees, S. Khalid, Thermochemically evolved nanoplatelets of bismuth selenide with enhanced thermoelectric figure of merit, *AIP Advances*, 4 (2014) 117129.

159. Q. Zhang, X. Ai, W. Wang, L. Wang, W. Jiang, Preparation of 1-D/3-D structured $AgNWs/Bi_2Te_3$ nanocomposites with enhanced thermoelectric properties, *Acta Mater.*, 73 (2014) 37.

160. G. Han, Z.-G. Chen, L. Yang, M. Hong, J. Drennan, J. Zou, Rational Design of Bi_2Te_3 Polycrystalline Whiskers for Thermoelectric Applications, *ACS Appl. Mater. Interfaces*, 7 (2015) 989.

161. K. Lee, S.-M. Choi, J. Roh, S. Hwang, S. Kim, W. Shin, H. Park, J. Lee, S. Kim, D. Yang, Enhanced Thermoelectric Performance of *p*-Type Bi-Sb-Te Alloys by Codoping with Ga and Ag, *J. Electron. Mater.* 44 (2015) 1531.

162. Y. Li, D. Li, X. Qin, X. Yang, Y. Liu, J. Zhang, Y. Dou, C. Song, H. Xin, Enhanced thermoelectric performance through carrier scattering at heterojunction potentials in BiSbTe based composites with Cu_3SbSe_4 nanoinclusions, *J. Mater.Chem. C,* 3 (2015) 7045.

163. Y. Luo, J. Yang, Q. Jiang, L. Fu, Y. Xiao, W. Li, D. Zhang, Z. Zhou, Y. Cheng, Melting and solidification of bismuth antimony telluride under a high magnetic field: A new route to high thermoelectric performance, *Nano Energy,* 15 (2015) 709

164. H. Mun, K. Lee, S. Kim, J.-Y. Kim, J. Lee, J.-H. Lim, H. Park, J. Roh, S. Kim, Fe-Doping Effect on Thermoelectric Properties of *p*-Type $Bi_{0.48}Sb_{1.52}Te_3$, *Mater. Today,* 8 (2015) 959.

165. F. Wu, W. Shi, X. Hu, Preparation and thermoelectric properties of flower-like nanoparticles of Ce-Doped Bi_2Te_3. *Electron. Mater. Lett.*, 11 (2015) 127.

166. Q. Zhang, X. Ai, L. Wang, Y. Chang, W. Luo, W. Jiang, L. Chen, Improved Thermoelectric Performance of Silver Nanoparticles-Dispersed Bi_2Te_3 Composites Deriving from Hierarchical Two-Phased Heterostructure, *Adv. Funct. Mater.,* 25 (2015) 966.

167. S. Gupta, N. Vijayan, A. Krishna, K. Thukral, K. K. Maurya, S. Muthiah, A. Dhar, B. Singh, G. Bhagavannarayana, Enhancement of thermoelectric figure of merit in Bi_2Se_3 crystals through a necking process, *J. Appl. Crystallogr.,* 48 (2015) 533.

168. Q. Lognoné, F. Gascoin, On the effect of carbon nanotubes on the thermoelectric properties of n-$Bi_2Te_{2.4}Se_{0.6}$ made by mechanical alloying, *J. Alloys Compd.* 635 (2015) 107.

169. G.-E. Lee, A. Y. Eum, K.-M. Song, I.-H. Kim, Y. Lim, W.-S. Seo, B.-J. Choi, C.-W. Hwang, Preparation and Thermoelectric Properties of *n*-Type $Bi_2Te_{2.7}Se_{0.3}$: D_m, *J. Electron. Mater.,* 44 (2015) 1579.

170. Y. Min, G. Park, B. Kim, A. Giri, J. Zeng, J. W. Roh, S. I. Kim, K. H. Lee, U. Jeong, Synthesis of Multishell Nanoplates by Consecutive Epitaxial Growth of Bi_2Se_3 and Bi_2Te_3 Nanoplates and Enhanced Thermoelectric Properties, *ACS Nano*, 9 (2015) 6843.

171. D. Suh, S. Lee, H. Mun, S.-H. Park, K. H. Lee, S. Wng Kim, J.-Y. Choi, S. Baik, Enhanced Thermoelectric Performance of $Bi_{0.5}Sb_{1.5}Te_3$-Expanded Graphene Composites by Simultaneous Modulation of Electronic and Thermal Carrier Transport, *Nano Energy,* 13 (2015) 67

172. M. Hong, Z.-G. Chen, L. Yang, G. Han, J. Zou, Enhanced Thermoelectric Performance of Ultrathin Bi_2Se_3 Nanosheets through Thickness Control, *Adv. Electron. Mater.,* 1 (2015) 1500025.

173. K. Ahmad, C.Wan, M. A. Al-Eshaikh, A.N.Kadachi, Enhanced thermoelectric performance of Bi_2Te_3 based graphene nanocomposites, *Appl. Surf. Science*, 474 (2019) 2.

174. T. Bland, K. Lee and S. Steinmuller, The spintronics challenge, *Phys. World,* 21(2008) 24.

175. D. D. Awschalom and M. E. Flatté, Challenges for semiconductor spintronics, *Nature Phys.,* 3 (2007) 153.

176. R. Janisch, P. Gopal and N. A. Spalding, Transition metal-doped TiO_2 and ZnO-present status of the field, *J. Phys.: Condens. Matter,* 17 (2005) R657.

177. J. K. Furdyna, Diluted magnetic semiconductors, *J. Appl. Phys.,* 64 (1988) R29.

178. D. Ferrand, J. Cibert, A. Wasiela, C. Bourgognon, S. Tatarenko, G. Fishman, T. T. Andrearczyk, J. Jaroszynski, S. Kolesnik, T. Dietl, B. Barbara and D. Dufeu,

Carrier induced ferromagnetism in p-Zn$_{1-x}$Mn$_x$Te, *Phys. Rev. B*, 63 (2001) 085201.

179. H. Munekata, H. Ohno, S. von Molnar, A. Segmaller, L. L. Chang and L. Esaki, Diluted magnetic III-V semiconductors, *Phys. Rev. Lett.*, 63 (1989) 1849.

180. H. Ohno, H. Munekata, T. Penney, S. von Molnar and L. L. Chang, Magnetotransport properties of p-type (In,Mn)As diluted magnetic III-V semiconductors, *Phys. Rev. Lett.*, 68 (1992) 2664.

181. H. Ohno, A. Shen, F. Matsukura, A. Oiwa, A. Endo, S. Katsumoto and Y. Iye, (Ga,Mn)As: A new diluted magnetic semiconductor based on GaAs, *Appl. Phys. Lett.*, 69 (1996) 363.

182. T. Jungwirth, J. Sinova, J. Masek, J. Kucera and A. H. MacDonald, Theory of ferromagnetic (III,Mn)V semiconductors, *Rev. Mod. Phys.*, 78 (2006) 809.

183. K. W. Edmonds, K. Y. Wang, R. P. Campion, A. C. Neumann, N. R. S. Farley, B. L. Gallagher and C. T. Foxon, High-Curie-temperature Ga1–xMnxAs obtained by resistance-monitored annealing, *Appl. Phys. Lett.*, 81 (2002) 4991.

184. D. Chiba, K. Takamura, F. Matsukura and H. Ohno, Effect of low-temperature annealing on (Ga,Mn)As trilayer structures, *Appl. Phys. Lett.*, 82 (2003) 3020.

185. T. Dietl, H. Ohno, F. Matsukura, J. Cibert, and D. Ferrand, Zener model description of ferromagnetism in zinc-blende magnetic semiconductors, *Science*, 287 (2000) 1019.

186. P. Sharma, A. Gupta, K. V. Rao, F. J. Owens, R. Sharma, R. Ahuja, J. M. O. Guillen, B. Johansson, G.A. Gehring, Ferromagnetism above room temperature in bulk and transparent thin films of Mn-doped ZnO, *Nature Mat.* 2 (2003) 673.

187. Y. J. Matsumoto, M. Murakami, T. J. Shono, T. Hasegawa, T. Fukumura, M. Kawasaki, P. Ahmet, T. Chikyow, S. Y. Koshihara and H. Koinuma, Room temperature ferromagnetism in transparent transition metal-doped titanium dioxide, *Science*, 291 (2001) 854.

188. K. Ueda, H. Tabata and T. Kawai, Magnetic and electric properties of transitionmetal-doped ZnO films, *Appl. Phys. Lett.*, 79 (2001) 988.

189. S. N. Kale, S. B. Ogale, and S. R. Shinde, M. Sahasrabuddhe, V. N. Kulkarni, R. L. Greene and T. Venkatesan, Magnetism in cobalt-doped Cu$_2$O thin films without and with Al, V, or Zn codopants, *Appl. Phys. Lett.*, 82 (2003) 2100.

190. S. B. Ogale, R. J. Choudhary, J. P. Buban, S. E. Lofland, S. R. Shinde, S. N. Kale, V. N. Kulkarni, J. Higgins, C. Lanci, J. R. Simpson, N. D. Browning, S. Das Sarma, H. D. Drew, R. L. Greene and T. Venkatesan, High temperature ferromagnetism with a giant magnetic moment in transparent Co-doped SnO$_{2-\delta}$, *Phys. Rev. Lett.*, 91 (2003) 077205.

191. J. Philip, N. Theodoropolou, G. Berera, J. S. Moodera and B. Satpati, High temperature ferromagnetism in manganese-doped indium-tin oxide films, *Appl.Phys. Lett.*, 85 (2004) 777.

192. K. Sato and H. Katayama-Yoshida, Material Design of GaN-Based Ferromagnetic Diluted Magnetic Semiconductors, *Jpn. J. Appl. Phys.* 40 (2001) L485

193. G. Lawes, A. S. Risbud, A. P. Ramirez, and R. Seshadri, Absence of ferromagnetism in Co and Mn substituted polycrystalline ZnO, *Phys. Rev. B* 71 045201 (2005).

194. C. N. R. Rao and F. L. Deepak, Absence of ferromagnetism in Mn- and Co-doped ZnO, *J. Mater.Chem.*15 573 (2005)

195. X. Liu, J. Iqbal, Z. Wu, B. He, R.Yu, Structure and Room-Temperature Ferromagnetism of Zn-Doped SnO_2 Nanorods Prepared by Solvothermal Method, *J. Phys. Chem.* C, 114 (2010) 4790.

196. Q. Ma, J. T. Prater, C. Sudakar, R. A. Rosenberg, J. Narayan, Defects in room-temperature ferromagnetic Cu-doped ZnO films probed by X-ray absorption spectroscopy. *J Phys: Condens Matter*., 24 (2012) 306002.

197. T. Fukumura, Z. Jin, A. Ohtomo, H. Koinuma and M. Kawasaki, An oxide-diluted magnetic semiconductor: Mn-doped ZnO, *J. Appl. Phys*, 75 (1999) 3366.

198. http://www.zyvex.com/nanotech/feynman.html

199. T. Fukumuraa, Y. Yamadaa, H. Toyosakia, T. Hasegawab, H. Koinuma and M. Kawasakia, Exploration of oxide-based diluted magnetic semiconductors toward transparent spintronics, *Appl. Surf. Sci*., 223 (2004) 62.

200. S. D. Yoon, Y. Chen, A. Yang, T. L. Goodrich, X. Zuo, D. A. Arena, K. Zeimer, C. Vittoria, V. G. Harris, Oxygen-defect-induced magnetism to 880 K in semiconducting anatase $TiO_{2-\delta}$ films, *J. Phys.: Condens. Matter*, 18 (2006) L355.

201. D. Kim, J. Hong, Y. R. Park, K. J. Kim, The origin of oxygen vacancy induced ferromagnetism in undoped TiO_2, *J. Phys.: Condens. Matter*, 21 (2009) 195405.

202. N. H. Hong, J. Sakai, N. Poirot, V. Brize, Room-temperature ferromagnetism observed in undoped semiconducting and insulating oxide thin films, *Phys. Rev. B*, 73 (2006) 132404

203. M. Venkatesan, C. B. Fitzgerald, J.M.D. Coey, Unexpected magnetism in a dielectric oxide, *Nature*, 430 (2004) 630.

204. X.-X. Zou, G.-D. Li, K.-X. Wang, L. Li, J. Su and J.-S. Chen, Light-induced formation of porous TiO_2 with superior electron-storing capacity, *Chem. Comm.*, 46 (2010) 2112.

205. C. Zener, Interaction between the d-Shells in the Transition Metals. II. Ferromagnetic Compounds of Manganese with Perovskite Structure *Phy. Rev.*, 82 (1951) 403.

206. C. Zener, Interaction between the d Shells in the Transition Metals, *Phys. Rev.* 81 (1951) 440.

207. C. Zener, Interaction between the d-Shells in the Transition Metals. III. Calculation of the Weiss Factors in Fe, Co, and Ni, *Phys. Rev.* 83 (1951) 299.

208. T. Dietl, H. Ohno, F. Matsukura, J. Cibert, and D. Ferrand, Zener model description of ferromagnetism in zinc-blende magnetic semiconductors, *Science*, 287 (2000) 1019.

209. K. Sato, H. Katayama-Yoshida, Stabilization of Ferromagnetic States by Electron Doping in Fe-, Co- or Ni-Doped ZnO, *Jpn. J. Appl. Phys.*, 40 (2001) L334.

210. A. Kaminski and S. Das Sarma, Polaron Percolation in Diluted Magnetic Semiconductors, Phys. Rev. Lett. 88 (2002) 247202.

211. J. M. D. Coey, M. Venkatesan, and C. B. Fitzgerald, Donor Impurity Band Exchange in Dilute Ferromagnetic Oxides, *Nature Mater.* 4 (2005) 173.
212. M. Berciu and R. N. Bhatt, Effects of Disorder on Ferromagnetism in Diluted Magnetic Semiconductors, *Phys. Rev. Lett.,* 87 (2001) 107203.
213. J. E. S. Haggerty, L. T. Schelhas, D. A. Kitchaev, J. S. Mangum, L. M. Garten, W. Sun, K. H. Stone, J. D. Perkins, M. F. Toney, G. Ceder, D. S. Ginley, B. P. Gorman, J. Tate, High-fraction brookite flms from amorphous precursors, *Sci. Rep.*, 7 (2017) Article number: 15232.
214. A. Linsebigler, G. Lu, J. T. Yates Jr., Photocatalysis on TiO_2 Surfaces: Principles, Mechanisms, and Selected Results, *Chem. Rev.*, 95 (1995) 735.
215. U. Diebold, The surface science of titanium dioxide, *Surf. Sci. Rep.*, 48 (2003) 53.
216. Q. Zhao, P. Wu, B.L. Li, Z.M. Lu, E.Y. Jiang, Activation of room-temperature ferromagnetism in nonstoichiometric $TiO_{2-\delta}$ powders by oxygen vacancies, *J. Appl. Phys.*, 104 (2008) 073911.
217. B. Santara, P.K. Giri, S. Dhara, K. Imakita, M. Fujii, Oxygen vacancy-mediated enhanced ferromagnetism in undoped and Fe-doped TiO_2 nanoribbons, *J. Phys. D: Appl. Phys.*, 47 (2014) 235304.
218. H. Peng, J. Li J, S.-S. Li, J.-B. Xia, Possible origin of ferromagnetism in undoped anatase TiO_2, *Phys. Rev. B*, 79 (2009) 092411.
219. S. Wang, L. Pan, J.-J. Song, W. Mi, J.-J. Zou, L. Wang, X. Zhang, Titanium-defected undoped anatase TiO_2 with p-type conductivity, room-temperature ferromagnetism, and remarkable photocatalytic performance, *J. Am. Chem. Soc.*, 137 (2015) 2975.
220. S. Zhou, E. Čižmár, K. Potzger, M. Krause, G. Talut, M. Helm, J. Fassbender, S. A. Zvyagin, J. Wosnitza, H. Schmidt, Origin of magnetic moments in defective TiO_2 single crystals, *Phys. Rev. B*, 79 (2009) 113201.
221. B. Choudhury, M. Dey, A. Choudhury, Defect generation, d-d transition, and band gap reduction in Cu-doped TiO_2 nanoparticles. *Int Nano Lett*., 3 (2013) 25
222. M. Parras, A. Varela, R. C. Gil, K. Boulahya, A. Hernando, J. M. G. Calbet, Room-temperature ferromagnetism in reduced rutile $TiO_{2-\delta}$ nanoparticles, *J. Phys. Chem. Lett.*, 2013, 4, 2171.
223. S. D. Yoon, Y. Chen, A. Yang, T. L. Goodrich, X. Zuo, D. A. Arena, K. Zeimer, C. Vittoria, V. G. Harris, Oxygen-defect-induced magnetism to 880 K in semiconducting anatase $TiO_{2-\delta}$ films, *J. Phys.: Condens. Matter*, 18 (2006) L355.
224. D. Kim, J. Hong, Y. R. Park, K. J. Kim, The origin of oxygen vacancy induced ferromagnetism in undoped TiO_2, *J. Phys.: Condens. Matter*, 21 (2009) 195405.
225. N. H. Hong, J. Sakai, N. Poirot, V. Brize, Room-temperature ferromagnetism observed in undoped semiconducting and insulating oxide thin films, *Phys. Rev. B*, 73 (2006) 132404
226. M. Venkatesan, C. B. Fitzgerald, J.M.D. Coey, Unexpected magnetism in a dielectric oxide, *Nature*, 430 (2004) 630.
227. X.-X. Zou, G.-D. Li, K.-X. Wang, L. Li, J. Su and J.-S. Chen, Light-induced formation of porous TiO_2 with superior electron-storing capacity, *Chem. Comm.*, 46 (2010) 2112.

228. B. Santara, P. K. Giri, K. Imakita and M. Fujii, Evidence of oxygen vacancy induced room temperature ferromagnetism in solvothermally synthesized undoped TiO_2 nanoribbons, *Nanoscale*, 5 (2013) 5476.

229. S. Duhalde, M. F. Vignolo, F. Golmar, C. Chiliotte, C. E. Rodríguez Torres, L. A. Errico, A. F. Cabrera, M. Rentería, F. H. Sánchez, and M. Weissmann, Appearance of room-temperature ferromagnetism in Cu-doped $TiO_{2-\delta}$ films, *Phys. Rev. B*, 72 (2005) 161313(R)

230. D. L. Hou, R. B. Zhao, H. J. Meng, L. Y. Jia, X. J. Ye, H. J. Zhou, X. L. Li, Room-temperature ferromagnetism in Cu-doped TiO_2 thin films, *Thin Solid Films*, 516 (10) (2008) 3223.

231. M. You, T. G. Kim, Y. –M. Sung, Synthesis of Cu-doped TiO_2 nanorods with various aspect ratios and dopant concentrations. *Cryst, Growth Des.*, 10 (2009) 983.

232. J.-Y. Zheng, S.-H. Bao, Y.-H. Lv, P. Jin, Activation and Enhancement of Room-Temperature Ferromagnetism in Cu-Doped Anatase TiO_2 Films by Bound Magnetic Polaron and Oxygen Defects, *ACS Appl. Mater. Interfaces*, 6 (24) (2014) 22243.

233. B. Anitha, M. Abdul Khadar, Dopant concentration dependent magnetism of Cu-doped TiO_2 nanocrystals, *J. Nanopart. Res.* 18 (2016) 149.

234. X. H. Wang, J. G. Li, H. Kamiyama, M. Katada, N. Ohashi, Y. Moriyoshi and T. Ishigaki, Pyrogenic Iron (III)-Doped TiO_2 Nanopowders Synthesized in RF Thermal Plasma: Phase Formation, Defect Structure, Band Gap, and Magnetic Properties, *J. Am. Chem. Soc.*, 127 (2005) 10982.

235. M. Hirano, T. Joji and M. Inagaki, Direct Formation of Iron(III)-Doped Titanium Oxide (Anatase) by Thermal Hydrolysis and Its Structural Property, *J. Am. Ceram. Soc.*, 87 (2008) 35.

236. S. George, S. Pokhrel, Z. Ji, B. L. Henderson, T. Xia, L. Li, J. I. Zink, A. E. Nel and L. Madler, Role of Fe doping in tuning the band gap of TiO_2 for the photo-oxidation-induced cytotoxicity paradigm, *J. Am. Chem. Soc.*, 133 (2011) 11270.

237. X. Li, R. Wang, F. Zhang and D. Zhao, Engineering homogeneous doping in single nanoparticle to enhance upconversion efficiency, *Nano Lett.*, 14 (2014) 3634.

238. Z. Wang, W. Wang, J. Tang, L. Tung, L. Spinu, and W. Zhou, Extraordinary Hall effect and ferromagnetism in Fe-doped reduced rutile, *Appl. Phys. Lett.* 83 (2003) 518.

239. Y. J. Kim, S. Thevuthasan, T. Droubay, A. S. Lea, C. M. Wang, V. Shutthanandan, S. A. Chambers, R. P. Sears, B. Taylor, and B. Sinkovic, Growth and properties of molecular beam epitaxially grown ferromagnetic Fe-doped TiO_2 rutile films on TiO_2 (110), *Appl. Phys. Lett.* 84 (2004) 3531.

240. N. H. Hong, W. Prellier, J. Sakai, A. Hassini, Fe- and Ni-doped TiO_2 thin films grown on $LaAlO_3$ and $SrTiO_3$ substrates by laser ablation *Appl. Phys. Lett.* 84 (2004) 2850

241. P. Xiaoyan, J. Dongmei, L. Yan, M. Xueming, Structural characterization and ferromagnetic behavior of Fe-doped TiO_2 powder by high-energy ball milling, *J. Mag. Magn. Mat.* 305 (2006) 388.

242. S. K. S. Patel, S. Kurian, N. S. Gajbhiye, Room-temperature ferromagnetism of Fe-doped TiO_2 nanoparticles driven by oxygen vacancy, *Mater. Res. Bulletin,* 48 (2013) 655.

243. A. M. M. Navarro, C. E. R. Torres, V. Bilovol, A. F. Cabrera, L. A. Errico, M. Weissmann, Study of the relation between oxygen vacancies and ferromagnetism in Fe-doped TiO_2 nano-powders, *J. Appl. Phys.*, 115 (2014) 223908.

244. B. Prajapati, S. Kumar, M. Kumar, S. Chatterjee, A. K. Ghosh, Investigation of the physical properties of $Fe:TiO_2$-diluted magnetic semiconductor nanoparticles, *J. Mater. Chem. C*, 5 (2017) 4257.

245. S. A. Ahmed, Ferromagnetism in Cr-, Fe-, and Ni-doped TiO_2 samples, *J. Mag. Mag. Mater.*, 442 (2017) 152.

246. Y. Matsumoto, R. Takahashi, M. Murakami, T. Koida, X.-J. Fan, T. Hasegawa, T. Fukumura, M. Kawasaki, S.-Y. Koshihara and H. Koinuma, Ferromagnetism in Co-doped TiO_2 rutile thin films grown by laser molecular beam epitaxy, *Jpn. J. Appl. Phys.*, 40 (2001) L1204.

247. J.-Y. Kim, J.-H. Park, B.-G. Park, H.-J. Noh, S.-J. Oh, J.S. Yang, D.-H. Kim, S.D. Bu, T.-W. Noh, H.-J. Lin, H.-H. Hsieh, C.T. Chen, Ferromagnetism induced by clustered Co in Co-doped anatase TiO_2 thin films, *Phys. Rev. Lett.* 90 (2003) 017401.

248. T. Fukumura, H. Toyosaki, K. Ueno, M. Nakano, M. Kawasaki, Role of charge carriers for ferromagnetism in cobalt-doped rutile TiO_2, *New J. Phys.* 10 (2008) 055018.

249. L. –T. Tseng, X. Luo, T.T. Tan, S. Li, Y. Jiabao, Doping concentration dependence of microstructure and magnetic behaviors in Co-doped TiO_2 nanorods, *Nanoscale Res. Lett.* 9 (2014) 673.

250. A. Chanda, K. Rout, M. Vasundhara, S. R. Joshi and J. Singh, Structural and magnetic study of undoped and cobalt doped TiO_2 nanoparticles, *RSC Adv.*, 8, (2018) 10939.

251. W. K. Park, R. J. Ortega-Hertogs, J. S. Moodera, A. Punnoose, and M. S. Seehra, Semiconducting and ferromagnetic behavior of sputtered Co-doped TiO_2 thin films above room temperature, *J. Appl. Phys.*, 91 (2002) 8093.

252. N.-J. Seong, S.-G. Yoon, and C.-R. Cho, Effects of Co-doping level on the microstructural and ferromagnetic properties of liquid-delivery metalorganic-chemical-vapor-deposited $Ti_{1-x}Co_xO_2$ thin films, *Appl. Phys. Lett.*, 81 (2002) 4209.

253. S. R. Shinde, S. B. Ogale, S. D. Sarma, J. R. Simpson, H. D. Drew, S. E. Lofland, C. Lanci, J. P. Buban, N. D. Browning, V. N. Kulkarni, J. Higgins, R. P. Sharma, R. L. Greene, and T. Venkatesan, Ferromagnetism in laser deposited anatase $Ti_{1-x}Co_xO_{2-\delta}$ films, *Phys. Rev. B,* 67 (2003) 115211.

254. P. A. Stampe, R. J. Kennedy, Y. Xin, and J. S. Parker, Investigation of the cobalt distribution in TiO_2 : Co thin films, *J. Appl. Phys.*, 92 (2002) 7114.

255. S. A. Chambers, T. Droubay, C. M. Wang, A. S. Lea, R. F. C. Farrow, L. Folks, V. Deline, and S. Anders, Clusters and magnetism in epitaxial Co-doped TiO_2 anatase, *Appl. Phys. Lett.*, 82 (2003) 1257.

256. S. R. Shinde, S. B. Ogale, J. S. Higgins, H. Zheng, A. J. Millis, V. N. Kulkarni, R. Ramesh, R. L. Greene, T. Venkatesan, Co-occurrence of superparamagnetism and anomalous hall effect in highly reduced cobalt-doped rutile $TiO_{2-\delta}$ films, *Phys. Rev. Lett.,* 92(16) (2004) 0166601.

257. J. D. Bryan, S. A. Santangelo, S. C. Keveren, D. R. Gamelin, Activation of High-T_C Ferromagnetism in Co^{2+}:TiO_2 and Cr^{3+}:TiO_2 Nanorods and Nanocrystals by Grain Boundary Defects, *J. Am. Chem. Soc.*, 127 (2005) 15568.

258. L. C. J. Pereira, M. R. Nunes, O. C. Monteiro, A. J. Silvestre, Magnetic properties of Co-doped TiO_2 anatase nanopowders, *Appl. Phys. Lett.*, 93, 222502 (2008)

259. B. Santara , B. Pal and P. K. Giri , Signature of strong ferromagnetism and optical properties of Co doped TiO_2 nanoparticles, *J. Appl. Phys.*, 110 (2011) 114322.

260. A. Kaushik, B. Dalela, S. Kumar, P. A. Alvi, S. Dalela, Role of Co doping on structural, optical and magnetic properties of TiO_2, *J. Alloys Compd.*, 552 (2013) 274.

261. L.-T. Tseng, X. Luo, T. T. Tan, S. Li, J. Yi, Doping concentration dependence of microstructure and magnetic behaviours in Co-doped TiO_2 nanorods, *Nanoscale Res. Lett.* 9 (2014) 673.

262. B. Anitha, M. Abdul Khadar, Alok Banerjee, Paramagnetic behavior of Co doped TiO_2 nanocrystals controlled by self-purification mechanism, *J. Solid State Chem.*, 239 (2016) 237

263. D. Jing, Y. Zhang, L. Guo, Study on the synthesis of Ni-doped mesoporous TiO_2 and its photocatalytic activity for hydrogen evolution in aqueous methanol solution, *Chem. Phys. Lett.* 415(1) (2005) 74.\

264. D. L. Hou, H. J. Meng, L. Y. Jia, X. J. Ye, H. J. Zhou, X. L. Li, Oxygen vacancy enhanced the room temperature ferromagnetism in Ni-doped TiO_2 thin films, *Phys. Lett. A*, 364(3–4) (2007) 318.

265. Y. L. Zhao, M. Motapothula, N. L. Yakovlev, Z. Q. Liu, S. Dhar, A. Rusydi, Ariando, M. B. H. Breese, Q. Wang, and T. Venkatesan, Reversible ferromagnetism in rutile TiO_2 single crystals induced by nickel impurities, *Appl. Phys. Lett.* 101 (2012) 142105.

266. B. Parveen, M.-ul Hassan, Z. Khalid, S. Riaz, S. Naseem, Room-temperature ferromagnetism in Ni-doped TiO_2 diluted magnetic semiconductor thin films, *J. Appl. Res. Tech.*, 15(2) (2017) 132.

267. M. Manzoor, A. Rafiq, M. Ikram, M. Nafees, S. Ali, Structural, optical, and magnetic study of Ni-doped TiO_2 nanoparticles synthesized by sol-gel method, *Inter. Nano Lett.*, 8 (2018) 1.

268. A. A. Dakhel, H. Hamad, A. Jaafar, Investigation to the Structural, Optical, and Magnetic Properties of Synthesized Ni-Doped Anatase Nanoparticles: Essential Role of Treatment in Hydrogen on Long-Range Ferromagnetic Order, *J. Supercond. Nov. Magn..*, 32 (2019) 253.

269. S.K.S. Patel, N.S. Gajbhiye, Oxygen deficiency induced ferromagnetism in Cr-doped TiO_2 nanorods, *J. Magn. Magn. Mater.*, 330 (2013) 21

270. B. Choudhury, A. Choudhury, Structural, optical and ferromagnetic properties of Cr doped TiO_2 nanoparticles, *Mater. Sci. Eng. B*, 178 (2013) 794.

271. F. Da Pieve, S. Di Matteo, T. Rangel, M. Giantomassi, D. Lamoen, G.M. Rignanese, X. Gonze, Origin of magnetism and quasiparticles properties in Cr-doped TiO_2, *Phys. Rev. Lett.*, 110 (2013)136402.

272. N. H. Hong, A. Ruyter, W. Prellier, and J. Sakai, Room temperature ferromagnetism in anatase $Ti_{0.95}Cr_{0.05}O_2$ thin films: Clusters or not? *Appl. Phys. Lett.* 85 (2004) 6212.

273. Z. Wang, J. Tang, H. Zhang, V. Golub, L. Spinu, and L. D. Tung, Cr-doped TiO_2 anatase: A ferromagnetic insulator, *J. Appl. Phys.*, 95 (2004) 7381

274. T. Droubay, S. M. Heald, V. Shutthanandan, S. Thevuthasan, S. A. Chambers, and J. Osterwalder, Cr-doped TiO_2 anatase: A ferromagnetic insulator, *J. Appl. Phys.,* 97 (2005) 046103.

275. Y. Liao, H. Zhang, J. Li, G. Yu, Z. Zhong, F. Bai, L. Jia, S. Zhang, P. Zhong, Ferromagnetism at room temperature in Cr-doped anodic titanium dioxide nanotubes, *J. Appl.Phys.*, 115 (2014) 17C304.

276. B. Santara, K. Imakita, M. Fujii, P. K. Giri, Mechanism of defect induced ferromagnetism in undoped and Cr doped TiO_2 nanorods/nanoribbons, *J. Alloys Comp.*, 661 (2016) 331

277. K. Haq, M. Irfan, M. Masood, M. Saleem, T. Iqbal, Ishaq Ahmad, M. A. Khan, M. Zaffar, M. Irfan, Enhanced room temperature ferromagnetism in Cr-doped ZnO nanoparticles prepared by auto-combustion method, *J. Semicond.*, 39 (2018) 043001.

278. S. Naseem, W. Khan, S. Khan, S. Husain, A. Ahmad, Dielectric response and room temperature ferromagnetism in Cr doped anatase TiO_2 nanoparticles, *J. Mag. Mag. Mater.*, 447 (2018) 155.

279. B. Lee, T. Jungwirth, A. H. MacDonald, Ferromagnetism in diluted magnetic semiconductor heterojunction systems, *Semicond, Sci, Technol,,* 17 (2002) 393.

280. Z. Wang, J. Tang, Y. Chen, L. Spinu, W. Zhou, L. D. Tung, Room-temperature ferromagnetism in manganese doped reduced rutile titanium dioxide thin films, *J. Appl. Phys.,* 95(2004) 7384.

281. N. H. Hong, J. Sakai, A. Ruyter, V. Brize, Does Mn doping play any key role in tailoring the ferromagnetic ordering of TiO_2 thin films? *Appl. Phys. Lett.*, 89 (2006) 252504.

282. G. M. Dalpain, J. R. Chelikowsky, Self-Purification in Semiconductor Nanocrystals, *Phys. Rev. Lett.,* 96 (2006) 226802.

283. S. Bhattacharyya, A. Pucci, D. Zitoun, A. Gedanken, One-pot fabrication and magnetic studies of Mn-doped TiO_2 nanocrystals with an encapsulating carbon layer, *Nanotechnology*, 19(2008) 495711.

284. Z. M. Tian, S. L. Yuan, Y. Q. Wang, J. H. He, S. Y. Yin, K. L. Liu, S. J. Yuan, L. Liu, Magnetic studies on Mn-doped TiO_2 bulk samples, *J. Phys. D: Appl. Phys.,* 41(2008) 055006

285. L. H. Mie, L. Min, Z. Y. Su, H. T. Cheng, Coexistence of antiferromagnetic and ferromagnetic in Mn-doped anatase TiO_2 nanowires, *J. Cent. South Univ. Technol.*, 17 (2010) 239.

286. G. Glaspell, A. Manivannan, Sol–Gel Synthesis and Magnetic Studies of Titanium Dioxide Doped with 10% M (M=Fe, Mn and Ni), *J. Cluster Sci.,* 16 (2005) 501.

287. Z. V. Saponjic, N. M. Dimitrijevic, O. G. Poluektov, L. X. Chen, E. Wasinger, U. Welp, D. M. Tiede, X. Zuo, T. Rajh, Charge Separation and Surface Reconstruction: A Mn^{2+} Doping Study, *J. Phys. Chem. B,* 110 (2006) 25441.

288. A. F. Cabrera, L. Errico, C. E. R. Torres, F. H. Sanchez, Influence of thermal treatments on phase formation and magnetic behaviour in metal transition doped TiO_2, *Physica B* 389 (2007) 103.

289. M. C. K. Sellers, E. G. Seebauer, Room temperature ferromagnetism in Mn-doped TiO_2 nanopillar matrices, *Mater. Lett.,* 114 (2014) 44.

290. X. Chen, L. Liu, P. Y. Yu, S. S. Mao, Increasing solar absorption for photocatalysis with black hydrogenated titanium dioxide nanocrystals, *Science*, 331 (2011) 746.

291. A. Naldoni, M. Allieta, S. Santangelo, M. Marelli, F. Fabbri, S. Cappelli, C. L. Bianchi, R. Psaro, V. D. Santo, Effect of Nature and Location of Defects on Bandgap Narrowing in Black TiO_2 Nanoparticles. *J. Am. Chem. Soc.*, 134 (2012) 7600.

292. L. Liu, P. P. Yu, X. Chen, S. S. Mao and D. Z. Shen, Hydrogenation and Disorder in Engineered Black TiO_2, *Phys. Rev. Lett.*, 111 (2013) 065505.

293. X. Chen, L. Liu, Z. Liu, M. A. Marcus, W.-C. Wang, N. A. Oyler, M. E. Grass, B. Mao, P.-A. Glans, P. Y. Yu, J. Guo, S. S. Mao, Properties of disorder-engineered black titanium dioxide nanoparticles through hydrogenation, *Sci. Rep.*, 3 (2013) 1510.

294. X. Liu, S. Gao, H. Xu, Z. Lou, W. Wang, B. Huang, Y. Dai, Green Synthetic Approach for Ti^{3+} Self-Doped TiO_{2-x} Nanoparticles with Efficient Visible Light Photocatalytic Activity, *Nanoscale*, 5 (2013) 1870.

295. W. Zhou, W. Li, J.-Q. Wang, Y. Qu, Y. Yang, Y. Xie, K. Zhang, L. Wang, H. Fu, D. Zhao, Ordered mesoporous black TiO_2 as highly efficient hydrogen evolution photocatalyst. *J. Am. Chem. Soc.* 136 (2014) 9280.

296. B. Liu, H.M. Chen, C. Liu, S.C. Andrews, C. Hahn, P.D. Yang, Large-Scale Synthesis of Transition-Metal-Doped TiO_2 Nanowires with Controllable Overpotential. *J. Am. Chem. Soc.*, 135 (2013) 9995.

297. S. N. R. Inturi, T. Boningari, M. Suidan, P. G. Smirniotis, Flame Aerosol Synthesized Cr Incorporated TiO_2 for Visible Light Photodegradation of Gas Phase Acetonitrile. *J. Phys. Chem. C*, 118 (2014) 231.

298. Z. Y. Chen, L. Fang, W. Dong, F. G. Zheng, M. R. Shen, J. L. Wang, Inverse Opal Structured Ag/TiO_2 Plasmonic Photocatalyst Prepared by Pulsed Current Deposition and its Enhanced Visible Light Photocatalytic Activity. *J. Mater. Chem. A*, 2 (2014) 824.

299. T. Kamegawa, S. Matsuura, H. Seto, H. A. Yamashita, Visible-Light-Harvesting Assembly with a Sulfocalixarene Linker between Dyes and a Pt-TiO_2 Photocatalyst. *Angew. Chem. Int. Ed*. 52 (2013) 916.

300. J.H. Pan, Z.Y. Cai, Y. Yu, X.S. Zhao, Controllable Synthesis of Mesoporous F-TiO_2 Spheres for Effective Photocatalysis. *J. Mater. Chem.* 21 (2011) 11430.

301. M. Senna, N. Myers, A. Aimable, V. Laporte, C. Pulgarin, O. Baghriche, P. Bowen, Modification of titania nanoparticles for photocatalytic antibacterial activity via a colloidal route with glycine and subsequent annealing, *J. Mater. Res.*, 28 (2013) 354.

302. S. Musić, M. Gotić, M. Ivanda, S. Popović, A. Turković, R. Trojko, A. Sekulić, K. Furić, Chemical and micro structural properties of TiO_2 synthesized by sol-gel procedure, *Mater. Sci. Eng. B*, 47(1) (1997) 33.

303. J. Rodriguez, M. Gomez, J. Lu, E. Olsson, C. G. Granqvist, Reactively sputter-deposited titanium oxide coatings with parallel penniform microstructure, *Adv. Mater.*, 12(5) (2000) 341.

304. S. A. O'Neill, R. J. H. Clark, I. P. Parkin, N. Elliott, A. Mills, Anatase thin films on glass from the chemical vapor deposition of titanium(IV) chloride and ethyl acetate, *Chem. Mater.*, 15(1) (2003) 46.

305. D. Bersani, G. Antonioli, P. P. Lottici, T. Lopez, Raman study of nanosized titania prepared by sol-gel route, *J. Noncryst. Solids*, 232 (1998) 175.

306. G. J. Wilson, A. S. Matijasevich, D.R.G. Mitchell, J.C. Schulz, G.D. Will, Modification of TiO_2 for enhanced surface properties: finite Ostwald ripening by a microwave hydrothermal process, *Langmuir*, 22(5) (2006) 2016.

307. P. K. Khanna, N. Singh, S. Charan, Synthesis of nano-particles of anatase-TiO_2 and preparation of its optically transparent film in PVA, *Mater. Lett.*, 61(25) (2007) 4725.

308. C. Y. Wang, C. Böttcher, D. W. Bahnemann, J.K. Dohrmann, A comparative study of nanometer sized Fe (III)-doped TiO_2 photocatalysts: synthesis, characterization and activity, *J. Mater. Chem.*, 13(9) (2003) 2322.

Chapter 3

Tailoring thermoelectric properties through structure and morphology in chemically synthesized Bi and Sb based chalcogenide nanostructures

This chapter demonstrates a simple, cost effective, surfactant-assisted and aqueous-based low-temperature reflux method for the synthesis of Bi_2Te_3 nanocrystals. Thermoelectric properties of n-type Bismuth Telluride nanostructures are reported by varying reaction times and surfactant concentration. Tuning the reaction time from 1 h to 36 h and surfactant concentration from 50 mmol to 100 mmol enables the phase transformation from BiTe to Bi_2Te_3 with hexagonal crystal structure. A deep insight into the chemistry of ethylenediaminetetraacetic acid assisted aqueous based reflux method in the synthesis of Sb_2Te_3, SnTe and Sb-doped Bi_2Te_3 is also demonstrated in this chapter.

3.1. Introduction

Current research on TE materials is focussed on improving the power factor with a drastic reduction of κ using mixtures of multiphase nanostructured materials[1-10] and hence the nanostructured TE materials have attracted much attention for achieving enhanced **ZT** for practical applications. Among the available class of TE materials, group V chalcogenides such as Bi_2Te_3 based materials have attracted as good TE materials known to exhibit very high **ZT** values over the temperature range of 200 K– 400 K.[8] Again, it is interesting to note that Bi_2Te_3 has a stable structure at room temperature and hence Bismuth Telluride (BT) structures can be considered as a magnificent system for understanding the preparation of nanostructured TE materials[11], which in bulk form exhibits a **ZT** of around 0.5 at room temperature[12]. Recent reports emphasize the importance of a variety of synthesis techniques such as solvothermal method[13], sonochemical method[14], aqueous chemical method[15], refluxing method[16] etc. as bottom-up approach and ball milling[17-19], melt spinning[20, 21] and exfoliation techniques[22] as top down approaches for obtaining nanostructured TE materials. Among the two approaches, bottom up approach is the best method to achieve uniformity in the synthesized nanoparticles and to have a morphological tuning. Earlier methods suggested a sufficient reduction in κ by preparing the solid solution of materials where point defects in solid solutions aided the phonon scattering.[23] Thus phonon glass electron crystal model well suits for materials having complex crystal structures[24] where voids and rattlers could be the phonon scattering centres. Almost all the modern approaches aim at enhancing the phonon scattering at the grain boundaries by quantum confinement effect. Nanostructuring approach enhances the density of states near Fermi level and decouples the inverse relationship among **S** and σ.[25] Despite the quantum confinement effect, mean free path of electrons and phonons plays a crucial role when nanostructuring is employed as it introduces a large density of interfaces. This large density of interfaces enables the preferential scattering of phonons than electrons and thus lattice contribution towards κ is reduced while preserving the carrier concentration and σ.[26] Structural changes can affect the TE properties of a material and one of the main advantages of nanostructuring and introducing structural changes is the reduced κ and improvement in the overall TE figure of merit.[8,27,28] The previous reports have

demonstrated that κ can be reduced drastically by nanostructuring. Extensive phonon scattering is one of the key reasons to employ nanostructured TE materials to have a low κ due to the grain boundary effect.[29, 30]

This chapter deals with the temperature dependence of TE properties and efficiency of chemically synthesized BT nanostructures in terms of ***ZT***. Here we used refluxing method, one of the bottom-up, surfactant-directed (ethylenediaminetetraacetic acid (EDTA) as the surfactant), simple, low-cost method and achieved the required product with precise control over the stoichiometric balance between Bi and Te. To the best of our knowledge, there is almost no report on the preparation of different phases of BT nanostructures with control over morphology using aqueous-based low temperature refluxing method. To fill this gap, we presented a systematic study to observe the effect of reaction time on the crystal structure, morphology and TE properties of BT nanostructures. Here EDTA is the molecular capping agent, responsible for inhibiting the oxidation apart from its role as a surfactant and hence stable BT nanostructures could successfully be synthesised. In addition to the control over crystal structure and morphology, the stoichiometry of the synthesised samples can be maintained as the method is a low temperature one. Hence, reproducible samples of n-type Bi_2Te_3 with different EDTA concentrations with perfect stoichiometry and a variety of structural as well as morphological variations could be synthesized which is one of the significant achievements of this study. A reaction mechanism suggesting the formation of these low dimensional nanostructures has also been presented and we have tried to demonstrate that both structural and morphological changes are appropriate ways to enhance the overall TE properties of materials belonging to the BT category. In addition Sb-doped BT samples have also been synthesized and the effect of hot pressing has been demonstrated. This will help in future for keeping the stoichiometry even after adding the suitable dopants for enhanced TE performance. Hence we tried to demonstrate that both structural and morphological changes are appropriate ways for enhancing the overall transport properties of materials belonging to BT category and that the synthesis technique plays a crucial role in keeping the stoichiometry of the synthesised samples. Thus, our low temperature refluxing provides potential

opportunities for the synthesis of defect free, stable nanostructured materials through the control of reaction parameters.

3.2.   Experimental section

3.2.1. Material Synthesis

In the synthesis of BT nanostructures, 0.2 m mol of $BiCl_3$, 0.3 m mol of Te powder were used as starting materials. Sodium borohydride ($NaBH_4$) acts as the reducing agent and EDTA as the surfactant. Deionised water was used as the reaction medium and the reaction was carried out at the boiling point of the medium. After being stirred for 10 minutes, the solution was refluxed which constitute the primary stage of reaction, where $BiCl_3$ splits up into bismuth and chloride ions. EDTA is essential to cap the bismuth ions and to control the morphology over different reaction times. Once the reaction temperature reached the boiling point of the medium, $NaBH_4$ was introduced into the mixture to facilitate the reduction reaction. Reaction has been carried out for different molarities of $NaBH_4$ (0.5-4.4 M) and different reaction timings from 1 h to 36 h to have a clear idea of the growth mechanism and TE properties of BT bulk and nanostructures. The BT nanostructures prepared for different EDTA concentrations namely 50 mmol, 75 mmol and 100 mmol and different reaction times (1 h, 6 h, 12 h, 24 h and 36 h) are labelled as shown in Table 3.1. In addition, Sb_2Te_3, SnTe and Sb-doped BT nanostructures are prepared using Sb powder, $SbCl_3$, $SnCl_2$ and Te powder as metal ion precursors and EDTA as the surfactant. The precipitated BT nanostructures after refluxing is washed with acetone, ethanol and deionised water several times until a clear solution is obtained. Vacuum dried BT powders at 393 K were subjected to high-pressure pelletizing with a uniaxial pressure of 1.2 GPa. These pellets were sealed in an evacuated quartz tubes and subjected to sintering at 600 K for 3h. Sintering at a temperature above 600 K is not favorable here due to the tendency of Te to vaporize especially at a sintering temperature above 600 K due to its high vapor pressure, and hence an insufficient amount of Te can significantly affect both stoichiometric chemical composition and material properties. Refluxing enables a perfect and ambient condition for the formation of BT structures by controlling the Te evaporation up to certain extent

even for prolonged reaction time.[16, 31, 32] The careful optimization of EDTA concentration could enable an ambient condition for the formation of low dimensional BT structures by decreasing the surface energy. Thus, optimizing both EDTA concentration and reaction time could deliver stable, phase pure compounds of BT nanostructures. The stability of the prepared samples is directly related to the concentration of capping agent and was confirmed by exposing them to open atmosphere for six months before measuring the transport properties.

3.2.2. Materials Characterization

The sintered pellets from each batch were powdered for X-ray diffraction (XRD), high-resolution transmission electron microscopy (HR-TEM) and energy dispersive X-ray spectroscopy (EDS) analysis, whereas X-ray photoelectron spectroscopy (XPS) and TE measurements were carried out on sintered pellets. Crystal structures of the synthesized BT nanostructures were determined by XRD (Bruker D8 Advance X-ray diffractometer), using Cu Kα radiation with an X-ray wavelength of 1.5406 Å in the 2θ range of $20°$-$90°$ with a step size of $0.0167°$. Structural refinement was carried out using GSAS-EXPGUI software and the crystal structures were obtained from Crystal Maker software. The morphologies of the synthesized BT nanostructures were investigated by Scanning Electron Microscopy, SEM (JEOL 7800, operated at 5 kV) and HR-TEM (FEI Tecnai F20, operated at 300 kV). The elemental compositions of all the BT nanostructures were determined using EDS. To understand the effect of EDTA concentration on nanosheet formation of the synthesized samples, atomic force microscopy (AFM) analysis in the tapping mode was carried out (Bruker Multimode, Germany). XPS measurements were carried out using a Kratos Analytical Instrument, UK (SHIMADZU group, Model: AXIS Supra). A monochromated Al K_{α} source (Energy= 1486.6 eV) was used to probe the BT samples. The binding energies were corrected by C 1s as reference energy (C 1s = 284.8 eV). A wide scan was collected to ensure that no foreign materials were present on the sample surface. Narrow scans of Bi 4f and Te 3d regions were collected. Curve fitting to the XPS spectrum was done using XPSPEAK 4.1 software. Background subtraction was done using the Shirley method.

Table 3.1. Codes of the synthesized samples for different molarity and reaction times.

Nanostructures	Molarity	Reaction time	Sample code
Bi₂Te₃	50 mmol	1 h	BT50-1
	50 mmol	12 h	BT50-12
	50 mmol	24 h	BT50-24
	75 mmol	1 h	BT75-1
	75 mmol	6 h	BT75-6
	75 mmol	12 h	BT75-12
	75 mmol	24 h	BT75-24
	75 mmol	36 h	BT75-36
	100 mmol	1 h	BT100-1
	100 mmol	12 h	BT100-12
	100 mmol	24 h	BT100-24
Sb₂Te₃ (using Sb powder)	75 mmol	24 h	ST1-75-24
Sb₂Te₃ (using SbCl₃)	75 mmol	24 h	ST2-75-24
SnTe	75 mmol	24 h	TT-75-24
Bi₂₋ₓSbₓTe₃ (x=0.01)	75 mmol	24 h	BS1T
Bi₂₋ₓSbₓTe₃ (x=0.03)	75 mmol	24 h	BS3T
Bi₂₋ₓSbₓTe₃ (x=0.05)	75 mmol	24 h	BS5T
Hot pressed Bi₂₋ₓSbₓTe₃ (x=0.01)	75 mmol	24 h	BS1T-HP
Hot pressed Bi₂₋ₓSbₓTe₃ (x=0.03)	75 mmol	24 h	BS3T-HP
Hot pressed Bi₂₋ₓSbₓTe₃ (x=0.05)	75 mmol	24 h	BS5T-HP

It is well reported that anisotropic behaviour in polycrystalline samples will be too weak to exhibit a significant changes in TE properties and hence isotropic *ZT* values are expected in both the directions. To avoid the influence of nanostructures orientation

on the TE properties of the synthesized BT sample, the measurements for electrical resistivity (ρ), S and κ were measured with the samples oriented identically (i.e., perpendicular to the press direction in this study). BT powders were subjected to high-pressure and high temperature sintering (HPHTS) where high-pressure pelletizing[33, 34] has been done with a uniaxial pressure of 1.2 GPa and sintering at a temperature of 600 K. The density of the BT pellets was determined using Archimedes set up and was found to be above 95% for all the samples with a maximum of 97% for higher reaction time samples, i.e. samples synthesised above 12 hours (h). The ρ of the BT rectangular pellets (8mm x 2mm x 2mm) were measured using the 4 probe method in electrical transport option (ETO) attached to Physical Property Measurement System (PPMS) supplied by Quantum Design, USA in the temperature range 2 K− 350 K. Hall resistivity (ρ_{xy}) of the BT rectangular pellets (8mm x 3mm x 2mm) were measured at room temperature using the ETO probe of PPMS. The κ and S of the pellets were measured using the thermal transport option of PPMS in the temperature range 260 K-380 K.

3.3.   Results and discussion

3.3.1.   Morphological tailoring and enhanced room temperature TE performance in n-type Bi$_2$Te$_3$ nanostructures synthesized via chemical route

Thermoelectric properties of n-type BT nanostructures are reported by varying the morphology and crystal structure whereas the EDTA concentration has been fixed as 75 mmol. Tuning the reaction time from 1 to 36 h enables the phase transformation from BiTe with a hexagonal crystal structure to Bi$_2$Te$_3$ with a rhombohedral crystal structure and the detailed structural, morphological and thermoelectric properties are discussed below.

3.3.1.1. Structural analysis

The XRD patterns of the samples prepared for different molarities of NaBH$_4$ and 1 h reaction time is shown in Fig.3.1. The synthesized samples were of molarities ranging from 0.5-4.4 M of NaBH$_4$. The sample prepared with 4.4 M NaBH$_4$ was confirmed to be BiTe as per the standard powder diffraction data for JCPDS: 83-1749

(ICSD code 30525). From the results obtained, it was confirmed that stable samples of BT structures could be synthesized using reflux method. There is no possibility for arising Boron in the matrix of the synthesized samples. This is due to the fact that reaction of Te and $NaBH_4$ could only lead to the production of Te^{2-} ions and $NaBO_3$ as byproducts. The combination of Bi^{3+} and Te^{2-} yields Bi_2Te_3, whereas, $NaBO_3$ is readily soluble even in water. Hence, washing of the final product several times in acetone, ethanol and deionized water and centrifuging will completely dissolve and wash out $NaBO_3$. The impurity peaks observed in the lower concentration samples are arising as a result of the formation of TeO_2 and the complete chemical reaction between Te and $NaBH_4$ is explained in detail in the coming sections.
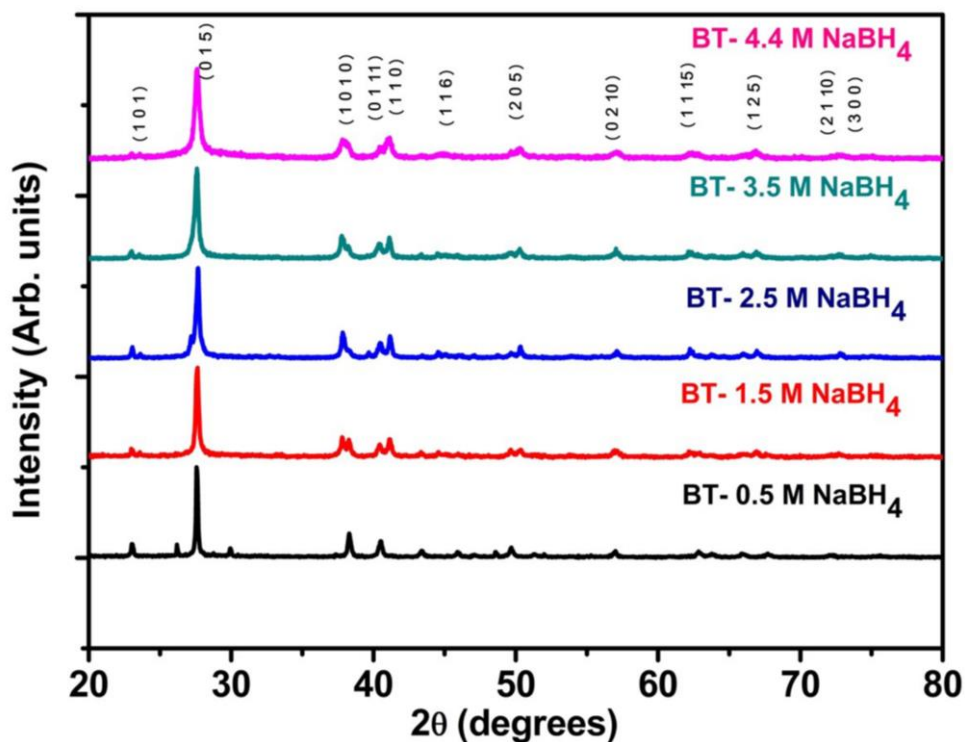
Fig. 3.1. XRD patterns of the BT structures prepared for different molarities of $NaBH_4$

Fig. 3.2 shows the XRD patterns along with Rietveld refinement of the BT samples prepared for different reaction times varying from 1 h to 36 h at an EDTA concentration of 75 mmol and keeping the molarity of $NaBH_4$ at 4.4M. The Rietveld refinement (shown in Fig.3.2 (a) – 3.2(e)) gives a clear idea about the structural changes and the structural parameters were determined and listed in Table 3.2. The χ^2 (goodness of fit) is defined as the square of the ratio between weighted profile R factor (R_{wp}) and

expected R factor (R_{exp}). A low value of χ^2 has been observed which justifies the quality and goodness of refinement. It is confirmed that a series of structural transition from BiTe hexagonal phase to the Bi_2Te_3 rhombohedral phase with JCPDS: 85-0439 (ICSD code 15753) takes place with the reaction time from 1 h to 36 h and further it is noticed that a combination of different BT structures dominates in BT75-6 and BT75-12 samples i.e., BiTe and Bi_2Te_3 phases for BT75-6 sample, whereas Bi_2Te_3 and Bi_4Te_3 phases for BT75-12 sample. Finally, a stable Bi_2Te_3 phase with hexagonal stacking is obtained with the reaction time of 24 h. However, upon further increase in the reaction time i.e., for 36 h, Bi_2Te_3 phase with rhombohedral crystal structure is formed.
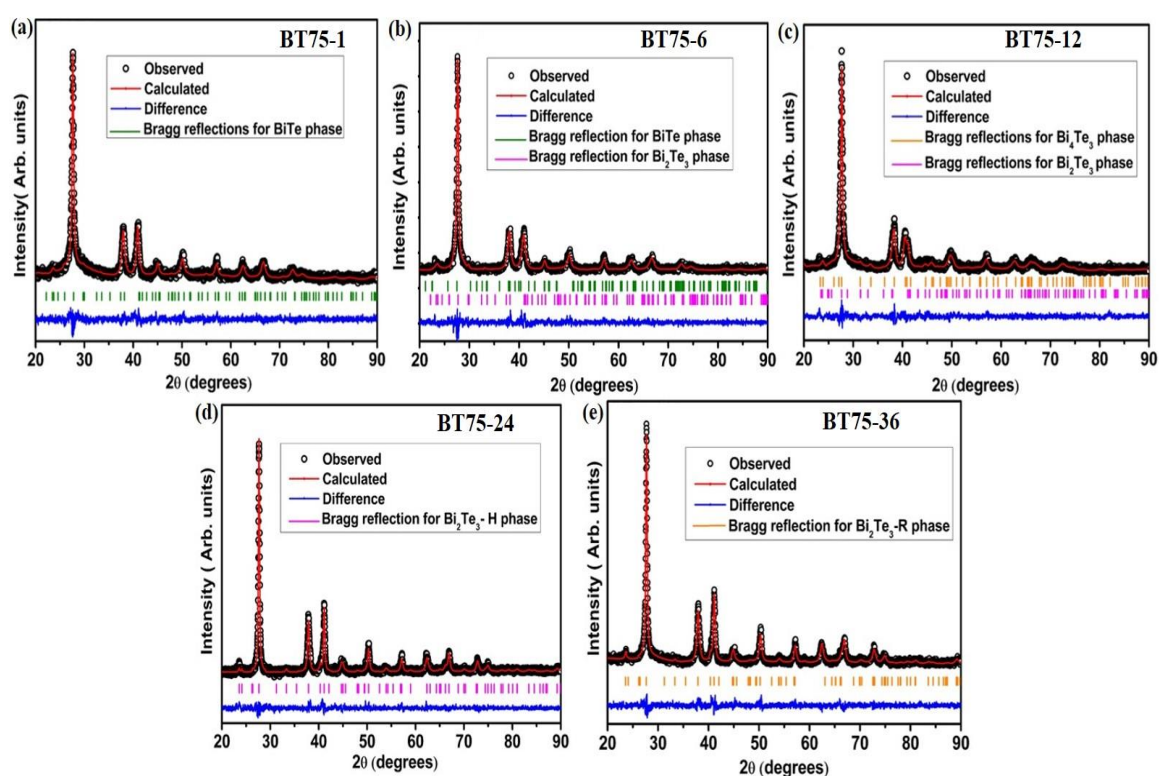
Fig. 3.2. Refined XRD patterns of BT nanostructures.

The crystal structure has been obtained using the refined parameters and is depicted in the Fig.3.3 and it clearly shows the structural transition from BiTe phase to Bi_2Te_3 phase for 1 h to 24 h reaction time.

Table 3.2. Refined parameters of BT nanostructures

BT nano-structures	BT75- 1	BT75-6		BT75-12		BT75-24	BT75-36
Phase	BiTe	Bi_2Te_3 + BiTe		Bi_2Te_3 + Bi_4Te_3		Bi_2Te_3 - H	Bi_2Te_3 - R
Crystal Structure	Hexagonal	Hexagonal		Hexagonal + Rhombohedral		Hexagonal	Rhombohedral
Space Group	P-3 m 1	R-3m + P-3 m 1		R-3m		R-3m	R-3m
Lattice Parameters							
a(Å)	4.38(4)	4.40(3)	4.35(8)	4.46(7)	4.43(8)	4.39(1)	10.44(1)
b(Å)	4.38(4)	4.40(3)	4.35(8)	4.46(7)	4.43(8)	4.39 (1)	10.44(1)
c(Å)	24.01(4)	30.08(5)	24.80(9)	29.57(7)	42.41(1)	30.39(3)	10.44(1)
γ(deg)	120	120	120	120	120	120	24.30(1)
Volume(Å)³	399.08(5)	504.99(6)	406.50(1)	508.80(1)	719.30(1)	506.51(4)	169.22(2)
Residual Parameters							
χ^2	1.05	1.12		1.10		1.08	1.14

.
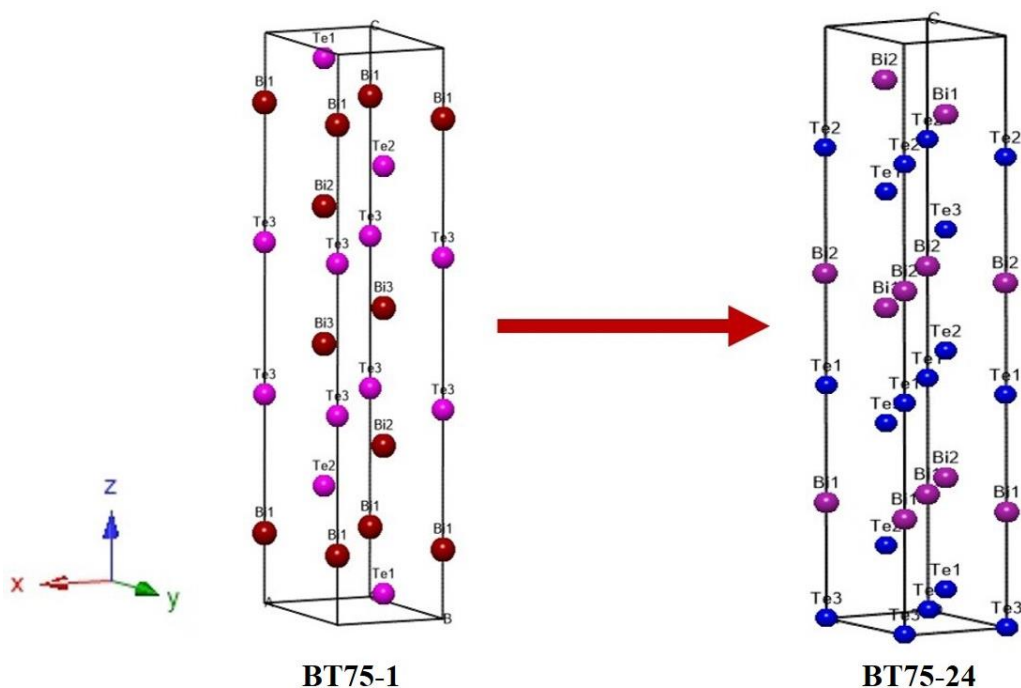
BT75-1   **BT75-24**

Fig. 3.3. Crystal structure of BT75-1 and BT75-24 samples.

3.3.1.2. SEM micrographs

SEM images and EDS spectrum of all the samples were taken and as a representative of the series, BT75-24 sample data is shown in Fig.3.4. All the samples show well-formed grains with less porosity revealing the high densification. The EDS spectrum of BT75-24 sample and the composition data for all the studied samples are tabulated in Table 3.3. As it can be seen from the spectrum and Table 3.3, the compositions of the lower reaction time sample matches with BiTe phase, as the sample is exposed to reaction temperature for a lesser time, in which unreacted Bi and Te ions will be washed off resulting in the formation of BiTe, whereas samples synthesized at a higher reaction time above 24 h and 36 h is experiencing reaction temperature for prolonged time and ambient reaction condition for the formation of Bi_2Te_3 phase. An intermediate composition is observed for BT75-6 and BT75-12 from the compositional data and reveals the co-existence of different BT phases which is confirmed by HR-TEM analysis and is discussed below.
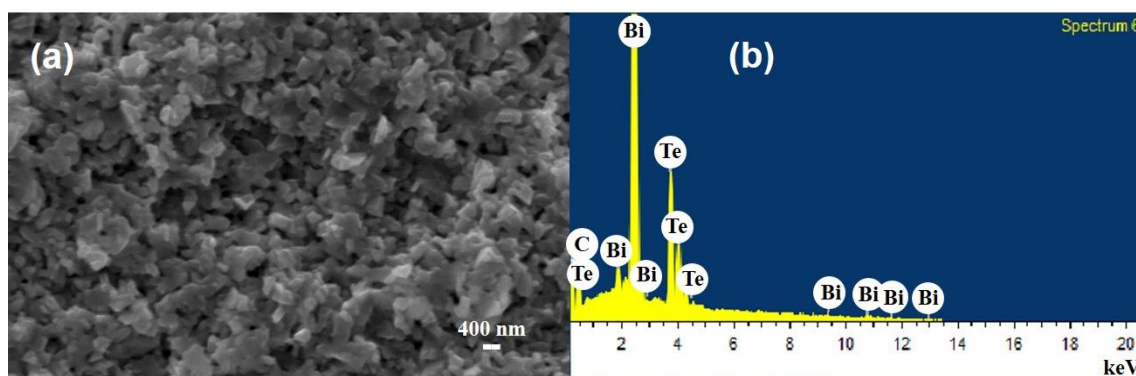
Fig. 3.4. BT75-24 sample (a) SEM image and (b) EDS spectra

Table 3.3. EDS data of BT nanostructures

Sample	Atomic percentage		Weight percentage	
	Bi	Te	Bi	Te
BT75-1	49.23	50.77	62.74	37.26
BT75-6	46.04	53.96	58.29	41.71
BT75-12	46.91	53.09	59.14	40.86
BT75-24	40.72	59.28	51.78	48.22
BT75-36	40.56	59.44	51.38	48.62

3.3.1.3. TEM analysis

Fig. 3.5 shows the TEM images of the BT nanostructures synthesized for different reaction times. The crystal structure of most of the chemically synthesized BT nanocrystals has two-dimensional plate-like structures.[8,35] Fig.3.5 (a-j) shows the morphology of the BT nanostructures. BT75-1 has nanocrystals with size ranging from 20–25 nm (shown in Fig.3.6 (a)). Initiation of growth mechanism is clearly seen in BT75-6 (Fig. 3.5(b) and 3.5(g)). In BT75-6 samples, plate-like morphology having around 100 nm width is noticed (Fig. 3.7 (a)). Upon increasing the reaction time to 12 h i.e., in BT75-12, fine and coarse nanostructures are observed with maximum particle size ranging up to 70 nm (Fig 3.5 (c), 3.5 (h) and 3.7 (b)). Interestingly, 24 h reaction time enables the formation of nanocrystals with an average particle size of 20 nm (shown in Fig.3.6 (b), Fig 3.5 (d) and 3.5 (i)) clearly illustrates the impact of reaction time on morphological aspects of the BT75-24 samples synthesised for 24 h. Further increase in the reaction time, i.e., for BT75-36 sample causes the morphological changes as shown in Fig. 3.5 (e) and 3.5 (j). BT75-36 sample shows an agglomerated kind of morphology where a significant change in the lattice parameters is seen with a transition to the Bi_2Te_3 rhombohedral structure. The corresponding lattice fringes and selected area diffraction patterns (SAED) patterns are shown in Fig. 3.5(k) – 3.5(t) (Fast Fourier Transform (FFT) is shown in the inset). It is well reported that the BT compounds have a layered structure with Te–Bi–Te–Bi–Te sequence showing weak Van der wall's interaction among the Te atoms which allows the cleavage along the perpendicular planes to that of c-axis[28, 36] as shown in Fig.3.3. Reflections corresponding to the (011), (104), (018) and (005) planes of BiTe phase are observed in Fig. 3.5(k) and FFT shows the crystalline nature of the BT75-1 sample. Nanocrystals in the BT75-6 samples synthesized for 6 h reaction time grew with a preferred orientation, as their morphology constituted coarse structures along with the fine structures as shown in Fig. 3.5(b) and 3.5(g). The (015) plane of grown Bi_2Te_3 phase is evident from both lattice fringes and SAED patterns as indicated in Fig. 3.5(l) and 3.5(q). An increase in the reaction time yields the formation of nanocrystals as a combination of fine and coarse structures which is in accordance with the earlier reports, where sintering

temperature was the varying parameter.[11]
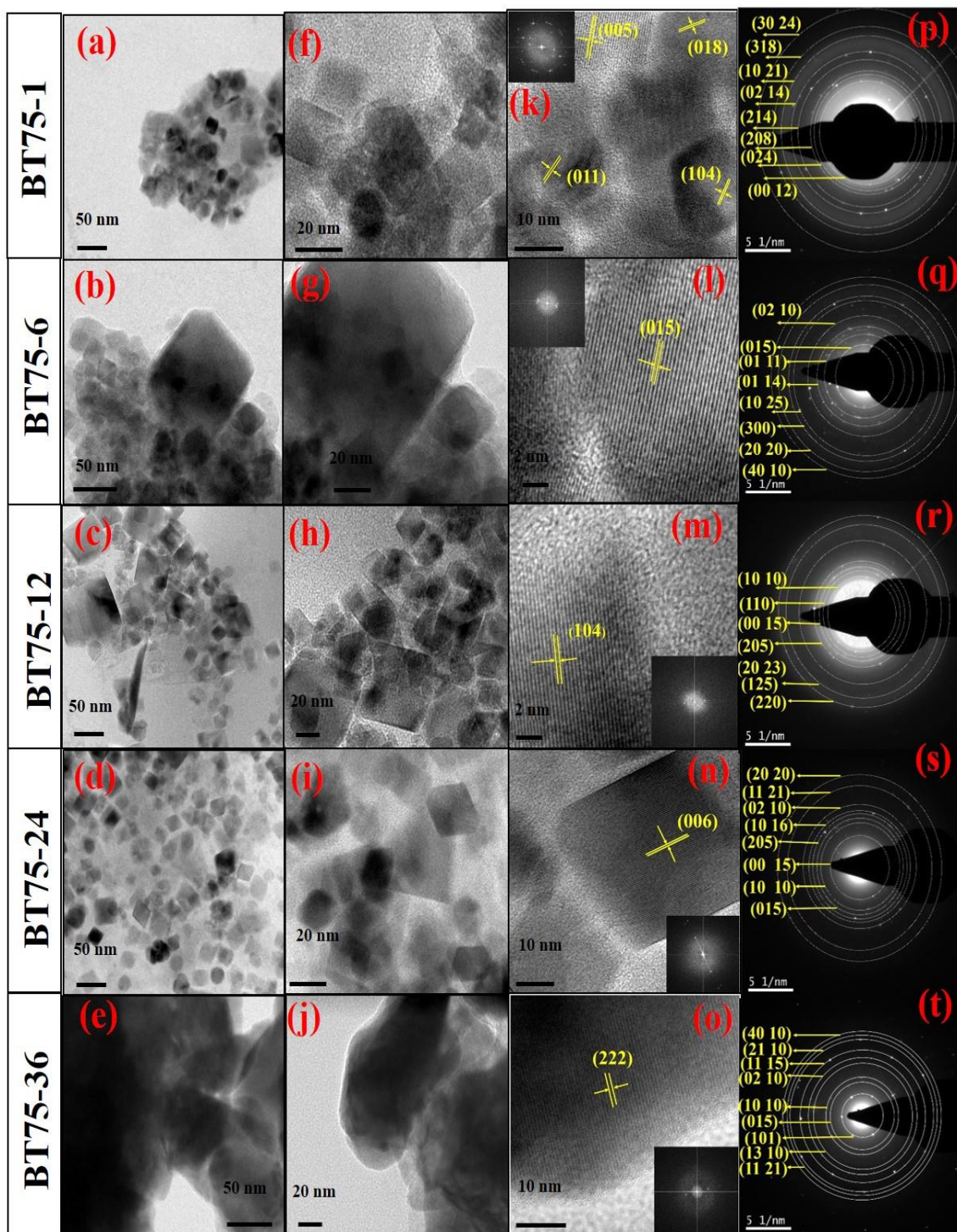
Fig. 3.5. BT nanostructures (a-j) TEM images showing plate-like nanocrystals, (k-o) HR-TEM images with lattice fringes (FFT is in the inset) and (p-t) SAED patterns.

The high-resolution TEM images and SAED patterns of BT75-12 and BT75-24 are shown in Fig. 3.5(m), 3.5(r) and Fig. 3.5(n), 3.5(s) respectively. It is evident from the FFT and SAED patterns of BT75-24 (Fig. 3.5(n) and 3.5(s)) that the size of the crystals and crystallinity has improved considerably with the reaction time. The lattice fringes correspond to the (006) plane of the Bi_2Te_3 phase is shown in Fig. 3.5(n), in which it can be observed that uniformly distributed cube like nanocrystals have been formed for BT75-24. Fig.3.5 (e and j) shows the morphological changes of BT75-36 samples. Lattice fringes and diffraction patterns of BT75-36 samples which are as shown in Fig.3.5 (o and t), confirms the rhombohedral crystal structure of BT75-36 sample.

In order to further confirm the existence of different phases in BT75-6 and BT75-12, high-resolution TEM images showing lattice planes of the corresponding phases are shown in Fig.3.8. In BT75-6, (015) plane of Bi_2Te_3 and (104), (018) planes of BiTe are coexisting whereas in BT75-12, (015) plane of Bi_2Te_3 and (009) plane of Bi_4Te_3 are coexisting (shown in Fig.3.8 (a) and 3.8 (b) respectively) which further corroborates the mixed phases of BT75-6 and BT75-12 samples as discussed in the XRD analysis.
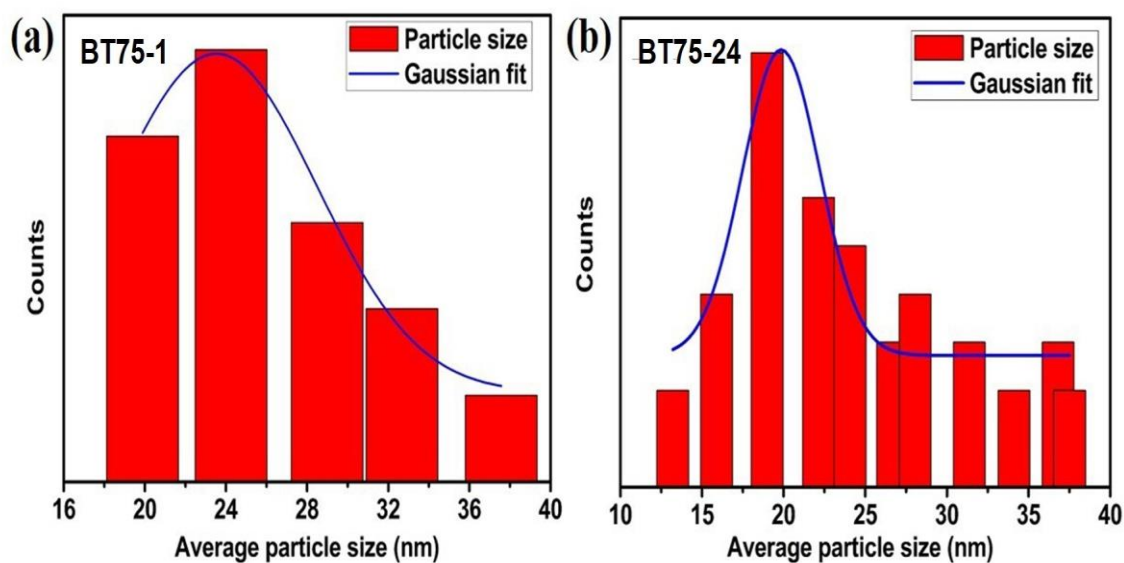
Fig. 3.6. Particle size distribution of (a) BT75-1 and (b) BT75-24
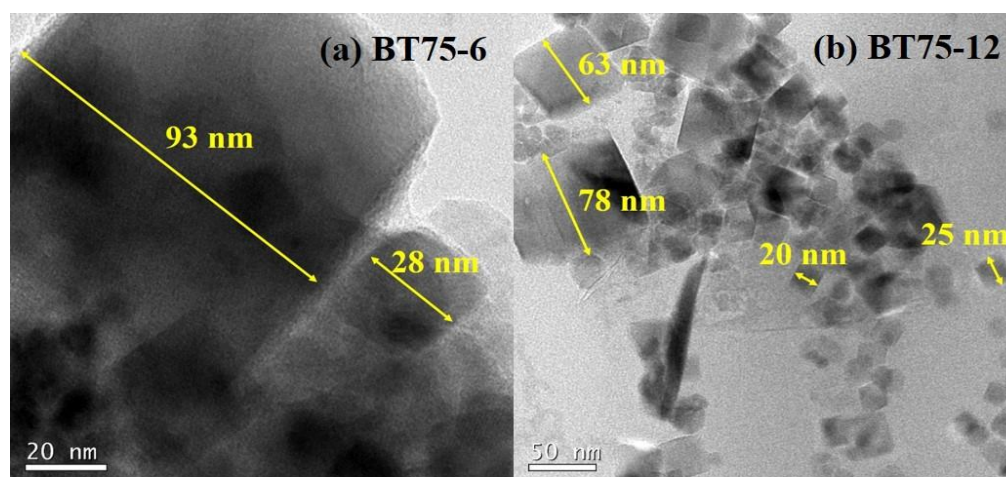
Fig. 3.7. TEM images: Coarse and fine structures (a) BT75-6 and (b) BT75-12
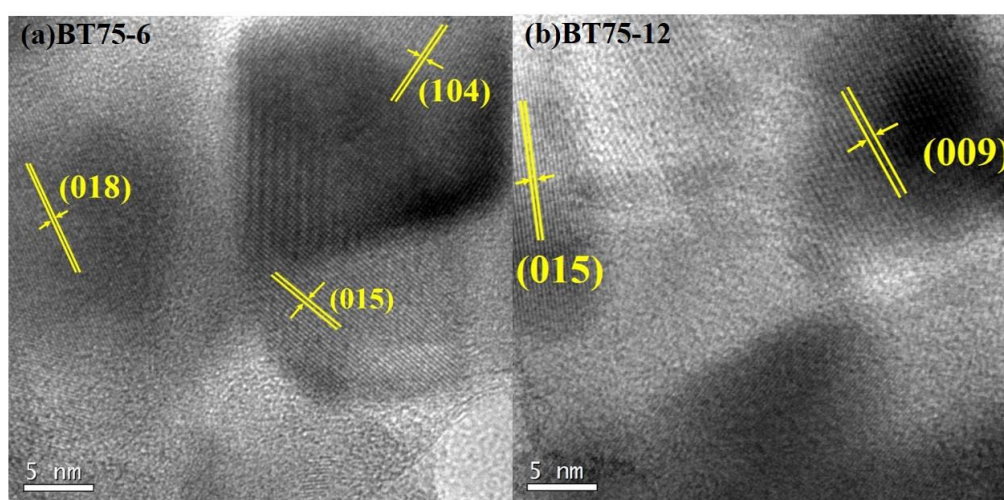
Fig. 3.8. HR-TEM images showing planes corresponding to different phases of BT nanostructures (a) BT75-6 and (b) BT75-12

3.3.1.4. Seebeck coefficient and thermal conductivity

Fig. 3.9 and Fig. 3.10 shows the temperature dependence of S and κ in the temperature range of 260 K-380 K. A negative value of S obtained for all the samples (shown in Fig. 3.9) indicates an n-type semiconducting behavior. BT75-1 with hexagonal BiTe phase shows the highest value of S as -145 μV/K around room temperature, whereas a considerable reduction of the same is observed for BT75-6 sample which shows a maximum S value of -85 μV/K at 380K. Upon increasing the reaction time further, S of BT75-12 and BT75-24 improved further and achieved a peak value of -147 μV/K and -270 μV/K respectively. It is noticed that the S value of the

BT75-36 sample reduced to a value below -130 μV/K. BT75-1 shows the typical range of S value for BiTe nanocrystals and it is well reported that Bi_2Te_3 phase of BT structures could exhibit the maximum value of S compared to other phases of the same.[6, 37] The reduction in S for the BT75-6 sample may be due to the transition of crystal structure from BiTe hexagonal phase to a combination of BiTe and Bi_2Te_3 phases with variation in the lattice parameters. Furthermore, the temperature dependence of S in case of BT75-12 and BT75-24 samples reveal that a significant enhancement in S is achieved as a result of nanostructuring and crystal structure variation. However, BT75-36 synthesised at 36 h shows, S value in the range -80 to -130 μV/K which may be due to the Bi_2Te_3 rhombohedral crystal structure.[11] In the present study, BT75-24 sample, the Bi_2Te_3 with hexagonal stacking possess the higher value of S and it is found to be near -260 μV/K at room temperature which is still higher in comparison to the conventional state-of-art materials.[29,32,35] It is well reported that S is in inverse proportion to carrier concentration and thus a decrease in S from BT75-1 to BT75-36 is expected. On the contrary, there is a deviation from the general trend and this could be due to the different phases present in different BT structures and potential barrier scattering. These potential barriers will aid the filtering of low energy carriers at the interface which is responsible for the reduction of S. Thus, filtering of these low energy carriers could successfully enhance the S value [38-40] and another reason for enhanced value of S in BT75-24 sample is the improved interface density. We have performed the Hall resistivity measurement to confirm that the majority charge carriers are electrons in all the samples, which are discussed in later sections.

Fig. 3.10 shows the measured κ value of the BT samples which are lower values than that of reported bulk ingots Bi_2Te_3 (1.5 W m^{-1}K^{-1}) and are comparable to that of recently reported Bi_2Te_3 nanostructures.[29,41] BT75-1 sample shows the least κ among the synthesised samples and exhibit a κ value of 0.34 W m^{-1}K^{-1} at room temperature. BT75-12 and BT75-24 also exhibit lower values of κ well below 0.5 W m^{-1}K^{-1}, which are much lesser than that of bulk values (0.8 W m^{-1}K^{-1} - 1.1 W m^{-1}K^{-1}) in the temperature range of 260 K−380 K and is approaching close to the minimum κ among

the reported values of Bi_2Te_3 series.[42,43]
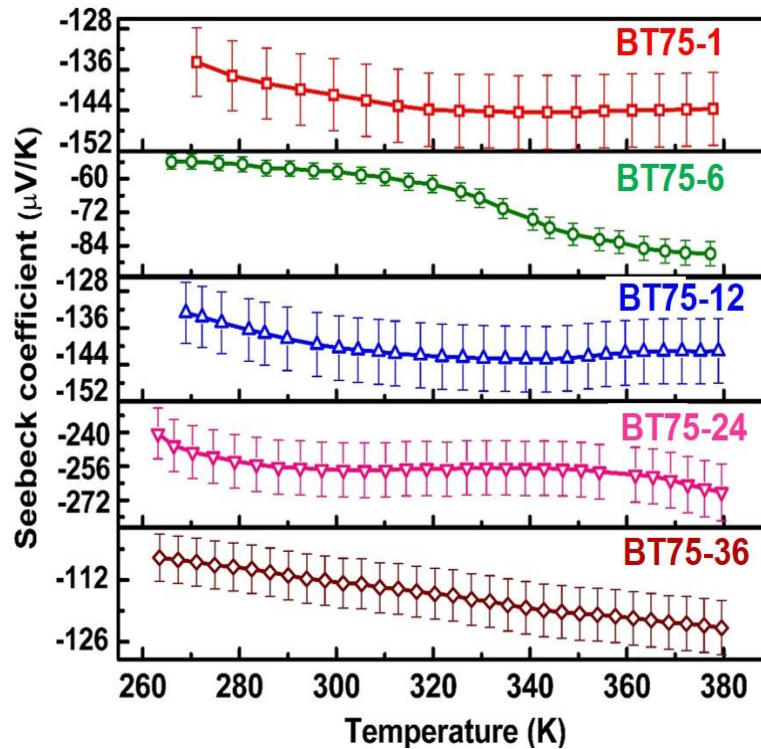
Fig.3.9. Temperature dependence of *S* of BT nanostructures.

Thus, for all the samples prepared at different reaction times, it was possible to tune the κ value in the range 0.32 $Wm^{-1}K^{-1}$ - 0.68 $Wm^{-1}K^{-1}$ from 260 K to 380 K except in the case of BT75-6 sample. BT75-6 sample which has formed as a combination of BiTe and Bi_2Te_3 phases, exhibits a κ of 1.5 $Wm^{-1}K^{-1}$ as in the case of bulk alloys. This is due to the grown Bi_2Te_3 coarse structures as shown in Fig. 3.8 (a), which has a κ value close to its bulk counterparts. Among the BT75-24 and BT75-36, BT75-24 is of less κ and this could be probably due to the fact that uniform nanocrystals with a large number of grain boundaries effectively enhances the scattering of the short-wavelength phonons. Moreover, the fine nanostructures promote the specified orientation along the press direction, which in turn further enhance the phonon scattering in the direction that is parallel to the press direction. Again, BT75-36 sample is of rhombohedral crystal structure with distorted geometry, where atomic packing is less compared to hexagonal stacking. A significant reduction in the κ value is observed in the nanostructured single phase samples with hexagonal stacking, especially in BT75-1 and BT75-24 which is understood to be due to extensive phonon scattering.[29]

3.3.1.5. Electrical and Hall resistivity

Fig. 3.11 shows the temperature variation of ρ for all the BT nanostructures in the range 5 K – 350 K. All the synthesised samples show a metal to semiconductor like transition near room temperature. It is observed that the ρ value of BT75-1 at 300 K is 1.39 x 10^{-4} ohm-m, which is decreased to 6.82 x 10^{-5} ohm-m for BT75-6 and 3.37 x 10^{-5} ohm-m for BT75-12 sample. It is to be noted that BT75-1 sample is having a single phase of BiTe, whereas the BT75-6 and BT75-12 samples contain multiphase and coarse structures, which results in the drastic decrease of ρ with the increase in reaction time. Again, in case of BT75-24 and BT75-36 samples where the single phase of Bi_2Te_3 is formed but with different crystal structure (i.e. hexagonal for BT75-24 and rhombohedral for BT75-36) is observed and ρ value is found to be 7.12 x 10^{-5} ohm-m and 8.22 x 10^{-5} ohm-m respectively which is close to that of BT75-6.

Further, Hall measurements were conducted on the BT pellets and the variation of Hall resistivity (ρ_{xy}) with temperature is shown in Fig. 3.12. All the samples show negative Hall coefficient (R_H) confirming that electrons are the majority charge carriers in the BT samples. This result is concordant with the values of S discussed in the earlier sections. The carrier concentration (n) has been calculated from the relation $n=1/R_H$ and the mobility (μ) from the relation $\rho= 1/(ne\mu)$ where e is the electronic charge, 1.6 x 10^{-19}C. The n and μ calculated from the hall measurements are plotted in Fig. 3.13.

BT75-1 has a n value of 5 x 10^{19}electrons/cm^3 which is increased from 2 x 10^{19} electrons/cm^3 for BT75-6 to 14 x 10^{19} electrons/cm^3 for BT75-36 and it is expected to have a decrease in the ρ values of these samples. But both electrical and thermal properties strongly depend on the crystal structure and the different combination of BT structures arising from different reaction time could be the reason for the lack of uniformity in the transport properties of different samples.[11] The ρ has achieved a decreased value of 3.37 x 10^{-5} ohm-m for BT75-12 sample with a n value of 5 x 10^{19}electrons/cm^3 and a μ of 35 cm^2/V-s. The value of n for BT75-24 and BT75-36 samples has increased to 8 x 10^{19} electrons/cm^3 and 14 x 10^{19} electrons/cm^3 with a decrease in the μ and σ. Thus, the electron concentration of different BT structures

increases from BT75-1 to BT75-36 and an increase in σ is expected as σ is proportional to n.
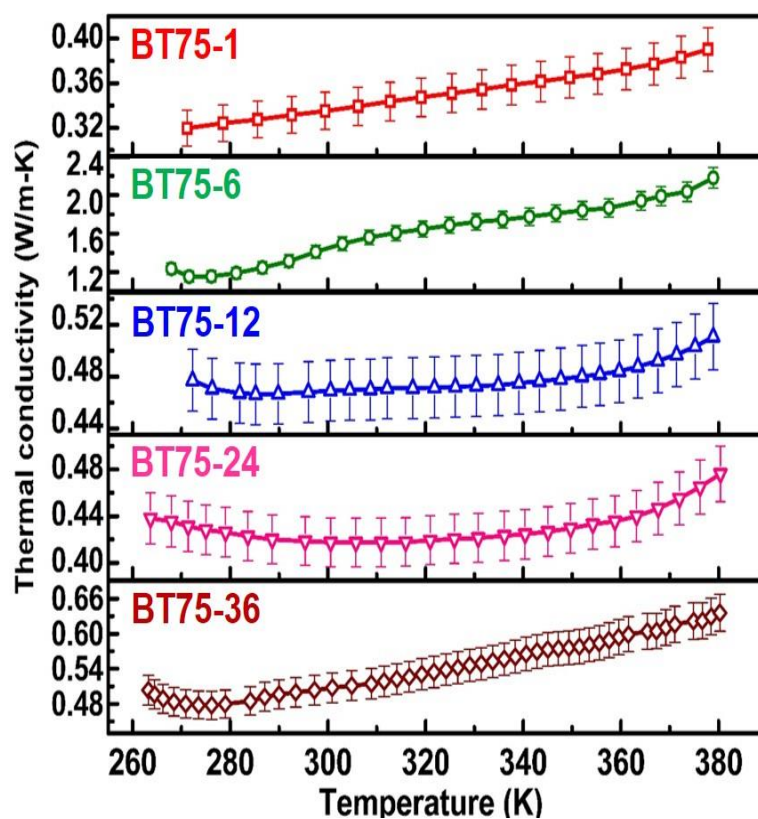
Fig.3.10. Temperature dependence of κ of BT nanostructures.
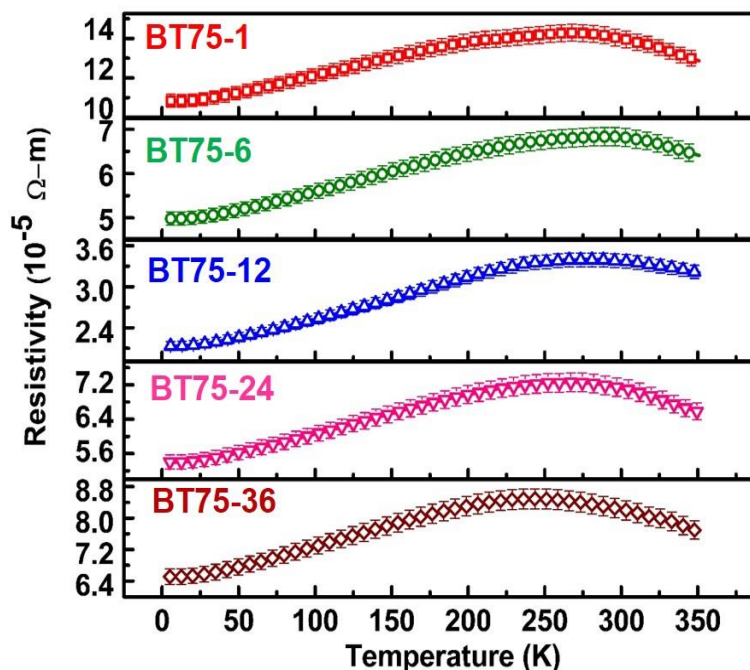
Fig. 3.11. Temperature dependence of ρ of BT nanostructures.
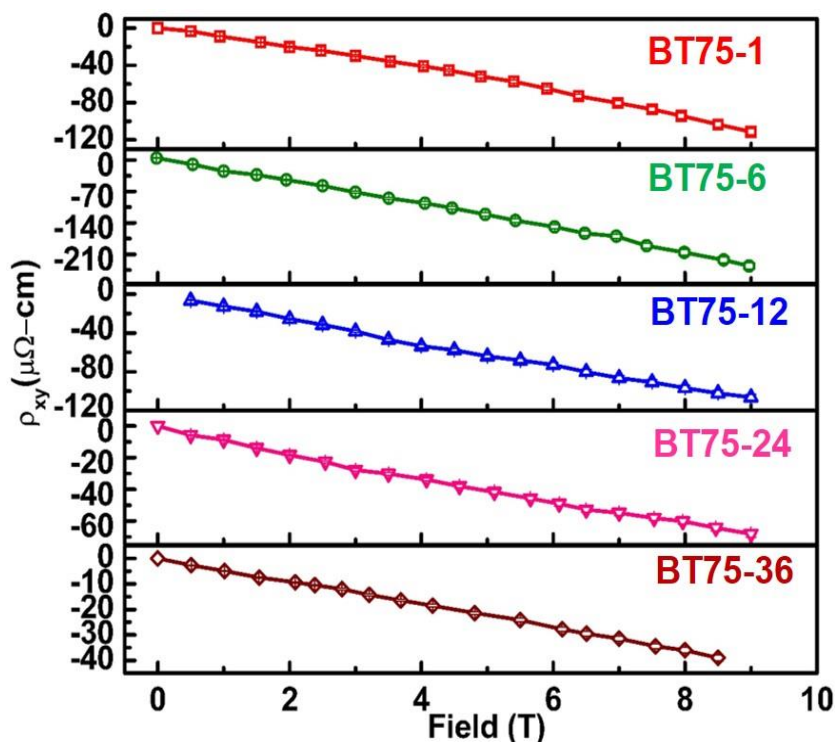
Fig. 3.12. Field dependence of ρ_{xy} of BT nanostructures measured at 300K.
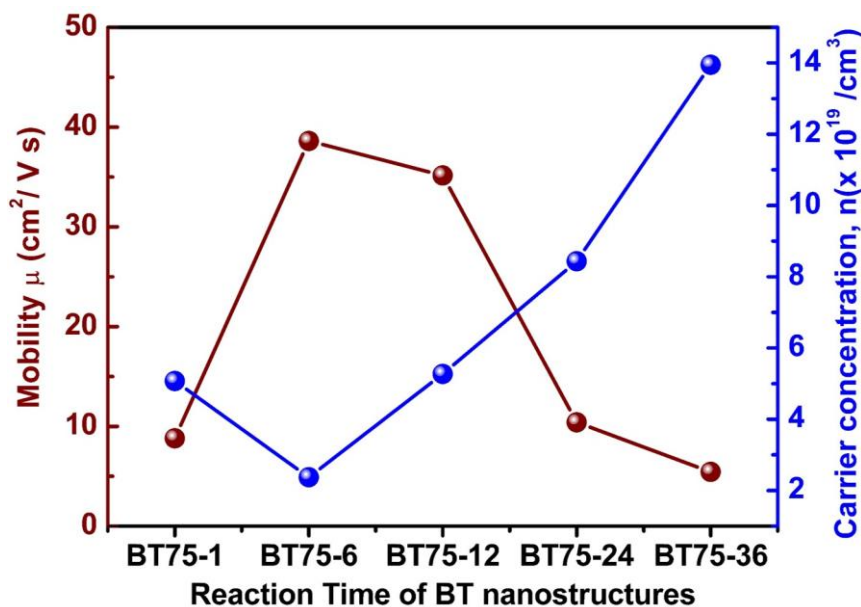
Fig. 3.13. Mobility and Carrier concentration versus reaction time of BT nanostructures.

The variation of σ in the temperature range 260 K–350 K has been plotted for all the BT samples and is shown in Fig. 3.14. The inverse proportionality among the n and σ can be observed in the conventional nanostructured TE materials synthesised by

bottom-up approach.[38, 43] The increased μ is expected in samples with coarse structures due to the fact that the reduced interface density will favour the mean free path of the carriers. Above 260 K, it is observed that σ has increased with an increase in the temperature for all the BT structures. This behaviour is in contradiction to the conventional BT structures where degenerate semiconductor behaviour is exhibited. However, if a non-degenerate semiconducting behaviour is exhibited by the system, where it can be expected this kind of unusual electrical behaviour. If potential barrier scattering is the dominant scattering mechanism as mentioned earlier, the σ of nanostructured materials increases with an increase in temperature in a particular temperature range as indicated in Fig. 3.14 and is exhibited by some of the recently reported systems.[43-45] If n increases, the concept of mean free path of electrons can be successfully explained the decrease of μ. Due to the drastic decrease in the μ and densification compared to spark plasma sintered samples, [29, 46, 47] the achieved results for σ is less compared to the reported values but still enhanced S with a peak value of about -260 μV/K at room temperature, is resulting in the overall improvement of PF and ZT for BT75-24 and is illustrated in Fig.3.15 and 3.16 respectively.
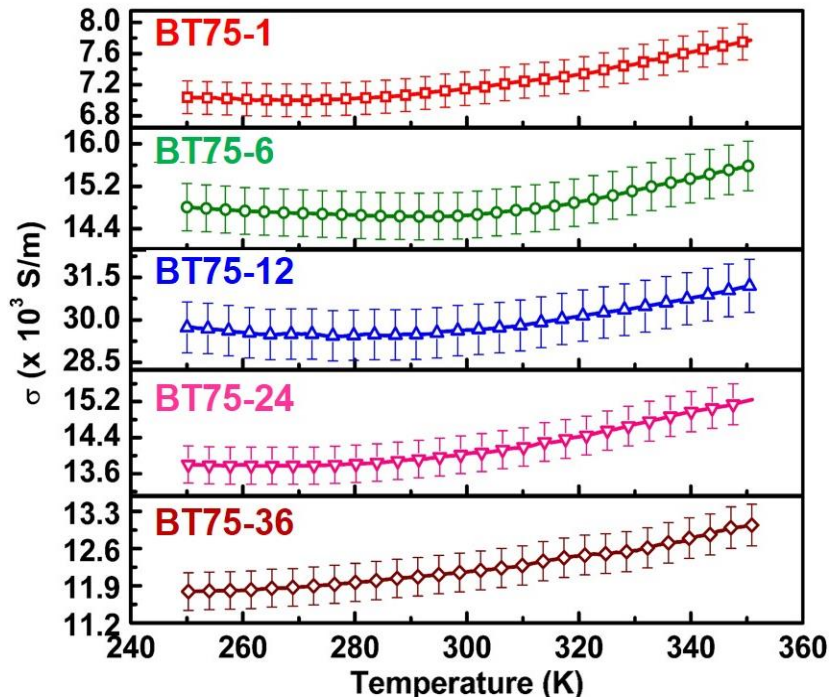
Fig. 3.14. Temperature variation of σ of BT nanostructures.

3.3.1.6. Power factor and figure of merit

The **PF**, which is calculated as $S^2\sigma$ is plotted with the variation of temperature and shown in Fig. 3.15. **PF** value of BT75-1 sample gave a maximum of 160 $\mu Wm^{-1}K^{-2}$ at 350 K which is decreased to 100 $\mu Wm^{-1}K^{-2}$ for BT75-6 sample because of the reduction in **S** value of BT75-6 as discussed in the earlier sections. The structural and morphological variation of BT75-6 could also be another reason for the decreased value of **PF**. The **PF** increased significantly for samples BT75-12 and BT75-24 when the reaction time increased beyond 6 h. The **PF** shows the maximum for BT75-24 which increased with temperature from 900 to 1000 $\mu Wm^{-1}K^{-2}$ as shown in Fig. 3.15. Compared to the bulk Bi$_2$Te$_3$ ingots, **S** of present sample is around 50% higher and it is also about two-to-three times higher than the state-of-the-art nanostructured bulk Bi$_2$Te$_3$ prepared by arc melting, ball milling and HPHTS BT structures.[11, 30, 48] It is expected that the considerably enhanced **S** in the BT75-24 nanostructures can compensate the moderately deteriorated σ, and in turn lead to the $S^2\sigma$ improvement.
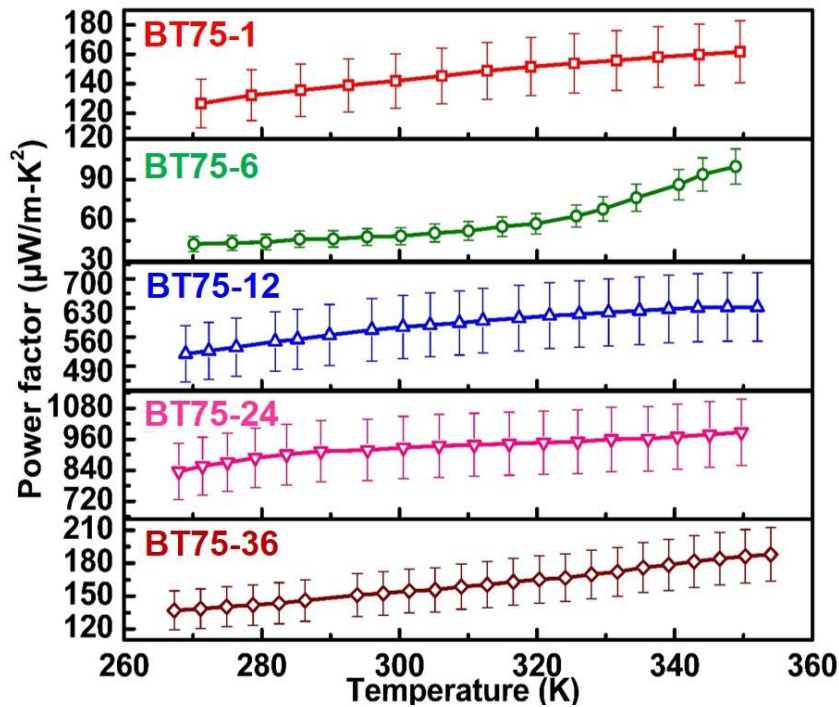
Fig. 3.15. Temperature dependence of **PF** of BT nanostructures.

Finally, *ZT* as a function of temperature has been determined and is depicted in Fig. 3.16, which shows the range of *ZT* values for different BT structures. *ZT* of BT75-1 shows a linear dependence with the temperature and achieved the highest value of 0.15 at 350 K. As a result of decrease in *S* and *PF*, BT75-6 sample shows a drastic reduction in the *ZT* value below 0.10 and is less effective to be used as a TE material. Significant improvement in *ZT* is observed for BT75-12 and BT75-24 samples synthesised for 12 h and 24 h showing a peak value of 0.45 and 0.81 respectively at 350 K. Further increase in reaction time causes a decrease in the TE properties in BT75-36 and overall reduction in the *ZT* value to 0.09 at 300 K. The enhanced *ZT* values of BT75-12 and BT75-24 are comparable to the previously reported Bi_2Te_3 nanostructures.[49-51] The measured *ZT* value for BT75-24 is higher than recently reported, solution synthesised Bi_2Te_3 samples.[52] Furthermore, both the increased *PF* and the reduced κ along with a resistivity range comparable to that of semi metallic materials result in an enhanced *ZT* in the BT75-12 and BT75-24 samples (Fig. 3.16). The TE parameters of all the BT samples at room temperature have been tabulated in Table 3.4.
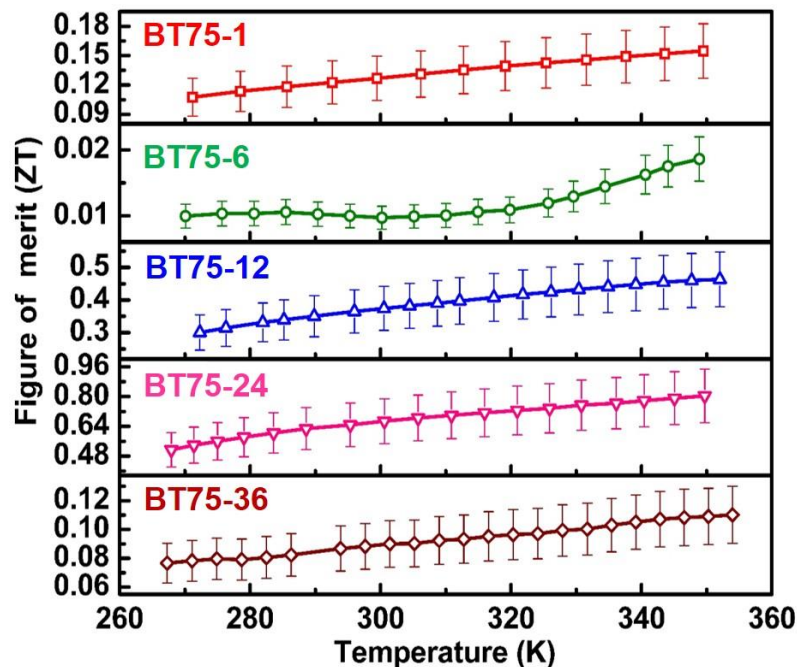
Fig. 3.16. Temperature dependence of *ZT* of BT nanostructures.

Table 3.4. TE parameters of BT nanostructures at 300 K. The estimated error in the measurement of *S* is ±5%, **κ** is ±5 % and resistance is ±0.1%

Sample	S (μW/K)	κ (W/m-K)	ρ (x10^{-5} Ω-m)	σ (S/m)	μ (cm^3/V sec)	n (x 10^{19} /cm^3)	PF (μW/m-K^2)	ZT
BT75-1	-141	0.34	13.99	7148	10	5	142	0.12
BT75-6	-57	1.49	6.82	14663	40	2	48	0.01
BT75-12	-140	0.47	3.37	29674	35	5	582	0.37
BT75-24	-258	0.42	7.12	14045	10	8	935	0.67
BT75-36	-113	0.51	8.22	12165	5	14	155	0.09

The variation in TE properties can be well explained with grain boundary scattering and formation of coarse structures.[11] The single phase samples are formed as fine nanocrystals whereas mixed-phase samples form coarse structures along with fine structures as shown schematically in Fig.3.17.

XRD and TEM images confirm the phase as well as structural changes of synthesized samples with reaction time. BT75-1 sample forms the BiTe phase with an average size of 24 nm. Due to the formation of nanocrystals, BT75-1 exhibits a *κ* value of 0.34 Wm^{-1}K^{-1} at room temperature and grain boundary scattering facilitates the reduction in *κ* for BT75-1 sample. *S* and *σ* exhibited by the BT75-1 sample are -141 μV/K and 7148 S/m respectively at 300 K which is the typical range of BiTe phase and is confirmed from the XRD refinement results. The formation of coarse structures is noticed for mixed phases (i.e. for BT75-6 and BT75-12 samples) which favors electron transport, as the number of grain boundaries have decreased due to the growth of coarse structures. Coarse and fine structures for BT75-6 and BT75-12 are clearly shown in Fig.3.7. Electrons can move easily in coarse structures and through the electrically neutral grain boundaries, unlike phonon scattering, which enhances electron transport in fine and coarse structures. This is the reason for the enhancement of *σ* in BT75-6 and on the other side *S* is reduced drastically to a value near -60 μV/K at room temperature. As the grain boundary effect is less in comparison to fine nanocrystals of BT75-1, BT75-6 sample exhibits the maximum *κ* and the microstructures are predominant over the fine structures as illustrated in Fig.3.7 (a).
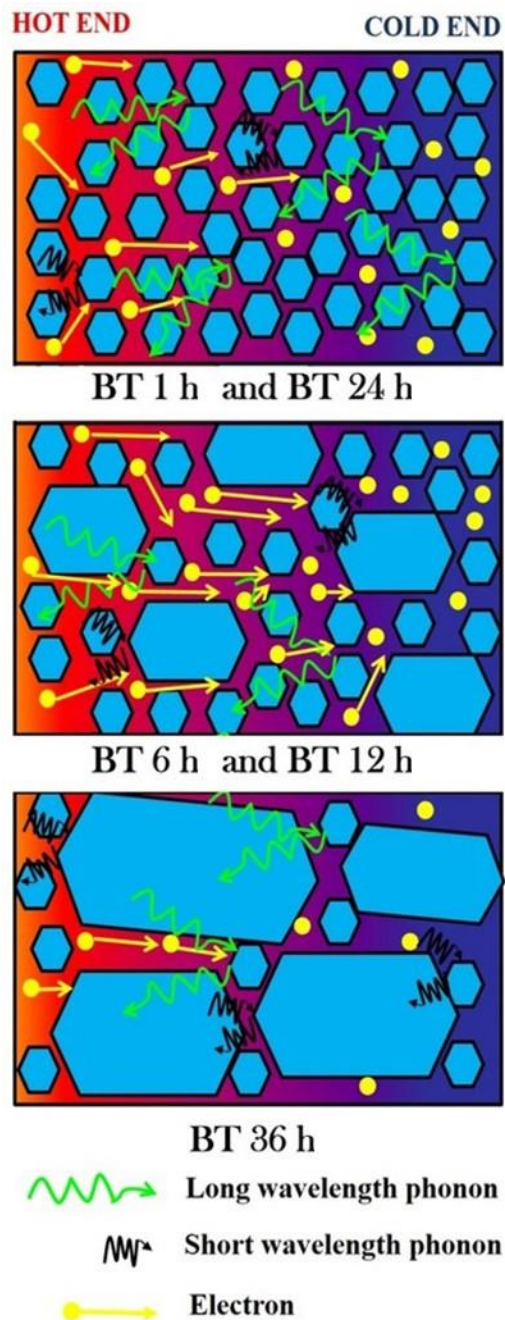
Fig. 3.17. Schematic diagram explaining the thermal and electrical transport properties of BT nanostructures.

Upon increasing the reaction time to 12 h, a perfect combination of fine and coarse structures is observed for BT75-12 and as a result both κ and σ is enhanced, where σ is maintained by the coarse structure and κ is maintained by the fine structure. A compromise is observed in the case of S as well and thereby the overall ZT is tuned to 0.5 for BT75-12 sample at 350 K. Further increase in reaction time to 24 h enables

the formation of nano crystals of single phase hexagonally stacked Bi_2Te_3 (BT75-24) where κ is less compared to BT75-6 and BT75-12 but slightly higher in comparison to BT75-1. BT75-24 nanostructures could considerably enhance the *PF* and preferentially scatter the phonons due to high densification and efficient stacking of the nanoplates. The slight increase in κ of BT75-24 compared to that of BT75-1 single phase could be due to the different phases exhibited by BT75-1 and BT75-24. As a result, the TE characteristics of the BT75-24 sample have been enhanced considerably. Further, increase in reaction time to 36 h induces structural and morphological changes which are responsible for inferior TE properties of BT75-36 sample in comparison to BT75-12 and BT75-24. Again, the hexagonal structure of BT75-24 sample has more atomic packing than that of rhombohedral structure of BT75-36 sample, which results in the enhanced TE properties in spite of having the same Bi_2Te_3 phase in both the samples. These results demonstrate that nanostructuring and careful optimization of coarse structures along with fine grains could enhance the overall TE properties of different BT nanocrystals.

3.3.2. Surfactant induced structural phase transitions and enhanced room temperature TE performance in n-type Bi_2Te_3 nanostructures synthesized via chemical route

A systematic study of surfactant-assisted aqueous-based low-temperature chemical method for the synthesis of different phases of Bi−Te-based nanostructures with different morphologies ranging from nanocrystals to nanorods/nanosheets is investigated in this section. Tuning the surfactant concentration from 50 to 100 mmol facilitates the formation of low-dimensional structures of Bi_2Te_3, the structural, morphological and TE properties of which is explained in the following sections.

3.3.2.1 Structural analysis

Fig. 3.18 shows the Rietveld refined XRD patterns of the BT samples prepared for different EDTA concentrations (i.e., 50 mmol and 100 mmol) and reaction times and the refined parameters of the same are tabulated in Tables 3.5 and 3.6 respectively. The quality and goodness of refinement is represented using the residual parameters which are well in accordance with the expected results. The Rietveld refinement of BT50

series (shown in Fig.3.18 (a) – 3.18 (c)) reveals the structural changes with the increase in reaction time. A combination of BiTe and Te is observed for BT50-1 whereas Bi_2Te_3, Bi_4Te_3 and Te is observed for BT50-12. Te impurity is seen to be present for lower reaction time (i.e., BT50-1 and BT50-12) which disappears for higher reaction time, i.e., for 24 h and forms a stable Bi_2Te_3 structure.
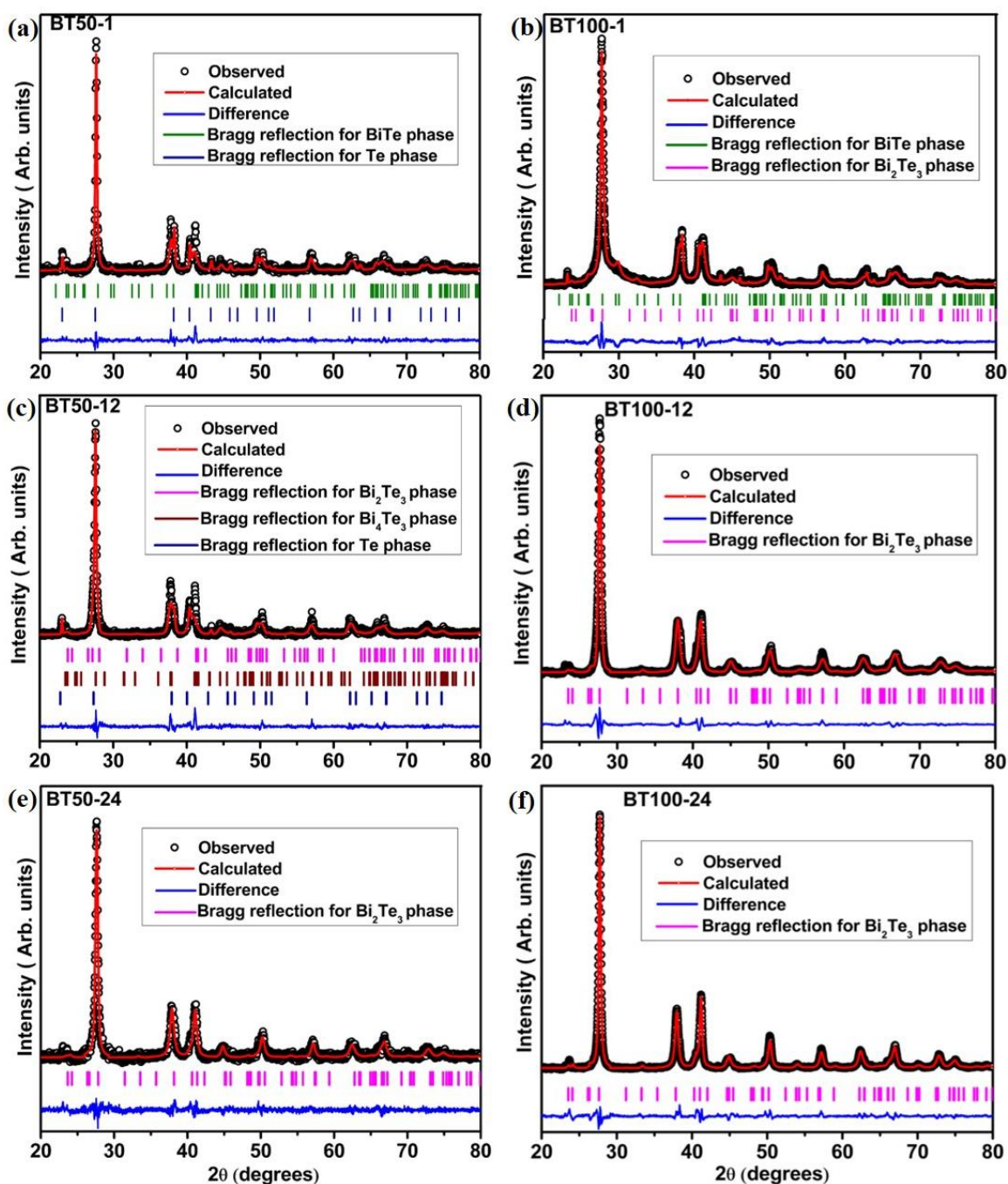
Fig. 3.18. Refined XRD patterns of BT nanostructures (a) BT50-1, (b) BT50-12, (c) BT50-24, (d) BT100-1, (e) BT100-12 and (f) BT100-24

An increase in EDTA concentration from 50 mmol to 75 mmol, the Te impurity completely disappears and facilitates the BT structure formation in the early stage, but 24 h reaction seems to be the best optimization for the formation of hexagonally stacked Bi_2Te_3.[54] When the EDTA concentration is further increased to 100 mmol, a similar observation is noticed but Bi_2Te_3 formation is facilitated even at the lower reaction time (i.e., BT100-1) along with BiTe phase. Finally, a stable Bi_2Te_3 phase is obtained for both 12 h and 24 h reaction time samples.

The Rietveld refinement of BT100 series (shown in Fig.3.18 (d) – 3.18 (f)) gives the observed structural changes. It is confirmed that structural transitions from mixed phases of different BT structures to hexagonal phase of Bi_2Te_3 take place with the reaction parameters from BT50-1 to BT100-24. There is a diffraction peak shift for the synthesized single phase Bi_2Te_3 and mixed phases of BiTe and Bi_2Te_3 which is due to the fact that solution based chemical synthesis can cause such phenomenon[55, 56].

Table 3.5. Refined Parameters of BT50 series

BT Structures	BT50-1		BT50-12			BT50-24
Phase	**BiTe + Te**		**Bi_2Te_3 + Bi_4Te_3 + Te**			**Bi_2Te_3**
Crystal Structure	Hexagonal + Trigonal		Hexagonal + Rhombohedral + Trigonal			Hexagonal
Space Group	P-3 m 1 + P 31 2 1		R-3m + P-3 m 1+ P 31 2 1			R-3m
Lattice Parameters						
a(Å)	4.36(0)	4.47(0)	4.35(1)	4.39(0)	4.50(0)	4.39(0)
b(Å)	4.36(0)	4.47(0)	4.35(1)	4.39(0)	4.50(0)	4.39(0)
c(Å)	24.11(1)	5.93(1)	29.52(2)	42.65(1)	5.96(1)	30.33(1)
γ(deg)	120	120	120	120	120	120
Volume(Å)³	396.68(1)	102.48(2)	483.41(0)	712.44(1)	104.66(3)	506.27(8)
Phase Fraction (%)	72.63	27.37	35.33	33.54	31.13	100
Residual Parameters						
wR$_p$	8.94		8.48			8.87
R$_p$	4.53		4.24			4.42
χ^2	1.15		2.03			1.27

Table 3.6. Refined Parameters of BT100 series

BT Structures	BT100-1		BT100-12	BT100-24
Phase	BiTe + Bi$_2$Te$_3$		Bi$_2$Te$_3$	Bi$_2$Te$_3$
Crystal Structure	Hexagonal		Hexagonal	Hexagonal
Space Group	P-3 m 1 + R-3m		R-3m	R-3m
Lattice Parameters				
a(Å)	4.39(0)	4.22(1)	4.40(0)	4.39(0)
b(Å)	4.39(0)	4.22(1)	4.40(0)	4.39(0)
c(Å)	24.10(1)	30.86(0)	30.24(0)	30.38(1)
γ(deg)	120	120	120	120
Volume(Å)^3	402.24(4)	474.83(0)	507.10(3)	507.17(2)
Phase Fraction (%)	48.11	51.89	100	100
Residual Parameters				
wR$_p$	7.85		6.95	6.51
R$_p$	3.70		3.23	3.12
χ^2	1.62		1.32	1.26
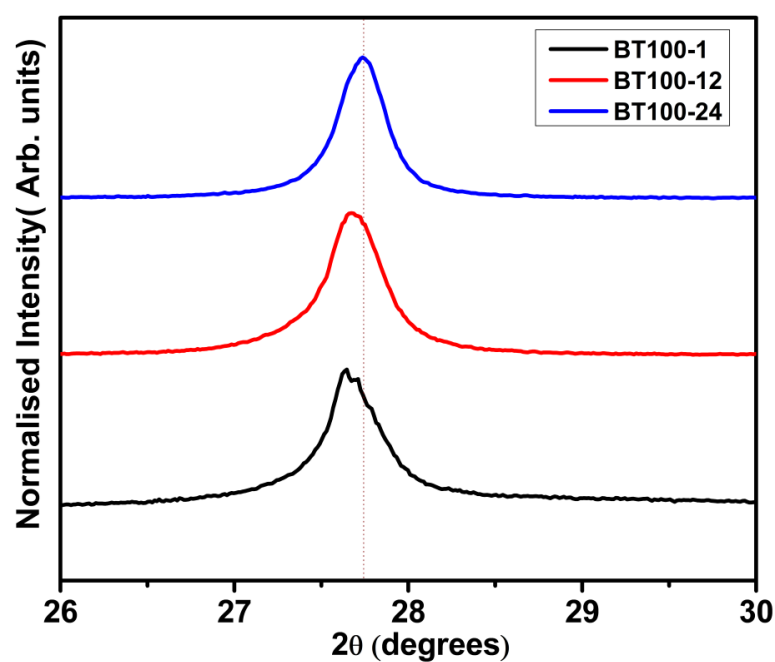
Fig. 3.19. Peak shift associated with different samples of BT100 series
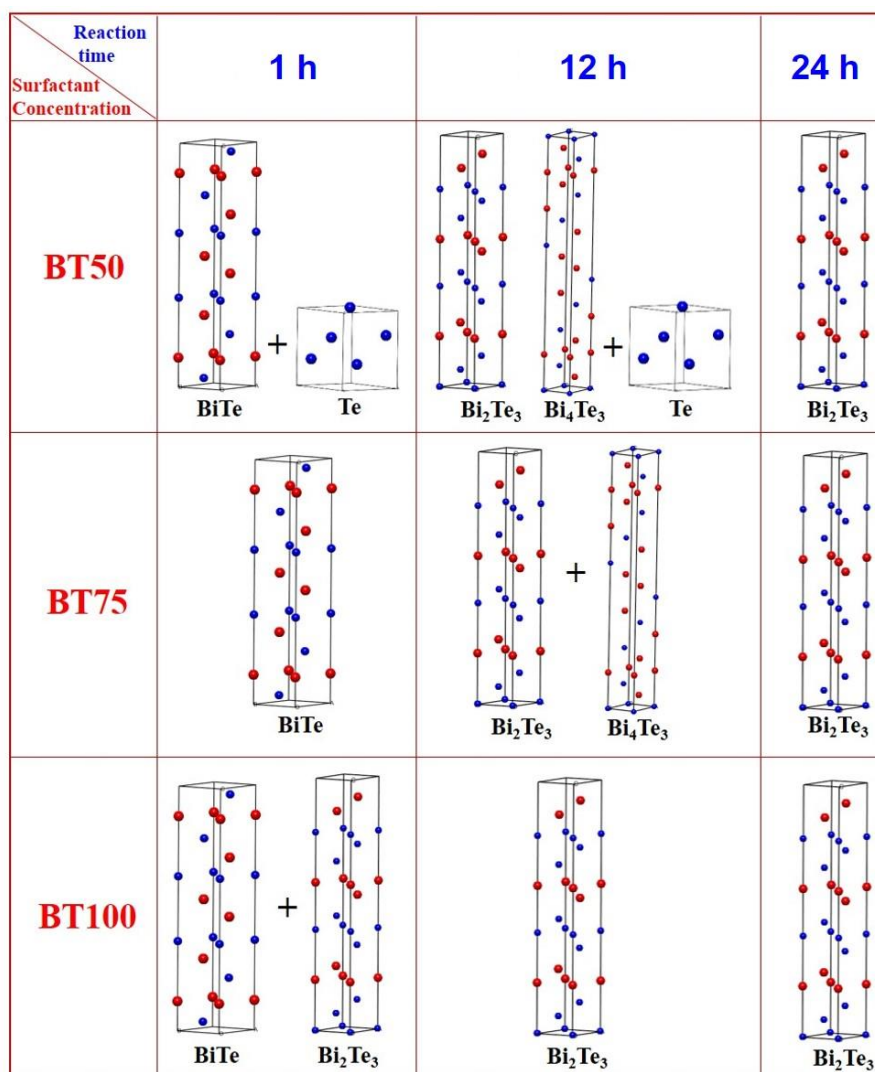
Fig. 3.20. Crystal structures of BT nanostructures for BT50, BT75 and BT100 series with varying reaction times of 1 h, 12 h and 24 h.

We tried to emphasise this peak shifts from the detailed refined XRD patterns and Fig.3.19 represents the peak shift associated with different samples of BT100 series. Again, consider Fig. 3.18 (d) where both BiTe and Bi_2Te_3 phases are coexisting, a clear shift is indicated for both BiTe and Bi_2Te_3 phases, green bars representing the Bragg's reflections of BiTe and pink bars indicating the Bragg's reflections of Bi_2Te_3. Hence the structural variations have resulted from the aqueous-based reflux method where EDTA concentration and reaction time acts as the key reaction parameters. As mentioned above, the shifting of stable Bi_2Te_3 phase formation towards lower reaction time with the increase in surfactant concentration is also clearly demonstrated in the crystal structure diagram as shown in Fig. 3.20.

3.3.2.2. Morphological Analysis

Detailed TEM micrographs are shown in Fig.3.21 for both BT50 series and BT100 series. From the morphology of BT50 series, it is evident that nanostructuring gets facilitated with reaction time even for the same EDTA concentration. Interestingly, the morphology is highly dependent on EDTA concentration as well and these reports suggest the formation of BT nanostructures with a variety of dimensions like nanorods, nanosheets and nanoplates.[57-61] Fig.3.21 (a-c), Fig. 3.21 (g-i) and Fig. 3.21 (m-o) shows the morphology of the BT50-1, BT50-12 and BT50-24. Both BT50-1 and BT50-12 shows an agglomerated morphology and is evident in Fig. 3.21 (m) and Fig. 3.21 (n). Upon further increasing the reaction time to 24 h, i.e., in BT50-24, a complete bridging among the adjacent nanocrystals are observed with maximum particle size ranging up to 50 nm (Fig. 3.21 (o)). The corresponding SAED patterns of BT50 series are shown in Fig. 3.21 (s) – Fig. 3.21 (u). Reflections corresponding to the (214), (208) and (00 12) in SAED pattern correspond to the BiTe and Te phases as shown in Fig. 3.21 (s), which is in corroboration with the XRD refinement results. Nanocrystals of BT50-12 sample show three different structures from the SAED patterns as indicated in Fig. 3.21 (t) those corresponds to Bi_4Te_3, Bi_2Te_3 and Te, which is well in agreement with XRD analysis. It is reported that the BT compounds can have mixed phases under some preferable conditions where reaction time, surfactant concentration and sintering temperature etc. could play a crucial role in determining the reaction conditions and formation mechanisms[11,54] which will be discussed in the later sections. An increase in the reaction time to 24 h, yields the formation of Bi_2Te_3 hexagonal nanocrystals in a connected morphology which is in accordance with the earlier reports[11,62] and SAED patterns of BT50-24 is shown in Fig. 3.21 (u), further confirm the hexagonal phase. The BT75 series exhibited a plate-like morphology up to 24 h reaction time[54] and we could suggest that EDTA plays an inevitable role in nanocrystal formation. Furthermore, it is evident from the TEM images of BT100 series that rod-like structures have formed in comparison with the other series of BT nanostructures. Fig. 3.21 (d-f) shows the morphology of the BT100-1, BT100-12 and BT100-24 respectively. BT100-1 shows a combination of nanorods and nanosheets along with some nanocrystals where the nanorod dimension is found to be of 98 nm width and 250 nm length shown in Fig.3.22.

Nanorod and nanosheet formation is facilitated with increased reaction time as well in BT100 series which could be seen in BT100-12 (Fig. 3.21 (e) and Fig. 3.21 (k)). In BT100-12 samples, nanorod morphology having around 35 nm width which is intercalated among nanosheets is noticed (Fig. 3.21 (k), Fig.3.23). Upon increasing the reaction time to 24 h, i.e., in BT100-24, a perfect combination of nanorods, nanosheets and nanoflakes are observed which is evident from the TEM images (Fig. 3.21 (f), Fig. 3.21 (l) and Fig.3.24).

Hence, the reaction time optimization enables the formation of nanorods along with nanosheets as given in Fig. 3.21 (l) and the dimensions of which are represented in Fig.3.24. The high-resolution image (FFT is shown in the inset) and SAED patterns of BT100 series are shown in Fig. 3.21 (p-r) and Fig. 3.21 (v-x). Reflections corresponding to the (1010), (002), (003) and (104) planes of BiTe phase are observed in BT100-1 which is represented in Fig. 3.21 (p) and FFT shows (inset of Fig. 3.21 (p)) the crystalline nature of the BT100-1 sample. Nanorods in the BT100-12 samples grew with a preferred orientation, as their morphology constituted both rod and sheet-like structures as shown in Fig. 3.21 (k) and Fig. 3.21 (q). The (003) and (006) planes of Bi_2Te_3 phase is evident from both lattice fringes and SAED patterns as indicated in Fig. 3.21 (q) and Fig. 3.21 (w). It is evident from the FFT and SAED patterns of BT100-12 that the formation of the nanorod/nanosheet and their crystallinity has improved considerably with reaction time.

The important observation is that Bi_2Te_3 single phase is achieved quickly as compared with BT-50 and BT-75 series which could be due to the reaction mechanism favored with EDTA concentration which will be discussed in later sections. A further increase in the reaction time to 24 h yields the formation of perfectly intercalated nanorods (Fig. 3.21 (l)) which is in accordance with the earlier reports, where synthesis conditions were different.[57,63-65] The high-resolution image and SAED patterns of BT100-24 is shown in Fig. 3.21 (r) and Fig. 3.21 (x) respectively. It is very much evident from the FFT and SAED patterns of BT100-24 that highly crystalline nanorods and nanosheets have been formed with 24 h reaction time.
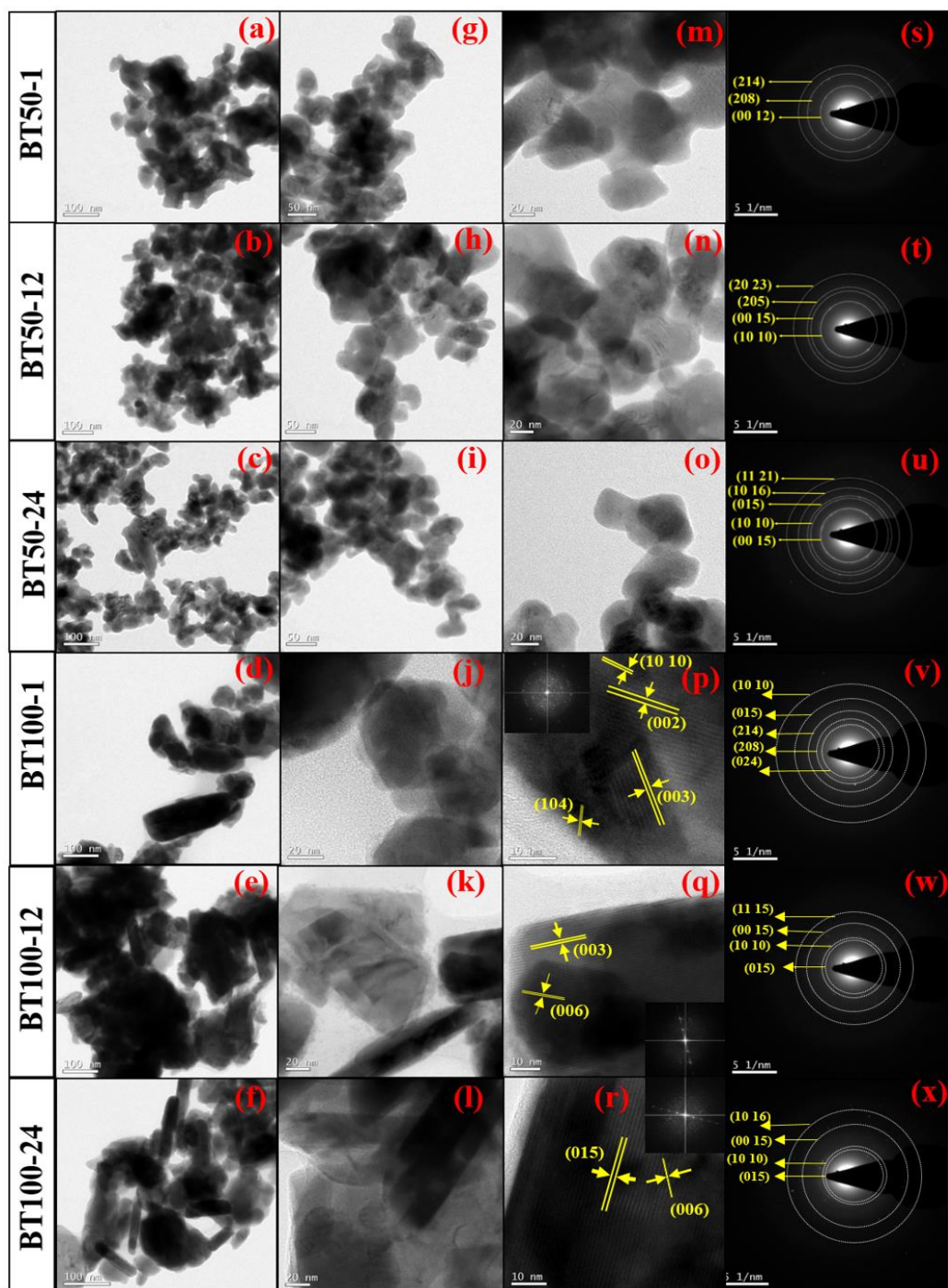
Fig. 3.21. BT50 and BT100 nanostructures (a-o) TEM images showing the formation of different nanostructures for 50 mmol and 100 mmol EDTA concentration with reaction time, (p-r) HR-TEM images showing lattice fringes of BT100 series with FFT shown in the inset and (s-x) SAED patterns of BT50 and BT100 series.

The lattice fringes correspond to the (015) plane of the Bi_2Te_3 phase is shown in Fig. 3.21 (r), in which it can be observed that nanorods have been grown in the preferred orientation.
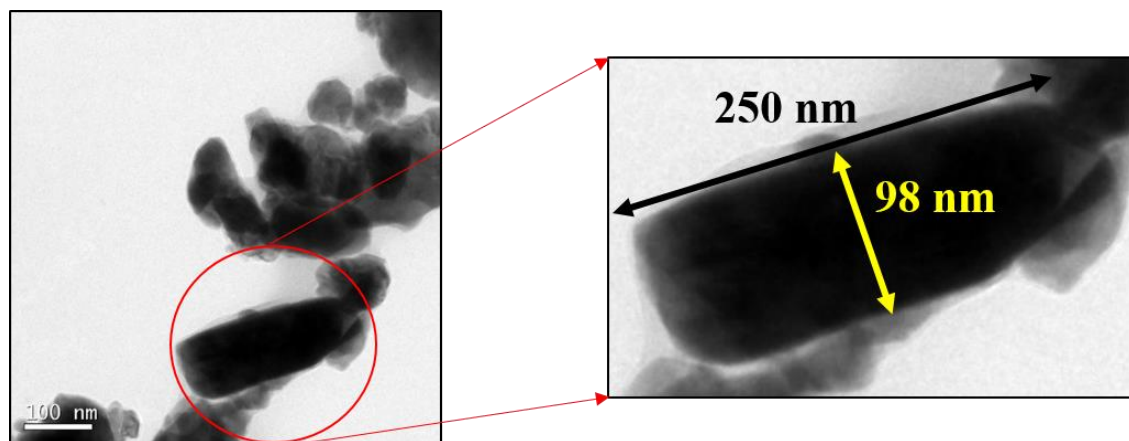
Fig. 3.22. Initiation of rod formation in BT100-1 sample
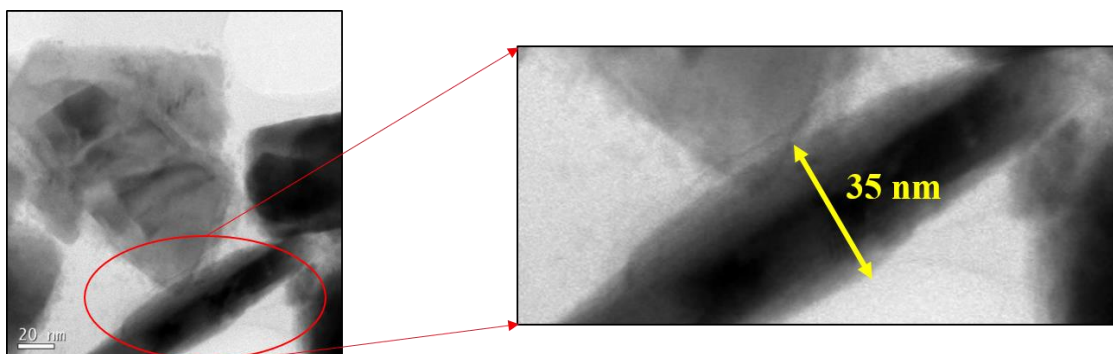
Fig. 3.23. Combination of sheet and rod formation in BT100-12 sample
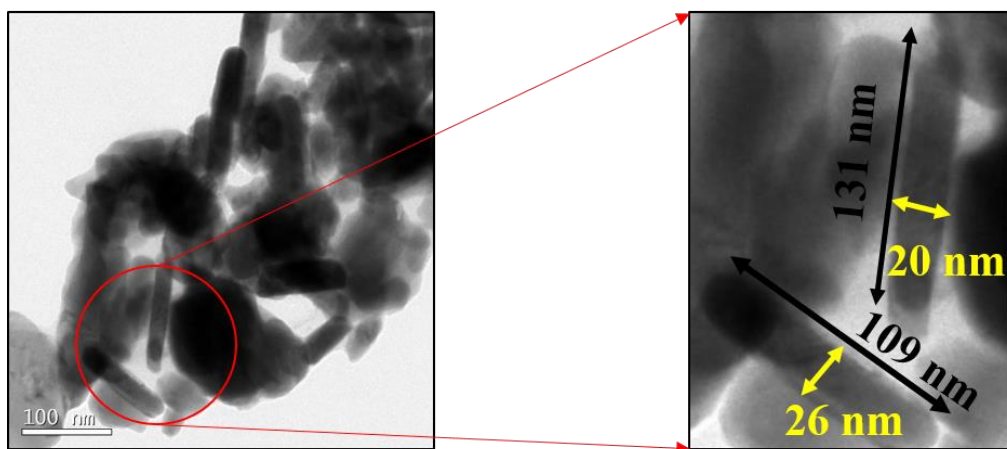
Fig. 3.24. Combination of sheet, rod and flake like structures in BT100-24 sample
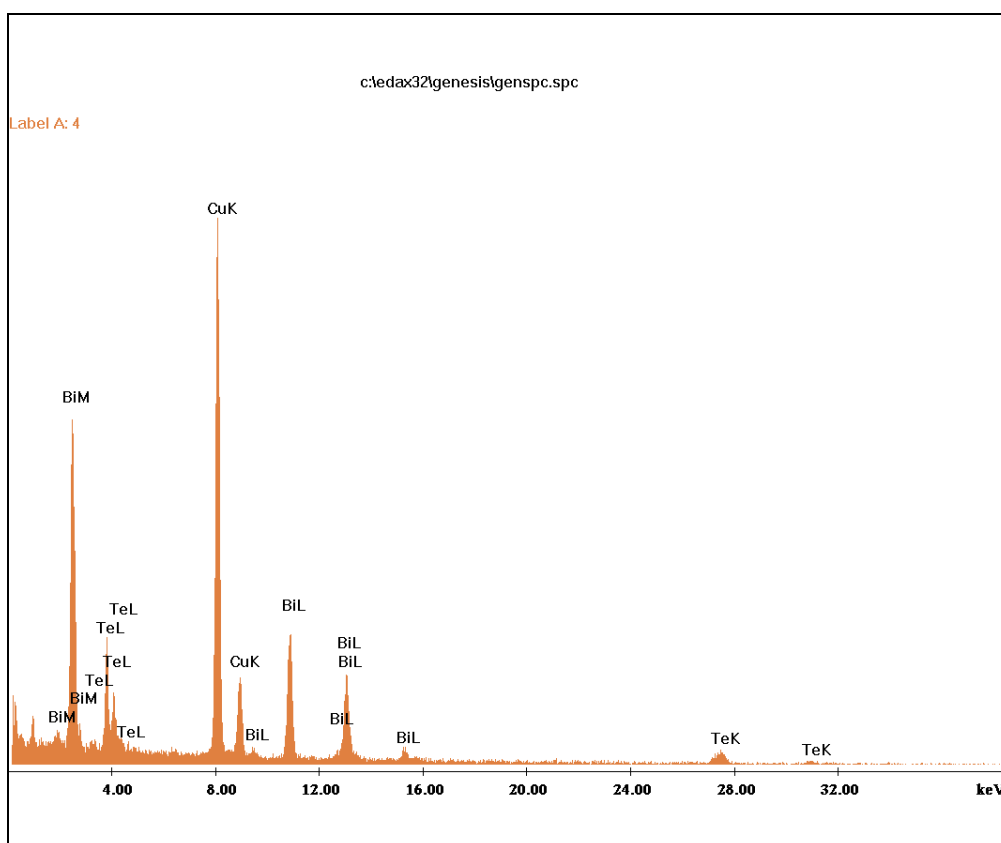
Fig. 3.25. EDS spectra obtained for BT100-24 sample showing the elemental peaks

Table 3.7. EDS data for BT50-1, BT50-12, BT50-24, BT100-1, BT100-12 and   BT100-24

Sample	Atomic percentage		Weight percentage	
	Bi	**Te**	**Bi**	**Te**
BT50-1	47.6	52.4	59.8	40.2
BT50-12	43.7	56.3	56.0	44.0
BT50-24	40.9	59.1	53.1	46.9
BT100-1	42.5	57.5	54.8	45.2
BT100-12	40.3	59.7	52.5	47.5
BT100-24	40.3	59.7	52.5	47.5

3.3.2.3 Reaction mechanism for BT nanostructure formation

In the previous section, it is presented that a reflux reaction technique using bismuth source (Bi^{3+} ions) from a bismuth precursor, bismuth chloride ($BiCl_3$), which could then be reacted with anions like Te^{2-} to obtain a nanostructured Bi_2Te_3 material. Unlike most of the chemical reactions using organic solvents as the reaction medium, we used deionized water to carry out the reaction where $BiCl_3$ reacts with water to form

bismuth (III) dihydroxide-chloride. When the temperature of the medium increases, this bismuth (III) dihydroxide-chloride could act as Bi^{3+} ion contributor and Te powder could give away two electrons upon reduction where Bi and Te ions could combine to form Bi_2Te_3 structures. Another possible mechanism for the formation of these nanostructures could be a direct combination of metals as in the case of a typical alloying process. In such a case Bi^{3+} ions will become Bi with the action of BH^{4-} ions and elemental Bi could combine with elemental Te to form bulk Bi_2Te_3 as in the case of typical alloying which is represented in equation (3.1) and (3.2).

$$BiCl_3 + 2H_2O \longrightarrow Bi(OH)_2Cl + 2HCl \tag{3.1}$$

$$3BH_4^- + Bi^{3+} + 24OH^- \longrightarrow 3H_2BO_3^- + 15H_2O + Bi \tag{3.2}$$

$$2Bi + 3Te \longrightarrow Bi_2Te_3 \tag{3.3}$$
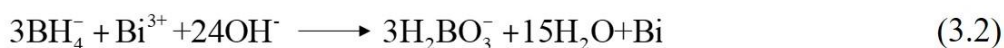
Because of the extensive precipitation and formation of $Bi(OH)_2Cl$, it is impossible to synthesize the desired nanomaterial in an aqueous medium without selecting a proper capping agent. In the absence of such a complementary agent, inorganic reducing agents like $NaBH_4$, which are commonly used for the reduction of metal ions, have significant reducing power to convert $Bi(OH)_2Cl$ directly to bismuth particles (Bi^0); and the reaction in equation (3.3) is more favourable in the chemical reaction. This reaction mechanism can be directed either towards unreacted metal ions or the existence of some unstable phases of these BT structures which could be the reason for impurity phases present in the BT50 series where an insufficient capping agent concentration exists. Hence reaction represented in (equation 3.3) can be treated as an undesirable one and which should be hindered especially in the synthesis of BT nanostructures.

Ligands such as EDTA can coordinate with several inorganic ions to form multinuclear complexes. It is well reported that such structures can also act as a template in self-assembly process.[66-68] It is expected that an oriented attachment may occur with the template effect of EDTA by adding appropriate ligands to the reaction mixtures. Here, we show that nanorods and nanosheets of Bi_2Te_3 structures (as shown in Fig.3.21) can grow via varying the EDTA concentration. In the refluxing process,

reaction occurs at the boiling point of water and ambient atmospheric conditions, it is expected that complete formation of 1D structure will be a tedious job[62] but still a combination of 1D and 2D structures could be developed where we could effectively control the κ and overall TE performance of these Bi_2Te_3 nanostructures. These rods and sheets are arranged through template action of the EDTA additive which is a favorable mechanism as per the recent reports where expensive techniques such as solvothermal/hydrothermal methods and a high reaction temperature were used to develop the desired materials.[3,8,63] Here, we could successfully lower the reaction temperature and executed an aqueous based reaction to deliver the nanostructured material with desired crystal structure and morphology. The TEM images in Fig. 3.21 show the various morphologies of the Bi_2Te_3 nanostructures prepared using $NaBH_4$ as the reductant with EDTA as a surfactant. The Bi_2Te_3 nanostructures synthesized by reflux method with less amount of EDTA concentration (Fig. 3.21 (a)) mainly contained irregular nanocrystals of about 50 - 100 nm width. The formation of non-uniform nanocrystals could be due to the lack of sufficient concentration of EDTA where the above-mentioned reaction mechanism will lead to the formation of agglomerated morphologies. When EDTA is used as a capping agent, the following reactions could be favorable on Bi since upon reaction with metals, EDTA shows a typical tendency to form EDTA-metal ion complexes as shown in Fig.3.26.

$$BiCl_3 + 2H_2O \longrightarrow Bi^{3+} + 2OH^- + Cl^- + 2HCl \tag{3.4}$$

$$C_{10}H_{16}N_2O_8 \xrightarrow[NaOH]{H_2O,\ heat} \left[C_{10}H_{12}N_2O_8\right]^{4-} + 4H^+ \tag{3.5}$$

$$\left[C_{10}H_{12}N_2O_8\right]^{4-} + 2NaOH \longrightarrow \left[Na_2C_{10}H_{12}N_2O_8\right]^{2-} + OH^- \tag{3.6}$$

$$Bi^{3+} + \left[Na_2C_{10}H_{12}N_2O_8\right]^{2-} \xrightarrow{H_2O} \left[Bi(C_{10}H_{12}N_2O_8)\right]^+ + 2NaOH \tag{3.7}$$
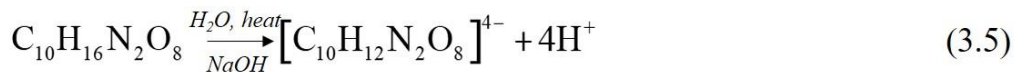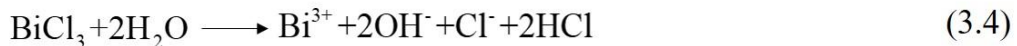
The chemical structures of EDTA are shown in Fig.3.26 where Fig.3.26 (a) shows $C_{10}H_{16}N_2O_8$ which is not completely soluble in water but in the presence of NaOH and H_2O where reactions mentioned in equation (3.5) and equation (3.6) is liable to occur. Na-EDTA can effectively involve in the chemical reaction where it could act as a capping agent and the structure of which is represented in Fig.3.26 (b). The real capping mechanism of Na-EDTA with Bi^{3+} ion is mentioned in equation (3.7) and is

diagrammatically depicted in Fig.3.26 (c). Now the reduction mechanism of Te in the ionic reaction process may be considered by the following chemical equations.

$$3Te + 6OH^- \longrightarrow 2Te^{2-} + TeO_3^{2-} + 3H_2O \tag{3.8}$$

$$5Te + 10OH^- + NaBH_4 \longrightarrow Te^{2-} + Te + NaBO_3 + H_2O + 2OH^- \tag{3.9}$$

$$2TeO_3^{2-} + NaBH_4 \longrightarrow 5Te^{2-} + NaBO_3 + 7H_2O \tag{3.10}$$

(a) **(b)** **(c)**
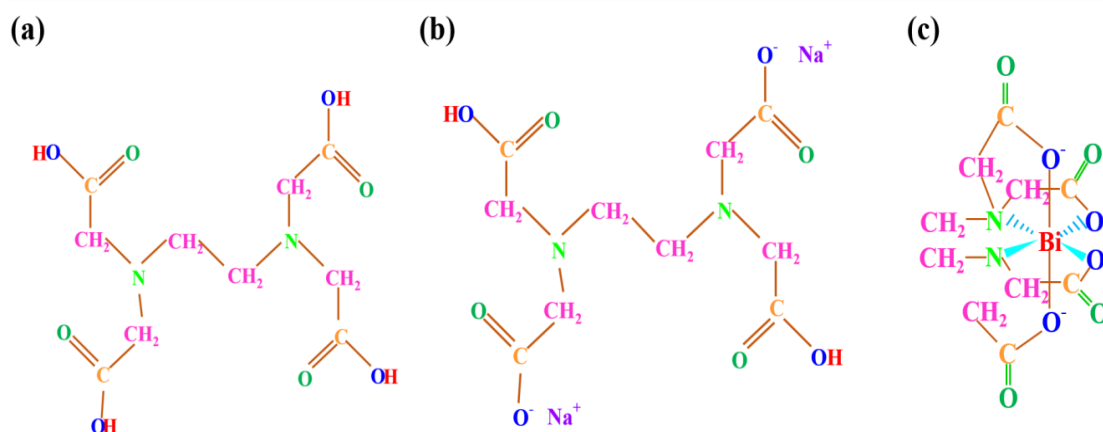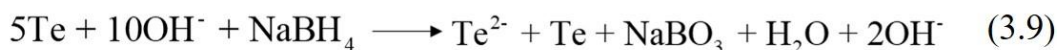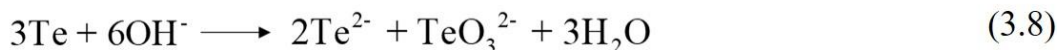
Fig. 3.26. Chemical structures of (a) EDTA, (b) Na-EDTA and (c) Bi-capped EDTA.

It is interesting to note that complete reduction of Te is not occurring in a single step. The reduction reaction can be subdivided into three where Te partially reduces to Te^{2-} and TeO_3^{2-}. This TeO_3^{2-} further reacts with $NaBH_4$ to form Te^{2-} but a portion of it will be reduced to its zero oxidation state which again undergoes the reduction reaction with $NaBH_4$ to further form the Te^{2-} ions which is represented in equations (3.8) to (3.10).[69] The overall reaction mechanism is shown in equation (3.11)

$$2\left[Bi(C_{10}H_{12}N_2O_8)\right]^+ + 3Te^{2-} \longrightarrow Bi_2Te_3 + \left[C_{10}H_{14}N_2O_8\right]^{2-} \tag{3.11}$$
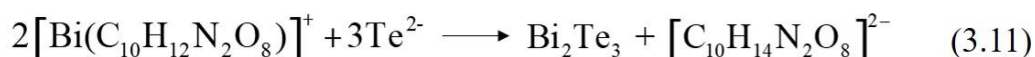
Fig.3.21 shows that the morphologies of the Bi_2Te_3 powders synthesized in the presence of EDTA include nanorods with diameter of 35 nm and length of about 150 nm. Uniform thin nanorods along with nanosheets of a few hundred nanometers were formed for BT100 series, as shown in Fig.3.21 (d-f) and Fig.3.21 (j-l). As shown in the supporting information, the nanosheets and nanorods formation among BT nanostructures is occurring with different reaction time in BT100 samples. It is

interesting to note that reaction time facilitates the formation of nanorods and nanosheets which is in accordance with the previous results (section 3.3.1.) where nanocrystal formation was optimized with reaction time alone.[54] From Fig. 3.21 (a) and Fig. 3.21 (g), it can be seen that nanocrystals with agglomerated morphology for BT50 series could be due to the fact that the amount of EDTA is not sufficient to cap the Bi^{3+} ions so that ionic reaction process will occur partially but the reactions mentioned in eq (3.1), (3.2) and (3.3) will allow the formation of Bi_2Te_3 agglomerates. When EDTA reaches a critical concentration sufficient amount of which could cap the entire Bi^{3+} ions and it will enable the formation of uniformly distributed nanocrystals of Bi_2Te_3. If EDTA concentration exceeds the critical concentration, these EDTA agglomerates can act as soft templates for the formation of nanorods/nanosheets which is schematically represented in Fig.3.27 which suggests the formation of 1D and 2D structures even in an aqueous medium by adopting a low temperature refluxing technique under ambient conditions. The above-mentioned reaction processes dominate the formation of Bi_2Te_3 nanostructures under different reaction conditions, which results in different morphologies of Bi_2Te_3 nanostructures as shown in Fig.3.26.
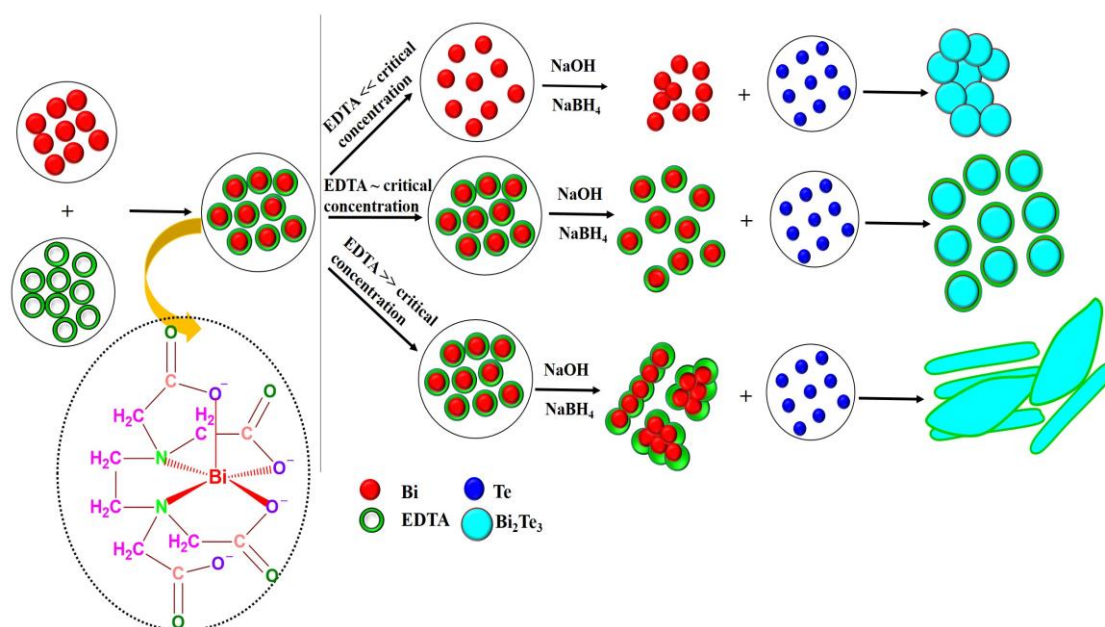
Fig. 3.27. Schematic diagram showing the proposed reaction mechanism for the formation of BT nanostructures

As discussed in the previous section when less amount of EDTA was used for BT50 series and increasing the concentration of which would likely to facilitate the formation of 1D/2D structures as nanorods or combination of sheet-rod structures. It is well known that EDTA is a multidentate ligand with polyfunctional groups and it could effectively serve as bridging ligands to form multinuclear complexes with metal ions above some critical concentration. Then chains of crystalline seeds would form in the nucleation process especially with reaction time, which finally yields sheet/rod-like structures of our desired compound. Here, EDTA acts as a structure directing agent in the formation of Bi_2Te_3 nanostructures. The present approach using reflux technique could favor the reaction mechanism through nucleation and growth process. The crystalline Bi_2Te_3 structures could form in the reflux reaction process through a homogeneous nucleation process if reaction time is a varying parameter along with EDTA concentration. It is well known that BT based materials have a highly anisotropic structure which favors the growth primarily confined to a particular direction and the crystalline seeds of the material tends to grow into the rod/sheet shape under the influence of EDTA which would be a soft template, and induce the formation of 1D/2D structures. Hence EDTA could promote a preferential directional growth under the template effect where the formation of inorganic nanoparticles in liquid media is associated with the monomer growth. Previous reports suggest that the nucleus is characterized by various shapes and facets with different surface energies, and grows by bonding with other monomers exist in the solution.[59] Crystal surface energy and facet attachment are highly influencing in the nanoparticle growth and shape formation. If any capping agent is present in the solution, they can bind to specific facets of the nucleus to coat it with a monolayer which is precisely happening between Bi and EDTA in the present technique. These attached surfactants could lower the total surface energy when Bi_2Te_3 nanocrystals are formed which is specifically by blocking high-energy facets and exposing low energy facets.

The formation of the nanostructures during the refluxing should be related to the layered anisotropic hexagonal lattice structure of Bi_2Te_3. During the refluxing process, covalent bonding enables free Te atoms or Te^{2-} ions to bond with the atoms on the growing crystal surface. The overall refluxing process at 24 h reaction time and

different EDTA concentrations is shown in Fig.3.28 where hexagonally stacked Bi_2Te_3 is shown. Due to the fact that Van der Waals force is insufficient to attach a Te^{2-} ions to a Te (1) layer crystal surface will probably remain in the reaction medium and which is not strong enough to hold the atoms onto the atomic surface. Hence a Bi_2Te_3 structure will always tend to grow significantly faster in a-axis / b-axis directions than in the c direction. This growth mechanism should lead to a crystalline morphology of agglomerated and connected flakes for BT50 series as shown in the Fig. 3.27, Fig.3.28 and Fig.3.29 (a).

When EDTA is present in the aqueous medium, this monolayer of surfactant could control the growth rate and facilitate the formation of individual nanocrystals by holding the surface energy of the nanocrystal facets. It is important to note that the morphologies of the synthesized Bi_2Te_3 nanostructures with various surfactant concentrations will be different from that without surfactants. EDTA acts as anion surfactant in the reaction medium, which could connect with Bi^{3+} ions to form large molecular groups as discussed in the previous sections, which facilitates Bi_2Te_3 nuclei to grow along the surfaces of EDTA agglomerates when EDTA exceeds the critical concentration, directing the growth structure in the preferred orientation of the Bi_2Te_3 crystals.
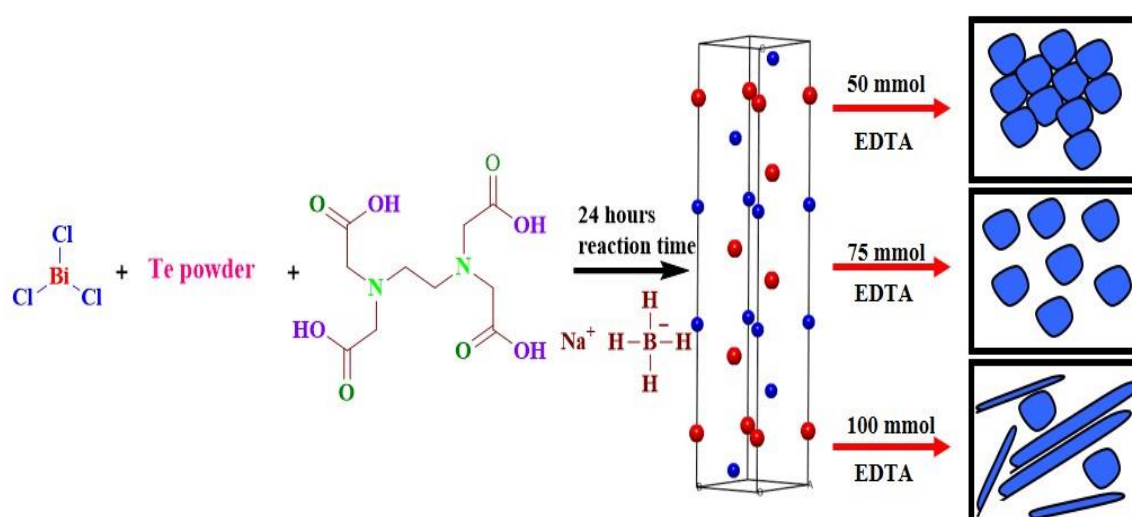
Fig. 3.28. Schematic diagram showing the overall morphological prediction for different EDTA concentrations
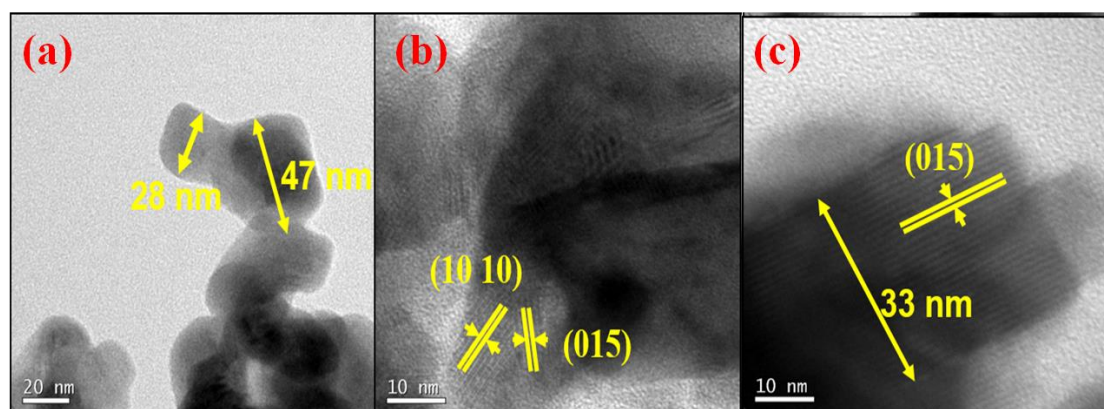
Fig. 3.29. Overview of TEM images (a) showing dimensions of nanocrystals formed for BT50-24, (b) HR-TEM image showing lattice fringes corresponding to the Bi_2Te_3 nanosheets, (c) HR-TEM image showing lattice fringes corresponding to the Bi_2Te_3 nanorod of 33nm width.

When sufficient amount of surfactant exists in the reaction medium it could selectively bind to one of the facets and interestingly, which kinetically slows down growth rate in a- or b-axis directions with a relative increase of growth in the c-axis direction. This reaction mechanism is applicable even in the low temperature reaction process as in the present case where the movements of fine crystals of Bi_2Te_3 capped with molecular groups in the aqueous medium make it possible for uniformly distributed nanocrystals of BT nanostructures to connect with each other by suspended bonds according to definite epitaxy in the c-axis direction as mentioned above and consequently to form nanorods or nanosheets of Bi_2Te_3 structures (Fig.3.29 (b)). The HR-TEM image of a nanosheet and nanorod in the BT100 series with EDTA as a surfactant (Fig.3.29 (b, c)) shows the lattice structure of the Bi_2Te_3 nanocrystal. The distance between two neighbouring (015) planes measured from Fig.3.29 (c) is about 0.32 nm, which corroborates with the lattice parameter of desired Bi_2Te_3 given by ICDD 82-0358.

The nanorods were formed during reflux technique like an intercalation in the nanosheet indicating a combination of rods/sheets of Bi_2Te_3 nanostructures where complete conversion of nanocrystals to form nanorods may not be possible due to the fact that low reaction temperature provided by the aqueous medium is insufficient to promote the entire nanorod formation even with the addition of a surfactant. HR-TEM observation of a nanorod with EDTA as the surfactant (Fig.3.29 (c) also shows a width

of 33 nm and a further high-resolution image along with AFM images are illustrated in Fig.3.30 to demonstrate the nanosheet formation and (015) plane of the Bi_2Te_3 nanorod. AFM was employed to have an idea about the impact of both surfactant concentration and reaction time on the height profile of nanosheets formed especially for BT100 series. BT100-12 and BT100-24 samples were subjected to AFM analysis. Fig.3.30 (a) and Fig. 3.30 (d) represent the typical AFM images and Fig. 3.30 (b) and Fig. 3.30 (e) shows the corresponding height profile in which the maximum thickness observed is less than 8 nm. With increasing the reaction time in BT100 series, the single-phase BT100-24 sample is exhibiting an ultra-low thickness of about 1nm and which can be considered as the nanoflakes of Bi_2Te_3. Fig. 3.30 (c) shows the evidence of a nanosheet formation from the TEM analysis and a combination of rod, sheet and flake like structures are obtained by the increase of EDTA concentration. Fig. 3.30 (f) indicates the (015) plane of the nanorod structure formed for BT100-24.

Further, we have recorded the XPS spectra of the bismuth 4f and tellurium 3d regions for BT100-24 sample are shown in Fig.3.31. The wide scan spectra of the same is shown in Fig.3.32 (a) which suggests the formation of stable and oxidation free surfaces of nanostructures specifically for higher EDTA concentration. Fig.3.31 (a) shows the photoelectron spectrum where core level XPS signals arising out of Bi 4f. The two distinct and highly intense peaks at an energy of 159.4 and 164.8 eV, corresponding to the binding energies of Bi 4f7/2 and Bi 4f5/2 of Bi_2Te_3, are in good agreement with the data observed from a Bi_2Te_3 nanostructured material.[11,63] Moreover Fig.3.31 (b) shows the photoelectron spectrum of the Te 3d core level which is also exhibiting a distinct doublet peaks. These doublet peaks at energies of 575.3 and 587.3 eV are in good agreement with the binding energies seen in the Te 3d spectra observed from Bi_2Te_3 single phase material. Previous reports suggest the formation of these nanostructures without surface oxidation is a tedious process[70] and here we could achieve an excellent oxidation inhibition specifically due to the higher EDTA concentration which acts as a capping agent to prevent the oxidation.
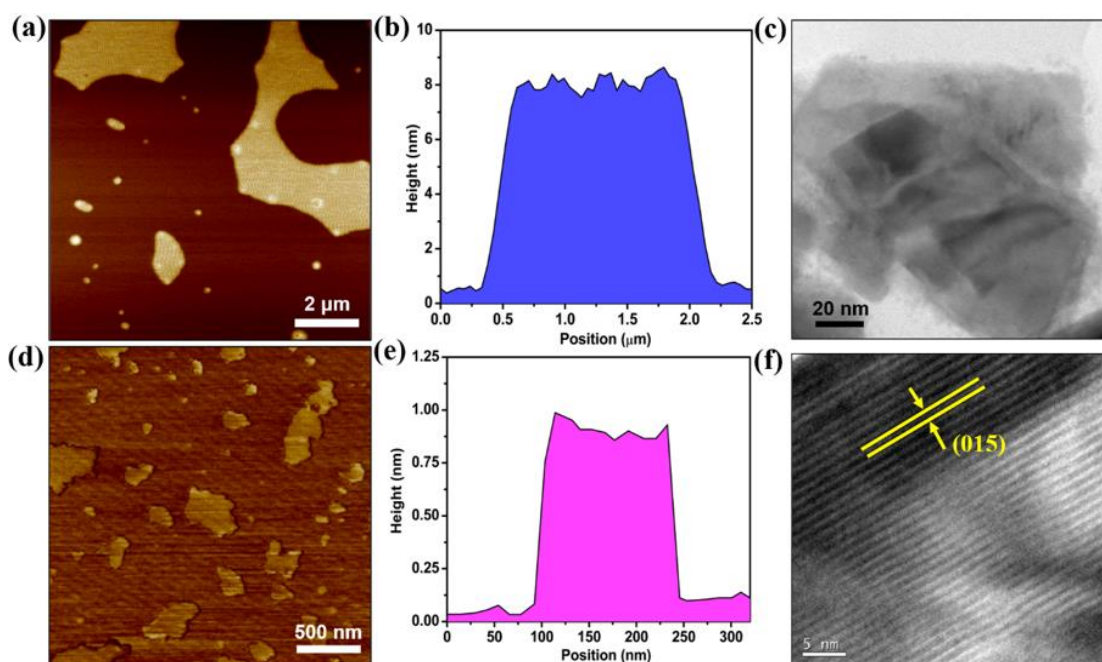
Fig. 3.30. Overview of AFM images (a) showing sheet formation for BT100-12, (b) Height profile pattern of BT100-12 (c) TEM image showing sheet formation corresponding to the BT100-12 (d) Nanoflakes formed for BT100-24 (e) Height profile pattern of BT100-24 and (f) HR-TEM image of BT 100-24 with (015) plane.

From quantitative analyses of the XPS spectra, the as-prepared sample had 41.23 and 59.77 atomic percentage of Bi and Te, respectively. Hence, it can be confirmed that the single phase formation of Bi_2Te_3 is evident which corroborates with XRD, TEM and EDS analyses. Meanwhile, the BT50-24 sample which was synthesized with a lower concentration of EDTA exhibit a surface oxidation which could be due to the insufficient EDTA concentration to cap the individual ions as discussed in the formation mechanism and the wide scan of BT50-24 is shown in Fig.3.32 (b). The core level spectra of both Bi and Te, in this case, is also clearly depicted in Fig.3.33 (a,b) respectively, which confirms the impact of EDTA concentration for the formation of Bi_2Te_3 nanostructures using the low-temperature reflux technique.

3.3.2.4. Temperature variation of *S*, *ρ* and *κ* of BT100 nanostructures

The temperature variation of *S* for BT100-12 and BT100-24 samples was measured in the temperature range 150 K – 350 K, and the results are shown in Fig. 3.34. A negative value of *S* has resulted in both the samples indicating a n-type behavior of the material.
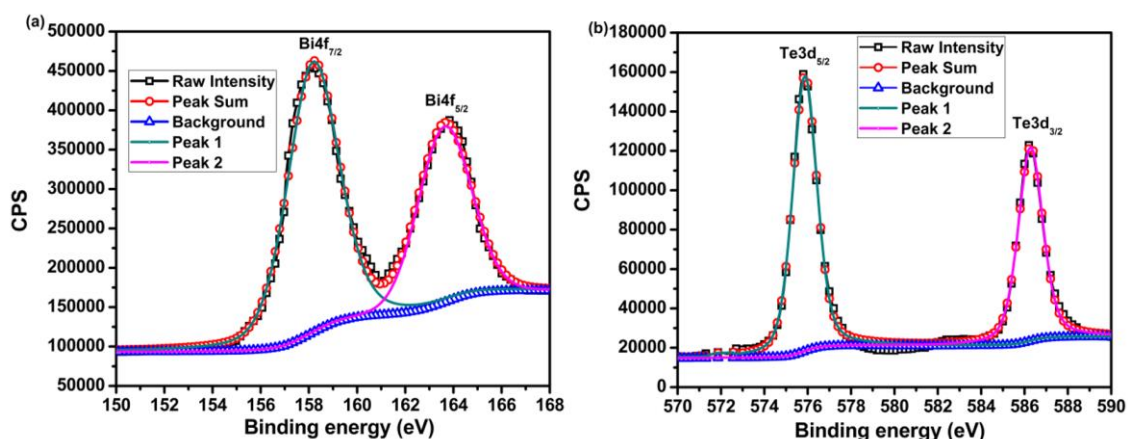
Fig. 3.31. XPS spectra of BT100-24 sample (a) Bi 4f and (b) Te 3d
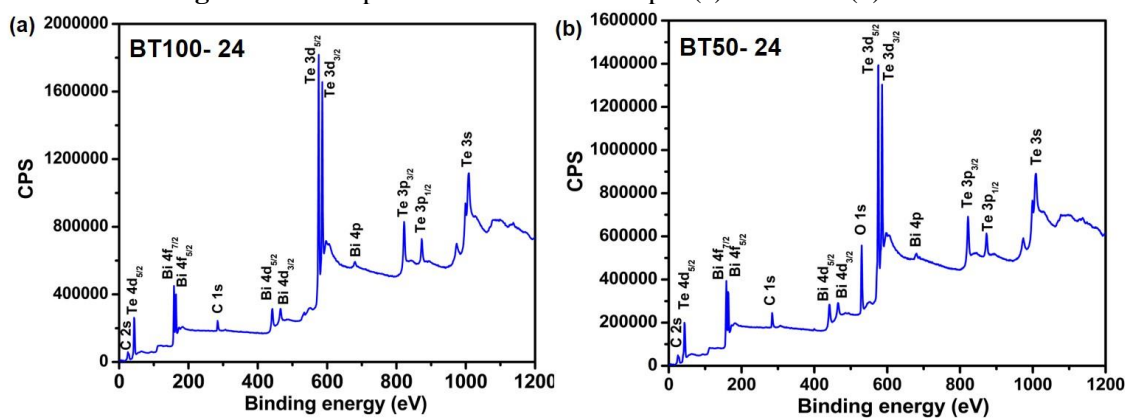
Fig. 3.32. XPS Survey spectrum (a) BT100-24 and (b) BT50-24
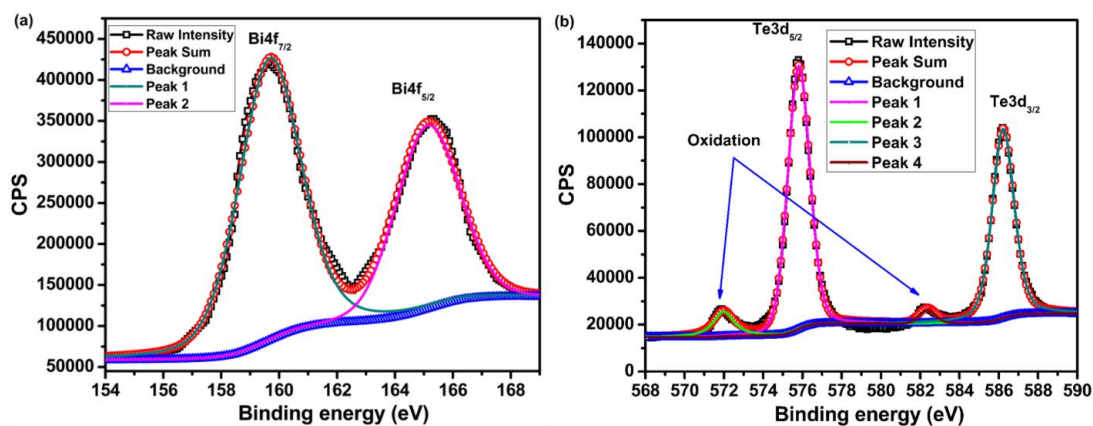
Fig. 3.33. XPS spectra of BT50-24 sample (a) Bi 4f and (b) Te 3d with surface oxidation

It is demonstrated that the S value increases linearly with the temperature and the same is enhanced with the reaction time. The S value observed for BT100-12 is −119.53 μV/K at 350 K and for BT100-24 is 127 μV/K at 350 K. This S value obtained at 350 K is comparable to the recently reported S values for other binary Bi_2Te_3

nanostructures which includes nanostring-cluster structures, mesoporous structures, ultrathin nanosheets, and polycrystalline nanotubes.[8,71,72] It is evident from the previous reports that the influence of the reaction time on BT nanostructures is positively attributed to the combination of enhanced crystal quality and increased TE properties.[54] Also, previous reports suggest that different parameters such as annealing temperature, nature of surfactants, etc. had a favorable effect on the improvement in overall TE performance of n-type BT nano and bulk compounds.
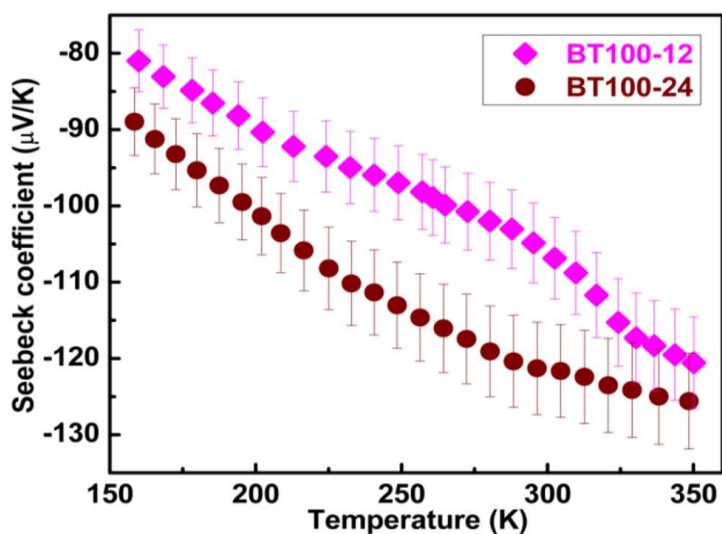
Fig. 3.34. Temperature dependence of *S* of BT100-12 and BT100-24.

It is interesting to note that the *S* measured for the nanostructures formed for an EDTA concentration of 100 mmol was decreased to about 50 % compared to those prepared with 75 mmol concentration. But a room temperature *S* value of 121 µV/K makes sense for the practical applications near 300 K which is also comparable with recently reported materials of the same class[47]. However, it is expected that the inverse relationship between *S* and σ could favourably enhance the electrical conduction[26,73] thus maintaining an overall *PF* comparable to some of the recent reports.[74]

To understand the electrical transport of the synthesized BT nanostructures, detailed ρ analysis was performed on BT100-12 and BT100-24 samples in the temperature range of 20 K – 300 K. Fig. 3.35(a) presents the temperature-dependent ρ of these samples, and reveals a metal to semiconducting transition near 225 K. BT100-12 exhibits a ρ value of 1.91 X 10^{-5} Ω-m and BT100-24 exhibits 1.85 X 10^{-5} Ω-

m at 300 K which could be a promising figure for a TE material. The σ versus T is represented in Fig.3.35(b) where a peak value of 53600 S m^{-1} is achieved for BT100-24 which is comparable and much higher than the recently reported n-type Bi$_2$Te$_3$ based materials prepared using different chemical approaches.[71,72] Such a moderate value of σ can be attributed to the highly crystalline nanostructures present in the BT100-12 and BT100-24 as represented in TEM and AFM analyses that performs a high density of interfaces of Bi$_2$Te$_3$ nanostructures as demonstrated in the previous sections (Fig.3.21, Fig.3.27 and Fig.3.30). High density of interfaces is very much required for improving the phonon scattering mechanisms and to obtain a better reduction in κ. The various phonon scattering mechanisms include Umklapp processes, electrons, grain boundaries, point defects and dislocations.[55] These mechanisms will be predominant in nanostructures in comparison to the bulk counterparts.[75] Hence, the reduction in κ is obviously observed in nanostructured materials. At the same time, it is really challenging to maintain a moderate value of σ as mentioned above without affecting κ so that a moderate value of **PF** can be maintained. In the present case, we tried to demonstrate a system where a combination of nanoflakes, nanorods and nanosheets that constitutes widely distributed grain sizes having different crystallographic orientations to tailor the overall TE performance. Interestingly, a combination of different nanostructures (nanorods, nanoflakes and nanosheets) can provide the means for getting high density interfaces without compromising the conflicting TE properties which is similar to the fine and coarse structure model discussed in recent reports.[11,54]
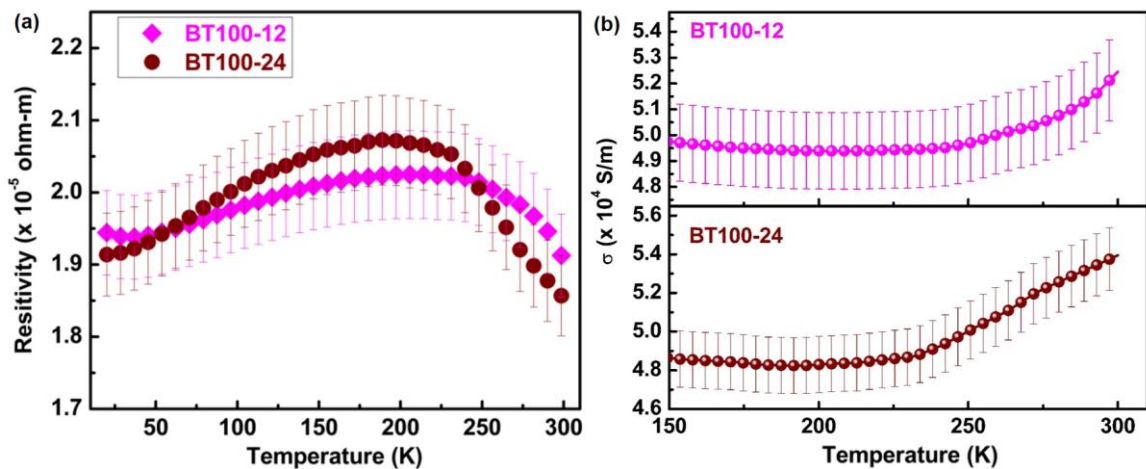
Fig. 3.35. Temperature dependence of (a) ρ and (b) σ of BT100-12 and BT100-24.

Fig.3.36 (a) gives the variation in κ of the BT100-12 and BT100-24 as a function of temperature. As can be seen, a very low κ for BT100-12 and BT100-24 (a peak value of 0.34 and 0.38 W m^{-1} K^{-1} respectively at 350 K) has been obtained, which is significantly lower than that of bulk Bi$_2$Te$_3$ materials and recently reported nanostructures of the same family synthesized via complex and expensive techniques.[42,43] Especially, low κ values of 0.30−0.35 W m^{-1} K^{-1} at room temperature have been obtained which is close to the lowest value reported for BT nanostructures which was 0.28 W m^{-1} K^{-1} synthesized at a relatively high reaction temperature using hydrothermal setup.[76] Despite its inherent structural properties of Bi$_2$Te$_3$, the lattice κ strongly depends on the presence of additional sources of phonon scattering. This scattering can be increased by reducing the phonon mean free path by decreasing the dimensionality of the lattice. The phonon scattering will be excellent here due to the fact that ultra-thin nanosheets and nanoflakes are improving the scattering mechanism whereas nanorod structures are helpful in maintaining the σ. Hence, the combination of different low dimensional nanostructures could behave like a 'phonon glass and electron crystal' to decrease the κ. Hence, the reason for low κ value may be due to the overlapping of different nanostructures, where the particle interfaces could significantly scatter phonons to achieve a maximum reduction in κ while preserving the σ in the range 55000 Sm^{-1} – 60000 Sm^{-1} which is clearly demonstrated in Fig. 3.35(b) from which a non-degenerative behavior of the synthesized nanostructures have been confirmed. The hiking trend in κ value, especially above 200 K, is specifically due to this electronic contribution towards κ as shown in Fig.3.36 (b). Hence, from the thermal transport studies together with HR-TEM and AFM analysis suggests the low dimensional and highly crystalline nanostructures inherited from the low temperature reflux reaction and their corresponding high-density interfaces in the HPHTS nanostructures can significantly scatter the phonons and thereby contribute to the significant reduction in κ to maximize the TE efficiency.

3.3.2.5. Power factor and Figure of Merit

The temperature variation of *PF*, which is calculated as $S^2\sigma$ is plotted and shown in Fig.3.37 (a).
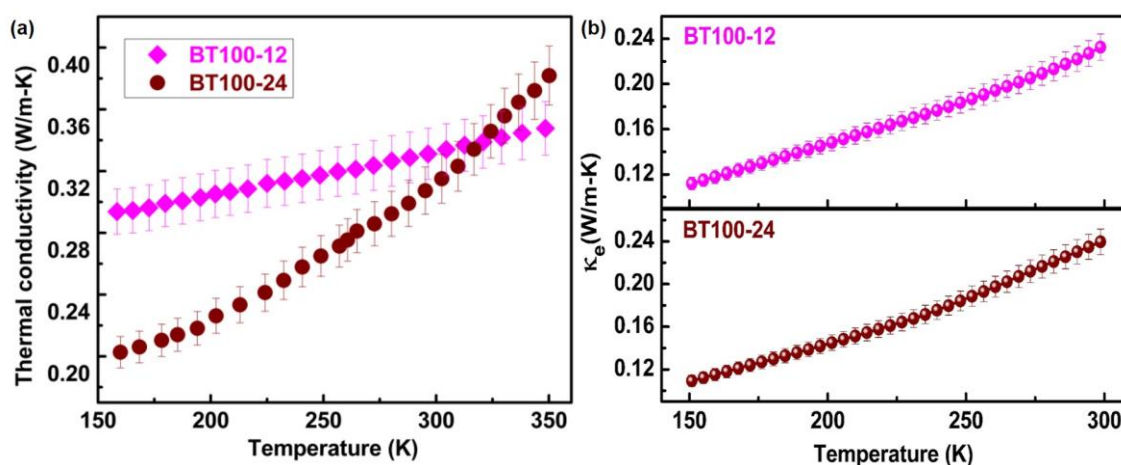
Fig. 3.36. (a) Variation of κ with temperature for BT100-12 and BT100-24 (b) Variation of electronic contribution towards κ with temperature (where Lorentz number is taken as 1.5 x 10^{-8} WΩK^{-2} for a non-degenerate semiconducting material)

Here, we selectively carried out the TE performance on BT100-12 and BT100-24 where structural as well as morphological control has been achieved. The **PF** increased significantly with reaction time which also corroborates the BT75 series[54] and shows the maximum for BT100-24 which increased with temperature from 320 to 750 μWm^{-1}K^{-2} as shown in Fig.3.37 (a). **S** and **PF** of the BT100 samples are comparable with most of the nanostructured Bi_2Te_3, but around 50% reduction is observed for **S** in comparison to BT75 samples on Bi_2Te_3 nanocrystals. Again, it is interesting to note that a two-fold increase in σ than the state-of-the-art nanostructured bulk BT is ultimately reflecting in the **PF** values of Bi_2Te_3 nanostructures prepared by varying the EDTA concentration. It is expected that the considerably enhanced σ in the BT100-24 nanostructures can compensate the moderately deteriorated **S**, and in turn lead to the enhancement of overall **PF** value.

Finally, the temperature variation of **ZT** has been determined and is depicted in Fig.3.37 (b), which shows a promising range of **ZT** values for Bi_2Te_3 nanostructures prepared for BT100-12 and BT100-24. **ZT** of BT100-12 shows a linear dependence with the temperature and achieved a maximum value of 0.52 at 300 K, which is comparable with the Bi_2Te_3 nanostructured bulk materials.
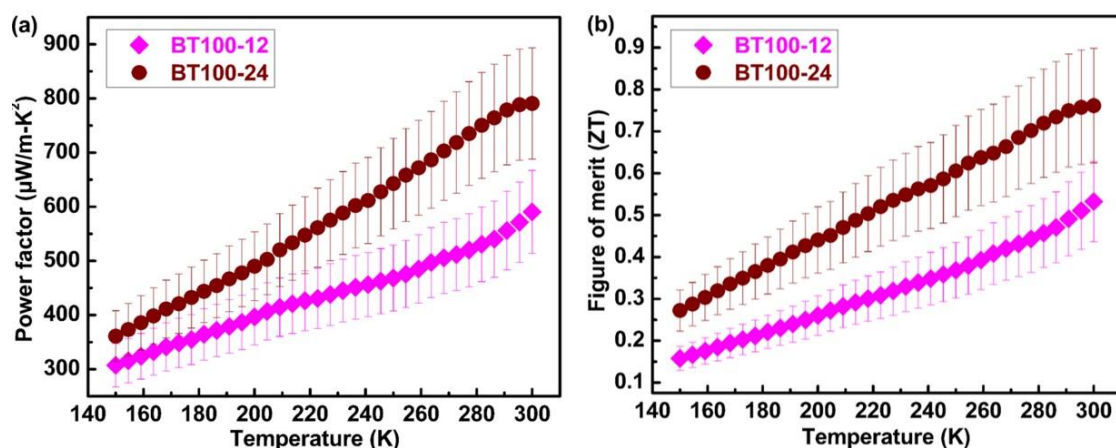
Fig. 3.37. Temperature dependence of (a) *PF* and (b) *ZT* of BT100-12 and BT100-24.

Significant improvement in *ZT* is observed for BT100-24 nanostructures showing a maximum value of 0.75 at 300 K. As explained in the reaction mechanism for the formation of Bi_2Te_3 nanostructures, complete conversion of 1D/2D structures may not be possible due to the very low reaction temperature of the aqueous medium. Still, the enhanced *ZT* value of BT100-24 at room temperature is comparable to the previously reported Bi_2Te_3 nanostructures synthesized especially via different chemical approaches.[29,54] Furthermore, both the moderate values of *S* and the reduced *κ* along with a significantly improved electrical transport comparable to that of the other materials in the chalcogenide family result in an enhanced *ZT* in the BT100-24 sample.

The variation in TE properties can be well explained with grain boundary scattering due to the formation of nanorods and nanosheets of Bi_2Te_3 nanostructures with increased EDTA concentration and the phase transitions and scattering mechanism of which is represented in Fig.3.38. The single phase samples of Bi_2Te_3 with morphological control are very much essential for high-performance TE material where both reaction time and EDTA concentration favors the formation of the desired structure using the reflux method and is depicted in Fig.3.38. Mixed-phase samples with coarse structures are formed when EDTA concentration is very less, i.e., in 50 mmol series as shown in the schematic representation where scattering centers will be minimum and may ultimately result in a drastic decrease of overall TE efficiency due to which we excluded the BT50 series from TE performance analysis. XRD and TEM images

confirm the mixed phases and coarse structures respectively for the samples in the BT50 series with lower reaction time. BT50-24 is the only sample in the series with 50 mmol surfactant concentration which formed with desired Bi_2Te_3 structure but still the insufficient EDTA concentration resulted in the formation of agglomerated morphology which is not recommended to decrease the κ. When the surfactant concentration is increased to 75 mmol, the formation of nanocrystals get facilitated and an excellent scattering mechanism was proposed in section 3.3.1.5 by which κ value decreased to 0.34 $Wm^{-1}K^{-1}$ at room temperature for the sample synthesized for 1h but this low reaction time favors the BiTe formation rather than Bi_2Te_3. The 12 h reaction time promotes the initiation of Bi_2Te_3 formation along with Bi_4Te_3 as shown in Fig.3.38. Here, in 75 mmol EDTA concentration with 24 h reaction time is helping in the formation of single phase Bi_2Te_3 structures where significant phonon scattering reduces κ to 0.42 $Wm^{-1}K^{-1}$ which is less compared to the conventional TE materials. In BT75-24, uniformly distributed fine nanocrystals have been formed which considerably enhanced the **PF** and **ZT** value.[54] When EDTA concentration increased to 100 mmol, EDTA agglomerates act as a soft template for the formation of low dimensional structures of Bi_2Te_3 as mentioned in the ionic reaction mechanism.
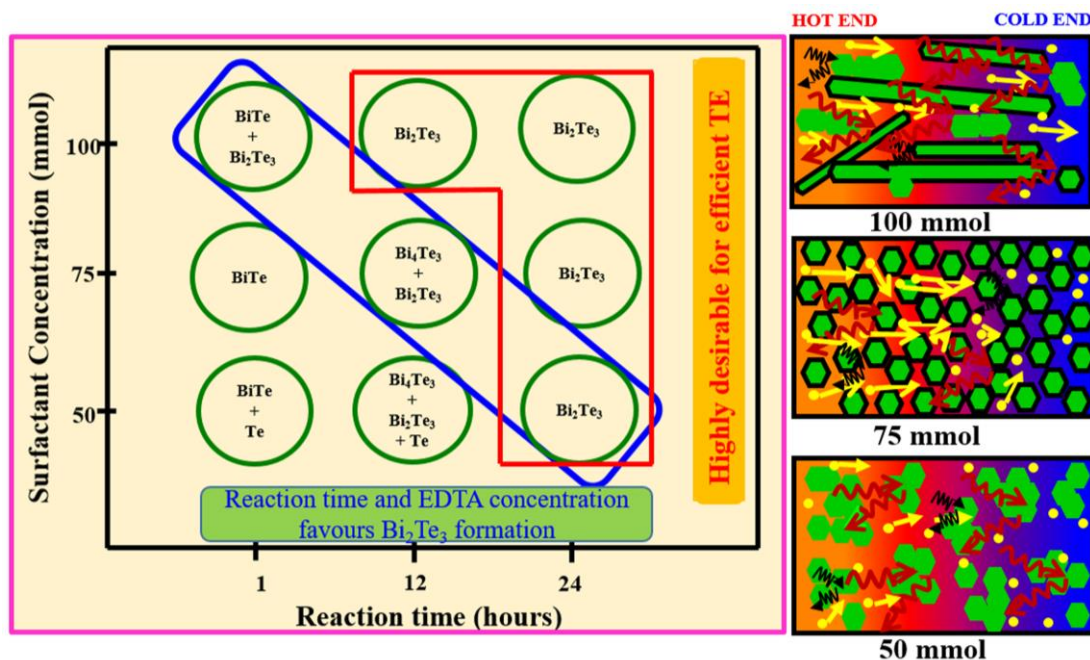
Fig. 3.38. Schematic diagram showing structural phase transitions and model explaining enhanced σ

Interestingly Bi_2Te_3 phase formation initiated even in the 1 h reaction and it is demonstrated in Fig.3.38 that the formation of desired Bi_2Te_3 structure is facilitated both by reaction time and EDTA concentration. Both BT100-12 and BT100-24 exactly allows the Bi_2Te_3 formation along with low dimensional nanostructures where phonon scattering could be efficient to significantly decrease the κ value that exhibits 0.31 $Wm^{-1}K^{-1}$ at room temperature. When the low dimensional structures are forming in the system (especially nanosheets and nanoflakes of 1-10 nm thickness), a high pressure could sufficiently stack these nanostructures in the press direction that increase the scattering centers at the interfaces and could provide an ultralow κ. The previous report suggests the mechanism for enhancement in σ by the formation of coarse structures and reduction in κ by the formation of fine structures.[11,54] Here, in the present study, our compound forms as a combination of rod, sheet and flake like morphology that facilitates the phonon scattering and reduction in κ whereas the combination of these nanostructures allows the electrical conduction; the combined effect is the overall improvement in the TE efficiency in terms of ***ZT***, which is depicted in Fig.3.39.

In a nutshell, Fig.3.39 represents the systematic variation of *S*, σ and κ along with ***ZT*** and morphological variations. Among the mixed phases BT75-12 is the best candidate with coarse and fine structures that showed a ***ZT*** value of 0.38 K. BT75-24 was best among the series which exhibited a ***ZT*** of 0.67 at room temperature. In comparison to BT75-12, BT100-12 is exhibiting significant enhancement of about 40% reaching a ***ZT*** value of 0.54 at room temperature. Similarly, in BT100-24 where nanorods are formed partially, the κ reduces significantly by maintaining a high σ which provides the improvement in ***ZT*** value to a maximum of 0.75 at 300 K which is about 12% higher than that reported for BT75-24.[54] These results demonstrate that both reaction time and surfactant concentration could carefully optimize the desired Bi_2Te_3 structures and could tailor the morphology to enhance the overall TE performance of different BT nanostructures.

As mentioned in the previous discussions, we obtained a reactive Bi source (i.e., Bi^{3+} ions) with EDTA capping through the simple manipulation of EDTA concentrations. By reacting this EDTA capped Bi ions with anions (Te^{2-}), we obtained

stable oxidation resistant nanomaterials with desired stoichiometry, structure and morphology.
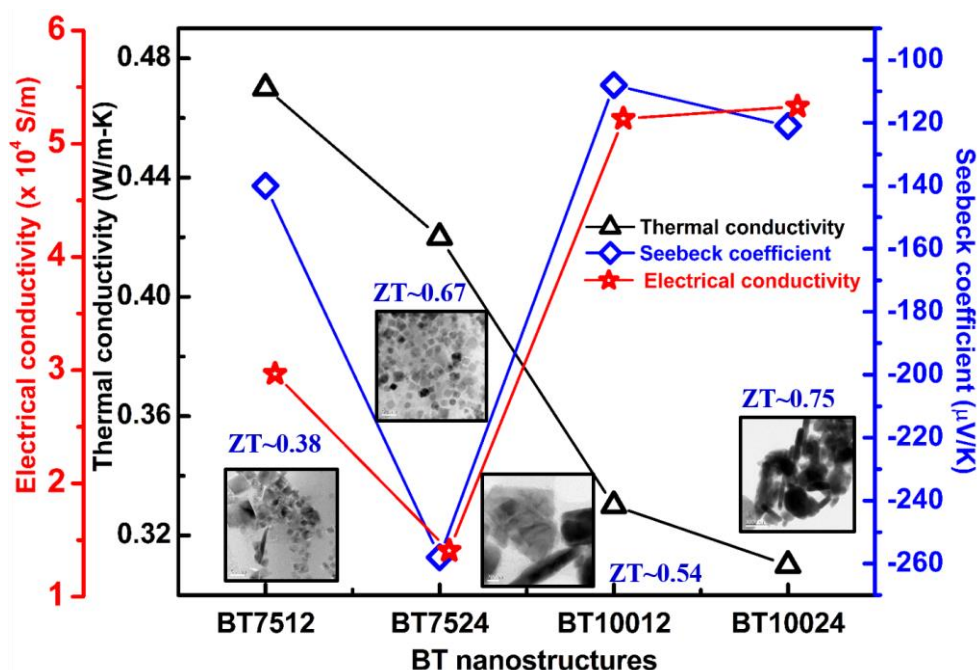
Fig. 3.39. A comparison of overall room temperature TE performance for different BT nanostructures

Table 3.8. A comparison showing σ, S, κ and *ZT* of Bi_2Te_3 nanostructures of present study with recent trends.

SL. No.	σ (x 10^4 S/m)	S (μV/K)	κ (W/m-K)	*ZT*	Reference
1	6.30	125	1.10	0.27 (at 300 K)	8
2	1.40	-258	0.42	0.67 (at 300 K)	54
3	8.00	-148	0.99	0.53 (at 300 K)	77
4	5.60	-142	0.75	0.45 (at 300 K)	78
5	7.30	-131	0.58	0.65 (at 300 K)	29
6	7.70	-151	0.97	0.54 (at 300 K)	55
7	3.43	-135	0.49	0.36 (at 313 K)	70
8	7.50	-185	1.10	0.70 (at 298 K)	75
9	1.82	-126	0.28	0.31 (at 300 K)	43
10	5.36	-121	0.31	0.75 (at 298 K)	Present work

We optimized the TE transport properties with the desired structural and morphological tailoring, which maximized the *ZT* value. A comparison of room temperature σ, S, κ

and ZT of our present study with some of the recent reports are represented in Table 3.8 and careful optimization of reaction conditions could favor the formation mechanism of Bi_2Te_3 nanostructures that enhance the overall TE properties.

3.3.3. Investigation on synthesis mechanisms of nanostructured (Bi,Sb,Sn) –Te TE materials via aqueous based reflux method

A series of different chalcogenide based thermoelectric materials have been synthesized using $BiCl_3$, $SbCl_3$, Sb powder and $SnCl_2$ as starting materials. A detailed understanding of the chemistry involved in the reaction mechanism and decomposition of EDTA is proposed for different precursors of Bi, Sb and Sn where possibilities of aqueous based low temperature synthesis of phase pure Bi_2Te_3 and Sb_2Te_3 is demonstrated.

3.3.3.1. Crystal structure of Bi_2Te_3/Sb_2Te_3 and SnTe

Bi_2Te_3 and Sb_2Te_3 are narrow band gap semiconductors with homologous layered crystal structure having a rhombohedral unit cell with an R-3m space group. These are semi-metals possessing good σ and low κ and are used for power generation and in cooling devices.[79-81] Bi_2Te_3 is reported to be an n-type semiconductor while Sb_2Te_3 is a p-type semiconductor. However, the presence of excess Te may change their type from n-type to p-type semiconductor. Fig. 3.40 (a) shows the layered crystal structure of M_2Te_3 (M=Bi, Sb). Sb_2Te_3 and its doped derivatives have been widely studied due to their excellent ZT in the temperature range of 300-500 K.[82-84]

Self-generation of antisite defects creates a large number of holes in bulk Sb_2Te_3 owing to low S.[82] As a consequence, the ZT values are still limited to about 1 over the entire temperature range which corresponds to low efficiencies of the TE device which limits wider applications. Venkatasubramaniam *et al.*[85] proposed a specially constructed Bi_2Te_3/Sb_2Te_3 superlattice with a ZT of 2.4 at room temperature. Recently, Yang *et al.*[86] employed surfactant-assisted reflux method for preparation of Sb_2Te_3 nanostructures using cold compaction followed by annealing and achieved a high ZT of 0.37 at 473 K. Several chemical methods have been developed so far to prepare nanostructures with

different shapes. However, single phase Sb_2Te_3 could not be easily achieved due to the spontaneous occupation of partial Sb atoms at Te lattice sites.[87]
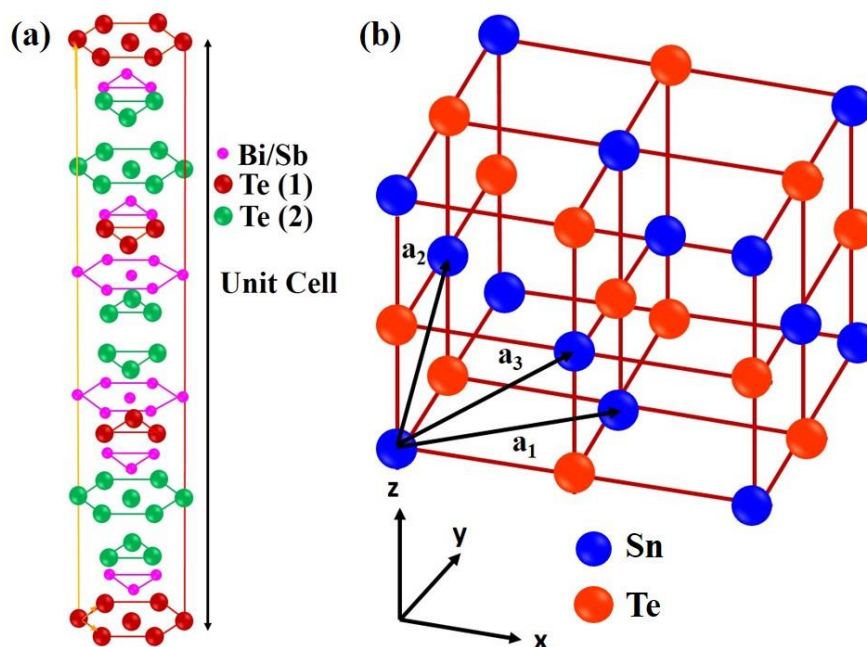
Fig. 3.40. Crystal structure of (a) Bi_2Te_3 / Sb_2Te_3 and (b) SnTe

Wang *et al.*[88] synthesized Sb_2Te_3 hexagonal nanoplates with an edge length of 200-2000 nm through solvothermal approach. However, they showed a low ZT due to the presence of Te impurity which reduced the electrical conductivity of the Sb_2Te_3 matrix. There have been also some reports on the synthesis of $Bi_{0.5}Sb_{1.5}Te_3$ nanocrystals by the solvothermal or hydrothermal process. However, the majority research work has been focused on the preparation of nanostructures with various methods, while studies on consolidation of Bi_2Te_3, Sb_2Te_3 and $Bi_{2-x}Sb_xTe_3$ nanocrystals and their TE properties are relatively rare.

SnTe is another narrow band gap semiconductor with a direct band gap of 0.18 eV. SnTe normally forms p-type semiconductor due to tin vacancies and at low temperatures, it becomes a superconductor. SnTe exhibits a very low ***ZT*** ~ 0.40 at 900 K [89] due to its intrinsically high carrier concentration, large $\Delta E_{L-\Sigma}$ of 0.3 eV and high κ_L.[90,91] SnTe exists in 3 crystallographic phases. At low temperatures, when the hole concentration is less than 1.5×10^{20} cm^{-3}, SnTe exists in rhombohedral structure and is

known as α-SnTe. At room temperature and atmospheric pressure, SnTe crystallizes in rock salt structure and is composed of a face-centered cubic lattice of Te atoms with Sn atoms filling all the octahedral voids and is known as β-SnTe.[92] β-SnTe transforms to γ-SnTe at 18 kbar pressure, with orthorhombic structure and space group Pnma. β-SnTe (referred to as SnTe in the chapter) with cubic structure and Fm-3m space group finds application as TE materials. The crystal structure of SnTe is shown in Fig. 3.40 (b).

SnTe has received limited attention as a TE material owing to its inability to control its very high carrier concentration of the order of 10^{21} cm^{-3} at 300 K which results in low S and high κ_e.[93] Large concentration of intrinsic Sn vacancies are responsible for the high p-type carrier concentration in SnTe.[94] In SnTe, the energy difference between the light hole valence band (L band) and the heavy hole valence band (Σ band) is 0.3 eV.[93,95-99] The large energy separation between light and heavy hole valence bands restricts the contribution of heavy hole mass to the S. Recently, alloying SnTe with other metal tellurides such as AgSbTe$_2$, MgTe, SrSe, CdSe, etc. was found to improve its TE performance.[100-104] A remarkable enhancement in the ***ZT*** was achieved due to the formation of resonance level in the valence band through In doping in SnTe synthesized by high energy ball milling and spark plasma sintering. [105] Alloying of SnTe with SnSe which has a high band gap of 0.9 eV, helps to reduce the κ value and also results in an improved S due to the convergence of the two valence bands of SnTe. Moreover, the κ value of SnTe can be further decreased by solid solution alloying with SnSe. Alloying Cd or Hg in SnTe also result in an enhancement in S due to the decreased energy separation between light and heavy hole valence band.[106-107] Hence, we have attempted to synthesize p-type Sb$_2$Te$_3$ and SnTe through EDTA assisted aqueous based synthesis which is an efficient synthesis method to get a good control over the morphology and study the TE properties of n-type Bi$_2$Te$_3$ nanostructures. Moreover, nanostructuring could help in improving the TE properties of SnTe through band convergence.

3.3.3.2. Thermal decomposition of EDTA

Ligands such as EDTA acts as a capping agent for tailoring the crystal growth and may also provide the possibility of breaking the nature of crystals, which may lead

to more different morphologies and wider applications.[108-110]. EDTA can coordinate with several inorganic ions to form multinuclear complexes. It is well reported that such structures can also act as a template in self-assembly process.[66-68] It is expected that an oriented attachment may occur with the template effect of EDTA by adding appropriate ligands to the reaction mixtures. Also EDTA added as anion surfactant in the solution could connect with Bi^{3+} ions to form large molecular groups, which facilitates Bi_2Te_3 nuclei to grow along the surfaces of EDTA agglomerates. When EDTA selectively bind to one of the facets, the growth rate in either a- or b-axis directions kinetically slows down, with a relative increase in the c-axis direction. The movements of these hexagonal fine crystals together with molecular groups in the solution make it possible for continuous particles to connect with each other by suspended bonds according to definite epitaxy in the c-axis direction and consequently to form long nanorods or nanosheets. These rods and sheets are arranged through template action of the EDTA additive which is a favorable mechanism as per the recent reports where expensive techniques such as solvothermal/hydrothermal methods and a high reaction temperature were used to develop the desired materials.[3,8,63]

However, if EDTA residue remains in the final product it can detrimentally affect the TE performance of the final product. In order to get nanostructured Bi_2Te_3, it is required to maintain a pH of 10 during the synthesis (using NaOH) and finally the precipitated product is to be washed with acetone, ethanol and deionized water several times. The residual EDTA can well dissolve in acetone when the pH is above 8; hence from the slurry of aqueous based Bi_2Te_3 final product, EDTA and other unreacted residues can be removed by treating it initially with acetone till obtaining a clear solution. Again, upon heat treatment, the EDTA primarily decomposes to N-(2-hydroxyethyl) iminodiacetic acid and iminodiacetic acid at 473 K. At higher temperatures, i.e., at 533 K, these primary products can yield ethylene glycol as the final product. Ethylene glycol can well control the morphology of the nanostructures even at a sintering temperature of 623 K. Hence EDTA is removed partially by washing with different solvents and partially by converting it to ethylene glycol at a higher temperature. However complete removal of EDTA is a tedious job, still 75 mmol EDTA could deliver Bi_2Te_3 nanostructures with good control over TE properties. The

temperature dependent decomposition of EDTA in the aqueous synthesis of chalcogenide nanostructures is explained as follows: At 533 K, EDTA decomposes into N-(2-hydroxyethy1)iminodiacetic acid and iminodiacetic acid as shown in equation (3.12). Further hydrolysis of N-(2-hydroxyethy1)iminodiacetic acid results in the formation of ethylene glycol and iminodiacetic acid (equation (3.13)). [111]

$$^-OOCH_2C \diagdown \atop ^-OOCH_2C \diagup NCH_2CH_2N \diagup ^{CH_2COO^-} \atop \diagdown CH_2COO^- \xrightarrow{H_2O} \; ^-OOCH_2C \diagdown \atop ^-OOCH_2C \diagup NCH_2CH_2OH \; + \; NH \diagup ^{CH_2COO^-} \atop \diagdown CH_2COO^- \qquad (3.12)$$

$$^-OOCH_2C \diagdown \atop ^-OOCH_2C \diagup NCH_2CH_2OH \; + \; H_2O \longrightarrow NH \diagup ^{CH_2COO^-} \atop \diagdown CH_2COO^- \; + \; OHCH_2CH_2OH \qquad (3.13)$$
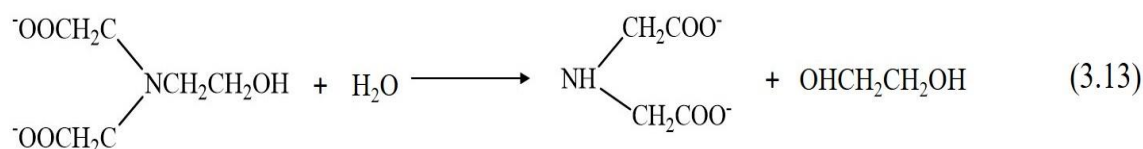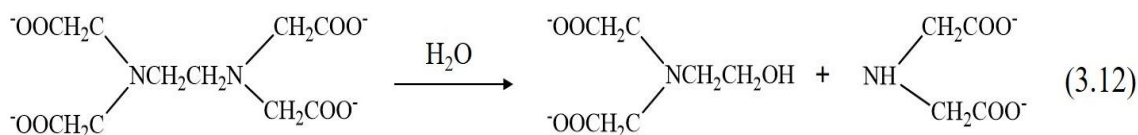
A portion of iminodiacetic acid decomposes to iminodiacetic anhydride with the evolution of water at 512 K (equation (3.14)).

$$NH \diagup ^{CH_2COO^-} \atop \diagdown CH_2COO^- \longrightarrow HN \diagup ^{CH_2-CO} \atop \diagdown CH_2-CO \diagdown O \; + \; H_2O \qquad (3.14)$$
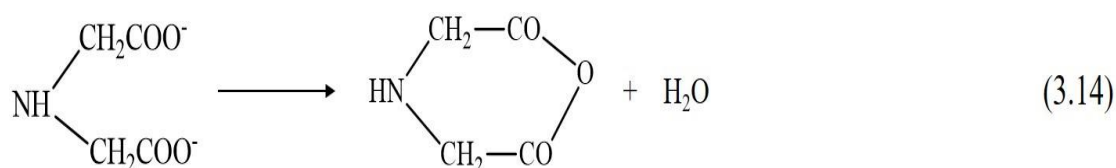
At around 593 K, iminodiacetic anhydride boils off. Beyond 593 K, iminodiacetic acid decomposes into water, carbondioxide, carcon monoxide, acetonitrile and hydrogen gas as by products as shown in equation (3.15). Acetonitrile boils at 354 K and ethylene glycol vaporises at 470.3 K.

$$NH \diagup ^{CH_2COO^-} \atop \diagdown CH_2COO^- \longrightarrow H_2O \; + \; CO \; + \; CO_2 \; + \; CH_3CN \; + \; H_2 \qquad (3.15)$$
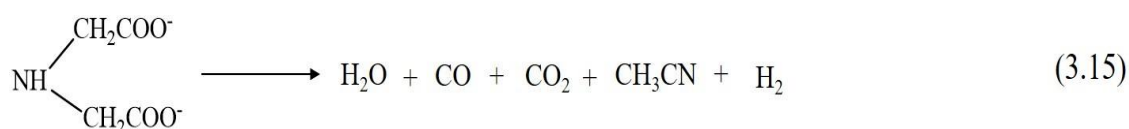
Deng *et al.* synthesized Bi_2Te_3 nanorods using EDTA as surfactant.[112] Srashti *et al.* synthesized BT nanostructures by refluxing method using EDTA as a surfactant, KOH and $NaBH_4$ and showed that the growth and morphology of the BT depends upon the surfactant, concentration of KOH and reaction timings.[113] Yang *et al.* showed that

EDTA-Na$_2$ could be used as complexing agent in the synthesis of nanocrystalline Sb$_2$Te$_3$ and achieved a ***PF*** of 2.04 μW cm^{-1} K^2 at 140°C and σ remained in the range 5–10 x 10^3 Sm^{-1}.[114] Dharmaiah *et al.* synthesized Sb$_2$Te$_3$ nanoplates using EDTA and achieved a high *S* of 181 μV/K, high σ of 763 Ω^{-1} cm^{-1} and low κ of 1.15 W/mK.[115]

3.3.3.3. Structural Analysis of Bi$_2$Te$_3$, Sb$_2$Te$_3$ and SnTe samples

Fig. 3.41 shows the XRD patterns of BT75-24, ST1-75-24, ST2-75-24 and TT75-24 samples prepared using different Bi, Sb and Sn precursors in aqueous medium. A phase pure Bi$_2$Te$_3$ is obtained for BT75-24 which forms in hexagonal crystal structure and neither the peaks of Bi additional phases nor Te impurity peaks are identified in BT75-24 sample. BT75-24 sample well matches the Bi$_2$Te$_3$ hexagonal phase with ICSD No: 20289. The observed peaks for ST1-75-24 are corresponding to the diffraction from hexagonal Sb$_2$Te$_3$ material having space group R-3m with the JCPDS number 15-0874.[116] It is noticed that ST2-75-24 contains both Sb$_2$Te$_3$ peaks and several impurity peaks of intermediate phases of SbCl$_3$ in the aqueous medium. A similar observation has been made on TT75-24 sample also where impurity peaks such as SnTe$_3$O$_8$ and TeO$_2$ are noticed. Hence, XRD results suggest the formation of phase pure compounds of chalcogenides through aqueous based chemical method only for selected cases, especially for BT75-24 and ST1-75-24.

3.3.3.4. Mechanism for the formation of secondary phases in Sb$_2$Te$_3$ and SnTe samples

In order to explore more on the unstable phases of ST2-75-24 and TT75-24, a detailed understanding of chemistry of these materials are necessary. Let us consider the chemical reactions that can happen in each case. Fig.3.42 represents the chemical compounds that can generate Bi^{3+}, Sb^{3+} and Sn^{2+}/Sn^{4+} in aqueous medium to combine with Te^{2-} to form corresponding chalcogenide materials. The existence of Te^{2-} ions in aqueous medium is validated with the chemical equations as represented in equation (3.16) – equation (3.18).
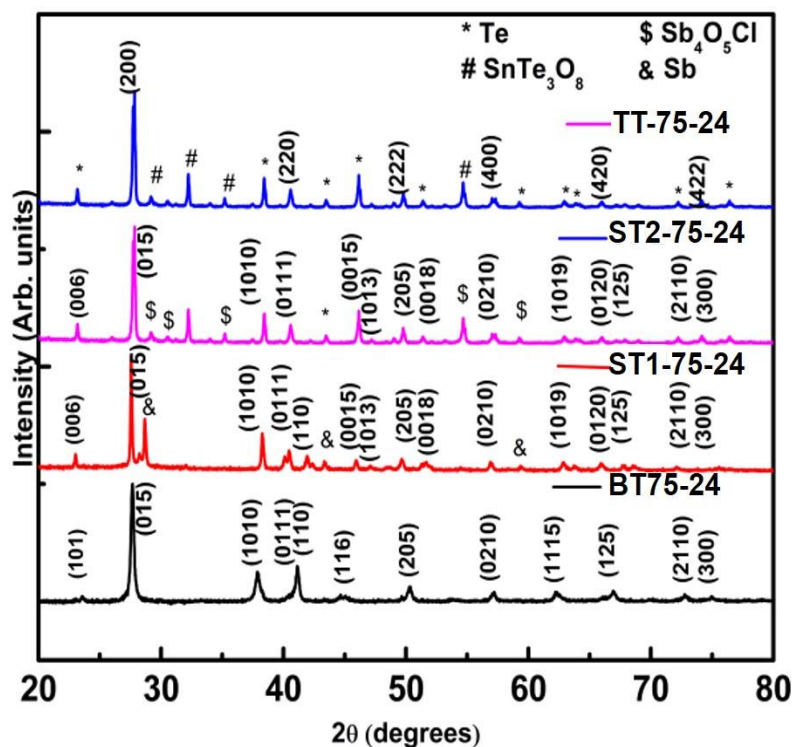
Fig. 3.41. XRD patterns of BT75-24, ST1-75-24, ST2-75-24 and TT-75-24 nanostructures
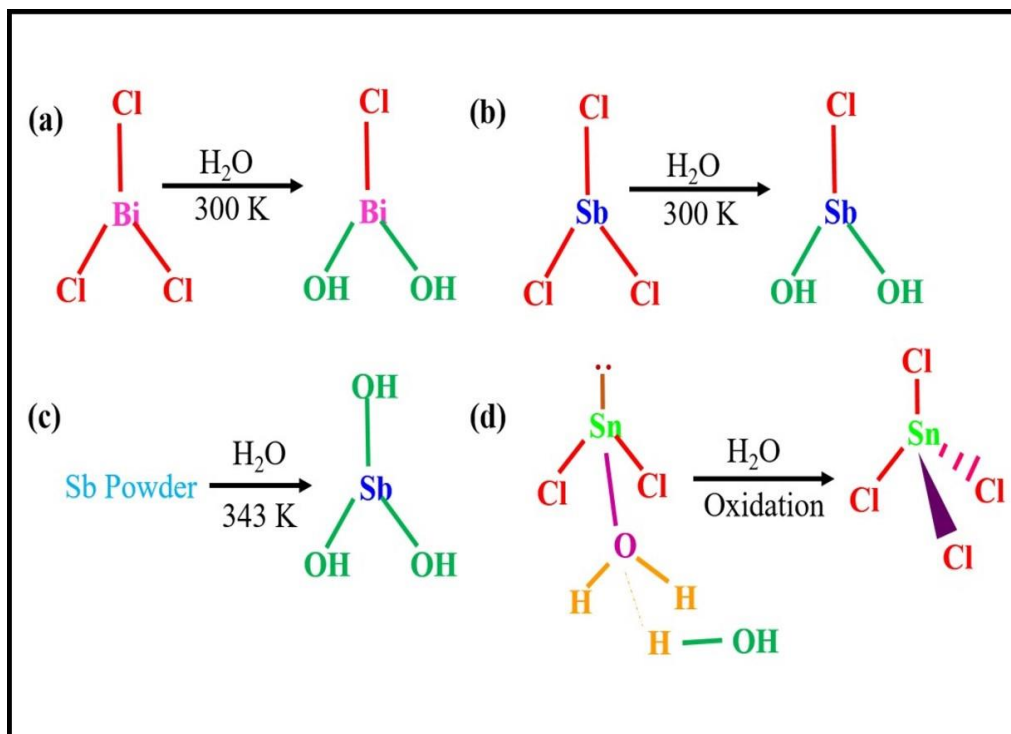
Fig. 3.42. Possible chemical compounds generating cations of (a) Bi, (b, c) Sb and (d) Sn to form corresponding chalcogenide nanostructures

$$3Te + 6OH^- \longrightarrow 2Te^{2-} + TeO_3^{2-} + 3H_2O \tag{3.16}$$

$$2TeO_3^{2-} + NaBH_4 \longrightarrow Te^{2-} + Te + NaBO_3 + H_2O + 2OH^- \tag{3.17}$$

$$5Te + 10OH^- + NaBH_4 \longrightarrow 5Te^{2-} + NaBO_3 + 7H_2O \tag{3.18}$$
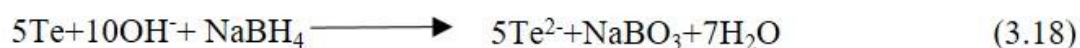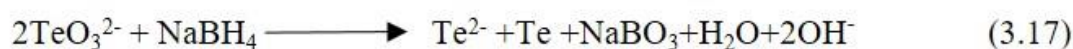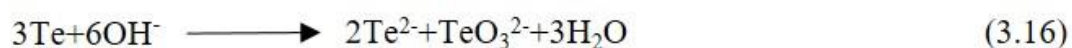
While using $BiCl_3$ in the formation of Bi_2Te_3, it is obvious that $Bi(OH)_2Cl$ which is stable in room temperature will generate Bi^{3+} ions in the aqueous medium whereas $Bi_4O_5Cl_2$ and $BiOCl$ will not take part in the chemical reaction[117] and is represented in equation (3.19) – equation (3.23).

$$4BiCl_3 + 5H_2O \xrightarrow{813\ K} Bi_4O_5Cl_2 + 10\ HCl \tag{3.19}$$

$$BiCl_3 + 2H_2O \xrightarrow{300\ K} Bi(OH)_2Cl + 2HCl \tag{3.20}$$

$$BiCl_3 + H_2O \xrightarrow{>400\ K} BiOCl + 2HCl \tag{3.21}$$

$$Bi^{3+} + [EDTA]^{2-} \longrightarrow [Bi(EDTA)]^+ \tag{3.22}$$

$$3[Bi(EDTA)]^+ + 2Te^{2-} \longrightarrow Bi_2Te_3 \tag{3.23}$$
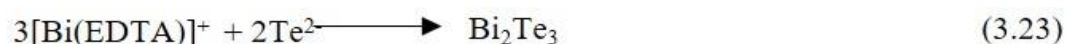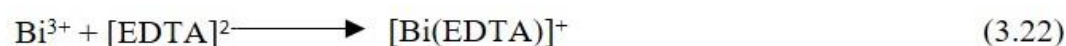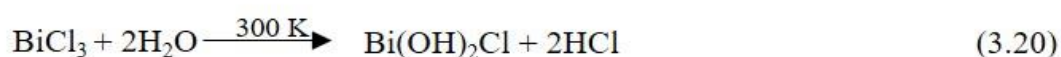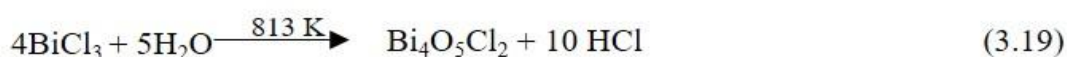
Thus, the formation of stable BT nanostructures is possible using $BiCl_3$. While using $SbCl_3$ as the starting material, the following possibilities can occur as mentioned below in equation (3.24) – equation (3.28).

$$4SbCl_3 + 5H_2O \xrightarrow{323\ K} Sb_4O_5Cl_2 + 10\ HCl \tag{3.24}$$

$$SbCl_3 + 2H_2O \xrightarrow{300\ K} Sb(OH)_2Cl + 2HCl \tag{3.25}$$

$$SbCl_3 + H_2O \xrightarrow{343\ K} SbOCl + 2HCl \tag{3.26}$$

$$Sb^{3+} + [EDTA]^{2-} \longrightarrow [Sb(EDTA)]^+ \tag{3.27}$$

$$3[Sb(EDTA)]^+ + 2Te^{2-} \longrightarrow Sb_2Te_3\ (partially) \tag{3.28}$$
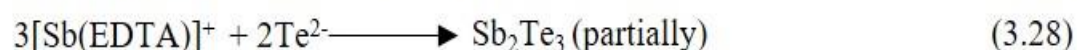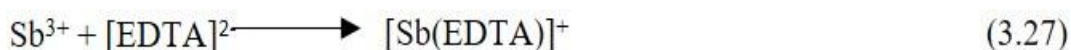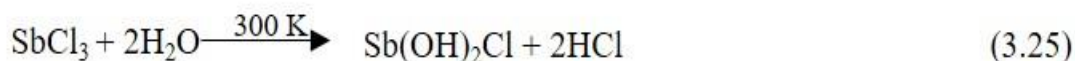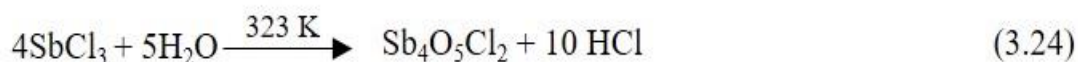
It is well understood from equation (3.24) and equation (3.26) that the formation of $Sb_4O_5Cl_2$ and $SbOCl$ is unavoidable here and only partial synthesis of Sb_2Te_3 is possible. An easy way to get phase pure Sb_2Te_3 in aqueous medium is through Sb metallic powder where $Sb(OH)_3$ can contribute Sb^{3+} as shown in equation (3.29).

$$Sb(\text{metallic powder}) + H_2O \xrightarrow{\text{343 K}} Sb(OH)_3 + Sb^0 \tag{3.29}$$
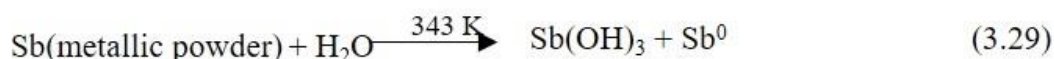
A small trace of metallic Sb could be present here, still this method holds good to carry out equation (3.27) and equation (3.28) to develop Sb_2Te_3 nanomaterials in aqueous medium which corroborates with XRD results of ST1-75-24.

Interestingly, it is observed that Sn based reactions are not recommended in aqueous medium as Sn^{2+} can easily undergo oxidation to form Sn^{4+} as represented in equation (3.30) to equation (3.32).

$$SnCl_2 + H_2O \underset{\text{323 K}}{\overset{}{\rightleftharpoons}} Sn(OH)Cl + HCl \tag{3.30}$$

$$6SnCl_2(aq) + O_2(g) + 2H_2O \longrightarrow 2SnCl_4(aq) + 4Sn(OH)Cl(s) \tag{3.31}$$

$$Sn^{2+} \xrightarrow[H_2O]{\text{oxidation}} Sn^{4+} \tag{3.32}$$
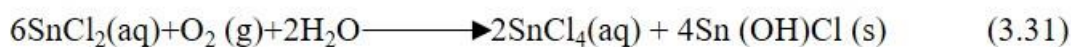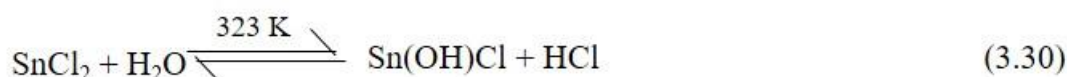
It could be well seen that $SnCl_2$ reacts with water to form an insoluble basic salt $Sn(OH)Cl$. This basic salt could further combine with Te ions present in the solution to form a secondary phase $SbTe_3O_8$ in addition to SnTe. Thus, aqueous based synthesis using EDTA is not suitable for the synthesis of SnTe. Other methods such as the one described in ref 118 needs to be adopted to synthesize phase pure SnTe nanopowders.

In this regard, it could be presumed that there are limitations to the formation of Sb_2Te_3 and SnTe in aqueous based reflux synthesis. However, the partial formation of Sb_2Te_3 using EDTA prompted us to synthesize Sb-doped Bi_2Te_3 and to investigate the n to p-type behaviour with Sb doping. Hence, we have attempted to synthesize Sb-doped Bi_2Te_3. Small amounts of Sb namely 1%, 3% and 5% were doped into Bi site using reflux method. The use of Sb powder may not bring satisfactory results and hence $SbCl_3$

was used as the precursor for the synthesis of Sb-doped Bi_2Te_3 as $SbCl_3$ will be suitable for replacing Bi ions to form the doped compound. The samples were prepared in 75 mmol EDTA with a reaction time of 24 h.

3.3.3.5. Structural Analysis of Sb-doped Bi_2Te_3

Fig. 3.43 shows the XRD patterns of the Sb-doped BT samples prepared for 1%, 3% and 5% concentrations by keeping the molarity of $NaBH_4$ at 4.4M. It could be seen that BS1T exists in single phase at lower concentrations of Sb and crystallizes into hexagonal Bi_2Te_3 structure. However, BS3T and BS5T contain small amounts of secondary phases of Sb and Sb_2O_3. Hence, it could be seen that for higher concentrations of Sb, the samples does not become phase pure. Hence reflux method and cold pressing is not sufficient to produce phase pure samples of Sb-doped Bi_2Te_3.

Hence, as a second step, these samples were hot pressed (HP) at a pressure of 50 MPa and a temperature of 723 K and the XRD patterns were taken for the Sb-doped samples which are shown in Fig 3.44. Upon hot pressing, all the Sb-doped BT samples crystallized into a combination hexagonal Bi_2Te_3 and BiTe phases. The Rietveld refinement of all the samples is shown in Fig 3.44. No peaks corresponding to Sb or Sb_2O_3 were indexed in the XRD patterns. The structural parameters determined from Rietveld refinement are listed in Table 3.9. A low value of χ^2 has been observed which justifies the quality and goodness of the refinement. It could be seen from the refinement data that there is decrease in unit cell volume with increase in Sb concentration. This is attributed to the small size of Sb^{3+} ions substituting Bi^{3+} ions in the lattice. Also upon hot pressing, there could be a redistribution of ions in the lattice and the insoluble compounds could have vaporised leading to the formation of phase-pure Bi_2Te_3 without any impurity peaks.

3.3.3.6. Morphological Analysis of hot pressed Sb-doped Bi_2Te_3

Fig 3.45(a) and (b) shows the TEM images of BS1T-HP. The TEM images of BS1T-HP indicate the formation of nanosheets. The formation of nanosheets in BS1T-HP could be attributed to the template action of EDTA as a result of which oriented attachment occurs along a preferred direction resulting in the formation of nanosheets.

The (006) plane and the SAED patterns shown in Fig. 3.45 (c) and 3.45 (d) correspond to the lattice planes of Bi$_2$Te$_3$.
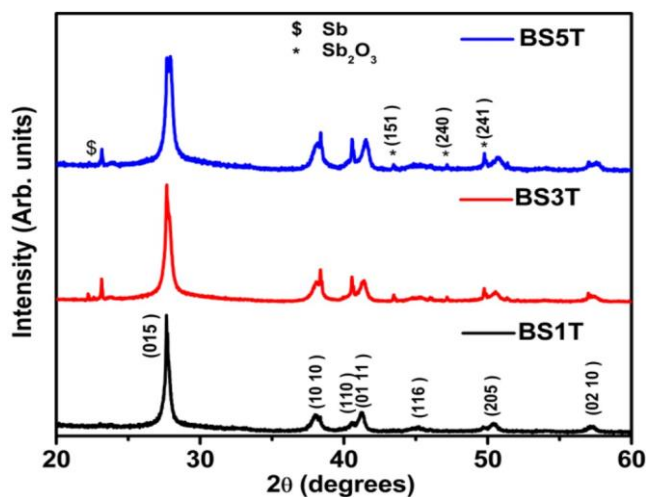
Fig. 3.43. XRD patterns of cold pressed Sb-doped BT nanostructures
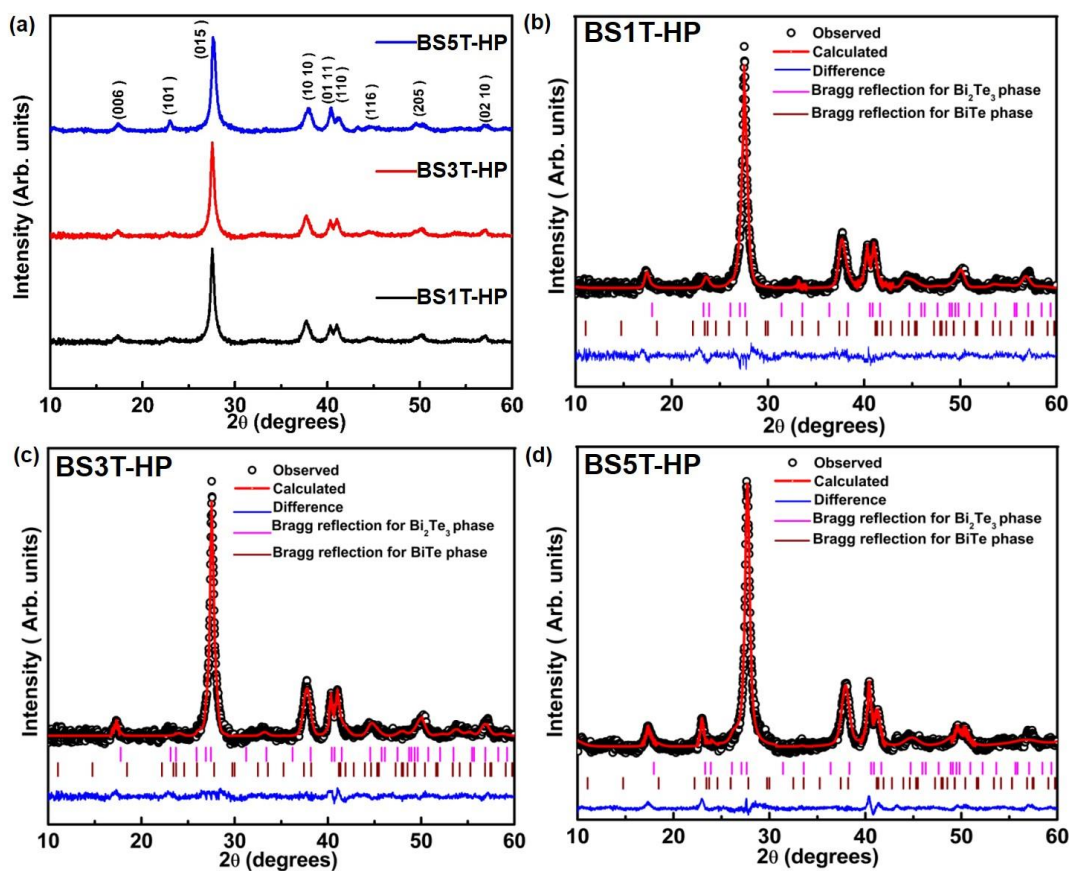
Fig. 3.44. (a) XRD patterns of hot pressed Sb-doped BT nanostructures, Refined XRD patterns (b) BS1T-HP, (c) BS3T-HP and (d) BS5T-HP.

Table 3.9. Refined parameters of BS1T-HP, BS3T-HP and BS5T-HP

BT Nano-structures	BS1T-HP		BS3T-HP		BS5T-HP	
Phase	Bi_2Te_3 + BiTe		Bi_2Te_3 + BiTe		Bi_2Te_3 + BiTe	
Phase fraction (%)	62+38		73+27		82+18	
Crystal Structure	Hexagonal + Rhombohedral		Hexagonal + Rhombohedral		Hexagonal + Rhombohedral	
Space Group	R-3m + P-3 m 1		R-3m + P-3 m 1		R-3m + P-3 m 1	
Lattice Parameters						
a(Å)	4.38(3)	4.34(8)	4.37(3)	4.34(8)	4.36(3)	4.35(8)
b(Å)	4.38(3)	4.34(8)	4.37(3)	4.34(8)	4.36(3)	4.35(8)
c(Å)	30.08(5)	24.80(9)	30.08(5)	24.80(9)	30.08(5)	24.80(9)
γ(deg)	120	120	120	120	120	120
Volume(Å)^3	504.99(6)	406.50(1)	504.99(6)	406.50(1)	504.99(6)	406.50(1)
Residual Parameters						
R_p	3.40		3.34		3.27	
wR_p	2.29		2.13		2.09	
χ^2	1.89		1.68		1.54	

3.3.3.7. Mechanism for the formation of hot pressed Sb-doped Bi_2Te_3

The detailed reaction mechanism showing the formation of Bi_2Te_3 nanostrucutres was explained in detail in previous section Fig. 3.27. The mechanism for the formation of $Bi_{2-x}Sb_xTe_3$ nanostructures using EDTA is demonstrated in Fig.3.46. Here, it could be seen that the secondary phases of Sb and Sb_2O_3 present in the cold pressed BS3T and BS5T disappears upon hot pressing. This could be due to the additional energy provided during hot pressing which results in the phase formation of $Bi_{2-x}Sb_xTe_3$ nanostructures. The TEM images indicate the formation of sheet-like structures for in BS1T-HP. It is well known that EDTA is a multidentate ligand with polyfunctional groups and it could effectively serve as bridging ligands to form multinuclear complexes with metal ions above some critical concentration. Then chains of crystalline seeds would form in the nucleation process especially with reaction time, which finally yields sheet/rod-like structures of our desired compound. Here, EDTA acts as a structure directing agent in the formation of $Bi_{2-x}Sb_xTe_3$ nanostructures. The present approach using reflux technique could favor the reaction mechanism through nucleation and growth process. The crystalline $Bi_{2-x}Sb_xTe_3$ structures could form in the

reflux reaction process through a homogeneous nucleation process if reaction time is a varying parameter along with EDTA concentration.
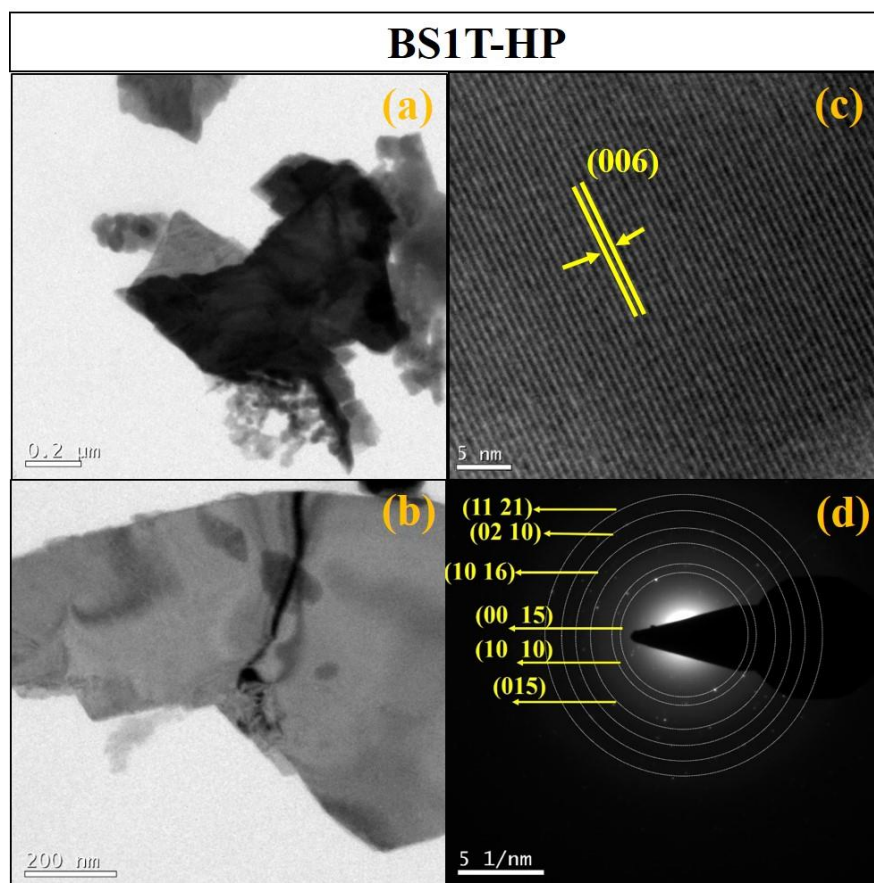
Fig. 3.45. (a, b) TEM images showing the formation of BS1T-HP nanosheets (c) (006) plane corresponding to Bi_2Te_3 and (d) SAED patterns of BS1T-HP.

It is well known that BT based materials have a highly anisotropic structure which favors the growth primarily confined to a particular direction and the crystalline seeds of the material tends to grow into the rod/sheet shape under the influence of EDTA which would be a soft template, and induce the formation of 1D/2D structures. Hence EDTA could promote a preferential directional growth under the template effect where the formation of inorganic nanoparticles in liquid media is associated with the monomer growth. Previous reports suggest that the nucleus is characterized by various shapes and facets with different surface energies, and grows by bonding with other monomers exist in the solution.[59] Crystal surface energy and facet attachment are highly influencing in the nanoparticle growth and shape formation. If any capping agent is present in the

solution, they can bind to specific facets of the nucleus to coat it with a monolayer which is precisely happening between Bi and EDTA in the present technique. These attached surfactants could lower the total surface energy when $Bi_{2-x}Sb_xTe_3$ nanocrystals are formed which is specifically by blocking high-energy facets and exposing low energy facets.
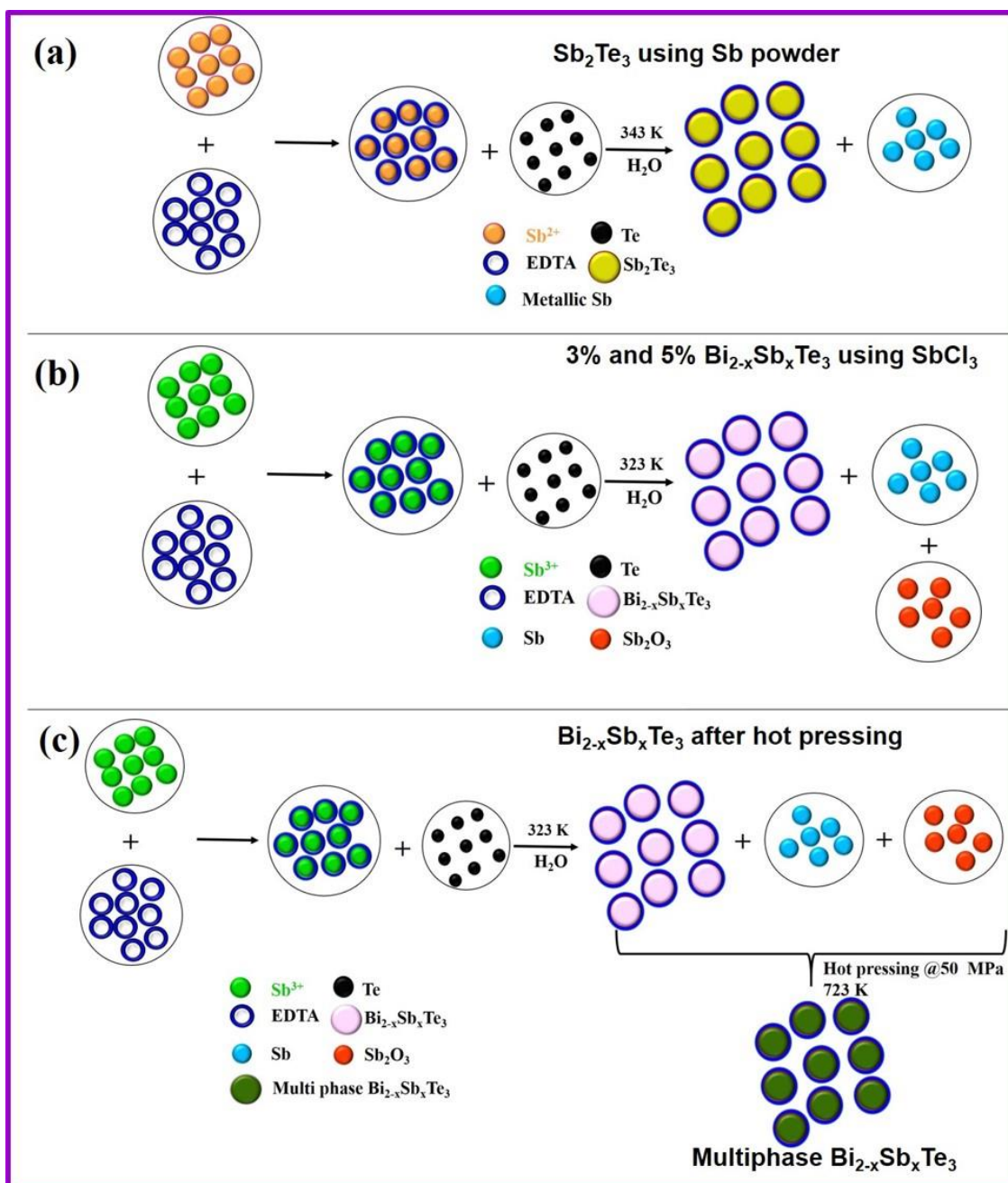
Fig. 3.46. Schematic diagram showing the formation of EDTA assisted (a) ST1-75-24, (b) 3% and 5% $Bi_{2-x}Sb_xTe_3$ and (c) hot pressed $Bi_{2-x}Sb_xTe_3$ nanostructures

3.3.3.8. Temperature dependence of *S*, *ρ* and *PF* of hot pressed Sb-doped Bi₂Te₃

Fig. 3.47 shows the temperature dependence of *S* in the temperature range of 280 K-480 K. A negative value of *S* is obtained for BS1T-HP at temperatures below 425 K revealing an n-type semiconducting behaviour indicating that electrons are the majority carriers upto 425 K. As the temperature increases to 425 K, a clear transition from negative to positive value of *S* is evident which marks a crossover from n-type to p-type. As the Sb doping concentration increases to 5%, the sample becomes completely p-type which is evident from the obtained positive values of *S* from Fig.3.47. Hence, an n-type to p-type semiconducting behaviour has been achieved with Sb doping in Bi₂Te₃. However, due to the presence of mixed phases in BS1T-HP, the value of *S* is quite low, reaching a maximum value of -54.78 µV/K at 306 K and 11.2 µV/K at 448 K. In case of BS5T-HP, a maximum value of 215.12 µV/K is achieved at 465 K which is quite remarkable.
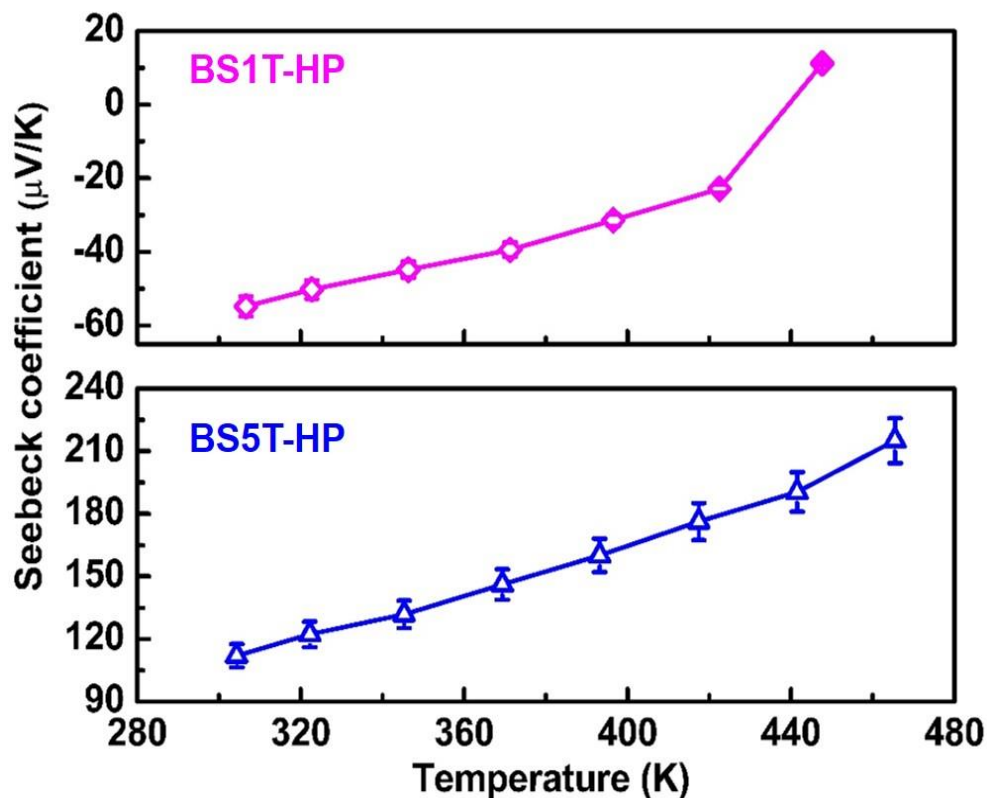
Fig. 3.47. Temperature dependence of *S* of BS1T-HP and BS5T-HP.
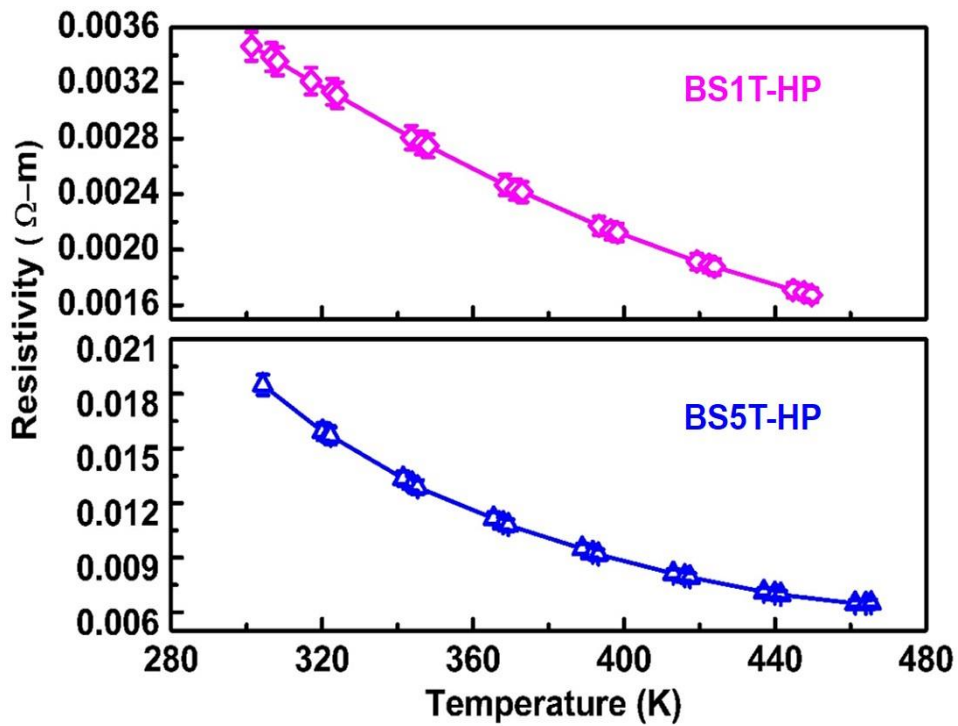
Fig. 3.48. Temperature dependence of *ρ* of BS1T-HP and BS5T-HP.
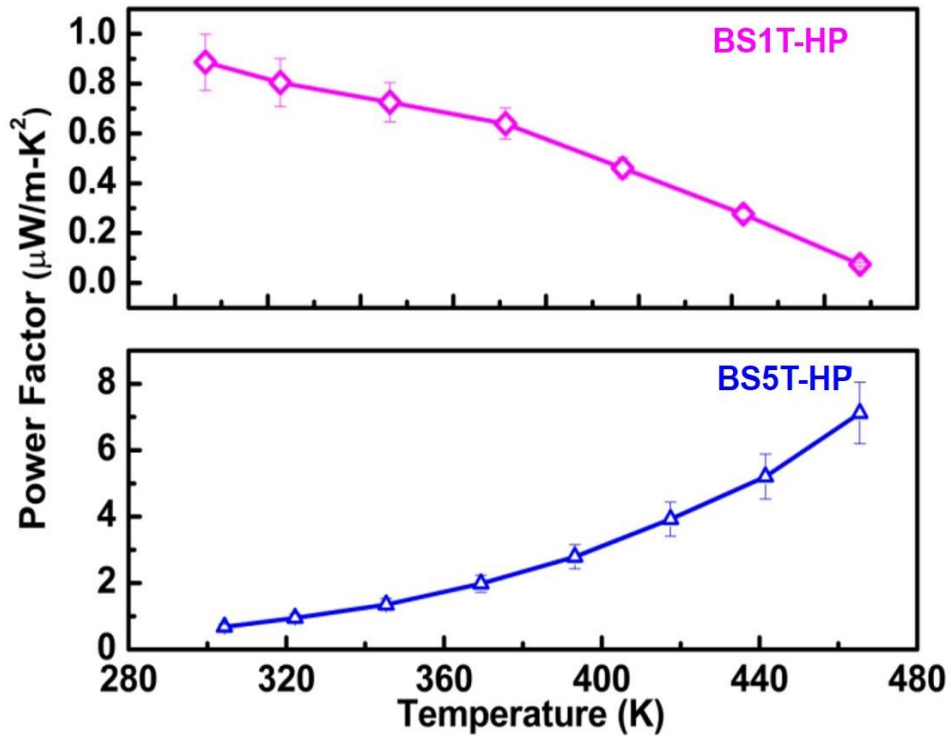
Fig. 3.49. Temperature dependence of *PF* of BS1T-HP and BS5T-HP.
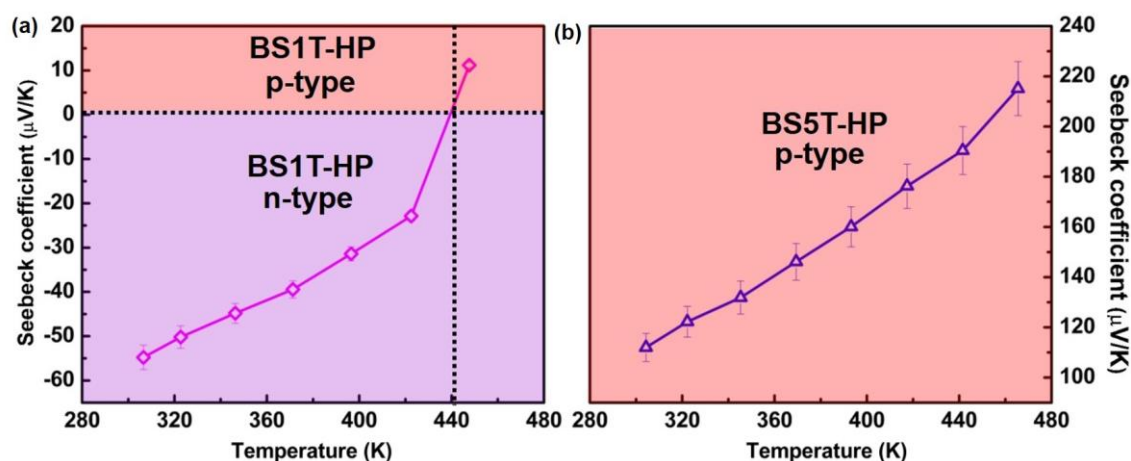
Fig.3.50. (a) Transition from n-type to p-type in BS1T-HP and (b) p-type semiconducting behaviour in BS5T-HP.

To understand the electrical transport of the synthesized Sb-doped BT nanostructures, detailed ρ analysis was performed on BS1T-HP and BS5T-HP samples in the temperature range of 280 K – 480 K. Fig. 3.48 presents the temperature-dependent ρ of these samples, and reveals semiconducting behaviour for BS1T-HP and BS5T-HP. BS1T-HP exhibits a ρ value of 0.00347 Ω-m and BS5T-HP exhibits 0.01848 Ω-m at 300 K which is much higher than the values obtained for the BT samples presented in previous sections. Due to this reason, a considerable decrease in the σ can happen and which could ultimately lower the **PF**. The temperature variation of **PF** is plotted and shown in Fig.3.49. **PF** value of BS1T-HP sample decreases with temperature giving a maximum of 0.89 $\mu Wm^{-1}K^{-2}$ at 306 K and this low value of **PF** is arising due to the decreased S and increased ρ value compared to the Bi_2Te_3 samples discussed in the previous section 3.3.1.5. and 3.3.2.5. With increase in Sb concentration in BS5T-HP, the **PF** follows an inverse trend where it increases with increase in temperature reaching a maximum value of 7.1 $\mu Wm^{-1}K^{-2}$ at 465 K. The decreased value of **PF** in BS1T-HP and BS1T-HP could be attributed to the presence of multiphases of Bi_2Te_3 and BiTe present in the system. It could also be seen that there is a crossover from n-type (negative Seebeck) to p-type (positive Seebeck) in BS1T-HP at 440 K which is represented in Fig 3.50(a). For BS5T-HP, the material becomes completely p-type as shown in Fig. 3.50(b). Brahmi *et al.* reported that this transition could be due to the movement of the Fermi level (E_f) away from the conduction band and towards the valence band caused by the increased contribution from acceptors by

changing the temperature.[119] This result could provide a new pathway towards finding correct doping scheme for tailoring the TE properties for novel technological applications.

3.4. Summary

- BT nanostructures have been synthesised successfully by a simple, low-cost and low-temperature reflux method using deionized water as the solvent.

- Structural and morphological changes were obtained by varying the reaction time in 75 mmol EDTA concentration where the reaction time facilitates the formation of different BT structures transforming from BiTe phase to Bi_2Te_3 phase and reaction time of 24 h shows the hexagonal stacking and exhibits the best TE properties among the synthesised samples.

- The EDTA concentration facilitates the formation of desired Bi_2Te_3 phase in lower reaction time and EDTA behaves not only as a capping agent but also acts as a soft template for lowering the surface energy to facilitate the formation of rod and sheet-like structures.

- BT sample synthesized for an EDTA concentration of 100 mmol and reaction time of 24h exhibits the best TE figure of merit among the synthesized samples.

- In addition to Bi_2Te_3, reaction mechanism has also been investigated in detail for Sb_2Te_3, SnTe and Sb-doped Bi_2Te_3 and it is suggested that aqueous based reflux reaction is not suitable for the synthesis of SnTe whereas partial formation of Sb_2Te_3 could be possible.

- Hot pressed Sb-doped Bi_2Te_3 samples prepared by reflux method exhibits an n- to p-type transition with significant improvement in thermopower value.

- The results achieved in this chapter indicate that optimization of reaction conditions could provide defect free, stoichiometric and stable products of Bi and Sb based chalcogenide nanostructures using a simple aqueous based reflux technique that provides appropriate ways for enhancing the overall TE performance of nanostructured chalcogenide materials.

3.5. References

1. L. E. Bell, Cooling, heating, generating power, and recovering waste heat with thermoelectric systems. *Science*, *321* (2008) 1457.
2. G.A. Slack, D.M. Rowe (Ed.) New materials and performance limits for thermoeletric cooling; CRC Handbook of Thermoelectrics: CRC Press, Boca Raton, (1995) 407.
3. R. J. Mehta, Y. Zhang, C. Karthik, B. Singh, R. W. Siegel, T. Borca-Tasciuc, G. Ramanath, A new class of doped nanobulk high-figure-of-merit thermoelectrics by scalable bottom-up assembly, *Nat. Mater.,* 11 (2012) 233.
4. Y. Min, J. W. Roh, H. Yang, M. Park, S. I. Kim, S. Hwang, S. M. Lee, K. H. Lee, U. Jeong, Surfactant-free scalable synthesis of Bi_2Te_3 and Bi_2Se_3 nanoflakes and enhanced thermoelectric properties of their nanocomposites, *Adv. Mater.* 25 (2013) 1425.
5. Y. Zhang, L. P. Hu, T. J. Zhu, J. Xie, X. B. Zhao, High yield Bi_2Te_3 single crystal nanosheets with uniform morphology via a solvothermal synthesis. *Cryst. Growth Des*., 13 (2013) 645.
6. J. P. Fu, S. Y. Song, X. G. Zhang, F. Cao, L. Zhou, X. Y. Li, H. J. Zhang, Bi_2Te_3 nanoplates and nanoflowers: synthesized by hydrothermal process and their enhanced thermoelectric properties. *Cryst.Eng.Comm.*, 14 (2012) 2159.
7. G. Zhang, B. Kirk, L. A. Jauregui, H. Yang, X. Xu, Y. P. Chen, Y. Wu, Rational synthesis of ultrathin n-type Bi_2Te_3 nanowires with enhanced thermoelectric properties. *Nano Lett*., 12 (2011) 56.
8. J. S. Son, M. K. Choi, M.-K. Han, K. Park, J.-Y. Kim, S. J. Lim, M. Oh, Y. Kuk, C. Park, S.-J. Kim, T. Hyeon, *n*-Type Nanostructured thermoelectric materials prepared from chemically synthesized ultrathin Bi_2Te_3 nanoplates, *Nano Lett.,* 12 (2012) 640.
9. G. Q. Zhang, H. Y. Fang, H. R. Yang, L. A. Jauregui, Y. P. Chen, Y. Wu, Design principle of telluride-based nanowire heterostructures for potential thermoelectric applications. *Nano Lett.,* 12 (2012) 3627.
10. L. Cheng, Z. G. Chen, L. Yang, G. Han, H. Y. Xu, G. J. Snyder, G. Q. Lu, J. Zou, T-Shaped Bi_2Te_3–Te heteronanojunctions: epitaxial growth, structural modeling, and thermoelectric properties, *J. Phys. Chem. C,* 117 (2013) 12458.
11. P. Anandan, M. Omprakash, M. Azhagurajan, M. Arivanandhan, D. Rajan Babu, T. Koyama, Y. Hayakawa, Tailoring bismuth telluride nanostructures using a scalable sintering process and their thermoelectric properties. *Cryst. Eng.Comm.,* 16 (2014) 7956.
12. H. J. Goldsmid, R. W. Douglas, The use of semiconductors in thermoelectric refrigeration. *Br. J. Appl. Phys*., 5 (1954) 386.
13. Y. Deng, C-W. Cui, Ni-la. Zhang, T-H. Ji, Q- L. Yang, L. Guo, Fabrication of bismuth telluride nanotubes via a simple solvothermal process. *Solid State Commun*, 138 (2006) 111.
14. Y. Y. Zheng, T. J. Zhu, X. B. Zhao, J. P. Tu, G. S. Cao, Sonochemical synthesis of nanocrystalline Bi_2Te_3 thermoelectric compounds. *Mater. Lett.*, 59 (2005) 2886.

15. Y. Q. Cao, T. J. Zhu, X. B. Zhao, Thermoelectric Bi_2Te_3 nanotubes synthesized by low-temperature aqueous chemical method. *J. Alloys Compd.*, 449 (2008) 109.
16. J. Z. Hu, X. B. Zhao, T. J. Zhu, A. J. Zhou, Synthesis and transport properties of Bi_2Te_3nanocomposites. *Phys. Scr.*, T 129 (2007) 120.
17. Ch. Papageorgiou, E. Hatzikraniotis, Ch. B. Lioutas, N. Frangis, O. Valasiades, K.M. Paraskevopoulos, T. Kyratsi, Thermoelectric properties of nanocrystalline PbTe synthesized by mechanical alloying. *J. Electron. Mater.*, 39 (2010) 1665.
18. L. Wang, X. Y. Qin, The effect of mechanical milling on the formation of nanocrystalline Mg_2Si through solid-state reaction. *Scr. Mater.*, 49 (2003) 243.
19. M. Ioannou, E. Hatzikraniotis, Ch.B. Lioutas, Th. Hassapis, Th. Atlantis, K. M. Paraskevopoulos, Th. Kyratsi, Fabrication of nanocrystalline Mg_2Si via ball milling process: Structural studies. *Powder Technol.*, 217 (2012) 523.
20. W. J. Xie, X. F. Tang, Y. G. Yan, Q. J. Zhang, T. M. Tritt, High thermoelectric performance BiSbTe alloy with unique low-dimensional structure. *J. Appl. Phys*, 105 (2009) 113713.
21. W. J. Xie, X. F. Tang, Y. G. Yan, Q. J. Zhang, T. M. Tritt, Unique nanostructures and enhanced thermoelectric performance of melt-spun BiSbTe alloys. *Appl. Phys. Lett.*, 94 (2009) 102111.
22. D. Teweldebrhan, V. Goyal, M. Rahman, A. A. Balandin, Atomically-thin crystalline films and ribbons of bismuth telluride. *Appl. Phys. Lett.*, 96 (2010) 053107.
23. G.-E. Lee, I.-H. Kim, Y. S. Lim, W.-S. Seo, B.-J. Choi, C.-W. Hwang, Preparation and Thermoelectric Properties of Doped Bi_2Te_3-Bi_2Se_3 Solid Solutions. *J. Electron. Mater.*, 43 (2013) 1650.
24. T. Takabatake, K. Suekuni, T. Nakayama, E. Kaneshita, Phonon-glass electron-crystal thermoelectric clathrates: Experiments and theory. *Rev. Mod. Phys.*, 86 (2014) 841.
25. M. G. Kanatzidis, Nanostructured Thermoelectrics: The New Paradigm. *Chem. Mater.*, 22 (2010) 648.
26. G. J. Snyder, E. S. Toberer, Complex thermoelectric materials. *Nat. Mater.*, 7, (2008) 105.
27. L. Xue-Dong, Y.-H. Park, Structure and transport properties of $(Bi_{1-x}Sb_x)_2Te_3$ thermoelectric material prepared by mechanical alloying and pulse discharge sintering. *Mater. Trans., JIM*, 43 (2002) 681.
28. O. Eibl, K. Nielsch, N. Peranio, F. Völklein, Thermoelectric Bi_2Te_3 Nanomaterials edited, *Wiley* (2015).
29. L. Yang, Z.-G. Chen, M. Hong, G. Han, J. Zou, Enhanced Thermoelectric Performance of Nanostructured Bi_2Te_3 through Significant Phonon Scattering. *ACS Appl. Mater. Interfaces,* 7 (2015) 23694.
30. M. Gharsallah, F. Serrano-Sánchez, J. Bermúdez, N. M. Nemes, J. L. Martínez, F. Elhalouani, J. A. Alonso, Nanostructured Bi_2Te_3 Prepared by a Straightforward Arc-Melting Method. *Nanoscale Res. Lett.,* 11 (2016) 142.
31. G. Kavei, M. A. Karami, Formation of anti-site defects and bismuth over stoichiometry in p-type $Sb_{2-x}Bi_xTe_3$ thermoelectric crystals. *J. Appl. Phys.*, 42 (2008) 67.
32. J. Horak, K. Cermak, L. Koudelka, Energy formation of antisite defects in doped Sb_2Te_3 and Bi_2Te_3 crystals. *J. Phys. Chm. Solids*, 47 (1986) 805.

33. S. V. Ovsyannikov, V. V. Shchennikov, High-Pressure Routes in the Thermoelectricity or How One Can Improve a Performance of Thermoelectrics. *Chem. Mater.*, 22 (2010) 635.
34. Y. Kang, Q. Zhang, C. Fan, W. Hu, C. Chen, L. Zhang, F. Yu, Y. Tian, B. Xu, High pressure synthesis and thermoelectric properties of polycrystalline Bi_2Se_3. *J. Alloys Compd.*, 700 (2017) 223.
35. A. Soni, Z. Yanyuan, Y. Ligen, M. K. Khiam Aik, M. S. Dresselhaus, Q. Xiong, Enhanced Thermoelectric Properties of Solution Grown $Bi_2Te_{3-x}Se_x$ Nanoplatelet Composites. *Nano Lett.*, 12 (2012) 1203.
36. S. Urazhdin, D. Bilc, S. D. Mahanti, S. H. Tessmer, Surface effects in layered semiconductors Bi_2Se_3 and Bi_2Te_3. *Phys. Rev. B*, 69 (2004) 085313.
37. C. L. Hsin, M. Wingert, C. W. Huang, H. Guo, T. J. Shih, J. Suh, K. Wang, J. Wu, W. W. Wu, R. Chen, Phase transformation and thermoelectric properties of bismuth-telluride nanowires. *Nanoscale*, 5 (2013) 4669.
38. J. Martin, L. Wang, L. Chen, G. S. Nolas, Enhanced Seebeck coefficient through energy-barrier scattering in PbTe nanocomposites. *Phys. Rev. B*, 79 (2009) 115311.
39. K. Kishimoto, T. Koyanagi, Preparation of sintered degenerate n-type PbTe with a small grain size and its thermoelectric properties. *J. Appl. Phys.*, 92 (2002) 2544.
40. B. Moyzhes, V. Nemchinsky, Thermoelectric figure of merit of metal–semiconductor barrier structure based on energy relaxation length. *Appl. Phys. Lett.*, 73 (1998) 1895.
41. C. Chiritescu, C. Mortensen, D. G. Cahill, D. Johnson, P. Zschack, Lower limit to the lattice thermal conductivity of nanostructured Bi_2Te_3 -based materials. *J. Appl. Phys.*, 106 (2009) 073503.
42. X. Yan, B. Poudel, Y. Ma, W. S. Liu, G. Joshi, H. Wang, Y. Lan, D. Wang, G. Chen, Z. F. Ren, Experimental studies on anisotropic thermoelectric properties and structures of n-type $Bi_2Te_{2.7}Se_{0.3}$. *Nano Lett.*, 10 (2010) 3373.
43. M. Scheele, N. Oeschler, I. Veremchuk, K. G. Reinsberg, A. M. Kreuziger, A. Kornowski, J. Broekaert, C. Klinke, H. Weller, ZT enhancement in solution-grown $Sb_{(2-x)}Bi_xTe3$ nanoplatelets. *ACS Nano*, 7 (2010) 4283.
44. M. Scheele, N. Oeschler, K. Meier, A. Kornowski, C. Klinke, H. Weller, Synthesis and Thermoelectric Characterization of Bi_2Te_3 Nanoparticles. *Adv. Funct. Mater.*, 19 (2009) 3476.
45. Y. Zhao, J. S. Dyck, B. M. Hernandez, C. Burda, Improving Thermoelectric Properties of Chemically Synthesized Bi_2Te_3-Based Nanocrystals by Annealing. *J. Phys. Chem. C*, 114 (2010) 11607.
46. D. L. Medlin, G. J. Snyder, Interfaces in bulk thermoelectric materials: A review for Current Opinion in Colloid and Interface Science. *Curr. Opin. Colloid Interface Sci.*, 14 (2009) 226.
47. J. Callaway, H. C. von Baeyer, Effect of Point Imperfections on Lattice Thermal Conductivity. *Phys. Rev.*, 120 (1960) 1149.
48. K. T. Kim, T. S. Lim, G. H. Ha, Improvement in thermoelectric properties of N-type bismuth telluride nanopowders by hydrogen reduction treatment. *Rev. Adv. Mater. Sci.*, 28 (2011) 196.
49. H-T. Zhu, J. Luo, J.-K. Lianga, Synthesis of highly crystalline Bi_2Te_3 nanotubes and their enhanced thermoelectric properties. *J. Mater. Chem. A*, 2 (2014) 12821.

50. G. Zheng, X. Su, T. Liang, Q. Lu, Y. Yan, C. Uher, X. Tang, High thermoelectric performance of mechanically robust n-type $Bi_2Te_{3-x}Se_x$ prepared by combustion synthesis. *J. Mater. Chem. A*, 3 (2015) 6603.

51. M. Saleemi, M. S. Toprak, S. Li, M. Johnsson, M. Muhammed, Synthesis, processing, and thermoelectric properties of bulk nanostructured bismuth telluride (Bi_2Te_3). *J. Mater. Chem.*, 22 (2012) 725.

52. H. Fang, J-H. Bahk, T. Feng, Z. Cheng, M. S. Mohammed Amr, X. Wang, X. Ruan, A. Shakouri, Y. Wu, Thermoelectric properties of solution-synthesized n-type Bi_2Te_3 nanocomposites modulated by Se: An experimental and theoretical study. *Nano Res*, 9 (2016) 117.

53. L. Giri, G. Mallick, A. C. Jackson, M. H. Griepa, S. P. Karna, P. Synthesis and characterization of high-purity, single phase hexagonal Bi_2Te_3 nanostructures. *RSC Adv.*, 5 (2015) 24930.

54. V. R. Akshay, M. V. Suneesh, M. Vasundhara, Tailoring Thermoelectric Properties through Structure and Morphology in Chemically Synthesised n-type Bismuth Telluride Nanostructures, *Inorg. Chem.* 56 (2017) 6264.

55. M. Hong, T. C. Chasapis, Z.-G. Chen, L. Yang, M. G. Kanatzidis, G. J. Snyder, J. Zou, n-Type $Bi_2Te_{3-x}Se_x$ Nanoplates with Enhanced Thermoelectric Efficiency Driven by Wide-Frequency Phonon Scatterings and Synergistic Carrier Scatterings, *ACS Nano*, 10 (4) (2016) 4719.

56. M. Hong, Z. G. Chen, L. Yang, J. Zou, $Bi_xSb_{2-x}Te_3$ Nanoplates with Enhanced Thermoelectric Performance due to Sufficiently Decoupled Electronic Transport Properties and Strong WideFrequency Phonon Scatterings, *Nano Energy*, 20 (2016) 144.

57. Y. Deng, X. S. Zhou, G. D. Wei, J. Liu, C. W. Nan, S. J. Zhao, Solvothermal Preparation and Characterization of Nanocrystalline Bi_2Te_3 Powder with Different Morphology. *J. Phys. Chem. Solids*, 63 (2002) 2119.

58. Y. Deng, G. D. Wei, C. W. Nan, Ligand-Assisted Control Growth of Chainlike Nanocrystals. *Chem. Phys. Lett*. 368 (2003) 639.

59. X. B. Zhao, X. H. Ji, Y. H. Zhang, B. H. Lu, Effect of Solvent on the Microstructures of Nanostructured Bi_2Te_3 Prepared by Solvothermal Synthesis. *J. Alloys Compd.* 368 (2004) 349.

60. D. Hsieh, D. Qian, L. Wray, Y. Xia, Y. S. Hor, R. J. Cava, M. Z. A. Hasan, Topological Dirac Insulator in a Quantum Spin Hall Phase (Experimental Realization of a 3D Topological Insulator) *Nature,* 452 (2008) 970.

61. H. Zhang, C. X. Liu, X. L. Qi, X. Dai, Z. Fang, S. C. Zhang, Topological Insulators in Bi_2Se_3, Bi_2Te_3 and Sb_2Te_3 with a Single Dirac Cone on the Surface. *Nature Phys.* 5 (2009) 438.

62. G. Bendt, A. Weber, S. Heimann, W. Assenmacher, O. Prymak, S. Schulz, Wet-Chemical Synthesis of Different Bismuth Telluride Nanoparticles using Metal Organic Precursors-Single Source vs. Dual Source Approach, *Dalton Transactions* 44 (2015) 14272.

63. P. Kumar, P. Srivastava, J. Singh, R. Belwal, M. K. Pandey, K. S. Hui, K. N. Hui, K. Singh, Morphological Evolution and Structural Characterization of Bismuth Telluride (Bi_2Te_3) Nanostructures. *J. Phys. D: Appl. Phys.* 46 (2013) 285301.

64. Y. M. Lin, M. S. Dresselhaus, Thermoelectric Properties of Superlattice Nanowires. *Phys. Rev. B*, 68 (2003) 075304.

65. W. Kullmann, J. Geurts, W. Richter, N. Lehner, H. Rauh, U. Steigenberger, G. Eichhorn, R. Geick, Effect of Hydrostatic and Uniaxial Pressure on Structural Properties and Raman Active Lattice Vibrations in Bi_2Te_3. *Phys. Stat. Sol. b* 125, (1984) 131.

66. Y. C. Ha, H. J. Sohn, G. J. Jeong, C. K. Lee, K. I. Rhee, Electrowinning of Tellurium from Alkaline Leach Liquor of Cemented Te. *J. Appl. Electrochem.* 30 (2000) 315.

67. R. S. Mane, B. R. Sankapal, C. D. Lokhande, Studies on Chemically Deposited Nanocrystalline Bi_2S_3 Thin Films. *Mater. Res. Bull.* 35 (2000) 587.

68. S. P. Summers, K. A. Abbound, S. R. Farrah, G. J. Palenik, Syntheses and Structures of Bismuth (III) Complexes with Nitrilotriacetic Acid, Ethylenediaminetetraacetic Acid, and Diethylenetriaminepentaacetic Acid. *Inorg. Chem.* 33 (1994) 88.

69. C. Kim, D. H. Kim, J. T. Kim, Y. S. Han, H. Kim, Investigation of Reaction Mechanisms of Bismuth Tellurium Selenide Nanomaterials for Simple Reaction Manipulation Causing Effective Adjustment of Thermoelectric Properties. *ACS Appl. Mater. Interfaces*, 6 (2014) 778.

70. J. Fu, S. Song, X. Zhang, F. Cao, L. Zhou, X. Li, H. Zhang, Bi_2Te_3 Nanoplates and Nanoflowers: Synthesized by Hydrothermal Process and Their Enhanced Thermoelectric Properties. *Cryst. Eng. Comm.* 14 (2012) 2159.

71. Y. C. Zhang, T. Day, M. L. Snedaker, H. Wang, S. Kramer, C. S. Birkel, X. L. Ji, D. Y. Liu, G. J. Snyder, G. D. Stucky, Mesoporous Anisotropic n-Type Bi_2Te_3 Monolith with Low Thermal Conductivity as an Efficient Thermoelectric Material. *Adv. Mater.* 24 (2012) 5065.

72. J. L. Mi, N. Lock, T. Sun, M. Christensen, M. Søndergaard, P. Hald, H. H. Hng, J. Ma, B. B. Iversen, Biomolecule-Assisted Hydrothermal Synthesis and Self-Assembly of Bi_2Te_3 Nanostring-Cluster Hierarchical Structure, *ACS Nano*, 4 (2010) 2523.

73. M. Cutler, J. F. Leavy, R. L. Fitzpatrick, Electronic Transport in Semimetallic Cerium Sulfide, *Phys. Rev.* 133 (1964) A1143.

74. M. Gharsallah, F. Serrano-Sánchez, J. Bermúdez, N. M. Nemes, J. L. Martínez, F. Elhalouani, J. A. Alonso, Nanostructured Bi_2Te_3 Prepared by a Straightforward Arc-Melting Method. *Nanoscale Res. Lett.* 11 (2016) 142.

75. Y. Lan, B. Poudel, Y. Ma, D. Wang, M. S. Dresselhaus, G. Chen, Z. Ren, Structure Study of Bulk Nanograined Thermoelectric Bismuth Antimony Telluride. *Nano Lett.* 9 (2009) 1419.

76. C. Yu, X. Zhang, M. Leng, A. Shaga, D. Liu, F. Chen, C. Wang, Preparation and Thermoelectric Properties of Inhomogeneous Bismuth Telluride Alloyed Nanorods. *J. Alloys Compd.* 570 (2013) 86.

77. M. Hong, Z.-G. Chen, L. Yang, J. Zou, Enhancing thermoelectric performance of Bi_2Te_3-based nanostructures through rational structure design, *Nanoscale*, 8 (2016) 8681.

78. G. Han, Z.-G. Chen, L. Yang, M. Hong, J. Drennan, J. Zou, Rational design of Bi_2Te_3 polycrystalline whiskers for thermoelectric applications, *ACS Appl. Mater. Interfaces*, 7 (2015) 989.

79. M. N. Touzelhaev, P. Zhou, R. Venkatasubramanian, K. B.Goodson, Thermal characterization of Bi$_2$Te$_3$/Sb$_2$Te$_3$ superlattices, *J Appl Phys*, 90 (2001) 763.
80. Y. Kim, A. DiVenere, G. K. L. Wong, J. B. Kelterson, S. Cho S, J. R. Meyer, Structural and thermoelectric transport properties of Sb$_2$Te$_3$ thin films grown by molecular beam epitaxy, *J Appl Phys*, 91 (2002) 715.
81. D. D. Frari, S. Diliberto, N. Stein, J.M. Lecuire, Comparative study of the electrochemical preparation of Bi$_2$Te$_3$, Sb$_2$Te$_3$, and (Bi$_x$Sb$_{1-x}$)$_2$Te$_3$ films, *Thin Solid Films*, 483 (2005) 40.
82. S. Schulz, S. Heimann, J. Friedrich, M. Engenhorst, G. Schierning, W. Assenmacher, Synthesis of hexagonal Sb$_2$Te$_3$ nanoplates by thermal decomposition of the single-source precursor (Et$_2$Sb)$_2$Te. *Chem Mater.* 24 (2012) 2228.
83. P. Dharmaiah, H. S. Kim, C. H. Lee, S. J. Hong, Influence of powder size on thermoelectric properties of p-type 25%Bi$_2$Te$_3$-75%Sb$_2$Te$_3$ alloys fabricated using gas-atomization and spark plasma sintering. *J Alloys Compd.* 686 (2016) 1.
84. J. Horak, C. Drasar, R. Novotny, S. Karamazov, P Lostak, Non-stoichiometry of the crystal lattice of antimony telluride. *Phys Status Solidi A.* 149 (1995) 549.
85. R. Venkatasubramanian, E. Siivola, T. Colpitts, B. O. Quinn. Thin-film thermoelectric devices with high room-temperature figures of merit. *Nature.* 413 (2011) 597.
86. H. Q. Yang, L. Miao, C. Y. Liu, et al. A facile surfactant-assisted reflux method for the synthesis of single-crystalline Sb$_2$Te$_3$ nanostructures with enhanced thermoelectric performance. *ACS Appl Mater Interfaces.* 7 (2015) 14263.
87. J. Horak, Z. Stary, J. Klikorka, Relations between structure, bonding, and nature of point defects in layered crystals of tetradymite structure. *Phys. Status Solidi B.* 147 (1988) 501.
88. W. Z. Wang, B. Poudel, J. Yang, D. Z. Wang, Z. F. Ren, High-yield synthesis of single-crystalline antimony telluride hexagonal nanoplates using a solvothermal approach. *J. Am. Chem. Soc.* 127 (2005) 13792.
89. M. Zhou, Z. M. Gibbs, H. Wang, Y. M. Han, C. N. Xin, L.F.Li, G.J.Snyder, Optimization of thermoelectric efficiency in SnTe: the case for the light band. *Phys. Chem. Chem. Phys.,* 16 (2014) 20741.
90. J. He, J. T. Xu , G. Q. Liu, H. Z. Shao, X. J. Tan, Z. Liu, J. Xu, H. Jiang, J. Jiang Enhanced thermopower in rock-salt SnTe–CdTe from band convergence, *RSC Advances*, 6 (2016) 32189.
91. X. J. Tan, H. Z. Shao, J .He , G. Q. Liu, J. T. Xu, J. Jiang, H. C. Jiang, Band engineering and improved thermoelectric performance in M-doped SnTe (M = Mg, Mn, Cd, and Hg). *Phys. Chem. Chem. Phys.,* 18 (2016) 7141.
92. V. Vedeneev; S. Krivoruchko; E. Sabo, Tin Telluride Based Thermoelectrical Alloys. *Semiconductors*, 32 (1998) 241.
93. R. F. Brebrick and A. J. Strauss, Anomalous Thermoelectric Power as Evidence for Two-Valence Bands in SnTe, *Phys. Rev.*, 131 (1963) 104.
94. R. F. Brebrick, Deviations from stoichiometry and electrical properties in SnTe, *J. Phys. Chem. Solids*, 24 (1963) 27.
95. L. M. Rogers, Br. Valence band structure of SnTe, *J. Appl. Phys.*, 1 (1968) 845.
96. B. A. Efimova, V. I. Kaidanov, B. Y. Moizhes, I. A. Chernik, Band model of SnTe, *Sov. Phys. Solid State*, 1966, 7, 2032.

97. W. Li, Y. Wu, S. Lin, Z.Chen, J. Li, X. Zhang, L. Zheng, Y. Pei, Advances in Environment-Friendly SnTe Thermoelectrics, *ACS Energy Lett. ,* 2(10) (2017) 2349.

98. A. Banik, U. S. Shenoy, S. Anand, U. V. Waghmare, and K. Biswas, Mg Alloying in SnTe Facilitates Valence Band Convergence and Optimizes Thermoelectric Properties, *Chem. Mater.*, 27 (2) (2015) 581.

99. A. Banik and K. Biswas, Lead-free thermoelectrics: promising thermoelectric performance in p-type $SnTe_{1-x}Se_x$ system, *J. Mater. Chem. A*, 2 (2014) 9620.

100. M. K. Han, J. Androulakis, S. J. Kim and M. G. Kanatzidis, Lead-Free Thermoelectrics: High Figure of Merit in p-type $AgSn_mSbTe_{m+2}$, *Adv. Energy Mater.*, 2012, 2, 157.

101. Y. Chen, M. D. Nielsen, Y.-B. Gao, T. J. Zhu, X. Zhao, J. P. Heremans, SnTe–$AgSbTe_2$ Thermoelectric Alloys, *Adv. Energy Mater.,* 2 (2012) 58.

102. L. D. Zhao, H. J. Wu, S. Q. Hao, C. I. Wu, X. Y. Zhou, K. Biswas, J. Q. He, T. P. Hogan, C. Uher, C. Wolverton, V. P. Dravid, M. G. Kanatzidis, All-scale hierarchical thermoelectrics: MgTe in PbTe facilitates valence band convergence and suppresses bipolar thermal transport for high performance, *Energy Environ. Sci.*, 6 (2013) 3346.

103. H. Wang, Z. M. Gibbs, Y. Takagiwa, G. J. Snyder, Tuning bands of PbSe for better thermoelectric efficiency, *Energy Environ. Sci.*, 7 (2014) 804.

104. B. Gao, J. Tang, F. Meng, W. Li, Band manipulation for high thermoelectric performance in SnTe through heavy CdSe alloying, *Journal of Materiomics,* 5 (1) (2019) 111.

105. Q. Zhang, B. Liao, Y. Lan, K. Lukas, W. Liu, K. Esfarjani, C. Opeil, D. Broido, G. Chen and Z. Ren, High thermoelectric performance by resonant dopant indium in nanostructured SnTe, *Proc. Natl. Acad. Sci. U. S. A.*, 110 (2013) 13261.

106. G. Tan, L.D. Zhao, F. Shi, J.W. Doak, S.-H. Lo, H. Sun, C. Wolverton, V. P. Dravid, C. Uher, M. G. Kanatzidis, High thermoelectric performance of p-type SnTe via a synergistic band engineering and nanostructuring approach, *J. Am. Chem. Soc.* 136 (2014) 7006.

107. G. Tan, F. Shi, J.W. Doak, H. Sun, L.D. Zhao, P. Wang, C. Uher, C. Wolverton, V.P. Dravid, M. G. Kanatzidis, Extraordinary role of Hg in enhancing the thermoelectric performance of p-type SnTe, Energy *Environ. Sci.*, 8 (2015) 267.

108. Y. D. Yin, Y. Lu, Y. G. Sun, and Y. N. Xia, Silver nanowires can be directly coated with amorphous silica to generate well controlled coaxial nanocables of silver/silica, *Nano Letters*, 2 (2002) 427.

109. X. Peng, L. Manna, W. Yang et al., Shape control of CdSe nanocrystals, *Nature*, 404 (6773) (2000) 59.

110. L. Manna, E. C. Scher, and A. P. Alivisatos, Synthesis of soluble and processable rod-, arrow-, teardrop-, and tetrapod-shaped CdSe nanocrystals, *J. American Chem. Society*, 122 (51) (2000) 12700.

111. A. E. Martell, R.J. Motekaitis, A.R. Fried, J. S. Wilson, D.T. Macmillian, Thermal decomposition of EDTA, NTA and Nitrilotrimethylenephosphonic acid in aqueous solution, *Can. J. Chem.*, 53 (1975) 3471.

112. Y. Deng, C.-W. Nan, L. Guo, A novel approach to Bi_2Te_3 nanorods by controlling oriented attachment, *Chem. Phys. Lett.,* 383 (2004) 572.

113. S. Gupta, S. Neeleshwar, V. Kumar, Y.Y. Chen, Synthesis of bismuth telluride nanostructures by refluxing method, *Adv. Mat. Lett.* 3(1) (2012) 50.

114. H. Q. Yang, L. Miao, C. Y. Liu, C. Li, S. Honda, Y. Iwamoto, R. Huang, and S. Tanemura, A Facile Surfactant-Assisted Reflux Method for the Synthesis of. Single-Crystalline Sb_2Te_3 Nanostructures with Enhanced Thermoelectric Performance, *ACS Appl. Mat. Interfaces*, *7* (26) (2015) 14263.

115. P. Dharmaiah, S.-J. Hong, Hydrothermal method for the synthesis of Sb_2Te_3 and $Bi_{0.5}Sb_{1.5}Te_3$ nanoplates and their thermoelectric properties, *Int. J. Appl. Ceram. Technol.*, 15 (1) (2017) 132.

116. U. Nithiyanantham, R.E. Sivasankara, M. Fevzi Ozaydin, H Liang. A. Rathishkumar, S. Kundu , Low temperature, shape-selective formation of Sb_2Te_3 nanomaterials and their thermoelectric applications, *RSC Adv.*, 5 (2015) 89621.

117. H. Kodama, S. Horiuchi, S and A. Watanabe, The hydrothermal synthesis of bismuth oxide chlorides, *J. solid state chem.*, 75 (1988) 279.

118. G. Han, R. Zhang, S. R. Popuri, H. F. Greer, M. J. Reece, J.-W. G. Bos, W. Zhou, A. R. Knox and D.H. Gregory, Large-Scale Surfactant-Free Synthesis of p-Type SnTe Nanoparticles for Thermoelectric Applications, *Materials*, 10 (2017) 233.

119. H. Brahmi, R. Neupane, L. Xie, S. Singh, M. Yarali, G. Katwal, S. Chen, M. Paulose, O. K. Varghese and A. Mavrokefalos, Observation of a low temperature n–p transition in individual titania nanotubes, *Nanoscale*, 10 (2018) 3863.

Chapter 4

Observation of Optical Band Gap Narrowing and Enhanced Magnetic Moment in Transition Metal Elements-Doped TiO$_2$ Nanocrystals derived by sol-gel route

This chapter illustrates the development of wide band gap semiconductors using sol-gel synthesis where undoped and transition metal elements doped anatase-TiO$_2$ nanocrystals have been synthesized with tailored band-gaps and enhanced magnetization. Here, in-depth understanding regarding the contribution of non-magnetic (Cu and Zn), magnetic (Fe, Co and Ni) and antiferromagnetic (Cr and Mn) transition metal ions in TiO$_2$ on the structural, morphological, optical and magnetic properties have been presented. The role of oxygen vacancy defects in the formation of bound magnetic polarons to induce a weak ferromagnetic behavior in oxide dilute magnetic semiconductors have been discussed in detail.

4.1. Introduction

The structural and optical properties of TiO_2 nanocrystals doped with different TM elements like Fe, Co, Ni, Cr, Mn, Cu, Zn, etc. and their influence on the magnetic properties and interaction of these doped ions with defects such as oxygen vacancies present in the TiO_2 lattice have been reported in this chapter.[1,2,3-7] Recently, few reports have suggested that successful incorporation of metal ions into the host lattice can induce a red shift in the band gap of TiO_2 material and create oxygen vacancies which contribute towards FM.[8] Very few studies have reported about the origin of magnetic behavior of TM-doped TiO_2 and the formation of both TM ion site vacancies and oxygen site vacancies. Thus, we have investigated in detail the structural, morphological, optical and magnetic properties of the following TM ion-doped TiO_2 nanocrystals synthesized by a simple and cost effective sol-gel technique.

(i) Non-magnetic elements, i.e. 3 atomic weight % doped Cu and Zn

(ii) Ferromagnetic elements i.e. 3, 6, 9 and 12 atomic weight % doped Fe, Co and Ni

(iii)Antiferromagnetic elements i.e. 3, 6, 9 and 12 atomic weight % doped Cr and Mn

4.2. Experimental section

Undoped and TM-doped (TM= Cu, Zn, Fe, Co, Ni, Cr and Mn) TiO_2 nanocrystals were synthesized by a simple sol-gel technique where titanium butoxide and corresponding metal nitrates were used as the Ti and metal ion precursors respectively. The synthesis approach enables the formation of stable anatase phase for all the studied samples and hence after named as shown in Table 4.1. The resultant sol-gel materials were calcined at 400°C for 3.5 h in a muffle furnace under ambient air atmosphere. Their structure and phase purity were studied by XRD at room temperature using PANalytical X'Pert Pro diffractometer with Cu-Kα radiation. The crystal structure of anatase TiO_2 was generated using Vesta software. Micro-Raman spectroscopy was performed using Horiba Jobin Yvon LabRAM HR 800 micro-Raman spectrometer using 1800 grooves mm^{-1} grating, with the spectral resolution of 2 cm^{-1} and an excitation wavelength of 405 nm. The particle size and morphology were studied using HR-TEM (FEI Tecnai F20, operated at 300 kV). Again, to confirm the elemental composition, an energy dispersive X-ray Fluorescence Spectrometry (ED-XRFS) study

was carried out using PANalytical Epsilon 3 and the obtained chemical compositions are tabulated in Table 4.2. The composition was further confirmed by Inductive Coupled Plasma-Mass Spectroscopy (ICP-MS, Thermofischer Scientific, Model iCAP-RQ-ICPMS) for the selected samples and are tabulated in Table 4.3. Functional group identification of the prepared nanocrystals was investigated by Fourier Transform-Infrared (FT-IR) spectra using a Bruker FT-IR spectrometer. The UV-Visible spectra of the samples were recorded by a Shimadzu UV 2401 PC spectrophotometer and the emission spectra were obtained from a spectrofluorometer (Cary Eclipse, Varian). The XPS study was carried out on powder samples at room temperature using a PHY 5000 Versa Probe II, ULVAC-PHI, Inc instrument. The binding energies were corrected by taking C 1s as reference energy (C 1s = 284.60 eV). Curve fitting to the XPS spectrum was done using MultiPak Spectrum: ESCA. Background subtraction was done using the Shirley method. Magnetic studies were performed at room temperature using vibrating sample magnetometer (VSM) attached to the physical property measurement system, Quantum Design Inc., (USA).

Table 4.1. Compositions and names of synthesized compounds

Chemical compositions	Sample Name
Un-doped TiO_2	T-P
3% Cu-doped TiO_2	T-Cu
3% Zn-doped TiO_2	T-Zn
3%, 6%,9% and 12% Fe-doped TiO_2	T3Fe, T6Fe, T9Fe and T12Fe
3%, 6%,9% and 12% Co-doped TiO_2	T3Co, T6Co, T9Co and T12Co
3%, 6%,9% and 12% Ni-doped TiO_2	T3Ni, T6Ni, T9Ni and T12Ni
3%, 6%,9% and 12% Cr-doped TiO_2	T3Cr, T6Cr, T9Cr and T12Cr
3%, 6%,9% and 12% Mn-doped TiO_2	T3Mn, T6Mn, T9Mn and T12Mn

Table 4.2. ED-XRFS data of TM-doped TiO_2 nanocrystals

Compound	Percentage of elemental oxides
T-P	99.97 % TiO_2
T-Cu	97.10 % TiO_2 + 2.90 % CuO
T-Zn	97.03 % TiO_2 + 2.97 % ZnO
T3Fe	96.91% TiO_2 + 3.09% Fe_2O_3
T6Fe	93.93% TiO_2 + 6.07% Fe_2O_3
T9Fe	90.90% TiO_2 + 9.10% Fe_2O_3
T12Fe	87.82% TiO_2 + 12.18% Fe_2O_3
T3Co	96.94% TiO_2 + 3.06% Co_3O_4
T6Co	93.92% TiO_2 + 6.08% Co_3O_4
T9Co	90.89% TiO_2 + 9.11% Co_3O_4
T12Co	87.88% TiO_2 + 12.12% Co_3O_4
T3Ni	97.05% TiO_2 + 2.95% NiO
T6Ni	93.85% TiO_2 + 6.15% NiO
T9Ni	90.83% TiO_2 + 9.17% NiO
T12Ni	88.02% TiO_2 + 11.98% NiO
T3Cr	97.20% TiO_2 + 2.80% Cr_2O_3
T6Cr	94.31% TiO_2 + 5.69% Cr_2O_3
T9Cr	91.43% TiO_2 + 8.57% Cr_2O_3
T12Cr	88.22% TiO_2 + 11.78% Cr_2O_3
T3Mn	97.15% TiO_2 + 2.85% MnO
T6Mn	94.31% TiO_2 + 5.69% MnO
T9Mn	91.28% TiO_2 + 8.72% MnO
T12Mn	88.47% TiO_2 + 11.53% MnO

Table 4.3. ICP-MS analysis of selected TM-doped TiO_2 nanocrystals

Compounds	Molar ratio of TM ions/Ti	Actual composition
T-P	0	TiO_2
T3Cu	0.032	$Ti_{0.97}Cu_{0.03}O_2$
T3Zn	0.034	$Ti_{0.97}Zn_{0.03}O_2$
T3Fe	0.027	$Ti_{0.974}Fe_{0.026}O_2$
T12Fe	0.118	$Ti_{0.896}Fe_{0.104}O_2$

4.3. Results and Discussion

4.3.1. Undoped, Cu and Zn- doped TiO₂ nanocrystals

The present investigation studies in detail the structural, morphological, optical and magnetic behavior of nonmagnetic element (Cu and Zn) doped TiO_2, synthesized via a simple sol-gel technique.

4.3.1.1. Structural Analysis

Fig. 4.1(a, b) shows the indexed XRD patterns along with peak shift associated with each sample. All the samples were found to crystallize in the tetragonal anatase phase of TiO_2 and match well with the JCPDS card No: 89-4921.[9,10] No diffraction peaks related to Cu and Zn can be seen in the XRD pattern of T-Cu and T-Zn. The shifting of highest intense (101) peak as well as change in full width at half maximum (FWHM) in T-Cu and T-Zn of XRD patterns indicate the incorporation of Cu and Zn in the host lattice. Fig.4.2 (a, b and c) shows the Rietveld refinement patterns of the T-P, T-Cu and T-Zn nanocrystals. The crystallite size calculated from XRD analysis for T-P, T-Cu and T-Zn are 12.10 nm, 13.31 nm and 11.27 nm respectively. Rietveld refinement was carried out by varying 16 parameters such as background parameters, unit cell, shape and isotropic thermal parameters, and oxygen occupancy using the Fullprof-98 program. The refined parameters of T-P, T-Cu and T-Zn are depicted in Table 4.4. The Rietveld refinement indicates the incorporation of Cu and Zn ions in the TiO_2 matrix. As a representative of the series, the anatase crystal structure of TiO_2 derived using Vesta software is depicted in Fig.4.2 (d).
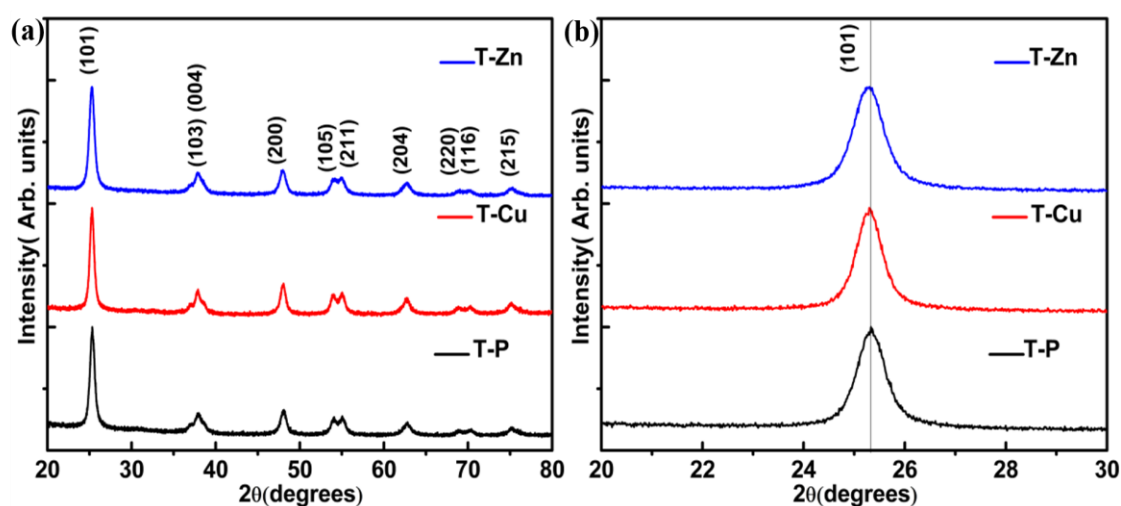
Fig.4.1. (a) Indexed XRD patterns of anatase T-P, T-Cu and T-Zn (b) peak shift associated with T-P, T-Cu and T-Zn

Raman spectroscopy has been used to find out the crystallinity, phase, presence of defects, strain and disorder induced in the crystal due to dopant incorporation in the host lattice. To confirm the phase and crystallinity of T-P, T-Cu and T-Zn nanocrystals,

Raman spectra were taken and are shown in Fig. 4.3. Raman spectrum of T-P nanocrystals exhibit peaks which are located at around 144, 196, 398, 520 and 640 cm^{-1}. These peaks correspond to the lattice vibration mode of the E_g (1), E_g (2), B_{1g} (1), $A_{1g}+B_{1g}$ (2), and E_g (3) mode of anatase TiO$_2$ respectively [11-13]. The E_g mode appears
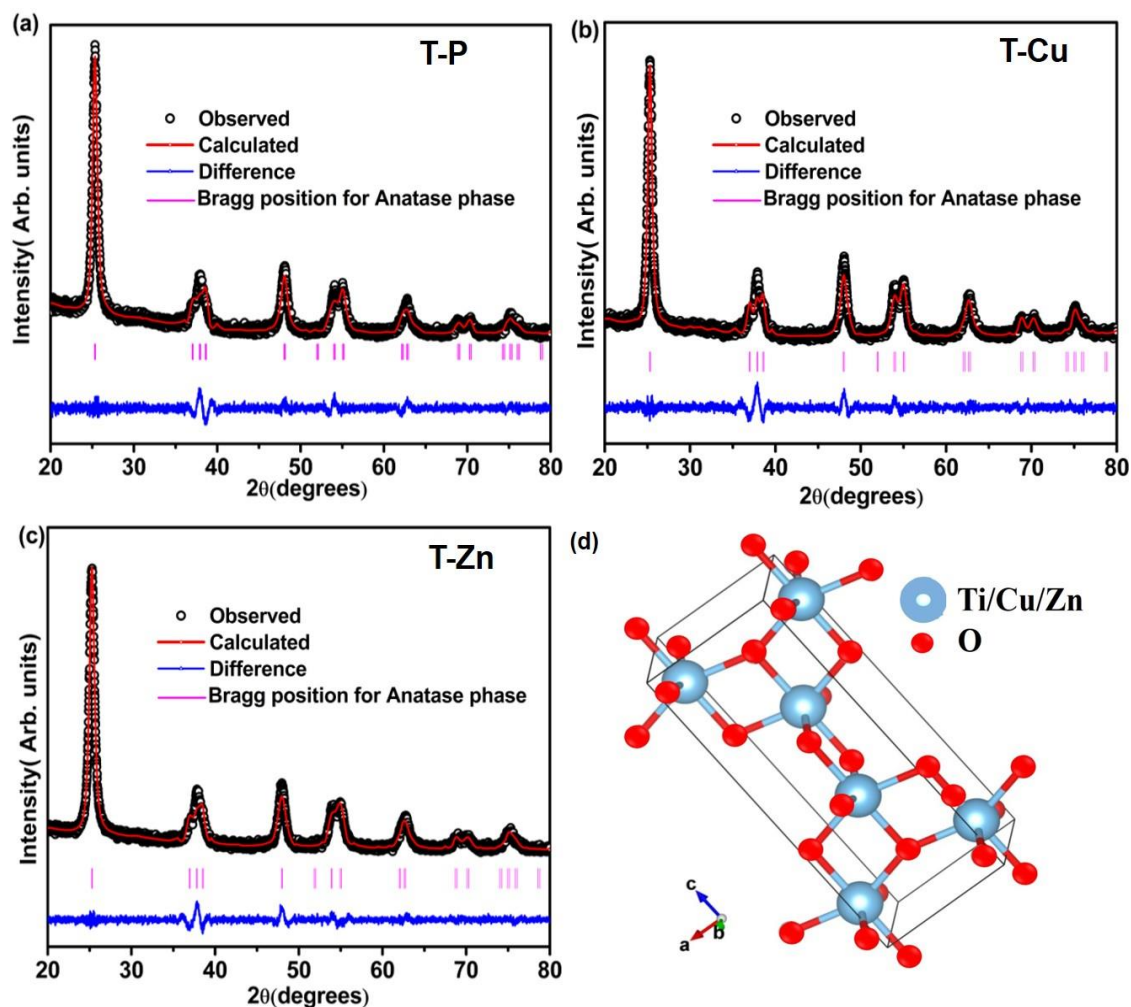
Fig.4.2. Rietveld refinement of XRD patterns of (a) T-P, (b) T-Cu, (c) T-Zn nanocrystals and (d) Crystal structure of anatase TiO$_2$

due to O-Ti-O symmetric stretching vibration. B_{1g} mode is associated with O-Ti-O symmetric bending vibration and the A_{1g} mode is related to O-Ti-O anti-symmetric bending vibrations.[14] Raman spectra of T-Cu and T-Zn show typical spectra of anatase TiO$_2$. Furthermore, there is no Cu or Zn related Raman peaks in doped TiO$_2$ samples. The absence of the characteristic Cu and Zn vibration modes in the Raman spectra reveals that there is no segregation of Cu or Zn in TiO$_2$ nanocrystals. These results

clearly suggest the solid solution formation in T-P, T-Cu and T-Zn samples, which is consistent with the XRD analysis. The absence of any other mode related to Cu, Zn, CuO, ZnO, Cu-Ti or Zn-Ti species within the detection limit of Raman spectra of doped samples indicates that the doped elements might have gone to the substitutional site

Table 4.4. XRD Refinement parameters obtained for T-P, T-Cu and T-Zn

Compound	T-P	T-Cu	T-Zn
Phase	Anatase		
Crystal Structure	Tetragonal		
Space Group	I 4$_1$/a m d		
Lattice Parameters			
a(Å)	3.7901 (1)	3.7932 (4)	3.7940 (5)
c(Å)	9.4923 (3)	9.5016 (3)	9.5162 (1)
Volume (Å)^3	136.35 (2)	136.71 (1)	136.98 (3)
Atomic positions			
Ti/Cu/Zn $_x$ (4a)	0.0000	0.0000	0.0000
Ti/ Cu/Zn $_y$ (4a)	0.7500	0.7500	0.7500
Ti/ Cu/Zn $_z$ (4a)	0.1250	0.1250	0.1250
O $_x$ (8e)	0.0000	0.0000	0.0000
O $_y$ (8e)	0.2500	0.2500	0.2500
O $_z$ (8e)	0.0848	0.0855	0.0833
B $_{iso}$ (Ti/ Cu/Zn) (Å)^2	0.0005	0.0008	0.0006
B $_{iso}$ (O) (Å)^2	0.0045	0.0013	0.0017
Residual Parameters			
R$_p$	4.56	3.98	3.38
R$_{wp}$	5.77	5.33	4.55
χ^2	1.89	1.94	1.83
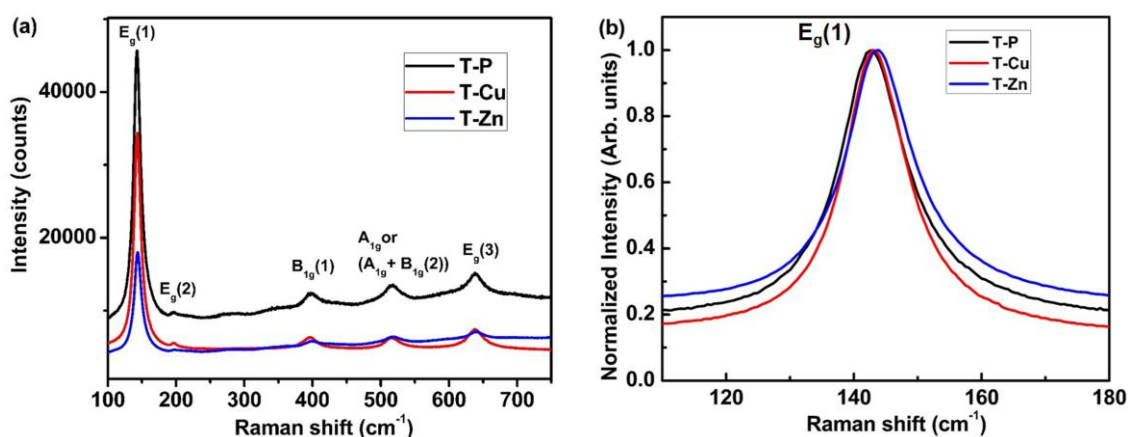
Fig.4.3. Raman spectra of (a) T-P, T-Cu and T-Zn samples (b) Raman peak shift of E$_g$ (1) mode associated with T-P, T-Cu and T-Zn samples

replacing Ti in TiO_2. The ionic size of Cu^{2+} (0.73 Å) is larger than that of Ti^{4+} (0.61 Å) and hence substitution of Cu on Ti site will distort the lattice structure. Also due to the charge difference between Ti^{4+} and Cu^{2+}, substitution of Cu will generate oxygen vacancies in the lattice to maintain charge neutrality. It is very clear that the phonon confinement and non-stoichiometry due to defects associated with the system could induce disorders in the lattice leading to the shifting and broadening of Raman lines [13]. Hence, it is believed that defects like oxygen vacancy in the material strongly affect the Raman modes. In our study, the most intense E_g (1) Raman mode at 144 cm^{-1} show blue shifting and slight broadening with doping (Fig. 4.3 (b)). So, both the phonon confinement and disorder in the host lattice induced due to the incorporation of Cu, Zn atoms/ions creating defects like oxygen vacancies in TiO_2 have caused the shifting and broadening of the Raman peaks [15–17].

4.3.1.2. Morphological Analysis

Detailed TEM micrographs showing the morphology of the samples are given in Fig.4.4. Interestingly, formation of nanocrystals with average particle size of about 12 nm in T-P which further agrees well with the crystallite size estimated from the XRD results. It is reported that sol-gel route facilitates the formation of nanostructures [18, 19]. Cu substitution into the Ti site could result in lattice expansion due to larger ionic size of Cu and hence an increase in particle size is also expected as mentioned in the crystallite size calculation from XRD analysis. TEM results of T-Cu indicate the formation of nanocrystals having higher particle size (13 nm) than T-P sample (12 nm). Interestingly, T-Zn sample shows a decrease in particle size (11 nm) which also agrees well with the crystallite size calculated from XRD results. Previous reports suggest the reduction in particle size of TiO_2 upon Zn doping [20]. The T-P sample shows an average particle size of 12 nm and T-Zn samples show an average size of 11 nm suggesting that Zn doping has significantly decreased the size distribution of nanocrystals. Fig.4.4 (d-f) demonstrates the high resolution HR-TEM images of T-P, T-Cu and T-Zn samples respectively. The HR-TEM images show clear lattice fringes without any distortion in TiO_2 and (Cu, Zn)-doped nanocrystals indicating the high crystallinity of the nanocrystals. The estimated interplanar spacing of adjacent lattice

fringes of T-P corresponds to the (101) and (004) planes of anatase TiO$_2$ which are shown in Fig. 4.4(d). Similarly, (101), (004) and (200) planes of T-Cu is represented in Fig. 4.4(e) and HR-TEM image and FFT suggests the crystalline nature and quality of the prepared samples. Further Fig.4.4 (f) demonstrates the (101) and (004) planes of T-Zn sample and the interplanar spacing obtained in each case are in accordance with the XRD patterns (Fig.4.1). Fig.4.4 (g-i) represents the SAED patterns of the T-P, T-Cu and T-Zn samples respectively which suggest the polycrystalline nature of all the samples and T-Cu shows an enhanced crystallinity among the three samples, which again corroborates with HR-TEM images and lattice fringes as discussed earlier.
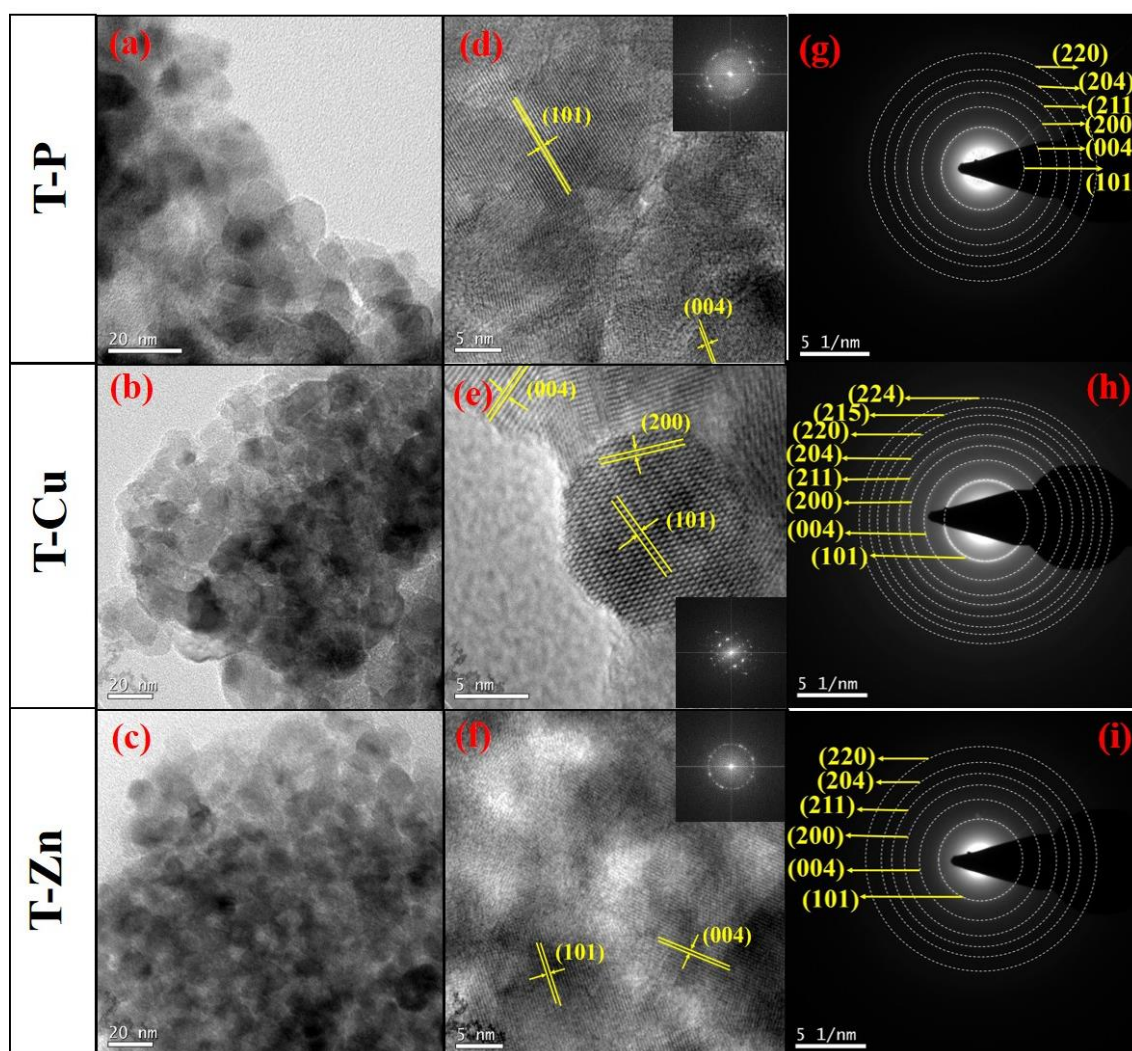
Fig. 4.4. (a-c) TEM images of T-P, T-Cu and T-Zn showing the formation of nanocrystals (d-f) HR- TEM images showing lattice fringes with FFT shown in the inset and (g-i) SAED patterns of samples.

4.3.1.3. FT-IR Analysis

FT-IR spectra of all the samples were taken at room temperature to identify the various functional groups and vibrational bands present in the samples which are shown in Fig. 4.5. Different bands observed in FT-IR spectra of T-P, T-Cu and T-Zn nanocrystals are summarized in Table 4.5. Among the different bands that appear in the spectra, the broad band around 3500 cm^{-1} corresponds to the stretching vibration of OH groups and could be due to the OH group associated with the Ti atoms, i.e., Ti–OH. The narrow band around 1650 cm^{-1} is well known for the characteristic bending vibrations of H–O–H. However, the peak close to 1400 cm^{-1} has been ascribed to C-O stretching bond present in the precursor material.

This peak might have arisen as a result of the organic radical from Ti- butoxide which is adsorbed in the nanocrystals. The presence of organic components in studied samples are clearly observed from TEM images shown in Fig.4.6, in which the amorphous regions have been shown which suggest the existence of organic residues along with crystalline TiO₂ nanocrystals. The FFT corresponding to different regions are also clearly demonstrated in Fig.4.6. The band centered at nearly 550 cm^{-1} are due to bonding among metal and oxygen, i.e., metal-oxygen bonds of (Ti-O) in undoped, (Ti-O, Cu-O) and (Ti-O, Zn-O) in Cu and Zn-doped TiO₂ nanocrystals[21,22]. Furthermore, no peak corresponding to any other oxide phases of doped elements appeared in the spectra. It reveals that doped metal ions are introduced into the Ti framework. This result corroborates with the results of XRD, and TEM as mentioned earlier.

Table 4.5. FT-IR spectra of different vibration bands of T-P, T-Cu and T-Zn

Vibration modes (cm^{-1})	T-P	T-Cu	T-Zn
O-Ti-O stretching	551	553	557
O-H-O bending	1630	1630	1630
O-H stretching	3455	3501	3504
C-O stretching	1384	1384	1384
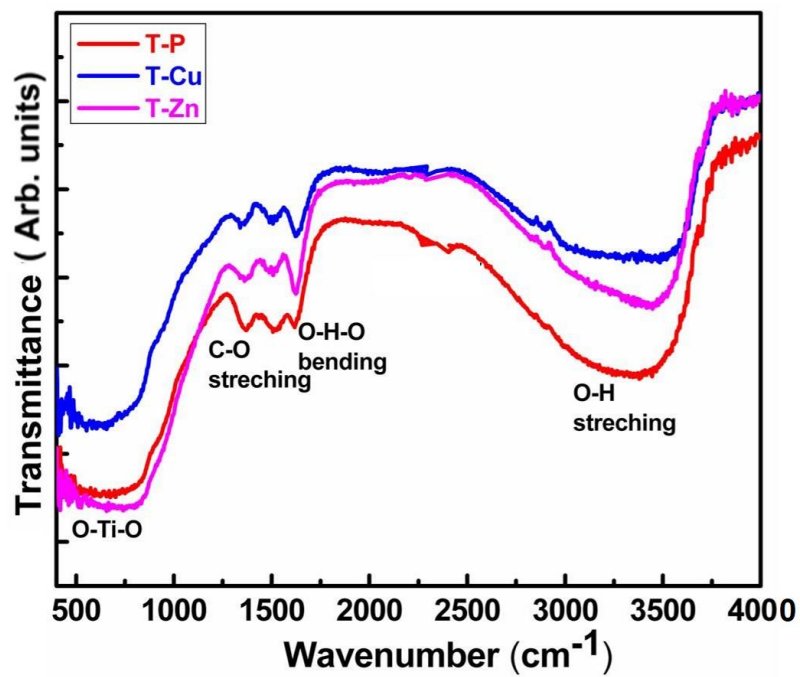
Fig.4.5. FT-IR spectra of T-P, T-Cu and T-Zn samples
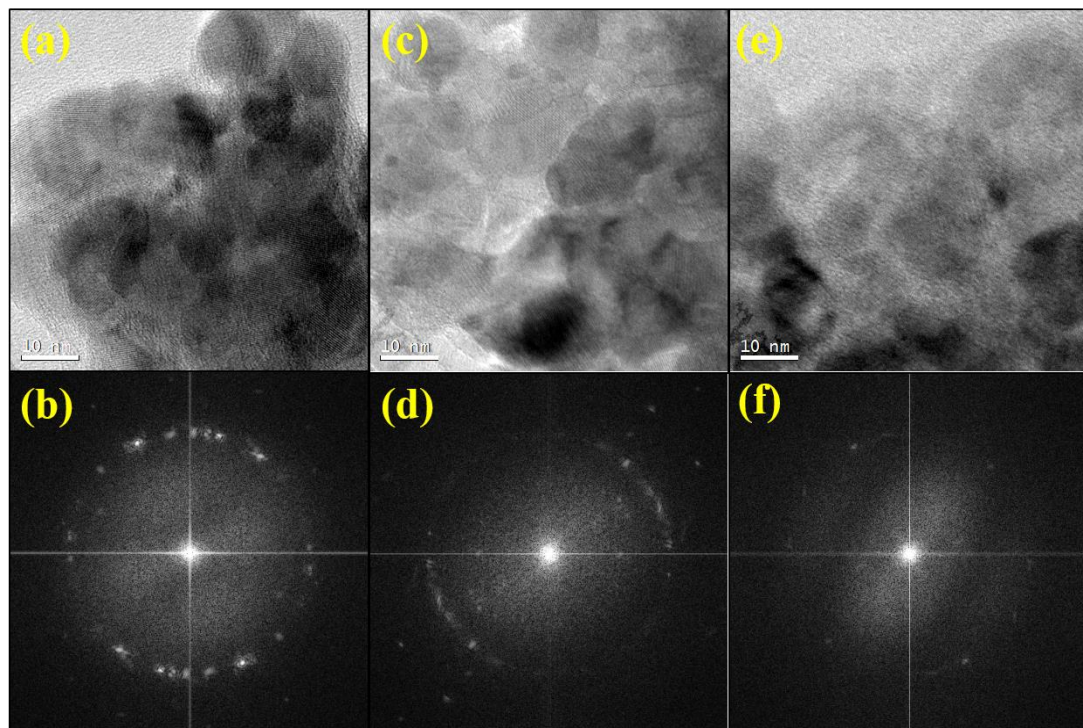
Fig.4.6. TEM images and corresponding FFT patterns of T-P (a,b) T-Cu (c,d) and T-Zn (e,f) showing the coexistence of both amorphous and crystalline regions

4.3.1.4. Optical Studies: UV-Visible and Photoluminescence Studies

UV-Visible absorption spectroscopy is an important tool to study the optical transitions and defect states due to the incorporation of dopants in the host lattice. The optical absorption of all the samples was obtained from the diffuse reflectance spectra using Kubelka–Munk equation, $F(R) = (1-R)^2/2R$ in the range 300-800 nm. Fig. 4.7 (a) shows the UV-Visible absorption spectra of all the samples. The absorption spectrum of TiO₂ sample generally exhibits sharp absorption around 385 nm which corresponds to the electronic transition from the valence band (O_{2p} state) to the conduction band (Ti_{3d} state).[23] The undoped sample shows strong absorption in UV region and high transparency in visible region. The Cu and Zn-doped TiO₂ nanocrystals show a regular shift of the absorption edge towards longer wavelengths due to incorporation of Cu and Zn in TiO₂. A slight shift in optical absorption edge is observed for T-Zn which is around 385 nm whereas a clear red shift is observed for T-Cu towards longer wavelength. It is clear from XRD and TEM analysis that particle size is decreased with Zn doping and previous reports suggests that the red shift of the absorption edge cannot be due to quantum confinement effect [24]. New energy bands are created within the band gap of TiO₂ due to these metal ion doping. The transition from valence band to intra-band energy levels or from these intermediate levels to the conduction band can cause the red shift of the absorption edge of TiO₂. This red shift can be taken as an evidence for the incorporation of doped metal ions into the TiO₂ lattice. The optical band gaps have been determined from the Tauc's relation, $\alpha h\upsilon = B(h\upsilon - E_g)^n$, where B is a constant and E_g is the optical band gap of the material, n is a number which characterizes the nature of electronic transition between valance band and conduction band and may have values 1/2, 2, 3/2 and 3 corresponding to the allowed direct, allowed indirect, forbidden direct, and forbidden indirect transitions, respectively[25]. Since anatase TiO₂ is an indirect band gap semiconductor, we have chosen n=2. A graph is plotted with $\alpha h\upsilon^{1/2}$ on the ordinate and $h\upsilon$ on the abscissa and then the band gap is determined by extrapolating the linear portion of the graph. The band gap observed for T-P, T-Cu and T-Zn are 3.16 eV, 2.38 eV and 3.05 eV respectively which is illustrated in Fig.4.7 (b). The decrease in band gap for T-Cu and T-Zn is due to the incorporation

of metal ions into host crystal lattice. The red shift in bandgap due to Cu and Zn doping can be due to sp-d exchange interactions between the band electrons and the localized d-electrons of Cu^{2+} and Zn^{2+} ions substituting Ti^{4+} ions. The s-d and p-d exchange interactions give rise to downward shifting of conduction band edge and upward shifting of valence band edge resulting in narrowing of bandgap. The interaction of these metal ions with the conduction band electrons could have shifted the valence band by lowering the conduction band which results in the reduction of band gap for the doped TiO_2 nanocrystals.
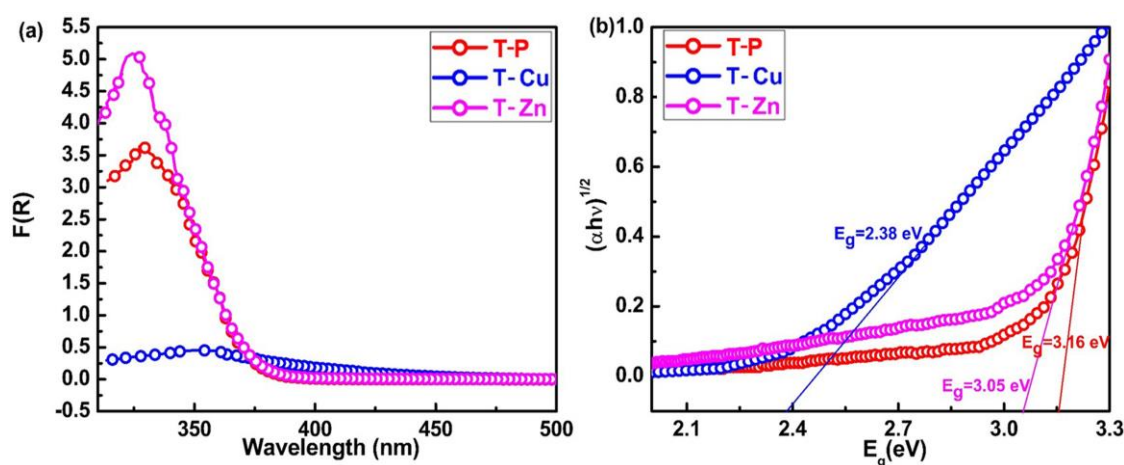
Fig.4.7. T-P, T-Cu and T-Zn samples: (a) UV-Visible spectra (b) Corresponding Tauc's plot

Photoluminescence (PL) spectra provides information regarding structural matters, defects in the crystal lattice and trap states of the material which decides the electronic structure of materials. Thus PL spectra recorded for all the samples are shown in Fig.4.8 (a). The deconvoluted PL spectra of T-P, T-Cu and T-Zn are represented in Fig.4.8 (b), (c), (d) respectively, from which strong emission peaks are observed in the range 370 nm – 600 nm. The emission peak observed around 390 nm is due to the near band edge emission of host TiO_2. The emission peaks located in between 400 - 450 nm have arisen as a result of self-trapped excitons (STE), oxygen vacancies, surface defects, etc. [26-29]. The STE arises when a trapped electron captures a hole in TiO_2, more clearly, the recombination occurs through oxygen vacancies present in the system. Since oxygen vacancies are intrinsic defects in TiO_2 and Cu/Zn doping also creates oxygen vacancies due to the substitution of Cu^+/ Cu^{2+}/ Zn^{2+} on Ti^{4+}, the emissions around 400 - 450 nm are probably due to STE [26-29].
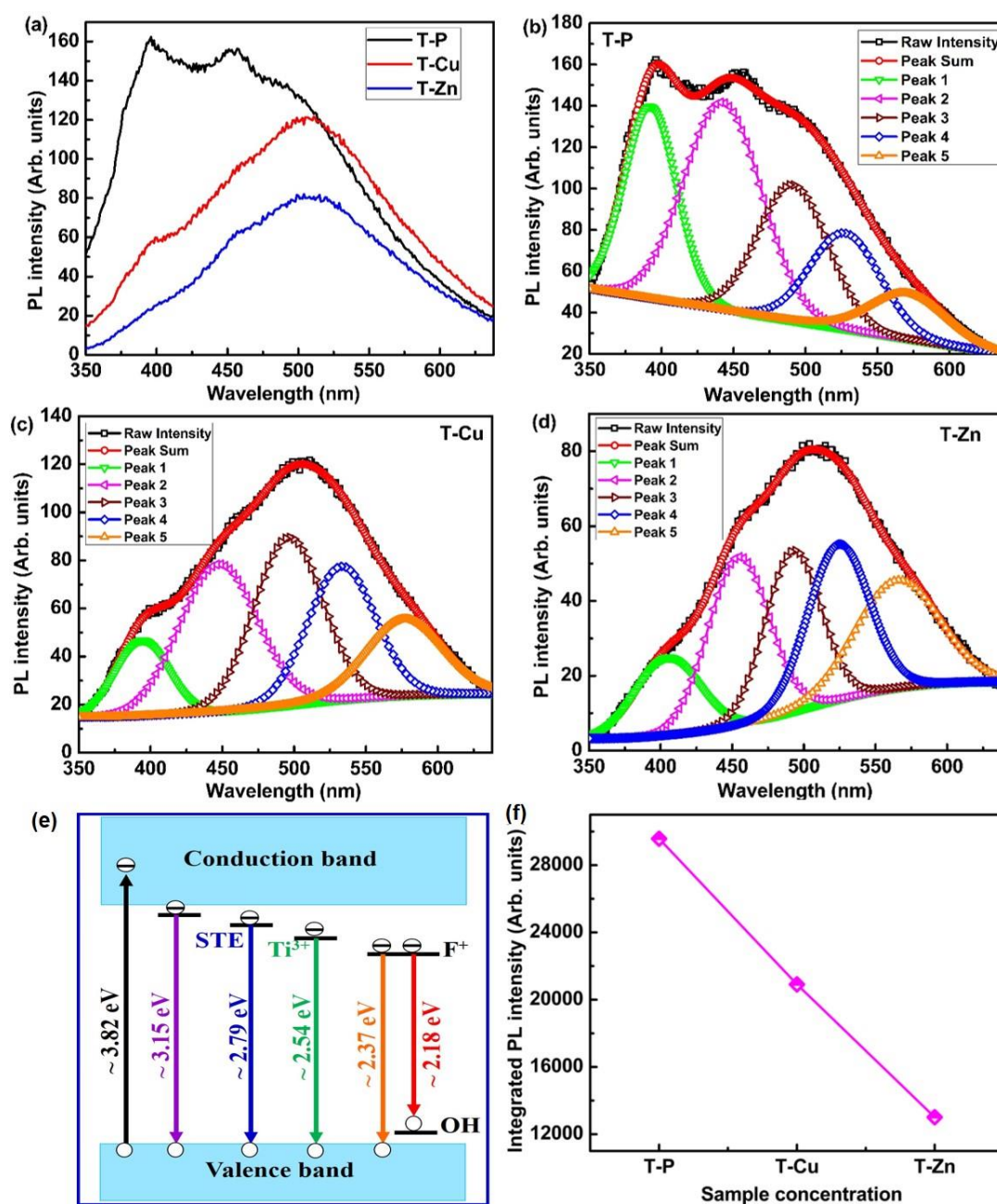
Fig.4.8. PL spectra of (a) T-P, T-Cu and T-Zn samples (b) deconvoluted PL spectra of T-P, (c) T-Cu, (d) T-Zn, (e) Schematic showing possible PL emissions and (f) Integrated PL intensity versus sample concentration.

The emission peak at 490 nm appears as a result of charge transition from Ti^{3+} to TiO_6^{2-} linked with oxygen vacancies [30] and the peak at nearly 520 nm may have appeared due to the F^+-center formation [31, 32]. The hydroxyl (OH) species as observed in the FT-IR spectra as well as confirmed from XPS analysis (which are discussed in the coming sections), can create an acceptor level just above the valence band and contributes for

the observed emission near 600 nm. It is expected that the presence of oxygen deficiency in small amounts cannot be ruled out in the air annealing process and hence the multiple oxidation states of Ti is expected in the system which is discussed in detail in the later sections.

4.3.1.5. Magnetic Studies

The M-H measurements of undoped, Cu-doped and Zn-doped TiO_2 were performed by varying the magnetic field from -90 kOe to +90 kOe at room temperature. and the plots are shown in Fig. 4.9 (a). A PM behavior is observed for T-P and T-Cu whereas a diamagnetic tail is noticed for T-Zn. However, it is interesting to note that the M–H loops show weak FM in T-P and T-Cu sample (Fig. 4.9 (b) and 4.9 (c)) at lower fields. There is a slight increase in the magnetic moment in T-Cu sample. The inset in Fig. 4.9 (b) shows the M-H plot (zoomed) at lower field of T-P sample at 300 K which gives H_c of 305 Oe. There is similar observation for T-Cu sample as shown in inset of Fig.4.9 (c) from which H_C of 120 Oe is noticed. It can be interpreted that different oxidation states of both Ti and Cu might have induced weak FM in the case of T-Cu sample. Hence, the electronic contribution from Cu^+ and Cu^{2+} could have played crucial role in determining the magnetism of the T-Cu material. The contribution from either Ti^{3+}/Cu^{2+} cannot be disregarded in T-P and T-Cu samples, due to which weak FM might have observed at lower fields. RTFM is generally observed when magnetic impurities are introduced into the host lattice due to the FM behavior of the magnetic impurities. Interestingly, very few reports have suggested the observation of PM and FM behavior due to the presence of non-magnetic impurities which could be mainly due to the charge carriers trapped by oxygen vacancies [33-41]. Some reports [42] have demonstrated the suppression of FM in TiO_2 even in the presence of magnetic impurities resulting in PM or AFM behavior due to the presence of secondary phases associated with the reported samples. In the present study, XRD and Raman analysis eliminate the presence of any other secondary phases like Cu or Cu related oxides in the case of T-Cu sample. It is interesting to note that undoped TiO_2 exhibit weak RTFM which may have arisen due to intrinsic defects such as Ti site vacancies, oxygen vacancies, Ti^{3+} ions or Ti interstitials.

This observation on the RTFM in TiO$_2$ based system reveals that magnetic properties may not be completely depending on the magnetic ions, but may be mediated effectively by the point defects such as oxygen vacancies or host lattice vacancies. Thus, point defects mediated FM is termed as 'd0 ferromagnetism' which is commonly noticed in nanostructures having high surface area to volume ratio and exhibiting notable surface defects [43, 44]. Hence, the size and morphology of nanostructures can strongly determine the observed FM, which is so crucial in studying the defect-related FM. The occurrence of intrinsic magnetic moment in TiO$_2$ nanoparticles can be explained by the magnetic interactions caused by the isolated magnetic moments arising as a result of partially filled electron shells due to imperfections at the surface and inter surface ultimately leading to the surface magnetic moments in nonmagnetic TiO$_2$ material. Hence, it can be assumed that surface defect states of TiO$_2$ nanoparticles could be responsible for the intrinsic origin of the macroscopic d0 FM in TiO$_2$ nanostructures.
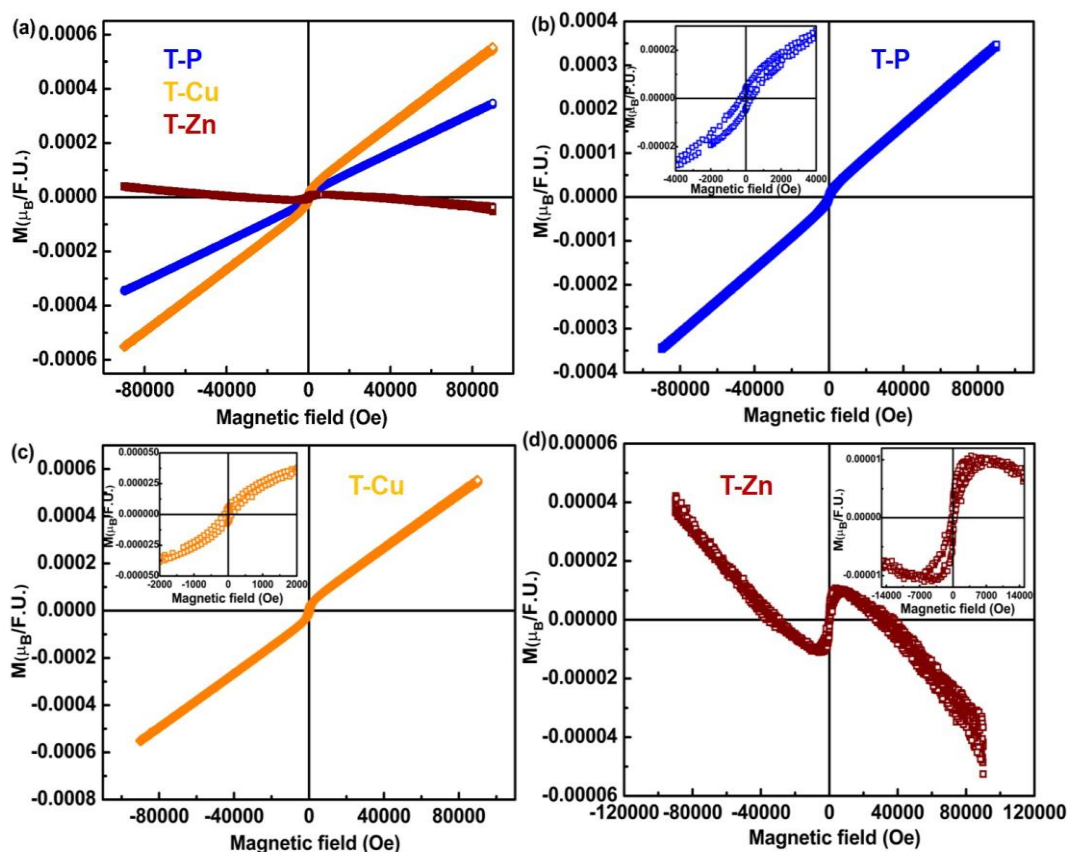
Fig.4.9. M-H curves measured at 300K (a) T-P, T-Cu and T-Zn nanocrystals, (b) T-P,(c) T-Cu and (d) T-Zn, Insets in (b), (c), (d) show the M-H plots (zoomed) at lower field.

The presence of FM in both T-P and T-Cu and an increase in magnetic moment in T-Cu indicate that magnetism can be enhanced due to Cu-doping which may have created more vacancies/Ti^{3+} ions which is well in accordance with the PL results. But in the case of Zn-doped samples although magnetization is observed at lower fields as shown in Fig. 4.9 (c), but an absence of clear PM/FM behavior indicates that long range FM ordering has been lost in the sample, which can be due to the interaction of oxygen vacancies/Zn^{2+} ions with Zn ions inhibiting FM/PM. Although, the T-Zn sample exhibits a diamagnetic behavior at higher magnetic fields, a positive response to the magnetic field well below 1 Tesla is observed (as shown in the inset of Fig.4.9 (d)). The observation of weak FM at lower magnetic fields might be due to the presence of oxygen vacancy defects and oxygen interstitial defects. In DMS materials, especially in nanostructured DMS materials, the existence of weak FM at lower fields and absence of which at higher fields is quite common. This is due to the defects associated with TiO_2 system, i.e., surface defects (such as oxygen vacancies, V_O) as well as interstitial defects. The V_O defects will be inherent in most of the nanomaterials (V_O defect's contribution towards magnetism is too small), at the same time, oxygen interstitials (O_i) also can contribute towards magnetism (O_i defect's contribution towards magnetism is significant compared to V_O). These defects could easily trap surface electrons and could provide magnetic moment. The FM order generated from O_i- and/or V_O-related defects, if possible, would be small with very small coercivity.[45]A very weak FM observed at lower fields could be attributed to the d0 mechanism as explained above. This could lead to the formation of BMPs similar to undoped and Cu-doped samples where small particle size could induce single domain in the system. Raman, UV-Visible analysis indicate the presence of defects like Ti/Cu/Zn site vacancies or oxygen vacancies in T-P, T-Cu, T-Zn samples. The presence of these deficiencies in both undoped and Cu, Zn-doped samples may have been obtained due to the synthesis conditions, surface defects especially arising when nanostructuring due to particle size reduction and these vacancy defects are responsible for variation in the magnetic behavior observed in undoped and doped samples of TiO_2. A perfect diamagnetism is absent in Zn-doped sample as shown in Fig.4.9 (d) and a diamagnetic tail is observed which is due to the effect of surface

defects and oxygen vacancy defects even though stable Zn^{2+} and Ti^{4+} exist in the T-Zn sample.

4.3.1.6. XPS Analysis

In order to have a detailed understanding of the relationship between magnetic properties and oxidation states of Ti, Cu, Zn and oxygen, XPS spectra have been recorded for all the samples and are shown in Fig. 4.10 – 4.12. Fig.4.10 (a) shows the wide scan spectra of undoped TiO_2. Elemental scan of Ti in undoped sample is shown in Fig.4.10 (b). The binding energies of Ti $2p_{3/2}$ and Ti $2p_{1/2}$ for the undoped sample are 458.09 eV and 463.76 eV, which are in consistent with that of Ti^{4+}. The small peaks at 457.31 eV and 461.10 eV confirm the presence of Ti^{3+} which indicates the existence of both Ti^{3+} and Ti^{4+} in the T-P sample [46]. Hence, the peaks corresponding to the binding energies of both Ti^{3+} and Ti^{4+} ions were observed [47], which suggests the delocalization of electrons between oxygen vacancies and Ti^{3+} ions on the surface. The O 1s spectrum of undoped sample is shown in Fig.4.10 (c) and the deconvoluted O 1s peak gives three peaks at 529.43 eV, 529.81 eV and 531.41 eV which are ascribed to lattice oxygen, hydroxyl groups and adsorbed water respectively. [48, 49] The XPS wide scan of T-Cu is represented in Fig.4.11 (a), which indicates the presence of Cu with the appearance of Cu2p peak [46]. The elemental scan of Ti, Cu and O are shown in Fig. 4.11 (b), (c) and (d) respectively. The peaks at 457.51 eV and 463.94 eV correspond to the presence of Ti^{3+} and at 458.97 eV and 464.72 eV corresponds to Ti^{4+} ions [46]. Hence, the presence of both Ti^{3+} and Ti^{4+} is confirmed in Cu doped samples. The binding energies of 931.64 eV and 933.45 eV of Cu $2p_{3/2}$ suggest the presence of Cu^+ and Cu^{2+} in the present system [46,50] rather than metallic Cu [51, 52] and hence $Ti^{3+}/Ti^{4+}/Cu^+/Cu^{2+}$ interactions are possible in the Cu-doped system. A slight shift in the peak position of O1s spectrum was observed in Cu-doped sample in comparison to the undoped sample indicating a change in the surface environments of Cu-doped sample. The O 1s spectrum of Cu-doped sample show a red shift at 531.49, 532.10 and 533.33 eV respectively, which indicates a lesser contribution from the Ti^{3+}-O bonds [53]. The contribution of surface oxygen is significantly more in T-Cu in comparison to undoped T-P as shown in Fig. 4.11 (d).
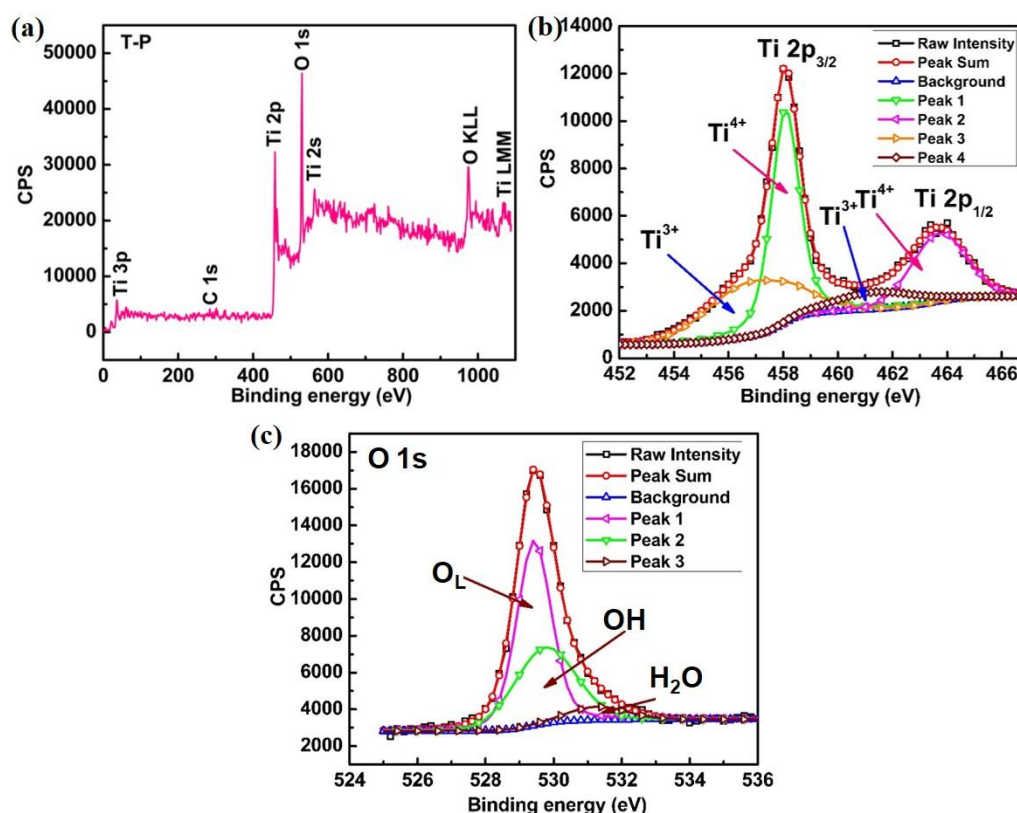
Fig.4.10. XPS spectra of T-P sample (a) Wide scan of T-P (b) Ti 2p and (c) O 1s

The appearance of Zn 3s and Zn 3p peaks in the wide scan of T-Zn sample indicates the presence of Zn in T-Zn sample which is represented in Fig. 4.12 (a). The detailed elemental scan of Ti, Zn and O is depicted in Fig.4.12 (b), (c) and (d) respectively. The peaks corresponding to 458.69 and 464.48 eV represent the Ti $2p_{3/2}$ and Ti $2p_{1/2}$ states which suggest that Ti exists as Ti^{4+} in T-Zn sample as shown in Fig.4.12 (b) where peaks corresponding to Ti^{3+} are completely absent. In the elemental scan of Zn, two peaks of Zn 2p spectrum corresponding to Zn $2p_{3/2}$ and Zn $2p_{1/2}$ electronic states of Zn (II) with binding energies of 1021.99 eV and 1045.08 eV are observed which are clearly shown in Fig.4.12 (c). Hence, it is confirmed that Zn is bivalent in T-Zn. Therefore, it is well understood that Zn^{2+} exist mainly in ZnO clusters dispersed on TiO_2 surface and this could be the reason for perfect diamagnetism exhibited by T-Zn as shown in Fig.4.9 (c). The O 1s spectrum of T-Zn sample is shown in Fig.4.12 (d) and after deconvolution, the O 1s peak of the sample is split into three peaks at 529.89, 530.01 and 531.58 eV. The behavior of O 1s spectrum of T-Zn is almost similar to T-P and slight peak shifts observed among T-P, T-Cu and T-Zn could

be due to the different surface oxygen contributions present in the respective samples. The intense peak at about 529.89 eV arises due to the oxygen in the TiO_2 crystal lattice (O_L), while the other oxygen peaks are the outcome of hydroxyl groups (OH, 530.01 eV) and adsorbed water (H_2O, 531.58 eV) respectively as shown in Fig.4.12 (d).
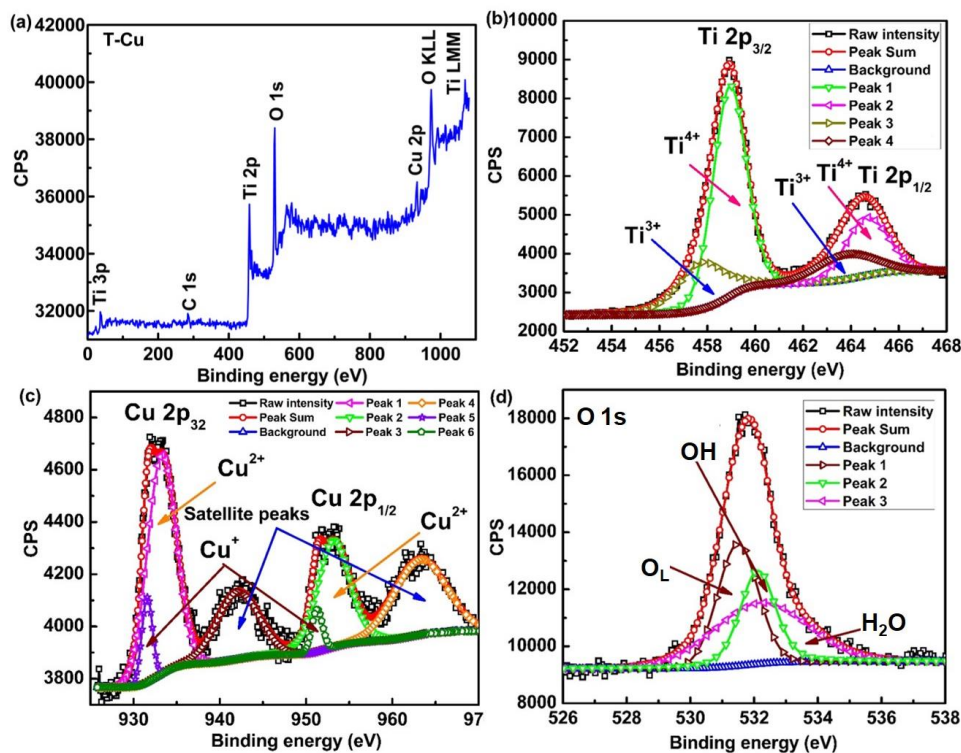
Fig.4.11. XPS spectra of T-Cu sample (a) Wide scan showing the presence of Cu (b) Ti 2p, (c) Cu 2p and (d) O 1s spectra along with deconvolution

4.3.1.7. Explanation of magnetic behaviour

Here, it is attempted to investigate the influence of TM ion site vacancies and oxygen vacancies on the magnetic behavior of the TiO_2 material due to the incorporation of non-magnetic elements in TiO_2. The origin of RTFM observed for the undoped sample (inset of Fig. 4.9 (b) has been mainly attributed to the particle size effect, defect concentration and Ti oxidation states. It has been observed that the reduction of particle size has a strong influence on the magnetic properties of nanostructured TiO_2 material. The observed results suggest that the nanocrystalline material form in such a way that larger particles would be preferentially doped over the smaller particles. As the grain size further decreases, the surface area to volume ratio increases and the contribution from the grain boundary defects increases.
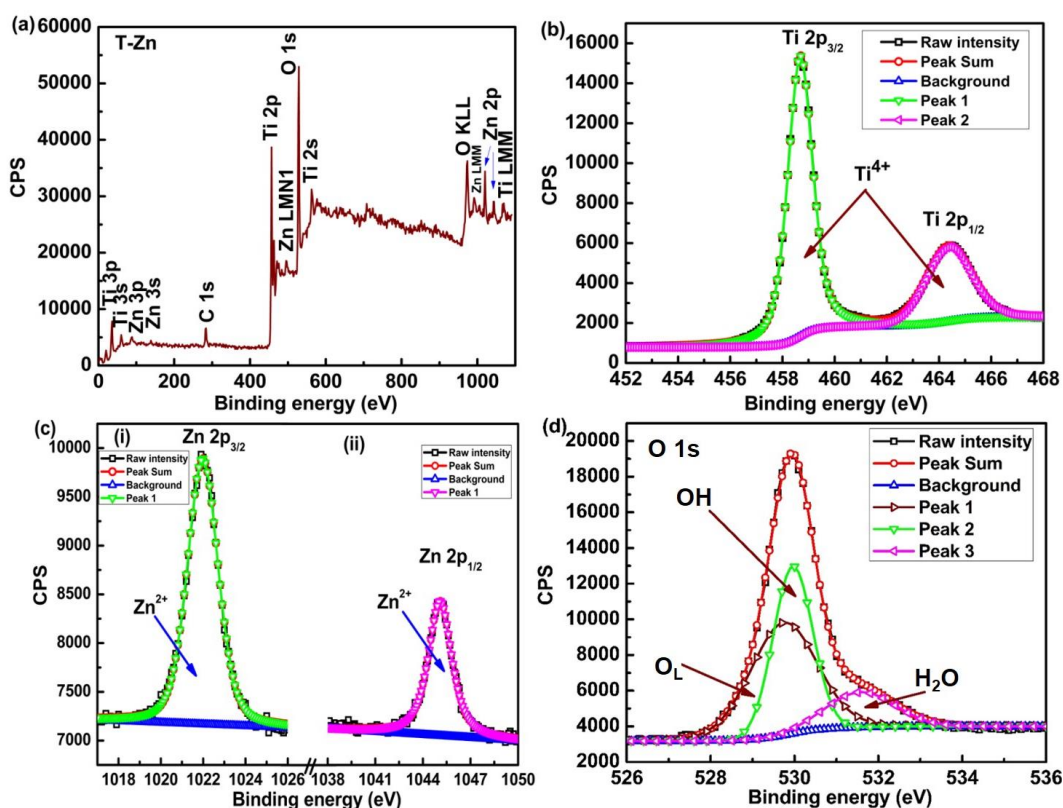
Fig.4.12. XPS spectra of T-Zn sample (a) Wide scan showing the presence of Zn (b) Ti 2p and (c) Zn 2p and (d) O 1s spectra along with the deconvolution

Thus, the inside of the nanocrystalline compound has magnetic properties same as that of the bulk counterpart while the amorphous outer layer is magnetically disordered due to more crystallographic defects and oxygen vacancies. Thus, due to the high disordered state of the outer region, the net magnetic moment of this amorphous region is zero, which in turn reduces the magnetization of the nanocrystalline compound compared to that of bulk counterpart. There is a strong exchange coupling taking place between the inner region and outer region of the nanocrystalline compound. The magnetically disordered state in the outer layer has a surface anisotropy contribution towards the effective anisotropy of the nanocrystalline compound. The effect of the surface anisotropy increases with a decrease in crystallite size. Thus, the broken symmetry due to the grain surface effects has a strong influence on the magnetic properties of nanocrystalline materials. The variation of H_C and magnetic moment with particle size for the undoped and Cu,Zu-doped TiO₂ has been plotted and is shown in Fig.4.13. In general, the effect of surface anisotropy increases with a decrease in

crystallite size. Thus the observed coercivity of the nanocrystalline compound is due to the surface anisotropy contribution by the insulating grain boundary growth. Thus the broken symmetry due to the grain surface effects has a strong influence on the physical properties of nanocrystalline materials. However, the variation shown in Fig. 4.13 could be primarily governed by oxygen defects rather than particle size effects.
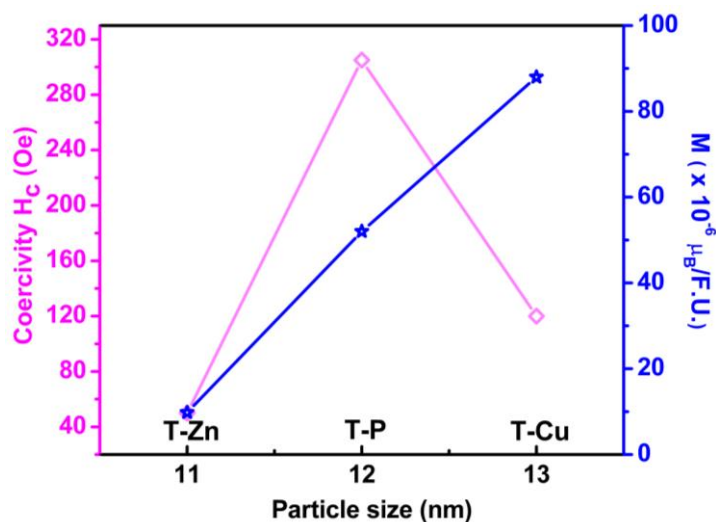
Fig.4.13. Variation of coercivity and magnetization with particle size

One of the theoretical reports suggest that a weak FM component in Ti can exist as a result of oxygen vacancy even without the presence of any secondary phases or magnetic impurities present at the Ti site. [39.] Even though there is a weak FM behavior, a considerable magnetic moment may not be observed with the generation of oxygen vacancy interaction with the trapped electrons in TiO₂ material.[54] Depending on the magnetic interactions present between the Ti^{3+}/Ti^{4+} ions and Ti^{3+} interaction with oxygen site vacancies, magnetic interactions such as diamagnetism, AFM, ferrimagnetism or FM could be liable to occur in undoped TiO₂ system. The charge redistribution associated with the oxygen vacancies can decide the magnetic properties of TiO₂ material, which is reflected in the controversial results obtained in different TiO₂ based systems.[39,54]

Oxygen vacancy is associated with the formation of F-centres and the interaction of these leads to the change in magnetic behavior of the material due to the trapping of electrons and charge redistribution occurring on the surface of TiO₂. When such an electron trapping occurs on the surface of TiO₂, it results in the formation of an F-centre

and an electron interacting with the F-centre could play with the nearby localized Ti^{4+} and subsequently, conversion of Ti^{4+} ions into Ti^{3+} ions occurs, leading to the formation of a F$^+$-centre.[55] The formation of Ti^{3+} is confirmed from the XPS analysis and F$^+$ defect centres are observed from the PL analysis as discussed in the previous section. BMPs may be generated as a result of localization of electrons in the F$^+$-centre and could develop magnetism by ordering the electron spin associated with Ti^{3+} (3d^1) located around oxygen vacancies. In the case of undoped TiO$_2$ sample, s–d exchange interaction associated with the 1s^1 electron spin of the F$^+$-centre and the 3d^1 electron spin originating from Ti^{3+} ions could easily favor a long-range FM ordering which is reflected in the magnetic measurements.

However, the magnetic properties and defects associated with TM-doped TiO$_2$ can effectively demonstrated by using the well-known BMP theory, proposed by Coey *et al.*,[56] as TiO$_2$ based systems can be considered as insulating system consisting of localized carriers. The BMP theory suggests that when oxygen vacancy comprising of a trapped electron (F$^+$ center) could effectively be treated as 1s hydrogenic type orbital with an electronic configuration of 1s^1. It can easily interact with nearby 3d orbitals of Ti/TM leading to the formation of BMPs. According to the BMP theory, it is believed that long range FM can be exhibited by the system when the size of BMPs is quite large to percolate through the host lattice. There are reports suggesting a weak FM behavior in the system due to the presence of oxygen vacancy even without the existence of any magnetic dopant occupying the Ti site.[54,57] Therefore, in DMS systems based on oxide materials having localized carriers, the most widely used and accepted theory is the BMP theory, proposed by Coey *et al.* when comparing with any other model for the explanation of defect assisted magnetic response.

Another possible way to get the FM behavior in undoped sample is the O 2p orbitals that arise from Ti site vacancy rather than the Ti 3d orbitals and oxygen vacancies. Hence, the intensity of d0 magnetism in the undoped TiO$_2$ nanostructures is determined by the population of Ti site vacancy at surface and or edge regions. To control the RTFM in undoped TiO$_2$ nanostructures, in general, factors towards surface defect state and defect density is to be manipulated. From these observations, the best

strategy to promote RTFM in undoped TiO_2 for spintronics related applications is to stabilize enough Ti vacancies near the surface in TiO_2 nanostructures by maintaining the crystalline quality of the material. Hence, a combined effort among the surface defects, Ti site vacancy and oxygen vacancy is ultimately leading to the electrons trapped at the defect sites leading to the BMP formation and ultimately deciding the magnetic behavior of undoped TiO_2 nanostructures. The interaction will be much stronger if the dopant ion contributes some 3d electrons which is exactly happening between the F^+-centre and Cu^{2+} ions to generate more number of BMPs, hence along with the s-d interaction mentioned above, another interaction in Cu-doped TiO_2 could arise among the F^+-centres and $3d^9$ electron spin of Cu^{2+} ions leading to FM ordering and enhanced magnetic moment. Previous reports suggest the formation of a $1s^2$ state with the doubly occupied F-centres, which leads to a weak AFM interaction.[56]

It is clear from these discussions that the ability of a system to generate more number of BMPs either due to Ti^{3+} or Cu^{2+} ions with the F^+-centre or both together, where an orbital overlapping with the unpaired $3d^1$ electron of Ti^{3+} ions or the unpaired $3d^9$ electron of Cu^{2+} ions is responsible for the observed RTFM which has happened in the present case, i.e., in T-Cu sample. Here, the concept of mixed valence ions also holds good along with the concept of surface defects and hence the possible role of charge transfer FM can also be used to explain the RTFM.[58,59] The room temperature M-H loop at lower fields show a weak FM behavior in T-Zn, which further corroborates the PL results and the formation of defect centres and surface free electrons inherently present in the TiO_2 system is crucial in determining the magnetic behavior in the T-Zn sample. Rather than the oxygen vacancies, O 2p orbitals resulting from Ti/Zn site vacancy could be favorable for the magnetic response of T-Zn at lower fields. However, the diamagnetic tail observed at higher fields indicates the presence of Ti^{4+} and Zn^{2+} in T-Zn sample which is in agreement with the XPS results. BMP fitting has been carried out on undoped and Cu, Zn-doped samples to investigate the impact of oxygen vacancy and non-magnetic ion concentrations.[60,61] According to this model, the measured magnetization can be fitted using the following relation;

$$M = M_0 L(x) + \chi_m H. \tag{4.1}$$

In the above mentioned equation, the first term accounts for BMP contribution and the second term is associated with the PM matrix contribution. The value of M_0 can be represented as the product of N and m_s, where N is the number of BMPs involved (per cm³) and m_s is the effective spontaneous magnetic moment per BMP. The Langevin function, $L(x)$ is defined as $L(x) = coth(x) - 1/x$ where $x = m_{eff} H/k_B T$. The term m_{eff} is the true spontaneous magnetic moment per BMP and is approximated to m_s. The parameters M_0, m_{eff} and χ_m are the variables in the fitting process. The experimental and fitted data to estimate the BMP concentration for undoped and Cu, Zn-doped samples are represented in Fig. 4.14 and it can be observed that the fitted data is very well in accordance with the experimental data. The obtained parameters are represented in Fig. 4.14 (d) from which the BMP concentration is found to be highest in T-Cu sample due to which the magnetic moment is more in comparison to T-P or T-Zn which is corroborated with the size versus moment plot shown in Fig.4.13.
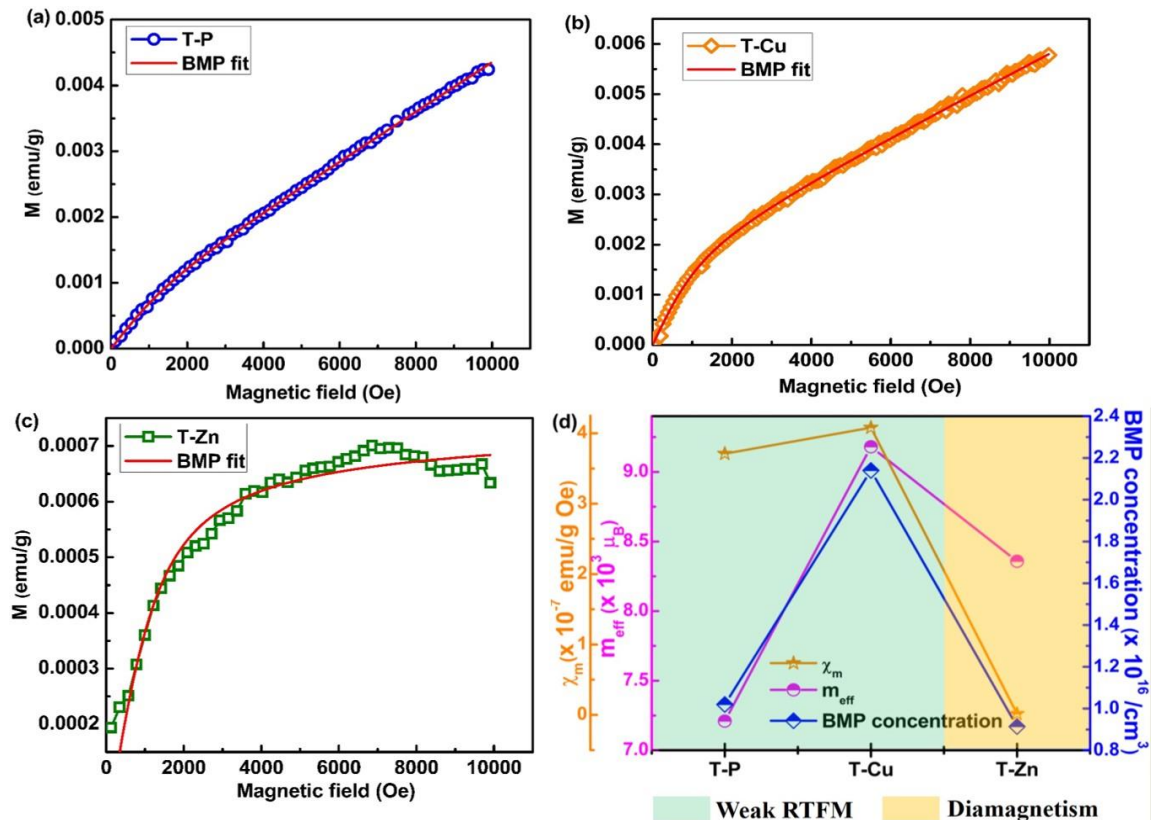
Fig.4.14. BMP fitting employed to estimate the concentration of magnetic polarons of (a) T-P and (b) T-Cu (c) T-Zn and (d) parameters obtained from langevin-fit for T-P,   T-Cu and T-Zn
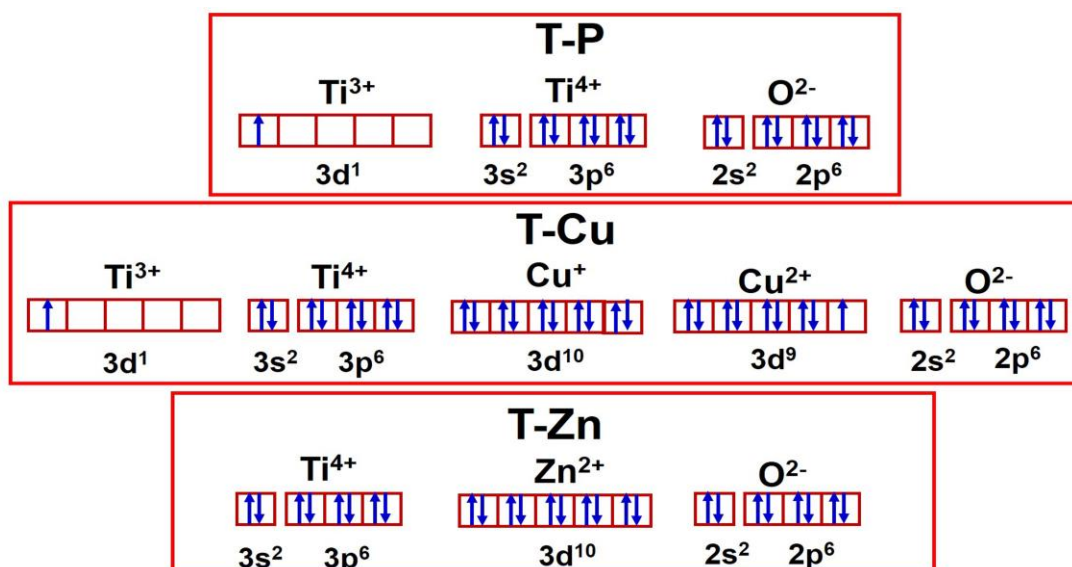
Fig.4.15. Schematic showing the spin states of valence shell electrons in T-P, T-Cu and T-Zn

In order to have a clear understanding regarding the spin interactions in these samples, a schematic representation is developed based on the results of XPS analysis which is depicted in Fig.4.15. As per the earlier discussions, the presence of Ti^{3+} is suggested in undoped T-P sample along with Ti^{4+}. The ratio of Ti^{3+} to Ti^{4+} is considerably small as shown in Fig.4.10 (b). Still, this small fraction of Ti^{3+} could have unpaired electrons in the 3d state as shown in Fig.4.15 and it can interact with the oxygen vacancy centres associated with the T-P sample as discussed previously. In the case of T-Cu, Cu^{2+} can be considered to be magnetic with one free electron and defect centres on the surface of TiO$_2$ system locally traps the electrons, ultimately leading to the formation of an F-centre where one of the electrons associated with the F-centre will have a tendency to interact with the adjacent localized Ti^{4+} and convert Ti^{4+} ions into Ti^{3+} ions, resulting in the formation of an F$^+$-centre. This mechanism can be well corroborated with the magnetic measurements also. But in the case of Zn-doped samples, Zn^{2+} is the most stable oxidation state which is diamagnetic in nature and the formation of both Ti^{3+} and F$^+$-centre will be hindered here ultimately leading to the diamagnetic tail like behavior of the sample. The formation of F-centres and F$^+$-centres will be facilitated due to the trapped electrons in these defect sites. The F$^+$-centre formation ultimately leads to the formation of BMPs, which favors the FM interaction. The room temperature M-H loop at lower fields show a weak RTFM which further

corroborates the PL results and the formation of defect centres and 3d^1 interaction of Ti^{3+}/Cu^{2+} plays a crucial role in generating the magnetic response in the undoped and Cu-doped sample.
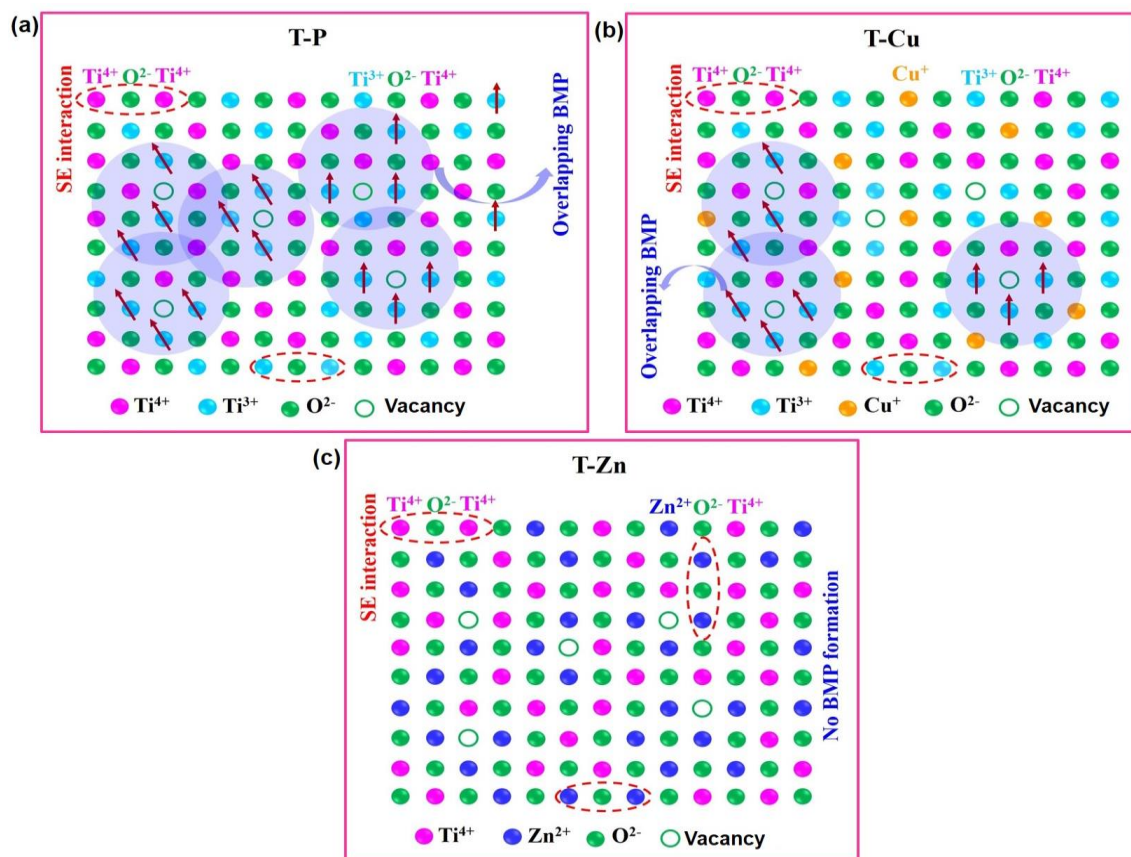
Fig.4.16. Schematic showing the BMP interactions in (a) T-P, (b) T-Cu and (c) absence of BMP formation in T-Zn

A similar behavior is observed for T-Zn also especially at lower magnetic fields, whereas at higher fields, i.e., above 10000 Oe, the magnetic contribution from Ti^{4+} and Zn^{2+} magnetic contribution is dominated and ultimately diamagnetic tails are observed and hence the ratio of Ti^{3+}/Ti^{4+} is crucial in determining the magnetic behavior in both undoped and doped samples. The previous discussions suggest the absence of expected perfect diamagnetism in T-Zn due to the defects associated with the system and the XPS results illustrate the presence of Ti^{4+} and Zn^{2+} in the T-Zn system, where there is no unpaired electrons at all to contribute towards a long range FM as shown in Fig.4.15 and Fig.4.16.

4.3.2. Ferromagnetic elements (Fe,Co,Ni)-doped TiO₂ nanocrystals

The study on ferromagnetic elements-doped TiO_2 nanocrystals could provide a new pathway in the field of spintronics and magneto optics by tuning the optical and magnetic properties through appropriate doping to accomplish the functional applications and the detailed investigations are given below.

4.3.2.1. Structural Analysis

X-ray diffraction studies corresponding to Fe, Co and Ni-doped TiO_2 are discussed in the following sub sections.

A. X-ray diffraction studies of Fe-doped TiO₂

XRD patterns of Fe-doped TiO_2 nanopowders are shown in Fig. 4.17. From Fig.4.17, the diffraction peaks could be well indexed and matches well with ICDD data of tetragonal anatase TiO_2 (space group I41/amd (ICDD 78-2486)). The diffraction patterns confirm the absence of any other impurity phases related to rutile or Fe or Fe_2O_3 showing that crystal structure and anatase phase is not disturbed due to Fe doping at Ti site.
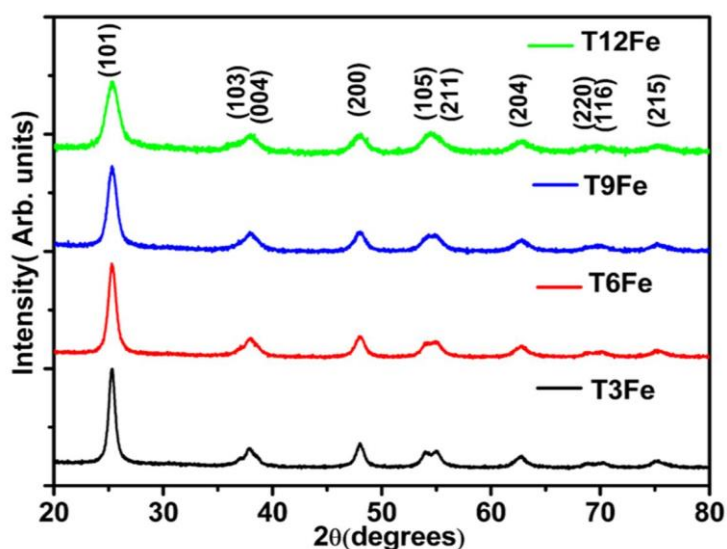
Fig.4.17. XRD patterns of T3Fe, T6Fe, T9Fe and T12Fe

Rietveld refinement has been carried out on the XRD data using Fullprof software which is depicted in Fig. 4.18(a–d) and the refined parameters are represented

in Table 4.6. Rietveld refinement also confirms the single-phase anatase tetragonal TiO_2 structure and the absence of any secondary phases in Fe-doped samples. Refined data, shows a slight decrease in lattice parameter and unit cell volume, which is expected as the ionic radius of Fe^{2+} (0.61 Å) is comparable with Ti^{4+} ions (0.61 Å) [62] and the ionic radius of Fe^{3+} (0.55 Å) is smaller than that of Ti^{4+} ions (shown in Table 4.6.).
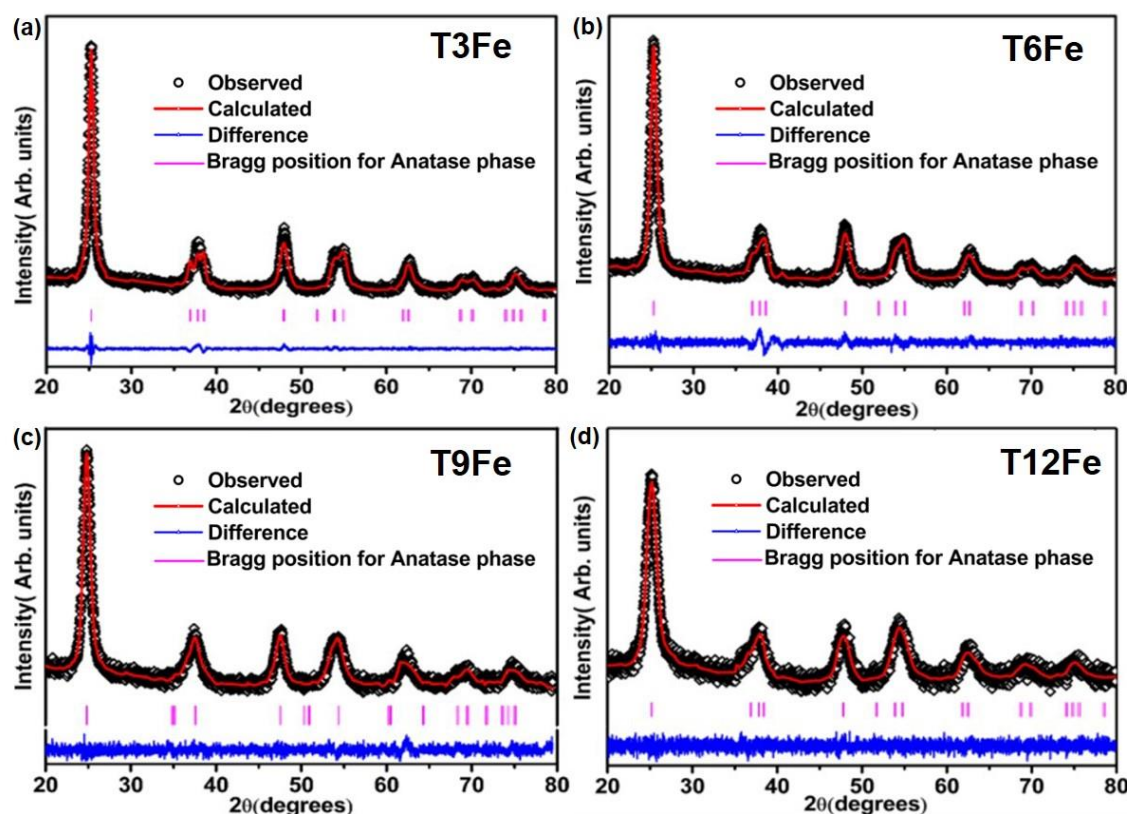
Fig.4.18. Refined XRD patterns of Fe-doped TiO_2 (a) T3Fe, (b) T6Fe, (c) T9Fe (d) T12Fe.

The decrease in particle size is also attributed due to the close agreement in ionic radius of dopant and host ions. A systematic decrease in the main peak intensity and a drastic reduction in the average crystallite size for Fe-doped TiO_2 are observed from T3Fe to T12Fe as shown in Fig.4.19 (a) and (b). The peak shift associated with varying Fe content is demonstrated in Fig.4.19 (c) for the most intense peak (101) and the variation in FWHM for doped samples justify the incorporation of Fe in TiO_2.[63] The intensity ratios associated with I_{101}/I_{004} and I_{101}/I_{200} for all the samples are shown in Fig. 4.19 (d). Rietveld refinement confirms TiO_2 with a Fe concentration of 12% do not cause any change in the phase, amorphization of the lattice and presence of any

impurity phases is eliminated within the detection limit of XRD. When we consider the intensity of an XRD peak, the atomic form factor (f_N) is a measure of an atom's scattering power while it doesn't depend on the atomic position of the atoms in a unit cell and is essentially different for different atoms. Structure factor (F) gives information regarding the total scattering power of all the atoms in the crystal. These are related through the following relation,[64]

$$F_{hkl} = \Sigma f_N \exp[2\pi i(hu_N + kv_N + lw_N)] \qquad (4.2)$$

In equation (4.2), u_N, v_N, w_N are the atomic positions in a unit cell and N corresponds to the total number of atoms in a unit cell. It is observed that the XRD peak intensity of Fe doped TiO₂ nanocrystals progressively decreases with Fe content compared to that of undoped TiO₂ nanocrystals.[65] By considering equation (4.2), we can represent the XRD peak intensity, I of Fe-doped TiO₂ nanocrystals as,

$$I = [Af_1(1 - x) - Bf_2x]^2 \qquad (4.3)$$

where f_1 and f_2 are the Ti and Fe ion's form factors. A and B are the parameters obtained from the fitting of equation (4.3) to experimentally obtained XRD patterns and x is the atomic ratio of Fe. Since f_N of oxygen is negligible, the contribution to XRD peak intensity by oxygen is neglected in equation (4.3). The most intense (101) peak is fitted with equation (4.3) and is shown in Fig. 4.19 (a). A large B value implies that the x value increases with Fe substitution suggesting that Fe atoms cause out of phase scattering of the waves compared to Ti atoms which is the reason for the decreased XRD peak intensity. This argument can be validated due to the fact that nanoparticles generally will try to drive out the dopant atoms, as a part of the self-purification mechanism to achieve the state of minimum energy.[66] Under such circumstances, it is interesting to note that the amount of dopant atoms would be greater near the surface of the nanocrystals than that at the core. In the fitting process, the larger the value of B, the higher the concentration of Fe ions present at the TiO₂ surface. A systematic decrease in the intensity of XRD peaks affirms the incorporation of Fe in to the TiO₂ lattice by the replacement of Ti ions with Fe and not by occupying the interstitial sites of TiO₂.

Table 4.6. Refinement parameters obtained for Fe-doped TiO_2 nanocrystals

Compound	T3Fe	T6Fe	T9Fe	T12Fe
Phase	Anatase			
Crystal Structure	Tetragonal			
Space Group	I 4_1/a m d			
Lattice Parameters				
a(Å)	3.7834 (5)	3.7810 (2)	3.7793 (3)	3.7772 (5)
c(Å)	9.4902 (1)	9.4881 (4)	9.4854 (1)	9.4843 (2)
Volume (Å)³	135.81 (1)	135.64 (3)	135.45 (1)	135.29 (4)
Atomic positions				
Ti/Fe $_x$ (4a)	0.0000	0.0000	0.0000	0.0000
Ti/ Fe $_y$ (4a)	0.7500	0.7500	0.7500	0.7500
Ti/ Fe $_z$ (4a)	0.1250	0.1250	0.1250	0.1250
O $_x$ (8e)	0.0000	0.0000	0.0000	0.0000
O $_y$ (8e)	0.2500	0.2500	0.2500	0.2500
O $_z$ (8e)	0.0846	0.0833	0.0829	0.0857
B $_{iso}$ (Ti/ Fe) (Å)²	0.0003	0.0007	0.0008	0.0005
B $_{iso}$ (O) (Å)²	0.0031	0.0014	0.0012	0.0008
Residual Parameters				
R$_p$	4.19	4.16	4.35	4.14
R$_{wp}$	5.23	5.44	5.33	5.39
χ^2	1.47	1.46	1.47	1.47

The average crystallite size obtained from the Scherrer's equation from the FWHM value of (101) peak of all the synthesized samples are shown in Fig. 4.19 (b) and Fig.4.20 which shows a decreasing trend with increasing Fe ions. This observation gives an impression that Fe ions in TiO_2 lattice can inhibit the TiO_2 crystal growth as a result of increased Fe atoms leading to subsequent grain size reduction. Earlier reports suggest a decrease in size with Fe doping in nanocrystalline TiO_2.[67] As mentioned earlier, the substitution of Fe^{3+}/ Fe^{2+} ions with comparatively low ionic radii than Ti^{4+} could be the reason for the decreased crystallite size.[68] In the bottom-up approach, a two-step mechanism can be suggested for the solution based synthesis of TiO_2 nanocrystals. Initial stage involves the formation of critical nuclei of the material and under preferable conditions which could grow considerably and allow the formation of nanocrystals in the second stage. In general, nucleation will be homogeneous and a poly-nuclear growth mechanism will determine the growth rate of the nanocrystals in

the case of mono-sized particles.[69] Thus, considering the semi-empirical kinetics equation, the rate of crystallization (R) can be represented as,

$$R = kF(g)\sigma \qquad (4.4)$$

where k denotes the crystal growth rate constant, F(g) is a function representing the available growth sites and σ is the relative supersaturation which is denoted as (C - Cα)/Cα, C and Cα representing the concentration of solute in the solution and at equilibrium state respectively.[70] In the present case, the function F(g) approaches the maximum when Ti atoms provide the maximum growth sites and approaches a minimum when Fe ions are maximum at the growth sites. If we assume a poly-nuclear process for the growth mechanism, there is a linear relation for the particle radius (r) with time (t) such that,

$$r = r_0 + k_p t \qquad (4.5)$$

where r_0 is the initial nuclear size and k_p is a constant dependent on temperature. Using the above equations, one can determine the nanocrystallite size and this can be represented in terms of Fe ion concentration (x) as,

$$r = r_0 - kF(g)x \qquad (4.6)$$

more appropriately as,

$$r = r_0 - D \qquad (4.7)$$

where D represents the negative growth rate of TiO₂ nanocrystals as a result of the incorporation of lesser ionic radii Fe atoms that subsequently leads to a considerable reduction in the growth centres. Fig. 4.19 (b) shows the reliability of the fit to the variation in crystallite size with Fe dopant concentration using equation (4.7). When we consider the growth of undoped TiO₂ nanocrystals, the binding energies of Ti and O ions will approach a maximum when the dopant ions are absent on a growing nucleus, while the incorporation of dopant ions effectively reduces their binding energies.[71] During the fitting process, when the D value is higher than unity in equation (6), surface concentration of Fe ions can be treated to be of maximum. The different intensity ratios, i.e., I_{101}/I_{004} and I_{101}/I_{200} corresponding to (101), (004) and (200) peaks are plotted against Fe concentration for each samples and are shown in Fig. 4.19 (d). It is clear from Fig. 4.19 (d) that an increase in Fe concentration causes a decrease in I_{101}/I_{004} and
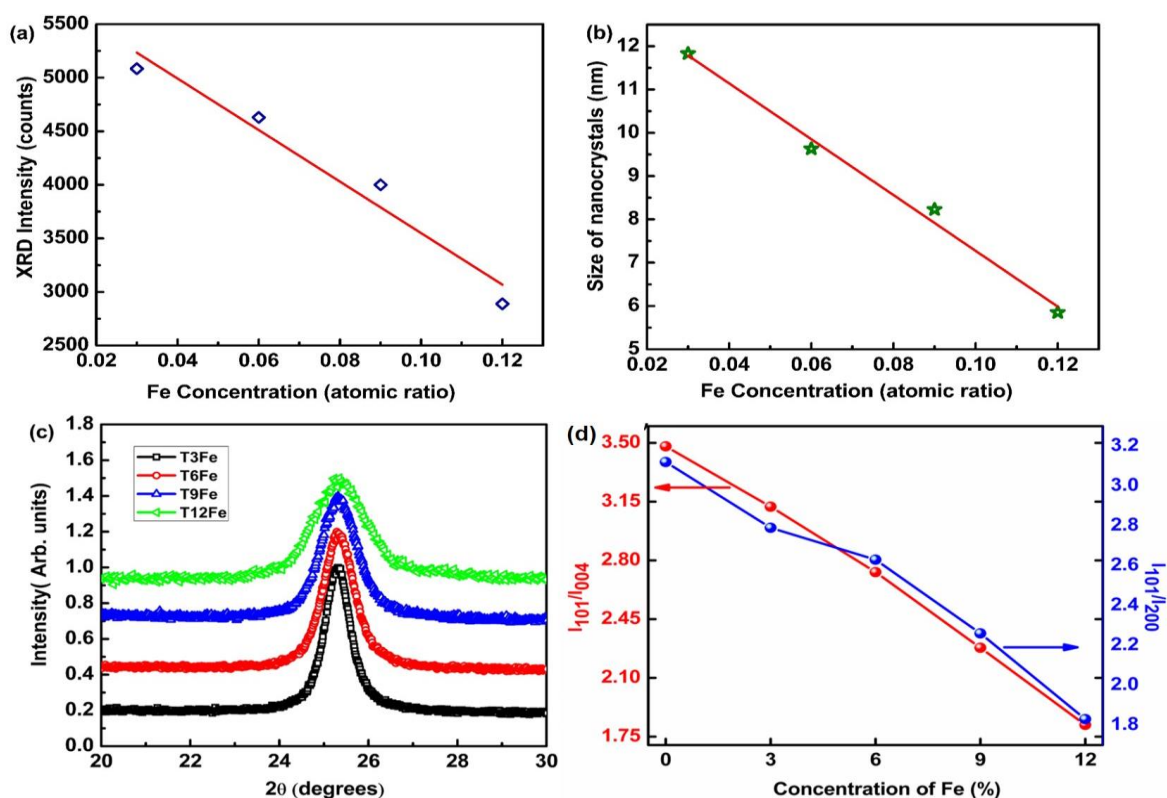
Fig.4.19. (a) Variation of XRD intensities with Fe concentration (b) variation of crystallite size (c) Peak shift associated with T3Fe, T6Fe, T9Fe and T12Fe (d) Intensity ratio corresponding to I_{101}/I_{004} and I_{101}/I_{200} with Fe concentration
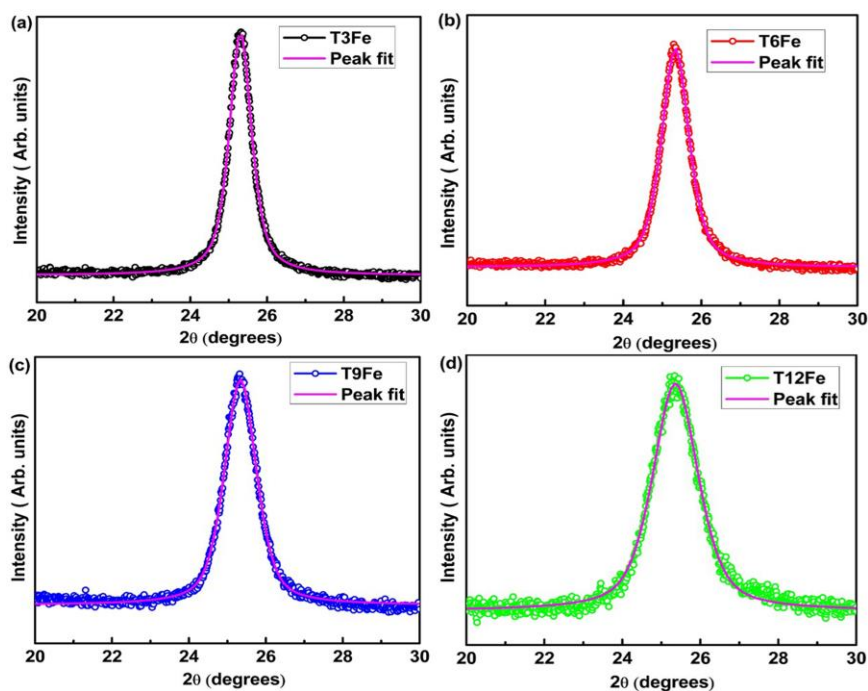
Fig.4.20. Estimation of FWHM from the most intense (101) peak of (a) T3Fe (b) T6Fe (c) T9Fe and (d) T12Fe

I_{101}/I_{200} which suggest the replacement of Ti^{4+} ions with Fe ions. Apart from the ionic radii concept, oxygen vacancies can inhibit the growth kinetics and a decrease in particle size can occur. This is specifically due to the Fe^{2+}/Fe^{3+} ions adsorbed at the TiO_2 nanoparticles surface during their formation. In the sol-gel process, doping with Fe^{2+}/Fe^{3+} significantly affects the adsorption sites and will retard the growth mechanism associated with the TiO_2 system. It is reported that samples annealed at higher temperatures show a significant reduction in size of nanocrystals with Fe concentration.[72] In the present investigation, the anatase TiO_2 samples are annealed at 673 K and hence it is possible to exhibit a similar behavior where the presence of slight amount of oxygen vacancies cannot be ruled out.

B. X-ray diffraction studies of Co-doped TiO₂

The XRD patterns of Co-doped TiO_2 powder with varying Co concentrations (T3Co, T6Co, T9Co and T12Co) are shown in Fig. 4.21 (a). All the diffraction peaks are well indexed and correspond to the tetragonal anatase phase of TiO_2 (space group I41/amd (ICDD 78-2486). The diffraction patterns do not show any secondary phase peak related to rutile or Co or CoO showing that anatase phase is not disturbed due to Co doping in TiO_2. A slight shift in the peak position of the most intense peak (101) (shown in Fig. 4.21 (b)) and the change in FWHM for the doped samples indicate the incorporation of Co in TiO_2.[27]
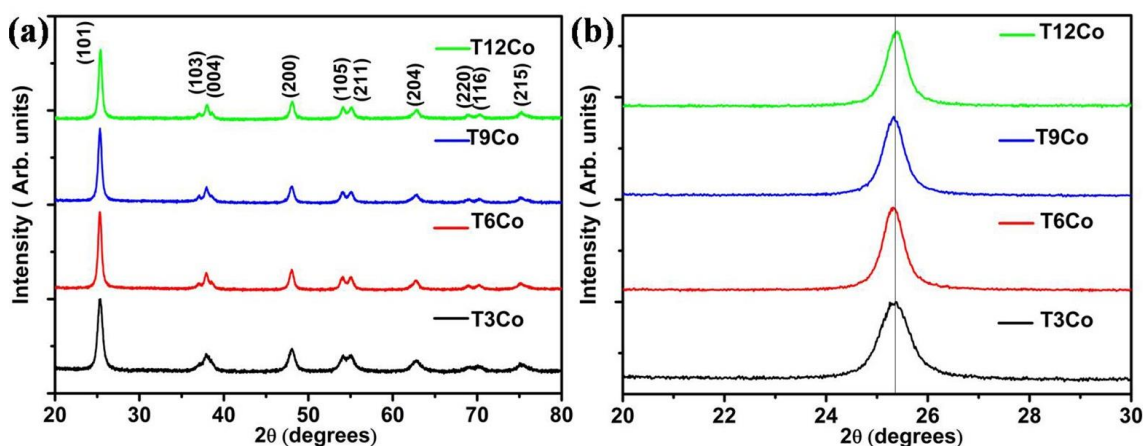
Fig.4.21. (a) XRD patterns of Co-doped TiO₂ nanocrystals (b) peak shift associated with T3Co, T6Co, T9Co and T12Co
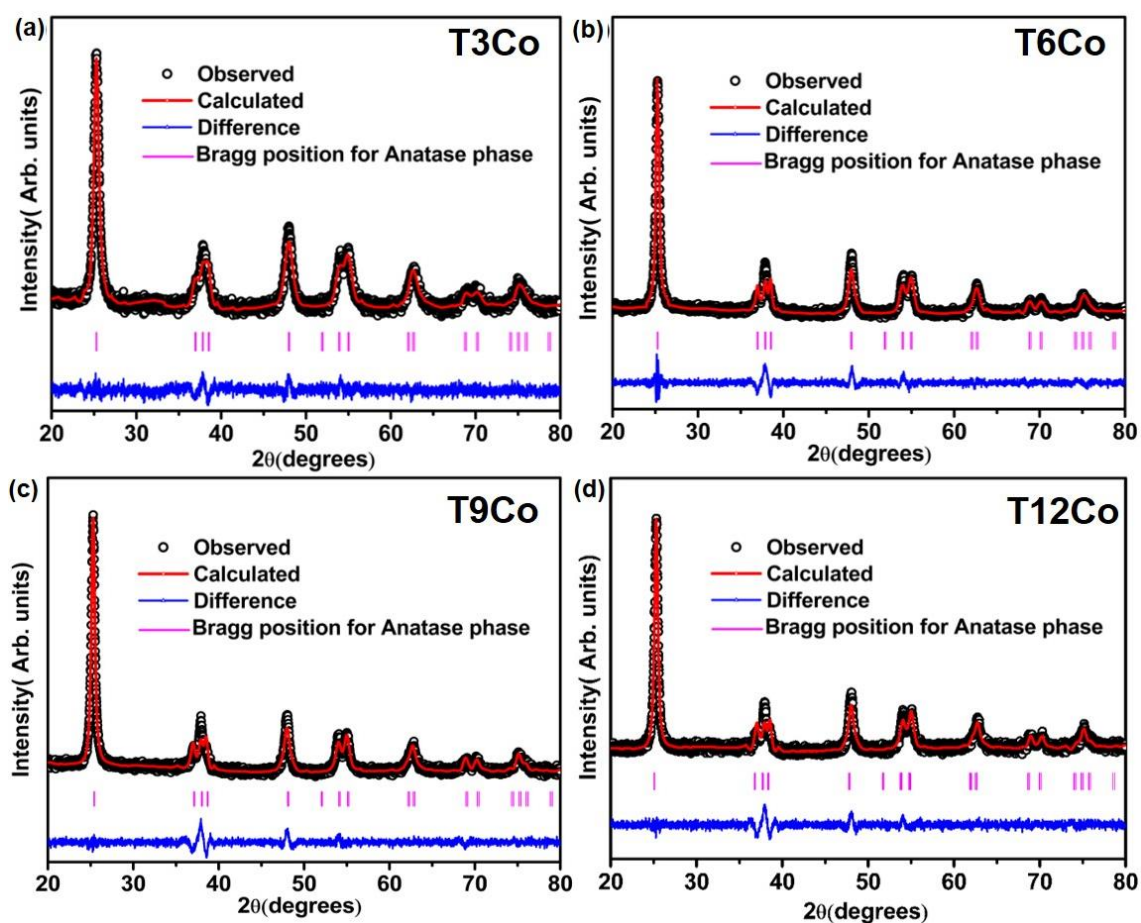
Fig.4.22. Refined XRD patterns of Co-TiO₂ nanocrystals (a)T3Co,(b)T6Co,(c)T9Co (d) T12Co

The average particle size of undoped and Co-doped TiO₂ powder determined from XRD pattern using Scherer's equation taking (101) peak as reference was found out to be around 14 nm and 14-20 nm respectively. The Rietveld refinement of the XRD data was done using Fullprof software which is shown in Fig. 4.22 (a–d) and the refined parameters are given in Table 4.7. The Rietveld refinement confirms that all the Co-doped TiO₂ samples crystallize in the anatase tetragonal structure and no secondary phase has been detected. Refined data, shows an increase in lattice parameter as well as unit cell volume with increase in Co concentration which is expected as the ionic radius of Co^{2+} (0.65 Å) is larger than that of Ti^{4+} ions (0.61 Å) [1] whereas the ionic radius of Co^{3+} (0.55 Å) is smaller than that of Ti^{4+} ions, but still increasing Co^{2+}/Co^{3+} ratio ultimately leads to the increased lattice parameters. Here, the coordination number of Ti^{4+} cation is considered to be 6, which is twice the coordination number of O^{2-} ion. The increase in particle size is also attributed to the difference in ionic radius of dopant and

Table 4.7. Refinement parameters obtained for Co-doped TiO_2 nanocrystals

Compound	T3Co	T6Co	T9Co	T12Co
Phase	Anatase			
Crystal Structure	Tetragonal			
Space Group	I 4₁/a m d			
Lattice Parameters				
a(Å)	3.7894 (1)	3.7906 (2)	3.7922 (4)	3.7951 (1)
c(Å)	9.4926 (3)	9.4942 (1)	9.5130 (3)	9.5029 (2)
Volume $(Å)^3$	136.31 (1)	136.42 (2)	136.81 (1)	136.87 (2)
Atomic positions				
Ti/Co $_x$ (4a)	0.0000	0.0000	0.0000	0.0000
Ti/ Co $_y$ (4a)	0.7500	0.7500	0.7500	0.7500
Ti/ Co $_z$ (4a)	0.1250	0.1250	0.1250	0.1250
O $_x$ (8e)	0.0000	0.0000	0.0000	0.0000
O $_y$ (8e)	0.2500	0.2500	0.2500	0.2500
O $_z$ (8e)	0.0848	0.0829	0.0813	0.0867
B $_{iso}$ (Ti/ Co) $(Å)^2$	0.0006	0.0004	0.0003	0.0008
B $_{iso}$ (O) $(Å)^2$	0.0043	0.0010	0.0007	0.0009
Residual Parameters				
R_p	2.326	2.380	3.183	3.253
R_{wp}	3.158	3.307	4.052	4.487
χ^2	1.793	1.994	1.399	2.520

host ions. The difference between ionic radii of the dopant and host ions is expected to cause a small enhancement of the TiO_2 unit cell and this increase in volume is proportionate with the increase in doping level which is in accordance with the Vegard's law.[73] Rietveld refinement data confirms that Co is incorporated into TiO_2 lattice and has substituted the Ti^{4+} ions and due to the small difference in ionic radii of both ions the local structure might have been little disturbed causing a change in FWHM.

C. X-ray diffraction studies of Ni-doped TiO₂

XRD patterns of all the Ni-doped samples are shown in Fig.4.23 (a). All the diffraction peaks have been indexed with the tetragonal anatase phase of TiO_2 with space group I 4₁/a m d (ICDD card no.78-2486). The presence of any impurity phases corresponding to NiO is ruled out within the detection limit of XRD. Fig.4.23 (b) shows

the peak shift of the most intense peak (101) in Ni-doped samples. It can be seen that there is a broadening of the (101) peak with increase in Ni concentration which suggests a decrease in crystallite size with Ni doping. The crystallite size is calculated using Scherrer's formula and the FWHM associated with each sample is also estimated and is represented in Fig. 4.23 (c). The change in FWHM with Ni doping indicates that Ni has been incorporated into TiO$_2$ lattice.[74] The average crystallite size of Ni-doped TiO$_2$ samples determined from the XRD patterns using Scherer's equation was found to be around 10-15 nm respectively. The reduction in the average crystallite size of Ni-doped TiO$_2$ nanocrystals could be attributed to the presence of Ni–O–Ti bonds, which inhibits the growth of the crystals. This suggests that the Ni^{2+} ion replaces the Ti^{4+} ions in the TiO$_2$ host lattice, which results in the decrease of the average crystallite size. The size-strain plot is shown in Fig. 4.23 (d) which follows a similar decreasing trend for crystallite size and it is clear that the strain associated with each sample is increasing with Ni substitution. This lattice strain could be the reason for peak broadening, variation in FWHM and decreasing trend observed for crystallite size with Ni doping.
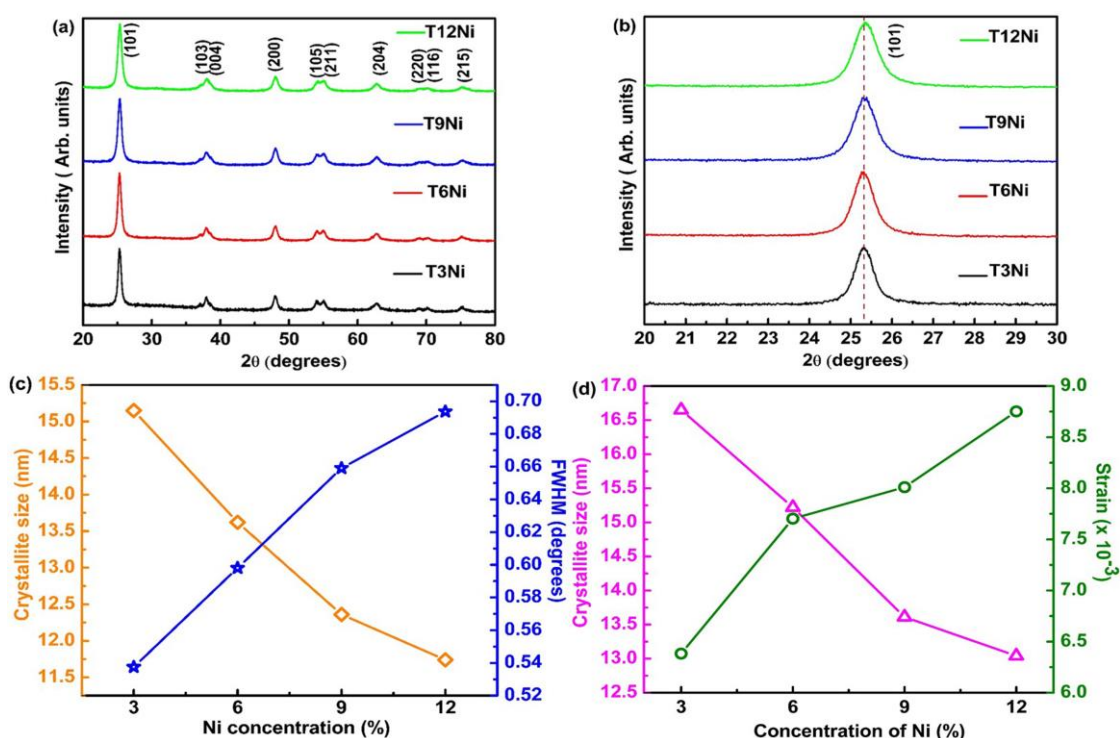
Fig.4.23. (a) XRD patterns of Ni-doped TiO$_2$ nanocrystals (b) peak shift associated with (101) peak in T3Ni, T6 Ni, T9 Ni and T12 Ni (c) The variation of crystallite size calculated from Scherrer's formula and FWHM associated with each sample (d) The variation of crystallite size and strain obtained from size-strain plot with Ni concentration.

Rietveld refinement of the XRD diffraction patterns has been carried out on all the samples using Fullprof software and is shown in Fig. 4.24 (a–d) and the parameters obtained from the refinement are given in Table 4.8. Rietveld refinement confirms that Ni-doped TiO_2 crystallizes in the anatase tetragonal structure. A slight increase in lattice parameter, as well as unit cell volume, is observed with increasing Ni concentration which is attributed to the large ionic radius of Ni^{2+} (0.69 Å) than that of Ti^{4+} ions (0.61 Å).[75] This difference in the ionic radii of Ni^{2+} and Ti^{4+} causes the small enhancement of the TiO_2 unit cell volume.[73] The detailed XRD analysis gives an impression that Ni ions have substituted the Ti ions and the size-strain plot reveals the possibility of causing a change in FWHM due to the lattice strain associated with the doped samples. The relative change in lattice parameter over the composition (0-12%) and crystallite size in the case of Co, Ni and Fe doped TiO_2 is included in the Appendix. A (Fig.A1 (a)-(d)).
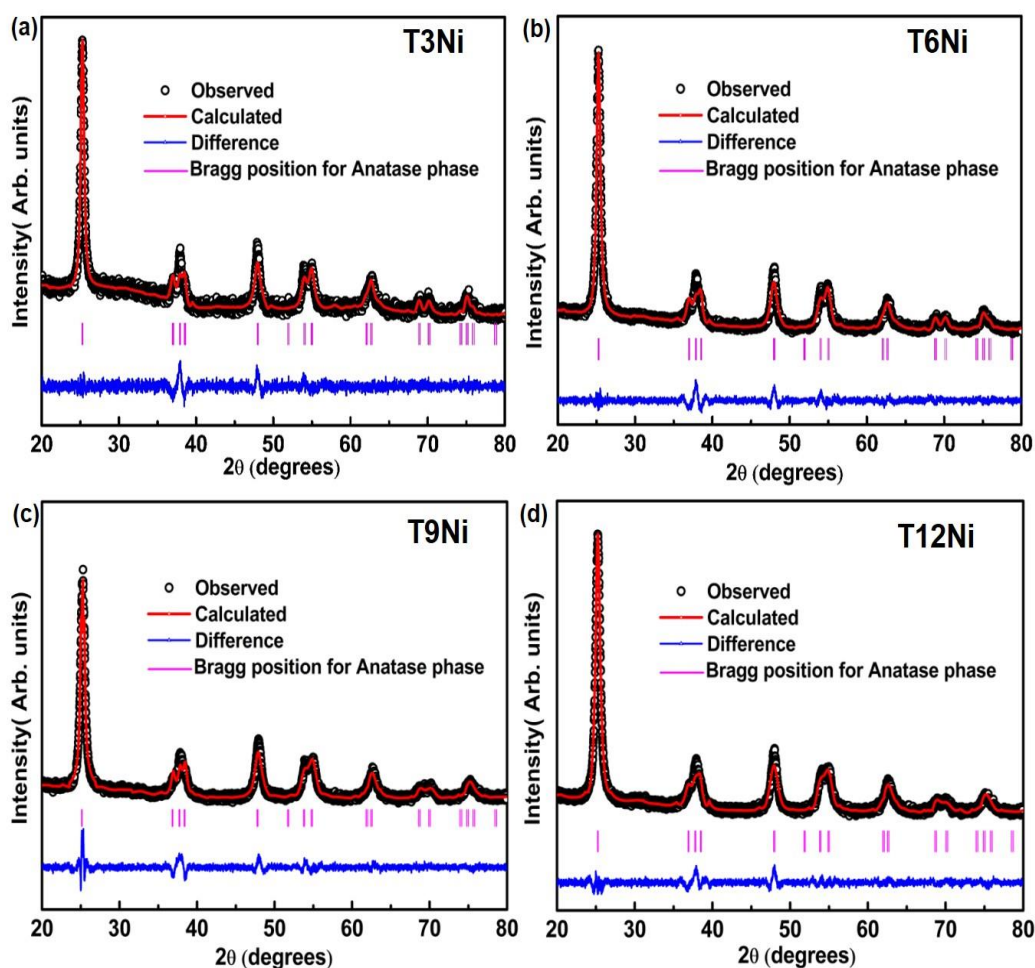
Fig.4.24. Refined XRD patterns of (a) T3Ni, (b) T6Ni, (c) T9Ni and (d) T12Ni.

Table 4.8. Refinement parameters obtained for Ni-doped TiO_2 nanocrystals

Compound	T3Ni	T6Ni	T9Ni	T12Ni
Phase	Anatase			
Crystal Structure	Tetragonal			
Space Group	I 4₁/a m d			
Lattice Parameters				
a(Å)	3.7934 (2)	3.7936 (4)	3.7956 (5)	3.7981 (1)
c(Å)	9.4947 (4)	9.5011 (6)	9.5109 (1)	9.5247 (4)
Volume (Å)^3	136.63 (1)	136.73 (3)	137.02 (3)	137.40 (5)
Atomic positions				
Ti/Ni $_x$ (4a)	0.0000	0.0000	0.0000	0.0000
Ti/ Ni $_y$ (4a)	0.7500	0.7500	0.7500	0.7500
Ti/ Ni $_z$ (4a)	0.1250	0.1250	0.1250	0.1250
O $_x$ (8e)	0.0000	0.0000	0.0000	0.0000
O $_y$ (8e)	0.2500	0.2500	0.2500	0.2500
O $_z$ (8e)	0.0827	0.0822	0.0838	0.0861
B $_{iso}$ (Ti/ Ni) (Å)^2	0.0011	0.0008	0.0002	0.0004
B $_{iso}$ (O) (Å)^2	0.0032	0.0013	0.0005	0.0007
Residual Parameters				
R$_p$	3.45	3.60	4.11	3.41
R$_{wp}$	4.50	4.84	5.42	4.45
χ^2	1.54	1.61	1.27	1.58

4.3.2.2. Raman analysis

Raman spectra corresponding to Fe, Co and Ni-doped TiO_2 nanocrystals are discussed below in detail.

A. Raman analysis of Fe-doped TiO₂

Fe-doped TiO_2 nanocrystals are subjected to micro-Raman analysis, the results of which are represented in Fig. 4.25 (a) which shows characteristic Raman active modes associated with anatase TiO_2. The observed peak at 144 cm^{-1} represents E_g (1) mode and all the other peaks located at 197, 399, 516, and 639 cm^{-1} corresponds to E_g (2), B_{1g} (1), A_{1g}, and E_g (3) modes, respectively. Neither the peaks corresponding to oxides of Fe nor other secondary phases is detected from Raman spectra which is well in accordance with the XRD results discussed earlier. With an increase in Fe content, E_g (1) intensity decreases systematically and signifies the substitution of Fe^{2+} and Fe^{3+} ions at Ti^{4+} sites.[65] The frequency shift and broadening of the most intense E_g (1) mode of all

the samples as a function of Fe concentration is depicted in Fig. 4.26 (b). A blue shift is observed with Fe concentration as shown in Fig.4.25 (b) in which the possible mechanisms causing this behavior could be the lattice strain, deficiencies and confinement effect on particle size. The creation of such deficiencies to maintain the charge neutrality of the system and is reported with the substitutional doping of Fe ions at the Ti site.[65] It is evident from literature that vacancies associated with oxygen sites are responsible for peak shift and broadening of Raman modes associated with TiO_2 system.[76] The broadening associated with the Raman modes of the doped samples could be due to the reduction in particle size of nanoparticles of TiO_2 which is well in accordance with results obtained from XRD analysis.
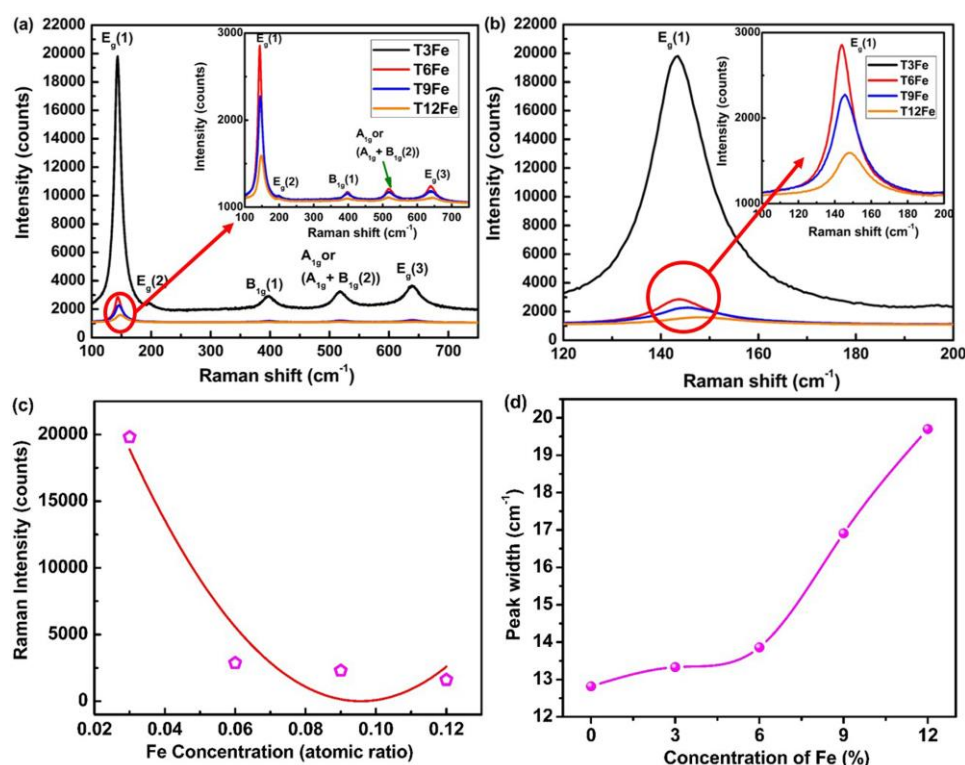
Fig.4.25. Raman spectra of T3Fe, T6Fe, T9Fe and T12Fe samples (a) complete spectrum, inset shows the enlarged view of higher concentration samples (b) Peak shift representation of T3Fe, T6Fe, T9Fe and T12Fe samples: inset shows the enlarged view of the marked region (c) Raman intensity versus Fe dopant concentration (d) peak width versus concentration of Fe.

Raman peak intensity can also be represented in terms of x, similar to XRD intensity as

$$I = I_0(1 - Ex)^2 \qquad (4.8)$$

here, I_0 corresponds to the Raman intensity of the undoped TiO_2 nanocrystals and E represents the Fe ion concentration close to TiO_2 surface. The fitting of equation (4.8) is depicted in Fig. 4.25 (c) and the same fitting is possible with the other Raman modes in the spectra also. Observation of higher value for the parameter E in equation (4.8) can be corroborated with earlier explanations regarding the increase in x value and self-purification mechanism could be responsible for this as discussed above. A peak shift towards higher wave numbers can be justified as the Fe^{3+} ions are having smaller ionic radius than Ti^{4+} and subsequently the bond length of O-Ti-O is expected to decrease followed by the O-Ti-O bond bending vibration due to substitutional doping. Broadening of Raman peaks on doping are also evident from the peak shifting as shown in Fig.4.25 (d).
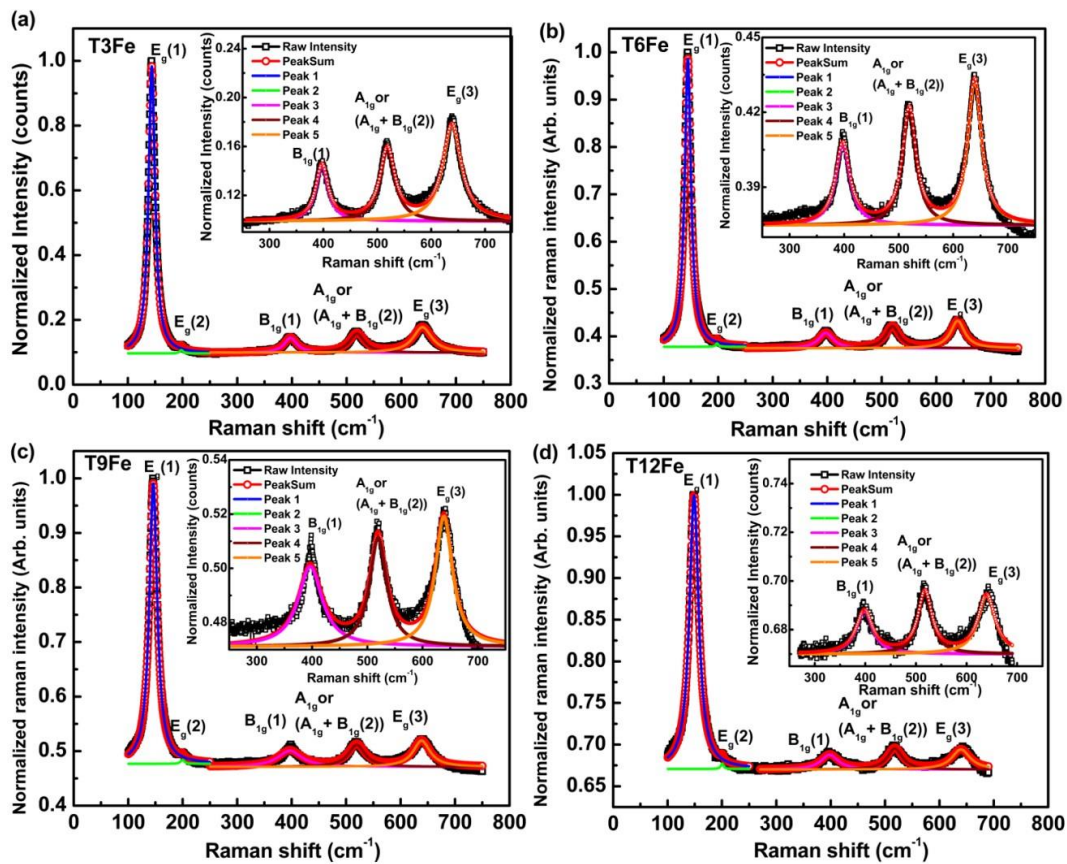
Fig.4.26. Deconvoluted Raman spectra of (a) T3Fe (b) T6Fe (c) T9Fe (d) T12Fe. Inset shows the enlarged view of the Raman peaks.

The deconvoluted Raman peaks of the samples have been represented in Fig.4.26. When we consider the undoped TiO_2, scattering of the TiO_6 octahedra

polarizes the system's Ti–O bonds, ultimately leading to a high intensity peak corresponding to E$_g$ mode. Interestingly, it is well known that doping of Fe can generate more number of oxygen vacancies and as a result, average number of Ti and O bonds reduces and leading to a decrease in TiO$_6$ octahedra to TiO$_{6-\delta}$, where δ is the number of oxygen vacancies. As a consequence of this reason, the scattering of Raman modes from TiO$_{6-\delta}$ may be able to polarize only a very few Ti–O bonds, resulting in broadening of the Raman peak. The impact of nonstoichiometric composition on E$_g$ (1) Raman mode in deficient TiO$_2$ samples is well reported.[77]

B. Raman analysis of Co-doped TiO$_2$

The Raman spectra of Co-doped TiO$_2$ nanocrystals taken at room temperature in the range 100-750 cm^{-1} are shown in Fig. 4.27 (a) and the inset shows the position of corresponding Raman modes. According to symmetry group analysis tetragonal anatase phase of TiO$_2$ has six active Raman modes and are reported to appear near 144 (E$_g$ (1)), 197 (E$_g$ (2)), 399 (B$_{1g}$ (1)), 516 (A$_{1g}$+B$_{1g}$ (2)) and 639 cm^{-1}(E$_g$ (3)).[58] When Co^{2+}/Co^{3+} substitutes Ti^{4+}, to balance the charge neutrality, there will be some disorder in the lattice which can be in the form of defects like oxygen vacancy or Ti interstitials. With the increase of the doping concentration, disorder increases and the ideal symmetry of the crystal will be destroyed which results in broadening of Raman bands.[76] The Raman bands at 144, 197, 399, 516, 639 cm^{-1} can be assigned as E$_g$ (1), E$_g$ (2), B$_{1g}$ (1), A$_{1g}$+B$_{1g}$ (2) and E$_g$ (3) modes of anatase phase respectively, the presence of these confirm the tetragonal anatase phase of TiO$_2$. The deconvoluted Raman spectra of all the doped samples are shown in Fig.4.28 and no mode corresponding to any other phase has been observed. The absence of any other mode related to Co or CoO or Co-Ti species within the detection limit of Raman spectra of doped samples indicates that Co might have gone to the substitutional site replacing Ti in TiO$_2$. The phonon confinement due to nanoscale crystallite size and non-stoichiometry due to defect induced disorder in the lattice results in shifting and broadening of Raman bands. Defects like oxygen vacancy in the material strongly affect the Raman modes. In the present study, the most intense E$_g$ (1) Raman mode at 144 cm^{-1} show blue shifting and broadening with doping (Fig. 4.27 (b)). So, both the phonon confinement and disorder in the host lattice due to the

incorporation of Co atoms/ions creating defects like oxygen vacancies in TiO_2 have caused the shifting of the position and broadening of the Raman bands[15-17].
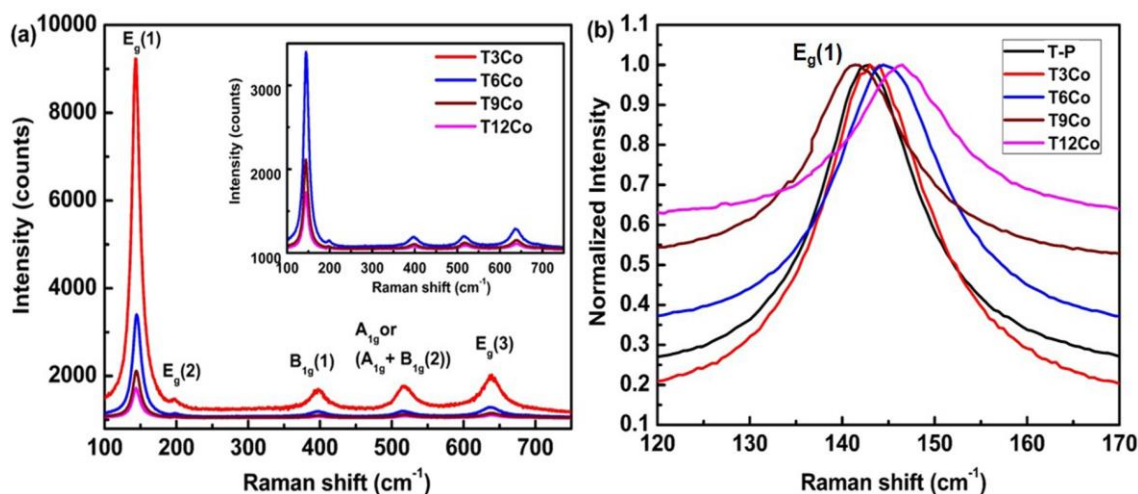
Fig.4.27. (a) Raman spectra of T3Co, T6Co, T9Co and T12Co samples. Inset shows the magnified view of Raman spectra of T6Co, T9Co and T12Co samples (b) Expanded region of $E_g(1)$ mode in the range 120-170 cm^{-1} of undoped and Co-doped TiO_2 nanocrystals.
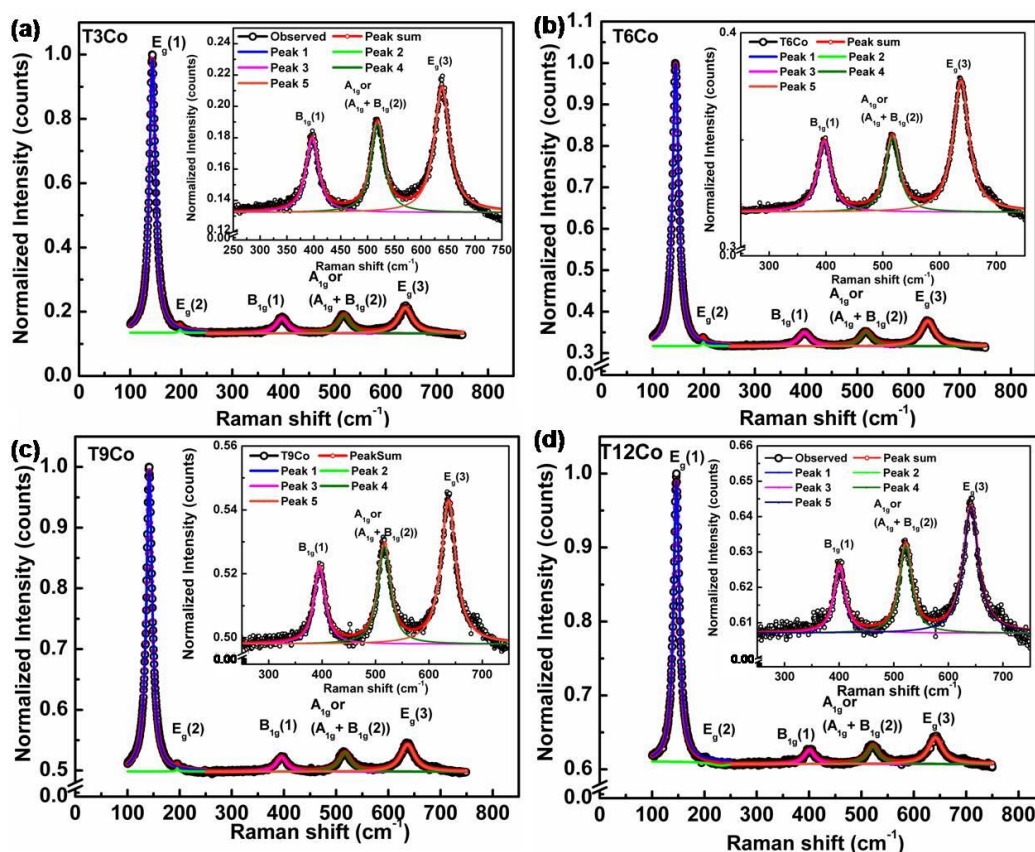
Fig.4.28. Deconvoluted Raman spectra of (a) T3Co, (b) T6Co, (c) T9Co and (d) T12Co. Inset shows the enlarged view of the Raman peaks.

C. Raman analysis of Ni-doped TiO$_2$

Raman spectra of all the Ni-doped samples have been taken at room temperature in the range 100-750 cm^{-1} and are shown in Fig. 4.29 (a). The inset shows the Raman spectra of T6Ni, T9Ni and T12Ni. It can be seen from Fig. 4.29 (a) that Ni-doped TiO$_2$ has six active Raman modes. The most intense peak near 144 cm^{-1} correspond to the E$_g$ (1) mode while the E$_g$ (2) and E$_g$ (3) modes are observed at 197 and 639 cm^{-1} respectively. No modes corresponding to any other secondary phases like NiO have been observed in the Raman spectra within its detection limit. This further confirms the incorporation of Ni into the Ti site in TiO$_2$. Defects like Ti interstitials or oxygen vacancies can be generated in Ni-doped TiO$_2$ to maintain the charge neutrality when Ni^{2+} partially replaces Ti^{4+}. The broadening of Raman lines with increasing Ni concentration is attributed to the increased disorder and destruction of ideal symmetry of the crystal.[76] More clearly, the shifting and broadening of Raman lines can be associated with nanoscale crystallite size and non-stoichiometry created due to the formation of defects leading to the phonon confinement. The broadening of the E$_g$ (1) Raman with Ni doping has been illustrated in Fig. 4.29(b) and the inset shows the variation of Raman intensity with Ni doping. Incorporation of Ni ions into TiO$_2$ host lattice is responsible for creating defects like oxygen vacancies that might have caused the shifting of the position and broadening of the Raman peak.[15,16,74] The deconvoluted Raman spectra of all the samples is shown in Fig. 4.30, which confirm the single anatase phase formation in all the samples and is corroborated with the XRD results.
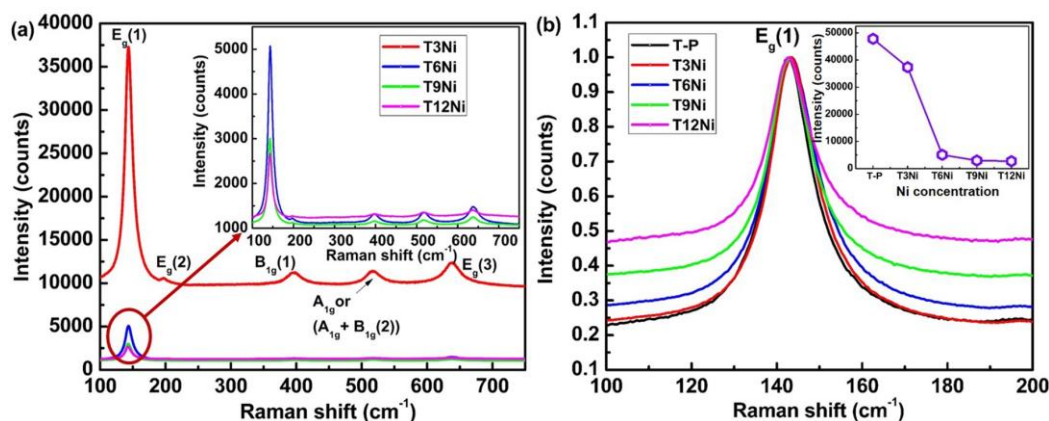
Fig.4.29. (a) Raman spectra of Ni-doped TiO$_2$. Inset shows the magnified view of Raman spectra of T6Ni, T9Ni and T12Ni (b) Expanded region of E$_g$(1) peak in the range 100-200 cm^{-1} of undoped and Ni-doped TiO$_2$ nanocrystals (inset shows the variation in Raman intensity).
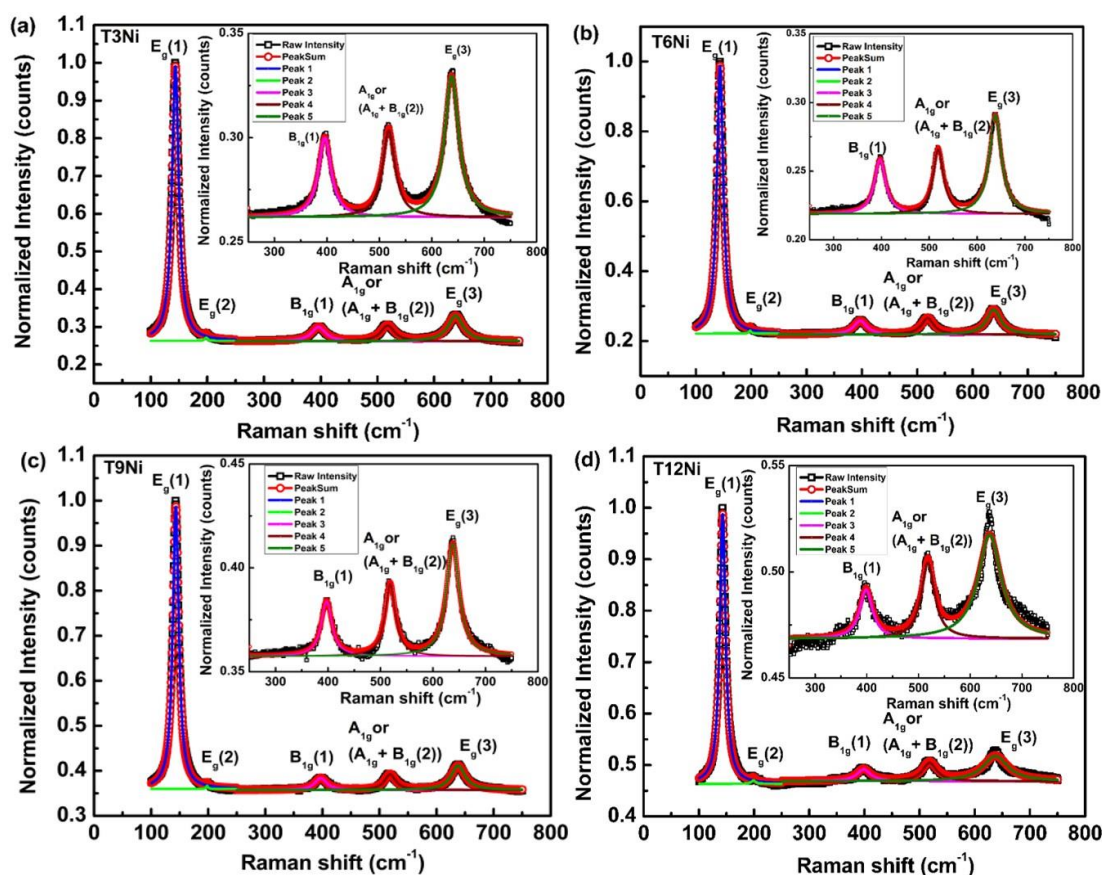
Fig.4.30. Deconvoluted Raman spectra of (a) T3Ni, (b) T6Ni, (c) T9Ni and (d) T12Ni. Inset shows the enlarged view of the Raman peaks.

4.3.2.3. Morphological analysis

Morphological analysis corresponding to Fe, Co and Ni-doped TiO₂ are discussed in the following sub sections.

A. Morphological analysis of Fe-doped TiO₂

The morphology of Fe-doped TiO₂ nanocrystals was analyzed by TEM. Typical TEM micrographs of T3Fe, T6Fe, T9Fe and T12Fe are shown in Fig.4.31 (a) – 4.31 (h). TEM has been taken for drop casted samples on C coated Cu grid. The presence of organic components in studied samples is clearly observed from TEM images, in which the amorphous regions have been shown which suggest the existence of organic residues along with crystalline TiO₂ nanomaterials. This peak might have arisen as a result of the organic radical from Ti-butoxide which is adsorbed in the nanocrystals. However, SAED is fine because the same grid with high concentration of drop casted

sample is used further to obtain good quality SAED patterns. It is clear from the TEM analysis that Fe-doped TiO₂ nanocrystals are almost spherical in shape where an agglomeration of particles is observed and the average crystallite size are ~12nm for T3Fe and ~ 6 nm for T12Fe respectively which corroborates with the result obtained from XRD analysis. Fig. 4.31 (i) - 4.31 (l) represents the HR-TEM images of T3Fe, T6Fe, T9Fe and T12Fe respectively. The HRTEM micrograph of T3Fe (Fig. 4.31 (i)) shows planes (101) and (004) corresponding to anatase TiO₂ and the interplanar spacing of (101) plane of T3Fe is about 0.36 nm. The lattice planes corresponding to (101), (004) of T6Fe, (101), (200) of T9Fe and (101), (004) of T12Fe
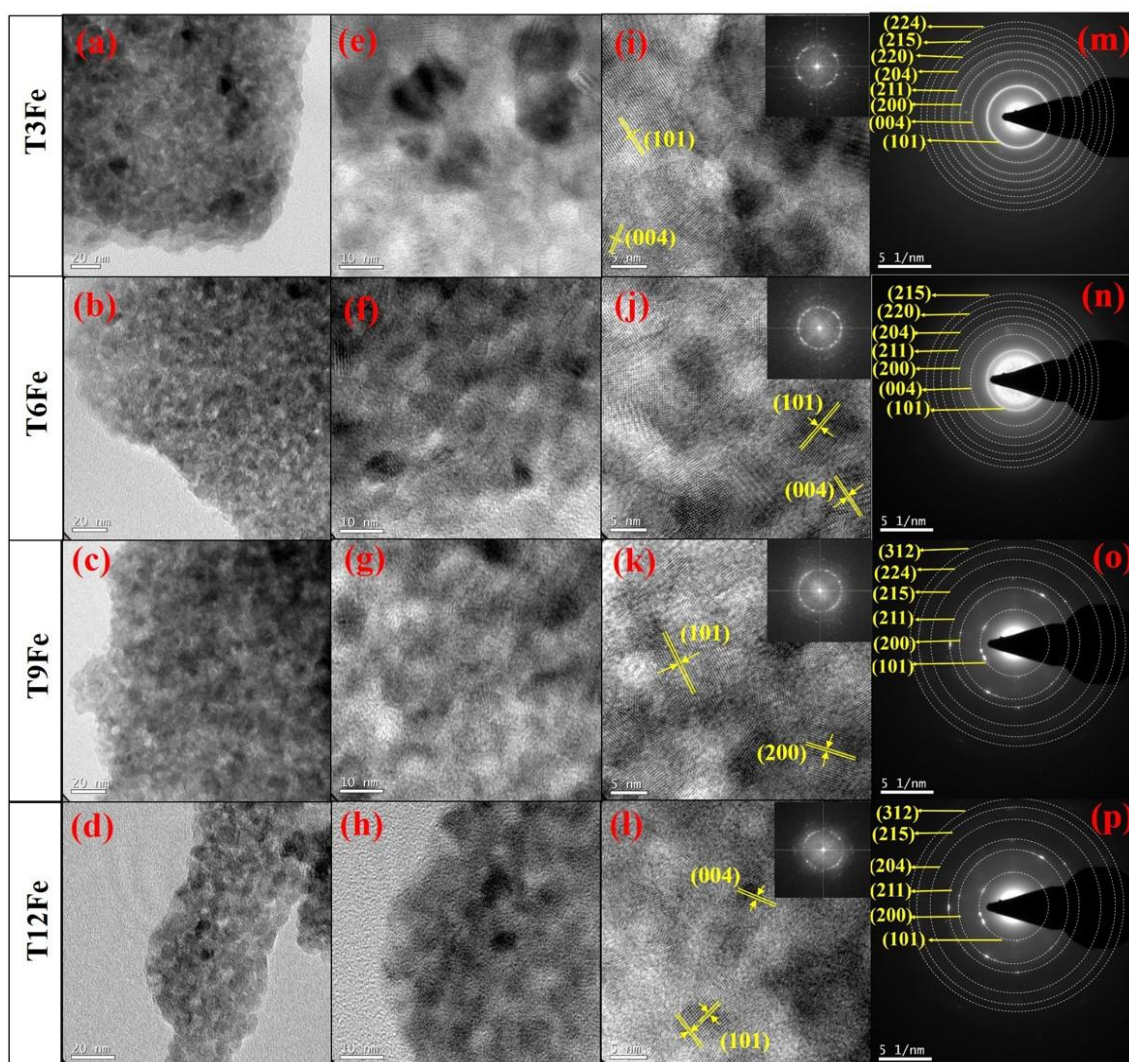
Fig.4.31. Fe doped TiO₂ (a-h) TEM images (i-l) High resolution images of the Fe-doped samples with FFT and (m-p) corresponding SAED patterns of T3Fe, T6Fe, T9Fe and T12Fe

shown in Fig. 4.31 (j - l) respectively, suggest that the interplanar spacing of (101) plane of all the samples are systematically decreasing in comparison with that of T3Fe and undoped sample. The d spacing value of all the samples determined from HR-TEM analysis is well matched with the results obtained from XRD measurements. The FFT of all the Fe-doped samples is given in the insets of Fig. 4.31 (i-l). Hence, from the HR-TEM analysis, it can be inferred that the fringe spacing (d) for anatase (101) planes systematically decreases from 0.36 nm for T3Fe (Fig. 4.31 (i)) to 0.32 nm for T12Fe (Fig. 4.31 (l)). These results can be validated with the fact that Fe^{3+} ions residing in the prepared TiO_2 samples substitutionally, creates a lattice contraction where the radius of Fe^{3+} (0.56 nm) is smaller than Ti^{4+} (0.61 nm). SAED patterns depicted in Fig. 4.31 (m)-4.31 (p) reveal the polycrystalline nature of the doped samples. The lattice planes were estimated from the inter-planar spacing using Image J software. All the planes were indexed to the tetragonal anatase phase of TiO_2. These results are concordant with the Raman results as well, as discussed earlier.

B. Morphological analysis of Co-doped TiO₂

TEM images of Co-doped TiO_2 powders are shown in Fig. 4.32 (a-d). The particles observed here are almost spherical in shape and agglomeration of particles can be seen in all the samples with an average size in the range 10-20 nm which agrees well with the particle size derived from XRD data.

The HR-TEM images (Fig. 4.32 (i-m)) clearly show the crystalline nature of the samples with lattice fringes corresponding to different planes like (101), (200), (004) planes of tetragonal anatase phase of TiO_2. Insets in Fig 4.32 (i-m) show the FFT pattern taken on all the samples which again confirm the crystalline nature of all the samples. SAED patterns taken on all the Co-doped samples show clear distinct rings corresponding to different planes of tetragonal anatase TiO_2 structures were similar to the planes obtained in XRD which indicate the formation of polycrystalline anatase TiO_2.
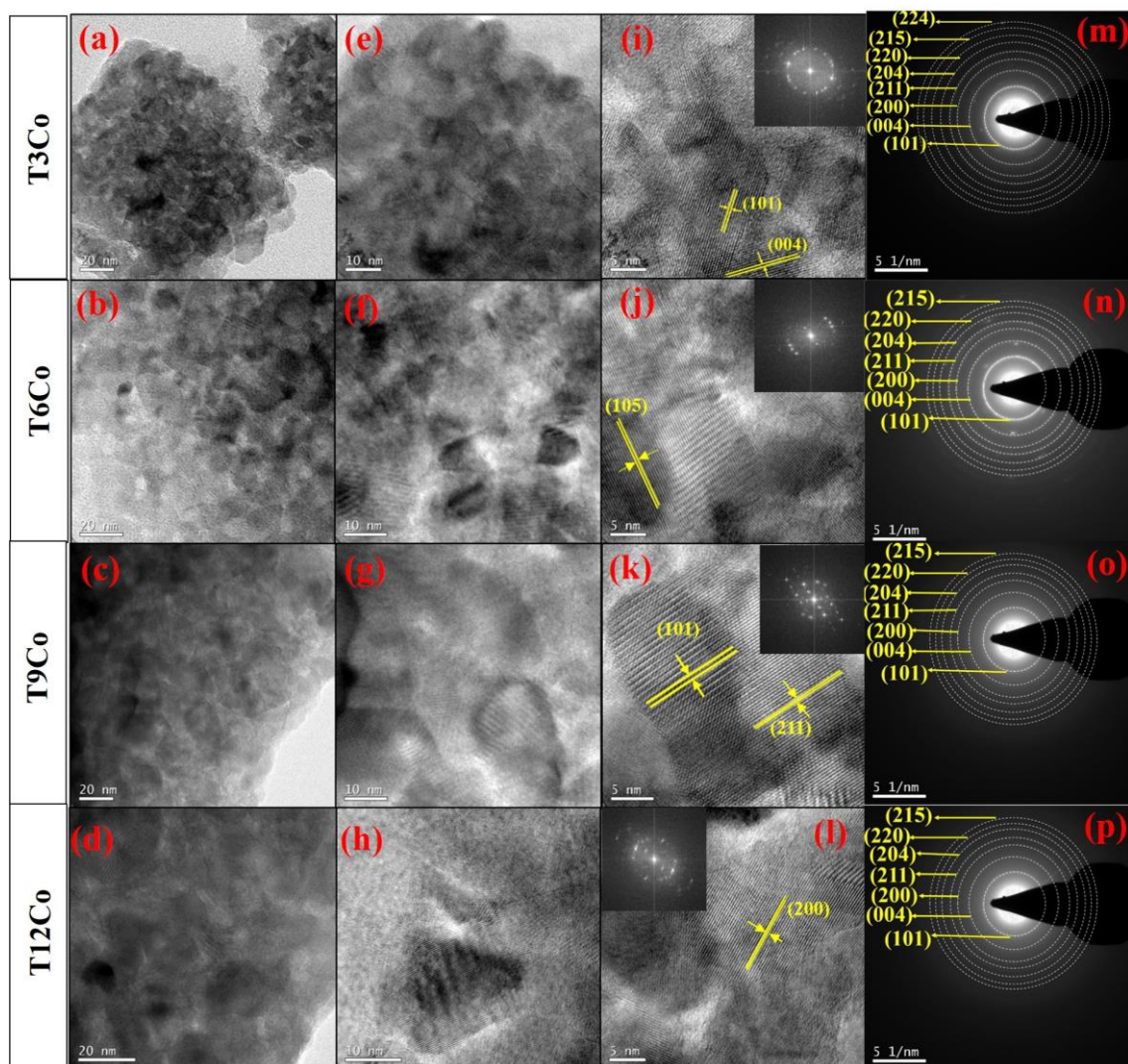
Fig.4.32. Co-doped TiO₂ (a-h) TEM images (i-l) HR-TEM images showing lattice fringes with FFT shown in the inset and (m-p) SAED patterns of T3Co, T6Co, T9Co and T12Co

C. Morphological analysis of Ni-doped TiO₂

TEM micrographs of Ni-doped TiO₂ nanocrystals are shown in Fig. 4.33 (a-h). Agglomeration of particles can be seen in all the samples with an average size of 10-15 nm which confirms with the crystallite size obtained from the Scherrer equation. The high-resolution TEM images (Fig. 4.33 (i-l)) indicate the crystalline nature of the samples and the lattice fringes corresponding to different planes has been indexed with (101), (004), (200), (101) and (211) planes of tetragonal anatase phase of TiO₂. Insets of Fig 4.33 (i-l) show the corresponding FFT which again confirm the crystalline nature of all the samples. SAED patterns of Ni-doped samples show a polycrystalline nature with

distinct rings corresponding to the different planes of tetragonal anatase TiO_2 as shown in Fig 4.33 (m-p).
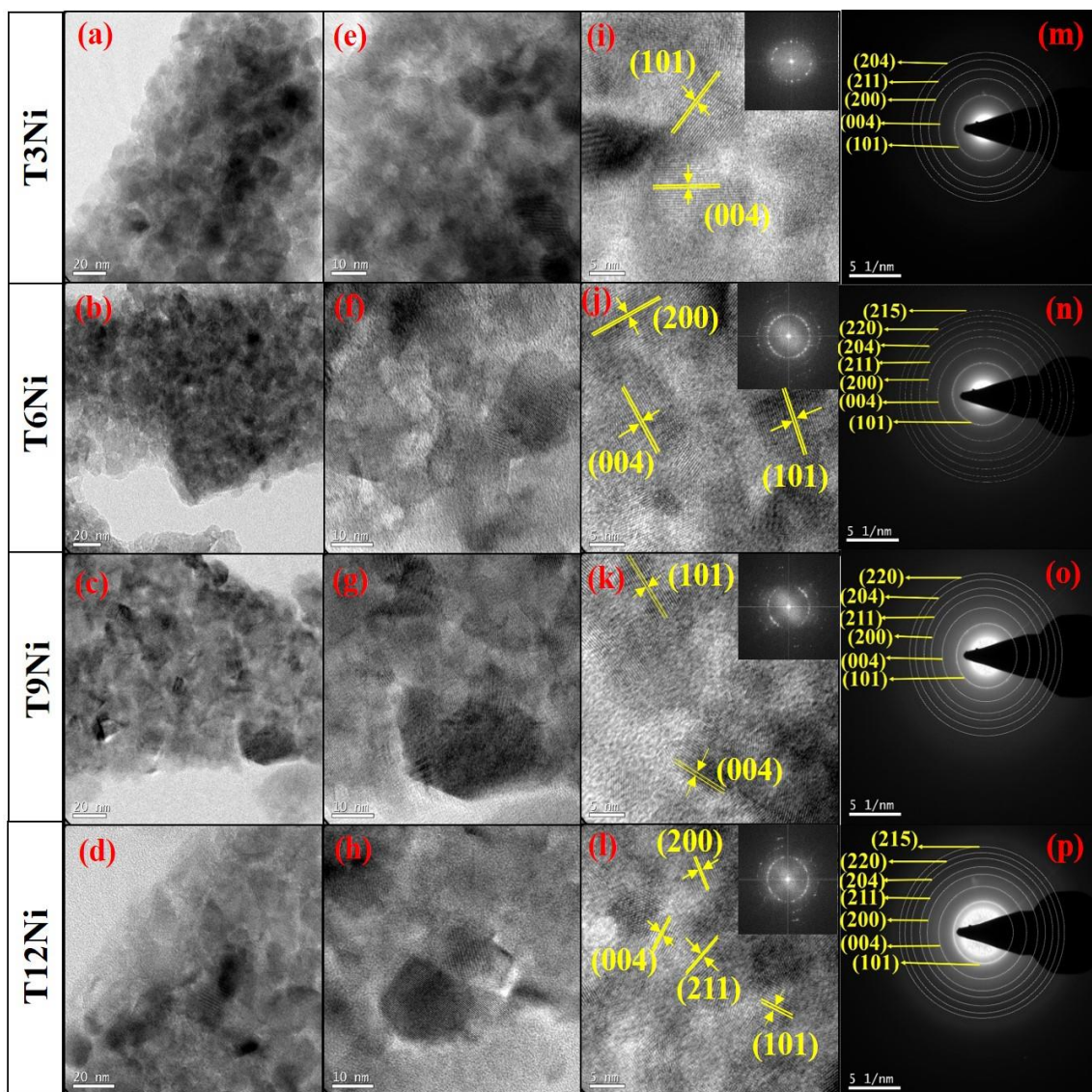
Fig.4.33. Ni-doped TiO_2 nanocrystals (a-h) TEM images (i-l) HR-TEM images showing lattice fringes with FFT shown in the inset and (m-p) SAED patterns of T3Ni, T6Ni, T9Ni and T12Ni.

4.3.2.4. FT-IR spectroscopy

FT-IR spectra corresponding to Fe, Co and Ni-doped TiO_2 are discussed in sub sections A, B and C repectively.

A. FT-IR spectroscopy of Fe-doped TiO₂

FT-IR spectra have been recorded for all the Fe-doped samples at room temperature to investigate more on the vibrational bands of Fe: TiO_2 system for metal-oxygen bond and its variation as a result of dopant ion contribution. The additional structural information obtained using FT-IR spectra is represented in Fig. 4.34. The less intensity peak located near 2360 cm^{-1} shown in Fig. 4.34 originates from CO_2 molecules present in the air.[78] It is well reported that the major bands corresponding to 400–700 cm^{-1} are originating from the vibration modes of TiO_6 octahedra.[21]
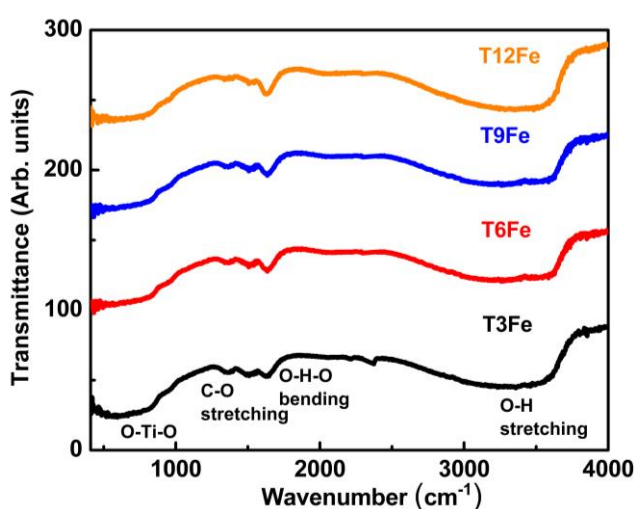
Fig.4.34. FT-IR spectra of Fe-doped TiO₂ nanocrystals

Among the different bands present in the spectra, a broad band observed near to 3500 cm^{-1} resulted from the stretching vibration of OH groups and could be attributed to the OH groups associated with the Ti atoms, i.e., Ti–OH. The characteristic bending vibrations of H–O–H can be represented by the narrow band near to 1650 cm^{-1}. The peak close to 1400 cm^{-1} is attributed to the C-O stretching bond present in Ti butoxide that contributes to agglomerated morphology as discussed earlier. More clearly, this peak can be associated with the organic radical from Ti- butoxide which is adsorbed in the synthesized nanocrystals. The band centered at nearly 550 cm^{-1} are due to bonding among metal and oxygen, i.e., metal-oxygen bonds of (Ti-O, Fe-O) for Fe-doped TiO₂ nanocrystals. Again, these results holds good agreement to most of the previous reports.[79] Furthermore, neither the peak corresponding to any other oxide phases of doped elements appeared in the spectra. Hence, the FT-IR spectra further reveal that Fe

ions are introduced into the Ti framework. This result corroborates with the results of XRD, Raman, TEM, and ED-XRFS as mentioned earlier.

B. FT-IR spectroscopy of Co-doped TiO₂

Fig. 4.35. shows the FT-IR spectra in transmission mode taken on Co-doped TiO_2 nanopowders. The IR band around 3600 cm^{-1} corresponds to O-H stretching vibration and the band around 1628 cm^{-1} attributes to H-O-H bending vibration of adsorbed atmospheric water on sample surface.[80] The band around 847 cm^{-1} corresponds to anatase TiO_2 and is attributed to Ti-O-Ti stretching vibration.[81] The shifting of band position around 847 cm^{-1} indicates the presence of defects especially oxygen vacancies due to Co incorporation in TiO_2 lattice.
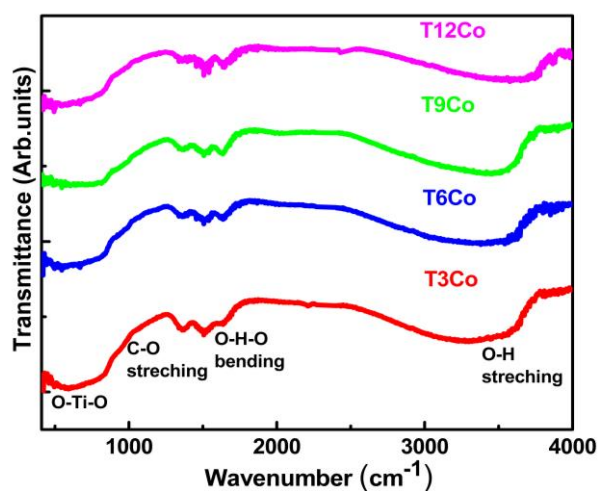
Fig.4.35. FT-IR spectra of Co-doped TiO₂ nanocrystals

C. FT-IR spectroscopy of Ni-doped TiO₂

Fig. 4.36 shows the FT-IR spectra of Ni-doped TiO_2 nanocrystals. The spectra of all samples are identical which indicates that increasing Ni concentration has no effect on nature of bonding present in the host material. The symmetric and antisymmetric stretching vibrations of a single-bond OH functional group are represented by the broadband around 4000–3200 cm^{-1}.[82] It is well reported that bending vibrations associated with the hydroxyl functional group appear between 1700 and 1300 cm^{-1} [80] and this arises as a result of adsorbed atmospheric water on the sample surface. A large hump around 847 cm^{-1} is attributed to the anatase TiO_2 and is due to stretching vibration

associated with the Ti-O-Ti bonding.[81] The shifting and broadening of band position corresponding to 847 cm^{-1} validate the presence of defects which arise as a result of oxygen vacancies owing to Ni incorporation in TiO$_2$ lattice. The presence of the different functional groups is associated with the organic solvents used in the synthesis procedure.
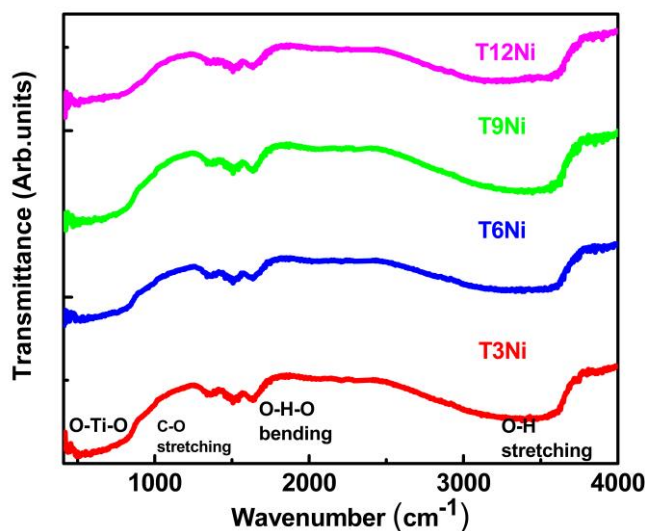
Fig.4.36. FT-IR spectra of Ni-doped TiO$_2$ nanocrystals

4.3.2.5. Optical spectroscopy results

UV-visible spectra and photoluminescence studies of Fe, Co and Ni-doped TiO$_2$ are discussed in the following sub sections.

A. UV-Visible and Photoluminescence analysis of Fe-doped TiO$_2$

UV-visible studies of the prepared samples are shown in Fig. 4.37 (a). All the samples are showing a clear red shift and a considerable visible region absorption is also observed. By increasing the Fe concentration, a considerable band gap narrowing is observed and is depicted in Fig. 4.37 (b). For undoped TiO$_2$, 380 nm absorption was attributed mainly due to the electronic transition from O and Ti orbitals, whereas a clear red shift of all the doped TiO$_2$ nanocrystals can be attributed to the exchange interactions.[58] A linear fit is employed to (αhυ)$^{1/2}$ and hυ plot to estimate the band gap of all the samples as given in Fig.4.37 (b). The estimated band gap of T-P was found to

be 3.30 eV,[58] whereas band-gap of T3Fe, T6Fe, T9Fe and T12Fe are 2.30 eV, 1.89 eV, 1.80 and 1.76 eV respectively. It is reported that the formation of Ti interstitials are mainly due to the synthesis conditions and heat treatment in the presence of air.[83] The Ti interstitial peak intensity is expected to be almost similar for all the samples as the calcination temperatures for all remains the same. Since higher calcination temperatures could promote the rutile phase formation, there is a high chance of having defect contribution as a result of structural transformation. Hence, from the absorption spectra, it is understood that the absorption edge of undoped TiO₂ material is near 380 nm, whereas the red shift associated with the Fe-doped samples may be arising as a result of surface trap centres generated by oxygen vacancy defect sites of Ti^{3+}, Fe^{2+}/Fe^{3+} or sp–d exchange interactions of the Fe^{2+}/Fe^{3+} ions residing at Ti^{4+} site and the band electrons resulting in a significant band gap narrowing. Band gap narrowing is attributed to the presence of localised defect states in TiO₂ which are responsible for the absorption tail in the absorption spectra which extends into the forbidden gap. This absorption tail is called Urbach tail and is associated with Urbach energy.[84,85] The Urbach energy estimation could be carried out by using the following relation;

$$\alpha = \alpha_0 + \exp(\frac{E}{E_u})$$
(4.9)

Here, α represents the absorption coefficient, E denotes photon energy and can be equated to hυ and E_u is considered as the Urbach energy.[84, 85] The Ln (α) versus E plot can effectively provide the Urbach energy and the reciprocal value of the slope of linear fit corresponding to Ln (α) versus E plot, below the optical band gap region, provides the Urbach energy, E_u.

The increase of Fe concentration yields an increase in Urbach energy as shown in Fig.4.38 indicating an increase in the number of oxygen vacancies with Fe substitution. This could be due to the oxygen vacancy defects present in the TiO₂ lattice with increased Fe concentration to maintain charge neutrality.[86] These localized defect states associated with Fe-doped TiO₂ is the reason behind lowering of band gap to 1.79 eV for T12Fe sample. More clearly, more number of defect states is created due to the

occurrence of additional oxygen vacancies in the system that perturbs the band structure, thus resulting in a significant band gap reduction.
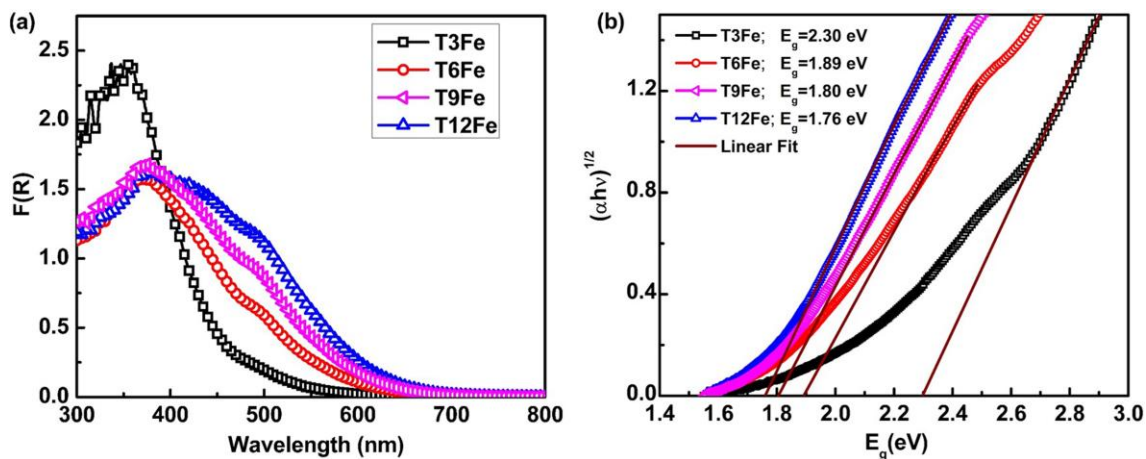
Fig.4.37. Fe-doped TiO_2: (a) UV spectra and (b) Tauc's plot
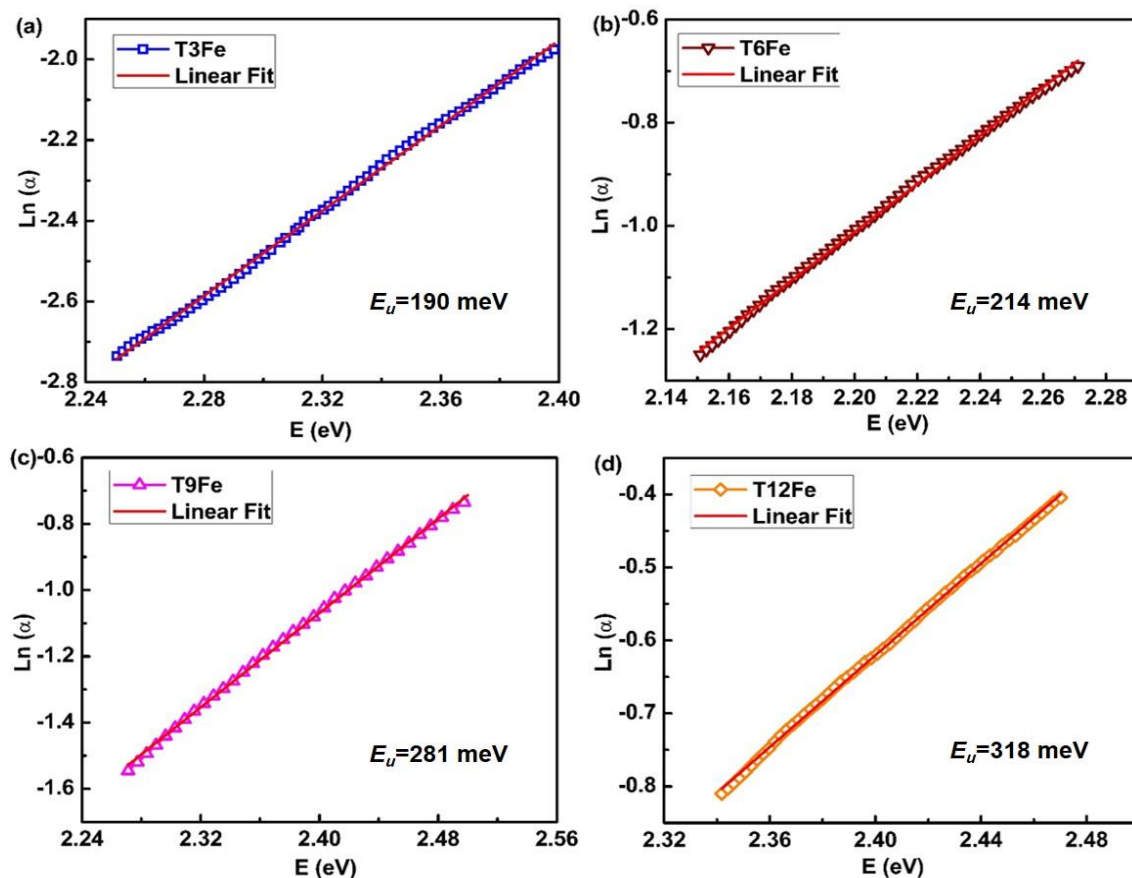
Fig.4.38. Plot for Urbach energy estimation of (a) T3Fe, (b) T6Fe (c) T9Fe and (d) T12Fe

To understand more information regarding the defects associated with Fe-doped TiO$_2$, emission spectra have been recorded. Fig. 4.39 (a) represents the PL spectra obtained at room temperature for all the samples with an excitation wavelength of 325 nm. A broad peak is noticed for all the samples which could be attributed to the STEs and defects associated with oxygen vacancy states in TiO$_2$.[28] To have a detailed understanding regarding the origin of broad PL emission, the peaks are deconvoluted for all the samples which are depicted in Fig.4.39 (b), (c), (d) and (e) respectively. The broad emission peak observed for all the samples is fitted properly with five Gaussian bands located at 390 nm, 450 nm, 500 nm, 550 nm and 600 nm as represented in the Fig. 4.39 (b) – (e). Near band edge emission of host TiO$_2$ may be responsible for the emission peak located near 390 nm. STE, defects associated with oxygen vacancies and other surface defects could be the reason for observed emission peaks at 400 nm and 450 nm.[28] The doping of Fe at Ti site results in the formation of Fe^{2+}/Fe^{3+} leading to the creation of oxygen vacancies. Due to the defect sites, F-centre formation will be facilitated and further, electrons occupied here will try to interact with the adjacent Ti^{4+} and provides Ti^{3+}-ions and F^{+}-centres which is clearly demonstrated in T3Fe as shown in Fig. 4.39 (b).[55] Hence, the peak observed at 489 nm may be due to Ti^{3+} to TiO$_6$$^{2-}$ charge transition, directly related to oxygen vacancies and the 520 nm emission could be due to the formation of F^{+}-center. Upon increasing the concentration of Fe ions, the incorporation of Fe^{2+}/Fe^{3+} into the Ti^{4+} substitutional site generates more number of vacancies at oxygen sites. Therefore, oxygen vacancies associated with Fe substitution is ultimately reflected in the emission spectra of T6Fe, T9Fe and T12Fe. Fig. 4.39 (f) shows the integrated PL intensity which clearly demonstrates a decreasing nature for higher Fe dopant concentration which could be due to the formation of more number of Fe^{2+}/Fe^{3+} ions which is to be further validated by the XPS measurement. Introducing Fe metal ions in to TiO$_2$ lattice shows a decreasing trend in the PL intensities; specifically as a result of shorter distance correspond to the inter-band metal ions that could lead to an energy transfer among nearby ions. As a result of which, a concentration quenching process is expected to be exhibited by the system which is a non-radiative decay process. As in the case of T12Fe, it is observed that PL intensity is much lower in comparison to other samples which suggest increased separation rates of photo-induced

charges and there is more chance for observing a band-gap narrowing as depicted in Fig. 4.37 (b) which is in accordance with the PL results.[87] As shown in Fig 4.39 (a), the comparison among the PL spectra of the entire doped samples exhibit a significant reduction in PL intensity, which is more evident for T12Fe in comparison to that of T9Fe. Hence, the PL spectrum of T12Fe is much broader with decreased intensity among all the other samples and this could be the reason for slight blue shift in the 390 nm peak for T12Fe.
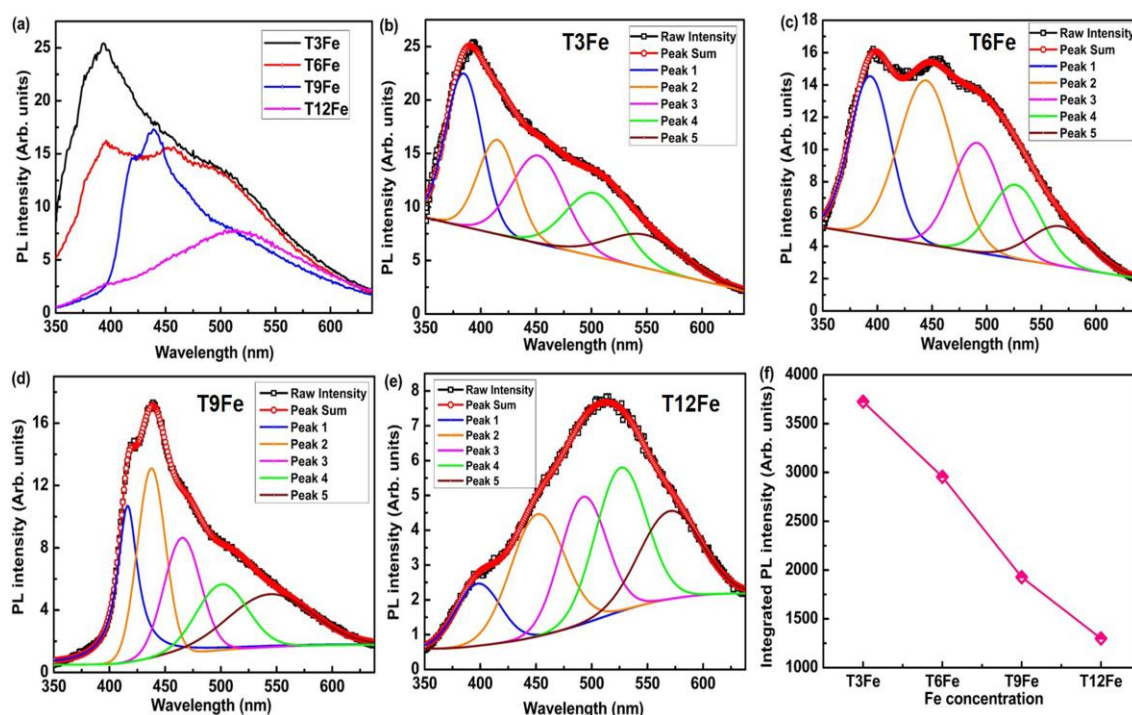
Fig.4.39. PL spectra of Fe-doped nanocrystals (a) PL spectra of all the samples (b) T3Fe (c) T6Fe (d) T9Fe (e) T12Fe samples and (f) Integrated PL intensity vs Fe concentration

B. UV-Visible and Photoluminescence analysis of Co-doped TiO₂

The absorption spectra of Co-doped samples are shown in Fig. 4.40 (a). The absorption spectra of Co-doped sample show shifting of the absorption edge towards visible region. The red shift of absorption edge due to the incorporation of Co ions in TiO₂ has been reported to be due to sp-d exchange interactions between band electrons and localized d electrons of dopant ions. The s-d and p-d exchange interactions result in downward shifting of conduction band edge and upward shifting of valence band edge due to which narrowing of bandgap occurs[1,27, 80]. Again, all the Co-doped samples show

a decrease in absorption in UV region and an increase in absorption in the visible region in comparison to undoped sample. Also, the Co-doped samples show a broad peak in the visible region. The broad absorption in the visible region in Co-doped samples is due to ligand field transition of Co^{2+} in octahedral coordination.[88] In anatase TiO_2, Ti^{4+} is surrounded by six oxygen ion O^{2-} forming TiO_6^{2-} octahedron.

In Co-doped TiO_2, with the substitution of Co^{2+}/Co^{3+} on Ti^{4+} site, the Co^{2+}/Co^{3+} will experience strong crystal force due to surrounding oxygen ions. Due to this strong crystal field interaction, especially the d-band states of Co^{2+} will split into ground and excited states giving rise to d-d electronic transition which falls in the visible region. This is a strong indication of Co^{2+} substitution for Ti^{4+} in TiO_2 lattice whereas Co^{3+} will not exhibit any d-d electronic transition while splitting into ground and excited states. The bandgaps of Co-doped samples were found out from Tauc's plot given in Fig. 4.40 (b) from which a reduction of bandgap to 2.24eV in T12Co sample is observed. In the case of T9Co and T12Co, the band gap values are close which corroborates with the intensity variation in PL spectra which is discussed in the coming section. It is expected that beyond certain dopant concentration it is very difficult to induce a drastic reduction in band gap and other associated properties and hence the dilute concentration of an impurity can tailor the material properties in a better way.

To further elucidate the nature of defects, PL studies were performed on all the samples and are shown in Fig.4.41 (a). All the PL spectra have been recorded for an excitation wavelength of 325 nm. Fig.4.41 (b) shows the deconvolution of PL spectrum of T3Co sample. The emission peak around 390 nm, 400-450 nm, 489 nm, 520 nm and around 600 nm can be ascribed to the near band edge emission of host TiO_2, due to STE, due to charge transition from Ti^{3+} to TiO_6^{2-} linked with oxygen vacancies, F^+-centre and due to OH species respectively as discussed earlier in section 4.3.1.4.[28,29] The presence of OH species is detected in the FT-IR spectra as shown in Fig.4.35.
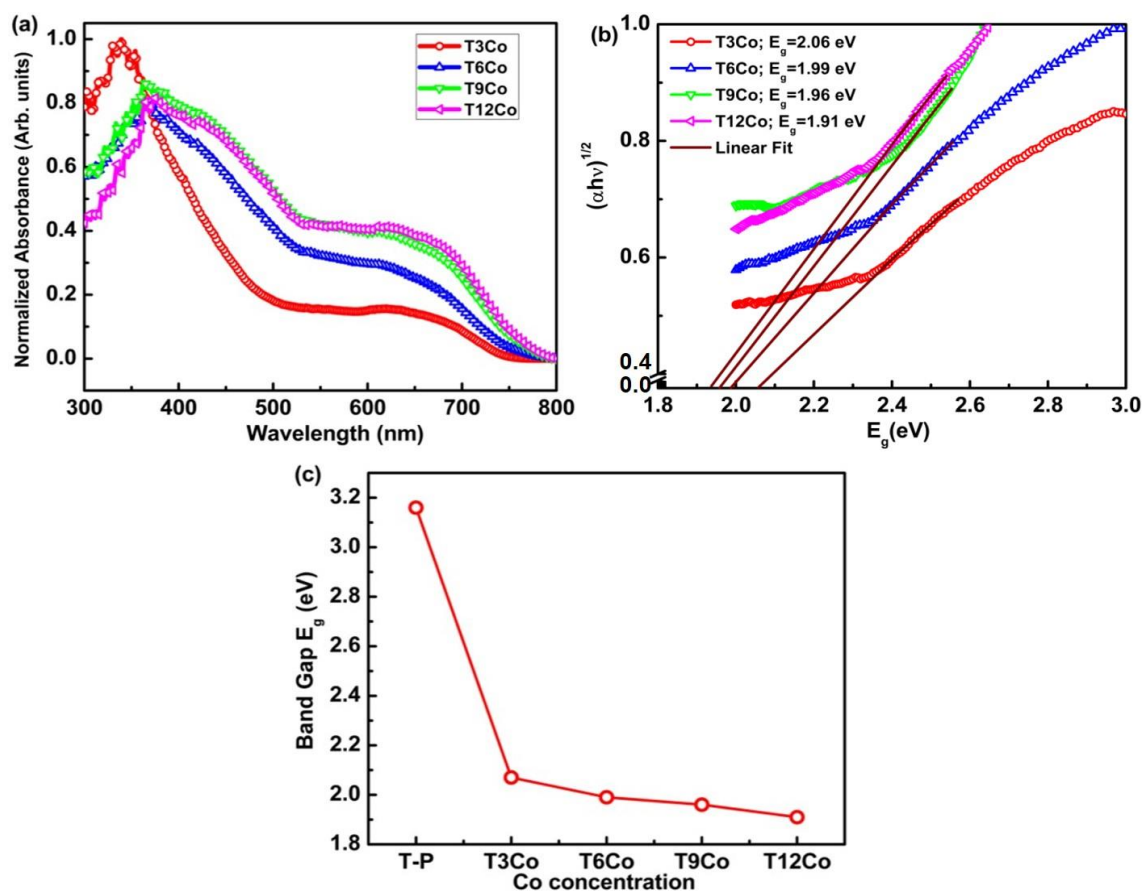
Fig.4.40. Co-doped TiO₂ nanocrystals (a) solid-state UV spectra and (b) Tauc's plot and (c) Observation of narrowed band gap with Co substitution.
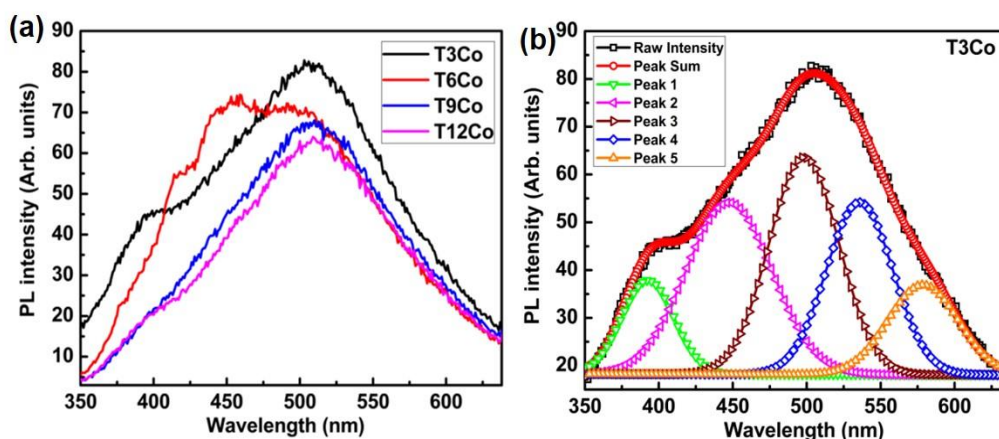
Fig.4.41. PL spectra of (a) Co-doped TiO₂ nanocrystals (b) Peak fitted PL spectra to T3Co

C. UV-Visible and Photoluminescence analysis of Ni-doped TiO₂

The UV-Visible absorption spectra of Ni- doped samples are shown in Fig. 4.42 (a). The absorption spectra of Ni-doped samples show a slight red shift which could be due to sp-d exchange interactions between the band electrons and the localized d

electrons of Ni^{2+} ions. The band-gaps of Ni-doped samples were estimated from Tauc's plot and is given in Fig. 4.42 (b). The ligand field transition of transition metal ions can cause a broad absorption in the visible region and in the present case the ligand field transition is due to Ni^{2+} in octahedral coordination. In Ni-doped TiO_2, when Ni^{2+} tries to occupy on Ti^{4+} site, a strong crystal force will be experienced by the Ni^{2+} as a result of oxygen ions surrounding it. As a result of this, the d-band states of Ni^{2+} split into ground and excited states by promoting d-d electronic transitions in the visible region. This concept strongly suggests the incorporation of Ni^{2+} in TiO_2 lattice and the existence of Ni^{2+} is validated from the XPS analysis which is discussed in the later sections.
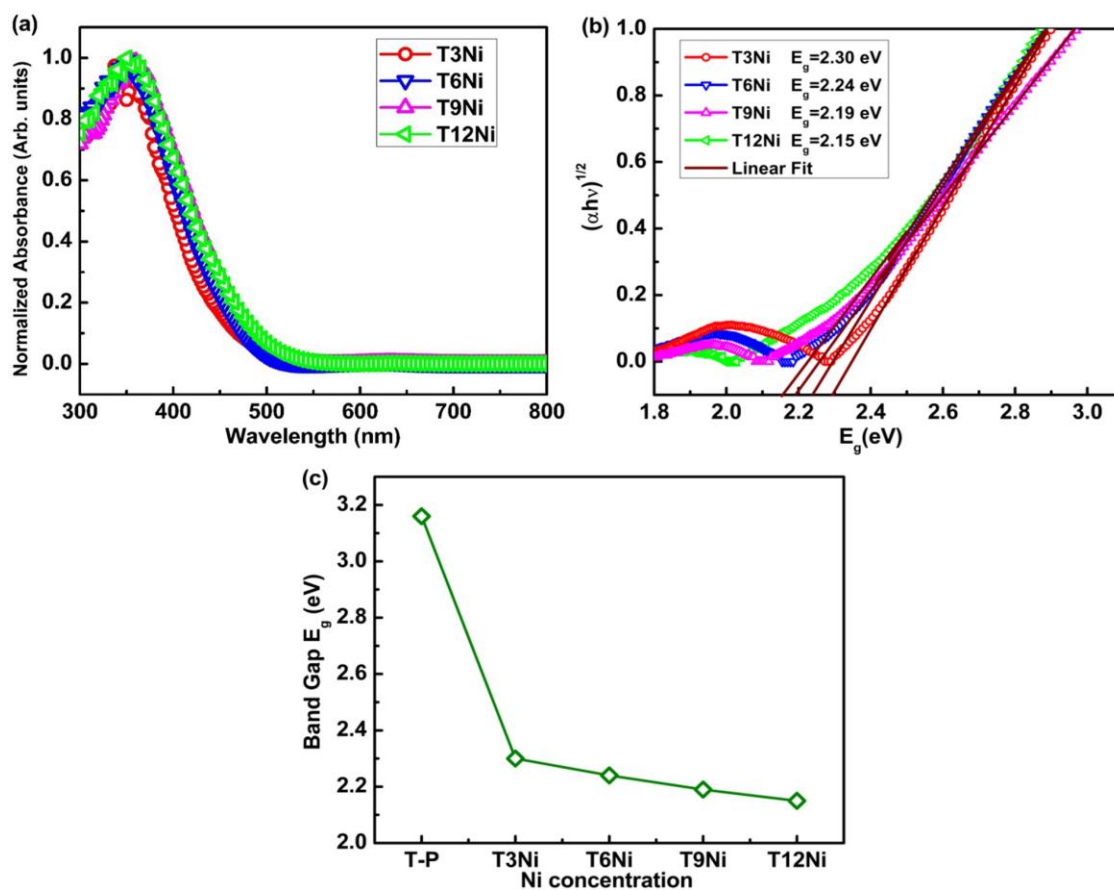
Fig.4.42. Ni-doped TiO_2 nanocrystals (a) solid-state UV spectra and (b) Tauc's plot and (c) Observation of narrowed band-gap with Ni substitution

The calculated band-gap of Ni-doped TiO_2 decreases significantly from 3.16 eV in undoped sample to 2.30, 2.24, 2.19 and 2.15 eV upon 3, 6, 9 and 12% Ni doping, respectively which could be attributed to the introduction of new electron states in the band structure of TiO_2 upon Ni doping and is shown in Fig. 4.42 (c). The band-gap

narrowing with Ni doping can be explained on the basis of oxygen vacancies produced as a result of doping. Both doping and oxygen vacancy together could decrease the band-gap where doping can induce a high vacancy concentration which forms a vacancy band just below the conduction band and the oxygen vacancy can narrow the band-gap by forming a miniband just below the conduction band.[89-91]

Fig. 4.43 (a) shows the PL spectra of Ni-doped samples, which have been recorded for an excitation wavelength of 325 nm. The deconvoluted PL spectra are shown in Fig.4.43 (b)-(e) which corresponds to T3Ni, T6Ni, T9Ni and T12Ni respectively. The emission peaks observed for all the Ni-doped samples are in the range 375 – 600 nm. A clear red shift is observed for all the samples with Ni-doping which is evident from the deconvoluted spectra. The first emission peak is considered as Peak 1 and rest towards higher wavelength is nomenclatured as Peak 2, Peak 3, Peak 4 and Peak 5 respectively where Peak 1 and Peak 2 are attributed to the near band edge emission of host TiO_2 and the formation of STE respectively along with other defects associated with the system.[28,29] Oxygen vacancies are intrinsic defects present in TiO_2 and Ni doping induces additional oxygen vacancies due to the substitution of Ni^{2+} at the place of Ti^{4+} may be responsible for the emissions corresponding to Peak 3. With Ni substitution, Peak 3 is shifting towards right and falls in the green emission which is a clear indication of additional oxygen vacancies created due to higher Ni concentration. In general, oxygen vacancy defects in most oxide systems contribute to green luminescence as observed in the case of higher Ni concentration and the blue emission observed for lower Ni concentration sample may be due to the decreased oxygen vacancies and much lower excitation wavelength in comparison to other oxide systems.[92] The Peak 4 might have appeared due to the F^+-centre formation and the OH group arising from Ti-butoxide creates an acceptor level near the valence band and contributes to the occurrence of Peak 5.[55] The variation of integrated PL intensity with Ni concentration is shown in Fig. 4.43 (f). Further, addition of transition metal ions in to TiO_2 lattice could successfully decrease the PL intensities, due to shorter distance of inter band metal ions, which is leading to an energy transfer between nearby ions.[87] Therefore, it can be suggested that the defect concentration and associated optical properties of samples can be effectively evaluated by means of PL measurements.[87,88]
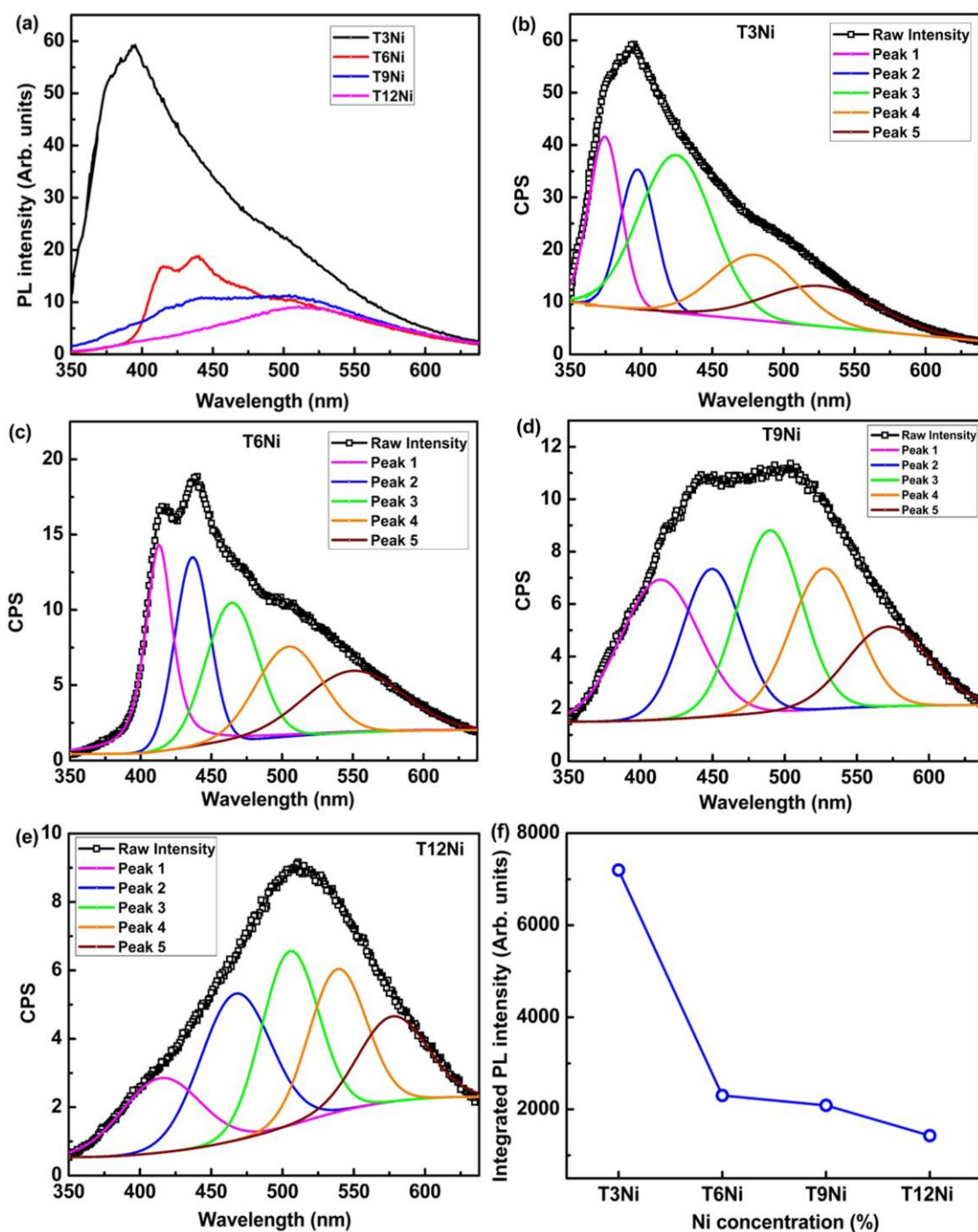
Fig.4.43. PL spectra of (a) T3Ni, T6Ni, T9Ni and T12Ni (b) deconvoluted PL spectra of T3Ni, (c) T6Ni, (d) T9Ni, (e) T12Ni and (f) Variation of integrated PL intensity with Ni doping

4.3.2.6. Magnetic studies

Magnetic studies of Fe, Co and Ni-doped TiO₂ nanocrystals are discussed in detail and is provided in the sub sections given below.

A. Magnetic studies of Fe-doped TiO$_2$

The M-H curves of Fe-doped TiO$_2$ nanocrystals at 300 K are shown in Fig. 4.44 (a) where a PM behavior is observed for all the samples. The low temperature M-H curves of all samples at 2 K is also shown in Fig. 4.44 (b). It is interesting to observe weak FM in undoped and T3Fe sample especially at lower field M–H measurements as depicted in Fig. 4.44 (c). The inset of Fig. 4.44 (c) shows the comparison of H$_C$ and retentivity of undoped compound and T3Fe sample which suggests a decrease in H$_C$ from 320 Oe to 70 Oe and an increase in retentivity from 4 x 10^{-4} μ$_B$/F.U. to 7.2 x 10^{-4} μ$_B$ /F.U. Magnetization is increased with Fe content which is expected due to the magnetic contribution from Fe ions. The variation in H$_C$ of all the samples is represented in Fig. 4.44 (d) which shows an H$_C$ of 70 Oe for T3Fe sample.
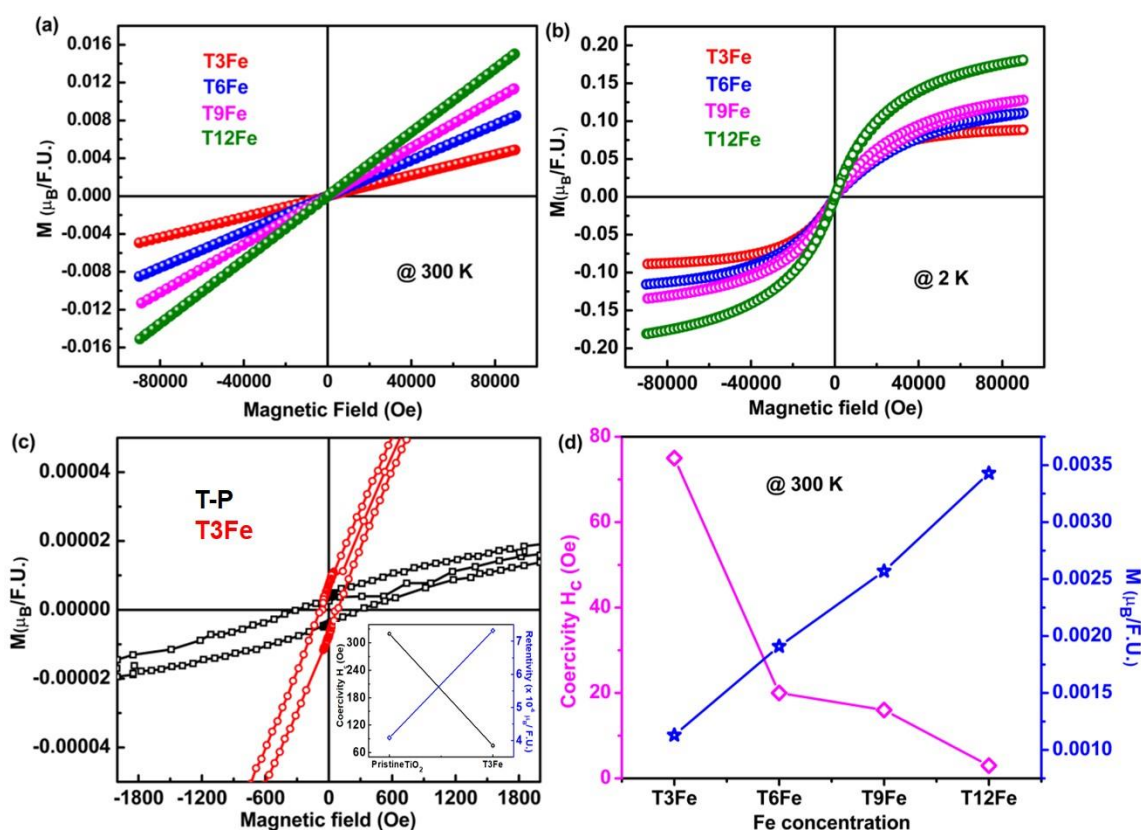
Fig.4.44. Magnetic response of Fe-doped TiO$_2$ nanocrystals (a) at 300K and (b) at 2 K (c) comparison of coercivity and retentivity of undoped TiO$_2$ and T3Fe (d) Variation of Hc and magnetic moment at 2 Tesla

There is a systematic decrease in the H_C value of T6Fe, T9Fe and T12Fe samples along with an enhancement in the net magnetic moment which indicates the perfect PM behavior in these samples. RTFM is expected in TiO₂ system with magnetic impurity doping which is due to the FM nature of Fe elements. A lot of reports on the origin of FM behavior due to magnetic impurity clusters, exchange coupling among magnetic ions and the charge carriers trapped by oxygen vacancies are discussed earlier. PM or AFM behavior is also reported[42] due to magnetic impurity doping which exhibited the suppression of FM in TiO₂, originating due to the segregation of elemental oxides. In the present case, XRD and Raman measurements reveal the absence of any secondary phases associated with Fe or Fe related oxides. The weak FM behavior exhibited by undoped TiO₂ which was understood to be arising as a result of intrinsic defects like oxygen vacancies/Ti^{3+} ions or Ti interstitials. The presence of weak RTFM in T3Fe similar to the undoped sample with a slight enhancement in magnetization reveals that the FM contribution cannot be exclusively from intrinsic factors. It is observed that upon increasing Fe ion concentration, the magnetization also shows some enhancement in terms of magnetic moment as shown in Fig. 4.44 (d), where a sufficient decrease in H_C value demonstrate an interaction of oxygen vacancy defects with Fe^{2+}/Fe^{3+} ions in different ways promoting PM interactions and FM ordering has been lost as a result of higher concentration of Fe ions. Further, as a representative of the series, temperature dependent magnetization data of undoped, 3% and 12% Fe doped samples have been recorded at 200 Oe and Curie-Weiss fit have been carried out which is provided in Appendix A (Fig.A2 (a) - (f)). There is no PM-FM transition in the temperature range 2 K - 300 K. Further, instead of a perfect paramagnetic behavior, there could be a mixed magnetic interaction as evident from Curie-Weiss fit. The 3% Fe doped sample shows a Weiss temperature of nearly 63 K and weak FM behavior is specifically due to the electrons trapped in the defect centers and BMP interactions.

B. Magnetic studies of Co-doped TiO₂

The M-H measurements Co-doped TiO₂ nanocrystals were carried out at 300K with field varying from -90 kOe to +90kOe and are shown in Fig. 4.45 (a) from which PM behavior of all samples could be seen. However, the M–H curves show weak

FM in T3Co sample similar to the undoped sample (Fig. 4.45 (b)) when taken at low fields. There is an increase in the magnetic moment with an increase in the concentration of Co. The inset in Fig. 4.45 (b) shows the variation in H_C with Co concentration. Some works suggested the observation of FM due to Co clusters while some reported that FM arise due to exchange coupling between substituted Co ions and the charge carriers trapped by oxygen vacancies.[33-41] Other reports [42] have also shown the suppression of FM in TiO₂ upon Co- doping resulting in PM or AFM which may have originated due to segregation of AFM CoO or Co₃O₄. But in our study, XRD, Raman analysis excludes the presence of any secondary phases like Co or Co related oxides. The presence of FM in T3Co indicates that the FM is not only intrinsic, but magnetism can be enhanced due to Co-doping which may have created more oxygen vacancy/Ti³⁺ ions. But in higher concentration of Co-doped samples, there is a decrease in H_C which indicates that FM ordering has been lost in these samples which may be due to the interaction of oxygen vacancy/Ti³⁺ ions with Co ions in different ways promoting FM/PM.
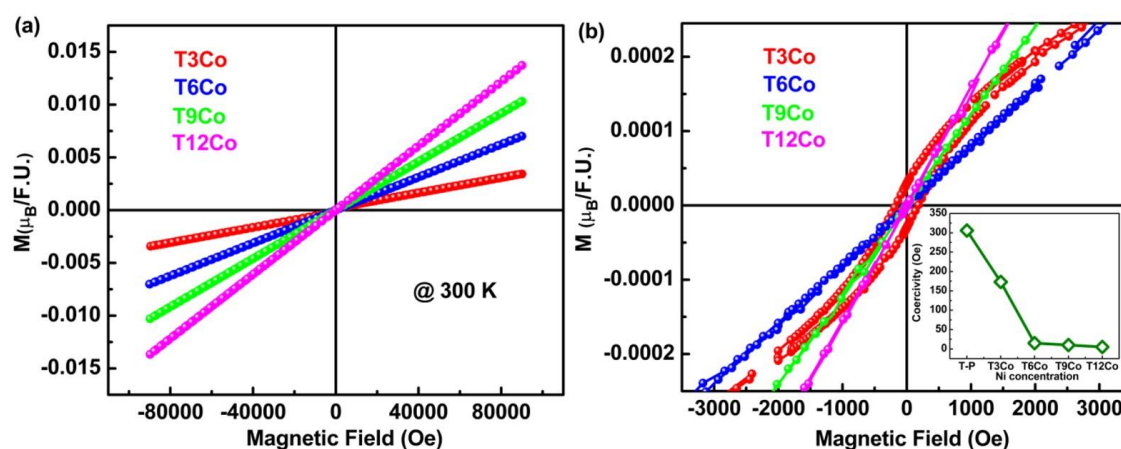
Fig.4.45. Magnetic response of Co-doped TiO₂ nanocrystals (a) at 300K and (b) Representation of weak FM in T3Co and PM in T6Co, T9Co and T12Co, inset shows variation of H_C with Co concentration.

C. Magnetic studies of Ni-doped TiO₂

The magnetic behavior of all the Ni-doped TiO₂ nanopowders at room temperature has been studied with field varying from -90 kOe to +90 kOe as shown in Fig. 4.46 (a), which show a PM behavior. In Ni-doped TiO₂, an increase in the magnetic

moment has been observed with the increase in Ni concentration from 3% to 12%. However, the doped samples possess much less H_C than undoped TiO_2. It can be affirmed that at higher Ni doping concentration, more oxygen vacancies are created which result in isolated vacancy clusters resulting in PM behavior for higher concentration of Ni-doped samples. Fig. 4.46 (b) shows the magnetic response of all the samples at lower fields and the inset gives a systematic decreasing trend in H_C for Ni-doped samples. A magnetic phase transition from weak FM to PM behavior has been observed at lower fields well below 2000 Oe for 3% Ni-doped samples similar to the undoped sample, whereas above 3% Ni-doped samples exhibit a perfect PM. The reason for the observed weak FM behavior in undoped and 3% Ni-doped samples could be specifically due to the trapped electrons in the defect centers. The presence of defects like oxygen vacancies has been observed in the UV-Visible and PL analysis which suggests that the presence of oxygen vacancies leading to the formation of one mini band closely below the conduction band as discussed earlier. Even though the oxygen vacancy defects are there, the formation of F^+-centres are effectively inhibited which is clear from the significant decrease in integrated PL intensity as discussed earlier. Under such a situation, where the F^+-centre formation is too low, the chance of Ti^{3+} formation also will be inhibited due to the absence of interaction between one of the electrons of F-centre and adjacent Ti^{4+} ions which is further discussed in the XPS analysis. The increasing trend in net magnetization for heavily doped Ni samples may be arising as a result of PM moment contributed by the isolated Ni^{2+} concentration.
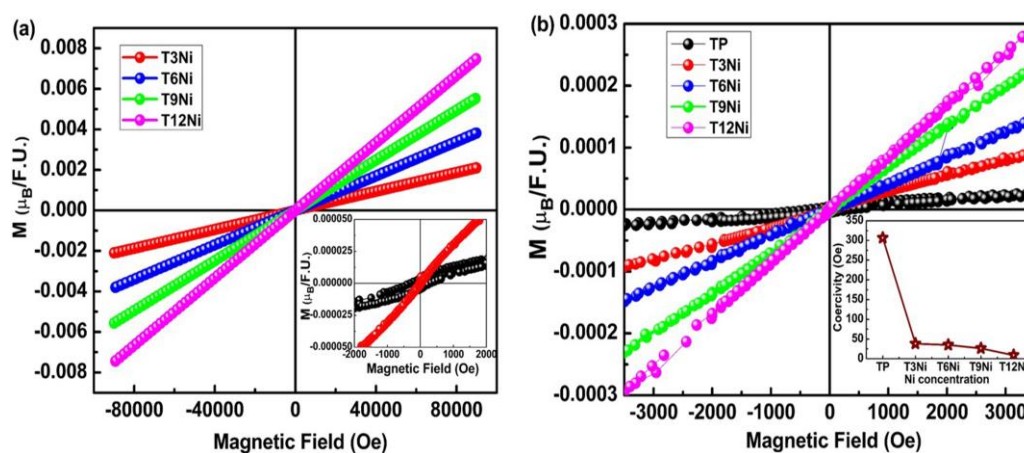
Fig.4.46. MH curves of (a) Ni-doped TiO_2 nanocrystals at 300K (inset shows the enlarged view of MH for T-P and T3Ni) and (b) An enlarged view of MH (inset shows H_C Vs Ni doping).

4.3.2.7. XPS analysis

XPS spectra corresponding to Fe, Co and Ni-doped TiO_2 are discussed in the following sub sections.

A. XPS analysis of Fe-doped TiO₂

XPS spectra were recorded on 3% and 9% doped Fe concentration as a representative of the series to understand the oxidation states of Ti and Fe. Fig.4.47 (a) signifies the peak of Fe along with the Ti, O and C peaks which were expected in both T3Fe and T9Fe. The high-resolution spectra obtained for Ti2p, Fe2p and O1s of T3Fe and T9Fe were recorded and are shown in Fig.4.47 (b-d) along with the deconvolution. The Ti2p spectrum of T3Fe sample can be fitted with four peaks corresponding to $Ti^{4+}2p_{3/2}$ at 458.45 eV, $Ti^{4+}2p_{1/2}$ at 463.92 eV and $Ti^{3+}2p_{3/2}$ at 456.86 eV, $Ti^{3+}2p_{1/2}$ at 460.63 eV which is consistent with the standard binding energy of TiO_2.[46] The Ti2p spectrum of T9Fe sample can also be fitted with four peaks corresponding to $Ti^{4+}2p_{3/2}$ at 458.23 eV, $Ti^{4+}2p_{1/2}$ at 464.05 eV and $Ti^{3+}2p_{3/2}$ at 455.81 eV, $Ti^{3+}2p_{1/2}$ at 461.42 eV.

It is observed that T9Fe sample exhibits a significantly low content of Ti^{3+} when compared with T3Fe and a clear binding energy shift is observed, which further signifies the decrease in band gap with Fe substitution. Furthermore, the Fe2p peak in T3Fe and T9Fe (Fig. 4.47 (c) consist of three peaks, a peak at 709.76 eV of $Fe^{2+}2p_{3/2}$, the second peak at 711.24 eV that of $Fe^{3+}2p_{3/2}$ and a clear satellite peak at 715.10 eV) revealing Fe atom in TiO_2 has a mixed oxidation state of +2/+3. It is also observed that Fe^{3+} concentration increases with Fe concentration. Broadening of the Raman peaks, a red shift in the optical absorption and XPS spectra strongly suggest the Fe ion incorporation at Ti site leading to the formation of vacancy related defects and hence, confirmation of Ti^{3+}, Fe^{2+} and Fe^{3+} from the XPS analysis of all the samples [79] are well in accordance with the Raman and PL studies mentioned earlier. There could be a slight difference between the number of oxygen vacancies with Fe ion content as T3Fe consists of Ti^{3+}, which is diminishing with Fe substitution. It is to be noted that the undoped sample also possess Ti^{3+}/Ti^{4+} and oxygen vacancies.[58] The slight shift in the O

1s peak could be due to the difference in the oxygen vacancies in the synthesized samples as shown in Fig.4.47 (d).
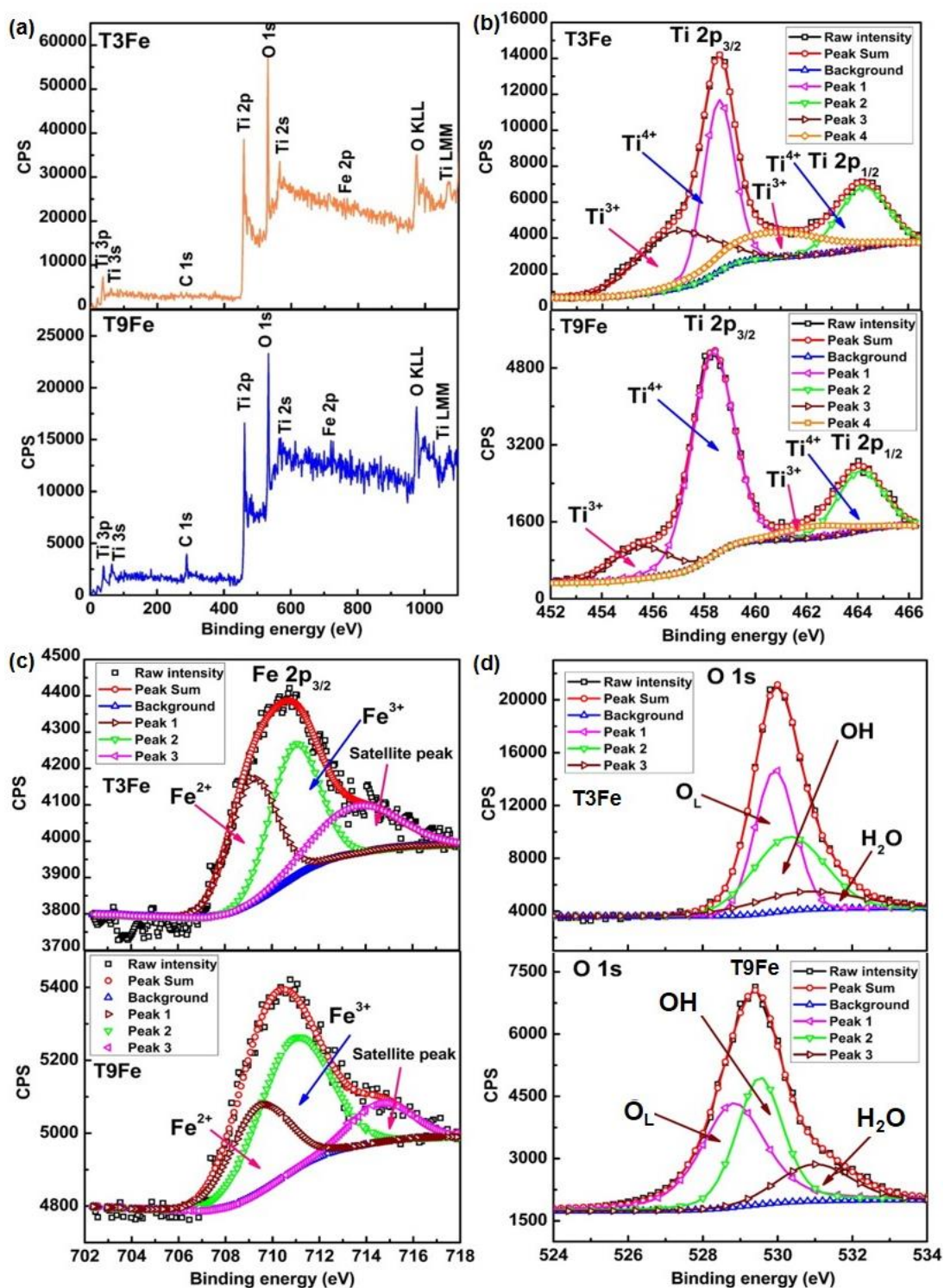
Fig.4.47. XPS spectra of T3Fe and T9Fe (a) wide spectrum (b) Ti 2p (c) Fe 2p and (d) O 1s

The deconvoluted O 1s spectra consist of three peaks.[72,93] The peak at 529.40 eV is attributed to the lattice oxygen (O_L) associated with TiO_2. The second peak with higher binding energy around 530.1 eV is due to the presence of OH groups. The final peak could be due to the water adsorbed on the surface as shown in Fig. 4.47 (d). Furthermore, it is observed that 2-δ value calculated from the XPS results[94] is 1.99 for T3Fe and 1.98 for T9Fe which clearly suggests the formation of minute amount of oxygen vacancy defects responsible for the magnetic interactions associated with the system. The presence of Fe^{2+} and Fe^{3+} as mentioned in the XPS analysis can be explained based on the residual carbon from organic radicals as evident from FT-IR spectra.[72] During the annealing process, the residual carbon associated with the system could interact with more oxygen, especially in the air annealing process which causes the oxidation of Fe^{2+} oxidation state to Fe^{3+} oxidation state. Hence both Fe^{2+} and Fe^{3+} are observed in the XPS spectra of Fe 2p.

B. XPS analysis of Co-doped TiO₂

The oxidation states of Co and Ti were further analyzed by XPS for T3Co, T9Co and T12Co samples as a representative of the series. The survey spectra of all the three samples are shown in Fig.4.48, from which the peak of Co can be seen along with the Ti, O and C peaks which were expected. The high-resolution spectra of Ti2p, Co2p and O1s were recorded and are shown in Fig. 4.49 (a-c) along with the deconvolution. The Ti spectrum of T3Co sample can be fitted with four peaks corresponding to $Ti^{4+} 2p_{3/2}$ at 458.19 eV, $Ti^{4+}2p_{1/2}$ at 463.92 eV and $Ti^{3+}2p_{3/2}$ at 456.03 eV, $Ti^{3+}2p_{1/2}$ at 461.67 eV as shown in Fig.4.49 (a). The line separation between $Ti^{4+}2p_{1/2}$ and $Ti^{4+}2p_{3/2}$ is 5.72 eV which is consistent with the standard binding energy of TiO_2.[29,46] Interestingly, T9Co sample exhibits a single oxidation state of Ti^{4+} and the peak positions are located at $Ti^{4+}2p_{3/2}$ at 458.54 eV and $Ti^{4+}2p_{1/2}$ at 464.27 eV respectively. Again in T12Co sample, a similar observation as T9Co is noticed with Ti^{4+} peaks at $Ti^{4+}2p_{3/2}$ at 458.54 eV and $Ti^{4+}2p_{1/2}$ at 464.27 eV respectively. Furthermore, the Co peak appeared in T3Co, T9Co and T12Co (Fig. 4.49 (b)) can be deconvoluted into four peaks, one at 780.66 eV which corresponds to $Co^{2+}2p_{3/2}$, second peak at 782.06 eV corresponds to $Co^{3+}2p_{3/2}$, other at 796.25 eV corresponding to $Co^{2+}2p_{1/2}$ and final peak at 797.64 eV corresponding to

$Co^{3+}2p_{1/2}$ in Co 2p spectra giving the line spacing of 15.8 eV between the two, along with two strong shake-up satellite peaks at 786.01 eV and 802.35 eV revealing Co atom in TiO_2 exist in a mixed oxidation states of +2/+3. The separation of Co 2p peak into $2p_{3/2}$ and $2p_{1/2}$ for both Co^{2+} and Co^{3+} indicates that the valence state of Co is 2+/3+.
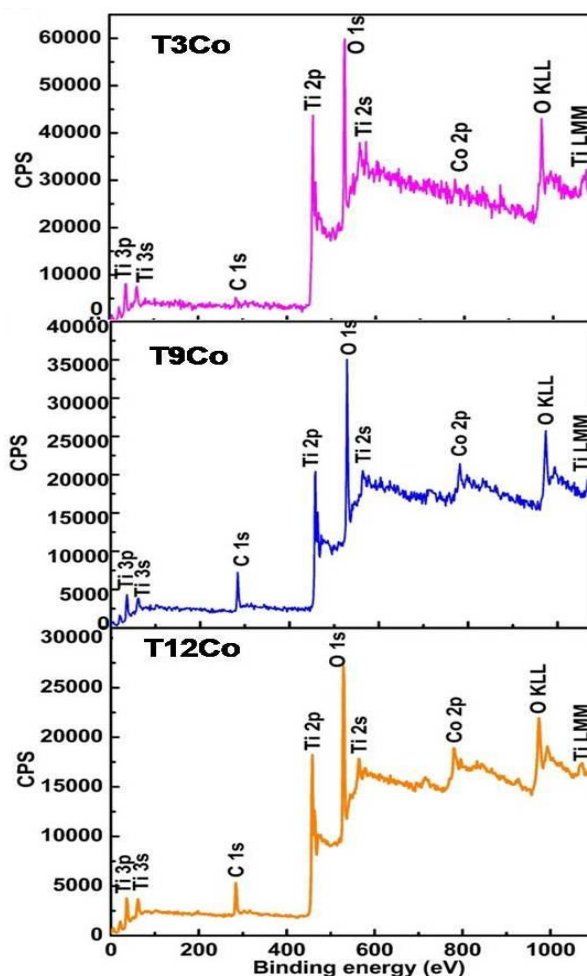
Fig.4.48. Wide scan XPS spectra of (a) T3Co, (b) T9Co and (c) T12Co

Broadening of the Raman modes, shifting of absorption edge to visible region and XPS data strongly support the substitution of Co ions for Ti^{4+} in the TiO_2 lattice which creates oxygen vacancy. Confirmation of the presence of Ti^{3+}, Co^{2+} and Co^{3+} in the XPS analysis indicates that Co-doped samples possess a certain amount of oxygen vacancies which further corroborates the Raman and optical absorption spectra data. There could be a slight difference between the number of oxygen vacancies of T3Co, T9Co and T12Co due to the fact that T3Co consists of Ti^{3+}, which is absent in T9Co and T12Co.

This difference in oxygen vacancies is ultimately reflected in the slight peak shifting of O 1s spectra as shown in Fig.4.49 (c). The deconvoluted O 1s spectra are represented by three symmetric Gaussian curves, similar to that of reported in the literature.[93] The intense peak at about 529.8 eV is arising due to the oxygen in the TiO_2 crystal lattice (O_L), while the other oxygen peaks are the outcome of OH bonds (531.0 eV) and the adsorbed water (532.0 eV) respectively as shown in Fig.4.49 (c). The concentration of Ti^{3+}, Ti^{4+}, Co^{2+} and Co^{3+} has been estimated from the XPS results [94] which are shown in Table 4.9.
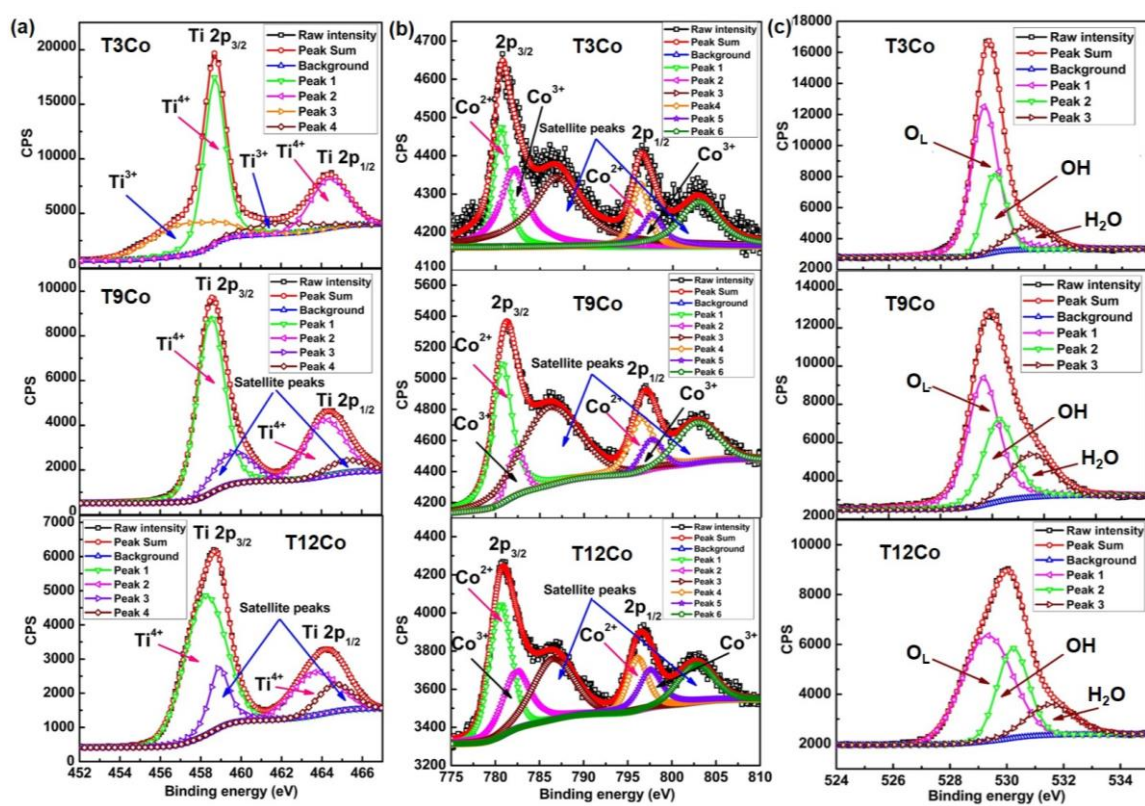
Fig.4.49. XPS spectra of T3Co, T9Co and T12Co sample (a) Ti 2p (b) Co 2p and (c) O 1s
Table 4.9. Estimated concentration of Ti^{3+}, Ti^{4+}, Co^{2+} and Co^{3+} from XPS spectra (δ represents the oxygen deficiency)

Compound name	Ti^{3+} (%)	Ti^{4+} (%)	Co^{2+} (%)	Co^{3+} (%)	O^{2-} (%)	2-δ
T-P	13.19	20.22	-	-	66.59	1.99
T3Co	11.02	21.34	0.55	0.75	66.34	1.99
T9Co	-	30.52	1.90	1.21	66.38	1.98
T12Co	-	29.35	3.65	0.76	66.24	1.98

C. XPS analysis of Ni-doped TiO₂

The wide scan XPS spectrum of T3Ni is shown in Fig. 4.50 (a) as a representative of the series. The high-resolution scans of Ti 2p, Ni 2p and O 1s are shown in Fig. 4.50 (b)-4.50 (d). The Ti 2p spectrum of T3Ni sample shows the presence of Ti^{4+} $2p_{3/2}$ at 458.45 eV, and $Ti^{4+}2p_{1/2}$ at 464.20 eV. No peaks corresponding to Ti^{3+} was observed in the high-resolution spectra of Ti 2p. The high-resolution scan of Ni 2p can be deconvoluted into four peaks: one peak at 855.57 eV corresponding to $Ni^{2+}2p_{3/2}$ and the second peak at 873.32 eV corresponding to $Ni^{2+}2p_{1/2}$.[46] Two strong satellite peaks at 861.79 eV and 879.71 eV reveals that Ni atom in TiO₂ has an oxidation state of +2.
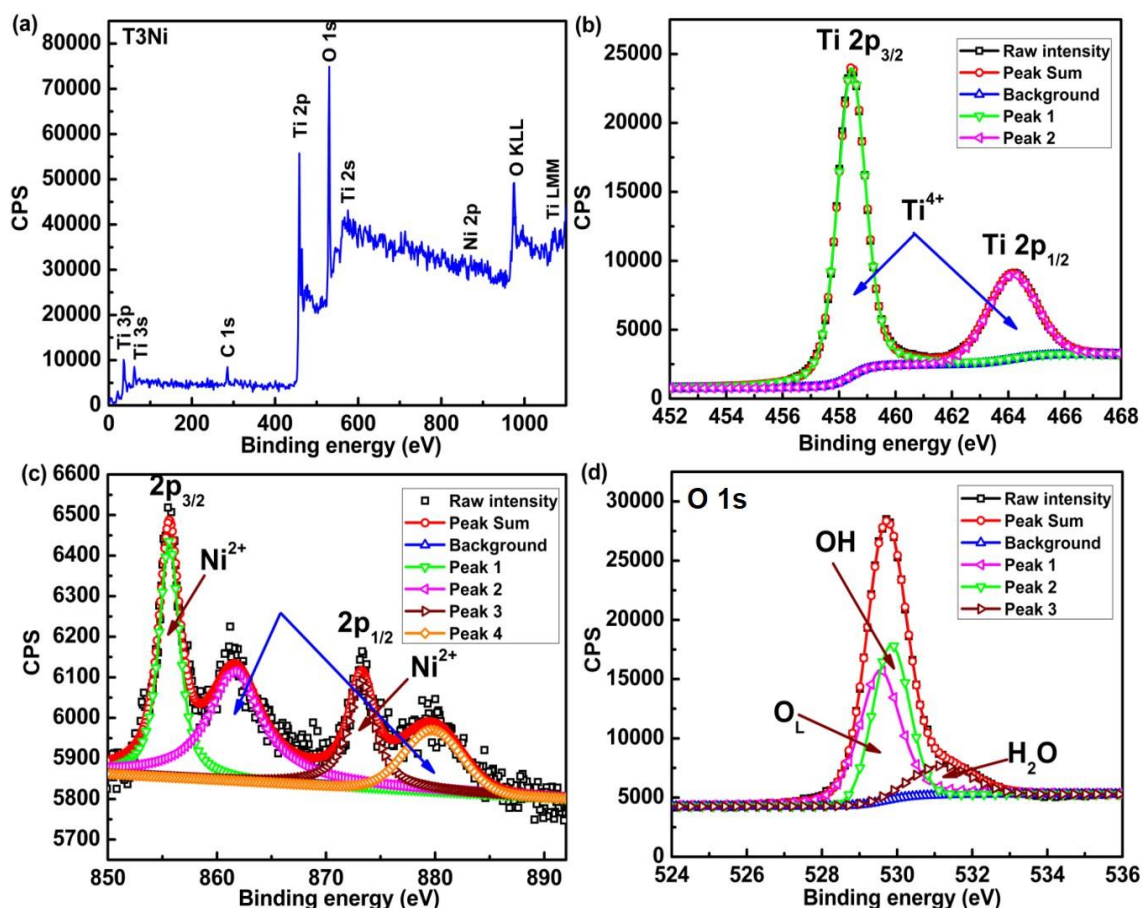
Fig.4.50. (a) Wide scan XPS spectra of T3Ni sample, High-resolution scan of (b) Ti 2p (c) Co 2p and (d) O 1s

Confirmation of the presence of Ni^{2+} in the XPS analysis indicates that Ni-doped samples possess a certain amount of oxygen vacancies which is in conformity with the

Raman spectra and shifting of absorption edge to visible region in the UV-Visible spectra. The O 1s spectrum shown in Fig. 4.50 (d) has been deconvoluted into three peaks observed at about 529.55 eV is attributed to the oxygen in the TiO_2 crystal lattice, while the other two peaks at 529.85 eV and 531.22 eV are due to the presence of OH bonds and the adsorbed water. It can be seen from the XPS analysis that no contribution from Ti^{3+} is observed even in 3% Ni-doped sample and there is a drastic decrease in H_C of 3% Ni-doped sample when compared with the undoped sample as discussed earlier in the M-H measurements.

4.3.2.8. Explanation for the magnetic behavior in Fe, Co, Ni-doped TiO₂

The oxygen vacancy defects associated with TiO_2 nanocrystals has a strong influence on the magnetic properties. In order to have an idea about the vacancy defects the Urbach energy estimation has been carried out on Fe-doped samples (Fig.4.38) and the presence of defects are validated which are in corroboration with the PL results as discussed in section 4.3.2.5.1. The origin of RTFM in the undoped sample has already been discussed in section 4.3.1.7. which was mainly attributed to the defect concentration and Ti oxidation states. While considering the Fe-doped or Co-doped TiO_2 nanocrystals, disorder in the host lattice arising as a result of incorporation of Fe/Co ions introduces oxygen vacancies as defects in TiO_2 and subsequent formation of BMPs could be the reason behind variation observed in both magnetic and optical properties.[56] BMP fitting has been carried out on Fe-doped TiO_2 samples to investigate the impact of oxygen vacancy and Fe ion substitution in the TiO_2 system. According to the previous reports, the fitting has been carried out on the recorded M versus H data represented in Fig.4.44.[60,61] The data fitted to the experimental curve are represented in Fig. 4.51 (a) and the parameters derived from the fitting process are represented in Fig. 4.51(b).

As per the earlier discussions, the presence of Ti^{3+} is confirmed in the Fe-doped samples along with Ti^{4+}. The ratio of Ti^{3+} to Ti^{4+} is decreasing which is evident from Fig.4.47 (b). Still, this minute fraction of Ti^{3+} along with Fe^{2+}/Fe^{3+} could have unpaired electrons in the 3d state and it can interact with the oxygen vacancy centres associated

with these sample as discussed previously. The trapped electrons in the defect sites energize the formation of F-centres and F^+-centres. The F^+-centre formation ultimately leads to the formation of BMPs, which may favor the weak FM interaction (Fig.4.51 (c)). The room temperature M-H loop at lower fields shows a weak RTFM for T3Fe where maximum H_C is observed which further corroborates the PL results and the formation of defect centres and $3d^1$ interaction of $Ti^{3+}/Fe^{2+}/Fe^{3+}$ plays a crucial role in generating the magnetic response in the Fe-doped sample. Similar behavior is expected for Fe-doped samples with higher concentration also, but the extrinsic PM contribution of Fe^{2+}/Fe^{3+} dominates over intrinsic defect-assisted FM behavior which is ultimately reflected in the decrease of H_C and enhanced PM behavior. The previous discussions suggest the absence of expected perfect FM in T9Fe and T12Fe which is due to extrinsic factors even though defects are associated with the system and the XPS results illustrate the presence of Ti^{3+}, Ti^{4+} and Fe^{2+}/Fe^{3+} in the Fe-doped TiO_2 system, where both intrinsic and extrinsic factors are ultimately deciding the magnetic behavior. From the M-H curve of Fe-doped TiO_2, it is observed that the net magnetic moment shows an increasing trend with Fe concentration and a systematic decrease in H_C is observed, that suggest a weak FM to PM transition at higher Fe concentration. The BMP concentration decreases with Fe substitution and at the same time paramagnetic susceptibility increases with increasing Fe concentration.

Now let us consider the decreased BMP concentration in T6Fe, T9Fe and T12Fe in comparison to T3Fe. It is interesting to observe that even with the increased number of Fe ions present in T6Fe, T9Fe and T12Fe, there is a decrease in H_C in comparison to T3Fe and the increased number of Fe^{2+} and Fe^{3+} sites may be generated to maintain the charge neutrality. Hence, when the Fe concentration increases, more number of Fe^{2+}/Fe^{3+} ions will be generated and the charge neutrality will be maintained by Fe sites and Ti^{4+} sites are less disturbed and less Ti^{3+} ions will get generated which is evident from the XPS results. More clearly, BMP formation at higher Fe concentration samples is solely due to the interaction of F^+-centres with 3d states of Fe ions and obviously will result in a decreased concentration of BMPs as the s-d exchange interaction among F^+-centre and Ti^{3+} is almost negligible in the T6Fe, T9Fe and T12Fe samples. The BMP

fitting of all the Fe-doped samples corroborates well with the above mentioned results where T12Fe is having the least number of BMPs among the Fe-doped samples and is found to be least FM with increased PM susceptibility. Along with this interesting magnetic behavior exhibited by the system, a significant band gap narrowing is also observed on these samples which are represented in Fig.4.51 (d).
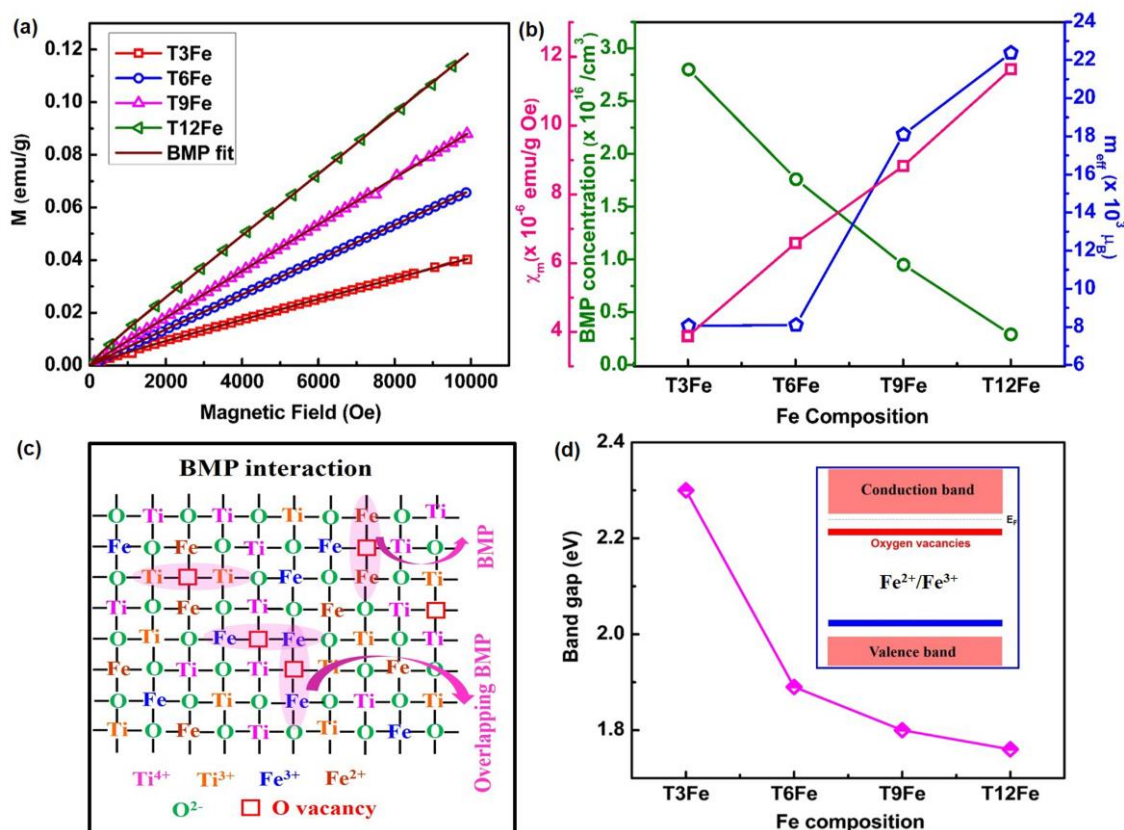
Fig.4.51. Fe-doped TiO₂ samples (a) BMP fit (b) Variation of BMP concentration, m_{eff} and χ_m with Fe-doping concentration obtained from Langevin-fitting (c) Schematic diagram representing the BMP model and (d) Schematic diagram of band-gap narrowing with Fe concentration

Now, let us consider the origin of RTFM observed for the lower doped T3Co sample. A similar interaction to that of Fe-doped samples is possible between the F^+-centre and Co^{2+} ions to develop further BMPs, hence another possible interaction in lightly Co-doped T3Co is between the F^+-centres and $3d^7$ electron spin of Co^{2+} ions leading to FM ordering. Hence the BMP formation due to Ti^{3+} and Co^{2+} ions with the F^+-centre, in which the electrons are locally trapped by oxygen site vacancies, where an orbital overlapping with the unpaired $3d^1$ electron of Ti^{3+} ions or the unpaired $3d^7$

electron of Co^{2+} ions is explored in detail to investigate the observed RTFM at lower fields in the present case, i.e., in T3Co sample. It is clear from Table 4.8 that Ti^{3+}/Ti^{4+} ratio is 0.65 for the undoped sample and 0.52 for T3Co. Again Co^{2+}/Co^{3+} ratio is observed to be 0.73 for T3Co, at the same time slight amount of oxygen vacancy is also evident from Table 4.8 and these results indicate the s–d exchange interaction associated with the $1s^1$ electron spin of trapped state, $3d^1$ electron spin of Ti^{3+} ions and $3d^7$ electron spin of Co^{2+} ions have induced magnetism in T3Co. The BMP fitting has been carried out on the observed M versus H data to get the BMP concentration as discussed in equation (4.1).[60,61] The experimental and fitted data to estimate the BMP concentration is represented in Fig. 4.52(a) for all the Co-doped samples and it can be observed that the fitted data is very well in accordance with the experimental data and the obtained parameters are tabulated in Table 4.10.
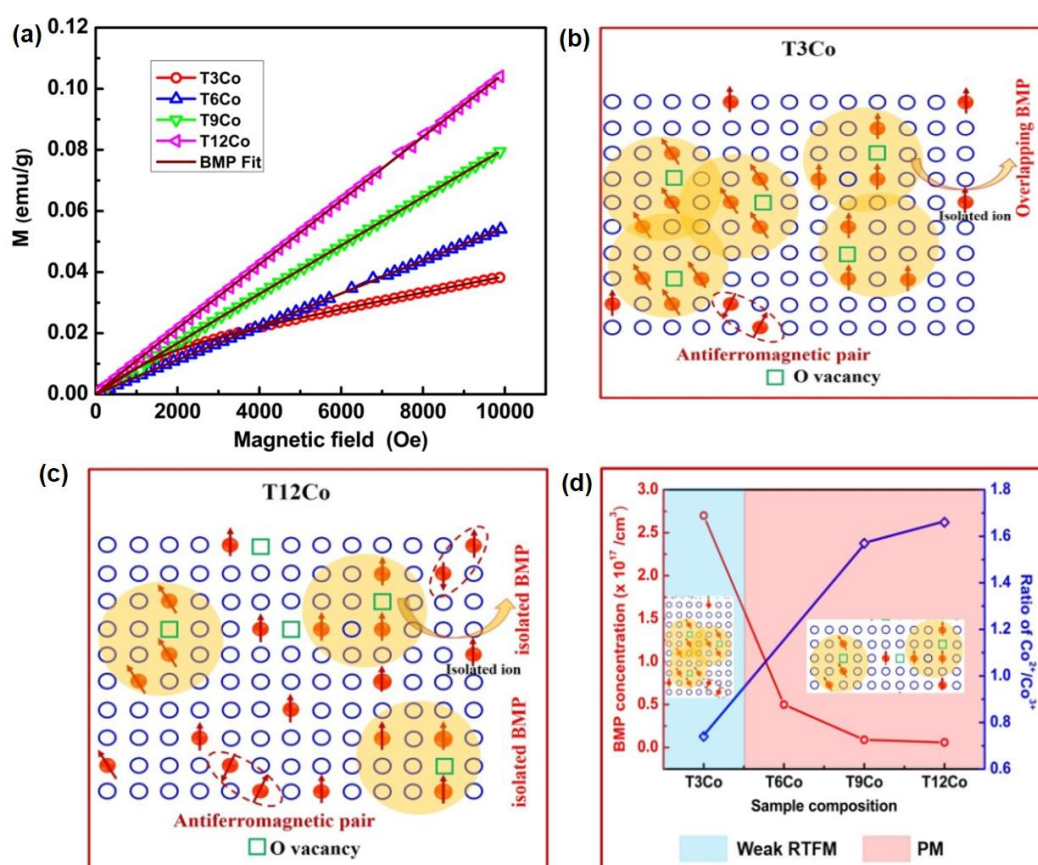
Fig.4.52. Langevin-fit to estimate the BMP concentration for (a) Co-doped samples, Schematic diagram showing the possible BMP formation involved in (b) T3Co and (c) T12Co for explaining the magnetic behavior of the Co-doped TiO₂ nanocrystals (d) The variation of BMP concentration and Co^{2+}/Co^{3+} ratio with Co substitution

The number of BMPs required to induce a long-range FM is reported to be of the order of $10^{20}/cm^3$, whereas the undoped sample contains 10^{16} BMPs and T3Co sample contains nearly 10^{17} BMPs and ultimately RTFM is observed only at lower fields. The low concentration of oxygen site deficiency due to air annealing is evident from the approximate low 2-δ value as shown in Table 4.8. When a less concentration of Co exists in T3Co, the system is bound to interact with Ti^{4+} defect sites to induce the formation of Ti^{3+} in order to maintain the charge neutrality. Here, a very few Co^{2+} ions from $Co(NO_3)_2$ will be converted to Co^{3+} ions which is the most stable state (but diamagnetic) among different Co ions due to d-orbital splitting into lower energy t_{2g} state and high energy e_g state. The results are well in agreement with the XPS results. Hence it is clear that BMPs formed as a result of both Co^{2+} ions and Ti^{3+} ions are responsible for the weak FM exhibited by T3Co.

The underlying mechanism of FM in heavily Co-doped TiO₂ samples is rather complicated due to the fact that doubly occupied F-centres and the formation of $1s^2$ state can adversely affect the FM interactions and a few mechanisms are put forward, which includes RKKY [95] model, FM double exchange and AFM superexchange coupling,[96] and coupling of BMPs formed at the F$^+$-centre and the Co^{2+} surrounding of doped nanocrystals,[97] etc. The inherent tendency of defect formation in TiO₂ nanocrystals increases the possibility of interactions among defects and carriers along with their coupling that could lead to a variety of magnetic interactions depending upon the defect concentration and dopant ion concentration. Considering the M-H curve represented in Fig.4.45, it is observed that the net magnetic moment increases with Co substitution and at the same time H_C decreases considerably leading to a weak FM to PM transition with the increased Co^{2+} concentration. The BMP concentration, total BMP magnetization and PM susceptibility obtained for T6Co are within the permissible limit and its BMP concentration considerably decreases with Co substitution whereas PM susceptibility increases systematically. Now let us consider the reason for the decreased BMP concentration in T6Co in comparison to T3Co. Obviously, more number of Co^{2+} ions is present in T6Co when compared with T3Co; hence, the system tend to interact with the increased number of Co^{2+} sites and again some amount of Co^{3+} generation occurs to

maintain the charge neutrality. The interaction with the Ti^{4+} site is hindered here due to the fact that the stability of Ti^{4+} (having noble gas configuration) is more in comparison to Co^{2+} (can easily oxidize to Co^{3+}). Hence, when more Co^{2+} ions is present, the charge neutrality concept is bound to Co^{2+} site and Ti^{4+} site get undisturbed as shown in Fig.4.49 (b). The BMP formation in T6Co case is only due to the interaction of F$^+$-centres with 3d states of Co^{2+} ions and obviously will result in a decreased concentration of BMPs as the s-d exchange interaction among F$^+$-centre and Ti^{3+} is absent in the T6Co sample. The BMP fitting of T9Co and T12Co is represented in Fig.4.52 (a), where a similar observation is noticed. Hence, T12Co is having the least number of BMPs among the Co-doped samples and is found to be least FM. It is evident from the XPS results that the ratio of Co^{2+}/ Co^{3+} is increasing with Co substitution which is represented in Table 4.9. The increasing trend in net magnetization results from the PM moment contributed by this hiking Co^{2+} concentration where the isolated Co spins in the trapped centres are responsible for the PM behavior of T6Co, T9Co and T12Co. Interestingly, the presence of Ti^{3+} ions have almost disappeared in these heavily doped samples. The Fig.4.52 (b, c) shows a schematic representation explaining the possible BMP formation involved in the Co-doped TiO$_2$ nanocrystals. The different possible mechanisms involved here can be explained in detail as discussed below. The higher concentration of Co yields the decreased FM behavior and a similar observation can be found in most of the recently reported systems.[96,98] It could be due to the fact that large concentration of Co^{2+} doping (as evident from the XPS analysis) can result in the following possibilities, (i) the AFM ordering between two nearby Ti^{4+}/Co^{2+} ions in the absence of oxygen vacancy sites by superexchange interaction, (ii) most of the Co^{2+} spins exist in the isolated PM spin system or (iii) may interact ferromagnetically by F$^+$-centre – Ti^{3+} ions/ F$^+$-centre – Co^{2+} ions. Even though (i) and (iii) is present in our system, (ii) is dominated by higher concentration of Co^{2+} resulting in an increased PM moment.

As discussed earlier in the PL results, the concentration of oxygen vacancies is considerably lower in T12Co in comparison to T3Co. Hence, a lower oxygen vacancy concentration is partly responsible for the decreasing FM behavior in T12Co. It is

observed that BMP concentration is the maximum for T3Co and there is a linear correlation between the increased Co-doping and BMP concentration, as shown in Fig.4.52 (d). It is extremely challenging to quantitatively estimate the defect concentration from the PL analysis, the observed correlation is in good agreement with the recent report [55] and it is reported that the correlation between BMP concentration and oxygen vacancies are rarely observed. These observations impart an expression that the observed RTFM is contributed significantly by oxygen vacancies created in the Co-doped samples. It is observed that the T3Co samples have numerous oxygen vacancies due to Ti^{3+} and Co^{2+}, leading to the formation of even small clusters of vacancies which could increase the chance of localization of the charges associated with the exchange interaction due to overlapping of BMPs. Hence it is understood that in the present samples, contribution of magnetization is due to the simultaneous occurrence of oxygen vacancies and BMP formation resulting in FM and PM behavior respectively. The oxygen vacancies and BMP formation are becoming weaker with the increase of Co ions, resulting in the weakening of FM behavior and the enhancement in magnetization occurs due to the increase in isolated Co^{2+} spins with the increase of Co substitution.

BMP fitting has been carried out on Ni-doped TiO$_2$ samples also to explore more on the role of oxygen vacancy and the impact of dopant ion concentrations. The measured magnetization has been fitted using equation (4.1). A plausible model for BMP formation in 3% Ni-doped TiO$_2$ is shown in Fig 4.53 (a). Fig 4.53 (b) shows the BMP fit for Ni-doped samples and it can be seen that the fitted data agrees well with the experimental data. The parameters obtained from the fitting are tabulated in Table 4.10. It is interesting to note that T3Ni sample contains nearly 10^{16} BMPs and a very low H$_C$ is observed at lower fields. The H$_C$ decreases with Ni doping and the maximum H$_C$ is observed for T3Ni. Hence it is clear that BMPs formed as a result of Ni^{2+} ions are determining the H$_C$ of the sample. Hence, it can be presumed that oxygen vacancies and Ti interstitials are responsible for the very weak FM exhibited by T3Ni. The increasing trend in net magnetization for heavily doped Ni samples result from the increased PM moment contributed by the increasing Ni^{2+} concentration.

When Ni^{2+} substitutes Ti^{4+}, to balance the charge neutrality, there will be some disorder in the lattice which can be in the form of defects like oxygen vacancies. When the Ni^{2+} concentration is present in a dilute manner the Ni–O, Ti–Ti, and Ti–O bond distances may change significantly and could contribute towards magnetism through different exchange interactions. The F-centre formation and interplay of spins associated with different elements present in the system are responsible for the magnetic behavior exhibited by transition metal oxides. Hence, it is desirable that the different elements present in doped TiO_2 should possess unpaired electrons so that the interaction will be strong enough to make the sample magnetic. It is also important to note that the transformation of F-centres to F^+-centres becomes so crucial in creating the magnetically active sites. In the case of Ni-doped TiO_2, different possibilities are there to determine the magnetic behavior of the sample.
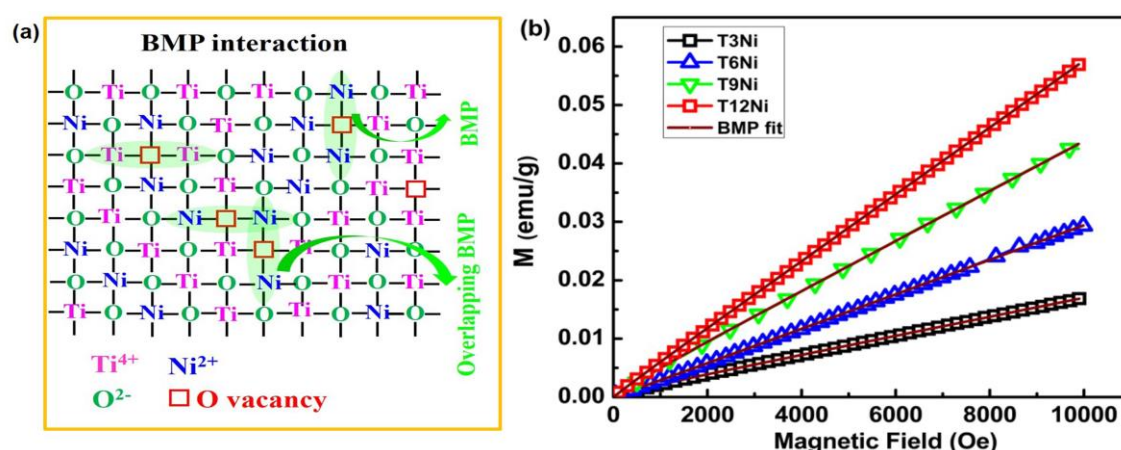
Fig.4.53. (a) BMP formation in T3Ni (b) BMP fitting in Ni-doped samples

From the XPS spectra of T3Ni, it is observed that only Ti^{4+} is present in the system along with a few Ni^{2+} substituting for Ti^{4+} ions. The electronic configuration for Ni^{2+} can be written as [Ar] $3d^8$ $4s^0$ which gives rise to two unpaired d-electrons in Ni-doped TiO_2 system. Even though this electronic configuration reveals the FM behavior of the dopant ion, it decreases the H_C in comparison to the undoped sample. This interesting observation is due to the fact that FM behavior in doped TiO_2 samples is difficult due to doubly occupied F-centres and the formation of $1s^2$ state in the trapped sites. From the different mechanisms discussed earlier, the BMP model holds good for the very weak FM in 3% Ni-doped TiO_2 at lower fields.[56] The BMP formation in T3Ni

is schematically represented in Fig 4.58 (a). With Ni substitution in TiO$_2$, especially in T3Ni, the simultaneous occurrence of oxygen vacancies and BMPs can be accounted for the very weak FM behavior at lower fields since Ni is a magnetic ion. Still, due to the absence of Ti^{3+} as revealed from the XPS spectra of T3Ni, a well accounted s-d interaction may not be present in these samples and due to this reason T3Ni exhibits a clear paramagnetic behavior at higher fields. Also, even with the existence of oxygen vacancies, BMP formation becomes weaker at higher Ni concentrations, leading to the PM behavior and the enhancement in magnetic moment is reflected from the increase in isolated Ni^{2+} spins which is evident from the M-H curves of T6Ni, T9Ni and T12Ni respectively.

Table 4.10. The parameters obtained from BMP fitting for Fe, Co, Ni-doped TiO$_2$ nanocrystals

Compound	$M_0 (x10^{-4} emu/g)$	$M_{eff} (x10^3 \mu_B)$	$\chi_m (x10^{-6} emu/g\text{-}Oe)$	$N(x 10^{17}/cm^3)$
T-P	6.81	7.21	0.37	0.11
T3Fe	20.91	8.06	3.88	0.28
T6Fe	15.11	8.1	6.585	0.18
T9Fe	13.52	18.1	8.824	0.09
T12Fe	6.23	22.38	11.64	0.03
T3Co	148.22	5.94	2.50	2.70
T6Co	17.23	4.01	5.40	0.46
T9Co	6.49	7.16	7.89	0.09
T12Co	3.97	7.13	10.48	0.06
T3Ni	12.11	10.32	1.63	0.12
T6Ni	7.88	11.33	2.96	0.08
T9Ni	4.39	7.18	4.27	0.07
T12Ni	2.34	8.47	5.72	0.01

4.3.3. Cr and Mn-doped TiO₂ nanocrystals

Here, we have carried out a detailed study of the morphological, structural, optical and magnetic properties of Cr and Mn-doped TiO_2 nanocrystals with doping concentrations varying from 3 to 12 atomic weight%.

4.3.3.1. Structural analysis

X-ray diffraction studies corresponding to Cr and Mn-doped TiO_2 are discussed in the following sub sections

A. XRD analysis of Cr-doped TiO₂

The XRD patterns of Cr-doped TiO_2 nanocrystals are shown in Fig. 4.54 (a). All the diffraction peaks have been indexed with the tetragonal anatase phase of TiO_2 with space group I 4_1/a m d (ICDD card no.78-2486). A slight left shift has been observed with the increase of Cr content, indicating an increase in d spacing and hence the unit cell volume. The broadening of the (101) peak suggests a decrease in particle size with increase in Cr content. The peak shift and broadening of the (101) peak is shown in Fig. 4.54(b). The Rietveld refinement patterns of all the samples are plotted in Fig. 4.55 and are tabulated in Table 4.11. The agreement between the observed and calculated intensities ensures the conformity of the XRD patterns with the tetragonal anatase phase of TiO_2. The lower values of the residual parameters indicate the goodness of fit.
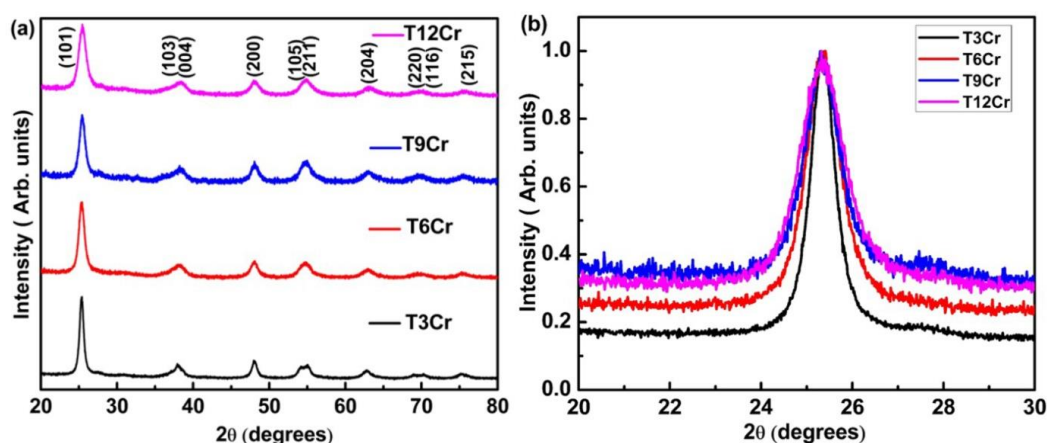
Fig.4.54. (a) XRD patterns of Cr-doped TiO_2 nanocrystals. (b) Peak shift associated with T3Cr, T6Cr, T9Cr, and T12Cr.
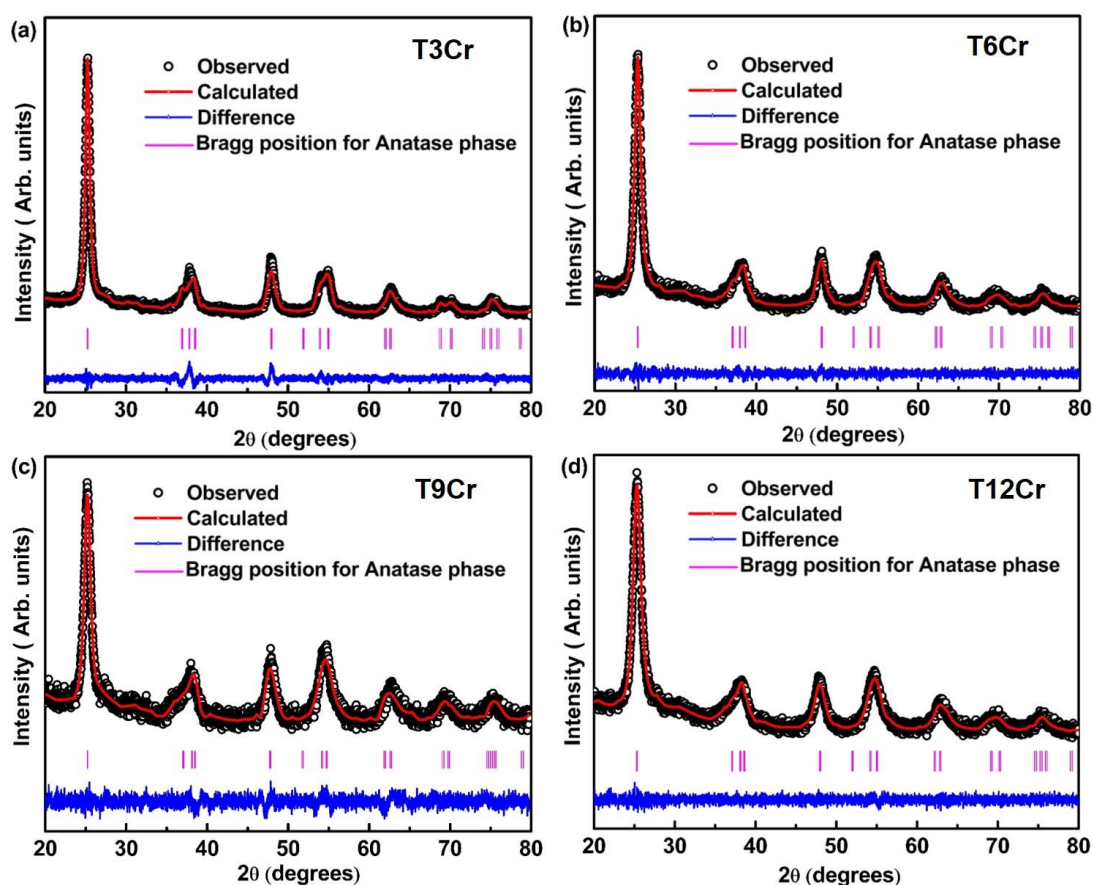
Fig.4.55. Refined XRD patterns of Cr-doped TiO₂ nanocrystals: (a) T3Cr, (b) T6Cr, (c) T9Cr, and (d) T12Cr.

It is observed from the detailed XRD refinement that incorporation of Cr doesn't affect the anatase phase of TiO₂ which remained the same for up to T12Cr. All the Cr-doped samples exhibit an intensity variation of the most intense (101) diffraction peak with a slight shift suggesting an expansion in the cell volume along with a slight decrease in the crystallite size. The observed expansion in the cell volume could be attributed to the difference in ionic radii between Cr dopant ion and the Ti ions occupying the host lattice.[99] The ionic radii corresponding to Cr^{3+} and Ti^{4+} ions are too close which is considered as 0.62 Å and 0.61 Å and as a result Cr^{3+} ion can cause a slight expansion of the unit cell, suggesting the substitutional doping of Cr in to the Ti site.[62]

The entire Cr-doped samples exhibit decreased intensity and increased FWHM of the most intense peak. This interesting behavior of decreased intensity could be due to the decreased nanoparticle size with Cr substitution, however at higher Cr

concentration all the dopant ions need not occupy the octahedral position in the present case.

Table 4.11. Refinement parameters obtained for Cr-doped TiO₂ nanocrystals

Compound	T3Cr	T6Cr	T9Cr	T12Cr
Phase	Anatase			
Crystal Structure	Tetragonal			
Space Group	I 4_1/a m d			
Lattice Parameters				
a(Å)	3.7902 (2)	3.7906 (4)	3.7915 (2)	3.7926 (4)
c(Å)	9.4926 (3)	9.4934 (1)	9.4948 (5)	9.4961 (3)
Volume (Å)³	136.37 (1)	136.41 (4)	136.49 (1)	136.59 (1)
Atomic positions				
Ti/Cr $_x$ (4a)	0.0000	0.0000	0.0000	0.0000
Ti/ Cr $_y$ (4a)	0.7500	0.7500	0.7500	0.7500
Ti/ Cr $_z$ (4a)	0.1250	0.1250	0.1250	0.1250
O $_x$ (8e)	0.0000	0.0000	0.0000	0.0000
O $_y$ (8e)	0.2500	0.2500	0.2500	0.2500
O $_z$ (8e)	0.0827	0.0833	0.0839	0.0855
B $_{iso}$ (Ti/ Cr) (Å)²	0.0007	0.0002	0.0006	0.0009
B $_{iso}$ (O) (Å)²	0.0036	0.0016	0.0005	0.0007
Residual Parameters				
R$_p$	3.18	2.80	3.43	2.47
R$_{wp}$	4.23	3.55	4.33	3.13
χ^2	1.82	1.06	1.16	1.03

A very few dopant ions could be expelled on to the surface due to self-purification mechanism or may occupy near the grain boundaries.[65] Due to this reason, the lattice periodicity may get disturbed leading to the inhibition of crystal growth that effectively decreases the crystallite size. Furthermore, there is no evidence for the occurrence of any other characteristic peaks corresponding to secondary phases or impurity ions in the prepared samples due to Cr incorporation.

The variation in the lattice parameters and unit cell volume could be also due to the development lattice strain with Cr doping. The value of interplanar spacing may increase or decrease depending on the strain present in the doped samples. The increase in d- spacing results in the shifting of 2θ-value towards lower angles which may be due to tensile strain while uniform compressive strain may be responsible for the decreased *d*-value corresponding to a shifting of 2θ toward higher values.[100] The size strain

parameters have been evaluated from the size strain plot (SSP) which has the advantage that it is reliable in case of isotropic line broadening and is shown in Fig. 4.56. In this plot, the data points from high angle reflections are given less weightage. In the SSP plots, it is assumed that Lorentzian function describes the ''crystallite size'' profile while Gaussian function describes the ''strain profile'' and is governed by the equation.[101]

$$\left(\frac{d_{hkl}\beta_{hkl}\cos\theta_{hkl}}{\lambda}\right)^2 = \frac{k\lambda}{D}\left(\frac{d_{hkl}^{\,2}\beta_{hkl}\cos\theta_{hkl}}{\lambda^2}\right) + \left(\frac{\varepsilon}{2}\right)^2 \qquad (4.10)$$

where d_{hkl} is the interplanar spacing between the (hkl) planes, β_{hkl} is the FWHM, λ is the wavelength of X-rays used, θ_{hkl} is the diffraction angle, k is the shape factor having values in between 0.9 and 1 and D is the apparent volume weighted average size and ε is the apparent strain related as[101]

$$\varepsilon_{rms} = \frac{\varepsilon}{2\sqrt{2\pi}} \qquad (4.11)$$

where ε_{rms} is the root mean square (rms) strain. Therefore, it can be seen that the incorporation of Cr produces a small lattice distortion giving rise a compressive strain which favor the reduction in d-value and shifting of Bragg angle toward higher angles. The average size and microstrain obtained from the SSP is plotted against Cr concentration in Fig. 4.57. It can be seen that with decrease in crystallite size, the microstrain increases suggesting the possible reduction in crystallite size which can be seen from the broadening of the diffraction peaks as shown in Fig. 4.54 (b). The crystallite size has also been evaluated from the Debye Scherrer equation on (101), (004), (200) and (105) peaks and the variation of crystallite size with Cr content is shown in Fig. 4.57. The reduction in the average crystallite size with Cr doping could be due to the presence of Cr–O–Ti bonds, which inhibits the growth of the crystals. This indicates that Cr ion replaces the Ti^{4+} ions in the TiO_2 host lattice, which results in the decrease of the average crystallite size.
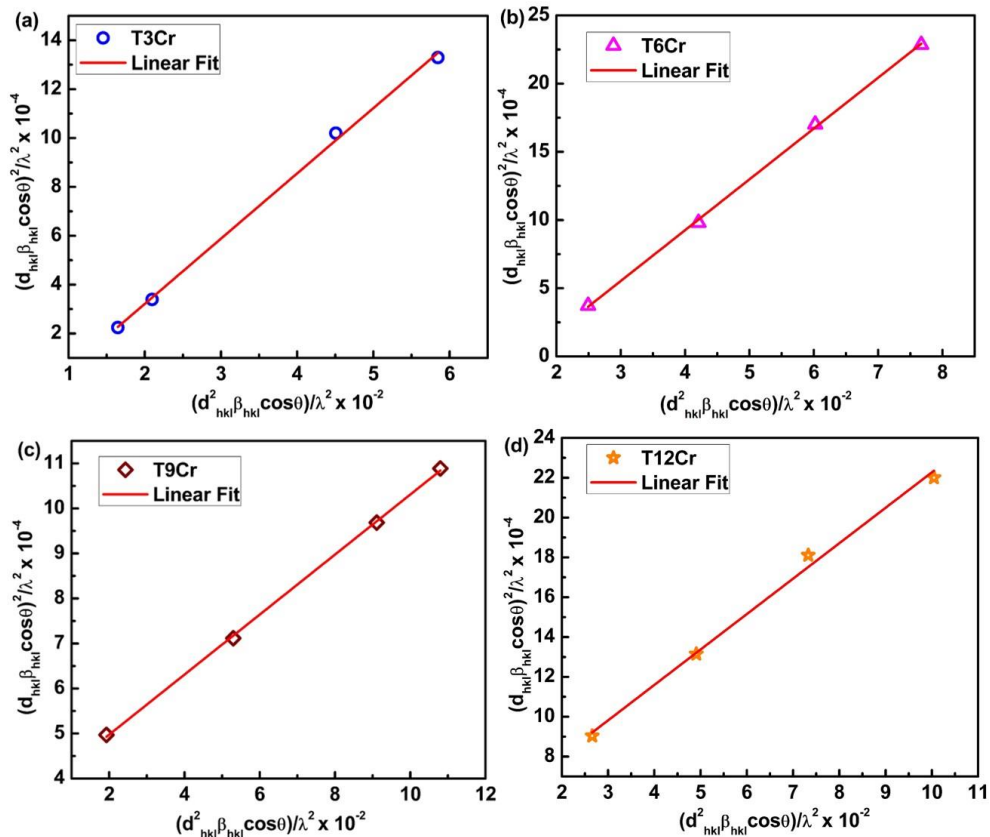
Fig.4.56. SSP of Cr-doped TiO₂ nanocrystals (a) T3Cr, (b) T6Cr, (c) T9Cr, and (d) T12Cr.
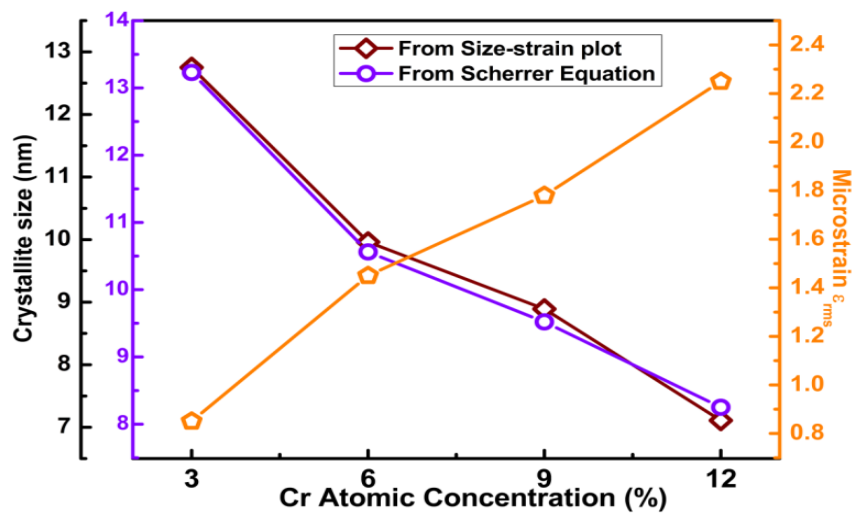
Fig.4.57. Variation of crystallite size and microstrain with Cr concentration

B. XRD analysis of Mn-doped TiO₂

Fig. 4.58 (a) shows the XRD patterns of all Mn-doped TiO₂ nanocrystals recorded in the range 20° to 80°. All the samples could be well indexed with the

tetragonal anatase phase of TiO_2 [JCPDS card No: 89-4921]. No diffraction peaks corresponding to MnO, Mn_2O_3 or Mn_3O_4 were observed in the XRD patterns indicating the phase purity of the synthesised samples. The peak shift associated with the most intense (101) peak shown in Fig. 4.58 (b) indicate the successful incorporation of Mn at the place of Ti in TiO_2. The FWHM has been estimated from the fitting of the (101) peak and is shown in Fig. 4.59. Rietveld refinement was carried out on all the samples using Fullprof software as shown in Fig. 4.60(a) - (d) and the parameters extracted from Rietveld refinement are tabulated in Table 4.12. The ionic radii of Mn^{2+} (0.67 Å) is slightly larger than Ti^{4+} (0.61 Å), while the ionic radii of and Mn^{3+} (0.58 Å) is slightly smaller than Ti^{4+}.[63] Hence, the slight increase in the lattice parameters could be due to the presence of Mn^{2+} ions in the system.[100]
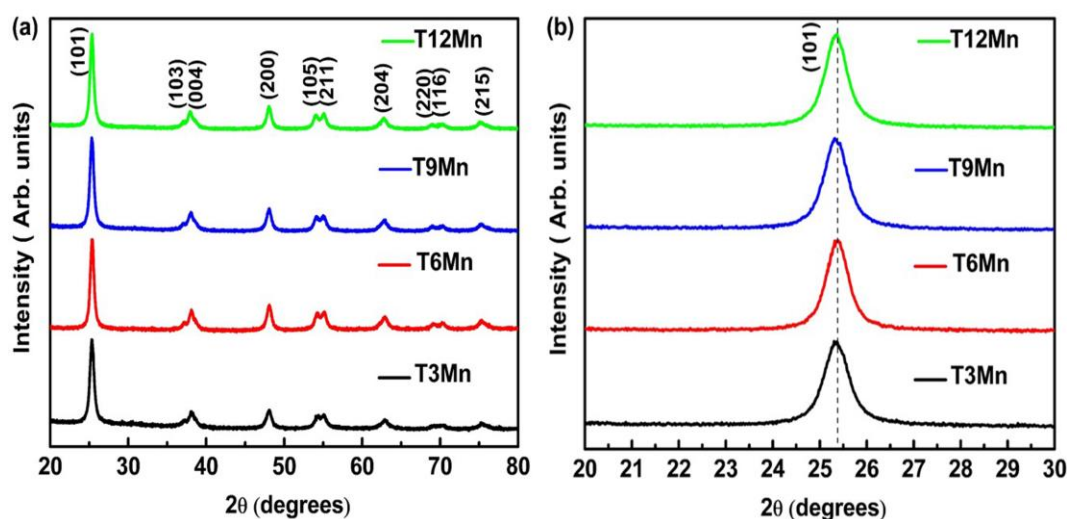
Fig.4.58. (a) XRD patterns of Mn-doped TiO_2 nanocrystals (b) peak shift associated with (101) peak for all the Mn-doped samples

The size strain parameters of the Mn-doped samples have been determined from the SSP and are shown in Fig. 4.61. In this plot, the data points from low angle reflections are given more weightage while the high angle reflections are given less weightage. In the SSP plots, it is assumed that Lorentzian function describes the ''crystallite size'' profile while Gaussian function describes the ''strain profile'' [101] and is governed by the equatios (4.10) and (4.11). From the SSP, the crystallite size and the micro strain were evaluated using the equations 4.10 and 4.11. The variation of crystallite size and micro strain with Mn concentration is shown in Fig. 4.62. The crystallite size has also been estimated from the Debye Scherrer equation and its

variation with Mn content is plotted in Fig. 4.62, which is in good agreement with the crystallite size derived from SSP.
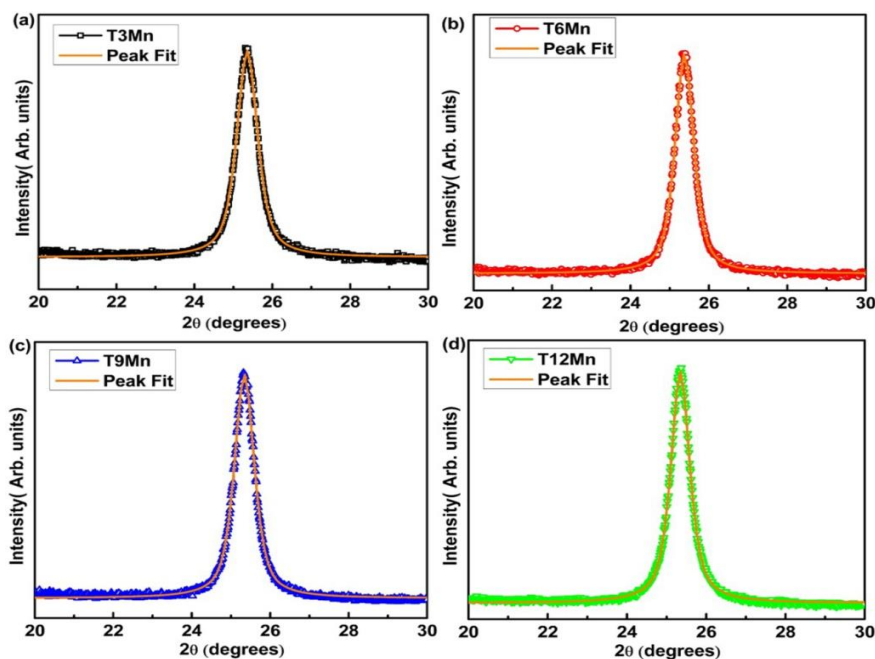
Fig.4.59. Estimation of FWHM from the most intense (101) peak of all the Mn-doped samples (a) T3Mn, (b) T6Mn, (c) T9Mn and (d) T12Mn
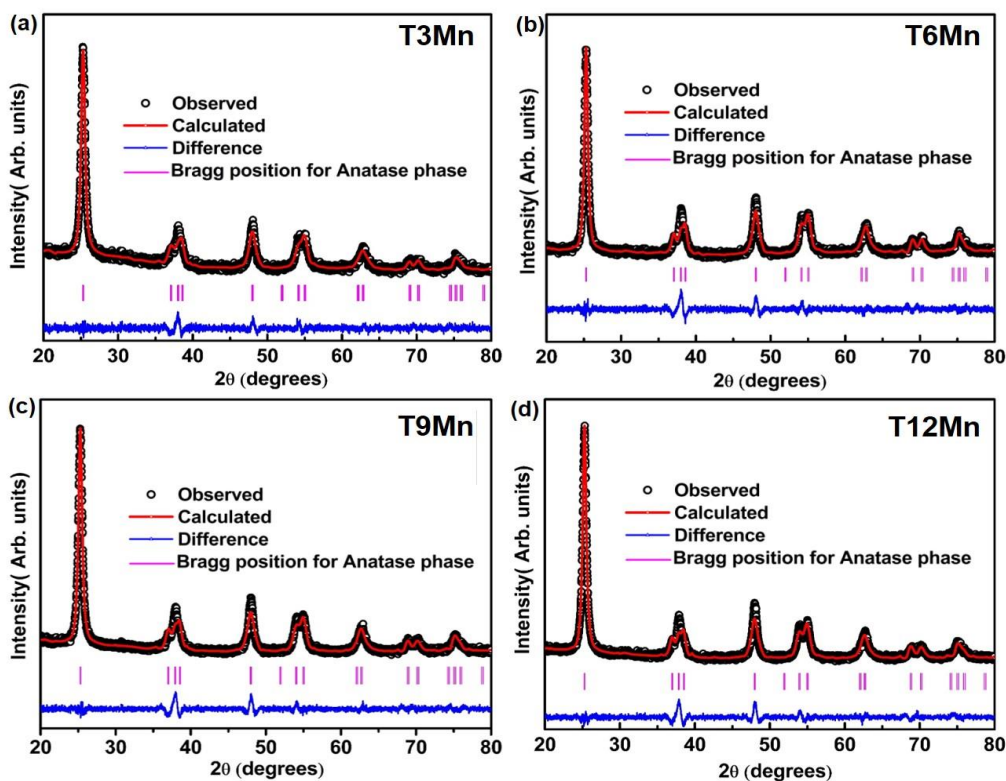
Fig.4.60. Refined XRD patterns of (a) T3Mn, (b) T6Mn, (c) T9Mn and (d) T12Mn

Table 4.12. Refinement parameters obtained for Mn-doped TiO$_2$ nanocrystals

Compound	T3Mn	T6Mn	T9Mn	T12Mn
Phase	Anatase			
Crystal Structure	Tetragonal			
Space Group	I 4$_1$/a m d			
Lattice Parameters				
a(Å)	3.7907 (4)	3.7911 (1)	3.7923 (4)	3.7953 (5)
c(Å)	9.4926 (2)	9.4928 (1)	9.5136 (3)	9.5035 (4)
Volume (Å)^3	136.40 (3)	136.43 (2)	136.82 (6)	136.89 (1)
Atomic positions				
Ti/Mn $_x$ (4a)	0.0000	0.0000	0.0000	0.0000
Ti/Mn $_y$ (4a)	0.7500	0.7500	0.7500	0.7500
Ti/Mn $_z$ (4a)	0.1250	0.1250	0.1250	0.1250
O $_x$ (8e)	0.0000	0.0000	0.0000	0.0000
O $_y$ (8e)	0.2500	0.2500	0.2500	0.2500
O $_z$ (8e)	0.0854	0.0862	0.0838	0.0861
B $_{iso}$ (Ti/ Mn) (Å)^2	0.0004	0.0003	0.0007	0.0005
B $_{iso}$ (O) (Å)^2	0.0041	0.0018	0.0011	0.0008
Residual Parameters				
R$_p$	3.68	3.51	3.55	2.98
R$_{wp}$	5.15	4.79	4.85	3.90
χ^2	1.49	1.22	1.15	1.55
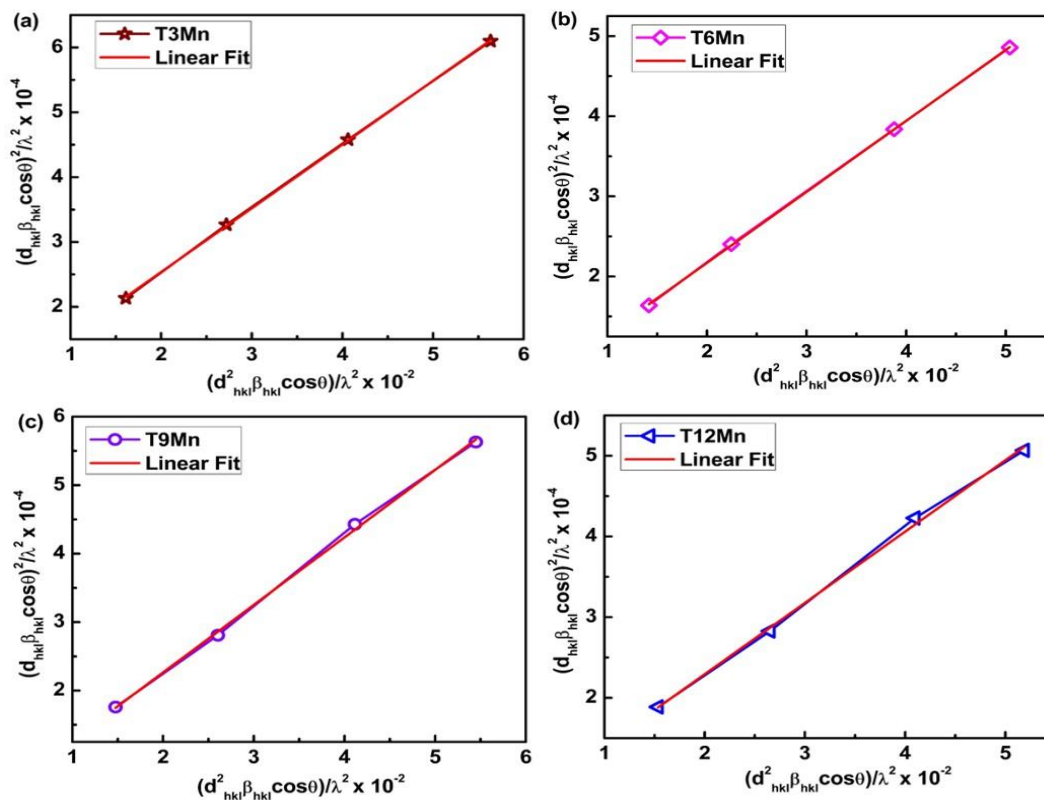
Fig.4.61. Size strain plots of (a) T3Mn, (b) T6Mn, (c) T9Mn and (d) T12Mn
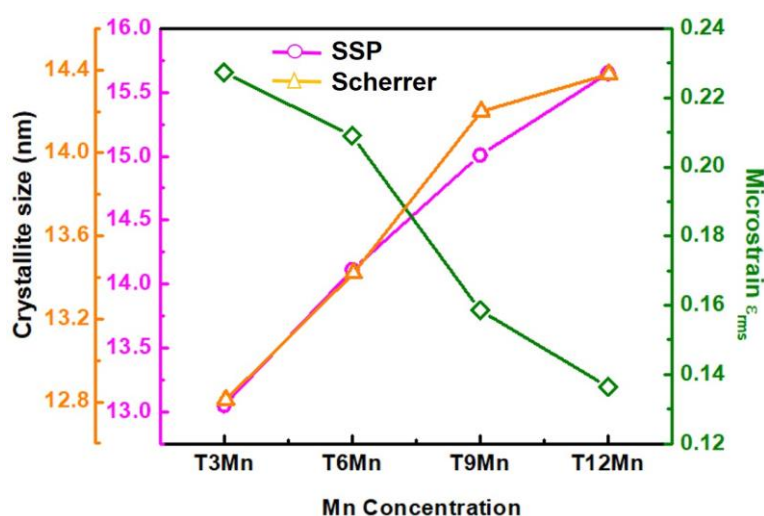
Fig.4.62. Variation of crystallite size and microstrain with Mn concentration

4.3.3.2. Raman Analysis

Raman spectra corresponding to Cr and Mn-doped TiO₂ are discussed in the following sub sections

A. Raman Analysis of Cr-doped TiO₂

Fig 4.63(a) shows the Raman spectra of all the Cr-doped samples. All the major peaks corresponding to anatase TiO_2 has been indexed in the Raman spectra. Anatase TiO_2 has six Raman active modes ($A_{1g} + 2B_{1g} + 3E_g$) and three IR active modes.[102] The irreducible representation of optical phonon mode at the G-point of the Brilliouin zones can be represented as: $\Gamma_{opt} = A_{1g}$ (R) + $2B_{1g}$ (R) + $3E_g$ (R) + B_{2u} (IR) + A_{2u} (IR) + $2E_u$ (IR). The peaks E_g at 144, 197 and 639 cm^{-1} corresponds to the symmetric stretching vibration of O-Ti-O bond while the A_g and B_g bands at 516 and 399 cm^{-1} indicates the symmetric and anti-symmetric bending vibrations of O-Ti-O bonds respectively.[14] No characteristic peaks of CrO_2 or Cr_2O_3 have been observed. The red shift and broadening of the major $E_g(1)$ peak suggests the incorporation of Cr ions into the TiO_2 lattice and is attributed to the increased disorder and destruction of ideal symmetry of the crystal and is plotted in Fig 4.63(b).[15,16,76] With increase in Cr concentration, it can be seen that there are no phases corresponding to Cr or related oxides suggesting that all the Cr atoms have been substituted into the lattice rather than occupying the interstitial sites associated with Ti. The deconvoluted Raman spectra of T3Cr is shown as a

representative of the series and all the modes corresponding to anatase TiO$_2$ has been deconvoluted in Fig 4.63 (c). Fig 4.63(d) shows the variation of Raman intensity with Cr content. It can be seen that the Raman intensity decreases with increase in Cr content indicates the breakdown of crystal symmetry arising as a result of the distortion of the
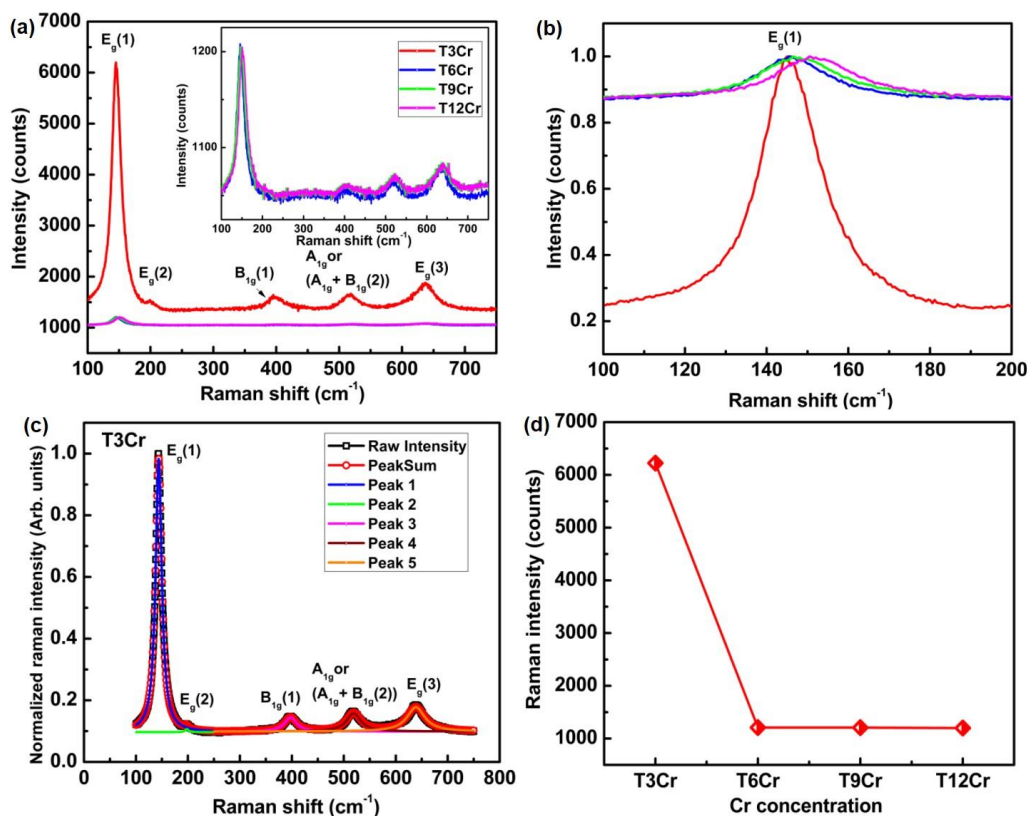
Fig.4.63. (a) Raman spectra of T3Cr, T6Cr, T9Cr, and T12Cr. Inset shows the magnified view of Raman spectra of T6Cr, T9Cr, and T12Cr (b) Expanded region of the E$_g$(1) mode showing peak shifting and broadening (c) Deconvoluted Raman spectra of T3Cr (d) Variation of Raman intensity with Cr concentration

O-Ti-O bond due to the incorporation of Cr ions at the Ti site. It can be seen that with increase in Cr content, the oxygen vacancies increases resulting in the decrease of Cr-O bonds and hence a decrease in unit cell volume is observed in conformity with the XRD refinement results. The shifting and broadening of the E$_g$ mode is due the increase in the concentration of oxygen vacancies.[77]

B. Raman Analysis of Mn-doped TiO$_2$

The room temperature Raman spectra Mn-doped TiO$_2$ nanocrystals are shown in Fig. 4.64 (a). It is well reported in literature that anatase TiO$_2$ has six Raman active

modes and three infra-red (IR) active modes.[103,104] The absence of modes corresponding to any other impurities are further validated by deconvoluting the Raman spectra and as a representative of the series deconvoluted spectra of T3Mn is shown in Fig. 4.65. As discussed earlier in section 4.3.1.1. and 4.3.2.2, the most intense Raman mode (E_g (1)) appears at 145 cm^{-1} and is very sensitive to the local oxygen surrounding the metal ion.[105] The other two E_g modes at 197 and 640 cm^{-1} corresponding to E_g (2) and E_g (3) respectively are less intense Raman modes. The B_{1g} peak and $A_{1g}+B_{1g}$ peak appear at 397 cm^{-1} and 516 cm^{-1} respectively.[106] The expanded view of the mode is shown in the Fig. 4.64 (b), which demonstrates that the broadening and red shifting of E_g(1) mode with the incorporation of Mn in TiO$_2$. This broadening and E_g(1) mode shifting is due to the disruption of lattice symmetry and generation of defects such as oxygen vacancies to maintain charge neutrality due to the substitution of Mn at the Ti site. As a result of the
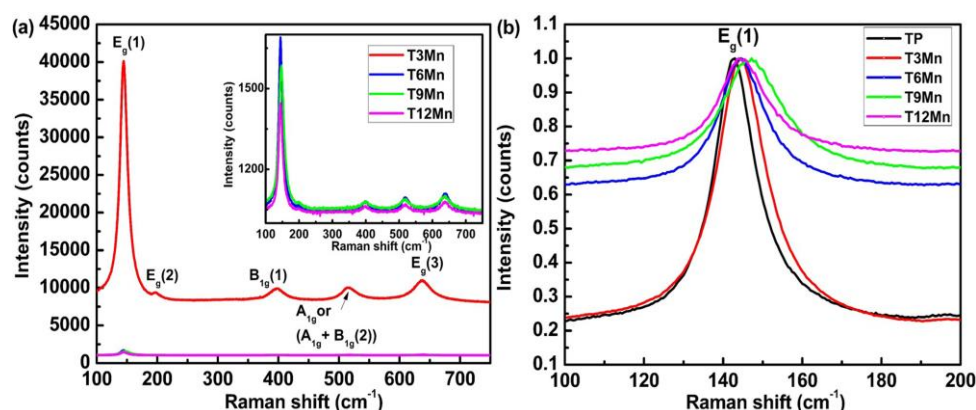
Fig.4.64. (a) Raman spectra of T3Mn, T6Mn, T9Mn and T12Mn at room temperature. Inset shows the magnified view of Raman spectra of T6Mn, T9Mn and T12Mn (b) Expanded region of E_g (1) peak in the range 100-200 cm^{-1} of undoped and Mn-doped TiO$_2$ nanocrystals

formation of oxygen vacancies, there would be a decrease in the number of Ti-O and Mn-O bonds, which would result in the contraction of the lattice as seen from the refinement table. This decrease in the number of Ti-O and Mn-O bonds is also responsible for the shifting of the E_g (1) mode to higher wave numbers.[77,107,108] Thus, it could be presumed that oxygen vacancies are key component contributing to the shifting and broadening of the Raman peaks.
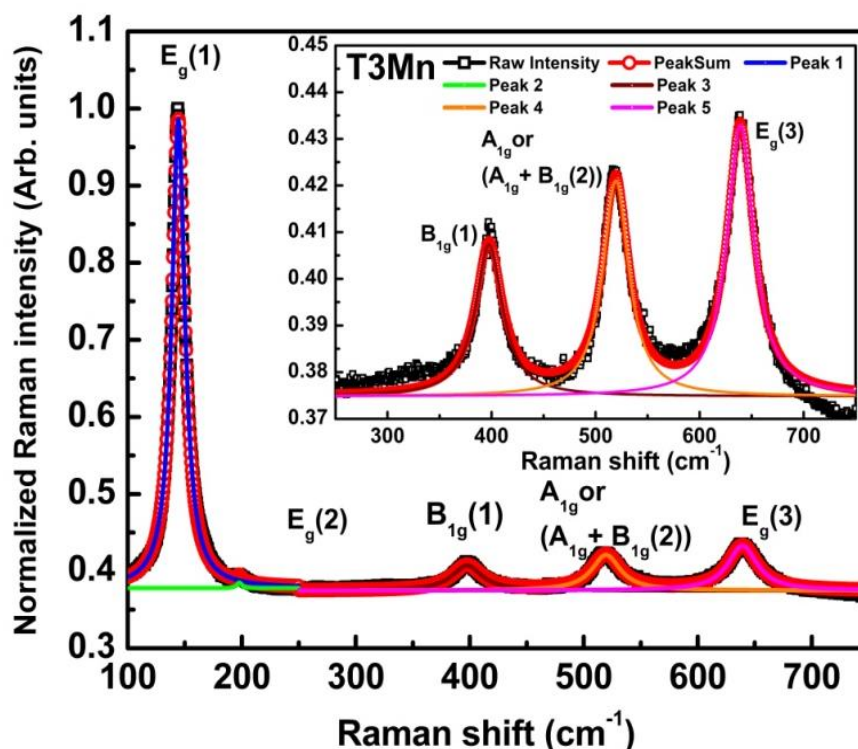
Fig.4.65. Deconvoluted Raman spectra of 3% Mn-doped TiO$_2$

4.3.3.3. Morphological analysis

TEM analysis have been carried out on Cr and Mn-doped TiO$_2$ nanocrystals and are discussed in the following sub sections

A. Morphological analysis of Cr-doped TiO$_2$

Fig.4.66 shows the high resolution TEM images of Cr-doped TiO$_2$ nanoparticles. The particles seem to be aggregated as seen from the TEM micrographs 4.66(a)-4.66(d). The high resolution TEM images show the presence of lattice fringes. The planes (101), (004), (211), (200) and (105) correspond to the tetragonal anatase phase of TiO$_2$ and have been indexed in Fig 4.66(i-l). The insets of Fig 4.66(i-l) show the corresponding FFT which indicate the high crystalline nature of the samples. SAED patterns corresponding to T3Cr, T6Cr, T9Cr and T12Cr are shown in Fig 4.66(m-p).
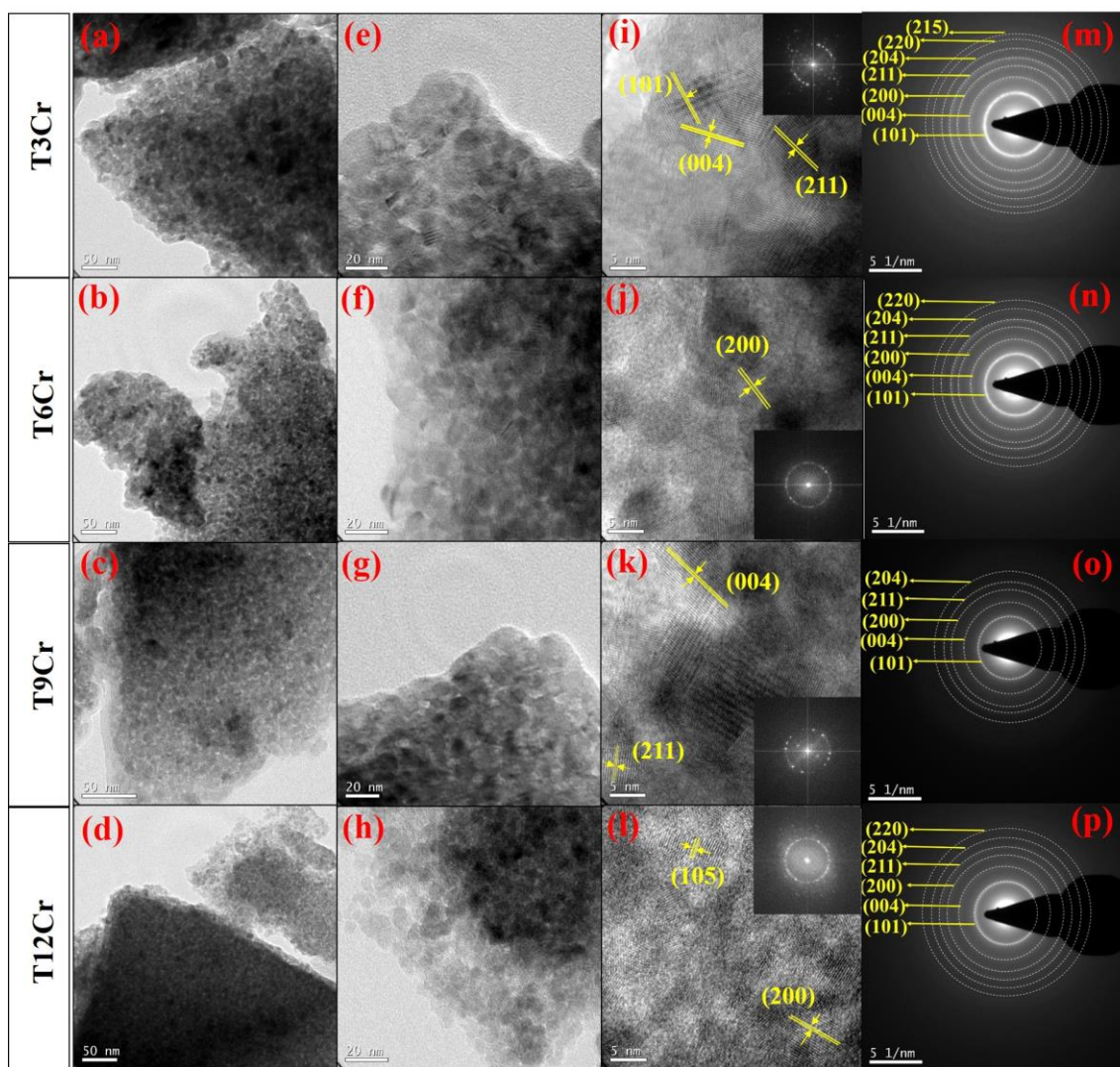
Fig.4.66. Cr-doped TiO₂ nanocrystals. (a–h) TEM images showing the nanocrystal formation. (i–l) HR-TEM images showing lattice fringes with FFT shown in the inset. (m–p) SAED patterns of Cr-doped TiO₂ nanocrystals

B. Morphological analysis of Mn-doped TiO₂

The morphological features of Mn-doped TiO₂ nanocrystals are shown in Fig. 4.67(a)-(h). All the samples have an average size ranging from 5-12 nm which is well in agreement with the particle size derived from the XRD data. The high-resolution TEM images shown in Fig. 4.67 (i)- (l) show the presence of lattice fringes corresponding to different planes of tetragonal anatase phase of TiO₂ like (101), (103) and (004) which indicate the high crystalline nature of the samples. The corresponding FFTs are shown in the insets in Fig. 4.67 (i) – (l). SAED patterns show the presence of distinct rings

corresponding to different planes of anatase TiO$_2$ and they have been indexed using Image J software for all the samples as shown in Fig. 4.67 (m - p).
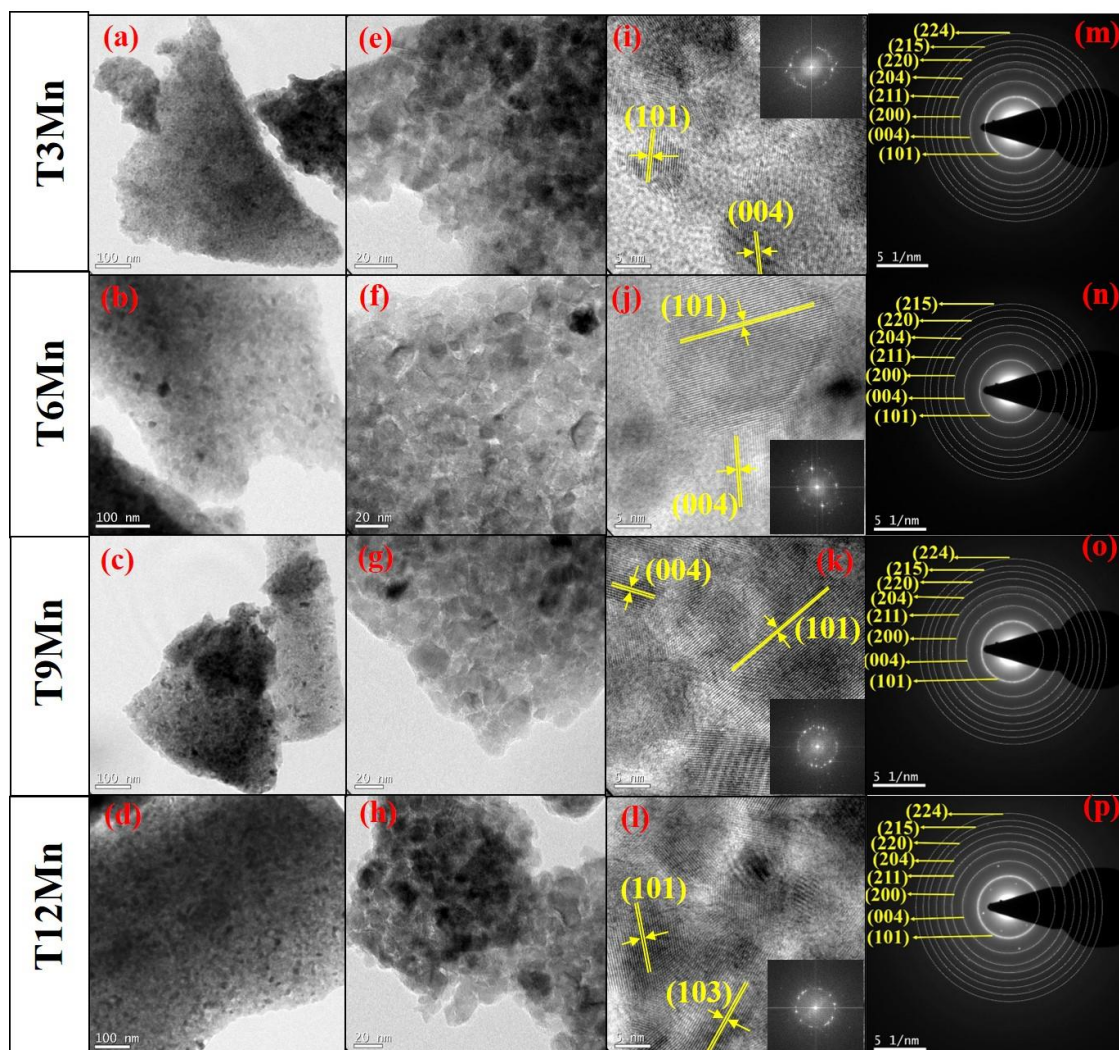
Fig.4.67. TEM images of Mn-doped TiO$_2$ nanocrystals (a-h) TEM images showing the nanocrystal formation, (i-l) HR-TEM images showing lattice fringes with FFT shown in the inset and (m-p) SAED patterns of Mn-doped samples.

4.3.3.4. FT-IR analysis

FT-IR analysis corresponding to Cr and Mn-doped TiO$_2$ are discussed below.

A. FT-IR analysis of Cr-doped TiO₂

Fig. 4.68 shows the FT-IR spectra of all the samples with increasing Cr content. A large hump around 847 cm^{-1} is attributed to the stretching vibration associated with the Ti-O-Ti bonding.[81] The shifting and broadening of band position at 847 cm^{-1} confirm the presence of defects arising due to oxygen vacancies existing in the system due to Cr

incorporation in TiO₂ lattice. The symmetric and anti-symmetric stretching vibrations of the OH functional group was represented by the broadband around 4000–3200 cm^{-1}.[82] Bending vibrations corresponding to the OH groups appear between 1700 and 1300 cm^{-1} and this arises as a result of the adsorbed atmospheric water on the sample surface.[80]
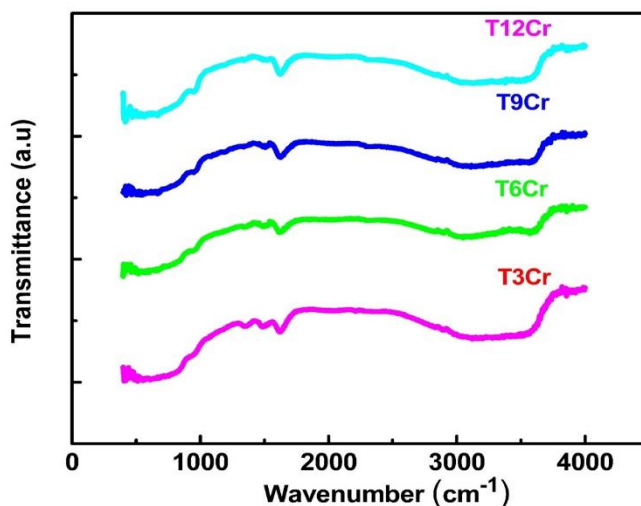
Fig.4.68. FT-IR spectra of Cr-doped TiO₂ nanocrystals

B. FT-IR analysis of Mn-doped TiO₂

Fig 4.69 shows the FT-IR spectra of all the samples with increasing Mn content. As discussed in section 4.3.3.4.1., the hump around 847 cm^{-1} is attributed to the O-Ti-O stretching vibration.[81] The stretching vibrations of the OH functional groups (symmetric and anti-symmetric) were represented by the broadband around 3200–4000 cm^{-1}.[82]
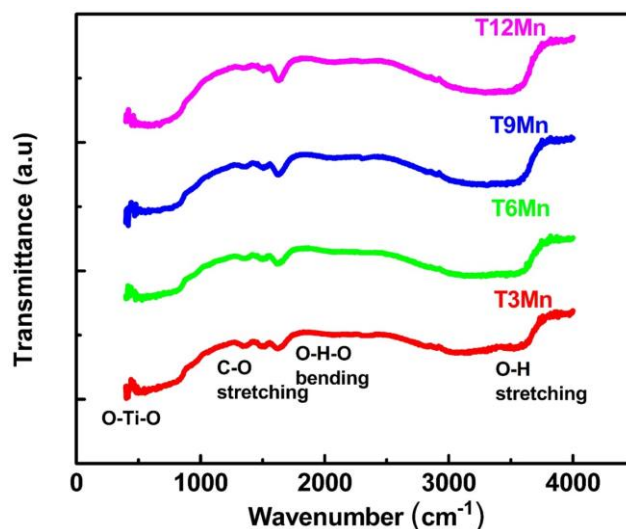
Fig.4.69. FT-IR spectra of Mn-doped TiO₂ nanocrystals

Bending vibrations corresponding to the OH groups appear between 1300 and 1700 cm^{-1} and this could be occurring as the adsorbed atmospheric water is present on the sample surface.[80]

4.3.3.5. Optical Studies

UV- Visible spectra and Photoluminescence studies corresponding to Cr and Mn-doped TiO_2 are discussed in the sub sections given below.

A. UV- Visible and Photoluminescence Studies of Cr-doped TiO₂

The changes in the optical absorption property with increasing Cr content can be studied with the help of UV-visible spectroscopy. The absorbance spectra of all the samples has been calculated using the Kubelka Munk equation and are shown in Fig 4.70 (a). However with Cr doping, the absorption spectra broadens and two peaks can be observed, one between 400 and 600 nm and the other at around 700 nm. These peaks are a result of the d-d transitions which arise under the influence of the octahedral crystal field when Cr ions are introduced into the lattice. The first absorption peak between 400 and 600 nm is due to $^4A_2$ (F) to $^4T_1$(F) transition and the second peak is due to the spin forbidden $^4A_2$(F) to 2E, $^2T_1$ transition.[104,109,110] When Cr ions are introduced into the TiO_2 lattice, it exists as Cr^{3+} ions forming a CrO_6 octahedra and the repulsion between these Cr^{3+} and oxygen ions results in the splitting of d orbitals into ground state ($^4A_2$) and excited states ($^4T_1$, 2E, etc.) The band gaps have been estimated from the Tauc's plot and are represented in Fig 4.70 (b). It can be seen that the band gap decreases abruptly with increase in Cr content suggesting the incorporation of Cr ions into the TiO_2 lattice. A red shift is observed for all the Cr-doped TiO_2 samples and this shift in absorption edge is attributed to the acceptor tendency exhibited by Cr and due to this reason the red shifting tendency is increased with Cr doping concentration as evident from Fig 4.70 (a). When Cr concentration increases, the shifting of conduction band edge can happen due to the acceptor tendency of Cr as discussed above which ultimately causes the red shift and endorses a decreased band gap in comparison to the undoped compound which is discussed below. At higher wavelengths, well above 600 nm, another low intensity absorption peak is evident and a similar result has been

reported recently[111] which is reported to be due to the d-d transition arising from Cr^{3+} ions as discussed earlier which can could effectively cause shifting of conduction band depending on the doping levels of Cr^{3+} ions.[111]

A significant narrowing of band-gap is observed with increasing Cr concentration and the estimated optical band-gap of all the samples with doping concentrations 3, 6, 9 and 12 at wt % are 1.90, 1.63, 1.57 and 1.43 eV respectively.
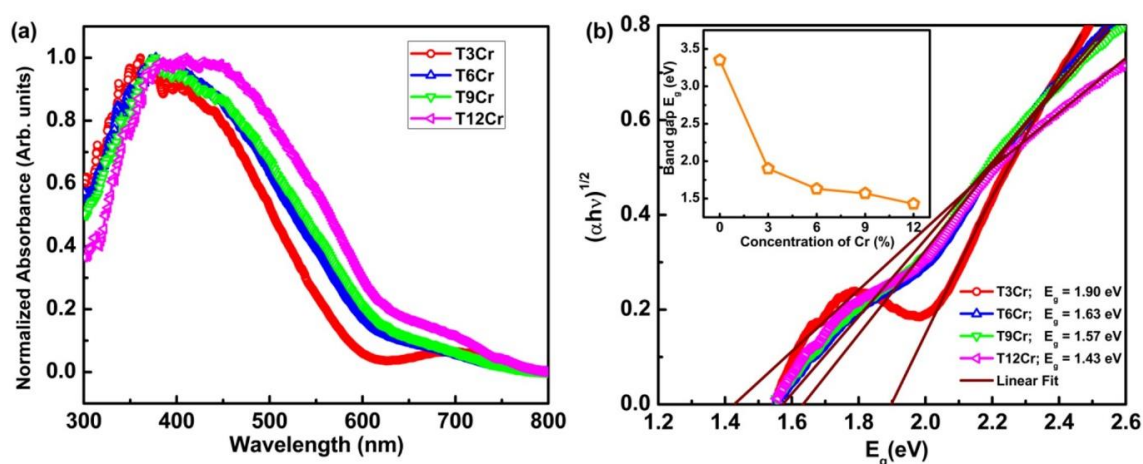
Fig.4.70. Cr-doped TiO₂ nanocrystals: (a) solid-state UV spectra and (b) Tauc's plot. Inset shows the variation of band gap with Cr substitution

It can also be seen that there is a significant lowering of band gap from 3.16 eV in undoped compound to 1.43 eV in T12Cr, which is clearly attributed to the presence of localised defect states in TiO₂ in comparison to the undoped TiO₂. These defect states are responsible for the absorption tail in the absorption spectra which extends into the forbidden gap. This absorption tail is called Urbach tail and is associated with Urbach energy.[84,85] The equation for calculating the Urbach energy is (4.9) and the Urbach energy is calculated by plotting Ln (α) against E. Since the absorption coefficient α is proportional to absorbance F(R), we have plotted Ln (F(R)) against the photon energy, E and is shown in Fig 4.71 for all the Cr-doped samples. The reciprocal of the slope of linear fit, below the optical band gap region, gives the value of Urbach energy, E_u and the values of Urbach energy is tabulated in Table 4.19.

It is observed that an increase in Cr dopant concentration causes Urbach energy enhancement indicating the formation of more number of oxygen vacancies with Cr

incorporation. The creation of more number of oxygen vacancy defects can be explained on the basis of charge neutrality concept which is essential to be maintained in the TiO_2 lattice when Cr concentration increases from 3% to 12%.[101] These localised defect states can effectively influence the valence and conduction band edges which could also be treated as another reason for triggering a decreased band gap in Cr-doped TiO_2.
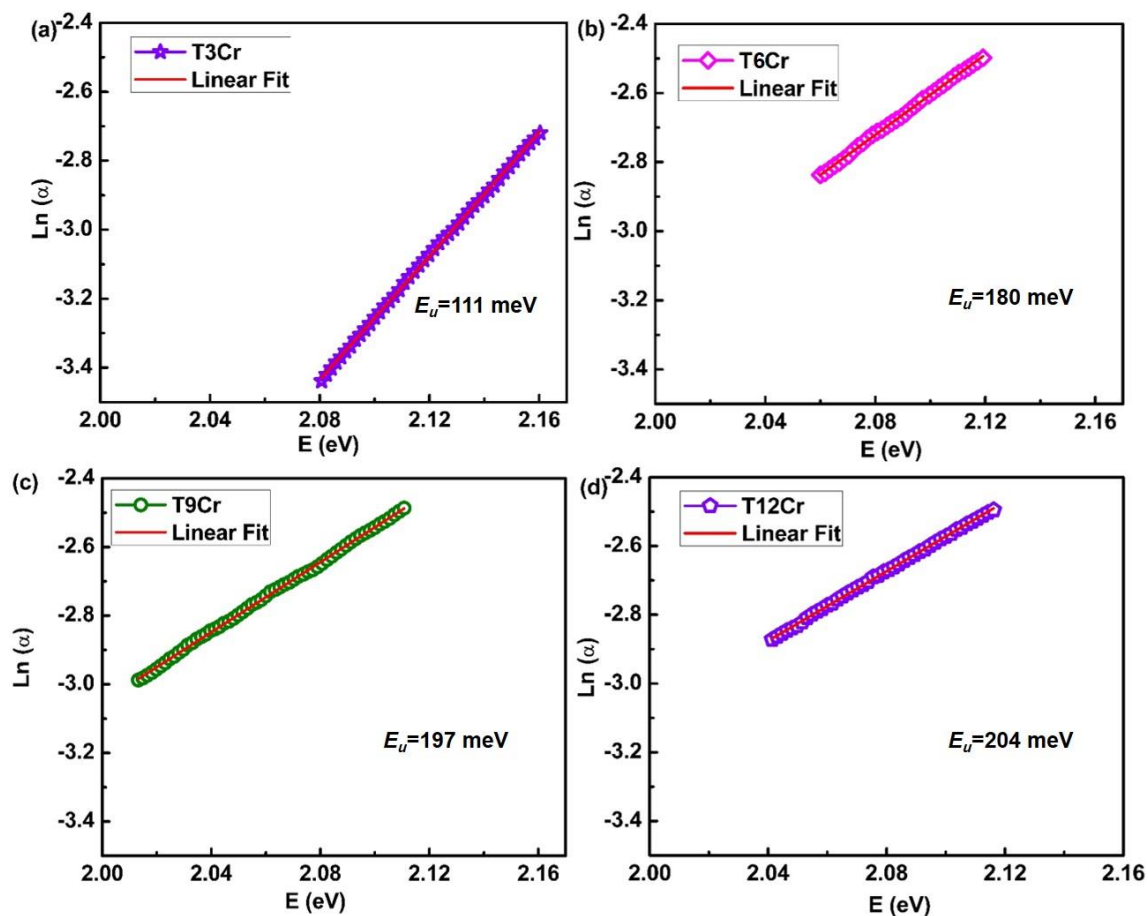
Fig.4.71. Plot of Urbach energy for (a) T3Cr, (b) T6Cr, (c) T9Cr, and (d) T12Cr.

PL spectra have been taken at an excitation wavelength of 325 nm and the emission spectra have been recorded for all the Cr-doped samples as shown in Fig 4.72(a). The spectra show a broad emission in the visible 350 - 600 nm range. The deconvoluted PL spectra shows five peaks at around 400, 460, 500, 540 and 580 nm as discussed earlier in sections 4.3.1.4, 4.3.2.5 and is represented in Fig 4.72(b). A schematic diagram showing the possible PL emissions in Cr-doped TiO_2 system is depicted in Fig.4.72 (c). The variation in PL intensity with Cr substitution shows a

decreasing trend as shown in Fig 4.72(d) and could ascertain the Cr incorporation into TiO_2 lattice based on the recent reports that explains the emission spectra of transition metal ion incorporated TiO_2 material.[112] Furthermore, this decrease in PL intensity can be well corroborated with optical absorption data and band-gap associated with the Cr-doped samples in such a way that when the doping concentration is heavy there will be higher separation rates associated with the photo-induced charges leading to a considerable decrease in the band-gap of the material and facilitate the broad range optical absorption.
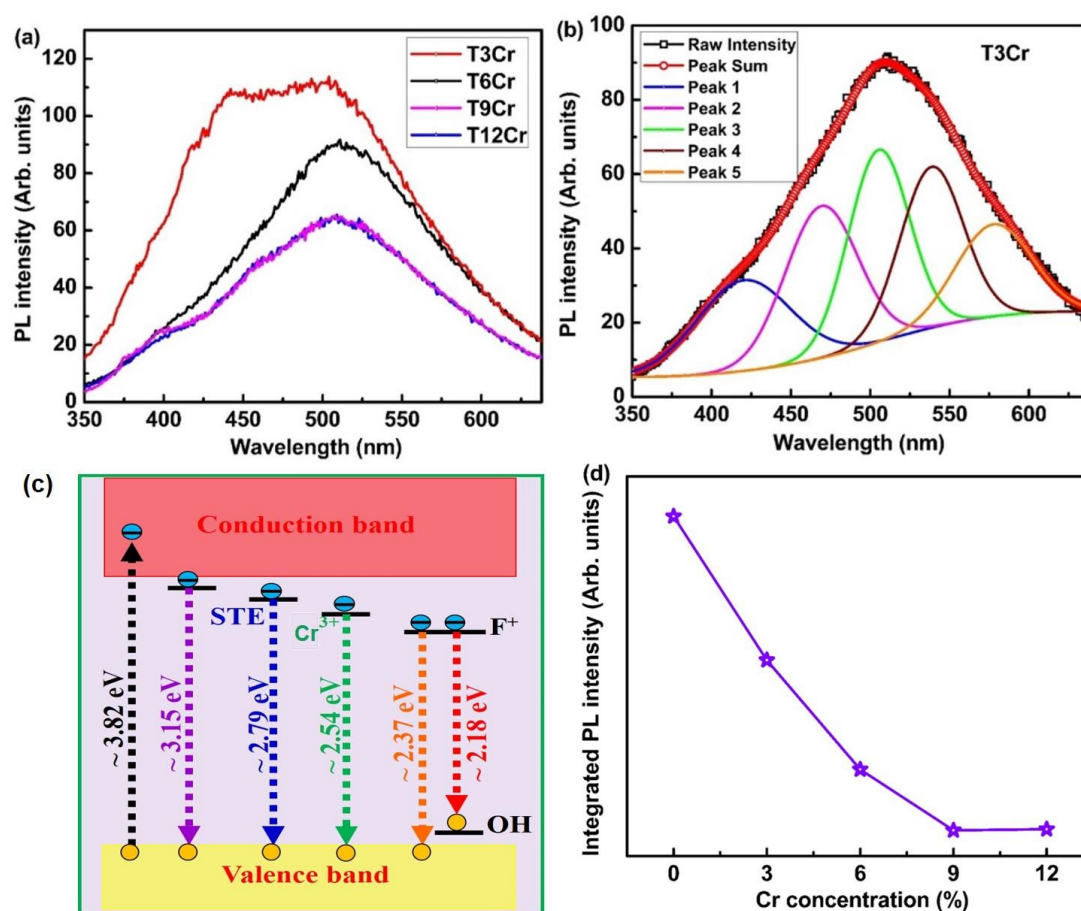
Fig.4.72. PL spectra: (a) Cr-doped TiO_2 nanocrystals. (b) Peak-fitted PL spectra corresponding to T3Cr. (c) Schematic diagram showing possible PL emissions in Cr-doped TiO_2 (d) variation of PL intensity with Cr substitution

B. UV- Visible and Photoluminescence Studies of Mn-doped TiO₂

The optical absorption spectra of all the Mn-doped samples are obtained from reflectance spectra in the range 300-800 nm and are shown in Fig. 4.73(a). The

introduction of Mn ions into the host lattice introduces intermediate states in the visible region. The peak at around 600 nm is attributed to ${}^4T_{1g}$ (G) $\rightarrow$ ${}^6A_{1g}$ (S) transition arising as a result of the d-d transitions.[113] When Mn ions substitutes for Ti, Mn-O bonds are also formed in addition to Ti-O bonds. Hence, according to the crystal field theory, electrons in the *d* orbital of Mn ions will experience repulsive forces from the electrons of the surrounding oxygen atoms, which results in the splitting of the *d* orbital to ground state and several excited states. In Mn substituted TiO₂, the band structure is perturbed by the presence of Mn ions which creates additional states within the band gap in the form of absorption tails called Urbach tail and the corresponding energy is called Urbach energy.[86] The Urbach energy is calculated using equation (4.9). Then, we have plotted Ln (α) versus E and the plots are shown in Fig. 4.74(a)-4.74(d). The reciprocal of the slopes of the linear portion below the optical band gap gives the Urbach energy. The presence of these localized defect states results in the lowering of band gap in Mn-doped TiO₂. It can also be seen that the estimated band gaps of Mn-doped TiO₂ nanocrystals are significantly lower than that of the recent report.[101]
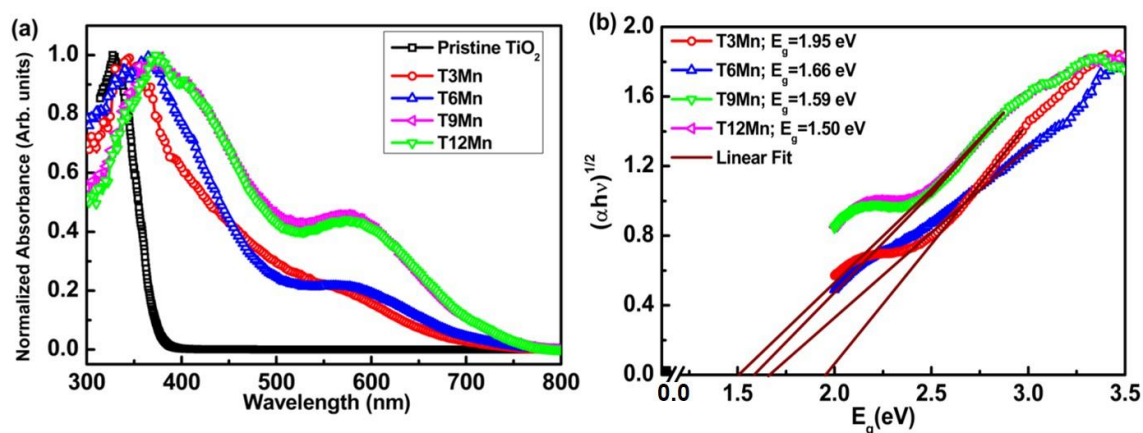
Fig.4.73. Mn-doped TiO₂ nanocrystals (a) solid-state UV spectra and (b) Tauc's plot

Fig. 4.75 depicts the PL spectra of Mn-doped TiO₂ nanoparticles taken at an excitation wavelength of 325 nm. The PL spectra of all the samples have been deconvoluted into five peaks. We have fitted the emission peaks with Gaussian and observed that five different emission peaks are present in the spectra. The deconvoluted PL spectra shows five peaks at around 400, 460, 500, 540 and 580 nm as discussed earlier in sections

4.3.1.4, 4.3.2.5 and is represented in Fig 4.75 (b)-(e). It can be seen that there are no peaks corresponding to Mn oxides in the PL spectra of the doped samples.
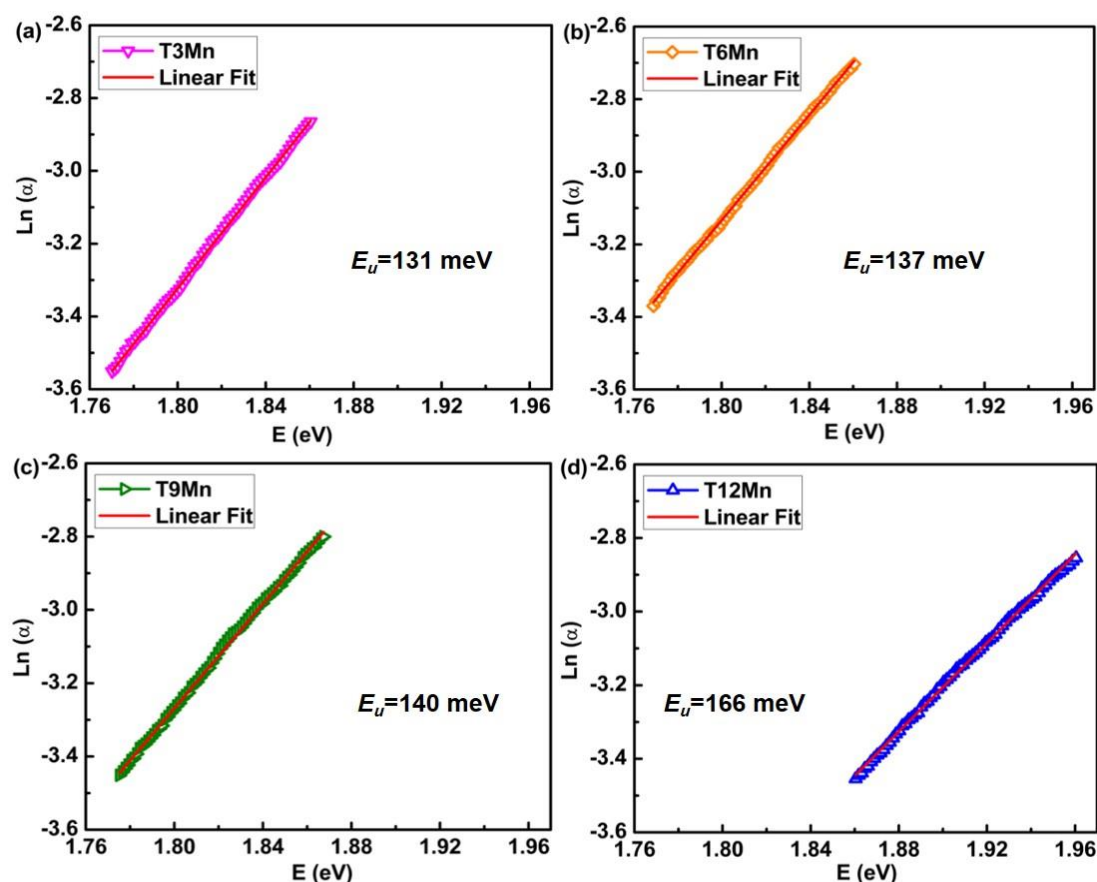
Fig.4.74. Urbach energy estimated for (a) T3Mn, (b) T6Mn, (c) T9Mn and (d) T12Mn

A decrease in PL intensity has been observed with increasing Mn concentration and is shown in Fig. 4.75(f). However upon doping TiO₂ with Mn disturbs the symmetry of the lattice resulting in the generation of oxygen vacancies as a result of the decrease in the number of Ti-O bonds as explained earlier in the Raman analysis. With increase in Mn doping, there would be an increase in the concentration of non-radiative oxygen vacancy centers. As the oxygen vacancy defects increases electrons get trapped and localized in these oxygen vacancies. Hence, electron hole recombination also decreases. As a result, the emission intensity also decreases with increase in Mn concentration. Another factor affecting the decrease in PL intensity is the reduction in mobility of the charge carriers due to the presence of defects or dopants on the grain boundaries, at the surface of the nanocrystals and in the interior. The mobile charge carriers get scattered when they approach charged dopants or oxygen defects resulting

in the decrease of their mobility which increases the separation of the charge carriers and hence reduces the PL intensity.[113]
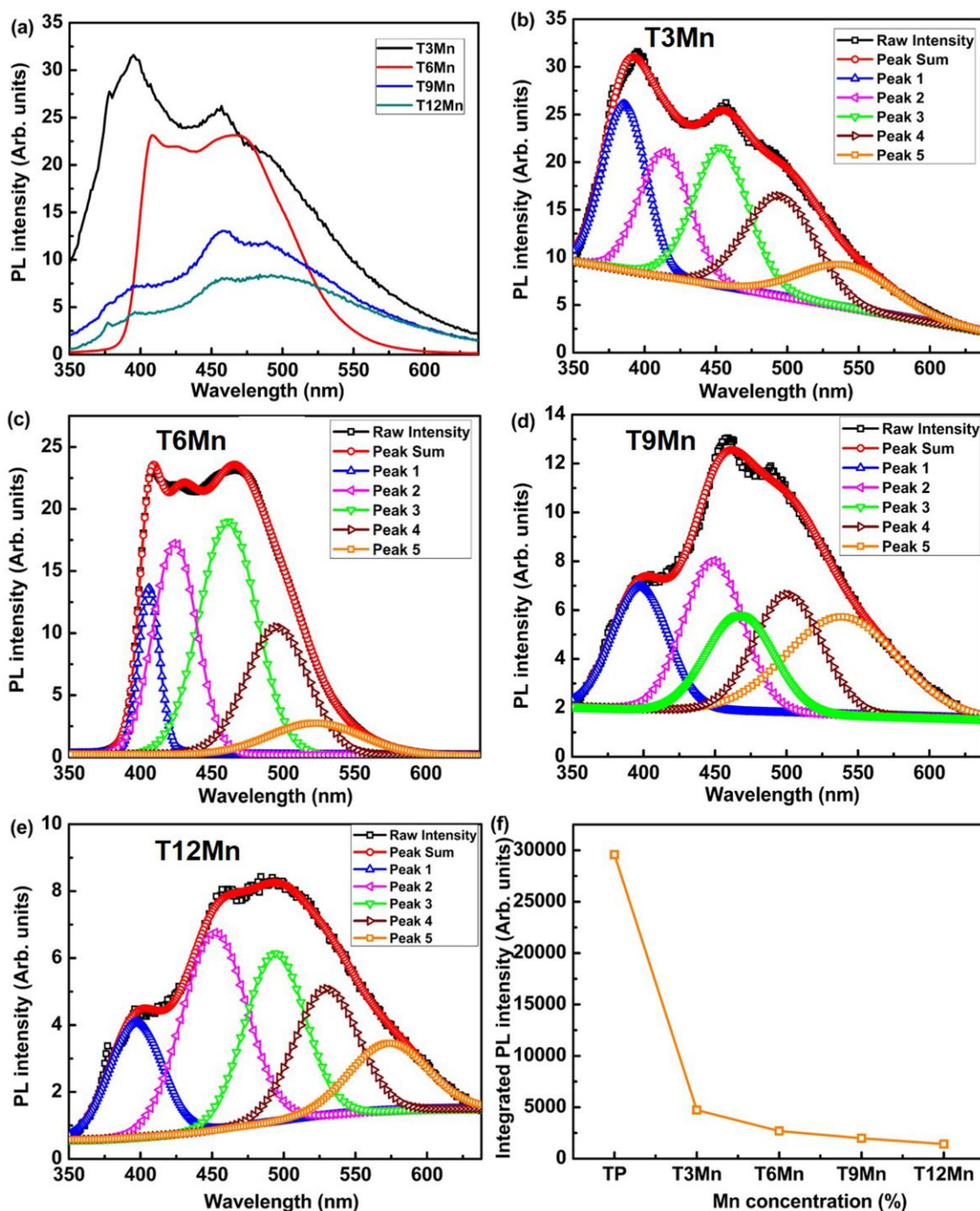
Fig.4.75. (a) PL spectra of Mn: TiO₂ nanocrystals (b) – (e) deconvoluted PL spectra of the individual compound and (f) Variation of integrated PL intensity with Mn doping

4.3.3.6. XPS analysis

XPS wide scan and high resolution spectra have been carried out on Cr and Mn-doped TiO$_2$ nanocrystals and the results are summarised in sub sections given below.

A. XPS analysis of Cr-doped TiO$_2$

In order to confirm the oxidation states of Cr and Ti in the doped samples, we have carried out the XPS analysis. The wide scan XPS spectra of T3Cr is shown in Fig 4.76(a). The high resolution scans of Ti, Cr and Oxygen is shown in Fig 4.76(b)-4.76(d) respectively. In the wide scan, only peaks corresponding to Ti, Cr and O are present which indicates that no foreign elements are present on the sample surface. The high resolution scan of Ti2p show the presence of Ti^{4+} and that of Cr2p indicate the presence of Cr^{3+} only. The Ti 2p spectrum of T3Cr shows the presence of Ti^{4+} 2p$_{3/2}$ at 458.35 eV, and Ti^{4+}2p$_{1/2}$ at 464.09 eV.[46]
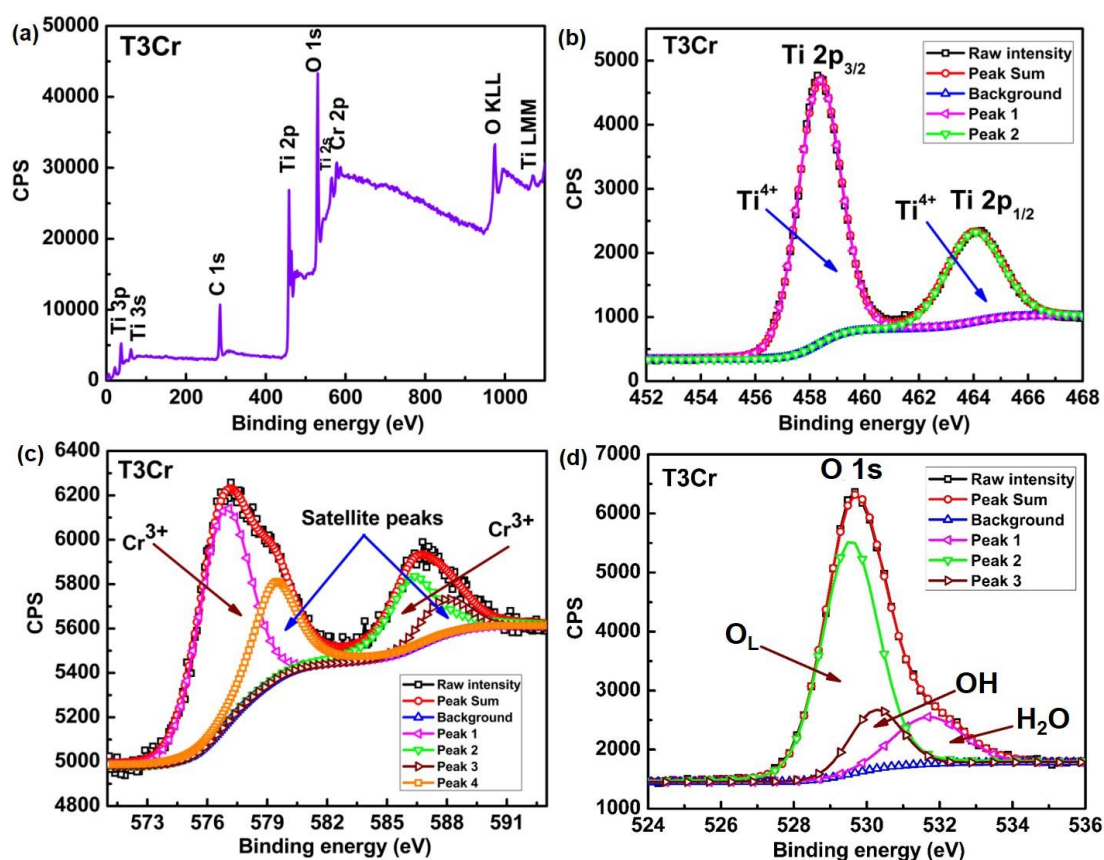
Fig.4.76. (a) Wide scan XPS spectra of T3Cr, High resolution scans of (b) Ti 2p, (c) Cr 2p, and (d) O 1s.
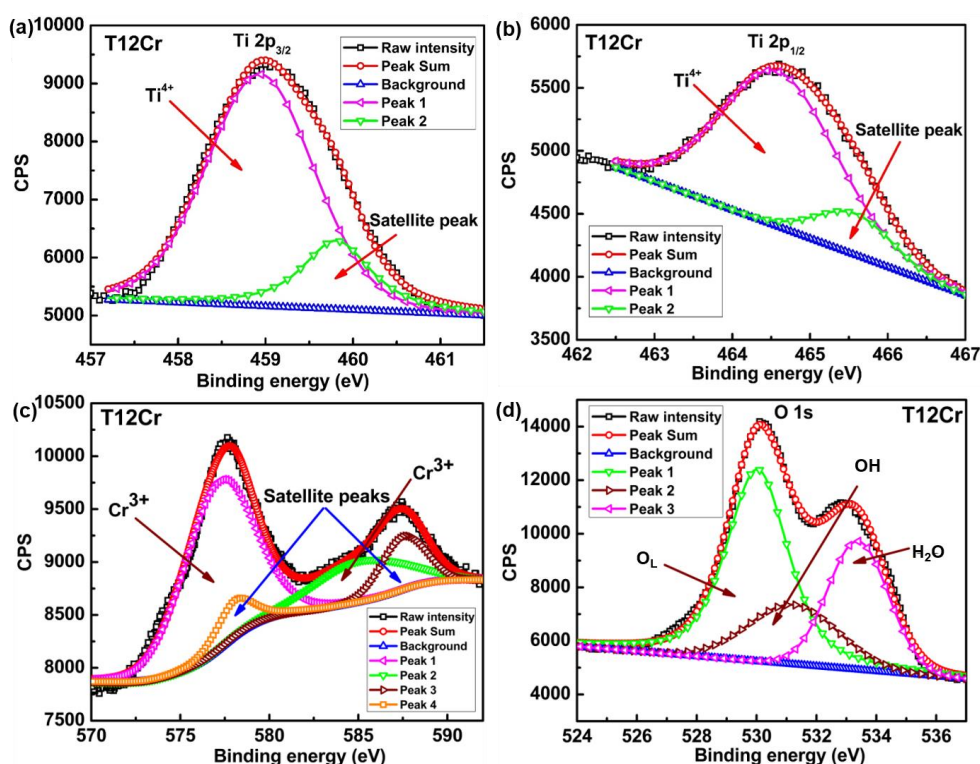
Fig.4.77. High resolution spectra of (a) Ti $2p_{3/2}$, (b) Ti $2p_{1/2}$ (c) Cr 2p, and (d) O 1s of T12Cr.

No peaks corresponding to Ti^{3+} was observed in the high-resolution spectra of Ti 2p. The high-resolution scan of Cr 2p can be deconvoluted into two main peaks: one peak at 576.74 eV corresponding to Cr $2p_{3/2}$ and the second peak at 586.47 eV corresponding to Cr $2p_{1/2}$.[46] Two strong satellite peaks at 579.50 eV and 588.09 eV reveals that Cr atom in TiO_2 exists in +3 oxidation state. A similar result has been observed for T12Cr which is shown in Fig. 4.77(a)-4.77(d). Confirmation of the presence of Cr^{3+} in the XPS analysis indicates that Cr-doped samples possess a certain amount of oxygen vacancies which corroborates the broadening of the Raman spectra and shifting of absorption edge to visible region in the UV-Visible spectra. Hence, it can be presumed that Cr ions substituted into the TiO_2 lattice exists in the form of Cr^{3+} and replaces Ti^{4+} ions. As a result of this, oxygen vacancies may be created in order to maintain charge neutrality in the TiO_2 lattice. The high resolution spectra of oxygen can be fitted with three distinct peaks corresponding to lattice oxygen, OH bonds and adsorbed water at 529.5, 530.3 and 531.8 eV respectively.[114]

B. XPS analysis of Mn-doped TiO₂

XPS analysis was carried out to investigate into the local chemical environments and oxidation states of all the Mn-doped samples. All the spectra were corrected for the reference energy C 1s peak at 284.6 eV. As a representative of the series, wide scan XPS spectrum of T3Mn is shown in Fig. 4.78 (a). The XPS spectra of Ti 2p core electron has a binding energy of 458.8 eV for Ti $2p_{3/2}$ and a binding energy of Ti $2p_{1/2}$, which are typically the binding energy values of Ti^{4+} in anatase TiO₂ which is shown in Fig. 4.78 (b).
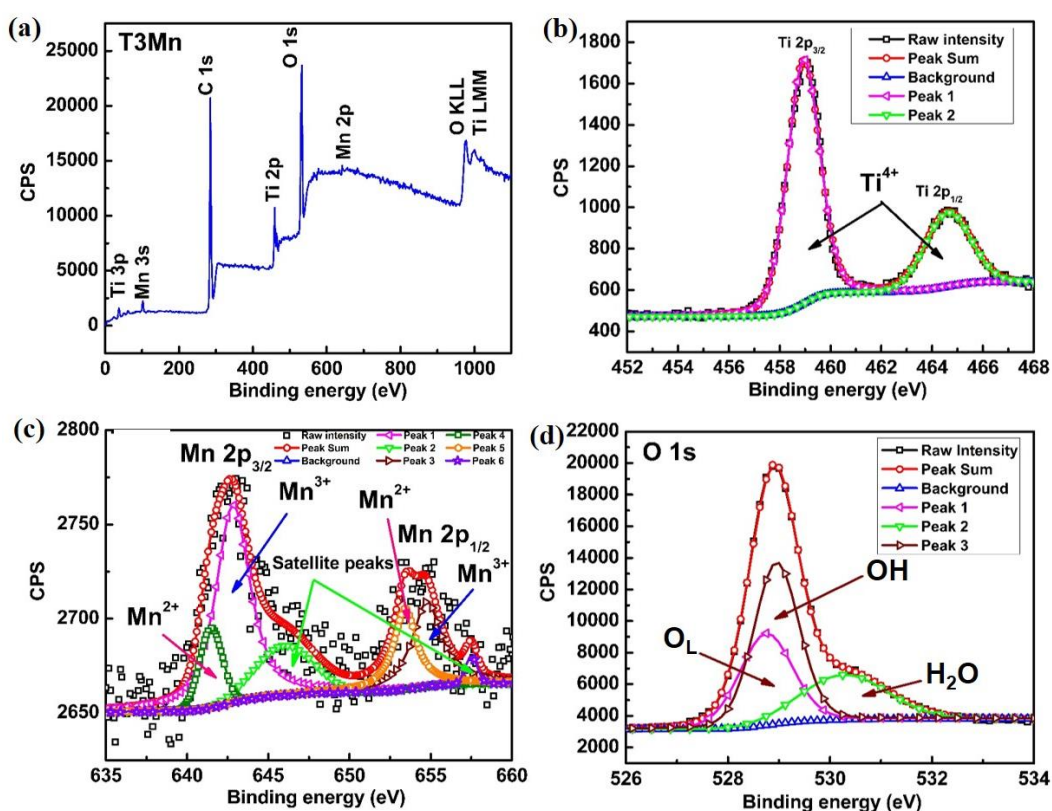
Fig.4.78. XPS spectra of T3Mn sample (a) Survey spectra, (b) High-resolution scan of Ti 2p (c) Mn 2p and (d) O 1s

The binding energy of Mn can be fitted into a combination of Mn^{2+} and Mn^{3+} peaks. The binding energies of Mn^{2+} for Mn $2p_{3/2}$ is and for Mn $2p_{1/2}$ is 641.48 eV and 653.53 eV respectively. Similarly, the corresponding binding energies of Mn^{3+} for Mn $2p_{3/2}$ and Mn $2p_{1/2}$ is 642.86 eV and 654.70 eV respectively.[46] Also, two satellite peaks are observed at 647.95 eV and 657.94 eV corresponding to the presence of Mn in the doped system are shown in Fig. 4.78(c). The O 1s spectra was fitted into three peaks

corresponding to O_L at 530.26 eV, OH bond at 531.85 eV and the adsorbed water at 533.07 eV as shown in Fig. 4.78 (d). Hence, the XPS spectra confirm the presence of Ti^{4+} without any evidence of the formation of Ti^{3+} and a mixed valence state of Mn^{2+}/ Mn^{3+} ions in T3Mn sample.

4.3.3.7. Magnetic studies

Magnetic studies have been carried out and all the Cr, Mn-doped samples exhibit a clear PM behavior at 300 K and the PM contribution increases as the Cr, Mn concentration is increased from 3% to 12%, significant results of which are discussed below.

A. Magnetic studies of Cr-doped TiO₂

In order to probe the magnetic behaviour of Cr-doped TiO₂, magnetic measurements were taken at room temperature in the field ranging from 90 kOe to -90 kOe. The M-H curve shows a PM behaviour for all the Cr-doped samples as seen in Fig 4.79(a). However, there is an increase in PM moment with increase in Cr concentration which could be due to the presence of isolated ions of Cr^{3+} existing in the doped system. Hence, a decrease in H_C with increase in Cr content is found. Oxygen vacancies play an important role in the observation of PM behaviour in Cr-doped samples.[33,35,38,39,115] It can be affirmed that at higher Cr doping concentration, more oxygen vacancies are created which result in isolated vacancy clusters resulting in PM behavior for higher concentration of Cr-doped samples.
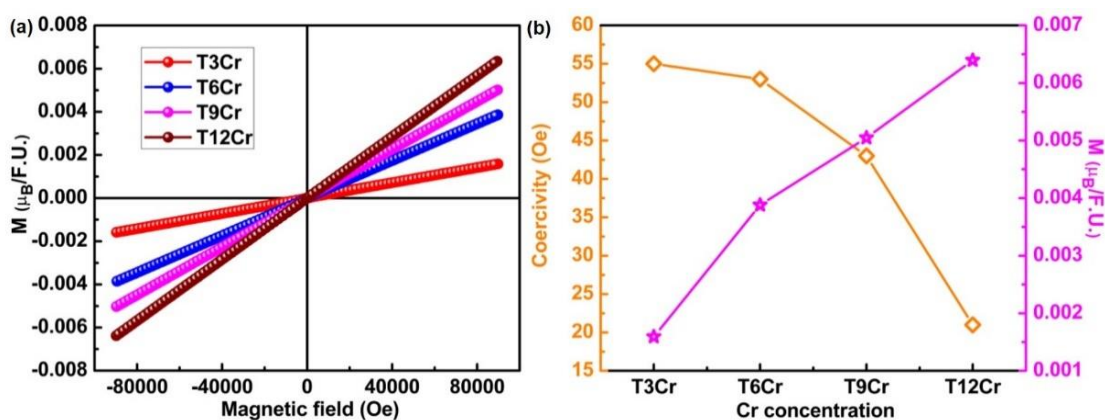
Fig.4.79. (a) Magnetic response of Cr-doped TiO₂ nanocrystals at 300 K (b) Variation of H_C and PM moment with Cr substitution

B. Magnetic studies of Mn-doped TiO₂

In order to understand the magnetic nature of the Mn-doped TiO_2, M-H measurements were carried out between 90 kOe and -90 kOe. The Mn-doped samples show PM behaviour as shown in Fig. 4.80(a). The inset of Fig. 4.80(a) shows the enlarged region of M-H curves of the Mn-doped samples. The decrease in H_C with Mn doping is shown in the inset of Fig. 4.80(b). However, it can be seen that the PM moment increases with increase in Mn doping which is attributed to the increase in the number of isolated Mn^{2+} and Mn^{3+} ions with Mn doping.
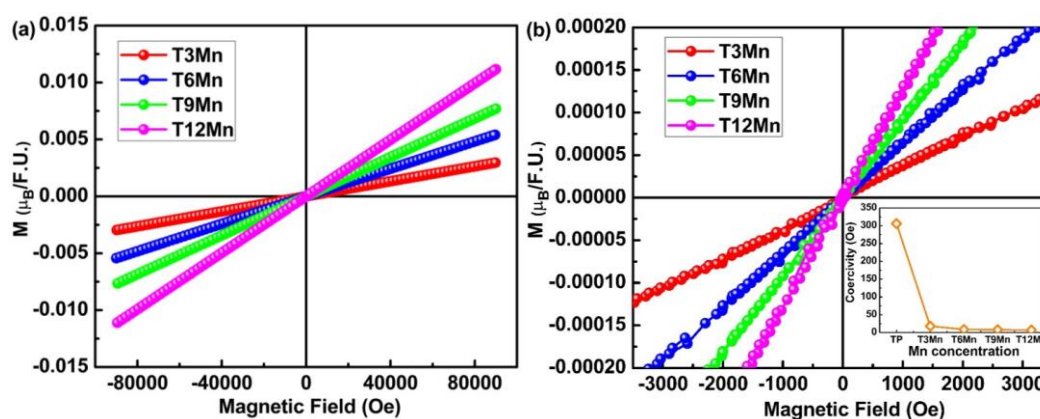
Fig.4.80. Magnetic behavior of (a) Mn-doped TiO_2 nanocrystals at 300K (inset shows the variation in coercivity of undoped and T3Mn sample) and (b) An enlarged view of the variation in H_C at lower fields (inset shows the decreasing trend in H_C with Mn doping).

C. Explanation of magnetic behavior in Cr, Mn-doped TiO₂ nanocrystals

The role of oxygen vacancy defects on the PM behavior exhibited by Cr-doped TiO_2 can be analysed by using the BMP fit. The measured magnetization has been fitted using equation (4.1). A BMP fit corresponding to Cr-doped TiO_2 samples is shown in Fig 4.81 (a) which is well in accordance with experimental data obtained from the magnetic measurements. Table 4.13 represents the BMP parameters derived out of fitting process. It is observed that all the samples contain BMP concentration in the range of 10^{16} and it is well reported that such a lower BMP concentration will not be sufficient to induce a long range RTFM. In the present case, significantly lower H_C are exhibited by all the doped samples and more specifically, a decreasing trend in H_C is observed with Cr doping as shown in Fig.4.81 (b). A systematic decrease in H_C with higher Cr concentration gives an impression that RTFM behavior is hindered in heavily

doped samples and hence defect concentration and BMP formation by incorporating Cr^{3+} ions in to Ti^{4+} site is not aiding the FM behavior due to some extrinsic factors rather it is increasing the PM moment of the doped samples. Hence, it is expected that along with the defect concentration associated with the DMS oxide system, the nature of dopant ions and their interaction with Ti ions deciding the RTFM behavior up to a certain extent.
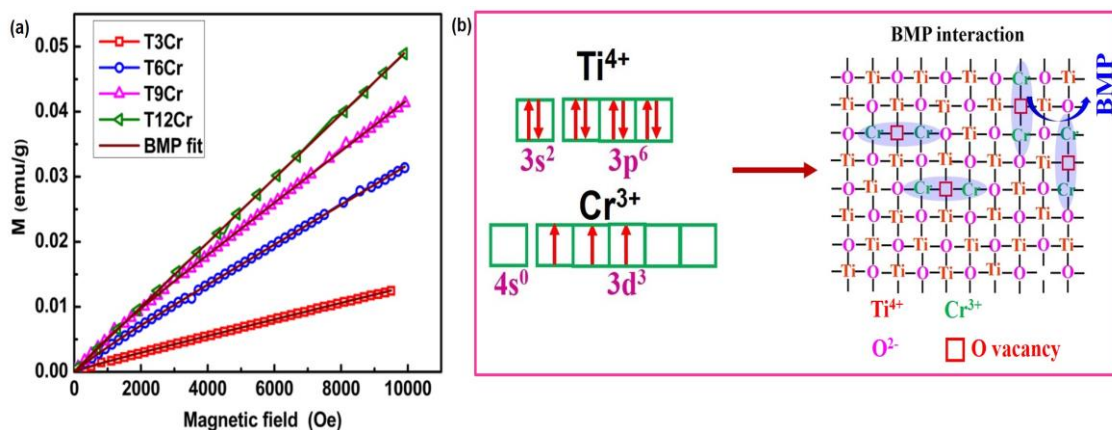
Fig.4.81. (a) BMP fit of Cr-doped samples (b) Schematic diagram showing the PM moment alignment with Cr doping in TiO_2

The BMP concentration, total BMP magnetization, and PM susceptibility shown by the Cr-doped TiO_2 samples are estimated to be within the permissible limit. The BMP concentration considerably decreases with increase in Cr concentration, while PM susceptibility increases systematically. From the above-mentioned observations, one could assume that some extrinsic PM contribution to the host lattice increases the magnetization value while suppressing the FM behavior. Let us consider the electronic configuration of Cr^{3+} which is [Ar] $3d^3$ and these *d* electrons is the key factor which interacts with the defect centres or *d* electrons of any other metal ions present in the system. Here, when Cr^{3+} ions are partially replacing Ti^{4+} in the nanocrystals of TiO_2, disorders in the form of oxygen vacancies may arise that helps in maintaining the charge neutrality. A decreasing trend in FM at higher Cr concentration is also reported which is attributed to the AFM ordering of Cr ions and observed RTFM is explained on the basis of BMPs. Similarly, with the help of theoretical studies, it is well reported that depending on the annealing condition such as oxygen poor or oxygen rich, Cr-doped TiO_2 system contribute towards PM or FM behavior.

However, the observed magnetic behavior can be well explained using the BMP theory, which is applicable in an insulating system with localized carriers. According to the theory, F centres are formed when a defect centre traps two electrons resulting in $1s^2$ hydrogenic type orbital. When one electron from the F centre interacts with the Ti/Cr site, F^+ centres are formed and it behaves like a $1s^1$ hydrogenic type orbital. In Cr-doped TiO_2, Ti^{3+} is absent as evident from the XPS measurements (Fig.4.76 8(b) and Fig. 4.77 (a and b)). When Ti^{3+} is absent, the chances of formation of F^+ centers are greatly minimized and hence FM is suppressed due to the absence of s-d interaction. In Cr-doped TiO_2, Ti^{3+} ions are absent and Cr exists in a single oxidation state. As a result, s-d interaction is absent and the formation of overlapping BMPs which contribute to FM is suppressed and hence a PM is observed in Cr-doped samples. The PM moment is due to the d electrons trapped in the defect centres and this increases with increase in Cr concentration. The above mentioned mechanism is responsible for observing an effective magnetic moment of $7.21 \times 10^3 \mu_B$ and a BMP concentration of $1.1 \times 10^{16} /cm^3$ respectively. Similarly, Cr-doped TiO_2 can exhibit weak FM if unpaired d electrons and defect mediated $1S^1$ configuration is present in the system. Even though there is a slight increase in BMP concentration of $1.38 \times 10^{16} /cm^3$ and effective magnetic moment of $14.05 \times 10^3 \mu_B$ in 3% Cr-doped sample, which exhibit a PM behavior with decreased H_C and increased magnetic moment. Hence, 1s configuration resembling hydrogenic like orbital due to the formation of F^+ center is one of the key factor in the BMP theory which can be equated to an oxygen vacancy having single trapped electron. The coupling of these $1s^1$ like orbital with 3d orbitals of Ti or Cr can form BMPs. When there is an overlapping of these BMPs, a long range FM behavior is expected in the system and hence, phonon confinement due to nanocrystal formation and defects arising due to Cr ions are responsible for the generation of BMPs that determine the magnetic and optical bahavior.

The BMP concentration for all the Mn-doped samples are calculated based on the previous reports and is shown in Fig. 4.82 (a). Again, in Mn-doped TiO_2, with the substitution of Mn ions, it is observed that there is no Ti^{3+} formation as validated from

the XPS analysis discussed earlier and we can assume that even though F-center formation is occurring with Mn-doping, it is not significantly generate the F^+-centers which could lead to less number of BMPs to form and may not contribute towards RTFM behavior. In turn, it is observed a clear PM response for all the samples with Mn-doping. To explain the PM behavior exhibited by the present system, let us first consider and explore more on the oxidation states shown by the Mn ions here. As explained earlier, the XPS analysis and magnetic studies suggest the occurrence of Mn^{2+} and Mn^{3+} in these samples with an electronic configuration of $Ar[3d^5]$ and $Ar[3d^4]$ respectively. When 3% Mn is loaded at Ti site, there is a possibility of majority of Mn^{2+} or Mn^{3+} ions occupy the Ti site substitutionally and there is a rare chance for a very few Mn ions to get oxidized to deliver Mn_3O_4. Depending on the BMP concentration formed as a result of this Mn substitution can impart FM and the formation of Mn_3O_4 may contribute towards a PM moment.[6,56,116-118] In the present case, the possibility of formation of Mn_3O_4 is completely ruled out through detailed XRD refinement analysis (Fig.4.60) and deconvoluted Raman spectra (Fig.4.65), hence it is assumed that whatever magnetic behavior exhibited by the present system is solely arising as result of Mn ions substitutionally replacing the Ti ions. As there is no significant s-d interaction, the d electrons present in the doped samples can respond to the magnetic field in different ways to exhibit the PM behavior. Especially, when we deal with nanocrystals of Mn-doped TiO_2 a strange phenomenon can occur in such a way that the Mn ion concentration towards the interior of the host system could be considerably low in comparison to Mn ions present near the grain boundary due to self-purification mechanism. In general, it is expected that such a huge number of Mn ions present near the grain boundary can oxidized to form corresponding oxides during the annealing process and these oxides can ultimately impart PM. However, in this case, as the oxide formation is not accounted significantly and we can suggest that there is a different mechanism for determining the PM behavior.
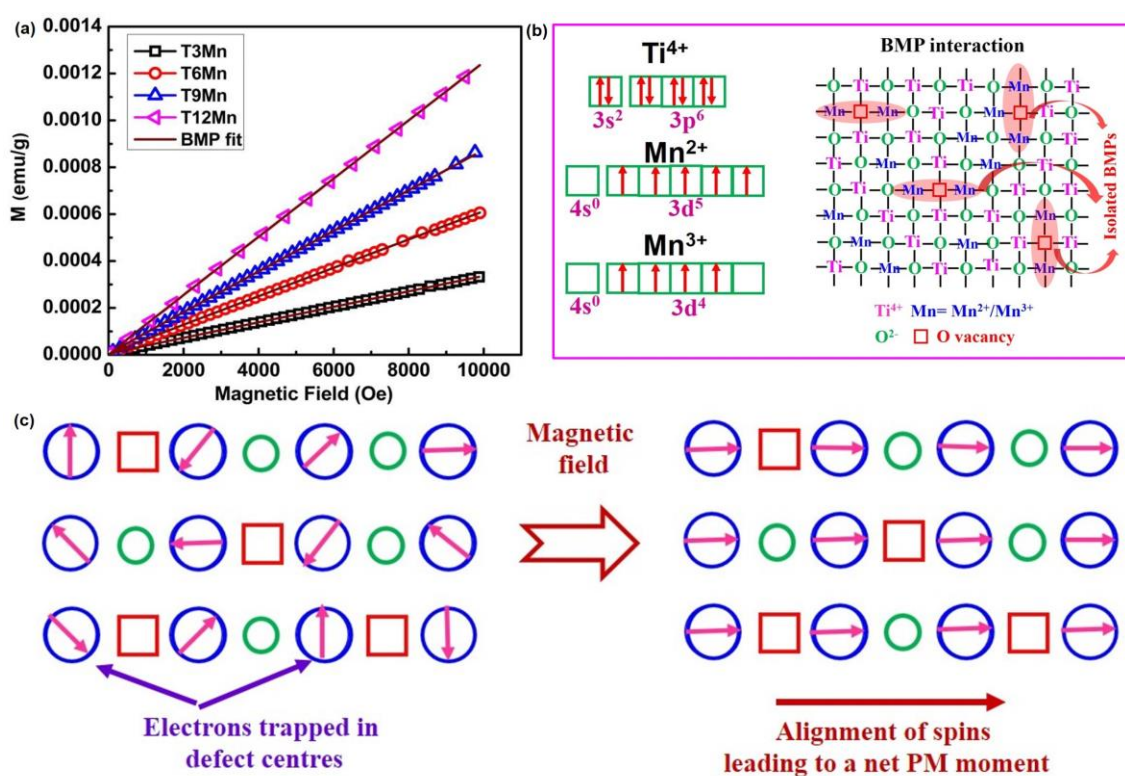
Fig.4.82. (a) Langevin-fitting of Mn-doped TiO$_2$ samples (b) Schematic diagram showing the PM moment alignment with Mn doping in TiO$_2$ and (c) alignment of trapped electron spin with magnetic field

Table 4.13. Parameters extracted from Langevin fitting for Cr and Mn-doped TiO$_2$ nanocrystals

Compound	M_0 (x 10^{-4} emu/g)	M_{eff} (x 10^3 μ_B)	χ_m (x 10^{-6} emu/g-Oe)	N (x 10^{15} /cm^3)
T3Cr	4.93	14.05	1.27	13.8
T6Cr	13.40	9.64	3.06	7.4
T9Cr	26.20	7.56	3.94	5.0
T12Cr	1.04	2.18	4.94	1.6
T3Mn	0.11	64.15	0.03	0.06
T6Mn	0.08	18.11	0.06	0.05
T9Mn	0.07	18.07	0.09	0.04
T12Mn	0.06	19.54	0.12	0.01

Among the different reports on Mn-doped TiO$_2$ systems, Sharma *et al.* recently reported that increasing Mn concentration can induce Mn$_3$O$_4$ impurity phase which

could contribute towards PM ordering.[119] Another report by Hong *et al.* suggest the effect of Mn doping on an inherently FM system and it is observed that Mn alone is not contributing towards the enhancing the FM and increasing the dopant concentration decreases the FM behavior.[120] Again, there are reports Li *et al.* suggesting the incapability of oxygen vacancies alone for introducing the FM pointing towards the need for a dopant in the host system.[121] Thus, we considered the situation where there is very less number of overlapped BMP concentration with Mn substitution as the s-d interaction has been suppressed then the PM contribution by the Mn ions is dominated over the exchange interaction present among these ions and oxygen vacancies leading to a perfect PM behavior. Hence, it is the isolated BMPs formed with higher Mn concentration that can align with the magnetic field to yield a PM response to the present Mn-doped TiO$_2$ system even without the formation of any secondary phases such as Mn$_3$O$_4$ as previously reported.[6] The free electrons associated with the Mn ions, the formation of isolated BMPs and aligning of isolated BMPs with applied magnetic field is schematically shown in Fig. 4.82(b) and the parameters extracted from the Langevin fitting are tabulated in Table 4.13. Even with the formation of oxygen vacancies with higher Mn concentration, it is the nature of the BMPs that determines whether to promote long range RTFM, weak RTFM or a PM behavior as suggested in the present study. Thus, it is suggested that oxygen vacancy concentration, concentration of the dopant Mn ions and the nature BMPs whether isolated or overlapped are the key factors determining the magnetic behavior of Mn-doped TiO$_2$ nanocrystals. Very few concentration of Mn may aid the weak RTFM and doping with extremely high concentration of Mn ions may suppress the RTFM behavior and may aid the PM behavior along with the formation of isolated BMPs.

4.4. Summary

- A detailed investigation on the crystal structure, optical properties and magnetic behavior of undoped and TM-doped TiO$_2$ nanocrystals (TM=Cu, Zn, Fe, Co, Ni, Cr and Mn) synthesized by a simple sol-gel route has been carried out.

- All the studied nanocrystals are crystallized into a tetragonal anatase structure

with space group I41/amd. Reitveld refinement of XRD patterns and Raman studies reveal that successful incorporation of TM ions (even upto 12 at. wt. %) into Ti site in TiO_2 lattice.

- Optical studies reveal that the band gap of TiO_2 (3.2 eV) significantly narrows down with the substitution of all TM elements (except Zn).

- XPS studies reveal the mixed valence states of Ti (Ti^{3+}/Ti^{4+}) are present in case of undoped and Cu,Fe,Co-doped TiO_2 whereas a single valance state of Ti (Ti^{4+}) is found in Cr,Mn,Ni and Zn-doped TiO_2 nanocrystals. Again, mixed valence states of Cu (Cu^+/Cu^{2+}), Fe (Fe^{2+}/Fe^{3+}), Co(Co^{2+}/Co^{3+}) and Mn (Mn^{3+}/Mn^{4+}) are found for Cu, Fe, Co and Mn-doped TiO_2 nanocrystals respectively. But, a single valance state of Zn (Zn^{2+}), Cr (Cr^{3+}) and Ni (Ni^{2+}) are found for Zn, Cr, and Ni doped TiO_2 nanocrystals respectively. However, presence of oxygen vacancies are witnessed in all the undoped and doped TiO_2 nanocrystals suggests the formation of BMPs

- The PL spectra confirm the formation of F^+ centres in all the synthesised nanocrystals leading to the formation of BMPs

- A very weak RTFM at lower magnetic fields has been observed for undoped and 3% Cu, Fe and Co-doped TiO_2 nanocrystals because impurity (dopant) ions associated with oxygen vacancies enables coupling between them to enhance BMPs overlapping and FM exchange interaction. But, a perfect PM behavior is witnessed for the higher dopant concentrations of Fe and Co, due to the individual magnetic contributions from the dopant ions. Again, all the Cr, Mn and Ni-doped samples exhibited a PM behavior with less coercivity due to the formation of isolated BMPs while 3% Zn-doped sample shows a diamagnetic tail.

- Magnetic behavior of undoped and doped TiO_2 nanocrystals is decided by either intrinsic contributions i.e, the nature of BMPs (isolated or overlapped) or extrinsic contributions (i.e the magnetic contributions of dopant ions) or both.

- A significant reduction in band gap is observed in all the TiO$_2$ naocrystals (except Zn-doped) and together with its interesting magnetic properties makes TM-doped TiO$_2$ a potential candidate for spintronics applications and magneto optic devices.

4.5. References

1. B. Santara, B. Pal, P. K. Giri, Signature of strong ferromagnetism and optical properties of Co doped TiO$_2$ nanoparticles, *J. Appl. Phys.*, 110 (2011) 114322.
2. A. Chanda, K. Rout, M. Vasundhara, S. R. Joshi, J. Singh, Structural and magnetic study of undoped and cobalt doped TiO$_2$ nanoparticles, *RSC Adv.*, 8 (2018) 10939.
3. B. Prajapati, S. Kumar, M. Kumar, S. Chatterjee, A. K. Ghosh, Investigation of the physical properties of Fe:TiO$_2$-diluted magnetic semiconductor nanoparticles, *J. Mater. Chem. C*, 5 (2017) 4257.
4. B. Parveen, M.-ul-Hassan, Z. Khalid, S. Riaz, S. Naseem, Room-temperature ferromagnetism in Ni-doped TiO$_2$ diluted magnetic semiconductor thin films, *J. Appl. Res. Tech.*, 15 (2017) 132.
5. B. Choudhury, S. Paul, G. A. Ahmed, A. Choudhury, Adverse effect of Mn doping on the magnetic ordering in Mn doped TiO$_2$ nanoparticles, *Mater. Res. Express*, 2 (2015) 096104.
6. B. Choudhury, A. Choudhury, Oxygen vacancy and dopant concentration dependent magnetic properties of Mn doped TiO$_2$ nanoparticle, *Curr. Appl. Phys.*, 13 (2013) 1025.
7. B. Choudhury, M. Dey, A. Choudhury, Defect generation, *d-d* transition, and band gap reduction in Cu-doped TiO$_2$ nanoparticles, *Int. Nano Lett*, 3 (2013) 25.
8. S. A. Ahmed, Ferromagnetism in Cr-, Fe-, and Ni-doped TiO$_2$ samples, *J. Mag. Mag. Mater.*, 442 (2017) 152.
9. J. Yu, T. Ma and S. Liu, Enhanced photocatalytic activity of mesoporous TiO$_2$ aggregates by embedding carbon nanotubes as electron-transfer channel, *Phys. Chem. Chem. Phys.*, 13 (2011) 3491.
10. Q.-H. Zhang, W.-D. Han, Y.-J. Hong and J.-G. Yu, Photocatalytic reduction of CO2 with H$_2$O on Pt-loaded TiO$_2$ catalyst, *Catal. Today*, 148 (2009) 335.
11. T. Ohsaka, F. Izumi and Y. Fujiki, Raman spectrum of anatase, TiO$_2$, *J. Raman Spectrosc.*, 7 (1978) 321.
12. D. Berdani, P. P. Lottice and A. Montenero, A micro-Raman study of iron-titanium oxides obtained by sol-gel synthesis, *J. Mater. Sci.*, 35 (2000) 4301.
13. H. A. Szymanski, Raman Spectroscopy: Theory and Practice, Plenum press, New York (1967).
14. T. Ohsaka, Temperature Dependence of the Raman Spectrum in Anatase TiO$_2$. *J. Phys. Soc. Jpn.*, 48 (1980) 1661.
15. W. F. Zhang, Y. L. He, M. S. Zhang, Z. Yin, Q. Chen, Raman Scattering Study on Anatase TiO$_2$ Nanocrystals. *J. Phys. D: Appl. Phys.*, 33 (2000) 912.
16. H. C. Choi, Y. M. Jung, and S. B. Kim, Size Effects in the Raman Spectra of TiO$_2$ Nanoparticles, *Vib. Spectrosc.*, 37 (2005) 33.

17. L. H. Liang, C. M. Shen, X. P. Chen, W. M. Liu, H. J. Gao, The Size-Dependent Phonon Frequency of Semiconductor Nanocrystals *J. Phys.: Condens. Matter*, 16 (2004) 267.

18. A. Ali, E. Yassitepe, I. Ruzybayev, S.I. Shah, A. S. Bhatti, Improvement of (004) texturing by slow growth of Nd doped TiO$_2$ films, *J. Appl. Phys.*, 112 (2012) 113505.

19. A. Punnoose, J. Hays, V. Shutthanandan, V. Gopal, *Appl. Phys. Lett.*, 85 (2004) 155.

20. M. Ahamed, M.A.M. Khan, M. J. Akhtar, H. A. Alhadlaq, A. Alshamsan, Role of Zn doping in oxidative stress mediated cytotoxicity of TiO$_2$ nanoparticles in human breast cancer MCF-7 cells, *Sci Rep.*, 6 (2016) 30196.

21. M. Cernea, C. Valsangiacom, R. Trusca, F. Vasiliu, Synthesis of iron-doped anatase -TiO$_2$ powders by a particulate sol-gel route, *J. Optoelectron. Adv. M.*, 9 (2007) 2648.

22. Z. Li, B. Hou, Y. Xu, D. Wu, Y. Sun, Hydrothermal synthesis, characterization, and photocatalytic performance of silica-modified titanium dioxide nanoparticles, *J. Colloid Interface Sci.*, 288 (2005) 149.

23. S. Mugundan, B. Rajamannan, G. Viruthagiri, N. Shanmugam, R. Gobi, P. Praveen, Synthesis and Characterization of Undoped and Cobalt-Doped TiO$_2$ Nanoparticles via Sol-Gel Technique, *Appl. Nanosci.*, 5 (2015) 449.

24. A. Bouaine, N. Brihi, G. Schmerber, C. Ulhaq-Bouillet, S. Colis, A. Dinia, Structural, Optical, and Magnetic Properties of Co-doped SnO$_2$ Powders Synthesized by the Coprecipitation Technique, *J. Phys. Chem. C*, 111(7) (2007) 2924.

25. P. Bindu, S. Thomas, Optical Properties of ZnO Nanoparticles Synthesised from a Polysaccharide and ZnCl$_2$, *Acta physica polonica A,* 131 (2017) 1474

26. K. Nagaveni, M. S. Hegde, G. Madras, Structure and Photocatalytic Activity of Ti$_{1-x}$M$_x$O$_{2\pm\delta}$ (M = W, V, Ce, Zr, Fe, and Cu) Synthesized by Solution Combustion Method, *J. Phys. Chem. B*, 108 (2004) 20204.

27. K. Das, S. N. Sharma, K. Mahesh, S. K. De, Morphology Dependent Luminescence Properties of Co Doped TiO$_2$ Nanostructures, *J. Phys. Chem. C*, 113 (2009) 14783.

28. W.Y. Wu, Y.M. Chang, J.M. Ting, Room-temperature synthesis of single-crystalline anatase TiO$_2$ nanowires *Crst. Growth Des.*, 10 (2010) 1646.

29. R. Sanjines, H. Tang, H. Berger, F. Gozzo, G. Margaritondo, and F. Lévy, Electronic structure of anatase TiO$_2$ oxide, *J. Appl. Phys.*, 75 (1994) 2945.

30. J. Liu, J. Li, A. Sedhain, J. Lin, H. Jiang, Structure and Photoluminescence Study of TiO$_2$ Nanoneedle Texture along Vertically Aligned Carbon Nanofiber Arrays, *J. Phys. Chem. C,* 112 (2008) 17127.

31. Y. Lei, L. Zhang, G. Meng, G. Li, X. Zhang, C. Liang, W. Chen, S. Wang, Preparation and photoluminescence of highly ordered TiO$_2$ nanowire arrays, *Appl. Phys. Lett.,* 78 (2001) 1125.

32. N. Serpone, Is the Band Gap of Pristine TiO$_2$ Narrowed by Anion- and Cation-Doping of Titanium Dioxide in Second-Generation Photocatalysts?, *J. Phys. Chem. B,* 110 (2006) 24287.

33. M. Parras, A. Varela, R. C. Gil, K. Boulahya, A. Hernando, J. M. G. Calbet, Room-Temperature Ferromagnetism in Reduced Rutile TiO$_{2-\delta}$ Nanoparticles, *J. Phys. Chem. Lett.*, 4 (2013) 2171.

34. J. Y. Zheng, S. H. Bao, Y. H. Lv, P. Jin, Activation and enhancement of room-temperature ferromagnetism in Cu-doped anatase TiO₂ films by bound magnetic polaron and oxygen defects, *ACS Appl. Mater. Interfaces*, 6 (2014) 22243.

35. S. Wang, L. Pan, J. J. Wang, W. Mi, J. J. Zou, L. Wang, X. Zhang, Titanium-defected undoped anatase TiO₂ with p-type conductivity, room-temperature ferromagnetism, and remarkable photocatalytic performance, *J. Am. Chem. Soc.*, 137 (2015) 2975.

36. K. Karthik, S. Kesava Pandian, K. Suresh Kumar, N. Victor Jaya, Influence of dopant level on structural, optical and magnetic properties of Co-doped anatase TiO₂ nanoparticles, *Appl. Surf. Sci.*, 256 (2010) 4757.

37. N. H. Hong, J. Sakai, N. Poirot, V. Brize, Room-temperature ferromagnetism observed in undoped semiconducting and insulating oxide thin films, *Phys. Rev. B.*, 73 (2006) 132404.

38. S. D. Yoon, Y. Chen, A. Yang, T. L. Goodrich, X. Zuo, D. A. Arena, K. Zeimer, C. Vittoria,V. G. Harris, Oxygen-defect-induced magnetism to 880 K in semiconducting anatase TiO$_{2-\delta}$ films, J. *Phys.: Condens. Matter*, 18 (2006) L355.

39. D. Kim, J. Hong, Y. R. Park, K. J. Kim, The origin of oxygen vacancy induced ferromagnetism in undoped TiO$_{(2)}$, *J. Phys.: Condens. Matter*, 21 (2009) 195405.

40. J.-Y. Kim, J.-H. Park, B.-G. Park, H.-J. Noh, S.-J. Oh, J. S. Yang, D.-H. Kim, S. D. Bu, T. W. Noh, H.-J. Lin, H.-H. Hsieh, C. T. Chen, Ferromagnetism induced by clustered Co in Co-doped anatase TiO₂ thin films, *Phys. Rev. Lett.,* 90 (2003) 017401.

41. J. Xu, S. Shi, L. Li, X. Zhang, Y. Wang, X. Chen, J. Wang, L. Lv, F. Zhang, W. Zhong, Structural, optical, and ferromagnetic properties of Co-doped TiO₂ films annealed in vacuum, *J. Appl. Phys.*, 107 (2010) 053910.

42. L.-T. Tseng, X. Luo, T. T. Tan, S. Li, J. Yi, Doping Concentration Dependence of Microstructure and Magnetic Behaviours in Co-Doped TiO₂ Nanorods *Nanoscale Res. Lett.*, 9 (2014) 673.

43. B. Qi, S. Ólafsson, H.P. Gíslason, Vacancy defect-induced d0 ferromagnetism in undoped ZnO nanostructures: Controversial origin and challenges, *Prog. Mater. Sci.*, 90 (2017) 45.

44. J.M.D. Coey, d0 ferromagnetism, *Solid State Sci.*, 7 (2005) 660.

45. T.-L. Phan, Y. D. Zhang, D. S. Yang, N. X. Nghia, T. D. Thanh, S. C. Yu, Defect-induced ferromagnetism in ZnO nanoparticles prepared by mechanical milling, Appl. Phys. Lett. 102 (2013) 072408.

46. http://srdata.nist.gov/xps.

47. J.C. Huo, Y. Hu, H. Jiang, Chunzhong Li, *In situ* surface hydrogenation synthesis of Ti^{3+} self-doped TiO₂ with enhanced visible light photoactivity, *Nanoscale*, 6 (2014) 9078.

48. H. Jensena, A. Solovieva, Z.S. Li, E.G. Sogaard, XPS and FTIR investigation of the surface properties of different prepared titania nano-powders, *Appl. Surf. Sci.*, 246 (2005) 239.

49. M. Xing, J. Zhang, F. Chen, B. Tian, An economic method to prepare vacuum activated photocatalysts with high photo-activities and photosensitivities, *Chem. Comm.* 47 (2011) 4947.

50. I. Nakai, Y. Sugitani, K. Nagashima, Y. Niwa, X-ray photoelectron spectroscopic study of copper minerals, *J. Inorg. Nucl. Chem.*, 40(5) (1978) 789.

51. B. R. Strohmeier, D. E. Levden, R. ScottField, D. M. Hercules, Surface spectroscopic characterization of $CuAl_2O_3$ catalysts, *J. Catal.*, 94(2) (1985) 514.

52. B. Sudakshina, B. Arun, K. Devi Chandrasekhar, H. D. Yang and M. Vasundhara, *Physica B Condens Matter.*, 539(15) (2018) 14.

53. Z. Wang, C. Yang, T. Lin, H. Yin, P. Chen, D. Wan, F. Xu, F. Huang, J. Lin, X. Xie, M. Jiang, *Adv. Funct. Mater.*, 23 (2013) 5444.

54. S. K. Pandey, R. J. Choudhary, Effect of Non-Magnetic Impurities on the Magnetic States of Anatase TiO_2, *J. Phys.: Condens. Matter,* 23 (2011) 276005.

55. B. Santara, P. K. Giri, K. Imakita and M. Fujii, Evidence of oxygen vacancy induced room temperature ferromagnetism in solvothermally synthesized undoped TiO_2 nanoribbons, *Nanoscale*, 5 (2013) 5476.

56. J. M. D. Coey, M. Venkatesan, and C. B. Fitzgerald, Donor impurity band exchange in dilute ferromagnetic oxides *Nature Mater.,* 4 (2005) 173.

57. V. R. Akshay, B. Arun, S. Dash, A. K. Patra, G. Mandal, R. M. Geetha, A. Chanda, M. Vasundhara, Defect Mediated Mechanism in Undoped, Cu and Zn-Doped TiO_2 Nanocrystals for Tailoring the Band gap and Magnetic Properties, *RSC Adv.*, 8 (2018) 41994.

58. D. Y. Inamdar, A. D. Lad, A. K. Pathak, I. Dubenko, N. Ali, S. Mahamuni, Ferromagnetism in ZnO Nanocrystals: Doping and Surface Chemistry, *J. Phys. Chem. C,* 114 *(*2010*)* 1451.

59. J. J. Beltrán, C. A. Barrero, A. Punnoose, Combination of defects plus mixed valence of transition metals: A strong strategy for ferromagnetic enhancement in ZnO nanoparticles, *J. Phys. Chem. C,* 129 (16) *(*2016) 8969.

60. C. Chiorescu, J. L. Cohin, J. J. Neumeier, Impurity Conduction and Magnetic Polarons in Antiferromagnetic Oxides. *Phys. Rev. B*, 76 (2007) 020404(R).

61. G. Madhu, K. Maniammal, and V. Biju, Defect Induced Ferromagnetic Interaction in Nanostructured Nickel Oxide with Core–Shell Magnetic Structure: The Role of Ni^{2+} and O^{2-} Vacancies. *Phys. Chem. Chem. Phys.*, 18 (2016) 12135.

62. R. D. Shannon, Acta Crystallogr., Sect. A: Cryst. Phys., Diffr., Theor. Gen. Crystallogr., 32 (1976) 751.

63. N. R. Mathews, M. A. Cortes Jacome, C. Angeles-Chavez, J. A. Toledo Antonio, Fe doped TiO_2 powder synthesized by sol gel method: structural and photocatalytic characterization, *J. Mater. Sci. Mater. Electron.* 26 (2015) 5574.

64. B. D. Cullity, Stock, S. R. Elements of X-ray Diffraction, Prentice Hall, USA (2001).

65. S. Manu, M. Abdul Khadar, Non-uniform distribution of dopant iron ions in TiO_2 nanocrystals probed by X-ray diffraction, Raman scattering, photoluminescence and photocatalysis, *J. Mater. Chem. C*, 3 (2015) 1846.

66. G. M. Dalpian, J. R. Chelikowsky, Self-Purification in Semiconductor Nanocrystals, *Phys. Rev. Lett.*, 96 (2006) 226802.
67. Y.-H. Zhang, A. Reller, Nanocrystalline iron-doped mesoporous titania and its phase transition, *J. Mater. Chem.*, 11 (2001) 2537.
68. J. Zhu, F. Chen, J. Zhang, H. Chen, M. Anpo, Fe^{3+}-TiO₂ photocatalysts prepared by combining sol–gel method with hydrothermal treatment and their characterization, *J. Photochem. Photobiol. A*, 180 (2006) 196.
69. G. Cao, Nanostructures & Nanomaterials: Synthesis, Properties & Applications, Imperial College Press (2004).
70. P. G. Koutsoukos, A. N. Kofina, D. G. Kanellopoulou, Solubility of salts in water: Key issue for crystal growth and dissolution processes, *Pure Appl. Chem.* 79 (2007) 825.
71. S. C. Erwin, L. Zu, M. I. Haftel, A. L. Efros, T. A. Kennedy, D. J. Norris, Doping semiconductor nanocrystals, *Nature*, 436 (2005) 91.
72. N. H. S. Nasralla, M. Yeganeh, Y. Astuti, S. Piticharoenphun, L. Šiller, Systematic study of electronic properties of Fe-doped TiO₂ nanoparticles by X-ray photoemission spectroscopy, *J. Mater. Sci.-Mater. Electron.* 29 (2018) 17956.
73. L. Vegard, The constitution of the mixed crystals and the space filling of the atoms, *Z. Phys.*, 5 (1921) 17.
74. K. Karthik, S. Kesava Pandian, N. Victor Jaya, Effect of nickel doping on structural, optical and electrical properties of TiO₂ nanoparticles by sol-gel method, *Appl. Surf. Sci.*, 256 (2010) 6829.
75. W. Zhou, H. Deng, L.Yu, P. Yang and J. Chu, Band-gap narrowing and magnetic behavior of Ni-doped $Ba(Ti_{0.875}Ce_{0.125})O_3$ thin films, *J. Phys. D: Appl. Phys.*, 48 (2015) 455308.
76. D. Bersani, P. P. Lottici, X.-Z. Ding, Phonon Confinement Effects in the Raman Scattering by TiO₂ Nanocrystals. *Appl. Phys. Lett.* 72 (1998) 73.
77. J. C. Parker, R. W. Siegel, Calibration of the Raman spectrum to the oxygen stoichiometry of nanophase TiO₂, *Appl. Phys. Lett.* 57 (1990) 943.
78. J. Gardy, A. Hassanpour, X. Lai, M. H. Ahmed, Synthesis of $Ti(SO_4)O$ solid acid nano-catalyst and its application for biodiesel production from used cooking oil *Applied Catalysis A*: *General*, 527 (2016) 81.
79. T. Lopez, J. A. Moreno, R. Gomez, X. Bokhimi, J. A. Wang, M. H. Yee, G. Pecchi, P. Reyes, Characterization of iron-doped titania sol–gel materials, *J. Mater. Chem.*, 12 (2002) 714.
80. M. Hamadanian, A. R. Vanani, A. Majedi, Sol-Gel Preparation and Characterization of Co/TiO₂ Nanoparticles: Application to the Degradation of Methyl Orange *J. Iran. Chem. Soc.*, 7 (2010) S52.
81. X. -H. Liu, X. -B. He, Y. -B. Fu, Effects of Doping Cobalt on the Structures and Performances of TiO₂ Photocatalyst. *Acta Chim. Sinica*, 66 (2008) 1725.
82. I. Ganesh, A.K. Gupta, P.P. Kumar, P.S.C. Sekhar, K. Radha, G. Padmanabham, G. Sundararajan, Preparation and characterization of Ni-doped TiO₂ materials for photocurrent and photocatalytic applications, *Sci. World J.*, 2012 (2012) 127326.

83. B. Santara, P. K. Giri, K. Imakita and M. Fujii, Evidence for Ti Interstitial Induced Extended Visible Absorption and Near Infrared Photoluminescence from Undoped TiO$_2$ Nanoribbons: An In Situ Photoluminescence Study, *J. Phys. Chem.* C, 117 (2013) 23402.

84. K. Boubaker, A physical explanation to the controversial Urbach tailing universality, *Eur. Phys. J. Plus*, 126 (2011) 10.

85. B. Choudhury, B. Borah, A. Choudhury, Extending Photocatalytic Activity of TiO$_2$ Nanoparticles to Visible Region of Illumination by Doping of Cerium, *Photochem. Photobiol.*, 88 (2012) 257.

86. B. Choudhury, A. Choudhury, Oxygen defect dependent variation of band gap, Urbach energy and luminescence property of anatase, anatase–rutile mixed phase and of rutile phases of TiO$_2$ nanoparticles, *Physica E:Low-dimensional Systems and Nanostructures,* 56 (2014) 364.

87. J. Liqiang, Q. Yichun, W. Baiqi, L. Shudan, J. Baojiang, Y. Libin, F. Wei, F. Honggang and S. Jiazhong, *Sol. Energy Mater. Sol. Cells*, 90 (2006) 1773.

88. Solomon, E.I.; Lever, A.B.P., Inorganic Electronic Structure and Spectroscopy, John Wiley and Sons, New York (1999).

89. S. Munir, S.M. Shah, H. Hussain, Effect of carrier concentration on the optical band-gap of TiO$_2$ nanoparticles, *Mater. Des.*, 92 (2016) 64.

90. J. Hu, L. Zhan, G. Zhang, Q. Zhang, L. Du, C.H. Tung, Y. Wang, Effects of substitutional dopants on the photoresponse of a polyoxotitanate cluster, *Inorg. Chem.*, 55 (2016) 8493.

91. F. Zuo, L. Wang, T. Wu, Z. Zhang, D. Borchardt, P. Feng, Self-doped Ti^{3+} enhanced photocatalyst for hydrogen production under visible light, *J. Am. Chem. Soc.*, 132 (2010) 11856.

92. N. Miriyala, K. Prashanthi, T. Thundat, Oxygen vacancy dominant strong visible photoluminescence from BiFeO$_3$ nanotubes, *Phys. Status Solidi RRL*, 7 (9) (2013) 668.

93. J. Zhuang, S. Weng, W. Dai, P. Liu, Q. Liu, Effects of Interface Defects on Charge Transfer and Photoinduced Properties of TiO$_2$ Bilayer Films. *J. Phys. Chem. C*, 116 (2012) 25354.

94. D. Schild, X-ray Photoelectron Spectroscopy, In: Léon A. (eds) Hydrogen Technology. Green Energy and Technology. Springer, Berlin, Heidelberg, Chapter 17c. *Hydrogen Technology*, (2008) 575.

95. Z. Wang, W. Wang, J. Tang, L. D. Tung, L. Spinu, W. Zhou, Extraordinary Hall Effect and Ferromagnetism in Fe-Doped Reduced Rutile. *Appl. Phys. Lett.,* 83 (2003) 518.

96. J. Chen, P. Rulis, L. Ouyang, S. Satpathy, W. Y. Ching, Vacancy-Enhanced Ferromagnetism in Fe-Doped Rutile TiO$_2$, *Phys. Rev. B*, 74 (2006) 235207.

97. K. Griffin Roberts, M. Varela, S. Rashkeev, S. T. Pantelides, S. J. Pennycook, K. M. Krishnan, Defect-Mediated Ferromagnetism in Insulating Co-Doped Anatase TiO$_2$ Thin Films, *Phys. Rev. B*, 78 (2008) 014409.

98. K. Dodge, J. Chess, J. Eixenberger, G. Alanko, C. B. Hanna, A. Punnoose, Role of Oxygen Defects on the Magnetic Properties of Ultra-Small Sn$_{1-x}$Fe$_x$O$_2$ Nanoparticles, *J. Appl. Phys.,* 113 (2013) 17B504.

99. R. S. Dubey, S. Singh, Investigation of structural and optical properties of pure and chromium doped TiO$_2$ nanoparticles prepared by solvothermal method, *Results in Phys.*, 7 (2017) 1283.

100. K. Maniammal, G. Madhu, V. Biju, X-ray diffraction line profile analysis of nanostructured nickel oxide: Shape factor and convolution of crystallite size and microstrain contributions *Physica E*, 85 (2017) 214.

101. B. Prajapati, S. Roy, S. Sharma, A. G. Joshi, S. Chatterjee, and A. K. Ghosh, Bandgap Engineering and Signature of Ferromagnetism in Ti$_{1-x}$Mn$_x$O$_2$ Diluted Magnetic Semiconductor Nanoparticles: A Valence Band Study, *Phys. Status Solidi B*, (2019) 1800262.

102. S.K.S. Patel, S. Kurian, N.S. Gajbhiye, Phase dependent room-temperature ferromagnetism of Fe-doped TiO$_2$ nanorods, *AIP advances*, 2 (2012) 012107.

103. M. G. Brojcin, M. J. Scepanovic, Z. D. Dohcevic-Mitrovic, I. Hinic, B. Matovic, G. Stanisic, Z. V. Popovic, Infrared study of laser synthesized anatase TiO$_2$ nanopowders, *J. Phys. D: Appl. Phys.* 38 (2005) 1415.

104. B. Choudhury, A. Choudhury, Dopant induced changes in structural and optical properties of Cr^{3+} doped TiO$_2$ nanoparticles, *Mater. Chem. Phys.,* 132 (2012) 1112.

105. H. Y. Lin, Y. Y. Chou, C. L. Cheng, Y. F. Chen, Giant enhancement of band edge emission based on ZnO/TiO$_2$ nanocomposites, *Opt. Express* 15 (2007) 13832.

106. J. Zhang, M. Li, Z. Feng, J. Chen, C. Li, UV Raman Spectroscopic Study on TiO$_2$. I. Phase Transformation at the Surface and in the Bulk, *J. Phys. Chem. B*, 110 (2006) 927.

107. J. G. Li, X. Wang, K. Watanabe, T. Ishigaki, Phase Structure and Luminescence Properties of Eu^{3+}-Doped TiO$_2$ Nanocrystals Synthesized by Ar/O$_2$ Radio Frequency Thermal Plasma Oxidation of Liquid Precursor Mists, *J. Phys. Chem. B,* 110 (2006) 1121.

108. Q. Wu, Q. Zheng, R. Krol, Creating Oxygen Vacancies as a Novel Strategy To Form Tetrahedrally Coordinated Ti^{4+} in Fe/TiO$_2$ Nanoparticles, *J. Phys. Chem. C*, 116 (2012) 7219.

109. J. E. Huheey, E. A. Keiter, R.L. Keiter, Inorganic Chemistry-Principles of Structure and Reactivity, 4th edition, Harper Collins college publishers, New York (2006).

110. A. Lempicki, L. Andrews, S.J. Nettel, B.C. McCollum, Spectroscopy of Cr^{3+} in Glasses: Fano Antiresonances and Vibronic "Lamb Shift", *Phys.Rev. Lett.*, 44 (1980) 1234.

111. L. Xuemin, G. Zhengkai, H. Tao, The doping mechanism of Cr into TiO$_2$ and its influence on the photocatalytic performance, *Phys. Chem. Chem. Phys.*, 15 (2013) 20037

112. B. Choudhury, A. Choudhury, Structural, optical and ferromagnetic properties of Cr doped TiO$_2$ nanoparticles, *Mater. Sci. Eng. B*, 178 (2013) 794.

113. B. Choudhury, A. Choudhury, Tailoring luminescence properties of TiO$_2$ nanoparticles by Mn doping, *J Lumin.*, 136 (2013) 339.

114. L. Rimoldi, E. Pargoletti, D. Meroni, E. Falletta, G. Cerrato, F. Turco and G. Cappelletti, Concurrent role of metal (Sn, Zn) and N species in enhancing the photocatalytic activity of TiO$_2$ under solar light, *Catal. Today*, 313 (2018) 40.

115. M. Manzoor, A. Rafiq, M. Ikram, M. Nafees, S. Ali, Structural, optical, and magnetic study of Ni-doped TiO$_2$ nanoparticles synthesized by sol-gel method, *Inter. Nano Lett.*, 8 (2018) 1.

116. J. M. D. Coey, A. P. Douvalis, C. B. Fitzgerald, M. Venkatesan, Ferromagnetism in Fe-doped SnO$_2$ thin films, *Appl. Phys. Lett.*, 84 (2004) 1332.

117. Z. L. Lu, H. S. Hsu, Y. H. Tzeng, F. M. Zhang, Y. W. Du, J. C. A. Huang, The origins of ferromagnetism in Co-doped ZnO single crystalline films: From bound magnetic polaron to free carrier-mediated exchange interaction, *Appl. Phys. Lett.*, 95 (2009) 102501.

118. L. R. Shah, B. Ali, H. Zhu, W. G.Wang, Y.Q.Song, H.W.Zhang, Shah S I, Xiao J Q, Detailed study on the role of oxygen vacancies in structural, magnetic and transport behavior of magnetic insulator: Co-CeO$_2$, *J. Phys. Condens. Matter.* 21(2009) 486004.

119. S. Sharma, S. Chaudhary, S. C. Kashyap, V. K. Malik, DC magnetization investigations in Ti$_{1-x}$Mn$_x$O$_2$ nanocrystalline powder, *J. Alloys Compd.,* 509 (2011) 7434.

120. N. H. Hong, J. Sakai, A. Ruyter, V. Brize, Does Mn doping play any key role in tailoring the ferromagnetic ordering of TiO$_2$ thin films, *Appl. Phys. Lett.,* 89 (2006) 252504.

121. X. Y. Li, S. X. Wu, L. M. Xu, C. T. Li, Y. J. Liu, X. J. Xing, S. W. Li, Effects of depositing rate on structure and magnetic properties of Mn:TiO$_2$ films grown by plasma-assisted molecular beam epitaxy, *Mater. Sci. Eng. B*, 156 (2009) 90.

Chapter 5

Defect Modulation by Varying Annealing Atmosphere on TiO$_2$ Nanocrystals to Tailor the NIR Range Optical Absorption, Band gap Narrowing and Ferromagnetic Response

This chapter demonstrates the impact of annealing conditions to tailor the optical and magnetic properties of TiO$_2$ nanocrystals. Optical and magnetic response of TiO$_2$ nanostructures are reported by varying the annealing atmospheres, i.e., under air, oxygen, argon, hydrogen and vacuum. Optimization of annealing conditions enables or hinders the Ti^{3+} formation which ultimately decides the optical band gap and room temperature ferromagnetism. A deep insight into the bound magnetic polaron approach that could decide the long range room temperature ferromagnetism is also demonstrated in this chapter.

5.1. Introduction

Recently, lot of attention has been given to produce dopant free pure TiO_2 phase to tailor both optical band gap and long-range RTFM. It has also been found that without doping, band gap can be reduced by using proper synthesis techniques like reduction or oxidation of TiO_2 in proper environment through which defects (oxygen vacancies and Ti^{3+}) can be enhanced/reduced which largely modify the optical and magnetic properties. Recently black TiO_2 obtained through hydrogenation has attracted great attention, which has been used as an effective technique to increase the visible and infrared light absorption under different conditions.[1] Therefore the black colour of anatase TiO_2 along with much reduced band gap have been attributed to multiple origins which invites great attention.

The concentration of intrinsic defects mostly depends on the growth conditions. Various techniques have been used to produce surface oxygen vacancies and Ti^{3+} such as UV irradiation, annealing TiO_2 in vacuum or in reducing atmosphere, ion sputtering and high energy particle bombardment, etc. Surface disorder and point defects such as O_v and Ti_i not only play the role in reducing the band gap and enhancing the optical absorption, these also largely affect the magnetic behavior of the materials. To the best of our knowledge, rare work has been reported on controlling simultaneously the optical and magnetic behavior of defective $TiO_{2-\delta}$. In this chapter, we have done calcinations of pure TiO_2 in five different atmosphere like air, argon, oxygen, vacuum and argon/hydrogen mixture and a detailed study is done on the structural, optical, electronic and magnetic properties. This study involves the interplay of defects like oxygen vacancies and Ti^{3+} ions on optical and magnetic behavior of TiO_2 exhibiting extended absorption in visible and IR region and much reduced band gap with RTFM.

5.2. Experimental section

Initially, a simple sol-gel technique using titanium butoxide as the precursor material and ethanol as the reaction medium was employed to prepare TiO_2 nanocrystals. Room temperature reaction was followed by the gel formation, which was further dried at 323 K. These samples have been prepared in five batches and have preheated at 423 K for 5 h in a muffle furnace under ambient air atmosphere enables the

removal of organic residues since the flash point of titanium butoxide is 350 K. The first batch of dried sample was calcined at 673 K in a muffle furnace under air atmosphere for 8 h (TPA). The second batch was calcined under O_2 gas at 673 K in a tube furnace for 8 h (TPO) to study the effect of oxygen vacancies. The third batch of sample was calcined by keeping the same conditions under Ar atmosphere (TPAr) and the fourth batch of sample was calcined under simple rotary vacuum at 673 K in a tube furnace for 8 h (TPV). In order to investigate more on the oxygen vacancies, hydrogenation has been carried out on final batch of TiO_2 nanocrystals using a gas mixture of 95% Ar and 5% Hydrogen (TPH). The structure and phase purity of all the samples were characterized by XRD at room temperature using PANalytical X'Pert Pro diffractometer using Cu-K_α radiation. The morphological analysis of all the samples were studied using HR-TEM, FEI Tecnai F20, operated at 300 kV. FT-IR spectra were taken to identify the functional groups present in the nanocrystals using a Bruker FT-IR spectrometer. The UV-Visible spectra of the prepared samples were obtained by a Shimadzu UV 2401 PC spectrophotometer and the emission spectra of the samples were recorded from a spectrofluorometer (Cary Eclipse, Varian). The XPS measurement was carried out on powder samples using a PHY 5000 Versa Probe II, ULVAC-PHI, Inc instrument with Al K_α X-ray source at room temperature. Field and temperature variation of magnetic measurements were performed using a vibrating sample magnetometer attached to the physical property measurement system, Quantum Design Inc., (USA).

5.3. Results and Discussion

5.3.1. Structural Analysis

Fig. 5.1(a) shows the XRD patterns taken on TiO_2 nanocrystals annealed under different atmospheres and the obtained Rietveld refinement of all the patterns are given in Fig. 5.1(b)-5.1(f). All the peaks were well indexed and identified as tetragonal anatase phase of TiO_2 (space group I4$_1$/amd (ICDD 78-2486)) without the presence of any other phases.
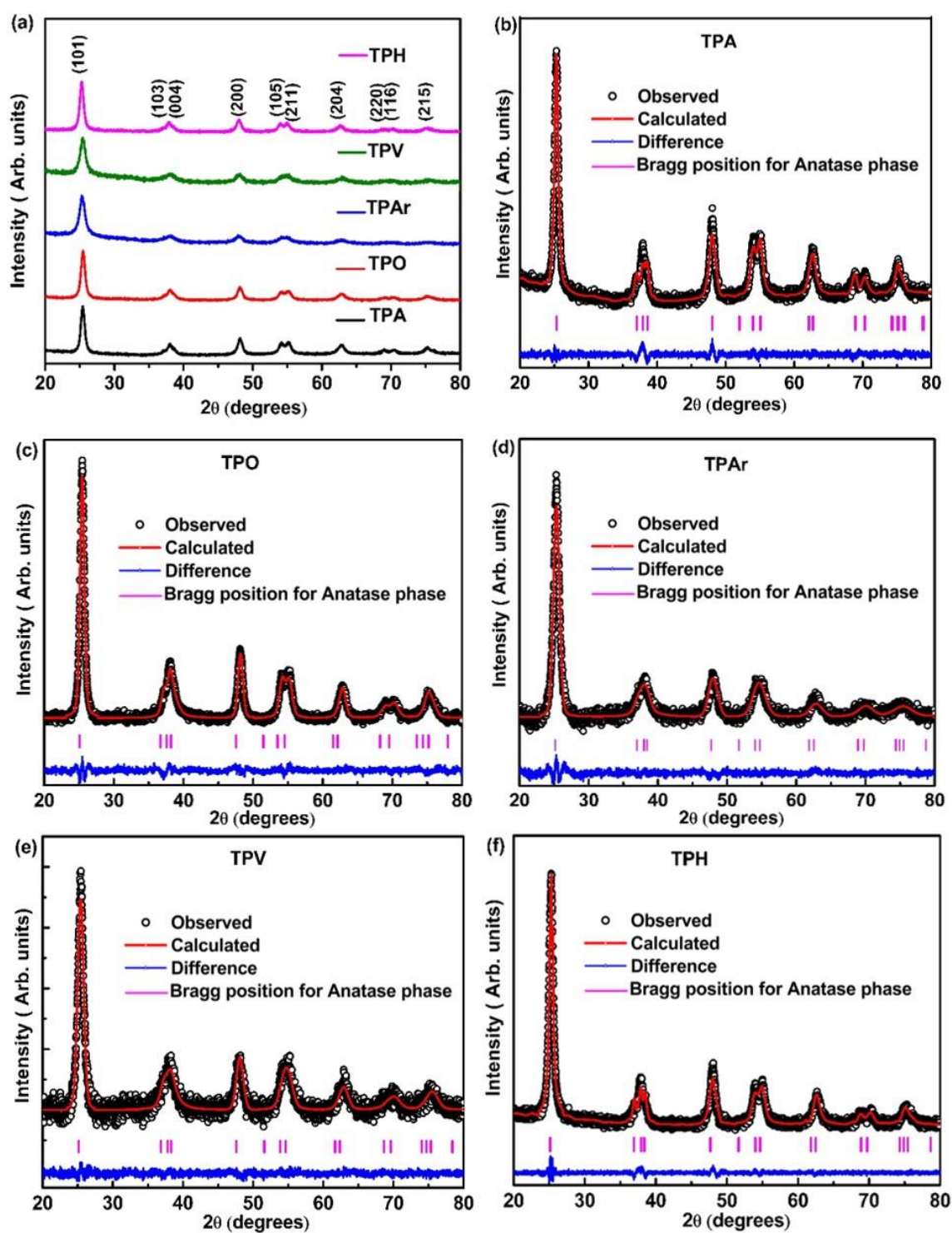
Fig.5.1. (a) XRD patterns of TiO$_2$ nanostructures, (b-f) Refined XRD patterns
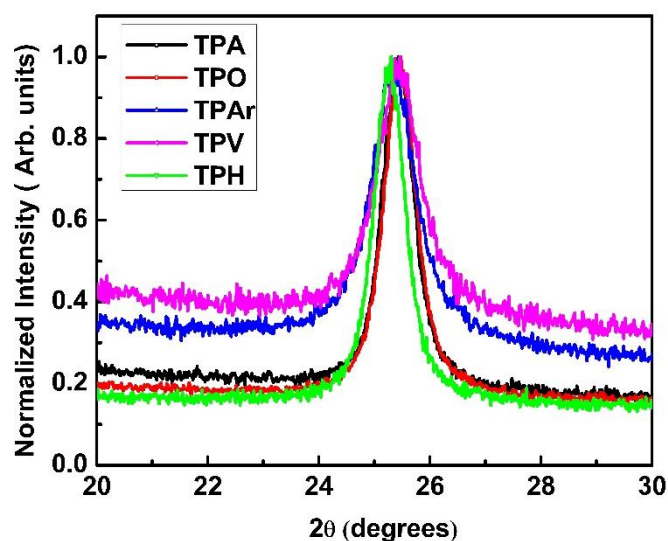
Fig.5.2. Peak shift and broadening associated with TPA, TPO, TPAr, TPV and TPH

The broadening and shifting of most intense (101) peak can be seen from the expanded plot (given in Fig. 5.2) taken from $20°$ to $30°$. The broadening is more in argon and vacuum annealed TiO_2 nanocrystals which may have arisen due to reduced particle size. The particle size was calculated from Scherrer's formula by taking into account the most intense diffraction peak (101) as the reference peak and the particle size was found out to be around 9 nm for TPAr and TPV samples and around 12 nm for TPA, TPO and TPH samples which closely agrees with the particle size obtained from TEM images (discussed later). The shifting of the (101) peak towards lower and higher angles suggests slight change in lattice constant which can be seen from the refinement parameters given in Table 5.1.

Although there is little change in both lattice parameters (a and c), it is interesting to observe that the axial ratio c/a which represents the lattice symmetry is nearly the same (2.50, except very small change in third decimal) for all the samples except in argon annealed TiO_2 nanocrystal. Due to the change in lattice parameter there is a little change in lattice volume but again this change (lattice expansion) is more in TPAr sample which is due to reduced particle size.[2] Although TPV has nearly same particle size, but it has slightly less lattice volume in comparison to TPAr sample. This may be due to the contradictory results of size dependence of lattice expansion/contraction in TiO_2, the mechanism of which is not understood clearly. Li *et*

al.[3] reported the size dependence of lattice expansion/contraction for extremely small nanocrystals i.e. less than 15 nm in anatase TiO_2. Again, within this small size many other factors such as quantum confinement effect, strain, intrinsic defects like oxygen vacancy, Ti interstitial, Ti vacancy etc. also play an important role, so it is not easy to determine the exact cause of lattice parameter variation in TiO_2 nanocrystals. Annealing in different gases have different impact on the samples, for eg., vacuum even has the advantage that the heating and cooling can be better controlled, which is favourable with regards to the dimensions of the products. Furthermore, after annealing in vacuum, it is possible to cool with overpressure nitrogen or argon so that a faster cooling compared to the annealing under Argon can be realized. In this way, particle size can be affected when sample is subjected to different conditions and this is the reason for varying peak width.

Raman spectra are recorded at room temperature for all the samples. The six active Raman modes $E_g(1)$, $E_g(2)$, $B_{1g}(1)$, A_{1g}, $B_{1g}(2)$ and $E_g(3)$ are assigned to anatase TiO_2. Fig. 5.3(a) shows the Raman spectra of samples TPA, TPO, TPAr, TPH and TPV and the inset shows the magnified spectra of TPA and TPO samples, the peaks of which were not clearly visible due to the much reduced intensity in comparison to TPAr, TPH and TPV samples. It is quite interesting to observe the presence of five characteristics modes of anatase TiO_2 ($E_g(1) \sim 143$ cm^{-1}, $E_g(2) \sim 196$ cm^{-1}, $B_{1g} \sim 394$ cm^{-1}, $A_{1g}+B_{1g} \sim 512$ cm^{-1} and $E_g(3) \sim 630$ cm^{-1}) in all the samples which confirm the anatase phase of TiO_2. But a large blue shift to 152 cm^{-1} accompanied by broadening of the most intense $E_g(1)$ mode is observed in TPAr, TPH and TPV samples (Fig. 5.3(b)). The $E_g(1)$ mode generally results from the vibration of Ti-O bonds and the Raman signal is very sensitive to the vibrational modes of O^{2-} ions in Ti-O bond. So the blue shift and peak broadening of anatase TiO_2 is attributed to the nonstochiometry in TiO_2 i.e. due to the presence of oxygen vacancy[4] which in turn affect the intensity, position and width of Raman signal. Thus the Raman spectra indicate the presence of large oxygen vacancies which in turn could be associated with the formation of Ti^{3+}.

Table 5.1. Refinement parameters obtained for TiO$_2$ nanocrystals prepared under different atmosphere

| Compound	Air annealed (TPA)	Oxygen annealed (TPO)	Argon annealed (TPAr)	Vacuum annealed (TPV)	Hydrogen annealed (TPH)
Phase	Anatase				
Crystal Structure	Tetragonal				
Space Group	I 41/a m d				
Lattice Parameters					
a(Å)	3.7887 (1)	3.7927 (4)	3.8086 (6)	3.7923 (2)	3.7938 (4)
c(Å)	9.4996 (4)	9.4878 (3)	9.4657 (3)	9.5124 (5)	9.5070 (2)
Volume (Å)^3	136.36 (5)	136.48 (1)	137.31 (2)	136.80 (1)	136.83 (5)
Atomic positions					
Ti $_x$ (4a)	0.0000	0.0000	0.0000	0.0000	0.0000
Ti $_y$ (4a)	0.7500	0.7500	0.7500	0.7500	0.7500
Ti $_z$ (4a)	0.1250	0.1250	0.1250	0.1250	0.1250
O $_x$ (8e)	0.0000	0.0000	0.0000	0.0000	0.0000
O $_y$ (8e)	0.2500	0.2500	0.2500	0.2500	0.2500
O $_z$ (8e)	0.0853	0.0857	0.0851	0.0848	0.0854
B $_{iso}$ (Ti) (Å)^2	0.0005	0.0002	0.0007	0.0006	0.0002
B $_{iso}$ (O) (Å)^2	0.0028	0.0016	0.0013	0.0007	0.0021
Residual Parameters					
R$_p$	4.18	3.25	3.51	3.70	5.17
R$_{wp}$	5.40	4.08	4.43	4.64	6.56
χ^2	1.62	1.12	1.01	1.13	1.62
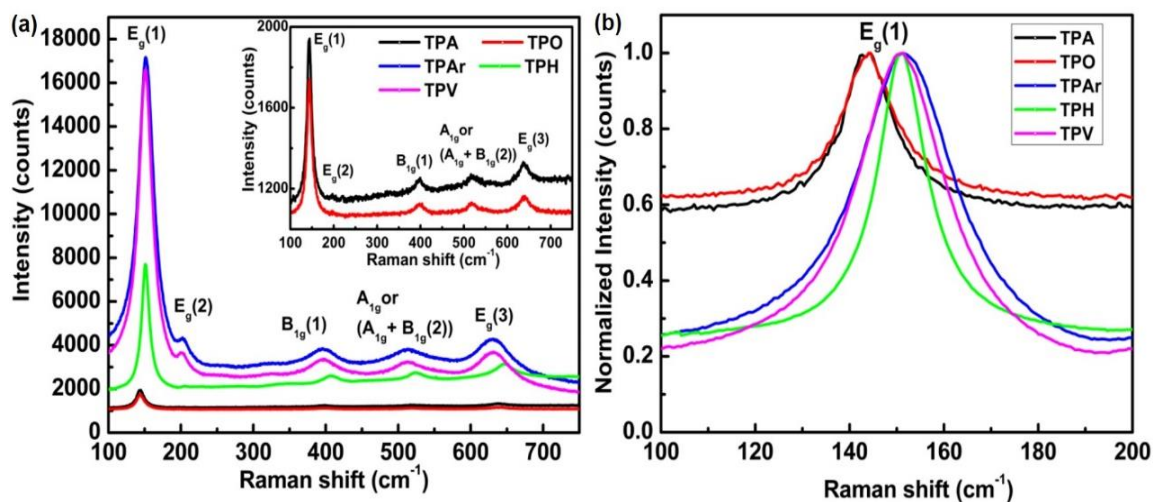
Fig. 5.3.(a). Raman spectra of TPA, TPO, TPAr, TPH and TPV, Inset shows the well resolved peaks of TPA and TPO samples, (b) Peak shift and broadening of $E_g(1)$ peak associated with TPA, TPO, TPAr, TPV and TPH

5.3.2. Morphological Analysis

The TEM images shown in Fig. 5.4(a-e) are almost spherical in shape with some agglomeration. The average particle size is found to be in the range 9-12 nm which well agrees with the particle size obtained from XRD analysis. The high resolution TEM images (Fig. 5.4(f-j)) show the highly crystalline nature of TiO₂ nanocrystals in all the samples with lattice fringes corresponding to different planes like (101), (103), and (004) planes corresponding to the tetragonal anatase phase of TiO₂. Insets of Fig. 5.4(f-j) show the Fast Fourier Transform (FFT) patterns taken on all the samples, which again confirm the crystalline nature of all the samples. SAED patterns taken on all the samples (Fig. 5.4 (k-o)) show clear distinct rings corresponding to different planes of tetragonal anatase TiO₂. The rings obtained in the SAED pattern are well indexed to different planes of anatase TiO₂, which were found out from the *d* spacing using Image J software. The planes obtained from SAED pattern were similar to the planes obtained in XRD which further confirms the tetragonal anatase phase of TiO₂.

5.3.3. FT-IR Analysis

FT-IR spectra of TiO₂ nanocrystals annealed in different atmosphere were taken to study the functional groups present in the samples. All the TiO₂ nanocrystals annealed at different environments displayed similar features.
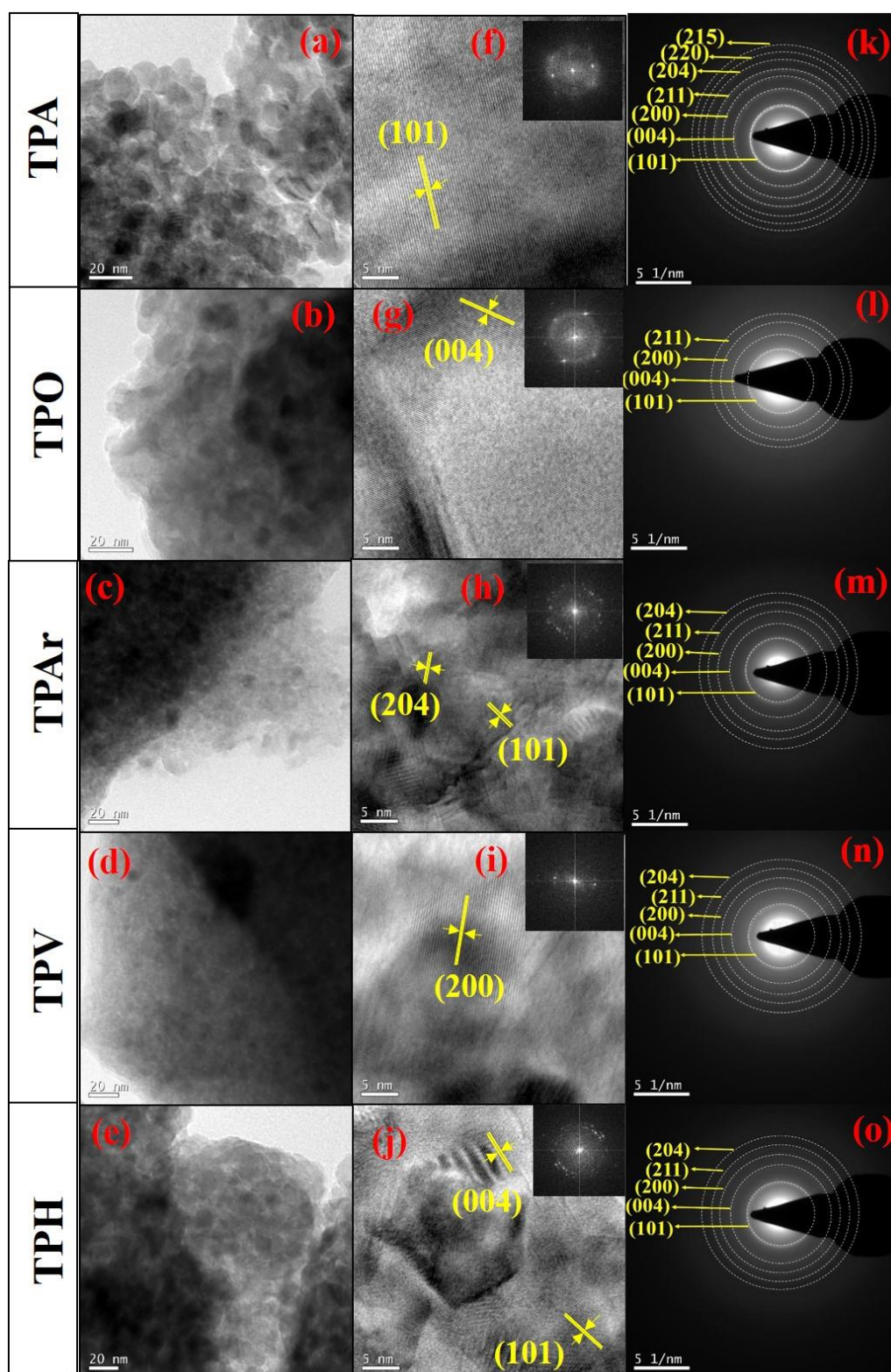
Fig.5.4. TiO₂ nanocrystals prepared under different atmosphere (a-e) TEM images showing the nanocrystal formation, (f-j) HR-TEM images showing lattice fringes with FFT shown in the inset and (k-o) SAED patterns.
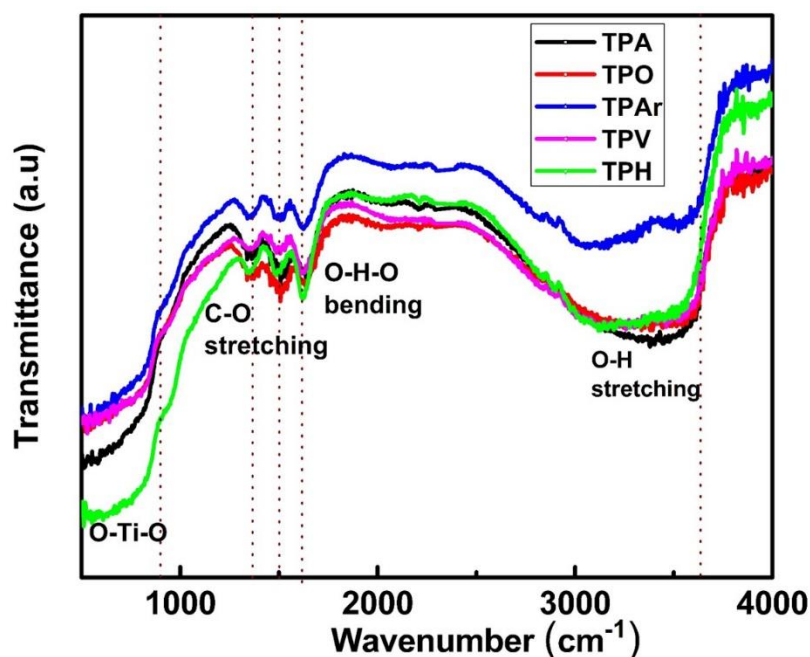
Fig.5.5. FT-IR spectra of TPA, TPO, TPAr, TPV and TPH samples

As seen from the Fig. 5.5, all the spectra have a broad band in the region 2900-3600 cm^{-1} which is attributed to O-H stretching vibrations of OH group present in the sample and the band around 1615 cm^{-1} is due to O-H-O bending mode of the adsorbed water molecule. The band around 1505 cm^{-1} corresponds to C-O stretching vibration indicating the presence of C=O group which is ascribed to acetate present in the precursor material and the band located around 1364 cm^{-1} corresponds to a vibration of T-Ligand bond. The band in the region below 1000 cm^{-1} is ascribed to the absorption band of TiO, Ti-O-Ti stretching and O-Ti-O bending vibrations.

5.3.4. Optical Studies

To investigate the influence of different annealing atmospheres on the absorbance of TiO₂, UV-Visible absorbance spectra were recorded from which the band gap of the TiO₂ nanocrystals was determined. All the samples show a steep increase in absorption at wavelengths shorter than 400 nm (Fig.5.6(a) and 5.6(b)) which can be attributed to the intrinsic band gap absorption of anatase TiO₂. TP-Ar, TP-H, TP-V samples exhibit broad absorption in visible and infrared region in contrast to TP-A and TP-O samples. This result is in good agreement with the colour change of the samples from grey to black TiO₂ (inset of Fig. 5. 6 (a)). The light grey (TPA) and white (TPO) samples

exhibit strong absorption in UV region while the dark brown (TPAr), black (TPV) and strong black (TPH) samples display absorption in the UV-VIS-NIR region.
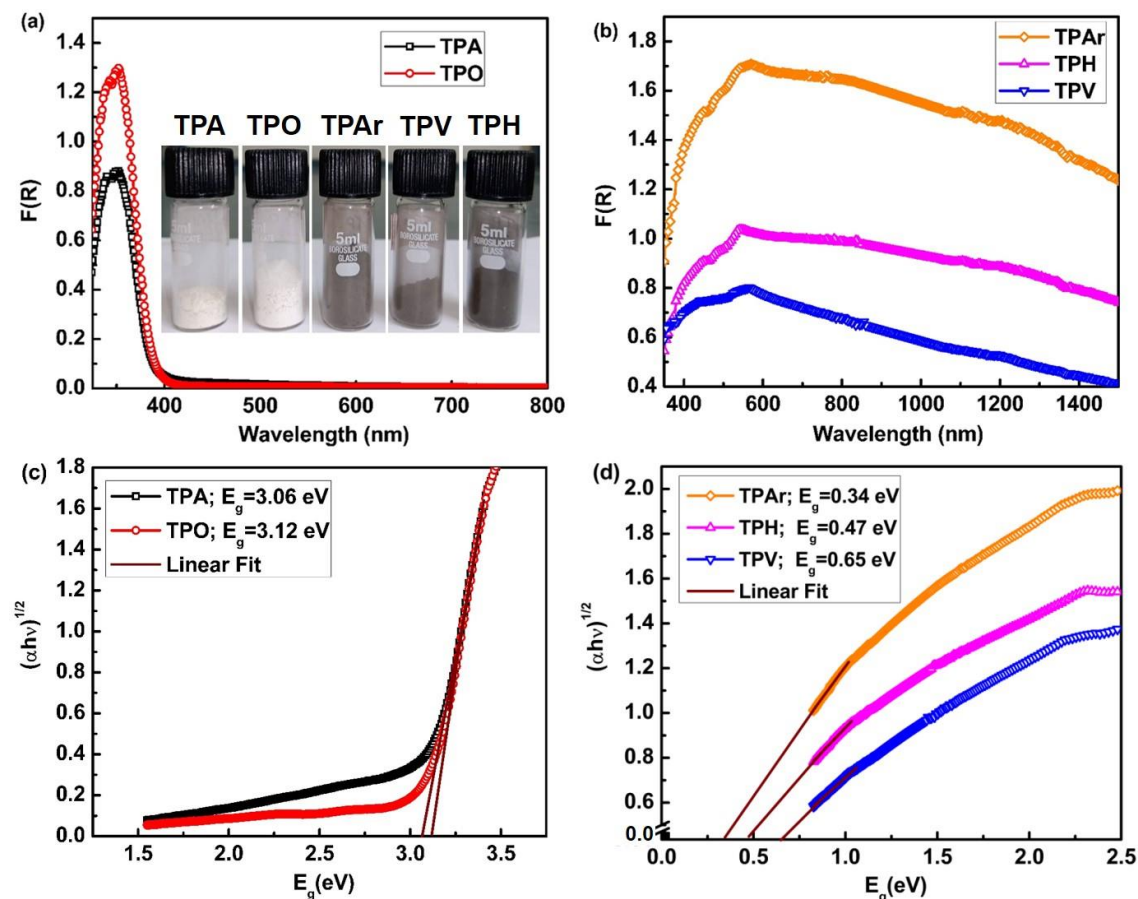
Fig.5.6. UV spectra corresponding to (a) TPA and TPO (inset shows the colour change associated with different samples) and (b) TPAr, TPV and TPH, Tauc's plot corresponding to (c) TPA and TPO and (d) TPAr, TPV and TPH

Assuming TiO_2 to be an indirect semiconductor and using Tauc plot (i.e. the Kubelka– Munk function versus the energy of the light absorbed) (Fig. 5.6(c) and 5.6(d)), the band gap of the TPA and TPO was extrapolated to be 3.06 and 3.12 eV, respectively while the band gap of TPAr, TPH, TPV was found to be 0.34, 0.47 and 0.65 eV respectively. It is known that in TiO_2, the formation of oxygen vacancies leads to the creation of unpaired electrons or Ti^{3+} centers, which could form donor levels in the electronic structure of TiO_2.[5] Under oxygen-rich conditions, oxygen vacancies are the favored defect type.[6] Oxygen vacancies V_o's (TiO_{2-x}) and Ti interstitials ($Ti_{1+x}O_2$) appear in TiO_2 due to reduction of TiO_2.[7] Here oxygen and air atmosphere are provided as oxygen rich while vacuum, hydrogen and argon are used as reducing atmosphere.

The narrowed band gap of TPAr, TPH, TPV are due to the introduction of oxygen vacancies and Ti^{3+} states. A new energy level must have introduced below the conduction band due to the introduction of oxygen vacancies and Ti^{3+}. Reports suggest that Ti^{3+} and/or oxygen vacancy can generate new energy level below the conduction band. Mostly black TiO_2 nanoparticles having crystalline core/disordered shell morphology, obtained by hydrogenation of TiO_2 studied by Chen *et al.*[8] and Naldoni *et al.*[7] exhibit visible-IR absorption and hence much reduced band gap was observed due to the presence of V_O and surface disorder. Chen *et al.* reported a substantial shift of valence band position in hydrogenated black TiO_2 nanoparticles due to surface disorder giving rise to a much reduced band gap of 1 eV. Wang *et al.*[9] and Naldoni *et al.* also reported remarkable band gap narrowing due to surface disorder. It is observed that highly reduced black anatase TiO_2 introduce localized defect states at 0.7-1.18 eV below the conduction band minimum and an optical band gap of 1.0 eV has been obtained in hydrogenated TiO_2. This value can also be reduced if we consider conduction band (CB)/valence band (VB) tailing. Therefore, in our case electronic transition from tailed VB and oxygen vacancy localized state to CB or from tailed VB to V_O localized state may have occurred giving rise to VIS-IR absorption and much reduced band gap in TPAr, TPV and TPH nanocrystals. Generally, hydrogen and vacuum environments have been used for creating reducing atmosphere in which anatase TiO_2 greatly reduces, giving black color and hence extended absorption in IR region. But in our case it is quite surprising that annealing in argon atmosphere exhibits enhanced absorption in visible and IR region giving rise to much reduced (lowest in this series) band gap of 0.34 eV and a very clear hysteresis behavior at room temperature (discussed later). Raman study shows large shift and broadening of $E_g(1)$ mode of TPAr sample which indicates presence of disorder and non-stoichiometry in the lattice. So, along with the disorder, a larger concentration of lattice defects like oxygen vacancy and titanium interstitials in comparison to other samples might have contributed largely to the enhanced absorption and much reduced band gap in argon annealed nanocrystals which are discussed in detail in coming section.

In order to understand the nature of defects PL spectra were recorded at room temperature on all the samples in the wavelength range 340-640 nm with excitation

wavelength of 325 nm. A strong broad visible PL emission (see Fig. 5.7) was observed for TPAr, TPV, TPH and a weak broad visible peak for TPA and TPO samples. Near band-edge emission around 377 nm can be seen in the PL spectra of air annealed sample which is shifted to 414 nm in TPO. The broad visible PL for all samples is mostly related to STE and oxygen vacancy related defect states.[10,11] Deconvolution of broad emission peaks was done on all the samples using Gaussian fittings. The emission spectra of air annealed sample shows UV emission peak around 375 nm which is shifted to 415 nm in all other samples. Along with violet emission peak around 429 nm, two blue emission peaks around 467 nm and 497 nm and one green emission peak around 535 nm can be seen in all the samples, the position of the peaks has shifted due to the interplay of defects. Oxygen vacancy-induced visible PL is well known in TiO₂ nanocrystals. However, there are very few reports on the PL signature of Ti_i defects in TiO₂. The 429 nm peak can be ascribed to STE localized on TiO_6 octahedra. The STE originates when a trapped electron captures a hole in TiO₂. In an STE emission, the recombination occurs through oxygen vacancies. The peaks at 467 and 535 nm are attributed due to the defects associated with oxygen vacancies where one or two electrons can be trapped with the oxygen vacancies producing F^+ center. The 497 nm emission is due to charge transition from Ti^{3+} to TiO_6^{2-} linked with oxygen vacancies. The emission around 580 nm may be due to the electron transition from F^+ center to the acceptor level just above the valence band. It can be seen from PL spectra that the intensity as well as the broadening of Argon annealed nanocrystal is more in comparison to other samples which indicates that the concentration of oxygen vacancy in TPAr sample is more. When an oxygen vacancy is created in TiO₂ lattice due to loss of oxygen, two electrons remain trapped in vacancy cavity giving rise to F centre and if one electron in F centre goes to occupy the neighboring Ti^{4+} ion giving rise to Ti^{3+} ion then F^+ (i.e. one electron trapped in oxygen vacancy site) centre states form within the band gap. It is reported that the NIR PL is attributed due to Ti interstitial defects in TiO₂.[12] Due to our experimental limitation we could not observe NIR PL. But the UV-Vis spectra indicate IR absorption. So, at this point we can say that both O_v and Ti_i play dominant role in IR absorption as well as reduced band gap which will be more clear from XPS analysis.
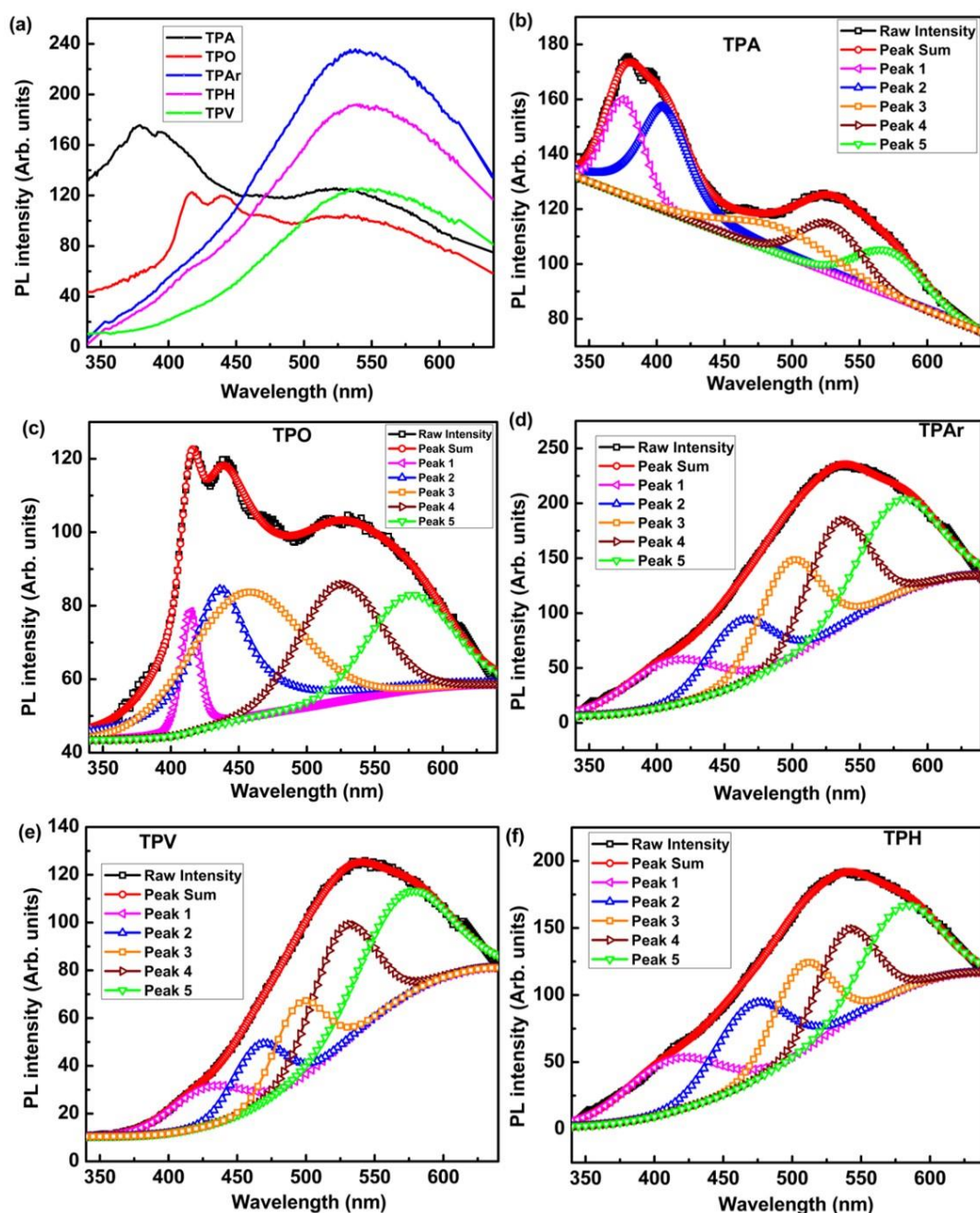
Fig.5.7. PL spectra of TiO₂ nanocrystals (a) PL spectra of all the samples, (b)-(f) deconvoluted spectra of TPA, TPO, TPAr, TPV and TPH

5.3.5. XPS Analysis

XPS being a surface sensitive technique provides information about the chemical environment of ion species present on the surface. The survey spectra of all samples are shown in Fig. 5.8. The high resolution spectra of Ti 2p and O1s were recorded and are shown in Fig. 5.9(a) − 5.9 (j) along with the deconvolution. The Ti

spectrum of TPAr, TPV and TPH samples can be fitted with four peaks corresponding to Ti^{4+} $2p_{3/2}$ at 457.51 eV, Ti^{4+} $2p_{1/2}$ at 463.26 eV, Ti^{3+} $2p_{3/2}$ at 457.11 eV and Ti^{3+} $2p_{1/2}$ at 462.47 eV as shown in Fig. 5.9 (c), (d) and (e) for TPAr, TPV and TPH sample with slight shift in TPH sample. The line separation between Ti^{4+} $2p_{1/2}$ and Ti^{4+} $2p_{3/2}$ is 5.74 eV, which is consistent with the standard binding energy of TiO_2.[13] Interestingly, TPA and TPO samples exhibit a single oxidation state of Ti^{4+} i.e. $Ti^{4+}2p_{3/2}$ and $Ti^{4+}2p_{1/2}$.

Further, the high resolution O1s XPS spectra obtained for all samples are shown in Fig. 5.9(f)–5.9(j). Each spectrum is fitted with three peaks i.e. 528.4 eV, 529.6 eV and 530.7 eV (for TPAr sample) that correspond to lattice oxygen of TiO_2, hydroxyl groups and adsorbed water, respectively. Now we can say the probable reason of band gap narrowing in TiO_2 due to different annealing environments. Due to annealing at higher temperature oxygen vacancies were formed which have created intermediate energy levels in the band gap. In our case, as discussed above Ti^{3+} is also formed which also creates energy level in the band gap, contributing to the reduction of band gap. Mostly, in TPAr, TPV and TPH samples both oxygen vacancies and Ti^{3+} are created which creates additional energy level in the band gap contributing to large reduction in the band gap.
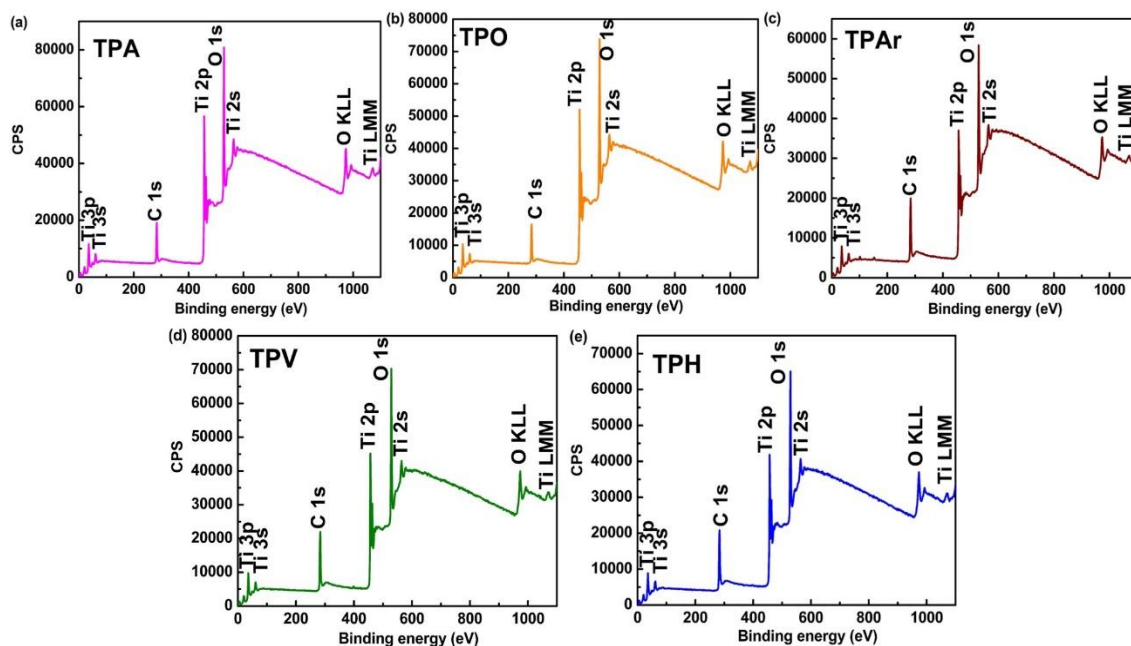

Fig.5.8. XPS wide scan spectra of TiO₂ nanocrystals (a) TPA, (b) TPO, (c) TPAr, (d) TPV and (e) TPH
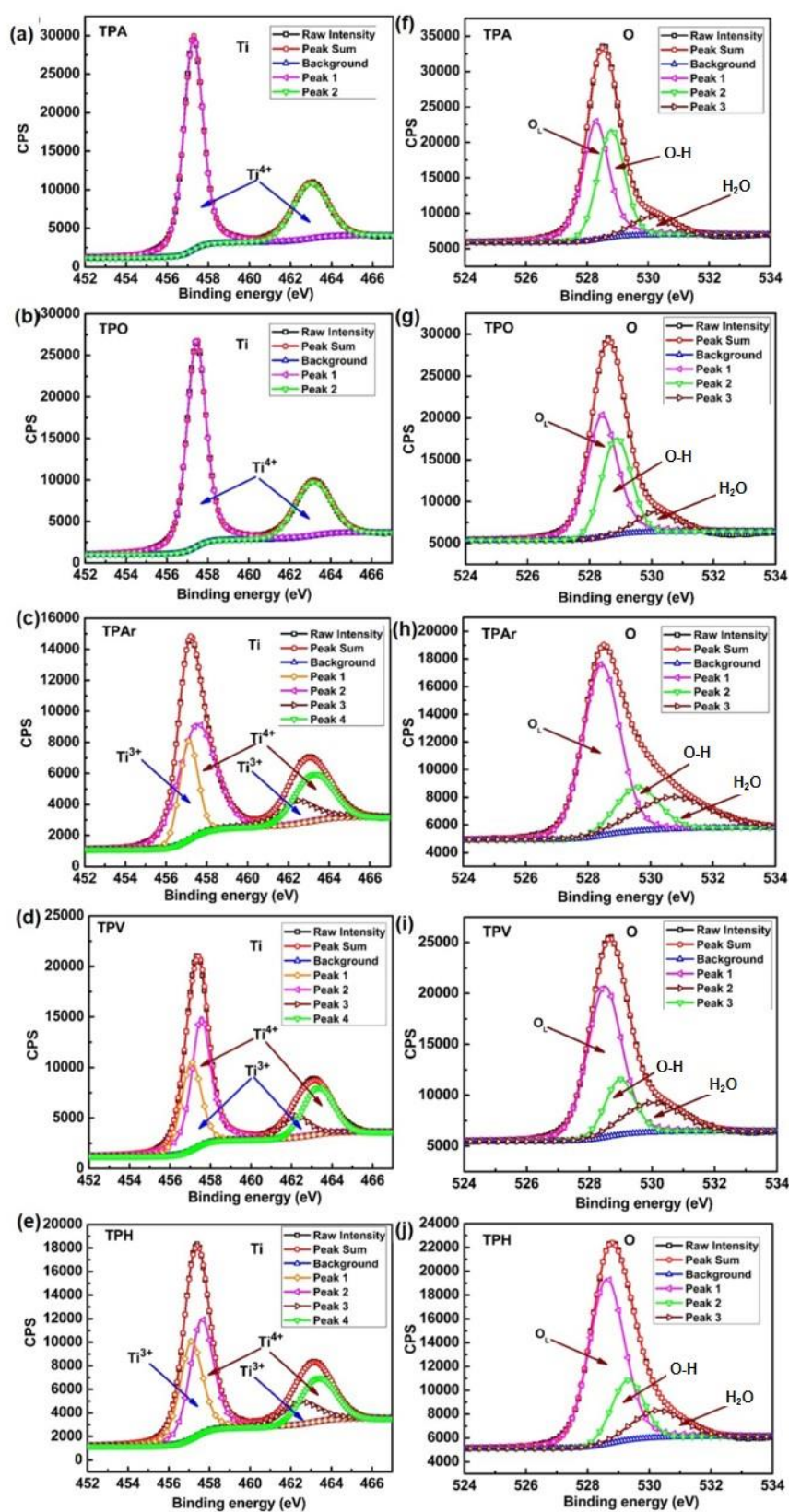
Fig.5.9. XPS spectra of TiO₂ samples (a)-(e) Ti 2p spectrum of TPA, TPO, TPAr, TPV and TPH (f)-(j) O 1s spectrum of TPA, TPO, TPAr, TPV and TPH

But in case of TPA and TPO samples, as there is no Ti^{3+} peak in XPS spectra, so only oxygen vacancies have played the major role in reducing the band gap due to which it is less in these samples. Hence, it can be seen that TPAr, TPV and TPH samples have much reduced band gap in comparison to TPA and TPO samples, so here it can be inferred that Ar, vacuum and hydrogen atmosphere annealing creates more number of oxygen vacancies contributing to significant reduction in band gap in comparison to air and oxygen annealed samples.

5.3.6. Magnetic studies

The effect of defects on the magnetic behavior due to the annealing of TiO₂ nanocrystals in different environment was investigated using a VSM. The M−H measurements were carried out at three different temperatures (300 K, 100 K, 2 K) with field varying from −90 to +90 kOe. The M−H curves of all samples at 300 K are shown in Fig. 5.10(a), from which a well-defined square shaped hysteresis loop can be observed for the TiO₂ nanocrystals annealed in argon atmosphere indicating that TPAr sample is FM at room temperature (Fig. 5.10(d)). From the M-T curve taken in a field of 200 Oe, the large difference between Zero Field Cooled (ZFC) and Field Cooled (FC) curve indicate the existence of ferromagnetism above room temperature i.e. the Curie temperature is above 300K as shown in Fig. 5.13 (a). Further, high temperature M-T curve clearly indicates a perfect ferromagnetic behavior as shown in Fig. 5.13 (b). The Curie-Weiss fit is also presented in Appendix.B and Fig.B1 (a) clearly demonstrates a Tc of 840 K. The spontaneous magnetic moment (from saturation magnetization) is found to be 1.77 x 10^{-4} μ$_B$/F.U. and the H$_C$ is about 30 Oe which are significantly higher than the reported magnetization obtained in Co-doped TiO₂ nanocrystals.[14] It can be observed that the TiO₂ nanocrystals annealed in hydrogen atmosphere (TPH) shows PM behavior at 2 K (Fig. 5.12 (f)), at 100 K and 300 K (Fig.5.11 (f) and 5.10(f)). But M-T curve (Fig. 5.13(c)) indicates coexistence of PM and very weak FM behavior upto 150 K and PM behavior at room temperature (with a very weak RTFM behavior at lower fields). This is further verified using Curie-Weiss fit and is shown in Fig.B1 (b).

Fig.5.10. Magnetic response of TiO₂ samples (a) M-H curve from -90 kOe to 90 kOe of all the samples measured at 300 K and (b)-(f) M-H curve from -10 kOe to 10 kOe of TPA, TPO, TPAr, TPV and TPH at 300 K

Fig.5.11. Low temperature magnetic response of TiO₂ samples (a) M-H curve from -90 kOe to 90 kOe of all the samples at 100 K and (b)-(f) M-H curve from -10 kOe to 10 kOe of TPA, TPO, TPAr, TPV and TPH at 100 K

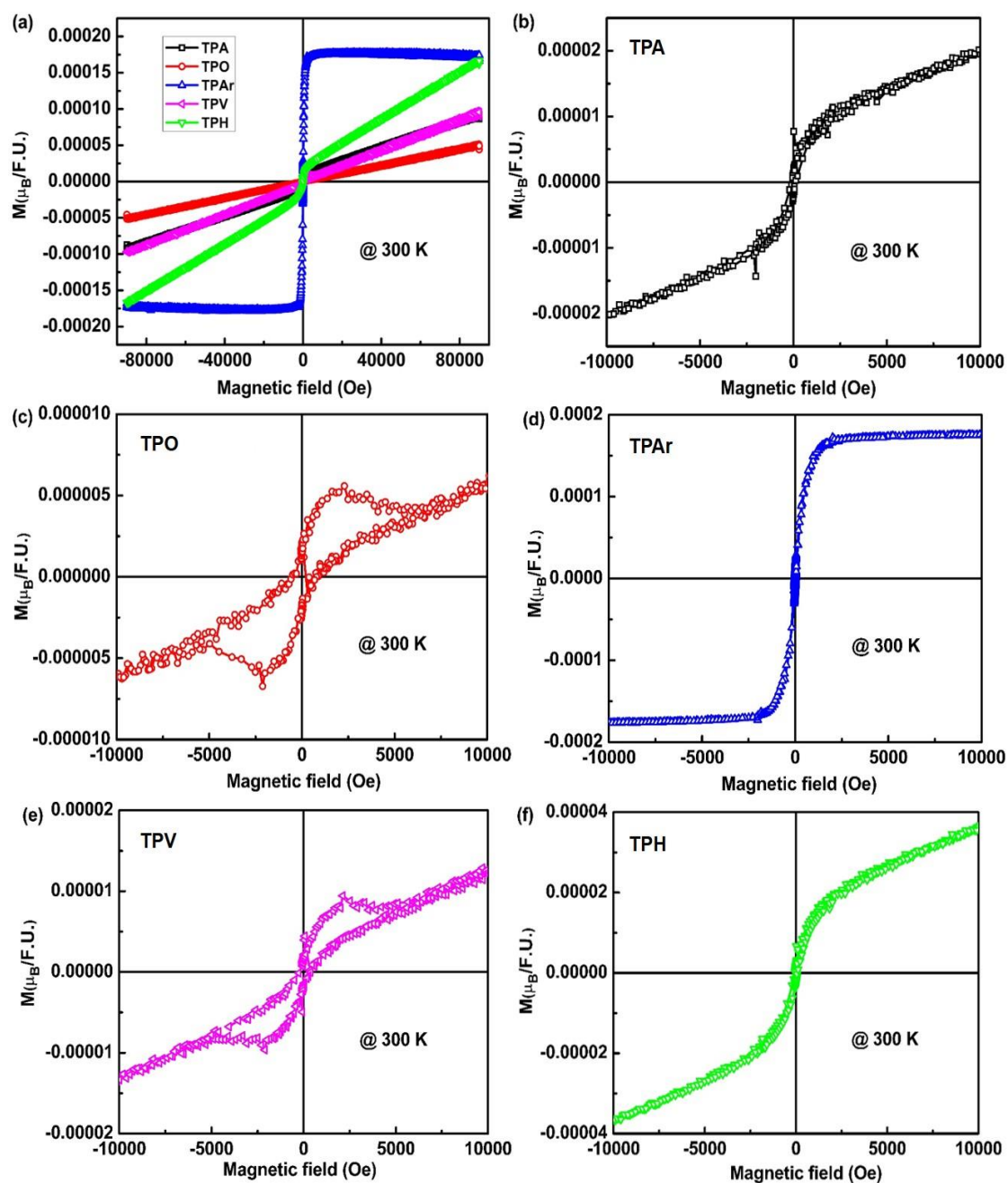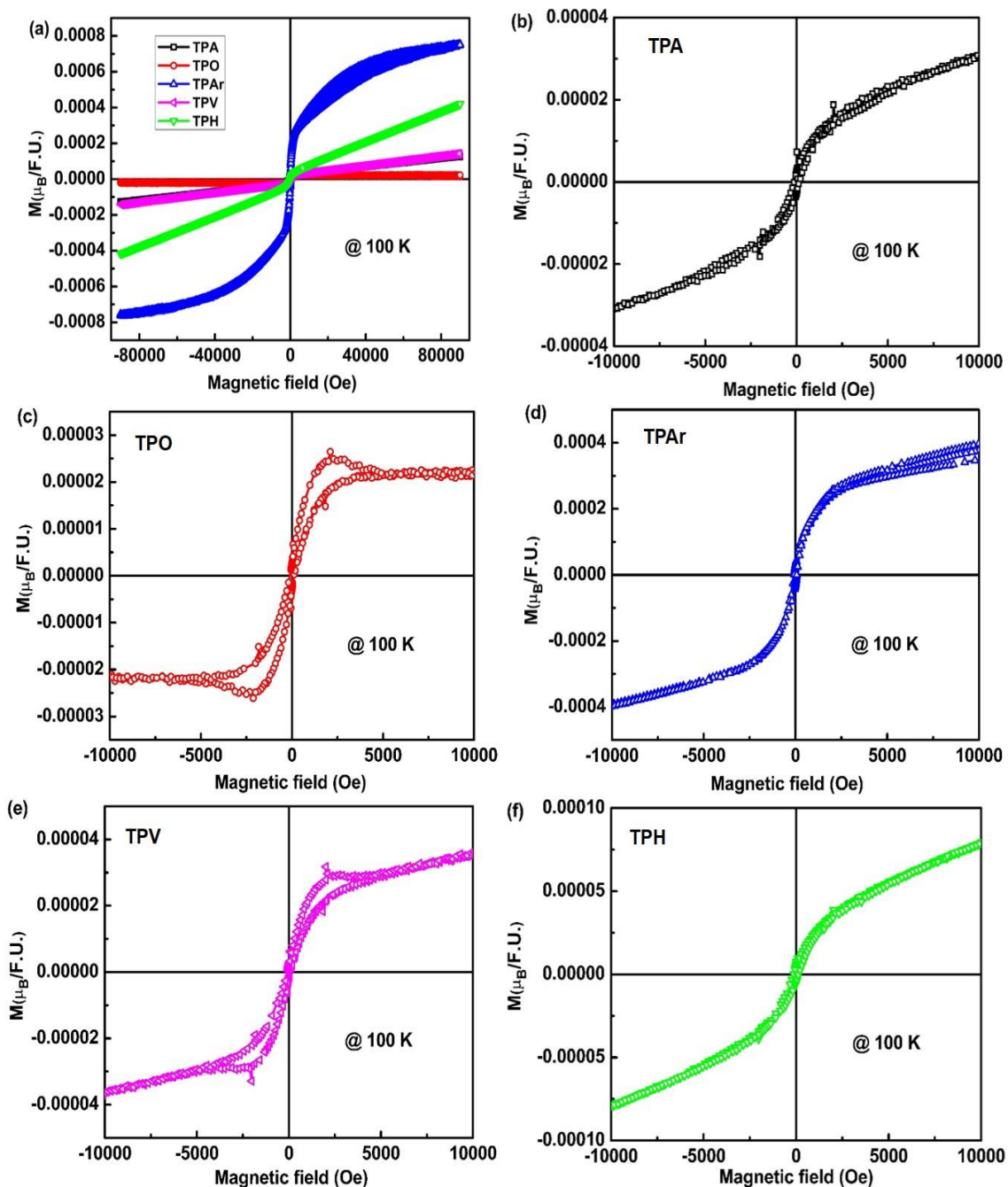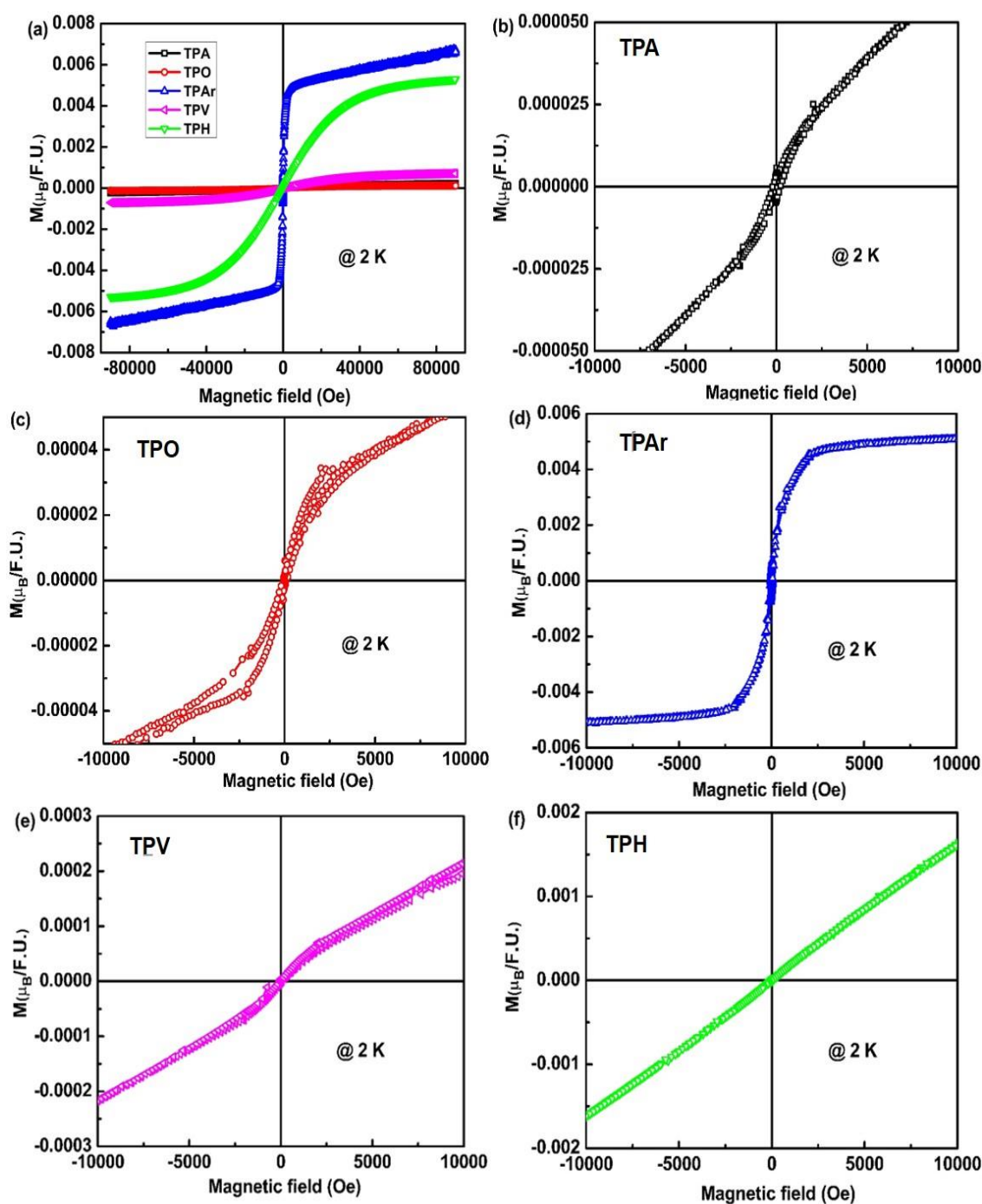**Fig.5.12.** Low temperature magnetic response of TiO₂ samples (a) M-H curve from -90 kOe to 90 kOe of all the samples at 2 K and (b)-(f) M-H curve from -10 kOe to 10 kOe of TPA, TPO, TPAr, TPV and TPH at 2 K
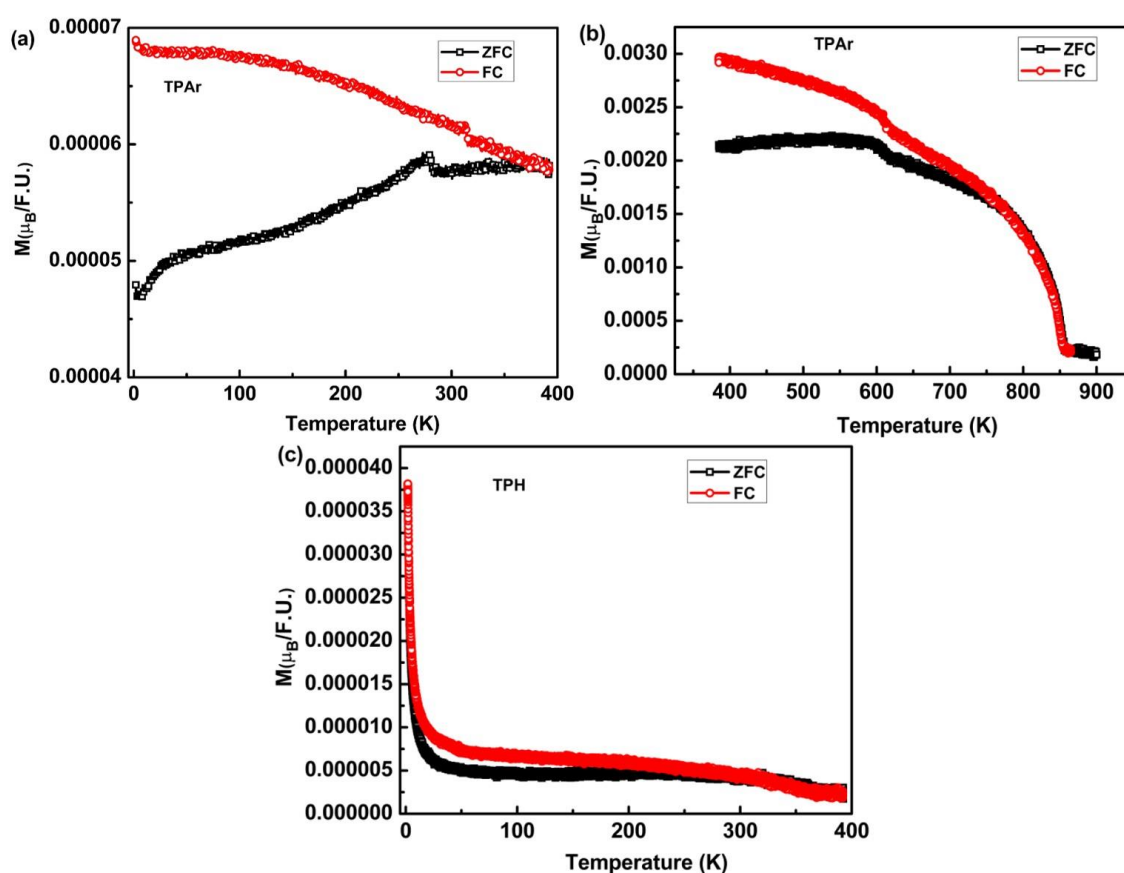
Fig.5.13. Temperature variation of magnetic moment corresponding to (a) TPAr at 200 Oe upto 385 K, (b) TPAr at 200 Oe upto 900 K (c) TPH at 200 Oe

Similar behavior is exhibited by TPV as well, as shown in Fig. 5.10 (e), Fig. 5. 11 (e) and Fig. 5. 12 (e) respectively. It can be seen from Fig. 5.10 (a) that TPA and TPO samples show PM behavior at room temperature and coexistence of FM and PM behavior at 100 K and 2 K. Even at 300 K we cannot say pure PM behavior of TPA and TPO samples if we consider lower fields. Although very weak hysteresis exists in TPA and TPO samples at 300 K and 100 K but the behavior is very different from pure FM and pure PM due to non-saturating behavior of M-H curve at higher field. So, mixed magnetic behavior of FM and PM exist in TPA and TPO sample. As for spintronics device application, RTFM is the practical requirement and thus it can be said that argon annealed TiO₂ is the best material for both optoelectronic and spintronics device applications.

5.3.7. Explanation of magnetic behaviour in TiO₂ nanocrystals annealed at different atmospheres

Here we have tried to explain the mechanism of clear hysteresis loop in TPAr sample at room temperature through the formation of BMP which is associated with oxygen vacancy and Ti^{3+} ions formed in the material. The BMP fit and the variation in BMP concentration for all the samples is represented in Fig. 5.14(a) and 5.14(b) respectively. BMP involves the overlapping of the orbital occupied by the locally trapped electron by an oxygen vacancy with the unpaired electron ($3d^1$) of Ti^{3+} ion. The estimated BMP concentration is 6.73×10^{19}, 8.09×10^{18}, 2.25×10^{16}, 1.38×10^{16} and 4.44×10^{14} for TPAr, TPH, TPV, TPA and TPO respectively. From the PL analysis, the presence of a significant number of oxygen vacancy defects (V_o) in the TiO₂ nanocrystals annealed in different atmospheres is evident. The V_o is a positively charged center, and when it traps an electron it forms a bound state V_o^+. Studies [15-19] have shown that such oxygen vacancy with single electron trap (V_o^+) can induce a local magnetic moment and when the concentration of such vacancies reaches a threshold limit, ferromagnetic exchange interaction between such V_o^+ defects can be stabilized to mediate the RTFM. Due to annealing in the air and O₂ atmosphere, the V_o concentration is very less, due to which very weak FM (negligible) is observed in TPA and TPO samples. In TPV sample, although vacuum is a reducing atmosphere and possibility of formation of oxygen vacancies is more in this case but the concentration of such vacancies is not enough to mediate FM interaction between the V_o^+ defects and at the same time XPS indicates the very less amount of Ti^{3+} peak which precludes the BMP involvement in inducing FM in TPV. In TPH sample, it can be observed from PL as well as XPS study that both oxygen vacancies and Ti^{3+} are much higher. So, the possibility of FM due to BMP is evident but the M-H and M-T measurement rules out the FM at room temperature. Here it can be assumed that BMP overlapping is not fulfilled, although an enhancement in magnetic moment is observed in comparison to TPV samples but it is not so strong to give ferromagnetic signal at room temperature. Also due to the very small (12 nm) particle size, the possibility of formation of clusters cannot be avoided which could have created different magnetic phases.
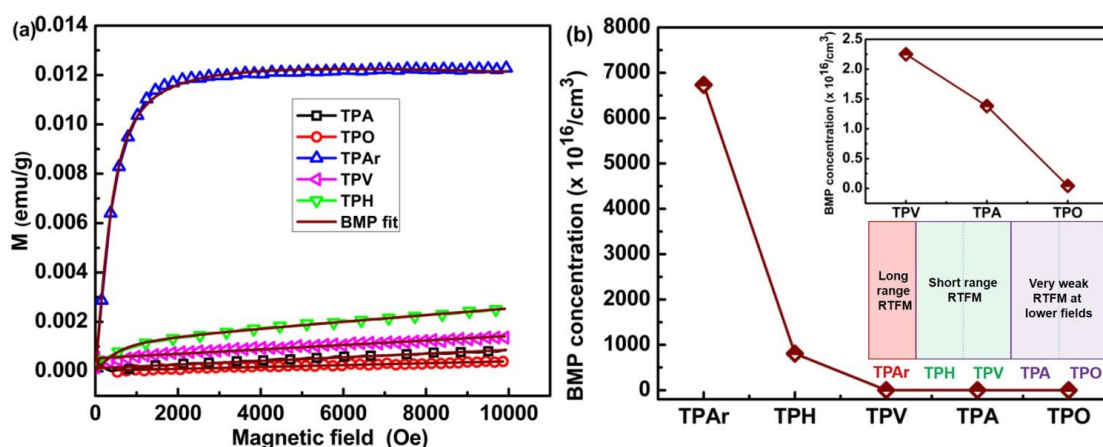
Fig.5.14. (a) BMP fit and (b) Number of BMP concentration at 300 K for all the TP samples. Inset shows the enlarged region.

Fig. 5. 15 (a) shows the variation of magnetic moment (at 2 Tesla) and band gap of all the samples. The magnetic moment shows a decreasing trend in magnetic moment in the sample order TPAr, TPH, TPV, TPA and TPO with a maximum value of 1.77×10^{-4} μ_B/F.U. for TPAr sample. Again, TPAr shows the least bandgap of 0.34 eV which is the least band gap ever reported in TiO_2. Fig. 5. 15 (b) shows the ratio of Ti^{3+} to Ti^{4+} in the case of TPAr, TPH and TPV which are in the order of 0.66, 0.63 and 0.48 respectively. This ratio is justified by the decreasing trend of FWHM values of $Ti2p_{3/2}$. Interestingly, in TPAr sample, both oxygen vacancies and Ti^{3+} ions are present producing large number of BMPs as shown in Fig. 5. 15 (c) and the overlapping among the BMPs is so strong to give enhanced magnetic moment and clear hysteresis loop at room temperature as shown in the figure. The FM in argon annealed sample is favoured due to the s–d exchange interaction between the $1s^1$ electron spin of trapped electron in the F^+ center and the $3d^1$ electron spin of Ti^{3+} ions within the orbital around oxygen vacancies. But if the electrons in oxygen vacancies form $1s^2$ state (F centre) then there is no possibility of FM but isolated BMP formation may have occurred which might be the case in TPA and TPO as in these samples. XPS indicate absence of Ti^{3+} ions and the formation of isolated BMPs are shown in Fig. 5. 15 (d). But in TPH and TPV samples although XPS shows the presence of Ti^{3+} ions and PL, Raman study indicate presence of oxygen vacancies but it seems that there is either very weak interaction between F^+ centre and Ti^{3+} ions because of F centre formation. Banerjee *et al.*[20] explained that oxygen vacancy clusters can induce FM while isolated oxygen vacancy or their clusters

can result in PM behavior at higher fields and very weak FM behavior at lower fields. So, it can be inferred here that oxygen vacancies in TPH and TPV samples have formed isolated clusters giving rise to PM behavior at higher fields. Thus the formation of BMPs, with the trapped electron in the F^+ center occupying an orbital overlapping with the unpaired electron ($3d^1$) of Ti^{3+} is proposed to explain the origin of FM observed in TPAr sample. It can be noticed that the samples exhibiting a high intensity of visible PL show a clear FM hysteresis loop. Shifting and broadening of E_g (1) Raman mode at 142 cm^{-1}, oxygen vacancy related strong visible PL emission, oxygen vacancy and Ti^{3+} concentrations observed from XPS spectra of Argon annealed samples confirm the fact that the FM in TPAr samples is due to oxygen vacancy mediated FM interaction.
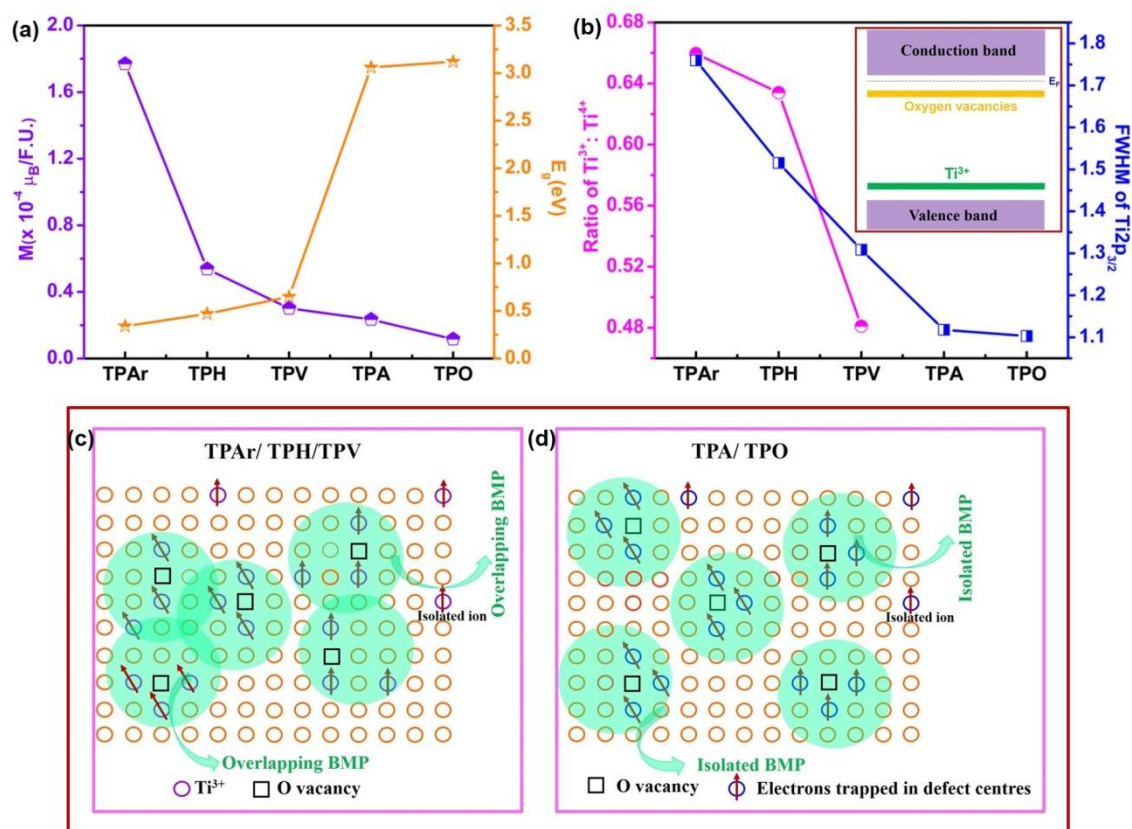

Fig.5.15. (a) Variation of magnetic moment and band gap (b) Ratio of Ti^{3+} to Ti^{4+} for TPAr, TPH and TPV with variation of FWHM for all the samples (c) Schematic showing the formation of overlapping BMPs in TPAr/TPH/TPV and (d) Isolated BMP formation in TPA and TPV samples

5.4. Summary

- Detailed structural, optical and magnetic study of TiO_2 nanocrystals prepared by sol-gel technique annealed in air, oxygen, argon, vacuum and hydrogen atmospheres for 8 h is done.

- Large absorption in Visible and IR region along with much reduced band gap, i.e. 0.34 eV, 0.47 eV and 0.65 eV is observed for argon, hydrogen and vacuum annealed samples respectively. These samples exhibit strong visible photoluminescence associated mostly with oxygen vacancies.

- XPS study reveals the formation of oxygen vacancies and mixed states of Ti (Ti^{3+}/Ti^{4+}) in argon, hydrogen and vacuum annealed samples.

- Magnetic measurements show a clear hysteresis loop with FM above room temperature in argon annealed sample while other samples show coexistence of paramagnetic and ferromagnetic behavior.

- RTFM observed in argon annealed TiO_2 nanocrystals is explained by taking into consideration of BMP which involves the overlapping of locally trapped electron orbital on the oxygen vacancy ($1s^1$) site with unpaired electron ($3d^1$) of Ti^{3+} ions.

- It is reported that without using any hazardous gases as well as without use of high temperature annealing conditions, TiO_2 nanocrystals with extended absorption in visible as well as in IR region with well-defined hysteresis loop at room temperature has been produced which can have wide applications in environmental remediation, photocatalysis and spintronics.

5.5. References

1. A. A. Dakhel, H. Hamad, A. Jaafar, Investigation to the structural, optical, and magnetic properties of synthesized Ni-doped anatase nanoparticles: essential role of treatment in hydrogen on long-range ferromagnetic order, *J. Supercond. Nov. Magn..*, 32 (2019) 253.
2. V. Swamy, D. Menzies, B. C. Muddle, A. Kuznetsov, L. S. Dubrovinsky, Q. Dai, V. Dmitriev, Nonlinear size dependence of anatase TiO_2 lattice parameters, *Appl. Phys. Lett.* 88 (2006) 243103.
3. G. Li, L. Li, J. Boerio-Goates, B. F. Woodfield, High purity anatase TiO_2 nanocrystals: near room-temperature synthesis, grain growth kinetics, and surface hydration chemistry *J. Am. Chem. Soc.* 127 (2005) 8659.

4. J.C. Parker, R.W. Siegel, Calibration of the Raman spectrum to the oxygen stoichiometry of nanophase TiO₂, *Appl. Phys. Lett.* 57 (1990) 943.
5. M. K. Nowotny, L. R. Sheppard, T. Bak and J. Nowotny, Defect chemistry of titanium dioxide. Application of defect engineering in processing of TiO₂-based photocatalysts, *J. Phys. Chem. C*, 112 (2008) 5275.
6. Xiaoyang Pan, Min-Quan Yang, Xianzhi Fu, Nan Zhang, Yi-Jun Xu, Defective TiO₂ with oxygen vacancies: synthesis, properties and photocatalytic applications, *Nanoscale*, 5 (2013) 3601.
7. A. Naldoni, M. Allieta, S. Santangelo, M. Marelli, F. Fabbri, S. Cappelli, C. L. Bianchi, R. Psaro, V. D. Santo, Effect of nature and location of defects on band gap narrowing in black TiO₂ nanoparticles. *J. Am. Chem. Soc.*, 134 (2012) 7600.
8. X. Chen, L. Liu, P. Y. Yu, S. S. Mao, Increasing solar absorption for photocatalysis with black hydrogenated titanium dioxide nanocrystals, *Science*, 331(2011) 746.
9. G. Wang, H. Wang, Y. Ling, Y. Tang, X. Yang, R. C. Fitzmorris, C. Wang, J.Z. Zhang, Y. Li, Hydrogen-treated TiO₂ nanowire arrays for photoelectrochemical water splitting, *Nano Lett.* 11 (2011) 3026.
10. B. Santara, P. K. Giri, K. Imakita and M. Fujii, Evidence of oxygen vacancy induced room temperature ferromagnetism in solvothermally synthesized undoped TiO₂ nanoribbons, *Nanoscale*, 5 (2013) 5476.
11. S. K. S. Patel, S. Kurian, N. S. Gajbhiye, Phase dependent room-temperature ferromagnetism of Fe-doped TiO₂ nanorods, *AIP Adv.,* 2 (2012) 012107.
12. H.Y. Lee, S.J. Clark, J. Robertson, Calculation of point defects in rutile TiO2 by the screened-exchange hybrid functional, *Phys. Rev. B* 86 (2012) 075209.
13. R. Sanjinés, H. Tang, H. Berger, F. Gozzo, G. Margaritondo, F. Lévy, Electronic structure of anatase TiO₂ oxide. *J. Appl. Phys.* **75,** 2945–2951 (1994).
14. J. D. Bryan, S. M. Heald, S. A. Chambers, D. R. Gamelin. Strong room temperature ferromagnetism in Co²⁺ doped TiO₂ made from colloidal nanocrystals, *J. Am. Chem. Soc.*, 245 (2004) 1772.
15. A. Sundaresan, R. Bhargavi, N. Rangarajan, U. Siddesh, C. N. R. Rao, Ferromagnetism as a universal feature of nanoparticles of the otherwise nonmagnetic oxides. *Phys. Rev. B*, 74 (2006) 161306(R).
16. F. Zheng, Y. Liu, Z. Liu, Y.-Q. Dai, P. Fang, S.-J. Wang, Study on defect properties of nanocrystalline TiO₂ during phase transition by positron annihilation lifetime. *J. Cryst. Growth*, 353 (2012) 55.
17. J. M. D. Coey, M. Venkatesan, C. B. Fitzgerald, Donor impurity band exchange in dilute ferromagnetic oxides. *Nat. Mater.* 4 (2005) 173.
18. M. Venkatesan, C. B. Fitzgerald, J.M.D. Coey, Unexpected magnetism in a dielectric oxide, *Nature*, 430 (2004) 630.
19. B. Choudhury, A. Choudhury, Room temperature ferromagnetism in defective TiO₂ nanoparticles: Role of surface and grain boundary oxygen vacancies, J. Appl. Phys. 114 (2013) 203906.
20. S. Banerjee, M. Mandal, N. Gayathri, M. Sardar, Enhancement of ferromagnetism upon thermal annealing in pure ZnO, *Appl. Phys. Lett.* 91 (2007) 182501.

Chapter 6

Summary and scope for future work

This chapter provides a brief summary of the observations made during the investigation on functional semiconductors for thermoelectrics and spintronics applications. The significant results of the investigation are also outlined in this chapter followed by scope for the future work.

6.1. Summary

The thesis is a detailed investigation on the development of nanocrystals of narrow band-gap Bi_2Te_3 based materials and wide band-gap TiO_2 based materials as functional semiconductors for TEs and spintronics applications. The primary interest for choosing these materials for the present investigation is to utilize the possibilities lying with charge of an electron pointing towards the TE applications and utilization of spin of an electron pointing towards the spintronics industry. From the existing literature on both the class of materials, it was understood that nanostructuring could provide improvement in both TE properties (due to phonon scattering) and optical/magnetic properties (due to defect induced mechanism). In this regard, efforts were made to develop Bi and Sb based chalcogenide materials with significant reduction in κ and improvement in the room temperature **ZT** value. Again, efforts for achieving optical band gap narrowing and RTFM in transition metal ion doped TiO_2 nanocrystals were carried out. Defect induced TiO_2 nanocrystals under different annealing atmospheres were also made a subject of study and long range RTFM with a significant narrowing of band gap is also investigated.

6.1.1. Bi and Sb based chalcogenide nanostructures

➢ Bismuth telluride nanostructures were successfully synthesised using a low-temperature reflux method with deionized water as the reaction medium. Both structural and morphological changes were obtained by varying the reaction time and EDTA concentration where reaction time of 24 h and EDTA concentration of 100 mmol shows the hexagonal stacking and exhibits the best TE properties among the synthesised samples.

➢ It is witnessed that the EDTA aids the formation of desired Bi_2Te_3 phase and behaves as both capping agent and soft template for lowering the surface energy to facilitate the formation of intercalated rod and sheet-like structures.

➢ A detailed reaction mechanism for Bi_2Te_3, Sb_2Te_3, SnTe and Sb-doped Bi_2Te_3 is investigated and understood that the aqueous based reflux reaction is a tedious job

for the synthesis of SnTe whereas partial formation of Sb_2Te_3 could be possible. However, hot pressed Sb-doped Bi_2Te_3 samples prepared by reflux method crystallizes in to mixed phases and exhibit an n- to p-type transition with improvement in thermopower value.

6.1.2. Transition metal elements doped TiO$_2$ nanocrystals

➢ Undoped and TM-doped TiO_2 nanocrystals (TM=Cu, Zn, Fe, Co, Ni, Cr and Mn) derived by sol-gel techniques are crystallized into a tetragonal anatase structure with space group $I4_1/amd$. Detailed structural studies reveal that successful incorporation of TM ions (even upto 12 at. wt. %) into Ti site in TiO_2 lattice.

➢ Optical studies reveal that the band gap of TiO_2 (3.2 eV) significantly narrows down with the substitution of all TM elements (except Zn). PL and XPS studies reveal the formation of BMPs in all the studied TiO_2 nanocrystals.

➢ A very weak RTFM is observed for undoped and 3% Cu, Fe and Co doped TiO_2 nanocrystals. But, a perfect PM behavior is witnessed for the higher dopant concentrations of Fe and Co, and all the Cr, Mn and Ni doped samples exhibited a PM behavior while 3% Zn doped sample shows a diamagnetic tail.

➢ Nature of magnetism in undoped and doped TiO_2 nanocrystals is decided by either intrinsic contributions i.e, the nature of BMPs (isolated or overlapped) or extrinsic contributions (i.e the magnetic contributions of dopant ions) or both.

➢ A significant reduction in band gap is observed in all the TiO_2 naocrystals (except Zn-doped) associated with its interesting magnetic properties make them a potential for spintronics applications and magneto optic devices.

6.1.3. Defect modulation by varying annealing atmosphere on TiO$_2$ nanocrystals

➢ TiO_2 nanocrystals are prepared by sol-gel technique and annealed for 8 h under different atmospheres, i.e, in air, oxygen, argon, vacuum and hydrogen. All the

samples are crystallized into a tetragonal anatase structure with space group $I4_1/amd$.

➢ Large absorption in Visible and IR region along with much reduced bandgap is observed in argon, hydrogen and vacuum annealed samples. The bandgap observed in theses samples are least ever reported so far in TiO_2 bases nanocrystals. These samples exhibit strong visible photoluminescence associated mostly with oxygen vacancies.

➢ XPS and PL studies reveal the formation of overlapped BMPs in Argon, hydrogen and vacuum annealed TiO_2 nanocrystals.

➢ RTFM is witnessed in argon annealed sample while other samples show coexistence of paramagnetic and ferromagnetic behavior.

➢ This study revealed that the RTFM with band gap of 0.34 eV is achieved in undoped TiO_2 nanocrystals which can have wide applications in environmental remediation, photocatalysis and spintronics.

6.2. Scope for future work

• Using the developed n and p-type TE materials, a device prototype can be fabricated.

• Detailed neutron diffraction and Mossbauer spectroscopy would give an insight in to the magnetic state of the TiO_2 DMS materials.

• For future applications, one could develop chalcogenide and TiO_2 DMS thin films which can actively control and manipulate charge, spin and heat flows in materials on the nanometer scale.

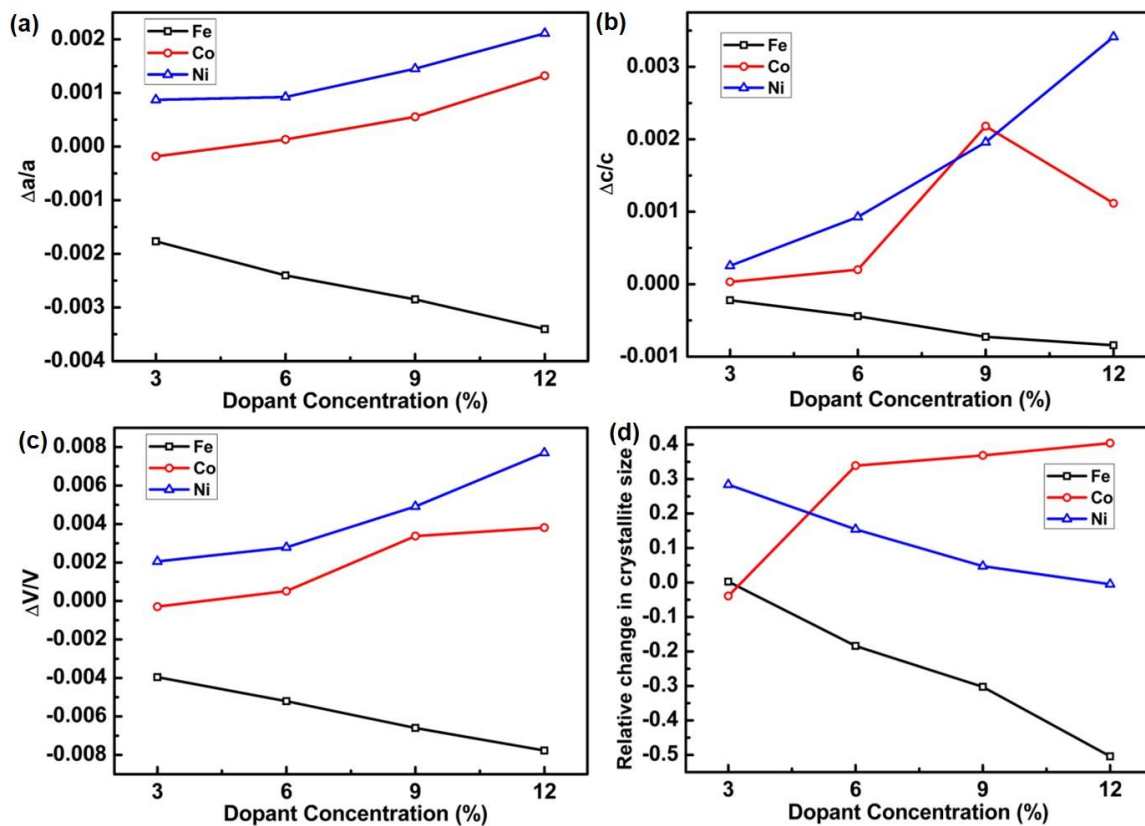# Relative change in lattice parameters and crystallite size in Fe, Co, Ni-doped TiO₂ nanocrystals

Fig. A1. (a) Relative change in lattice parameter *a,* (b) Relative change in lattice parameter *c,* (c) Relative change in cell volume *V,* (a) Relative change in crystallite size.

Temperature variation of magnetization and Curie-Weiss fit of undoped, 3% and 12% Fe doped TiO₂ nanocrystals
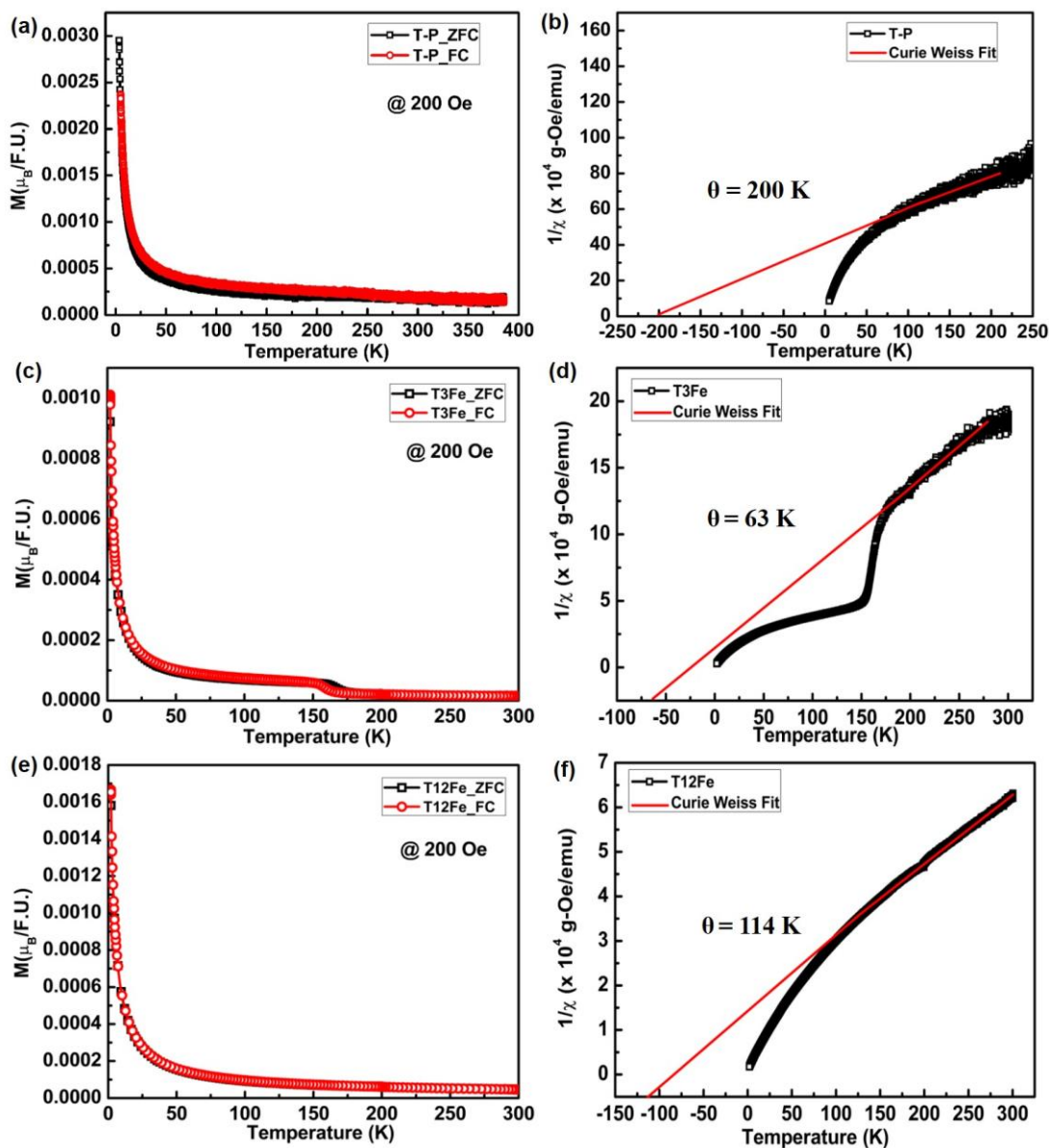

Fig. A2. (a) MT curves and (b) Curie Weiss Fit of T-P, (c) MT curves and (d) Curie Weiss Fit of T3Fe (e) MT curves and (f) Curie Weiss Fit of T12Fe.

Curie Weiss Fit corresponding to TiO$_2$ samples annealed in Argon and Hydrogen atmosphere
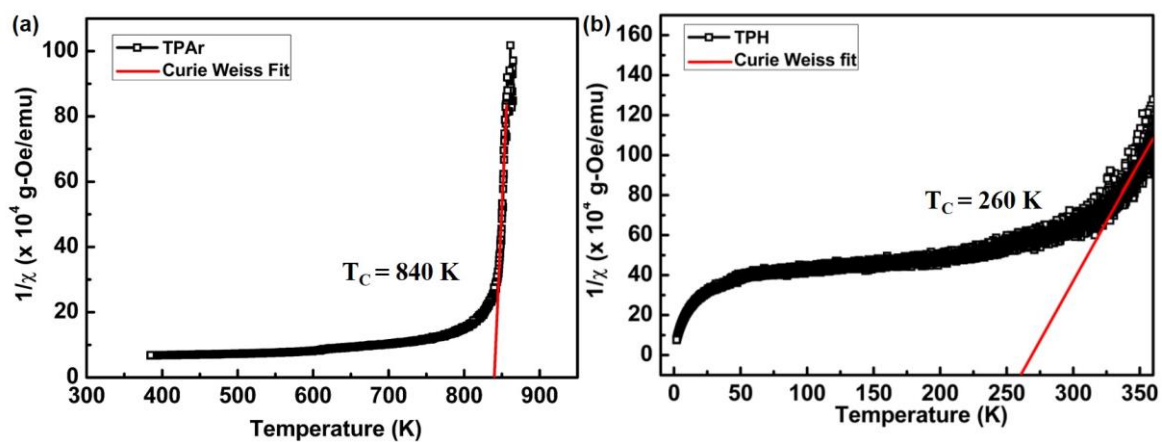

Fig. B1. Curie Weiss Fit of (a) TPAr, (b) TPH

List of publications in SCI journals

Publications related to thesis work:

1) **V. R. Akshay**, B. Arun, Guruprasad Mandal, Geeta R Mutta, Anupama chanda and M.Vasundhara, "*Observation of Optical Band-gap Narrowing and Enhanced Magnetization in Co-doped Sol-gel derived Anatase TiO₂ Nanocrystals*" **J. Phys. Chem. C,** J. Phys. Chem. C. 122 (2018) 26592−26604.

2) **V. R. Akshay**, B. Arun, B, M. V. Suneesh, M. Vasundhara, "*Surfactant Induced Structural Phase Transitions and Enhanced Room Temperature Thermoelectric Performance in n-Type Bi₂Te₃ Nanostructures Synthesized via Chemical Route*" **ACS Appl. Nano Mater.** 1 (2018) 3236−3250.

3) **V. R. Akshay**, M. V. Suneesh and M. Vasundhara, "*Tailoring Thermoelectric Properties through Structure and Morphology in Chemically Synthesized n-Type Bismuth Telluride Nanostructures*", **Inorg. Chem.**, 56(11) (2017) 6264-6274.

4) **V. R. Akshay**, B. Arun, Shubhra Dash, Ajit K. Patra, Guruprasad Mandal, Geeta R. Mutta, Anupama Chanda and M.Vasundhara, "*Defect Mediated Mechanism in Undoped, Cu and Zn-Doped TiO2 Nanocrystals for Tailoring the Band gap and Magnetic Properties*", **RSC Adv.** 8 (2018), 41994.

5) **V. R. Akshay**, B. Arun, Guruprasad Mandal and M. Vasundhara, "*Structural, optical and magnetic behavior of sol–gel derived Ni-doped dilute magnetic semiconductor TiO₂ nanocrystals for advanced functional applications*", **Phys.Chem.Chem.Phys.,** 21 (2019), 2519.

6) **V. R. Akshay**, B. Arun, Guruprasad Mandal, Anupama Chanda and M. Vasundhara, "*Significant Reduction in the Optical Band-gap and Defect Assisted Magnetic Response in Fe-Doped Anatase TiO₂ Nanocrystals for Spintronics and Magneto-Optics Applications*", **New J. Chem.,** 43 (2019), 6048 – 6062.

7) **V. R. Akshay**, B. Arun, Guruprasad Mandal and M. Vasundhara, "*Visible Range Optical Absorption, Urbach Energy Estimation and Paramagnetic Response in Cr-Doped TiO₂ Nanocrystals by Sol-Gel Method as Dilute Magnetic Semiconductors*", **Phys.Chem.Chem.Phys.,** 21 (2019), 12991.

8) **V. R. Akshay**, B. Arun, Guruprasad Mandal and M. Vasundhara, "*Impact of Mn-Dopant Concentration in Observing Narrowing of Band-Gap, Urbach tail and Paramagnetism in Anatase TiO₂ Nanocrystals*", **New J. Chem.,** 43 (2019), 14786.

9) **V. R. Akshay**, B. Arun, Guruprasad Mandal, Anupama Chanda and M. Vasundhara, *"Defect Modulation by Varying Annealing Atmosphere on TiO_2 Nanocrystals to Tailor the NIR Range Optical Absorption, Band-gap Narrowing and Ferromagnetic Response"*, *J. Mater. Chem.C,* 2019 (Under review)

10) **V. R. Akshay**, B. Arun and M. Vasundhara, *"Investigation on Synthesis Mechanisms of Nanostructured (Bi,Sb,Sn) -Te Thermoelectric Materials via Aqueous based Reflux Method"*, *RSC Adv.,* 2019 (Under review)

Publications out of the thesis work:

11) B. Arun, **V. R. Akshay**, K. D. Chandrasekhar, Geeta R. Mutta, M. Vasundhara, *"Comparison of structural, magnetic and electrical transport behavior in bulk and nanocrystalline Nd-lacunar $Nd_{0.67}Sr_{0.33}MnO_3$ manganites"*, *J. Magn. Magn. Mater.* 472 (2019) 74–85.

12) B. Arun, M.V.Suneesh, B Sudakshina, **V. R. Akshay**, K. D. Chandrasekhar, M.Vasundhara, *"Effect of Mn-site substitution on magnetic ordering and critical behavior in $Nd_{0.67}Sr_{0.33}MnO_3$ manganite"*, *J. Physics and Chemistry of Solids* 123 (2018) 327–335.

13) B. Arun, **V. R. Akshay**, M.Vasundhara, *"Observation of enhanced magnetocaloric properties with A-site deficiency in $La_{0.67}Sr_{0.33}MnO_3$ manganite"* *Dalton Trans.*, 47 (2018) 15512.

14) B. Arun, M. Athira, **V.R. Akshay**, B. Sudakshina, Geeta. R. Mutta, M. Vasundhara, *"Investigation on the structural, magnetic and magnetocaloric properties of nanocrystalline Pr-deficient $Pr_{1-x}Sr_xMnO_{3-\square}$ manganites"*,*J. Magn. Magn. Mater.* 448 (2018) 322–331.

15) P. Shukla, S. Tiwari, S. R. Joshi; **V. R. Akshay**, M. Vasundhara, S. Varma, J. Singh and Anupama Chanda, *"Structural, Morphological and Optical Study of Cobalt Doped ZnO Thin Films"*, *Physica B: Condensed Matter* 550 (2018) 303–310

16) B. Arun, B. Sudakshina, **V. R. Akshay**, K. D. Chandrasekhar, H. D. Yang, M. Vasundhara, *"Structural and magnetic behaveor of (Ni, Cu) substituted $Nd_{0.67}Sr_{0.33}MnO_3$ perovskite Compounds"*, *AIP Conf. Proc.* 1953 (2018) 120016/1–4.

17) Annrose Sunny, **V. R. Akshay** and M. Vasundhara, *"Effect of Annealing Temperature on the Size and Magneticproperties of $CoFe_2O_4$ Nanoparticle"*, *AIP Conf. Proc.*, 1953 (2018) 030162/1–4.

18) B. Arun, <u>**V. R. Akshay**</u>, Geeta R. Mutta, Ch. Venkatesh, M. Vasundhara, "*Mixed rare earth oxides derived from monazite sand as an inexpensive precursor material for room temperature magnetic refrigeration applications*", **Mater. Research. Bullt.** 94 (2017) 537–543.

19) B. Arun, **V. R. Akshay**, D. Chandrasekhar Kakarla, M. Vasundhara, "*Impact of Nd and Sr-site deficiencies on the structural, magnetic and electrical transport properties in Nd0.67-xSr0.33MnO3-δ (x=0.09, 0.17, 0.25, 0.33) and Nd0.67Sr0.33-yMnO3-δ (y=0.09, 0.17) manganites*", **J. Mag. Mag. Mater. 489** (2019) 165418.

20) B. Arun, **V. R. Akshay**, M. Vasundhara, "*Observation of enhanced magnetic entropy change near room temperature in Sr-site deficient La$_{0.67}$Sr$_{0.33}$MnO$_3$ manganite*", **RSC. Adv. 9** (2019) 23598.

21) M. Mukesh, K. K. Thejas, **V. R. Akshay**, B. Arun, M. Vasundhara, "*Effect of Annealing conditions on Particle size, Magnetic and Optical Properties of Gd2O3 Nanoparticles*"**AIP Conf. Proc.**, 2162 (2019) 020091/1–6.

Contributory Talks:

1) **V. R. Akshay** and M. Vasundhara "Development of n-Type Bismuth Telluride Alloy Nanostructures for Room Temperature Thermoelectric Applications", presented in **Best Paper Award Category** of 29th session of Kerala Science Congress (29th KSC) conducted from 28th to 30th January 2017 at Mar Thoma College, Thiruvalla, Pathanamthitta, Kerala.

2) **V. R. Akshay** and M. Vasundhara, "Development of BiTe nanostructures for thermoelectric applications near room temperature", won the Best Presentation Award in the Research Scholars Symposium organised by IIM, Trivandrum chapter, held on April 6, 2018 at CSIR-NIIST.

Conference Presentations:

1) **V. R. Akshay** and M. Vasundhara, "The quest for dilute ferromagnetism in TiO2 wide band gap semiconductors for spintronic dvices", presented at the Research Scholars Symposium organised by IIM, Trivandrum chapter, held on April 3, 2019 at CSIR-NIIST.

2) **V. R. Akshay** and M. Vasundhara, "Structural Phase Diagram and Reduction in Thermal Conductivity of Bismuth Telluride Nanostructures Synthesised via Chemical Route", presented a paper in International Conference on Condensed Matter and Applied Physics (ICC-2017) held during November 24-25, 2017.

3) B. Arun, B. Sudakshina, **V. R. Akshay**, K. D. Chandrasekhar, H. D. Yang, M. Vasundhara, "Structural and magnetic behavior of (Ni, Cu) substituted $Nd_{0.67}Sr_{0.33}MnO_3$ perovskite Compounds", 2nd International Conference on Condensed Matter & Applied Physics (ICC-2017), held at Govt. Engineering College, Bikaner, Rajasthan, India, during Nov. 24-25, 2017.

4) **V. R. Akshay** and M. Vasundhara, "Response of high temperature thermoelectric efficiency in A-site deficient $SrTiO_3$", presented a paper at the National Conference on critical and strategic materials for advanced Technologies (CSMAT-2017) during March 9-11, 2017.

5) B. Arun, M. Athira, **V. R. Akshay**, B. Sudakshina, Geeta. R. Mutta, M. Vasundhara, "Investigation on the structural, magnetic and magnetocaloric properties of nanocrystalline Pr-deficient $Pr_{1-x}Sr_xMnO_{3-\delta}$ manganites", International Conference on Magnetic Materials and Applications (ICMAGMA-2017) in association with Magnetics Society of India, held at Defence Metallurgical Research Laboratory (DMRL), Hydrabad, India, during February 01-03, 2017

6) **V. R. Akshay** and M. Vasundhara, "Thermoelectric Properties of Chalcogenide Based Materials for Room Temperature Applications", presented at the National Conference on Materials Science and Technology (IUMRS-ICYRAM 2016) held at J. N. Tata Auditorium, IISc, Bangalore-560012 during December 11-15.

7) **V. R. Akshay** and M. Vasundhara, "Structural and Thermoelectric Properties of Bi-Te Based Materials Synthesised by Chemical Route", presented at the National Conference on Materials Science and Technology (NCMST 2016) organized during July 12-14, 2016 at the IIST (Valiamala) campus.

8) **V. R. Akshay** and M. Vasundhara, "Rare-earth doped $SrTiO_3$ and its Thermoelctric applications", at International Conference on Science, technology and Applications of rare earths (ICSTAR-2015) at CSIR-NIIST during April 23-25, 2015.

9) **V. R. Akshay** and M. Vasundhara, "Structural and thermoelectric properties of Fe_2VAl based Heuslar alloys", presented a paper as poster at International Conference on Magnetic Materials and Applications (MAGMA-2013) at IIT Guwahati during December 5-7, 2013.